



**University of Brighton**



University of Sussex

**The generation of cartilage  
extracellular matrices using  
bioprinting**

**Ella Hodder (EH)**

**Submitted for the degree of Doctor of  
Philosophy, July 2019**

**The School of Computing,  
Engineering and Mathematics,  
University of Brighton**

## Table of Contents

Abstract.....	X
Acknowledgements.....	xi
Declaration.....	xi
List of Figures.....	xii
List of Tables.....	xxi
List of Abbreviations.....	xxiv
Chapter 1 Introduction.....	1
<b>1.1 Project aim.....</b>	<b>5</b>
<b>1.2 Contribution to knowledge, significance and innovation.....</b>	<b>5</b>
<b>1.3 Research questions and rationale.....</b>	<b>7</b>
1.3.1 Question 1: Using bioprinting how can a clinically feasible fabrication approach be developed that would allow for the generation of scaffolds which support chondrocyte survival?.....	7
1.3.2 Question 2: What methods can be used to assist cartilage tissue generation with an extracellular matrix similar to IVDs?.....	8
1.3.3 Question 3: Can medically available MRI be used to effectively evaluate the macromolecular composition of developing cartilage tissues within bioprinted scaffolds <i>in vitro</i> ?.....	9
Chapter 2 Literature review.....	10
<b>2.1 Intervertebral disc tissue.....</b>	<b>10</b>
2.1.1 Physiology.....	10
2.1.2 Mechanical properties.....	12
<b>2.2 Disc herniation and lower back pain.....</b>	<b>14</b>
2.2.1 Current clinical interventions.....	16
2.2.1.1 Surgical solutions.....	16
2.2.1.2 Artificial disc replacements.....	18
<b>2.3 Tissue-engineered scaffolds in regenerative medicine.....</b>	<b>20</b>
<b>2.4 Tissue engineering for intervertebral disc restoration.....</b>	<b>20</b>
2.4.1 Clinical feasibility.....	21
2.4.2 Mechanobiology.....	22
2.4.2.1 Mechanical properties of tissue-engineered scaffolds.....	24
2.4.2.2 Monitoring tissue development.....	26
2.4.3 Magnetic Resonance Imaging.....	27
<b>2.5 Current-tissue-engineered intervertebral disc approaches.....</b>	<b>32</b>

2.5.1 Conventional fabrication techniques for intervertebral disc scaffolds.....	32
2.5.1.1 Additive manufacturing.....	36
2.5.1.2 Materials for bioprinting.....	40
2.5.1.3 Hydrogels for cell-laden bioprinting.....	41
2.5.1.4 Alginate hydrogels.....	43
2.5.2 Additive manufacturing approaches for intervertebral disc scaffolds .....	45
<b>2.6 Bioprinting of articular cartilage for the guidance of intervertebral disc scaffold fabrication .....</b>	<b>50</b>
<b>2.7 Summary .....</b>	<b>54</b>
Chapter 3 Experimental screening of alginate and collagen based biomaterials for the fabrication of scaffolds using bioprinting .....	55
<b>3.1 Introduction .....</b>	<b>55</b>
<b>3.2 Materials and Methods .....</b>	<b>56</b>
3.2.1 List of Materials.....	56
3.2.2 Material Selection .....	57
3.2.3 Material preparation for bioprinting.....	58
3.2.3.1 Alginate methyl cellulose .....	58
3.2.3.2 Alginate-gelatine (ADA-Gel) .....	58
3.2.3.3 Collagen .....	59
3.2.4 Material characterisation.....	62
3.2.4.1 Fourier transform infrared spectrometer analysis .....	62
3.2.4.2 Shear Rheometer testing .....	62
3.2.5 Plotting of materials.....	64
3.2.5.1 Multi-head printing.....	66
3.2.6 Scaffold characterisation.....	68
3.2.6.1 Cryogenic-scanning electron microscopy of alginate methyl cellulose scaffolds .....	68
3.2.6.2 Stereo light microscopy of collagen methyl cellulose scaffolds .....	69
3.2.6.3 Compression testing.....	70
3.2.7 Statistical analysis .....	72
<b>3.3 Results.....</b>	<b>73</b>
3.3.1 Material Characterisation with Fourier transform infrared spectroscopy.....	73
3.3.2 Material properties .....	78
3.3.3 Fabrication of scaffolds .....	84
3.3.4 Morphological characterisation of scaffolds .....	86
3.3.4.1 Cryogenic-scanning electron microscopy of alginate methyl cellulose scaffolds .....	87

3.3.4.2 Optical microscopy of collagen methyl cellulose scaffolds.....	89
3.3.5 Scaffold mechanical properties .....	90
3.3.5.1 Shear testing of cross-linked alginate methyl cellulose scaffolds.....	90
3.3.5.2 Compression loading of alginate methyl cellulose scaffolds .....	91
3.3.5.3 Successive compression testing of collagen methylcellulose scaffolds .....	92
3.3.6 Biomaterial comparison .....	94
<b>3.4 Discussion .....</b>	<b>95</b>
<b>3.5 Summary .....</b>	<b>101</b>
Chapter 4 Investigating the effect of sterilisation methods on the physical properties and cytocompatibility of methyl cellulose used in combination with alginate for bioprinting chondrocytes.....	
	102
<b>4.1 Introduction .....</b>	<b>102</b>
<b>4.2 Materials and methods .....</b>	<b>106</b>
4.2.1 List of materials.....	106
4.2.2 Tissue processing and cell culture .....	106
4.2.3 Sterilisation .....	107
4.2.4 Plotting material preparation.....	108
4.2.5 Bioprinting of alginate methyl cellulose constructs .....	108
4.2.6 Methyl cellulose characterisation .....	109
4.2.6.1 Fourier Transform Infrared Spectroscopy .....	109
4.2.6.2 Gel permeation chromatography.....	109
4.2.7 Alginate methyl cellulose paste characterisation.....	110
4.2.7.1 Viscosity .....	110
4.2.8 Scaffold evaluation – structure and composition.....	110
4.2.8.1 Release of methyl cellulose.....	110
4.2.8.2 Scanning electron microscopy.....	111
4.2.8.3 Calcium release .....	111
4.2.8.4 Compression testing.....	112
4.2.9 Alginate methyl cellulose scaffold – cell compatibility.....	112
4.2.9.1 Cell survival live/dead assay .....	112
4.2.9.2 DNA quantification.....	114
4.2.9.3 Glycosaminoglycan histology .....	115
4.2.10 Statistical analysis .....	119
<b>4.3 Results.....</b>	<b>119</b>
4.3.1 Methyl cellulose characterisation .....	119

4.3.2 Alginate methyl cellulose paste characterisation .....	122
4.3.3 Alginate methyl cellulose scaffold evaluation .....	123
4.3.4 Cell compatibility of alginate methyl cellulose scaffolds – towards cartilage tissue engineering .....	129
<b>4.4 Discussion .....</b>	<b>133</b>
4.4.1 Effects of methyl cellulose sterilisation on alginate methyl cellulose properties for bioprinting .....	133
4.4.2 Effects of methyl cellulose sterilisation on alginate methyl cellulose scaffold characteristics .....	135
4.4.3 Sterilisation effects of methyl cellulose on cell survival and matrix production in alginate methyl cellulose scaffolds .....	137
<b>4.5 Conclusion .....</b>	<b>139</b>
Chapter 5 The effect of hydrostatic pressure application on proteoglycan production in mammalian articular cartilage <i>in vitro</i> : a meta-analysis review .....	
	141
<b>5.1 Introduction .....</b>	<b>141</b>
<b>5.2 Methodology .....</b>	<b>143</b>
5.2.1 Study Eligibility Criteria .....	143
5.2.2 Data Sources .....	143
5.2.3 Study Selection.....	144
5.2.4 Data Extraction.....	145
5.2.5 Missing Data Extraction .....	145
5.2.6 Statistical Analysis .....	146
<b>5.3 Results .....</b>	<b>151</b>
5.3.1 Hydrostatic pressure interventions.....	151
5.3.1.1 Proteoglycan gene expression .....	151
5.3.1.2 Glycosaminoglycan content .....	151
5.3.2 Static and dynamic hydrostatic pressure .....	152
5.3.2.1 Proteoglycan gene expression .....	152
5.3.2.2 Glycosaminoglycan content .....	153
5.3.3 Pressure magnitude .....	154
5.3.3.1 Proteoglycan gene expression .....	154
5.3.3.2 Glycosaminoglycan content .....	155
5.3.4 Study Duration .....	157
5.3.4.1 Gene expression.....	157
5.3.4.2 Glycosaminoglycan content .....	159
<b>5.4 Discussion - summary of main results.....</b>	<b>160</b>

5.4.1 Methodology criteria .....	160
5.4.2 The overall outcome of hydrostatic pressure versus control conditions.....	161
5.4.3 The effect of static versus dynamic hydrostatic pressure application.....	162
5.4.4 The influence of pressure magnitude.....	164
5.4.4.1 Gene expression analysis .....	164
5.4.4.2 Glycosaminoglycan content .....	166
5.4.5 The impact of experiment duration .....	167
5.4.6 The influence of loading time.....	168
<b>5.5 Conclusion.....</b>	<b>170</b>
Chapter 6 Hydrostatic pressure stimulated cell culture of bioprinted alginate methyl cellulose scaffolds embedded with BPCs or hIVD cells for the purposes of cartilage tissue engineering .....	
.....	172
<b>6.1 Introduction .....</b>	<b>172</b>
<b>6.2 Methods.....</b>	<b>174</b>
6.2.1 Isolation of human intervertebral disc cells .....	176
6.2.2 Bioprinting material preparation .....	177
6.2.3 Bioprinting of alginate methyl cellulose constructs .....	177
6.2.4 Hydrostatic pressure application .....	177
6.2.4.1 Sample preparation.....	177
6.2.4.2 The hydrostatic pressure vessel .....	178
6.2.4.3 Hydrostatic pressure application protocol .....	179
6.2.5 Cell survival .....	181
6.2.5.1 Cell survival live/dead .....	181
6.2.5.2 Cell survival using MTT dye compound .....	181
6.2.6 Gene expression analysis .....	182
6.2.6.1 RNA ScreenTape analysis .....	182
6.2.7 Glycosaminoglycan content .....	185
6.2.7.1 DMMB assay .....	185
6.2.7.2 Histochemical analysis .....	186
6.2.8 Mechanical properties .....	187
6.2.9 Statistical analysis .....	189
<b>6.3 Results.....</b>	<b>189</b>
6.3.1 Screen-tape analysis.....	189
Experiment 1- Hydrostatic pressure duration experiments using bovine primary chondrocytes .....	192
.....	192
6.3.2.1 Cell survival .....	192

6.3.2.2 Proteoglycan production.....	194
Experiment 2 - 21 day hydrostatic pressure experiment with bovine primary chondrocytes...	195
6.3.2.2 Cell survival .....	195
6.3.2.3 Proteoglycan production.....	198
6.3.3.3 Mechanical properties .....	200
6.3.4 Experiment 3- 21 day hydrostatic pressure experiment with human intervertebral disc cells	201
6.3.4.1 Cell survival .....	201
6.3.4.2 Proteoglycan production.....	204
<b>6.4 Discussion .....</b>	<b>206</b>
6.4.1 Experiment 1 – Hydrostatic pressure duration experiments using bovine primary chondrocytes .....	207
6.4.2 Experiment 2 -21 day hydrostatic pressure experiment with bovine primary chondrocytes .....	210
6.4.3 Experiment 3- 21 day hydrostatic pressure experiment with human intervertebral disc cells .....	211
<b>6.5 Conclusion.....</b>	<b>212</b>
Chapter 7 Characterisation of macromolecular composition in healthy intervertebral discs and BPC-laden alginate methyl cellulose scaffolds using quantitative magnetic resonance imaging and spectroscopy .....	215
<b>7.1 Introduction .....</b>	<b>215</b>
<b>7.2 Materials and Methods .....</b>	<b>216</b>
7.2.1 <i>In vivo</i> quantitative MRI disc study – human volunteers.....	217
7.2.1.1 Transverse relaxation time $T_2$ and $T_2^*$ .....	218
7.2.1.2 Quantitative spectroscopy .....	220
7.2.2 Experiment 2 - <i>in vitro</i> quantitative MRI study of bioprinted scaffolds.....	222
7.2.2.1 Cell preparation .....	222
7.2.2.2 Scaffold fabrication .....	223
7.2.2.3 Hydrostatic pressure application .....	224
7.2.2.4 Quantitative MRI of bioprinted alginate methyl cellulose structures .....	225
7.2.3 Statistical analysis .....	228
<b>7.3 Results.....</b>	<b>228</b>
7.3.1 Experiment 1 - <i>in vivo</i> quantitative MRI of human intervertebral discs .....	228
7.3.1.1 Transverse relaxation constant $T_2$ and $T_2^*$ .....	228
7.3.1.2 Quantitative Spectroscopy .....	230
7.3.2 Experiment 2 – <i>in vitro</i> quantitative MRI of bioprinted scaffolds.....	231

7.3.2.1 Transverse relaxation constant $T_2$ .....	231
7.3.2.2 Quantitative spectroscopy .....	233
<b>7.4 Discussion .....</b>	<b>235</b>
7.4.1 quantitative MRI for the investigation of human intervertebral discs <i>in vivo</i> .....	235
7.4.2 Quantitative MRI for the investigation of bioprinted chondrocyte-laden scaffolds .....	237
7.4.2.1 Bespoke sample holders .....	240
7.4.2.2 Sample submersion in Fomblin .....	241
7.4.2.3 High field strength MRI .....	241
7.4.3 Comparison of quantitative MRI experiments performed <i>in vivo</i> and <i>in vitro</i> .....	241
7.4.4 Overall confidence in the quantitative MRI measurements obtained .....	242
<b>7.5 Conclusion .....</b>	<b>243</b>
Chapter 8 Discussion .....	245
8.1 Bioink selection .....	245
8.2 Bioprinted alginate methyl cellulose scaffolds for chondrocyte culture .....	248
8.3 Hydrostatic pressure and supplement based stimulated culture of alginate methyl cellulose chondrocyte-laden scaffolds .....	250
8.4 Translation from bovine primary cells to human intervertebral disc cells in alginate methylcellulose with hydrostatic pressure stimulated culture .....	254
8.5 The application of biomedical imaging for the guidance of engineered tissues .....	258
8.6 Summary .....	260
Chapter 9 Conclusion .....	262
Chapter 10 Future research .....	264
<b>10.1 Biomaterial development for improved human annulus fibrosus cell compatibility .....</b>	<b>264</b>
<b>10.2 Clinical feasibility .....</b>	<b>266</b>
<b>10.3 Analysis of tissue-engineered matrix development using medical imaging .....</b>	<b>267</b>
References .....	269
Appendix .....	306
<b>Appendix A: Preliminary investigation of polycaprolactone for bioprinting – Relating to Chapter 3 .....</b>	<b>306</b>
Introduction .....	306
Methods .....	306
Material Selection .....	306
Polycaprolactone preparation .....	306
Polycaprolactone printing .....	306

Multi-material plotting.....	308
Scaffold characterisation .....	308
Results.....	311
Material Characterisation with Fourier transform infrared spectroscopy .....	311
Fabrication of scaffolds .....	312
Morphological characterisation of scaffolds .....	313
Static compression of polycaprolactone scaffolds with and without alginate methyl cellulose	315
Discussion .....	317
Conclusion.....	318
<b>Appendix B: Supplementary figures related to Chapter 4 .....</b>	<b>319</b>
<b>Appendix C: Documents related to Chapter 6.....</b>	<b>323</b>
<b>Appendix D: Documents related to Chapter 7 .....</b>	<b>328</b>
<b>Appendix E: Makerbot fabrication of anatomic disc model - related to Chapter</b>	<b>335</b>

## Abstract

Damage to intervertebral discs (IVD) is a leading contributor to disability worldwide. Current disc replacements have been pursued using artificial devices made from polymers and metal. However, artificial discs are typically unable to comply with the physiological motions of the spine and can damage adjacent tissue. This project focused on the regeneration of IVDs using bioprinted scaffolds. Firstly, the bioink options of collagen, alginate methylcellulose (alg/MC) and alginate–gelatin were screened. The alg/MC hydrogel was selected as the most conducive to accurate, stable and cell friendly scaffold production. Alg/MC was further characterised for bioprinting with bovine primary chondrocytes (BPCs) and the effect of MC sterilisation on cell compatibility investigated. It was identified that the alg/MC supported a chondrogenic phenotype, with a collagen type I: collagen type II gene expression ratio of 0.45:99.55 on day 21 of cell culture, and that autoclaved MC had a significant ( $P \leq 0.05$ ) beneficial effect relative to super critical CO<sub>2</sub>, based on DNA content (194% increase, in ng/scaffold) and matrix production (61% increase in safranin O stain intensity). Hydrostatic pressure (HP) stimuli was utilised with the aim to enhance the cartilage extracellular matrix (ECM). As a part of this, a meta-analysis review of HP literature was performed to identify key experimental parameters. Factors found to influence proteoglycan production to the greatest degree were identified as pressure magnitude ( $\leq 5$ -10 MPa), length of study ( $\geq 2$  weeks) and HP application style (static over dynamic). Guided by the outcome of the meta-analysis an HP protocol was employed on alg/MC scaffolds laden with BPC or human IVD cells. The daily application of HP was shown to significantly ( $P \leq 0.05$ ) upregulate proteoglycan gene expression in both the BPC ( $78.1 \pm 16.1$  %) and human nucleus pulposus (hNP) cells ( $81.9 \pm 26.4$  %) relative to controls on day 21 of culture, supported also by histological staining and dimethyl methylene blue assay. Furthermore, the increase in proteoglycan (and associated water content) following HP was demonstrated using quantitative MRI (qMRI). Molecular quantities of water content (inferred by T<sub>2</sub>) and proteoglycan (measured by <sup>1</sup>H MR spectroscopy) increased in HP treated samples relative to controls and were comparable to measurements taken from IVDs *in vivo* using the same methods. The results of this investigation suggested the potential of bioprinted chondrocyte-laden alg/MC with HP stimulation for engineering disc cartilage.

## **Acknowledgements**

I would like to extend great thanks to my supervisory team comprising of Dr Derek Covill, Dr Peter Bush, Dr Mark Best, Dr Nicholas Dowell and Professor Mara Cercignani for their kind support and assistance in the development and guidance of this work.

I would also like to thank my fellow PhD students, post-docs and friends in particular Sarah Duin, Tilman Ahlfeld, Madeleine Conaghan, Dr Jenny Venton, Olivia White and Dr Alexander Pitkin whose advice, support and entertainment has helped me in the completion of this work. I am also very appreciative of members of staff both at this University and other establishments including Professor Matteo Santin, Dr Andrew Overall and Dr Fergus Guppy from the University of Brighton, Dr Lisa Harris from Brighton and Sussex University Hospitals NHS Trust, Dr Lisa Mullen from the Brighton and Sussex Medical school, Professor Michael Gelinsky and Dr Anja Lode from the Dresden University of Technology, Dr Max Gay from the University Hospital of Basel and Dr Andrew Hall from the University of Edinburgh. Above all else I would to thank my family for their unwavering love and support throughout my study.

## **Declaration**

I declare that the research contained within this thesis, unless otherwise stated, is the original work of the author. The thesis has not been previously submitted in any form to any other university in fulfilment of any degree or qualification, nor has any of its material contained within.

Ella Hodder

## List of Figures

**Figure 1.1** Schematic of thesis structure and content sorted by chapters.

**Figure 2.1** Compositional diagram of a healthy human intervertebral disc, consisting of a nucleus pulposus, annulus fibrosus and the cartilage endplates. Original image sourced from encyclopaedia of occupational health and safety: [www.ilocis.org/documents/chpt6e.htm](http://www.ilocis.org/documents/chpt6e.htm).

**Figure 2.2** Diagram to demonstrate the distribution of an axial compressive force on intervertebral discs, the load is resisted by the swelling pressure of the nucleus. During NP compression water is extruded outwards and the stress is then dissipated across the disc through the annulus layers. Image sourced from: <https://ittcs.wordpress.com/2010/06/01/anatomy-and-physiology-the-intervertebral-discs/>.

**Figure 2.3** Diagrams to demonstrate the current surgical interventions for disc herniation (A) Disc fusion, first the damaged disc is removed and replaced by a spacer, then the spinal cage is screwed in place to fuse adjacent vertebrae into a fixed position (B) Surgical process of discectomy, the herniated and damaged tissue is removed using a microsurgical instrument. Images sourced from [www.newhealthadvisor.com/Spinal-Fusion-Recovery.html](http://www.newhealthadvisor.com/Spinal-Fusion-Recovery.html) and <http://spineonline.net>.

**Figure 2.4** Artificial disc models (A) ProDisc® implanted in position, (B) ProDisc® alone, (C) SB Charité®, (D) Maverick®. Images sourced from <https://ryortho.com/>.

**Figure 2.5**  $T_2^*$  map of an intervertebral disc with locations overlaid, NP: Nucleus Pulposus, AF: Annulus Fibrosus, aAF: anterior AF, pA: posterior AF, oAF: outer AF, and iAF: inner AF. A high  $T_2^*$  (ms) infers a high water content (red) and a low  $T_2^*$  (ms) represents a low water content (Blue).

**Figure 2.6** Conventional strategies used in disc tissue engineering. (A) Hybrid alginate/chitosan fibres fabricated for annulus fibrosus (AF) tissue using freeze-drying and wet-spinning (Shao and Hunter, 2007). (B) Carboxymethylcellulose mould-casted gel seeded with nucleus pulposus (NP) cells (Reza and Nicoll, 2009a). (C) Atelocollagen honeycomb scaffolds from natural extracellular matrix, using ammonia gas, freeze-drying and UV-irradiation (Sato *et al.*, 2003). (D) A disc scaffold with photo-crosslinked collagen and glycosaminoglycans formed by temperature sensitive mould-casting (Choy and Chan, 2015). (E) An AF replica constructed from poly(polycaprolactone-triol-malate) with chondrocytes, and a demineralized bone matrix formed via gas-foaming, cast-moulding and freeze-drying (Wan, *et al.*, 2008). (F) Scaffolds fabricated out of porous silk seeded with AF cells and a hyaluronic acid hydrogel with chondrocytes; using silicon moulds and high-temperature crystallisation, with freeze-drying (Park *et al.*, 2012).

**Figure 2.7** A schematic of conventional scaffold fabrication techniques (modified from Puppi *et al.*, (2010). (A) Solvent-casting and particulate-leaching process. (B) Gas foaming process (C) Phase separation process. (D) Melt moulding process. (E) Freeze drying process.

**Figure 2.8** Schematic of bioprinting. Image sourced from Naghieh *et al.*, (2018), formatted by author.

**Figure 2.9** Molecular structure of alginate, a linear polymer consisting of (1-4)-linked  $\beta$ -D-mannuronate (M) and  $\alpha$ -L-guluronate (G) residues (Draget *et al.*, 2006). Diagram taken from Lee and Mooney, (2012).

**Figure 2.10** Intervertebral disc models fabricated using additive manufacturing (A-B) fabricated using bioprinting by Whatley (2013), (C-D) using fused-filament modelling by van Uden *et al.*, 2015a. (A-B) High magnification scanning electron microscopy images of a chitosan/gelatin disc scaffold by Whatley (2013) with lamellae type structures similar to native annulus tissue. (C) Computer aided design model of a rabbit intervertebral disc at 200% scale. (D) Polycaprolactone disc scaffold after printing.

**Figure 3.1** Images showing stages of the non-fibrillar 4% collagen paste preparation. (A) Precipitation in saline solution. (B) Pellet formation after centrifugation. (C) Collection of pellets. (D) Freeze-dried collagen.

**Figure 3.2** Schematic of the 3D BioScaffolder 3.1 (GeSIM, Germany) with labelled elements. Modified image sourced from GeSIM online brochure <http://GeSIM-bioinstruments-microfluidics.com>.

**Figure 3.3** The multi-material printing of an intervertebral disc model based on true dimensions (A) The anatomical area of interest was isolated on a pixel by pixel bases in 3D using Mimics® software from a patients MRI scans. (B-D) The attained model was separated into two regions using Blender®. (E) Two cartridges of alginate methyl cellulose, coloured red or green were prepared. (F) The digital file was imported to the bioscaffolder 3.1 software (GeSIM, Germany) and a print code generated. The code script was edited for printing with two print heads and printing commenced.

**Figure 3.4** Procedure for measuring (A) material strut widths ( $w$ ) and (B) macropore height ( $h$ ) and widths from Cryo-SEM images of alginate methyl cellulose scaffolds using the smart Tiff imaging software package (Zeiss Zen 2).

**Figure 3.5** Flow diagram to demonstrate the compression protocol (1-4) used for mechanical testing of alginate methyl cellulose and collagen + 1% methyl cellulose scaffolds.

**Figure 3.6** Software interface of the AR G2 dynamic rheometer (TA Instruments) dynamic test set up on alginate methyl cellulose scaffolds. Demonstrating the use of the 'gap settings' to apply a defined compressive strain (entered as 3.791 for 15% and 3.122 for 30%) based on scaffold height. A step wise procedure was performed as follows: (1) Positioning/lifting of the lower plate to either 15% or 30% of the scaffold heights (as defined by gap setting) (2) Application of a compressive strain of 5 Pa and oscillation frequencies ranging from 0.05 Hz to 1.05 Hz, performed at 37°C. (3) Separation of the plates to remove compressive force on the sample.

**Figure 3.7** Fourier transform infrared (FTIR) spectra of (A) alginic salt powder (B) methyl cellulose powder and (C) freeze-dried alginate methyl cellulose scaffolds ionically crosslinked with calcium chloride.

**Figure 3.8** (A) Fourier transform infrared (FTIR) spectrum of alginate dialdehyde and alginate dialdehyde-gelatin, alongside spectra of the material components alginate and gelatin taken from Sarker *et al.*, (2014) for comparison with (B) FTIR spectrum of alginate dialdehyde and alginate dialdehyde-gelatin. Comparisons of the two spectra show shared characteristic peaks for the alginate dialdehyde material.

**Figure 3.9** Fourier transform infrared (FTIR) spectra of freeze-dried collagen (A) 1% collaplex (B) comparative spectra of five collagen types from the publication by Belbachir *et al.*, (2009).

**Figure 3.10** Mean dynamic viscosity of alginate methyl cellulose (alg/MC batch 1) measured over time following initial MC addition, to monitor MC swelling effect on material viscosity, where time '0' represents the alginate only control ( $n = 4$ ,  $P \leq 0.05$ , mean  $\pm$  stdev). Batch 1 was made with liquid sterile-filtered phosphate buffer saline (Dulbeccos) and stirred overnight after alginate addition.

**Figure 3.11** Representative rheogram of alginate methyl cellulose paste from batch 2, (material before ionic cross-linking) the plotted curves represent the shear stress (blue line) and viscosity (red line) as a function of shear rate. Batch 2 was prepared with phosphate buffer saline tablets from Sigma-Aldrich and stirred for five hours.

**Figure 3.12** Example rheometer curves of four (A-D) batch one alginate methyl cellulose replicates, demonstrating repeatability as well as a characteristic decreasing viscosity with increasing shear rate. Batch one was made with liquid sterile-filtered phosphate buffer saline (Dulbeccos) and stirred overnight after alginate addition.

**Figure 3.13** Rheograms demonstrating the dynamic shear properties of the (A) collagen paste alone and (B) collagen + 1% methyl cellulose. Storage shear modulus ( $G'$ ) and loss modulus ( $G''$ ) were plotted over time.

**Figure 3.14** The modification of print parameters for the printing of alginate methyl cellulose (alg/MC) through a 0.51 mm ID polyethylene tapered tip (Nordson) (A) alg/MC plotted using unrefined parameters of (1) 80 kPa, speed 10 mm/s (2) 80 kPa speed 15 mm/s (3) 75 kPa, speed 10 mm/s (4) 75 kPa speed 15 mm/s (5) 75 kPa speed 10 mm/s (B-D) alg/MC printed with adjusted settings of 70 kPa, speed 10 mm/s. Scale bars represent 5 mm.

**Figure 3.15** (A) Cartridges prepared for multi-material printing containing coloured alginate methyl cellulose (alg/MC) paste which were loaded into the GeSIM bioscaffolder 3.1 and recognised as print head A (red) and C (green) by the printer software. Multi-head printing of alg/MC scaffolds with different designs were achieved using the print sequences: (A) ACCAACCA (B) ACACA (C) AACCCCAA (D) AC (E) an up-scaled intervertebral disc model comprised of two regions printed using separate print heads, with coloured alg/MC. Scale bars represent 10 mm.

**Figure 3.16** 4% Collagen + 1% methyl cellulose scaffolds. Images taken with a stereo light microscope (Leica M205 C equipped with DFC295 camera, Germany). (A) Four strand scaffold plotted using stainless steel cannula tip, 0.84  $\mu\text{m}$  ID (mag x10). (B) Five strand scaffolds produced using a flexible

conical nozzle, 0.61 mm ID, (mag x10). (C) Close-up view of five strand variant macropores, plotted with nozzle size 0.61 mm (mag x20). (D) Side view of a 12 layer five strand scaffold to demonstrate full height (mag x10). (E-F) Early collagen scaffolds produced with non-refined print parameters, (E) pressure of 70 kPa, speed 8 mm/s, (F) 80 kPa, speed 5 mm/s.

**Figure 3.17** Cryogenic-scanning electron microscopy images of alginate methyl cellulose (alg/MC) scaffolds. (A) Six strand scaffold printed using a tip with an inner diameter (ID) of 0.61 mm. (B) Eight strand scaffold printed using a tip with an ID 0.61 mm. (C) Six strand scaffold produced with a tip ID of 0.51 mm. (D) Eight strand scaffold printed with ID of 0.51 mm with evidence of material breakage between struts.

**Figure 3.18** Stereo microscopy images of collagen + 1% methyl cellulose scaffolds (A-B) printed with 0.61 mm inner diameter (ID) steel cannula tip (C-D) or 0.84 mm ID flexible conical tip (scalebar = 1 mm).

**Figure 3.19** Example stress-strain graphs of the same collagen + 1% methyl cellulose scaffold (A) full stress-strain curve recorded on day 1 of incubation. (B) The regions of linearity used for extrapolating the Young's moduli on days 1, 2 and 3 of recurrent compression, using a threshold of between 0.5-2.0% strain.

**Figure 4.1** Schematic to demonstrate live/dead cell quantification using Image J V1.44p (FIJI) analysis software. Step 1: Channels were split, Step 2: Images were converted to an 8-bit format, Step 3: Maxima point selection found and cell number counted per channel.

**Figure 4.2** Schematic to demonstrate the image analysis process prior to safranin O stain intensity measurement. (1) Original image. (2) Image converted to 8-bit and grayscale inverted, mean intensity measured and multiplied by a fixed value of 0.4 to give the threshold value for use in next step. (3) Image thresholded and the mean intensity of the safranin O regions measured. (4) Threshold reversed and the mean intensity of the unstained background measured. (5) Calculations were performed to correct for differences in background intensity or for any false positive alginate staining.

**Fig 4.3** Fourier transform infra-red (FTIR) analysis of methyl cellulose (MC) powder treated by different sterilisation methods. (A) Example FTIR spectrum of MC powder with labelled peaks. The spectra of all MC types measured (autoclaved, scCO<sub>2</sub> treated, UV and  $\gamma$ -irradiated) were identical in appearance. (B) Identification of MC spectrum peaks.

**Figure 4.4** Gel permeation chromatography, weight and numerical average molecular mass (M<sub>w</sub> and M<sub>n</sub>) as well as polydispersity index (PDI) of methyl cellulose (MC) powders prepared using non-sterilised MC and MC sterilised by autoclave, scCO<sub>2</sub>, UV and  $\gamma$ -irradiation. Mean  $\pm$  stdev, n = 3, \*P  $\leq$  0.05.

**Figure 4.5** Viscosity measurements of alginate methyl cellulose (alg/MC) pastes. MC was mixed into dissolved alginate and left to swell overnight (A) Viscosity over shear rate of alg/MC pastes prepared

using non-sterilised MC and MC sterilised by autoclave, scCO<sub>2</sub>, UV and  $\gamma$ -irradiation. One representative measurement is shown from each variant to demonstrate material behaviour. At all-time points, the viscosity of the alg/MC paste with  $\gamma$ -irradiated MC was significantly lower than the other variants. (B) Viscosity of alg/MC pastes at a defined shear rate of 10 s<sup>-1</sup> prepared with non-sterilised MC and sterilised MC. Mean  $\pm$  stdev, n = 3, \**P*  $\leq$  0.05 compared to the non-sterilised MC. (C) Examples of plotted scaffolds prepared using non-sterilised MC and MC sterilised by autoclave, scCO<sub>2</sub>, UV and  $\gamma$ -irradiation (scale bars = 2 mm).

**Figure 4.6** Methyl cellulose (MC) content and microstructure of alginate methyl cellulose (alg/MC) scaffolds (A) Stereomicroscopy images of alg/MC scaffolds after 1, 7 and 21 days of cell culture stained with chlorine–zinc–iodine solution, prepared with untreated MC and sterilised MC via autoclave, scCO<sub>2</sub>, UV and  $\gamma$ -irradiation, (scale bars = 2 mm). (B) Quantitative measurement of cumulative percentage of MC release over time. Mean  $\pm$  stdv, n = 3. At all time points, release of the  $\gamma$ -irradiated MC was significantly higher; at days 14, 19 and 21, release of the scCO<sub>2</sub>-treated MC was significantly higher than those of the autoclaved and UV-treated MC; after 21 days, release of all sterilised MC types was significantly higher than those of the untreated MC \**P*  $\leq$  0.05. (C) Representative scanning electron microscopy images of alg/MC scaffolds prepared with the different MC variants at a magnification of x250 (I) and x10,000 (II) after one day of incubation under cell culture conditions (scale bars for I = 200  $\mu$ m and II = 50  $\mu$ m).

**Figure 4.7** The effect of different sterilisation procedures on scaffold stability of cell-free scaffolds kept under cell culture conditions (A) Compressive strength of alginate methyl cellulose (alg/MC) scaffolds prepared with the MC variants treated with autoclave, scCO<sub>2</sub> and UV on days 1, 10 and 21 of incubation. Mean  $\pm$  stdv, n = 12, \* *P*  $\leq$  0.05. (B) Cumulative calcium release by alg/MC scaffolds prepared using the different MC sterilisation methods, autoclaving, scCO<sub>2</sub> and UV, measured after 1, 10 and 21 days of incubation. Mean  $\pm$  stdv, n = 9, \**P*  $\leq$  0.05.

**Figure 4.8** Cytocompatibility of bovine primary chondrocyte (BPC)-laden alginate methyl cellulose (alg/MC) scaffolds prepared with MC treated by autoclave, scCO<sub>2</sub> and UV at days 1, 7, 14 and 21 of cell culture (A) Survival of live BPCs within the scaffolds, mean  $\pm$  stdv, n = 12, \* *P*  $\leq$  0.05. (B) Total DNA content of BPCs embedded in the scaffolds, mean  $\pm$  stdv, n = 6, \**P*  $\leq$  0.05.

**Figure 4.9** Glycosaminoglycan histology staining of bovine primary chondrocyte (BPC)-laden and cell-free alginate methyl cellulose (alg/MC) scaffolds prepared with autoclave, scCO<sub>2</sub> and UV treated MC (A) Histological images of scaffold sections, fixed at day 21 of cell culture and stained with safranin O, taken by light microscopy (I) 20x magnification showing areas of high stain intensity (II) 20x magnification images to represent regions of low staining (III) 10x magnification images (IV) 10x magnification of a cell-free scaffold prepared with autoclaved MC and fixed at day 14 of incubation under cell culture conditions (V) 20x magnification of BPC-laden scaffold prepared with autoclaved MC and fixed at day 7 of culture scalebars for all images represent 10  $\mu$ m. (B) Relative intensity of safranin O staining taken from histology images (20x magnification) of scaffolds on days 7, 14 and 21 of cell culture. Mean  $\pm$  stdv, n = 9, \**P*  $\leq$  0.05.

**Figure 5.1** Visual demonstration of the publication selection process.

**Figure 5.2** Representation of how the raw data was extracted from graphs using engage digitizer (10.5) software. (A) Screen shot of the engage digitizer software after three axis co-ordinates had been allocated to define the graph area. (B) Example of co-ordinate plotting for the extraction of data values using a bar graph. (C) Exported y-axis data from the plotted co-ordinates.

**Figure 5.3** Forest plots representing the relationship between hydrostatic pressure (HP) stimulated 3D cultured samples on proteoglycan gene expression measured via RT-PCR compared to control samples kept at atmospheric pressures.

**Figure 5.4** Forest plot representing the relationship between hydrostatic pressure stimulated 3D cultured samples on total glycosaminoglycan content measured via DMMB colorimetric assay relative to samples kept at atmospheric pressure conditions.

**Figure 5.5** Forest plots representing the relationship between hydrostatic pressure stimulated 3D cultured samples applied either as static or dynamic loads on proteoglycan gene expression measured via RT-PCR compared to control samples cultured under atmospheric pressures.

**Figure 5.6** Forest plots representing the relationship between hydrostatic pressure stimulated 3D cultured samples applied as either static or dynamic loads on measured glycosaminoglycan content, via DMMB colorimetric assay, compared to control samples cultured under atmospheric pressure.

**Figure 5.7** Forest plots demonstrating the relationship between hydrostatic pressure stimulated 3D cultured samples using magnitudes of  $\leq 5$  MPa, 10 MPa and 50 MPa applied as either static or dynamic loads on measured proteoglycan gene expression, via RT-PCR analysis, compared to control samples kept at atmospheric pressure.

**Figure 5.8** Forest plots representing the relationship between hydrostatic pressure stimulated 3D cultured samples using pressure magnitudes of under 1 MPa, 5 MPa and 10 MPa on measured glycosaminoglycan content, via DMMB colorimetric assay, compared to unpressurised control samples.

**Figure 5.9** Forest plots demonstrating the relationship between proteoglycan gene expression measured by RT-PCR of hydrostatic pressure stimulated 3D cultured chondrocytes and experiment duration; of one week or under and two weeks or over, compared to unpressurised control samples.

**Figure 5.10** Forest plots showing the relationship between glycosaminoglycan content measured by DMMB colorimetric assay in stimulated 3D cultured chondrocytes and experiment duration; of under one week, one week or over, and two weeks or over, compared to unpressurised control samples.

**Figure 6.1** Flow diagram schematic of the experimental layout within this chapter: (1) Duration experiments with bovine primary chondrocytes (BPCs). (2) 21 day hydrostatic pressure experiment with BPCs. (3) 21 day hydrostatic pressure experiment with human intervertebral disc cells.

**Figure 6.2** Schematic diagram of the hydrostatic pressure vessel set up. Water from the reservoir was manually pumped through the inlet valve and into the top of the full pressure vessel. Gas from solution was released using the outlet valve into the waste line. Once all gas was removed the outlet valve was closed and pressure within the vessel was raised to the desired magnitude using the hand-driven pump at approximately 0.04 MPa/sec. Once pressurisation was completed the outlet valve was gradually opened to allow for depressurisation into the waste line at approximately 0.04 MPa/sec. Image created by author.

**Figure 6.3** Images to demonstrate the hydrostatic pressure vessel in use (A) Loading of samples into the vessel. (B) Tightening of the vessel lid. (C) Clearing the line of gas by opening the outlet valve to release pressure into the waste line. (D) Pressurisation of the vessel (as indicated on the gauge).

**Figure 6.4** Hydrostatic pressure (HP) application timeline: For the duration screening in Experiment 1 the HP pressurisation started on day eight of bovine primary chondrocyte (BPC) scaffold culture, 6 MPa was applied once a day for five days for either 5 or 45 minutes, 4 hours or dynamically (5 min on/ 2 min off, x3). Two days after the last pressurisation the final samples were taken for analysis. For the 21 day investigations in Experiment 2 and 3 the HP pressurisation started on day eight of BPC or human intervertebral disc cell culture, HP was applied for 45 minutes a day for 5 days, followed by a two day rest period, this was then repeated and the final samples taken on day 21 after a two day period at atmospheric conditions. For all experiments the control samples were kept under atmospheric incubation conditions for the entire study duration. Image created by author.

**Figure 6.5** Flow diagram to demonstrate the compression protocol used for mechanical testing in Experiment 2 on bovine primary chondrocyte-laden alginate methyl cellulose scaffolds.

**Figure 6.6** Diagram to demonstrate the secant method used to extract the Young's moduli of alginate methyl cellulose scaffolds.

**Figure 6.7** Screen-tape analysis and nano-spectrophotometer results of RNA isolated using the RNeasy kit (Qiagen) from bovine primary chondrocytes (BPC) or human annulus fibrosus (hAF) and nucleus pulposus (hNP) cells at successive time-points, purified from alginate methyl cellulose scaffolds which were cultured under control conditions or with hydrostatic pressure (HP) exposure. (A1) RNA ladder (B1) BPC Day 7 control (C1) BPC Day 14 control (D1) BPC Day 21 control (E1) BPC Day 14 HP (F1) BPC Day 21 HP (G1) hAF Day 14 control (H1) hNP Day 14 Control. (A) RNA RINe values provided by the 'TapeStation Analysis software A.02.02' (Agilent technologies). (B) Nano-spectrophotometer (QIAxpert) results of measured RNA quantity (ng/ $\mu$ l) and 260/280 ratio, values presented as mean  $\pm$  standard deviation of three repeated measurements.

**Figure 6.8** (A) Percent bovine primary chondrocyte survival in alginate methyl cellulose scaffolds calculated via live/dead staining analysis on day one (D1) and day 15 (D15) of culture. Measurements were taken of samples kept at atmospheric control conditions (Ctrl) or exposed to five days of HP (6 MPa) applied for 5 minutes, 45 minutes, 4 hours or dynamic intermittent applications (IHP) of 5 minutes on/2 minutes off x3, (mean  $\pm$  stdv)  $n = 4$ ,  $*P \leq 0.05$ . (B) Examples of MTT stained scaffold sections

taken on day 15 of incubation, taken from samples subjected to the different HP duration protocols A) 5 minutes B) 45 minutes C) IHP D) 4 hours or from scaffolds kept under atmospheric conditions E) cell-laden controls F) cell-free controls. The three scaffold sections for each sample type represent one sample from three different cell sources ( $n = 3$ ).

**Figure 6.9** (A) Percent survival of bovine primary chondrocytes (BPCs) within alginate methyl cellulose (alg/MC) scaffolds over time on days 1,8,15 and 21 of incubation, separated by sample type; atmospheric controls or those exposed to 6 MPa of HP 5 days on/ 2 days off, after seven days of static atmospheric culture. Mean  $\pm$  stdv,  $n = 4$ , \*  $P \leq 0.05$ . (B) MTT staining of BPC cells within scaffolds taken on day 21 of incubation, following culture under atmospheric conditions for the entire study duration (controls) or subjected to HP. Samples represent sections taken from three separate scaffolds and are grouped by their cell source (1-4). Cell-free (CF) samples were also stained for comparison. Scalebar represents 5 mm. (C) Examples of MTT staining of BPC-laden (A-H) and cell-free alg/MC scaffolds (I-K) on day 21 of incubation (A-D) control samples, (E-H) samples exposed to the 45 minute/day HP protocol. Each column represents samples from a different cell source ( $n = 4$ ), with the exception of the cell-free samples (I-K). Images taken by light microscopy (Axiovert-25, Carl- Zeiss), magnification  $\times 10$ , scalebar represents 10  $\mu\text{m}$ .

**Figure 6.10** Young's modulus of bovine primary chondrocyte-laden and cell-free alginate methyl cellulose scaffolds over time, measured on days 8, 15 and 21 of incubation. Samples were either kept consistently under atmospheric conditions (control) or exposed to a daily 45 minute 6 MPa hydrostatic pressure protocol starting on day 8 (5 days on/2 days off). Mean  $\pm$  stdv,  $n = 4$ , \*  $P \leq 0.05$ .

**Figure 6.11** (A) Percent cell survival calculated from live/dead imaging of human annulus fibrosis (hAF) and nucleus pulposus (hNP) cells in alginate methyl cellulose (alg/MC) scaffolds after 8 or 21 days of incubation, including samples cultured under atmospheric control conditions or hydrostatic pressure (HP). Mean  $\pm$  stdv,  $n = 4$ , \*  $P \leq 0.05$ . (B) MTT staining of alg/MC scaffold sections embedded with hAF or hNP cells, sorted by cell source, on day one (the day of scaffold fabrication) or day 21 of culture under atmospheric control or HP conditions,  $n = 3$ , scale bar represents 5cm. Images taken with iphone v6.

**Figure 7.1** Sagittal  $T_2$ -weighted magnetic resonance image of the lumbar spine labelled to show the level 3,4 and 5 vertebrae. The lumbar discs chosen for voxel placement in this study were located between either L3-L4 or L4-L5.

**Figure 7.2** The manual region of interest (ROI) selection process taken from the slice positioned at the centre of the IVD. Regions were defined using ImageJ software (Fiji, V1.44p). (A) Un-edited image (B) ROI of the whole disc (WD) (C) ROI drawn around the annulus fibrosus region (D) ROI of the nucleus pulposus.

**Figure 7.3** Example linear regression plot of the Log of Signal against Echo Time, gradient used to extrapolate the  $T_2/T_2^*$  values.

**Figure 7.4** Voxel placement shown in three orthogonal planes, in which the voxel was fully contained within the intervertebral disc between the third lumbar disc (L3) and the fourth lumbar disc (L4). The hatched lines represent the saturation bands which were placed surrounding the voxel to remove external signal.

**Figure 7.5** (A) AMARES fitting of disc spectra (B) Observable peaks including carbohydrate at 3.54 ppm, lipids and macromolecules at 1.3 ppm and the proteoglycan (N-Acetyl) peak of interest at 2.04 ppm.

**Figure 7.6** (A) Scaffolds transferred into 50ml syringes (B) Cell-free (CF), control and hydrostatic pressure (HP) treated scaffolds were divided into separate syringes and filled with 40mls of culture medium. All syringes were capped with Luer lock 0.2-micron filters during incubation to allow for gas-exchange.

**Figure 7.7** Luer lock capped syringes containing scaffolds for hydrostatic pressurise (HP) treatment (B) Syringes inside the pressure vessel chamber.

**Figure 7.8** (A) Scaffold samples entering the Siemens Avanto 3 Tesla scanner, placed inside a 20-channel receive-only head-coil (B) Localisation scan image of an alginate methyl cellulose scaffold inside a syringe.

**Figure 7.9** (A) The positioning of imaging slices for  $T_2$  mapping in the three imaging planes sagittal, coronal and axial, using the Siemens Avanto 3T software interface (B) Shows the positioning of the region of interest on  $T_2$  scans of scaffolds using ImageJ software (Fiji, V1.44p).

**Figure 7.10** Mean  $T_2$  and  $T_2^*$  values (ms) of the annulus fibrosis (AF) and nucleus pulposus (NP) disc regions. Error bars represent standard deviations;  $n = 10$ ,  $P \leq 0.05$ .

**Figure 7.11** Example parameter maps generated using ImageJ (Fiji, V1.44p) of a lumbar disc in a healthy 29 year old male participant (A)  $T_2$  and (B)  $T_2^*$ .

**Figure 7.12** AMARES fit to the intervertebral disc spectrum (A) The black line represents the mean spectrum of all 10 study volunteers, and the grey line is the  $\pm$  standard deviation. Notable peaks are labelled and include Carbohydrate at 3.54 ppm, Proteoglycan (N-Acetyl) peak at 2.02 ppm and a Lipids and Macromolecules peak at 1.3 ppm. (B) Mean relative proteoglycan content of  $301.4 \pm 61.2$  water/proteoglycan ratio (error bars represent standard deviation,  $n = 13$ ). (C) Mean residual background noise measured (fitted model was subtracted from the spectrum data).

**Figure 7.13** Mean  $T_2$  measurements of bovine primary chondrocyte-laden and cell-free alginate methyl cellulose scaffolds on days 14, 21 and 28 which were either subjected to daily hydrostatic pressure (HP) treatment or cultured under atmospheric control conditions, error bars represent standard deviations, ( $n = 3$ ).  $P \leq 0.05$ .

**Figure 7.14** Examples of clipped  $^1\text{H}$ -spectra obtained for the alginate methyl cellulose scaffolds. (A) Cell-free scaffold after 21 days (B) Control scaffold after 21 days of culture. (C) Hydrostatic pressure

(HP) treated scaffold after 14 days. (D) HP treated scaffold after 21 days. (E) HP treated scaffold after 28 days.

## List of Tables

**Table 2.1** Difference in intervertebral disc composition and mechanical properties between the annulus fibrosus and nucleus pulposus (Marchand and Ahmed, 1990; Best *et al.*, 1994; Antoniou *et al.*, 1996; Wilke *et al.*, 1999; Klisch and Lotz, 2002; Elliott *et al.*, 2004; Mow, Huiskes and Abreu, 2005; Périé, Korda and Iatridis, 2005; Whatley, 2013).

**Table 2.2** The results of changes to relaxation quantitative magnetic resonance imaging parameters  $T_1$  and  $T_2$  monitored over time in different cartilage tissue-engineered constructs for the study of tissue-growth dynamics carried out by Kotecha *et al.*, (2013).

**Table 2.3** Advantages and disadvantages of biomaterials used in articular cartilage repair, taken from the review paper by Campos *et al.*, (2012).

**Table 3.1** Biomaterial scaffold criteria for clinical implementation.

**Table 3.2** Bioscaffolder 3.1 (GeSIM, Germany) print parameters, with definitions and ranges.

**Table 3.3** Screened print parameters for the printing of alginate methyl cellulose and non-fibrillar collagen + 1% methyl cellulose using the 3.1 Bioscaffolder (GeSIM, Germany).

**Table 3.4** Chemical bond assignments of the FTIR spectra for alginic salt and methyl cellulose.

**Table 3.5** Dynamic shear viscosity for alginate methyl cellulose material batches prepared with different phosphate-buffered saline sources at  $s^{-1}$  of applied shear rate.

**Table 3.6** Mean dynamic shear viscosity of collagen and collagen + 1% methyl cellulose material batches after 0 minutes, 30 minutes or 2 hours after paste formulation at  $s^{-1}$  of shear rate.

**Table 3.7** Pore morphology measurements of alginate methyl cellulose scaffold variants printed with either six or eight materials strands using nozzles with the inner diameter of 0.61 mm or 0.51 mm.

**Table 3.8** Mean dynamic shear moduli values of the alginate methyl cellulose scaffolds under compressive strains of 15% and 30%.

**Table 3.9** Young's modulus values of the alginate methyl cellulose scaffold at cycles 5,10,15,20,25. Means calculated from linear regression curves of stress versus strain. A general trend of decreasing compressive modulus was seen over the course of the test.

**Table 3.10** Measured heights of collagen + 1% methylcellulose scaffolds before and after compression testing on three successive days of incubation and mechanical testing.

**Table 3.11** A comparison of alginate methyl cellulose, non-fibrillar collagen + 1% methyl cellulose and alginate dialdehyde-gelatin materials based on their feasibility for bioprinting.

**Table 4.1** Protocol used to embed alginate methyl cellulose samples in paraffin using a *LEICA TP 1050* tissue processor.

**Table 5.1** Overview of physical hydrostatic pressure factors selected for meta-analysis taken from papers reviewed in this study.

**Table 5.2** Overview of the cell-based experiment factors within the studies selected for meta-analysis review.

**Table 6.1** Human intervertebral disc tissue information.

**Table 6.2** Bovine primer sequences.

**Table 6.3** Human intervertebral disc primer sequences.

**Table 6.4** RT-PCR reaction mixture composition.

**Table 6.5** Percent difference in proteoglycan gene expression and glycosaminoglycan content relative to controls measured in bovine primary chondrocytes extracted from bioprinted alginate methyl cellulose scaffolds exposed to either 5 minutes, 45 minutes, 4 hours or dynamic hydrostatic pressure (6 MPa for 5 days on/2 days off) taken on day 15 of cell culture.

**Table 6.6** Relative aggrecan gene expression, glycosaminoglycan content and safranin O stain intensity of bovine primary chondrocytes alginate methyl cellulose samples subjected to 6 MPa of hydrostatic pressure (5 days on/2 days off) after 8 days of incubation (one day of hydrostatic pressure exposure), 15 days (5 days of pressurisation) and 21 days of incubation (10 days of total hydrostatic pressurisation).

**Table 6.7** The calculated mean ratio of collagen type I : collagen type II relative gene expression in bovine primary chondrocytes isolated from alginate methyl cellulose scaffolds exposed to hydrostatic pressure (6 MPa; 5 days on/2 days off) or atmospheric control conditions taken on day 21 of cell culture.

**Table 6.8** Mean measurements of the relative aggrecan gene expression, glycosaminoglycan content and safranin O stain intensity of human annulus fibrosus and nucleus pulposus cells cultured in alginate methyl cellulose and subjected to 1 MPa of hydrostatic pressure (5 days on/2 days off) represented as percent change from control samples.

**Table 6.9** Relative gene expression ratios of collagen type I: collagen type II in human annulus fibrosus and nucleus pulposus cells cultured in alginate methyl cellulose scaffolds on day 8 or 21 of cell culture. Measurements taken from samples exposed to 1 MPa of hydrostatic pressure (5 days on/2 days off) or cultured under constant atmospheric control conditions.

**Table 7.1** Mean  $T_2$  and  $T_2^*$  relaxation parameters measured *in vivo* for the whole disc as well as the annulus fibrosus and nucleus pulposus disc regions.

**Table 7.2** Values of spectral noise level measured in root mean square voltage (RMS), proteoglycan amplitude and water/proteoglycan ratio taken from the  $^1\text{H}$ -spectra of cell-free and bovine primary chondrocyte laden alginate methyl cellulose scaffolds exposed to hydrostatic pressure or control conditions after 14, 21 and 28 days of cell culture conditions. All values were attained using Tarquin software.

## List of Abbreviations

AF	Annulus fibrosus
Alg/MC	Alginate methyl cellulose
ANOVA	Analysis of variance
BPC	Bovine Primary Chondrocytes
CMFDA	5-chloromethylfluorescein diacetate
ECM	Extracellular matrix
DMMB	Dimethyl methylene blue assay
DMEM	Dulbecco's Modified Eagle Medium
FCS	Fetal calf serum
FDA	Food and Drug Administration
FTIR	Fourier transform infrared
GAG	Glycosaminoglycan
$G'$	Storage modulus
$G''$	Loss modulus
$G^*$	Complex shear modulus
HP	Hydrostatic pressure
ID	Inner diameter
IVD	Intervertebral disc
MC	Methyl cellulose
MHRA	Medicines and healthcare products regulatory agency
MRI	Magnetic resonance imaging
MRS	Magnetic resonance spectroscopy

MTT	3-(4,5-Dimethylthiazol-2-yl)-2,5-diphenyltetrazolium bromide
MW	Molecular weight
NP	Nucleus pulposus
PBS	Phosphate buffered saline
RMS	Root mean square voltage
RT-PCR	Real time – polymerase chain reaction
scCO <sub>2</sub>	Super critical carbon dioxide sterilisation treatment
SEM	Scanning electron microscopy
TA	Tannic acid
T <sub>2</sub>	Transverse relaxation
TGF-β	Transforming growth factor – beta
UV	Ultraviolet
qMRI	Quantitative magnetic resonance imaging

## Chapter 1 Introduction

Severe back pain caused by intervertebral disc (IVD) degeneration and disc herniation is a major public health concern, stated to affect up to 35% of people within their lifetime (Maniadakis and Gray, 2000; Sabzalisenejani and Nikraz, 2013). In the Global Burden of Disease Study (GBD) performed in 2010 it was shown that lower back pain was among the top ten high burden diseases and injuries, with the summated years of disability higher than for HIV, road injury, tuberculosis, lung cancer, pulmonary disease and preterm birth complications (Murray *et al.*, 2012; Reinhart *et al.*, 2012). Furthermore, lower back pain has been stated as the leading cause of inactivity and work absence worldwide which causes an enormous economic burden on individuals, families, communities, industry and governments (Maniadakis and Gray, 2000; Wong *et al.*, 2010; Reinhart *et al.*, 2012; Sabzalisenejani and Nikraz, 2013). The total socioeconomic cost of lower back pain has been estimated in excess of £12 billion per year in the UK alone, including direct medical costs, insurance, lost productivity and disability benefits (Maniadakis, 2000; Sabzalisenejani and Nikraz, 2013).

As a result of the broad severity of lower back pain a substantial number of patients are treated surgically for IVD conditions. In the year 2009–10 there were over 9300 patients who underwent lumbar intervertebral disc excision operations on the NHS in England (NHSdigital, 2010). With an additional 12,500 lumbar decompression surgeries performed, to treat a condition related to the rupture of IVDs (NHSdigital, 2010). The current medical alternative to IVDs on the market are used in excision surgeries and typically consist of generically sized artificial devices made of polymeric and metallic materials (Abi-Hanna *et al.*, 2018). The artificial discs are employed during surgery to fill an excised disc space and have the intended role of disc height preservation upon mechanical loading (Bao *et al.*, 1996; Nerurkar *et al.*, 2010). However, due to the difference in properties of the materials used for artificial discs the devices are often unable to comply with the natural physiological motions of the spine and are subject to wearing (Setton *et al.*, 2007; Rosen *et al.*, 2009). With the resultant debris caused by artificial disc degradation having been linked to inflammatory processes, surrounding tissue necrosis and ultimate device failure (Reeks and Liang, 2015). Correspondingly, prosthesis related complications have

been reported in up to 39.3% of patients who underwent total disc replacement surgery, with reoperation rates of up to 28.6% of patients, as was established in the review on the effectiveness and safety of disc devices by Van Den Eerenbeemt *et al.*, (2010).

However, as a result of recent technological advancement a promising alternative to artificial disc models can be considered in the form of implantable tissue-engineered constructs made from biomaterials and living cells (Hu *et al.*, 2018). The prospect of tissue-engineered spinal discs, compared to artificial cell-free alternatives, would offer the advantage of biologically functional tissue regrowth capable of restoring full spinal motion and disc space maintenance (Este, Eglin and Alini, 2018; Hu *et al.*, 2018). However, the engineering of cartilage tissue represents one of the biggest challenges for regenerative approaches to date, in part due to its innate incapacity for self-regeneration and regionally distinct physiology (Fox *et al.*, 2009; Zhang, Hu and Athanasiou, 2009). As a result, despite the potential benefits of tissue-engineered discs, modern research has yet to yield a clinically approved IVD cellular scaffold capable of mimicking native disc tissue (Ducheyne *et al.*, 2015, Gullbrand, Ashinsky, *et al.*, 2018; Stergar *et al.*, 2019). Therefore, progress towards the medical feasibility of cartilage tissue engineering could hold substantial implications on the future treatment of degenerated or damaged discs, and subsequently was the main incentive for the research employed in this study. Consequently, the topic investigated in this thesis was the development of bioprinting and 3D cell culture methods for the improvement of cartilage engineering, with a particular emphasis on the restoration of IVDs.

In order to achieve engineered cartilage tissue which is suitable for medical implementation, the fabrication and biological components of the engineered structures (e.g. biomaterials and living cells) must adhere to the rules of good manufacturing processes i.e. all processes involved in the scaffold creation must be highly regulated, sterile and reproducible (O'Brien, 2011; Aimar, Palermo and Innocenti, 2019). Through the use of conventional (manual) tissue engineering approaches multiple experiments have been performed under the intention of replicating IVD properties (Nam *et al.*, 2000; Oh *et al.*, 2006; Sin *et al.*, 2010; Wu *et al.*, 2010). However, as a result of strict clinical regulations viable tissue-engineered disc products which are suitable for use in patients have yet to be identified (Gullbrand,

Ashinsky, *et al.*, 2018; Stergar *et al.*, 2019). Nonetheless, due to the advancement of additive manufacturing technology and the advent of cell-laden bioprinting (2003) the possibility of computer-controlled, high-resolution scaffold generation has become a recent reality (Fisher and Mauck, 2013; Liaw and Guvendiren, 2017; Aimar, Palermo and Innocenti, 2019). Within the last decade examples of additive manufacturing approaches for various tissue types has become a well-established research area (Cohen *et al.*, 2010; Mota *et al.*, 2012; Zhu and Chen, 2013; Huang and Zhang, 2014; Do *et al.*, 2015; Jung, Lee and Cho, 2016; Hangge *et al.*, 2018). Yet, despite the development in this field the potential of cell inclusive printing for IVD scaffolds remains underutilised, with sparse evidence of progress towards a cell-laden and clinically approvable full disc approach (Whatley *et al.*, 2011; Whatley, 2013; van Uden *et al.*, 2015a; Rosenzweig *et al.*, 2015). It was this observed gap in current literature that inspired the work carried out in this project and was addressed via the application of cell encapsulated bioprinting for IVD cartilage engineering (layout of the full thesis structure can be found in Fig.1.1).

The development of a cell-laden and one-step fabrication method was a leading motivation for this thesis. Wherein, an all-inclusive bioprinting approach for scaffold production minimises the need for manual processing steps such as cell seeding. In addition, bioprinting is associated with high process repeatability and regulatory control relative to conventional approaches, which enhances the possibility of clinical implementation (Leong *et al.*, 2014). Furthermore, an additional incentive of this work was to use biomedical magnetic resonance imaging (MRI) to assist tissue-engineered scaffold design and non-invasively monitor tissue development. The use of MRI for this purpose included the investigation of biologically significant quantitative MRI (qMRI) parameters which are sensitive to essential cartilage macromolecules (water, collagen and proteoglycan) and were employed in a further attempt to enhance the medical feasibility of the produced scaffolds (Do *et al.*, 2015).

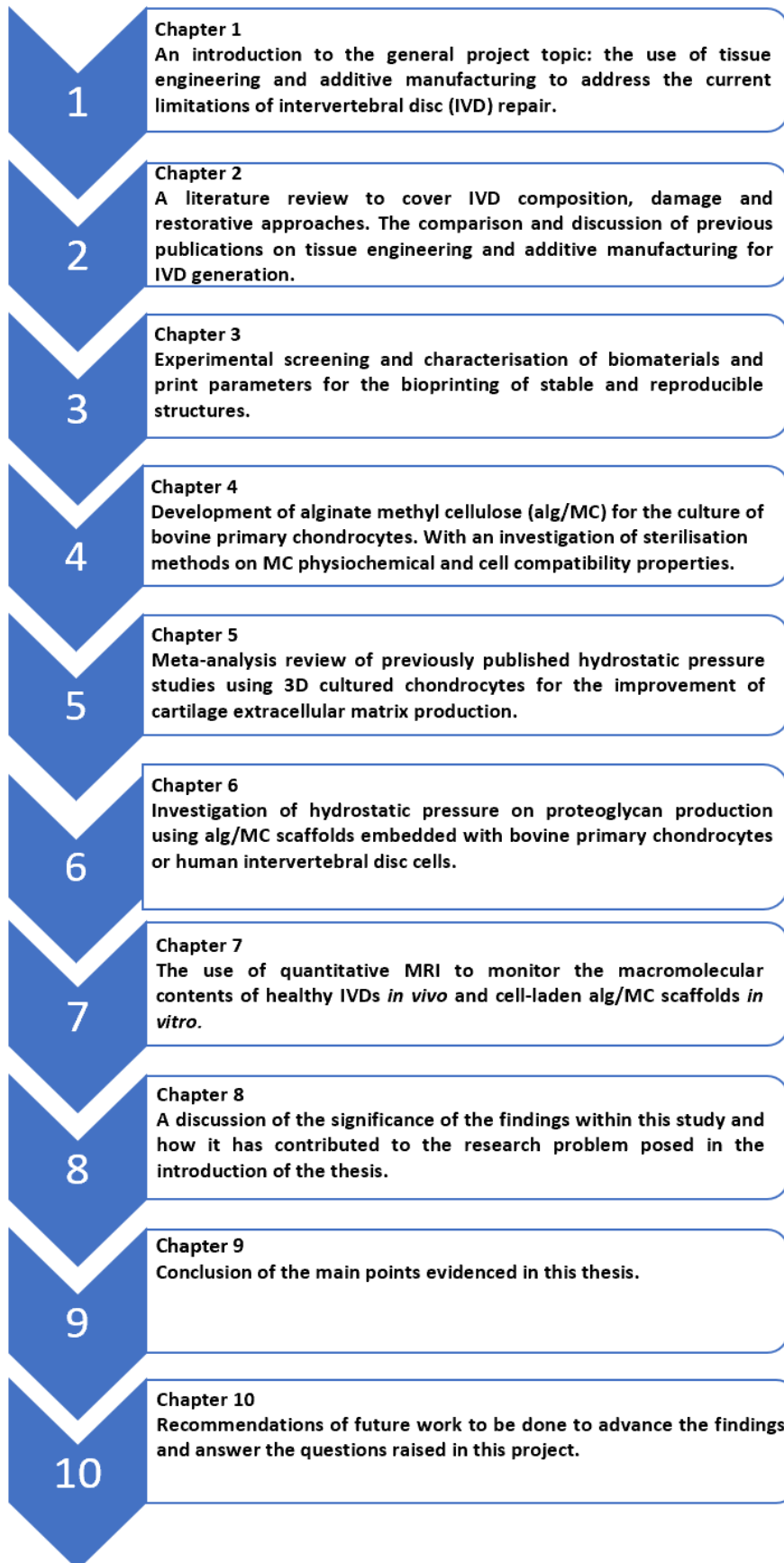


**Figure 1.1** Schematic of thesis structure and content sorted by chapters.

## 1.1 Project aim

The main objective of this research was to develop a clinically feasible fabrication approach to generate tissue-engineered cartilage. Specifically, the project aim was to fabricate scaffolds using bioprinting which can support and maintain chondrocytes, including IVD cells, for the generation of extracellular matrices similar to native disc tissue.

## 1.2 Contribution to knowledge, significance and innovation

The degeneration and damage to spinal discs is one of the most expensive public health issues to date and is a leading cause of disability worldwide (Urban and Roberts, 2003). Despite this, the use of cell-laden bioprinting for disc regeneration remains an under-utilised area of investigation. In part, the lack of research towards bioprinted disc replacements has been justified by the complex and bi-phasic structure of IVDs, as well as their inherently low regenerative capacity (Whatley *et al.*, 2011; Whatley, 2013; Rosenzweig *et al.*, 2015; van Uden *et al.*, 2015; Hu *et al.*, 2018). However, based on a range of previous studies which focused on IVD (Gruber *et al.*, 2004; Mizuno *et al.*, 2004; Choy and Chan, 2015) and articular cartilage engineering (Klein *et al.*, 2009; Oliveira *et al.*, 2009; Bhardwaj *et al.*, 2011) a novel bioprinting approach for generating disc tissue was developed within this thesis. Consequently, an alginate methyl cellulose (alg/MC) bioink was chosen for IVD scaffold development and was selected based on the wide-spread use of alginates in medicine, as well as its biocompatible and mild gelation attributes (Lee *et al.*, 2013; Detsch *et al.*, 2015; Axpe and Oyen, 2016). The addition of MC provided the alginate hydrogel with the properties suitable for bioprinting, and represented an approach which has only been recently established in literature (Ahlfeld *et al.*, 2017; Schütz *et al.*, 2017; Seidel *et al.*, 2017).

In the early stages of the investigation (Chapter 4) the MC component of the alg/MC pastes was fully characterised. Within this work, the effect of MC sterilisation approaches autoclave, super critical CO<sub>2</sub> treatment (scCO<sub>2</sub>), UV and gamma ( $\gamma$ )-irradiation on alg/MC physiochemical and cell compatibility were screened (Hodder *et al.*, 2019). Wherein, natural polysaccharides are commonly susceptible to sterilisation side effects and modifications (Munarin *et al.*, 2013). Consequently, the highly relevant

challenge in bioprinting known as ‘the balance between printability and biocompatibility’ (Bhardwaj, Devi and Mandal, 2015) was addressed within these experiments. The outcome of the sterilisation method experiments on MC demonstrated that the autoclave treatment was significantly improved over the use of scCO<sub>2</sub>, UV and  $\gamma$ -irradiation, and was based on both alg/MC BPC cell compatibility and printability (Hodder *et al.*, 2019). In addition, the findings of this work hold a wider implication in tissue engineering, whereby the use of MC as a sterile and cell-compatible viscosity modifier has the potential to enhance other materials for bioprinting, and has thus far only been employed with alginate (Ahlfeld *et al.*, 2017; Schütz *et al.*, 2017) and hyaluronic acid (Law *et al.*, 2018). The standardised use of MC additives for bioinks would therefore assist the future development of bioprinting approaches, which is currently limited by the poor availability of suitable material candidates (Zhang *et al.*, 2018). Furthermore, the use of alg/MC for bioprinting was the first example of this material being used for the culture of both bovine primary chondrocytes (BPCs) and human IVD (hIVD) cells in literature.

An additional original outcome of the work presented in this thesis was the use of hydrostatic pressure (HP) for 3D cultured bioprinted chondrocytes and was demonstrated in a series of experimental approaches. Firstly, an investigation of HP stimuli for chondrogenesis was carried out in the form of a review based on previous HP literature (Chapter 5). Within this review a meta-analysis of raw data was performed to isolate key experimental factors when using HP with 3D cultured chondrocytes, since such a synthesis of findings for the production of a standardised protocol has not been demonstrated in available literature. Within the next stage of study (Chapter 6) the use of HP factors which were revealed by the meta-analysis work were applied for the 3D culture of BPC and hIVD cell-laden alg/MC scaffolds. The results of the HP experiments repeatedly demonstrated a significantly enhanced cartilaginous matrix following HP exposure when relative to control samples, with a significant up-regulatory effect to proteoglycan production measured by relative gene expression and glycosaminoglycan (GAG) content analysis. Moreover, the anabolic effect of HP exposure on bioprinted BPC and hIVD cells is an approach which has not been previously evidenced in literature and therefore attributed further novelty to this thesis.

In the final experiments presented in this thesis (Chapter 7) another innovative outcome was demonstrated and was achieved through the investigation of quantitative magnetic resonance imaging (qMRI) for tissue engineering. Within these studies the use of the qMRI parameters 'T<sub>2</sub>' and '1H MR Spectroscopy (MRS)' were applied for the measurement of compositional information from both hIVDs *in vivo* and chondrocyte-laden alg/MC scaffolds *in vitro*. The findings of this work revealed that the quantitative measurements related to water (T<sub>2</sub>) and proteoglycan content (MRS) could be obtained from discs and alg/MC samples, and furthermore were sensitive enough to monitor tissue development over time in the engineered tissue. In addition, the MRS measurements recorded in native human discs were the first to have been reported using a 1.5 Tesla (T) MRI. Thus, the results of this study showed that the use of clinical qMRI can be sensitive enough to assist tissue engineering approaches and can be used for monitoring disc matrices in patients.

In summary, this thesis has increased our practical knowledge relating to the development of engineered cartilage using primary chondrocyte and hIVD cell-laden alg/MC bioprinting. Moreover, this work contributed to the field of tissue engineering by furthering the characterisation of clinically feasible bioinks, as well as the development of HP stimulation for enhanced ECM production monitored by non-invasive medical imaging.

### 1.3 Research questions and rationale

The questions posed within this project will aid to generate conceptual advances in cartilage and IVD engineering using bioprinting, with the combined potential of medically available qMRI characterisation.

#### 1.3.1 Question 1: Using bioprinting how can a clinically feasible fabrication approach be developed that would allow for the generation of scaffolds which support chondrocyte survival?

Rationale: Current methods focused on creating IVD scaffolds have been limited in their ability to fabricate scaffolds under conditions compatible to cell inclusive printing (Whatley *et al.*, 2011a; Whatley, 2013; van Uden *et al.*, 2015a). The availability of the

3.1 bioscaffolder (GeSIM, Germany) for this project is capable of multi-material and temperature-controlled material deposition. Through the screening of biocompatible materials with appropriate viscosity and shear thinning behaviour it was theorised that the production of sterile cell-laden and biocompatible structures would be possible.

1.3.2 Question 2: What methods can be used to assist cartilage tissue generation with an extracellular matrix similar to IVDs?

Rationale: It is the aim of a biofabrication approach to create scaffolds with characteristics of native tissues. Via a cell-based approach this would be achieved by the directed stimulation and support of the encapsulated cells to synthesise cartilaginous extracellular matrix (ECM). However, so far, no cell-based methods of IVD replacement have been approved for clinical trial in humans and could be attributed to the biological complexity of tissue-engineered scaffolds in research (O'Connell, Leach and Klineberg, 2015a; Gullbrand, Ashinsky *et al.*, 2018). Typically, the fabrication of IVD scaffolds has involved processes including drug or hormone functionalisation, the use of immunogenic or animal derived biomaterials and a requirement for harsh solvents or UV-irradiated and temperature based cross-linking methods (Reitmaier *et al.*, 2014; O'Connell, Leach and Klineberg, 2015; Gullbrand *et al.*, 2018; Xiongfa *et al.*, 2018; Cuidi Li *et al.*, 2019). All of which can invoke regulatory issues and hinder both cell compatibility and medical device implementation. A hypothesis posed in this study, based on previous research, was that through the combination of suitable biomaterials (biocompatible and mimicking a native tissue environment) with regulatory approvable, cell compatible fabrication conditions (mild temperatures and pressures), appropriate scaffold architectures (high porosity) and cell stimulatory culture conditions that the fabrication of clinically feasible scaffolds with similar ECM compositions to native IVD tissue can be generated.

1.3.3 Question 3: Can medically available MRI be used to effectively evaluate the macromolecular composition of developing cartilage tissues within bioprinted scaffolds *in vitro*?

Rationale: Prior to medical approval for use in patients tissue-engineered structures must be evaluated for their potential as suitable structures for effective tissue replacement (Brockbank, 2013). Based on the current successful utilisation of qMRI parameters for the assessment of tissues and implanted medical devices *in vivo*, it can be theorised that qMRI could also be implemented as a tool for the analysis of engineered tissues *in vitro* (Mwale, Iatridis and Antoniou, 2008; Iatridis and Mwale, 2014; Grunert *et al.*, 2015). The use of clinical 1.5 Tesla (T) and 3 T MRI machines for the quantification of macromolecular properties within tissues other than the brain has been limited, due to measurement sensitivity (Tanenbaum, 2006). However, the use of clinical MRI, if applied effectively, would provide a more widely and financially accessible method of attaining MR data from specialised body parts such as the IVDs or biological scaffolds. Furthermore, a non-destructive method for monitoring engineered tissues such as qMRI represents an important attribute for the future of biological implant verification (Kotecha *et al.*, 2013; Kotecha, Klatt and Magin, 2013); one which is not currently available using laboratory based methods such as gene expression analysis, protein assays, histological staining or immunohistochemistry.

## Chapter 2 Literature review

Before the laboratory based investigations of this thesis were commenced an exploration of the relevant and previously published literature on IVD cartilage and cartilage tissue engineering approaches were discussed and evaluated. The methodologies used by other researchers were studied and key topics including conventional fabrication versus additive manufacturing, the clinical requirements of tissue-engineered products and the biocompatible use of materials and mechanical stimulation for cell phenotype and ECM guidance were discussed. The aim of this literature review was to identify gaps in the current literature on additive manufacturing for tissue-engineered IVD replacements and to guide the research undertaken in the remainder of this thesis towards the goal of a clinically feasible bioprinting approach for disc tissue generation.

### 2.1 Intervertebral disc tissue

#### 2.1.1 Physiology

The IVD is a shock absorbing cartilage type tissue, found sandwiched between each vertebrae in the spine as shown in Fig.2.1. There are 23 IVDs in the human spine, and they account for approximately one-third of the height of the entire spinal column (Setton, Bonassar and Masuda, 2007). Healthy discs consist of a unique structure that enables them to perform their main functions. These functions include the ability to resist compression, support body weight and allow the bending and twisting motion of the spine (Oxland, 2015). The IVD is composed of an extracellular matrix (ECM) made up of a mesh of inter-connecting proteins which are secreted by chondrocytes (Setton *et al.*, 2007; Steele *et al.*, 2014). Like all tissues, the IVD ECM surroundings serve many important functions including structural support, tissue segregation, regulation of intercellular communication, the distribution of growth factors and the ability for response mediated degradability (Chan and Leong, 2008). Differences in the ECM composition across IVDs separate the disc into three main regions, each with its own molecular make-up and resulting function (Chan and Leong, 2008). The three major sections of an IVD include the following (Fig.2.1):

- The nucleus pulposus (NP): A gelatinous-like centre, rich in proteoglycans, collagen type II, elastin and water. Proteoglycan proteins osmotically exert a swelling pressure to bear compression.
- The annulus fibrosus (AF): A type I collagen-rich fibrous structure with ~15-25 highly orientated lamellae surrounding and confining the NP; oriented at ~60° to each other, with fibrils within each adjacent lamella alternating at ~28°.
- The vertebral endplates: Are composed of a layer of thickened cancellous bone and allow for nutrient transport exchange between the vertebral bone marrow and the discs.

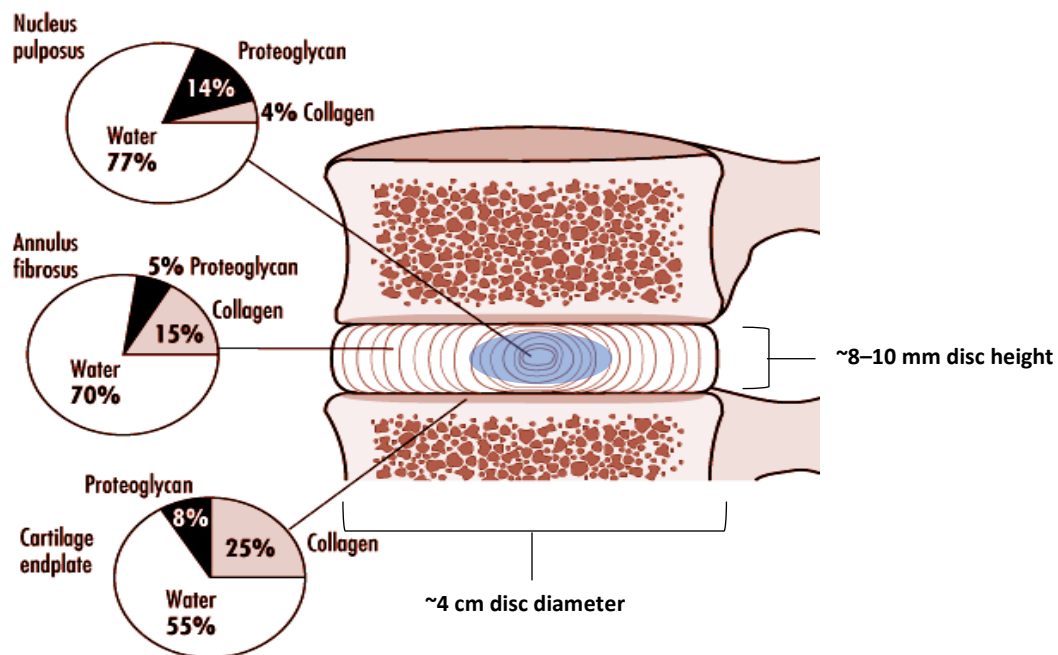


**Figure 2.1** Compositional diagram of a healthy human intervertebral disc, consisting of a nucleus pulposus, annulus fibrosus and the cartilage endplates. Original image sourced from encyclopaedia of occupational health and safety: [www.ilocis.org/documents/chpt6e.htm](http://www.ilocis.org/documents/chpt6e.htm).

### 2.1.2 Mechanical properties

The unique composition of the IVD ECM provides the tissue with important physical properties to consistently distribute and withstand the mechanical loading of the spine, including compressibility (supported by the NP) and shear strength (imparted by the AF) (White, 1989). The disc sections work in a synchronistic way so that when the external compressive load is high the pressure inside the NP region increases and water is squeezed outwards to resist compressive stress, it is then the job of the enclosing AF to contain this re-distribution and avoid protrusion (Fig.2.2). When the NP pressure decreases the water returns, exchanging nutrients and waste via the external capillaries within the adjacent vertebral end plates (Bao *et al.*, 1996). The pump like action of exchanging nutrients is an important feature of IVDs since they are avascular structures and rely on this method of creating osmotic gradients for obtaining nutrients from blood vessels at the disc's margins (Bao *et al.*, 1996).

The compressive modulus of the IVD varies between the AF and NP regions, a result of the different ECM macromolecule ratios (Table.2.1). Proteoglycan and water content increases from the outer AF towards the proteoglycan rich NP, while collagen content decreases from the outer AF to the NP. This macromolecular distribution gives each disc region its own physical properties (Table.2.1). For example, the compressive modulus of the AF has been reported to range from 0.116-2.3 MPa (Mow *et al.*, 2004) and this is associated with the high concentration of collagen type I fibres within the AF ECM. Conversely, in the NP the compressive modulus has been reported to range from 0.003-0.031 MPa (Mow *et al.*, 2004) and deforms less due to a lower level of collagen and a higher water content (Mow *et al.*, 2004; Whatley, 2013). Compressive modulus values inclusive of the whole disc are stated to range from 0.5-16.37 MPa (Setton, Bonassar and Masuda, 2007; Pei *et al.*, 2013).

Furthermore, the IVD while undergoing physical deformation is known to exhibit both viscous and elastic characteristics, and so is considered to be a visco-elastic tissue i.e. it has a time dependent linear force resistance but it will recover to its original form once the stress is removed (Oxland, 2015). However, when disc structures are disrupted, for example through degeneration or the result of injury, the disc ECM can

break down and the tissue integrity, elasticity and viscoelasticity is lost (Andersson, 1998).

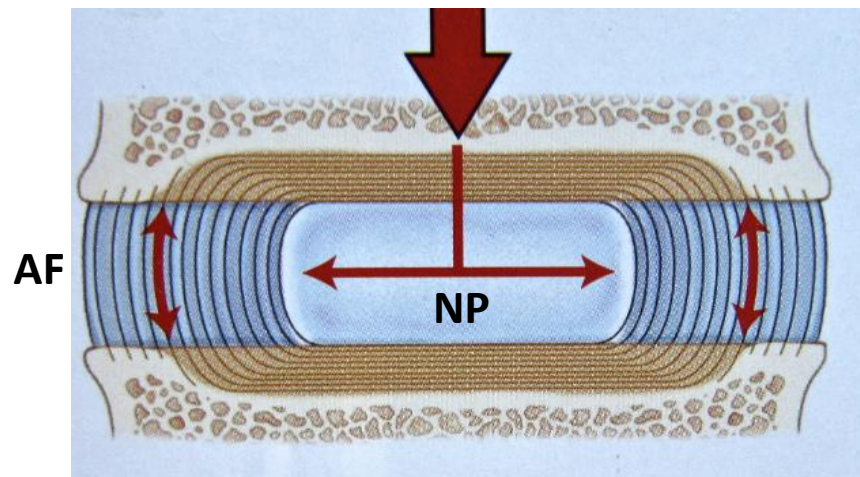


**Figure 2.2** Diagram to demonstrate the distribution of an axial compressive force on intervertebral discs, the load is resisted by the swelling pressure of the nucleus. During NP compression water is extruded outwards and the stress is then dissipated across the disc through the annulus layers. Image sourced from: <https://ittcs.wordpress.com/2010/06/01/anatomy-and-physiology-the-intervertebral-discs/>.

**Table 2.1** Difference in intervertebral disc extracellular matrix composition and mechanical properties between the annulus fibrosus and nucleus pulposus (Marchand and Ahmed, 1990; Best *et al.*, 1994; Antoniou *et al.*, 1996; Wilke *et al.*, 1999; Klisch and Lotz, 2002; Elliott *et al.*, 2004; Mow, Huiskes and Abreu, 2005; Périé, Korda and Iatridis, 2005; Whatley, 2013).

	<b>Outer AF</b>	<b>Inner AF</b>	<b>NP</b>
<b>*1 Water (per weight)</b>	65-75%	75-80%	75-90%
<b>*2 Collagen (per dry weight)</b>	75-90%	40-75%	25%
<b>*3 Proteoglycans (per dry weight)</b>	10%	20-35%	20-60%
	<b>AF</b>	<b>NP</b>	
<b>Compressive Modulus (MPa)</b>	0.116-2.3	0.003-0.031	

\*1 Samples in this analysis were dried at 110° C for four days to obtain the dry weight. Water weight was measured based on the wet weight subtracted by the dry weight of the tissue samples (Antoniou *et al.*, 1996). \*2 Hydroxyproline content was obtained from the dried tissues, whereby hydroxyproline content was considered as equivalent to 10% of the weight of each collagen alpha chain, total collagen content per dry weight was estimated. \*3 Extracts derived from the alpha-chymotrypsin and proteinase K digestions were used for measurement of the total proteoglycan content as sulfated GAG content per dry weight with the dimethyl methylene blue dye binding colorimetric assay.

## 2.2 Disc herniation and lower back pain

Spinal trauma can be categorised by a variety of injuries including damage to the vertebrae and vertebral endplates, ligaments, intervertebral discs or the spinal cord (Oxland, 2015). However, the most common failure mechanisms of the spine include endplate fractures and disc herniation (Fields *et al.*, 2010; Wade *et al.*, 2014).

Disc herniation is considered to be a leading contributor to the condition known as lower back pain, which has been one of the most common medical conditions in the western world (Bao *et al.*, 1996) and significantly affects over 70% of people within developed countries (Choy and Chan, 2015). In the USA, lower back pain is reported as the leading cause of disability in people under the age of 45, the second main cause of physician visits with days missed from work and the third most common cause for surgical procedures (Weber *et al.*, 2015).

The term disc herniation is a condition in which the NP 'herniates' or slips through the surrounding protective AF layers, ultimately leaking into the spinal canal and putting pressure onto adjacent nerves, associated with pain and sciatica (Weber *et al.*, 2015). Disc herniation is commonly found to afflict the lumbar region of the spine, which is the most mobile and load bearing spinal section, between the fifth lumbar vertebra and the first sacral vertebra (O'Connell *et al.*, 2015). The cause of disc herniation can be combined into three main categories: injury, degeneration and both injury and degeneration combined (Oxland, 2015).

Injury instigated herniation can be caused by a variety of factors including external trauma such as sports injury, repetitive strain (frequently experienced by workers in manual trades e.g. building/painting), or high impact accidents for example following a car crash (Pradeep *et al.*, 2010). Within the last half-century significant progress has been made towards understanding spinal mechanics through a series of laboratory based studies to recreate and explore spinal motion (Kemper *et al.*, 2007; Kingma *et al.*, 2007). In general, the investigations looked at the effect of spinal stresses such as rapid out of plane loading, long-term cyclic loading and high-rate single impacts on the biomechanical functions of IVDs, to successfully recreate and demonstrate the main features which lead to disc herniation (Veres *et al.*, 2009). The combination of physical studies alongside mathematical modelling concluded that disc herniation can be considered the result of initial AF stretching (often to its limit) followed by a subjection to high compressive loads (Wade *et al.*, 2014; Oxland, 2015). Thus, any direct, forceful and vertical pressure can cause the nucleus to be pushed outwards towards the vertebral body and any sudden lifting, twisting or repetitive movements can worsen the condition to become a full disc herniation (Veres, Robertson and Broom, 2009).

Disc herniation and lower back pain can also be caused by gradual degenerative changes, in which intensifying symptoms are often reported by patients as the annulus becomes weakened over time (Wang *et al.*, 2012). Disc degeneration, either due to disease or natural ageing involves a structural, functional, mechanical, nutritional and chemical alteration in the affected discs (Iatridis *et al.*, 1997). One of the first markers of disc degeneration is the breakdown of the protein proteoglycan within the NP (Zuo *et al.*, 2012). The loss of proteoglycan, essential for hydration, is responsible for the loss of osmotic pressure of the IVD (Raj, 2008). This loss of water from the NP then decreases the disc's ability to resist compressive forces and triggers a knock on effect

of the mechanical properties of the whole disc. The weakened disc ultimately leads to a loss of demarcation between the two disc phases as the AF breaks down (van Uden *et al.*, 2015a). In this way, disc degeneration can also be considered as a predisposing factor to disc herniation, as the annulus is weakened it is more sensitive to disruption, leading to an increased potential for NP leakage. The weakening of the AF over time is an attributing reason as to why the tendency for disc herniation increases with age (Van Den Eerenbeemt *et al.*, 2010).

## 2.2.1 Current clinical interventions

### 2.2.1.1 Surgical solutions

The tremendous financial impact of lower back pain (such as lost productivity and increased health costs) as well as the damaging effects to patient quality of life, provide a huge incentive for new clinical solutions for IVD restoration (Renema *et al.*, 2007). However, the current prevailing treatments for disc repair remain primarily symptomatic rather than curative and rely mostly on two types of surgical interventions (Bao *et al.*, 1996; Grane and Lindqvist, 2009; Punt *et al.*, 2012) (Fig.2.3):

- Spinal fusion: The immobilisation of the damaged region using an implanted 'cage' to fuse adjacent vertebral bones together, preventing movement
- Discectomy: The surgical removal of the herniated disc portion

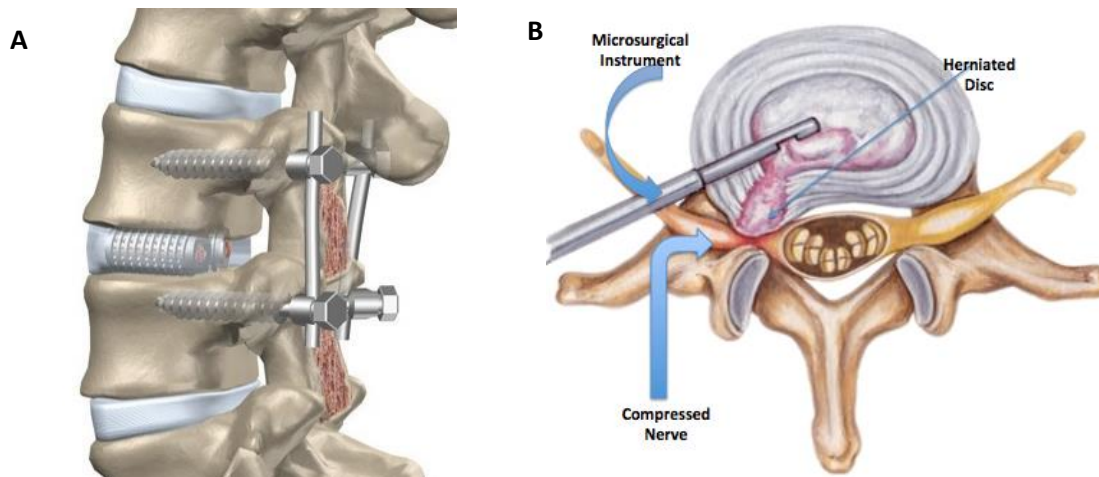


**Figure 2.3** Diagrams to demonstrate the current surgical interventions for disc herniation (A) Disc fusion, first the damaged disc is removed and replaced by a spacer, then the spinal cage is screwed in place to fuse adjacent vertebrae into a fixed position (B) Surgical process of discectomy, the herniated and damaged tissue is removed using a microsurgical instrument. Images sourced from [www.newhealthadvisor.com/Spinal-Fusion-Recovery.html](http://www.newhealthadvisor.com/Spinal-Fusion-Recovery.html) and <http://spineonline.net>.

Discectomy and fusion are widely used invasive procedures that provide a relatively good clinical result in relieving pain and are especially appropriate for the treatment of elderly patients with less actively demanding lifestyles (Wan *et al.*, 2008). However, the positive outcomes of spinal procedures are often short lived with both discectomy and fusion treatments being linked to a change in spinal biomechanics that cause the degeneration of surrounding tissue at adjacent levels (Gloria *et al.*, 2007; Bowles *et al.*, 2012). An example of the long-term outcome of discectomy surgery on disc herniation patients was demonstrated by the study by Loupasis *et al.*, (1999). This work was based upon the answers of a self-report questionnaire and was completed by 109 patients with questions on their satisfaction following surgery, whether they had a need for pain relief medication, their level of activity, their working capacity and if there was a need for reoperation. The study revealed a 46% dissatisfaction in reviewed patients, with more than one quarter still experiencing significant residual pain (Loupasis *et al.*, 1999). Similarly, a follow-up report by Nguyen *et al.*, (2011) demonstrated the short-term relief of spinal fusion and reviewed records from 1,450

patients. The study found that within a two year time span patients following fusion surgery had a statistically significant increase in disability, with a 43% increase in pain relief use and only 26% returning to work compared to 76% of non-surgically treated patients (Nguyen *et al.*, 2011). Therefore, it is accepted that despite short-term symptom relief the conventionally used surgical options of discectomy and fusion are not considered a long term solution for disc hernia patients. The reason for the failure of current surgical interventions is linked with the reparative approach, in which neither discectomy or fusion is capable of restoring disc function or replacing the natural motion of the spine which subsequently leads to the limitation of patient mobility. As a result, new efforts have been made to develop an artificial disc to replace degenerated or damaged discs (Beer and Merwe, 2013; van Uden *et al.*, 2015b) with the incentive of restoration of natural biomechanics after disc excision, to relieve pain and prevent further degeneration to nearby segments. The issue with artificial replication, however, is the complex and functionally demanding environment of a native disc, which makes the long-term mimicry of biomechanics difficult for device materials and designs (Bao *et al.*, 1996).

#### 2.2.1.2 Artificial disc replacements

Artificial disc replacements have been established for medical use in Europe for over a decade and are gaining interest and clinical approval in the United States (Salzmann *et al.*, 2017) (FDA U.S. Food and drug administration, 2018) (Fig.2.4). The artificial discs have conventionally come in a range of designs and sizes, made from mostly polymers (polyethylene, polyether ether ketone, PEEK) and elastomers (silicone, polyurethane) as well as metallic materials (titanium, cobalt chromium alloys), to suit the variation of disc excisions (Bao *et al.*, 1996; Reeks and Liang, 2015). Examples of current commercially available FDA approved artificial discs include the European devices known as the SB Charité® and ProDisc®. Both of which have since been approved in the US and have been shown to decrease operative time, blood loss, and length of hospitalisation when compared to spinal fusion (Whatley, 2013). The SB Charité® is made up of two cobalt chromium alloy endplates coated with titanium and hydroxyapatite to promote external bone integration, and a polyethylene mid-section spacer (Reeks and Liang, 2015). Similarly, the ProDisc® has endplates made of a cobalt chrome molybdenum alloy and a bearing surface containing porous coatings or

screws to promote bone ingrowth for fixation (Van Den Eerenbeemt *et al.*, 2010). Another, the Maverick® is an all metal implant and is undergoing clinical trials for longevity (Punt *et al.*, 2012, Sharifi *et al.*, 2015).

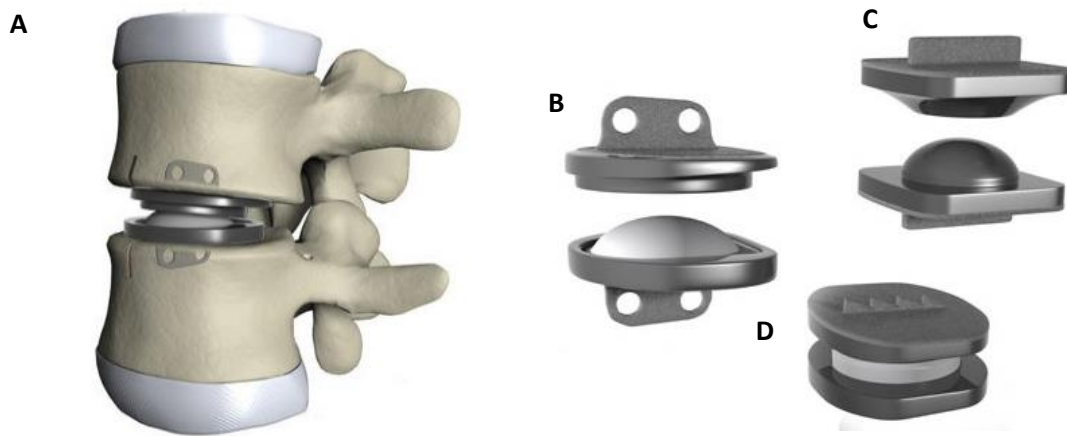


**Figure 2.4** Artificial disc models (A) ProDisc® implanted in position, (B) ProDisc® alone, (C) SB Charité®, (D) Maverick®. Images sourced from <https://ryortho.com/>.

However, although artificial discs can aid disc height preservation there are still significant limitations in their use, mostly due to their rigid material make up which inhibits their ability to replicate physiological motions or to absorb compressive forces (Gloria *et al.*, 2007). The metallic/polymeric compositions used in the disc devices are chosen for strength and longevity, however in multiple cases these materials have been linked with the production of damaging wear particles as well as causing osteolysis (bone cell death) (Shuff and An, 2005). Furthermore, the artificial implants commonly possess increased physical compliance and density in comparison to native disc tissue. This disparity between the physical properties of artificial IVDs and native disc tissue can result in the phenomenon of ‘stress shielding’, in which abnormal forces are generated along the spine during motion leading to damage of adjacent discs, as well as possible implant migration (Bono and Garfin 2004). Thus, although artificial disc interventions can alleviate some symptoms of disc degeneration in clinical use, they can lead to further degeneration at adjacent vertebrae levels, similar to discectomy and fusion. However, there is another promising solution to tackle the

problem of herniated or diseased discs, and this lies in the field of tissue engineering and regenerative medicine.

### 2.3 Tissue-engineered scaffolds in regenerative medicine

Tissue engineering is a multidisciplinary field that combines the use of cells, engineering materials, and physicochemical factors to improve, replace and regenerate the biological functions of damaged tissues or organs (Chan and Leong, 2008). An expanding area of interest for tissue engineering is the development of structures or 'scaffolds' as implantable devices for site-directed tissue synthesis. Tissue-engineered scaffolds function by contributing to the regenerative process of tissues and have been well implemented in the research of anatomy such as bone, cartilage, ligament, skin, vascular tissues, neural tissues, and skeletal muscle (Fisher and Mauck, 2013).

The role of a scaffold is to provide a protective and structural framework to support cell adhesion and proliferation, for directed tissue generation and survival *in vivo* (Chan and Leong, 2008; Woodfield *et al.*, 2009). When designing a scaffold, the general aim is to reproduce the ECM of the target tissue by using materials, factors and growth conditions which appropriately guide cells towards the desired cell phenotype and resultant tissue type (Fisher and Mauck, 2013). Thus, the scaffold operates with the intent of promoting tissue growth as biologically close to the native state as possible (Terzic and Nelson, 2013). However, bodily tissues are highly diverse, made up of a mesh of inter-connecting proteins with numerous tissue-specific compositions and for this reason they are difficult to mimic (Chan and Leong, 2008).

### 2.4 Tissue engineering for intervertebral disc restoration

The fabrication of cell-based biomimetic disc alternatives holds significant potential for the improved treatment of intervertebral disc degeneration/damage compared to current artificial disc replacements (Este, Eglin and Alini, 2018; Hu *et al.*, 2018; Gullbrand *et al.*, 2018). The successful application of tissue-engineered IVD scaffolds would result in the restoration of healthy tissue and thus return the ability to support

the physiological motions of the spine (Woods *et al.*, 2010). Consequently, to date it can be considered that the most promising avenue for meeting the both the biological demands of native tissue as well as clinical feasibility is through the use of computer controlled additive manufacturing approaches. Wherein, the customisability and reproducibility of additive manufacturing processes fair well on both repeatability and the generation of complex architectures, suited to mimicking native tissues. However, a cell-laden tissue engineering approach to disc replacement is innately more complex than the currently employed acellular artificial models and must overcome multiple obstacles before their clinical implementation is possible.

#### 2.4.1 Clinical feasibility

The implementation of patient-specific 3D printed anatomical models in healthcare has become increasingly useful in today's practice of precision medicine and personalised treatments (Aimar, Palermo and Innocenti, 2019), with many bespoke biomedical products already used in a wide range of healthcare settings including, cardiothoracic surgery (Kurenov *et al.*, 2015), cardiology (Vukicevic *et al.*, 2017), neurosurgery (Randazzo *et al.*, 2016), gastroenterology (Jeon *et al.*, 2017), oral and maxillofacial surgery (Saijo *et al.*, 2009), ophthalmology (Aldaadaa, Owji and Knowles, 2018), orthopaedic surgery (Eltorai, Nguyen and Daniels, 2015; Auricchio and Marconi, 2016), plastic surgery (Chae *et al.*, 2015), podiatry (Williams *et al.*, 2015), transplant surgery (Zein *et al.*, 2013) and aortic surgery (Hangge *et al.*, 2018).

The widespread use of additive manufacturing has therefore already become well established in medicine. However, more revolutionary manufacturing applications such as bioprinting also known as 'bioplotting' or 'extrusion printing' of organs and tissues have taken more time to evolve, hindered by the possibility of cell associated issues (Ventola, 2014; Cui *et al.*, 2017) including:

1. The foreign body reaction: when the implantation of foreign material triggers the host's innate immune system and causes a mass infiltration of white blood cells and change in the healing response.

2. Fibrosis: The thickening and scarring of connective tissue which encapsulates the implant and reduces blood supply, as well as nutrient exchange to the cells inside. Fibrosis is the result of a foreign body reaction.
3. Inflammation: Redness, heat, swelling and pain caused by the immune response. During swelling the capillaries become constricted so blood cannot be taken away from the area and white blood cells initiate localised apoptosis.
4. Calcification and cancer: Growth factors often used in cell culture can enter the body during implantation and may lead to unpredictable cell behaviour such as an unregulated growth of cells (cancer) or calcification (the build-up of calcium in the body). A calcification build-up can harden and disrupt the body's normal processes.

As a result of the potential issues with biologically active scaffolds, the majority of tissue-engineered products have failed to achieve clinical approval by regulatory bodies such as 'the medicines and healthcare products regulatory agency (MHRA)' in the United Kingdom and the 'food and drug administration (FDA)' of the United States of America (Abi-Hanna *et al.*, 2018). It is therefore of high importance to take into consideration these potential side-effects during IVD scaffold design and to come up with novel fabrication and culture methods which limit unwanted physiological responses in patients. According to these guidelines, methods with improved clinical feasibility would likely include the use of appropriate cell-compatible and degradable biomaterials that are capable of cell guidance, without a reliance on supplements such as growth factors (Gstraunthaler, 2003; Murphy and Atala, 2014; Cui *et al.*, 2017).

#### 2.4.2 Mechanobiology

From a review of the current and past tissue engineering literature, mechanobiology was identified as a promising field of research for directing chondrogenic culture by mimicking the native *in vivo* conditions of articular joints (Thompson, 1917; Hsieh and Twomey, 2010; Chen *et al.*, 2013; Martino *et al.*, 2018). The topic of mechanobiology focuses on how the use of mechanical stimulated cell culture can be used to contribute to guided cell development, differentiation and physiology (Weber *et al.*, 2015).

The employment of mechanobiology dates back to as early as the 20th century with the 1917 publication of 'On Growth and Form' by D'Arcy Thompson (Thompson,

1917), as one of the first researchers to pay attention to the effects of physical stress on cells. Work on mechanobiology and its influence on how cells migrate, interact and adhere to one another eventually became more popular in the 1980s, driven forward by new techniques which made it possible to observe the mechanical forces exerted on cells and their environment (Wheeler, Fitzgerald and Grodzinsky, 2005; Chen *et al.*, 2013; Lee *et al.*, 2018). Since the 1980s, the use of mechanobiology for chondrocytes and stem cells has been employed in an array of scientific studies and effectively mimics the dynamic conditions found within articular cartilage, such as hydrostatic pressure (HP) (Candiani *et al.*, 2008; Elder *et al.*, 2009a; Li *et al.*, 2016a), compression (Guilak, Ratcliffe and Mow, 1995; Diferico and Shelton, 2017) and shear stress (Fitzgerald, Jin and Grodzinsky, 2006; Nugent *et al.*, 2006). As a result, it is commonly accepted that when chondrocytes or stem cells are cultured with exposure to mechanical forces, an improved cartilaginous physiology can be achieved (O'Connor, Case and Guilak, 2013; Anderson and Johnstone, 2017).

Although the biophysical and biochemical events involved in mechanotransduction (the process which convert mechanical stimulus into an anabolic response) are still not fully understood, primarily due to the complex nature of signalling pathways and ECM interactions with cells. It has been suggested that chondrocyte mechanoreceptors such as mechanosensitive ion channels (Martinac, 2004) and integrins (Ingber, 1991) are likely to be involved in relaying mechanical stimuli into cellular response. In brief, these receptors upon activation initiate intracellular signalling cascades leading to tissue remodelling (Ramage, Nuki and Salter, 2009; Zhang, Chen and Pei, 2016). Tissue remodelling as a result of mechanobiology is induced by either anabolic responses, which cause the production of new tissue (proteoglycan and/or collagen II), or catabolic reactions which remove damaged cells. Maintenance of healthy tissues depends on the balance between matrix anabolism and catabolism and is shown to be directly influenced by mechanical pressures, such as the magnitude and frequency of their application (Ramage, Nuki and Salter, 2009). However, despite evidence of mechanical stimulation for the improvement of cartilage ECM development (an area of high importance for the future of cartilage healthcare) an effective protocol for long-term pressurised cell culture has yet to be standardised. The confusion around the protocol parameters required for mechanotransduction has been especially evident in studies which have utilised HP and is made clear by a

comparison of the experimental setups used. Examples of this disparity among experiments have included a wide variation in pressure magnitude application, ranging from 0.3 MPa (Heyland *et al.*, 2006) and 0.35 MPa (Hutton *et al.*, 2001) to 10 MPa (Hu and Athanasiou, 2006; Elder and Athanasiou, 2008; Kunitomo *et al.*, 2009). As well as, the method of HP application within papers which have shown a mixed use of either dynamic HP loading, such as intermittent or cyclical HP applications (Suzuki *et al.*, 2006; Heyland *et al.*, 2006; Kawanishi *et al.*, 2007; Tatsumura *et al.*, 2013), or static loading approaches (daily or one-off loading) (Toyoda *et al.*, 2003; Kunitomo *et al.*, 2009). Thus, the lack of a unified approach for HP based mechanotransduction experiments can be seen as a considerable gap in knowledge. Furthermore, the identification of a repeatable HP method for effective cartilage ECM stimulation would offer a highly beneficial outcome, which would be widely applicable for cartilage engineering.

#### 2.4.2.1 Mechanical properties of tissue-engineered scaffolds

In addition to the culture conditions employed, the overall mechanical properties of tissue-engineered structures represents a key determining feature in their ultimate clinical application. At the stage of implantation, it is important that a scaffold or artificial replacement has the mechanical properties which are suitable for the injury/tissue site (Nerurkar, Elliott and Mauck, 2010).

The compressive modulus of IVD scaffolds should typically range from 0.5-5.0 MPa, with a compressive strength of at least 8-10 MPa (Setton *et al.*, 2007, Nerurkar *et al.*, 2010, Oxland, 2015) measured in both static and dynamic compressive test conditions. In addition, viscoelastic properties are also important for replicating disc mechanics (Wang *et al.*, 2012) as are properties during bending and torsion (Krismer *et al.*, 2000; Oxland, 2015).

For acellular artificial disc designs such as the Charité® and Maverick®, the ability to withstand spinal loading is made possible as a result of their physical composition, made primarily of metal such as titanium or high strength polymeric materials such as PEEK (Bao *et al.*, 1996). However, in the case of tissue-engineered cell-laden constructs, a high innate strength is more difficult and timely to attain, due to the

reliance on the cells to produce an ECM over time which sufficiently mimics the physical properties of the native tissue (Nerurkar, Elliott and Mauck, 2010). The main reason for this is the limited availability of materials suitable for cell-laden scaffold fabrication. The most common utilisation of biomaterials within the field of tissue engineering has been hydrogels, such as collagen, chitosan, gelatine and alginates (Hoffman, 2002; Zhu and Marchant, 2011; Hunt *et al.*, 2014). The popularity of hydrogels is the result of their cell compatibility, which is associated with their high-water content matrices of polymers (Zhang *et al.*, 2015). However, hydrogels by nature have a relatively low resistance to being deformed with an elastic moduli in the range of 0.01 to 10 kPa (Okay, 2009). Thus, in cell-laden constructs the material used for scaffold fabrication is not typically capable of immediately withstanding the high physical demands such as those found in joints *in vivo* (Zhu and Marchant, 2011). Although, hydrogel properties can be manipulated to increase their mechanical properties by altering the conditions under which the hydrogel is formed i.e. the cross-linker concentration, the initial degree of dilution of the monomers and the chemistry of the units building the network structure, as well as by combination with other materials (Orakdogan and Okay, 2006). In general, to sufficiently overcome the physical disparity between hydrogels and tissue the chosen material must be able to support the development of cells towards the production of an ECM that will mimic the native tissue strength (Duarte Campos *et al.*, 2012). Thus, the selection of a material for tissue engineering is not necessarily determined by its physical properties but rather by how effectively the material can guide cells to generate functional tissue (Maher *et al.*, 2009; Melchels *et al.*, 2012; Xiongfa *et al.*, 2018). The aim of the cell-laden scaffolds, therefore, differs from the artificial acellular counterparts, in that the intended outcome is for the material to be replaced by a biological matrix. It is thus the task of the tissue-engineered scaffold to be able to encourage, maintain and direct cell growth to achieve an ECM for physical sustenance (Hunt *et al.*, 2014; Bhardwaj, Devi and Mandal, 2015).

#### 2.4.2.2 Monitoring tissue development

Before the implantation of tissue-engineered structures the scaffolds must be able to meet the physiological demands of the native tissue they are replacing, wherein the physical properties of the scaffolds are dependent on the ECM that has been produced by the cells within it (Martino *et al.*, 2012; Do *et al.*, 2015). It is, therefore, essential to monitor the ECM within the scaffolds during cell development to assess tissue viability (Kular, Basu and Sharma, 2014). The assessment of tissue ECM composition is determined by the quantification of key macromolecules and their relative proportions (Kular, Basu and Sharma, 2014). For the assessment of cartilage the main ECM molecules of importance include collagen type I and II and proteoglycan (Gentili and Cancedda, 2009). Examination of the ECM macromolecular composition is commonplace in tissue engineering and can be performed via many different methods including:

- Reverse transcription polymerase chain reaction (RT-PCR): A laboratory technique which combines the reverse transcription of RNA into DNA. Specific DNA targets are amplified using the polymerase chain reaction. It is used to quantitatively measure the amount of specific RNAs associated with a chosen tissue phenotype (Matyas *et al.*, 2002; Ponchel *et al.*, 2003).
- Histological staining: The use of dyes which selectively stain cells or extracellular matrix proteins and can be observed using microscopy (Schmitz *et al.*, 2010).
- Immunostaining: A procedure to detect specific proteins within a sample which relies on the use of antibody-antigen binding reactions (Manabe *et al.*, 1995).
- Protein micro-assays: a spectroscopic based analytical method used to measure the concentration of protein in solution (Barbosa *et al.*, 2003).

However, once a scaffold has been developed to a stage nearing clinical application, the lab-based methods of ECM assessment are no longer well suited (Kotecha, Yin and Magin, 2013). The laboratory-based analytical methods of ECM commonly rely on sample destruction for measurement acquisition i.e. once the tissue has been sampled it is irreversibly altered and the cells are no longer alive or functional. The

destructive system of scaffold monitoring is acceptable for early stage assessment of scaffold progress (Fisher and Mauck, 2013). Conversely, with the generation of new tissues for medical implementation a large quantity of a patient's cells is needed and the continual destruction of the cell-laden samples during measurement would be a highly inefficient way of monitoring tissues progress (Kotecha, Yin and Magin, 2013). Subsequently, the use of non-invasive methods for monitoring ECM composition such as quantitative medical imaging offer a promising solution to assist the translation of engineered tissues for use in patients (Schulz *et al.*, 2007; Li *et al.*, 2010; Lalande *et al.*, 2011; Jeffries and Macdonald, 2012; Weber *et al.*, 2012; Kotecha, Yin and Magin, 2013).

#### 2.4.3 Magnetic Resonance Imaging

MRI techniques have been applied in medicine, primarily in brain imaging, since their advent in the 1980's (Boulby, 2003). Non-invasive MRI scanners can be utilised to provide insight into tissue properties and processes at varying depths and dimensions. In particular, MRI has been applied as a useful method for the assessment of injury sites prior to medical device implantation, as well as a way of monitoring tissue integration of the structures following surgery (Grane and Lindqvist, 2009; Xian, Chen and Jin, 2015). Furthermore, the application of MRI offers important advantages over other medical imaging techniques such as computed tomography (CT), by obtaining images with high sensitivity and resolution (~0.5-1mm in each direction) without the use of potentially harmful or carcinogenic ionizing radiation (Murphy and Atala, 2014).

MRI scanners use strong magnetic fields and radio-waves to generate images for the study of intrinsic processes in biological tissue (Gründer, 2006). A sample under MRI investigation is first placed in a large magnetic field and becomes magnetised. Radio-frequency pulses are applied to the samples within the MRI machine at a frequency which causes the hydrogen-1 nuclei (protons commonly present in biological water or fat) to produce a MR signal (Grunert *et al.*, 2015). Magnetic field gradients are used to spatially encode these signals (Lalande *et al.*, 2011). The intensity of the MR signal from a given region within a sample depends on a number of intrinsic properties of the

object: the number of  $^1\text{H}$  nuclei<sup>1</sup> in a given volume (proton density), the lifetime of the signal (expressed as the time constant  $T_2$ ), and the recovery of the magnetisation following a radiofrequency pulse (expressed as the time constant  $T_1$ ) (Grunert *et al.*, 2015). Each of these properties is sensitive to the microstructural environment of biological tissue and results in some tissues producing more signal (and therefore yielding brighter pixels) than others. This is the origin of image contrast in conventional MRI (Wheeler-Kingshott *et al.*, 2003).

### Quantitative Magnetic Resonance Imaging

While the spatial resolution of conventional MRI is sufficient to image gross anatomical structures it is not possible to directly image tissue microstructure (Tofts, 2010). To address this limitation, a number of quantitative MRI (qMRI) techniques have been developed, to provide MR biomarkers that can be used to infer the internal composition of tissues (Jungmann *et al.*, 2014). Consequently, in contrast to conventional MRI, qMRI is capable of providing biologically-relevant quantities from within tissues (Tofts, 2010). For this reason qMRI is predominantly used for the characterisation and measurement of changes within a tissue caused by disease, and has been used extensively in neurology (Nijeholt *et al.*, 1998). In addition, the use of qMRI analysis has become an important diagnostic tool in the determination of cartilage and IVD matrix functional state and is recognised as a method for the 'grading' stages of degeneration in IVD disease (Nerurkar, Elliott and Mauck, 2010). A variety of qMRI parameters can be utilised to monitor the micro-compositional changes within tissues including the IVD, with some of the most favoured methods including the following:

- $T_1$ : The longitudinal relaxation time of a tissue's net magnetisation i.e. the time in which protons excited by a radiofrequency pulse return back toward the original equilibrium ( $B_0$ ), wherein tissues return back to equilibrium at different rates depending on their composition. In  $T_1$  weighted images water has a low signal and appears dark (Taylor *et al.*, 2016).
- $T_2$ : The transverse relaxation time constant which determines the rate at which excited protons reach equilibrium or go out of phase. In  $T_2$  weighted images

---

<sup>1</sup> Different nuclei can be used for MR assessment but not all nuclei are suitable, hydrogen-1 ( $^1\text{H}$ ) and Carbon-13 (C13) are the most popular for MRI with the highest natural abundance in tissue. Other nuclei include sodium-23 ( $^{23}\text{Na}$ ), Fluorine-19 (F19) and Phosphorus-31 (P31).

water comes out as bright pixels. Changes in  $T_2$  reflect changes in tissue properties effecting water contents (Boulby, 2003).

- $T_2^*$ : The  $T_2^*$  is the same concept as  $T_2$  but with external factors such as magnetic field inhomogeneity also captured and factored in (Hoppe *et al.*, 2012; Bittersohl *et al.*, 2015).
- Magnetisation transfer ratio imaging (MTR): A method that can detect alterations in protein-water interactions such as those between proteoglycan and water molecules and is inferred from the energy transfer between free and bound water within a sample (Tofts and Steens, 2003).
- MR Spectroscopy (MRS): A technique that can be used to determine the relative concentrations of a variety of metabolites. The outcome of MRS is a spectra of chemical shifts. Each metabolite or biochemical in a sample can be identified by its unique chemical shift peak in the spectrum, which appears at a known frequency measured in parts per million (ppm). Metabolites of interest, such as proteoglycan (2 ppm) can be looked for within the spectrum (Rebuzzi *et al.*, 2013).

Quantitative MRI is typically performed by collecting a number of 3D image sets on a region of interest within the subject and each image set is acquired under different conditions. The change in signal intensity throughout the region of interest can be monitored and ultimately mathematically modelled to extract parameters that are known to correlate with specific tissue properties (Tofts, 2010). Furthermore, the application of  $T_1$ ,  $T_2$  and  $T_2^*$  mapping is commonly employed technique for determining tissue pathology, wherein each pixel of a qMR image represents the  $T_1/T_2/T_2^*$  value in each voxel and can be used to visually depict even relatively small variations in measurements across a tissue (Keenan *et al.*, 2011; Taylor *et al.*, 2016) (Fig.2.5). The use of qMRI in medicine has been mostly employed for the examination of tissues *in vivo*, however *in vitro* measurement such as for the external analysis of tumours has also been utilised (Schopp and Whitman, 2014).

Thus, based on the known capabilities of qMRI *in vivo* (already used in multiple tissue types and for post-implantation purposes) (Punt *et al.* 2012; Gelber *et al.*, 2014) the application of qMR techniques for the assessment of engineered tissue has also been explored. For example, the work by Weber *et al.*, (2012) and Schulz *et al.*, (2007) has

shown the advantage of using Phosphorus-31 (P31) and Carbon-13 (C13) MRS for bone tissue engineering and regeneration, Cheng, Loai and Farhat (2012) have applied  $T_2^*$  to study the growth dynamics of engineered bladders and Jeffries and Macdonald (2012) and Constantinidis *et al.*, (2006) have used high-resolution hydrogen-1 ( $^1\text{H}$ ) C13, Fluorine-19 (F19) and P31 MRS to study the growth, metabolism and vitality of artificial liver samples (Jeffries and Macdonald, 2012) and pancreatic constructs (Constantinidis, *et al.*, 2006).

Furthermore, the application of MR for the purposes of cartilage tissue engineering has also been considered, wherein Li *et al.*, (2010) applied MTR to study the growth of engineered neo-cartilage, Miyata *et al.*, (2007) used  $T_1$  mapping to calculate the fixed charged density of engineered cartilage samples, Irrechukwu *et al.*, (2012) used  $T_2$  relaxation analysis for cartilage matrix characterization and Magin *et al.*, (2013) used sodium-23 ( $^{23}\text{Na}$ ) MRS and  $^1\text{H}$  spectroscopy for the study of matrix anisotropy using 3D cultured chondrocytes or stem cells. The qMR measurements obtained from tissue-engineered cartilage samples are subsequently used to demonstrate the changing microstructural features of the tissue matrix at various time points of development. For example, in the study by Kotecha, Yin and Magin (2013) a quantifiable change in MR relaxation with a decrease in  $T_1$  and  $T_2$  measurement within bovine chondrocytes (pellet culture) and human mesenchymal stem cells was shown to correlate well with the growth of the engineered tissues following two or four weeks of culture. Within the work by Kotecha, Yin and Magin (2013), the decrease of  $T_1$  and  $T_2$  within these culture models was subsequently stated to infer an increase in both proteoglycan deposition ( $T_1$ ) (Akella *et al.*, 2001; Xu, Othman and Magin, 2008) and collagen content ( $T_2$ ) (Crema *et al.*, 2011) (summarised in Table.2.2). Increased proteoglycan has been associated with a decrease in water permeability and subsequently the lower free water content is related to a lower  $T_1$  (Keenan *et al.*, 2011; Van Rossom *et al.*, 2017) whereas the reduction of  $T_2$  has been linked with increased collagen content and organisation, due to the water within macromolecules having a shorter  $T_2$  than free water (Li *et al.*, 2011; Matzat *et al.*, 2013).

Furthermore, despite the non-invasive advantages of qMRI for the monitoring of engineered tissue the availability of high magnetic field strength machinery (typically 9.4, 11.7 or 14.1 Tesla) has been a limiting factor for the widespread implementation of qMR parameters in medicine (Li *et al.*, 2010; Jeffries and Macdonald, 2012). At

present, clinically available MRI scanners have either a standard magnetic field strength 1.5 or 3 Tesla (T) (Wood *et al.*, 2012; Nowogrodzki, 2018). Therefore, to improve the clinical feasibility of qMRI as a tool for monitoring tissue-engineered scaffolds the sensitivity of the quantitative parameters must be further advanced so that reliable qMR measurements can be achieved using clinical MRI equipment.

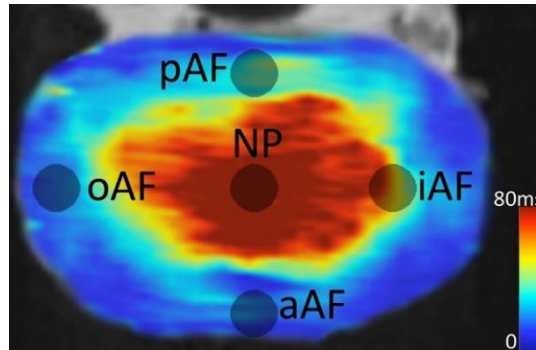


**Figure 2.5**  $T_2^*$  map of an intervertebral disc with locations overlaid, NP: Nucleus Pulposus, AF: Annulus Fibrosus, aAF: anterior AF, pA: posterior AF, oAF: outer AF, and iAF: inner AF. A high  $T_2^*$ (ms) infers a high water content (red) and a low  $T_2^*$  (ms) represents a low water content (Blue). Image sourced from Ellingson *et al.*, (2014).

**Table 2.2** The results of changes to relaxation quantitative magnetic resonance imaging parameters  $T_1$  and  $T_2$  monitored over time in different cartilage tissue-engineered constructs for the study of tissue-growth dynamics carried out by Kotecha *et al.*, (2013).

Experiment type	Culture time	MRI results
Chondrocytes in pellets	4 weeks	$T_1$ decreased 18% $T_2$ decreased 42%
Human MSCs in collagen/chitosan scaffolds	2 weeks	$T_1$ decreased 66% $T_2$ decreased 49%

\*The abbreviation MSCs signifies Mesenchymal stem cells,  $T_1$  the longitudinal relaxation time and  $T_2$  the transverse relaxation time. The MRI results represent the mean percent change from samples measured on day 0 of cell culture.

## 2.5 Current-tissue-engineered intervertebral disc approaches

### 2.5.1 Conventional fabrication techniques for intervertebral disc scaffolds

A full IVD replacement at the point of implantation should be able to replicate the native tissue type with properties including viscoelasticity, durability to repetitive stress, low friction and biocompatibility (non-toxic) (Whatley, 2013; Este, Eglin and Alini, 2018; Hu *et al.*, 2018). Thus far, a variety of material combination approaches for IVD regeneration have been attempted and have primarily been achieved using conventional techniques (Fig.2.6) (Mizuno *et al.*, 2004; Shao and Hunter, 2007; Choy and Chan, 2015). With some examples of conventional tissue engineering techniques including processes such as (Fig.2.7, A-E):

- Solvent-casting with particulate-leaching (Sin *et al.*, 2010) A polymer solution is cast into a mould filled with porogen particles, then the solvent is allowed to evaporate and the porogen is leached out (Fig.2.7, A)
- Gas foaming (Nam *et al.*, 2000) Polymer samples are exposed to high pressure allowing saturation of the gas into the polymer, the subsequent gas pressure reduction causes the nucleation of bubbles (Fig.2.7, B)
- Phase separation (Liu and Ma, 2010) A thermodynamic instability is established in a homogeneous polymer solution that separates into a polymer-rich and a polymer-poor phase (Fig.2.6, C)
- Melt moulding (Oh *et al.*, 2006) A mould filled with polymer powder and porogen component is heated to above the polymer glass-transition temperature ( $T_g$ ) and a pressure ( $P$ ) is applied to the mixture. The porogen is then leached out, leaving a porous structure (Fig.2.6, D)
- Freeze drying (Wu *et al.*, 2010) A polymer solution is cooled down, leading to the formation of solvent ice crystals. Then the solvent is removed by using a pressure lower than the equilibrium vapor pressure of the solvent ( $P^\circ$  solution), leaving a porous structure (Fig.2.6, E)

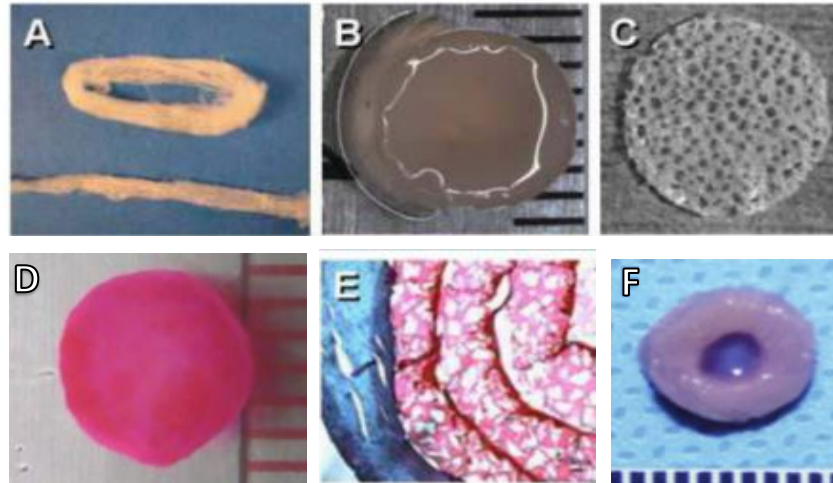


**Figure 2.6** Conventional strategies used in disc tissue engineering. (A) Hybrid alginate/chitosan fibres fabricated for annulus fibrosus (AF) tissue using freeze-drying and wet-spinning (Shao and Hunter, 2007). (B) Carboxymethylcellulose mould-casted gel seeded with nucleus pulposus (NP) cells (Reza and Nicoll, 2009a). (C) Atelocollagen honeycomb scaffolds from natural extracellular matrix, using ammonia gas, freeze-drying and UV-irradiation (Sato *et al.*, 2003). (D) A disc scaffold with photocrosslinked collagen and glycosaminoglycans formed by temperature sensitive mould-casting (Choy and Chan, 2015). (E) An AF replica constructed from poly(polycaprolactone-triol-malate) with chondrocytes, and a demineralized bone matrix formed via gas-foaming, cast-moulding and freeze-drying (Wan, *et al.*, 2008). (F) Scaffolds fabricated out of porous silk seeded with AF cells and a hyaluronic acid hydrogel with chondrocytes; using silicon moulds and high-temperature crystallisation, with freeze-drying (Park *et al.*, 2012).

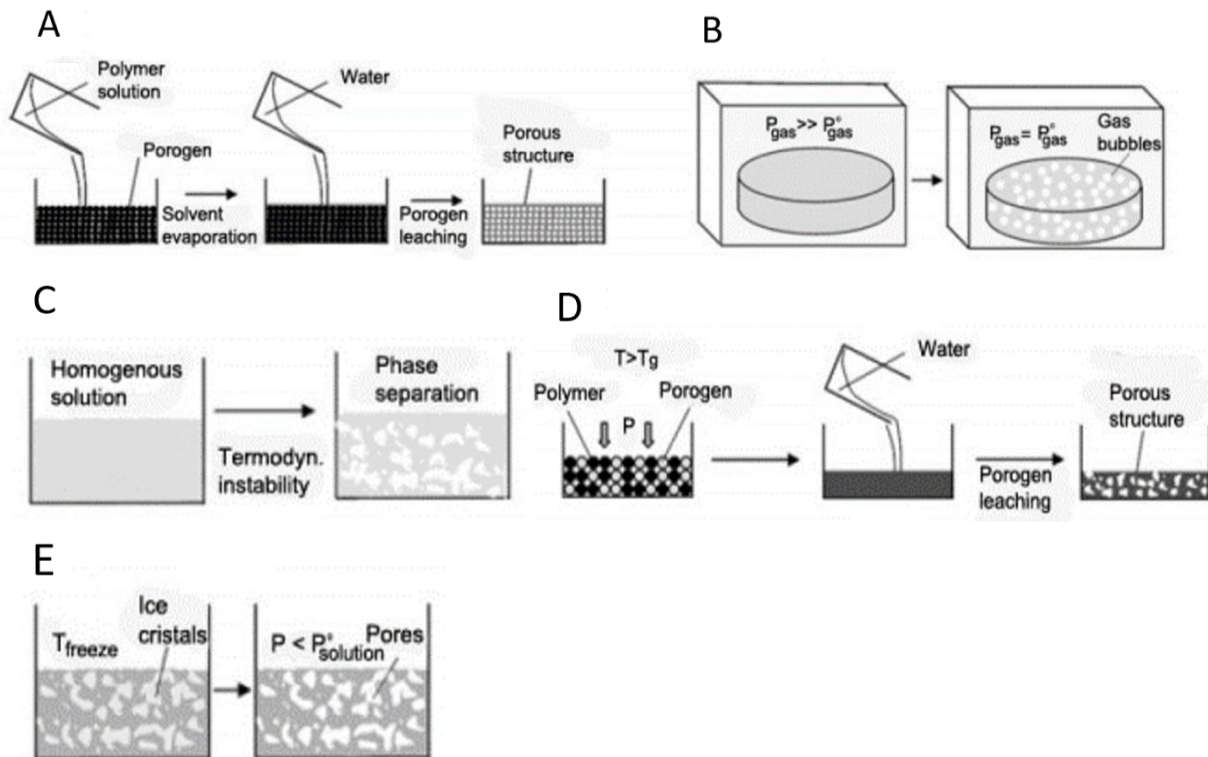


**Figure 2.7** A schematic of conventional scaffold fabrication techniques (modified from Puppi *et al.*, 2010). (A) Solvent-casting and particulate-leaching process. (B) Gas foaming process (C) Phase separation process. (D) Melt moulding process. (E) Freeze drying process.

The variety of conventional methods that have been employed for generating tissue-engineered IVD scaffolds have made noteworthy developments and gained significant progress towards the mimicry of native disc mechanical properties. For example, in the study by Choy and Chan (2015) compressive tests of mould-casted collagen and glycosaminoglycan (GAG) scaffolds were shown to reach a compressive moduli of 0.6 MPa following stress application, a value which is within the range of compressive moduli measured within native human discs of 0.5-5.0 MPa (Setton *et al.*, 2007, Nerurkar *et al.*, 2010, Oxland, 2015). The scaffolds further demonstrated a height recovery of between 82–89% which approached the 99% recovery that was achieved by native rabbit discs which endured the same pressures. In addition, conventional scaffold approaches for IVDs have revealed a variety of methods capable of

maintaining the IVD cell phenotype, as well as the generation of an ECM similar in composition to healthy discs (assessed via histology and immunohistochemistry analysis) (Park *et al.*, 2012). Thus, conventional methods have offered innovative ways to approach the discrete bi-phasic tissue challenges posed by native discs (Choy and Chan, 2015).

However, a commonly shared and major limitation of conventional scaffold approaches is their inability to regulate scaffold architecture during fabrication which has led to batch-batch product variation and unconnected pore networks (Zhu and Chen, 2013). Furthermore, conventional techniques have frequently demonstrated a reliance on potentially toxic solvents for the casting and/or removal of porogens (as used in solvent-casting and melt-moulding), as well as cell damaging conditions including extreme pressures or temperatures (melt-moulding and freeze drying) (Nam, Yoon and Park, 2000). The use of harmful environments during conventional processing, alongside the requirement for numerous wash steps and post-processing before cells seeding, has subsequently hindered the clinical feasibility of conventional scaffolds (Zhu and Chen, 2013).

Due to regulatory reasons as enforced by agents such as the 'Food and Drug Administration' (FDA) and 'The Medicines and Healthcare products Regulatory Agency' (MHRA) biological scaffolds for medical purposes should be manufactured in a reproducible, controlled and sterile fashion under conditions which are conducive to the inclusion of biological components such as living cells (O'Brien, 2011). As a result conventionally fabricated IVD biological scaffolds despite their advances, have not yet been clinically achieved (Whatley, 2013). However, the collective research on conventional scaffolds for IVDs has made significant progress towards disc tissue mimicry and biomaterial understanding and therefore should be utilised as a platform for the development of new fabrication methods, such as additive manufacturing.

### 2.5.1.1 Additive manufacturing

Additive manufacturing is an automated production process that encompasses a series of computationally directed, layer-by-layer, printing techniques which generates highly-controlled 3D objects (Kumar *et al.*, 2016; Aimar, Palermo and Innocenti, 2019). The progression of additive manufacturing technology has consequently revolutionised product tailored automisation (Melchels *et al.*, 2012) and is currently utilised in a variety of industry processes, due to additive manufacturing's high throughput efficiency and quality control features (Murphy and Atala, 2014).

In recent years, a number of automated fabrication methods have been employed within the field of tissue engineering to create scaffolds with well-defined architectures (Peltola *et al.*, 2008; Woodruff and Hutmacher, 2010; Melchels *et al.*, 2012). The application of additive manufacturing for scaffold fabrication has brought a new era of scaffold production possibilities and represents an important technological milestone in tissue engineering. With numerous examples of cell-free scaffolds produced by additive manufacturing already on the market e.g. for bone, osteochondral tissue repair, cartilage and skin (Melton *et al.*, 2010; Aimar, Palermo and Innocenti, 2019). Consequently, the successful clinical implementation of these devices can be attributed to the advantages of additive manufacturing including high reproducibility, customisability and an adherence to the rules of GMP, a system used for ensuring products are consistently produced and controlled according to high quality standards (Lysaght *et al.*, 2008; Melchels *et al.*, 2012).

In comparison to acellular additive manufacturing, automated fabrication with the inclusion of live cells, proteins and biomaterials has only been available for approximately 16 years, since the pioneering work of Wilson and Boland (2003) who first utilised a desktop printer to deposit cells. Thus, the fabrication of biological constructs with living cells is a much more recent concept than standard additive manufacturing. Subsequently, since the advent of cell-laden printing a number of additive manufacturing techniques have been developed or modified to incorporate cells (Melchels *et al.*, 2012) including: bio-laser printing (Guillemot *et al.*, 2010) (since 2004), stereolithography (Arcaute *et al.*, 2010) (since 2004) and robotic dispensing

(Pescosolido *et al.*, 2011) (either fused deposition modelling or bioprinting, available since 2005) (Melchels *et al.*, 2012).

However, one of the most commonly applied methods for cell-laden printing to-date is bioprinting, a computationally controlled, layer-by-layer 3D fabrication technique (Detsch *et al.*, 2014; Marchioli *et al.*, 2015) (Fig.2.8). Bioprinting permits the combined plotting of numerous different polymers within a single scaffold, and as such has been considered to be the most material-versatile of the additive manufacturing methods (Carvalho *et al.*, 2004). The bioprinting process is driven by pressurised gas and combines ultra-fine pipettes (micron-range diameters) for precise, spatially orientated liquid polymer extrusion (Billiet *et al.*, 2012). Furthermore, bioprinting has yielded a multitude of viable and functional scaffolds and has been used for a variety of medical research applications, ranging from soft-hard tissue types such as vascular vessel creation (Singh *et al.*, 2015), nerve engineering (Rajaram *et al.*, 2014) pancreatic islet printing (Marchioli *et al.*, 2015), bone repair (Haberstroh *et al.*, 2010; Zehnder *et al.*, 2015) and ear regeneration (Lee *et al.*, 2014). The use of bioprinting processes for scaffold generation can be summarised in the following steps:

1. Data Input: A digital blueprint of the desired tissue or structure is the first requirement. This can be achieved via the manual generation of a corresponding computer model via computer aided design (CAD) software (e.g. Pro/Engineer or Solidworks) (Leong and Llo, 2014) or imported from medical imaging techniques such as computed tomography (CT) or MRI, or 3D laser scanning (Melchels *et al.*, 2012). For bio-imaging the data acquisition is made up of a stack of 2D image slices to form a representative 3D volume and captures the contours and dimensions of the scanned structure. The medical images are then thresholded to separate out the darker and lighter pixels present, which are indicative of different tissue types within the image, (such as bone and soft tissue) to allow for a more accurate selection of the chosen region of interest. The 3D model is then processed and smoothed to eliminate overhanging unsupported regions, which would present issues during printing. The generation of these models can be performed using specialised software, such as 'Materialise Mimics®' or 'Simpleware®', which are capable of providing personally tailored 3D models with sub-millimeter geometrical accuracy (Van den Broeck *et al.*, 2014) .

2. Data file preparation and structure building: The visual data obtained are then imported and tessellated as an STL file into the additive manufacturing system software and converted to a buildable 3D mesh model (made up of tetrahedrons and supportive struts). The final digitised model acts as a heterogeneous representation of the scanned tissue, and comprises of material information in terms of composition, distribution and geometry (Melchels *et al.*, 2012). The precise printing parameters are then selected and the image is mathematically sliced into horizontal layers, ready for data communication to the additive manufacturing machine (Arafat *et al.*, 2013). The anatomically accurate model is subsequently built via a layer-by-layer spatial deposition of materials.

Thus, the improved mechanical properties and high resolution control of additive manufacturing, alongside printable biocompatible materials, has opened up new avenues for scaffold design and implementation (Murphy and Atala, 2014) with a potential to accelerate our understanding of tissue-engineered bio-mimicry and scaffold function. Furthermore, additive manufacturing's automated and refined printing process reliably generates reproducible and customisable scaffold products and represents major advantages when compared to manual labour heavy conventional approaches (Aimar, Palermo and Innocenti, 2019). However, despite these technological advances, unlike 3D printed acellular devices, bioprinted cell-laden scaffolds have yet to hit the clinical market. With the major limitation of cellular scaffolds in medicine being attributed to the availability of materials which meet all the criteria necessary for bioprinting, including printability with a consistent fluid flow, a stable structure upon deposition, high cell compatibility and tissue relevance (Kang *et al.*, 2016). In addition, another limiting factor of note for cell-laden tissue engineering is the availability of cell sources. With numerous factors influencing the cell source decision such as the chondrogenic potential, the cell yield, the accessibility and availability of the cells as well as the acquisition costs, the age-related function decline of cells and the potential for donor-site morbidity (Leijten *et al.*, 2013).

A further challenge related to additive manufacturing scaffolds, in comparison to conventional methods, is the scaffold geometry, whereby layered architectures are inherently weaker than scaffolds which have been milled or moulded out of a solid material (Gleadall *et al.*, 2018). The structural geometry of bioprinted scaffolds are primarily determined by the position and orientation of individual material filaments,

with a wide range of scaffold geometries used in literature (Gleadall *et al.*, 2018). Consequently, the architectural design of tissue-engineered scaffolds have been shown to significantly influence both mechanical properties and cell behaviour (Hutmacher *et al.*, 2001). Investigation towards the optimisation of layered scaffold architecture has however been explored. For example, the study by Domingos *et al.*, (2012) concluded that the mechanical performance of scaffolds was highly dependent on the level of scaffold macroporosity, and was further supported by De Ciurana, Serenó and Vallès (2013) and Trachtenberg *et al.*, (2014) who developed models to relate mechanical properties to porosity. In addition, studies have investigated filament positioning during bioprinting and subsequently showed that varied material deposition patterns, such as aligned versus staggered filament layering, significantly imparted differences in scaffold physical properties (Zein *et al.*, 2002; Domingos *et al.*, 2012).

Nevertheless, in spite of the developments in architectural design and related mechanical control, it is stated that the true capabilities of additive manufacturing systems remain under-utilised (Gleadall *et al.*, 2018). Wherein, it has been claimed that the the generic software supplied by commercial system manufacturers are incapable of reaching the wide-ranging needs required to fully meet the complexity of replicating tissue architectures and properties (Gleadall *et al.*, 2018). In particular, advancements in the control of multi-material printing will likely be key to the generation of scaffolds which require an interface between tissues types, such as cartilage and bone. In which, the generation of separate tissues relies on different material properties, such as stiffness, hydration and mineral composition, to guide the respective cell phenotypes (Steele *et al.*, 2014). Furthermore, scaffolds consisting of multiple materials should be well combined to prevent eventual interphase separation and breakage; a task that can be achieved by the precise positioning, overlapping and integration of multi-material filaments during fabrication (Lopes, Silva and Carneiro, 2018). In support of this, cases of custom bioprinting software have been developed by researchers to achieve different filament orientations and to offer more precise multi-material print control (Kang *et al.*, 2016; Gleadall *et al.*, 2018). Therefore, although some advanced capabilities have been developed within additive manufacturing for tissue engineering there is still unmet potential for bioprinting, whereby further progress could allow for more advanced and customisable tailoring of scaffold physical properties (Gleadall *et al.*, 2018).

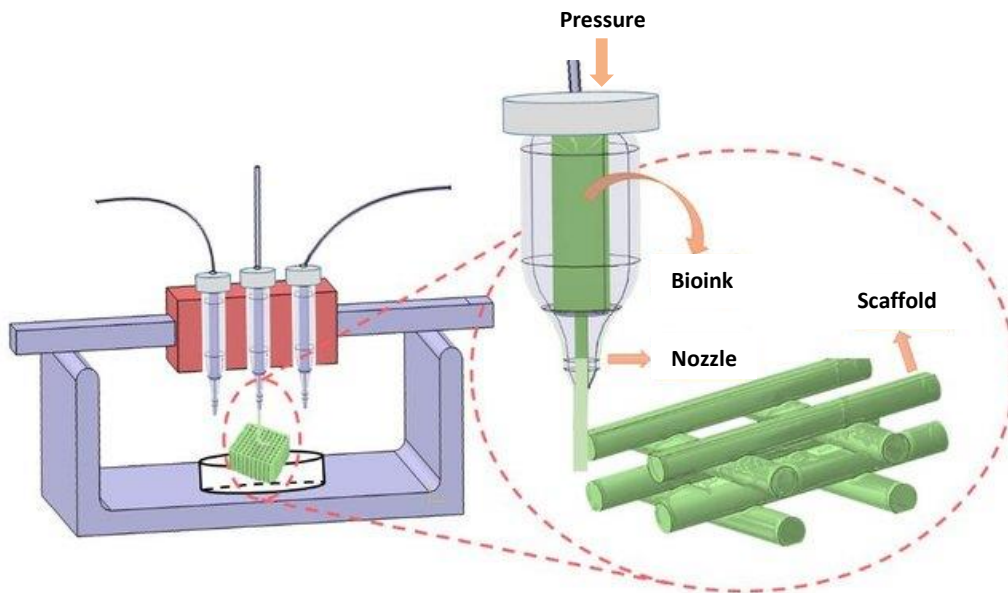


**Figure 2.8** Schematic of bioprinting. Image sourced from Naghieh *et al.*, 2018 and edited by author.

### 2.5.1.2 Materials for bioprinting

The correct application of functionally appropriate biomaterials (a biological or synthetic substance which can be introduced into the body) is an essential component in the fabrication of tissue-tailored scaffolds. The chosen material must be suitable for medical use and should be capable of supporting cell directed tissue growth (Malda *et al.*, 2013). Furthermore, the demands on material properties are increasingly more complex when the material is intended for cell-laden bioprinting (referred to as a 'bioink'<sup>2</sup>) (Malda *et al.*, 2013; Zhang *et al.*, 2018).

A good bioink should be highly biocompatible to accommodate live cells, be mechanically stable after printing, and be capable of high resolution during printing (Gopinathan and Noh, 2018). A critical aspect of bioink selection therefore is their ease of processability, in which the material must be printed under conditions that are favourable for both structurally sound scaffold fabrication and cellular inclusion

---

<sup>2</sup> A biomaterial comprised of living cells that can be extruded through a printing nozzle into shape sustaining structures is known as a bioink (Groll *et al.*, 2019).

(Xiongfa *et al.*, 2018). Furthermore, variations in the preparation or treatment of bioinks have been shown to potentially influence material molecular weight and chemical structure (Munarin *et al.*, 2013; Abraham *et al.*, 2019) and subsequently these changes can have a significant implication on the material properties for printing, such as melt temperature, gelation rate or viscosity (Naficy *et al.*, 2013). An example of this is a material which has been modified to have an increased molecular weight which typically results in a higher material viscosity (Zhu and Marchant, 2011). Materials with higher viscosities have different rheological properties and subsequently will commonly require higher pressures for material extrusion using bioprinting, as well as the potential adjustment of other print conditions such as increased temperature (Naficy *et al.*, 2013; Axpe and Oyen, 2016; López-Marcial *et al.*, 2018). In addition, print parameters can have a direct influence on cell survival within the bioinks, wherein high print pressures (>60 MPa) and temperatures above 37 °C can damage cells (Gopinathan and Noh, 2018). In essence, the ideal material for bioprinting should be viscous enough to print with integrity but not so viscous that it requires cell damaging pressures to be extruded (Naficy *et al.*, 2013). Furthermore, the material property known as 'shear thinning' is particularly sought after for bioinks and is defined as the behaviour of fluids whose viscosity decreases under strain (López-Marcial *et al.*, 2018). Shear thinning materials are well suited to bioprinting because when a print pressure is applied the shear thinning material becomes less viscous and is readily capable of extrusion, whereas, once the pressure is removed (after the material has been deposited) the initial higher viscosity of the material returns and is capable of maintaining the scaffold architecture (Gopinathan and Noh, 2018).

#### 2.5.1.3 Hydrogels for cell-laden bioprinting

Among the different biomaterials, hydrogels are most prominent materials used as bioinks in bioprinting. This is mainly due to their ability to support living cells, their modifiable chemical structures and adjustable mechanical and biodegradation properties as well as their previously evidenced good resolution during printing (Gopinathan and Noh, 2018).

Hydrogels are composed of a three-dimensional polymeric structure and water and can be formed from synthetic (e.g. poly (ethylene glycol), poly (hydroxyethyl methacrylate)) or naturally occurring polymers (e.g. collagen, alginate, chitosan, gelatine). The physical properties of hydrogels can range from soft-weak to hard-tough dependent on their molecular weight and cross-linking (Hennink and van Nostrum, 2002; Murphy and Atala, 2014). The preferential use of hydrogels over other printable materials is the result of their innately biomimetic properties with similar mechanical, swelling, and lubricating behaviours to the native ECM of many tissue types (López-Marcial *et al.*, 2018). Additional attributes of hydrogels include their tested affinity for cell or drug carrying and their pro-chondrogenic capabilities (Sechriest *et al.*, 2000; Kisiday *et al.*, 2004) and ease of surgical implantation (Hunt *et al.*, 2014).

However, a commonly stated limiting factor of hydrogels, has been their poor long-term mechanical strength, wherein their intrinsically high water content dilutes structural polymer chains (Melchels *et al.*, 2012). Consequently, the low innate strengths of hydrogels can impair a materials ability to physically support cells during tissue growth. To combat this, numerous research approaches have yielded hybrid hydrogels such as: gelatine/hyaluronic acid scaffolds (Chang *et al.*, 2012), Collagen/Chitosan–polylactide (CH–PLA) (Yin *et al.*, 2014), alginate-methylcellulose (Schütz *et al.*, 2017) and alginate-gelatine hydrogels (Zehnder *et al.*, 2015), with the intent to improve the physical capabilities of these hydrogels (Jayakumar *et al.*, 2011; Nguyen *et al.*, 2011). An example of the significant influence of hybrid hydrogels on the mechanical properties of the material was made clear in the work by Li *et al.*, (2014). In this work Li *et al.*, demonstrated that through the hybridisation of an alginate gel with polyacrylamide a stiff hydrogel with an elastic moduli of ~1 MPa could be formed, whereas the alginate alone had an elastic moduli of ~10 kPa. Subsequently, the increased durability of hybrid hydrogels has demonstrated them to be promising candidates for use in tissue-engineering (Malda *et al.*, 2013). However, the adjusted properties of hybrid hydrogels are not always suitable for cell inclusion or for extrusion bioprinting, due to their commonly increased polymeric concentration and thus their reduced micro porosity (essential for cell ingrowth, mass transfer and nutrient exchange) as well as differences in rheological properties (Li *et al.*, 2014; Mano, Reis and Gasperini, 2014). An alternative method which has been considered for improving the compressive stiffness of hydrogels, and is compatible with additive manufacturing,

is cryogenic 3D printing (Tan *et al.*, 2017). In this work, prior to printing the composite hydrogel was cooled below its freezing point using solid carbon dioxide (CO<sub>2</sub>) in an isopropanol bath, the material solution was then extruded and solidified by freezing upon contact with the stainless steel print plate. The cryogenic printing setup as was demonstrated in the Tan *et al.*, (2017) study was shown to successfully create stable 3D complex macroporous structures, with an average compressive stiffness of  $0.49 \pm 0.04$  kPa stress (at 30% compressive strain). A stiffness which mimics the mechanical properties of the soft tissues found in the human body (Tan *et al.*, 2017). However, despite the benefits of this approach on scaffold physical properties a current limitation of this work is its inability for live cell incorporation during processing.

#### 2.5.1.4 Alginate hydrogels

Alginate solutions encompass one of the most well established and extensively investigated hydrogels for biomedical applications, in part this has been due to its non-toxicity, high cell compatibility, ability to support a chondrogenic phenotype, relatively low cost, mild gelation capabilities via ionic crosslinking (Lee *et al.*, 2013) and non-animal origin, which has been related to a lowered immune response (Andersen, Auk-Emblem and Dornish, 2015).

Alginate is a naturally occurring polysaccharide extracted from brown seaweed and consists of 1,4-linked  $\beta$ -D mannuronic acid (M) and  $\alpha$ -L-guluronic acid (G) units (Fig.2.9) (Lee and Mooney, 2012). The composition of the monomer's units along the alginate polymer chain directly influence the material properties. For example, alginates with more MG blocks (MGMGMGM) will form more flexible chains in comparison to those predominantly made with G blocks (GGGGGGG) that will form stiffer chains (Lee *et al.*, 2000). The versatility of these compositional attributes has resulted in the use of alginate hydrogels for the purposes of a broad array of applications including tissue engineering: for wound healing, cell transplantation with the delivery of bioactive agents (Xinxin Shao, 2006; Lee and Mooney, 2012; Detsch *et al.*, 2015) and cell-embedded bioprinting (Zehnder *et al.*, 2015; Axpe and Oyen, 2016; Schütz *et al.*, 2017).

Furthermore, alginate hydrogels have been the most widely used material for IVD tissue engineering applications (Maldonado and Oegema, 1992; Chelberg *et al.*, 1995; Xinxin Shao, 2006; Gebhard *et al.*, 2010; Bowles *et al.*, 2012). With alginate materials primarily being researched as a replacement for NP IVD regions (Bron *et al.*, 2011; Huang *et al.*, 2012; Kuo and Ma, 2001), due to their shared rheological and thixotropic consistencies (fluid viscosity changes in response to stress) and swelling behaviour. Furthermore, ionically cross-linked alginates, like other natural materials, have a material stability which decreases over time (Lee and Mooney, 2012). Under physiological conditions alginate is dissolved, caused by the release of divalent ions into surrounding solutions, due to an exchange reactions with monovalent cations. The ability for degradation is a key feature of biomaterials and is required to allow room for new tissue ingrowth (Bouhadir *et al.*, 2001; Zhu and Marchant, 2011; Axpe and Oyen, 2016). It has additionally been shown that through alteration to the molecular weight and/or monomer units of alginate that degradation can be tailored to suit the rate of ECM production (Bouhadir *et al.*, 2001; Abraham *et al.*, 2019).

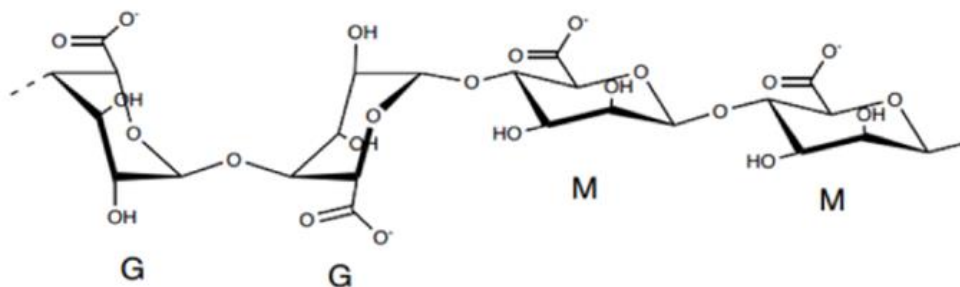


**Figure 2.9** Molecular structure of alginate, a linear polymer consisting of (1-4)-linked  $\beta$ -D-mannuronate (M) and  $\alpha$ -L-guluronate (G) residues (Draget *et al.*, 2006). Diagram taken from Lee and Mooney, (2012).

### 2.5.2 Additive manufacturing approaches for intervertebral disc scaffolds

Since the advent of bioprinting in 2003 (Wilson and Boland, 2003) the use of additive manufacturing for IVD regeneration has been underrepresented, and is a finding that was supported by the results of a Boolean style database search using the key words 'tissue engineering' 'intervertebral disc', 'bioprinting', 'printing' and 'additive manufacturing' on 'Web of Science' and 'PubMed'. The outcome of this search produced five relevant publications: Whatley *et al.*, (2011), Whatley (2013), van Uden *et al.*, (2015a), Rosenzweig *et al.*, (2015) and Hu *et al.*, (2018). Subsequently, the utilisation of additive manufacturing capabilities for the fabrication of tissue-engineered IVDs represents a relatively new area of investigation (2011-2018).

In the available examples of disc engineering using additive manufacturing, the majority of approaches have separated the fabrication of the AF and NP disc sections. The region specific approach for scaffold generation has been primarily trialled through the use of viscous hydrogels for the NP disc region, with stronger synthetic materials such as thermoplastics to replicate the annulus. The use of thermoplastic for this purpose was employed in three of the five studies on IVD engineering using additive manufacturing approaches (Van Uden *et al.*, 2015; Rosenzweig *et al.*, 2015; Hu *et al.*, 2018). However, despite the frequented use of thermoplastics (Woodruff and Hutmacher, 2010; Cho *et al.*, 2014; van Uden *et al.*, 2015b) these materials for tissue engineering are often hindered by their innate properties including: cell incompatibility, poor degradability, excess stiffness and a need for high temperature printing, which prevents cell inclusive fabrication (Rosenzweig *et al.*, 2015). An example of this is the common thermoplastic polycaprolactone (PCL), which is hydrophobic by nature and subsequently requires material treatments known as surface 'wetting' to achieve cell adhesion (Guarino *et al.*, 2017). The use of surface wetting was similarly evidenced in the study by Rosenzweig *et al.*, (2015) which used a collagen type I coating on PLA printed scaffolds to enhance NP cell spreading. Furthermore, the high stiffness of thermoplastics can present issues for tissue engineering, resulting in the phenomenon of stress shielding (when the compressive moduli of the device is higher than that of the intended tissue type). Stress-shielding is an existing hindrance of artificial disc replacements and has been known to cause both bone loss and the need for revision surgery (Chuen Wong, 2016; Honigmann *et al.*, 2018; Honigmann *et al.*, 2018; Liu,

Kamara and Yan, 2018). In the work by van Uden *et al.*, (2015a) which used PCL to print disc structures the mechanical properties of the produced scaffolds were no exception to this. Wherein, the PCL scaffolds demonstrated a compressive stiffness that varied from 5.9–6.7 kN/mm<sup>-1</sup> (van Uden *et al.*, 2015) which upon conversion to MPa <sup>\*3</sup> approximately equated to a stiffness of 131-250 MPa, a range which is orders of magnitude above the maximum range of discs (1.5 MPa) (Setton, Bonassar and Masuda, 2007). Thus, despite their popularity in literature the use of thermoplastics can present a range of significant issues for the fabrication of tissue-engineered implants.

Furthermore, the additive manufacturing methods which have been previously employed for engineering IVDs have been seen to vary between recent studies, in which the experiments by van Uden *et al.*, (2015a) and Rosenzweig *et al.*, (2015) used a fused-deposition modelling approach whereas Whatley *et al.*, (2011), Whatley (2013) and Hu *et al.*, (2018) used bioprinting. Following on from this, it was observed that amongst the IVD experiments which used bioprinting for disc tissue engineering that a similar biomimetic architectural design approach was used to replicate IVD structures. For example, in the Whatley *et al.*, (2011) and Whatley (2013) studies, a synthetic polyurethane material was bioprinted in concentric circles to replicate the AF lamellae (Fig.2.10, A-B). Comparatively in the work by Hu *et al.*, (2018) Polylactic acid (PLA) was printed into ring like structures with aligned parallel fibres to serve as the outer AF (with staggered infill densities) and a GG- PEGDA hydrogel was deposited to replicate the NP. However, in the experiments which employed a fused-deposition modelling approach, a printing process which works by the extrusion of flattened molten filaments to form layers, the scaffold designs were less reflective of native disc architecture. For example, in the van Uden *et al.*, (2015a) publication, a solid infill thermoplastic 'shell' was printed with an external shape based on true disc dimensions with varying outer macropore geometries (Fig.2.10, C-D). The work by Rosenzweig (2015) demonstrated a similar approach using fused-deposition, in which simple and macro-porous acrylonitrile butadiene styrene (ABS) and polylactic acid (PLA) scaffolds

---

<sup>3</sup> The kN/mm<sup>-1</sup> to MPa conversion used to check the van Uden *et al.*, (2015) methods was achieved via the digitisation of the scaffold figures provided in the publication, which were thresholded in a computer aided design software (CAD) to estimate an equivalent cross-sectional area and height (figure scale bars were used to ensure correct scaling).

were created, based on an orthogonal “matrix” construct taken from the .stl file of an IVD. The observed disparity between the IVD scaffold design approaches used in literature can likely be explained by the differences in the additive manufacturing approaches utilised. Wherein, typically bioprinting allows for the fabrication of more complex and intricate architectures than fused-deposition modelling (Ning *et al.*, 2015). Consequently, the use of bioprinting by Whatley *et al.*, (2011), Whatley (2013) and Hu *et al.*, (2018) resulted in more ambitious scaffold designs which aimed to mimic the complex internal structures of discs.

Furthermore, the Hu *et al.*, (2018) IVD scaffold approach was the only method out of the five examples in literature to demonstrate the incorporation of living cells during fabrication (Hu *et al.*, 2018). Comparatively, the studies by Whatley *et al.*, (2011), Whatley (2013), Van uden *et al.*, (2015) and Rosenzweig *et al.*, (2015) required the incorporation of cells after processing, via the manual pipetting of cell suspensions over the structures known as ‘cell seeding’. The use of cell seeding in the studies which employed fused-filament modelling was expected, due to the inherent use of high-temperatures during printing (Rosenzweig *et al.*, 2015; van Uden *et al.*, 2015a). However, the work by Whatley (2011) and Whatley *et al.*, (2013) employed bioprinting for scaffold fabrication, which is a gas-driven process, and subsequently the lack of cell-laden bioinks represented a key flaw within this work.

The computer-controlled and customisable spatial placement of cell-laden materials using bioprinting has been shown to infer a multitude of advantages when compared to cell seeding (Billiet, Vandenhaute, Schelfhout, Van Vlierberghe, *et al.*, 2012; Zhu and Chen, 2013), with reduced manual-error and improved cell penetration, as well as cell homogeneity and spreading within scaffolds. Furthermore, cell-laden bioprinting has been demonstrated to generate scaffolds with increased cell-cell interactions and matrix production relative to cell-seeded structures (Billiet, Vandenhaute, Schelfhout, Van Vlierberghe, *et al.*, 2012; Zhu and Chen, 2013). Consequently, it has been predicted that by 2023 cellular bioprinting is expected to become a \$8.9 billion industry, with \$1.9 billion (21%) projected to be spent on medical applications, using additive manufacturing, 3D printing and rapid product development (Wohlers Associates, Inc, 2013).

Thus, the experiments by Whatley *et al.*, (2011) and Whatley (2013) for IVD regeneration did not utilise the full cellular capacity of bioprinting, instead these studies focused on the architectural and mechanical recreation of IVD structures, which resulted in fabrication conditions that were not permissive for cell survival during printing. For instance, in the work by Whatley (2013) the manufacturing of the polyurethane IVD scaffolds were performed using a frozen print platform (-4°C) to allow for the fast solidification of the polymer solution and for scaffold shape retention, which was also followed by a freeze-drying procedure to further stabilise the porous structures (Whatley, 2013). Similarly, in the chitosan/gelatin scaffolds designed by Whatley (2013) potentially cell damaging UV light and a toxic photo-crosslinking chemical initiator was used for material photo-crosslinking and hardening of the printed structures and was followed by numerous solvent wash steps (Whatley, 2013). In brief, the outcome of the work by Whatley *et al.*, (2011) and Whatley (2013) evidenced two variants of bioprinted scaffolds with high resolution concentric layers, with a thickness of 50-100 µm and spacing of 100-200 µm (Fig.2.10, A-B). The scaffolds created by Whatley (2013) were stated to accurately mimic the native structures of the AF in human IVDs, and therefore demonstrated the feasibility of bioprinting for intricate scaffold fabrication. However, the harsh fabrication conditions which were required for precise extrusion and scaffold stabilisation demonstrated a significant compromise to the use of cell incorporation and overall clinical feasibility. Wherein, the optimal bioprinting protocol for tissue-engineered IVD scaffolds in medicine will likely require a fine balance between a favourable scaffold geometry and a high cell compatibility.

In comparison, the recent work by Hu *et al.*, (2018) demonstrated a bioprinting method which deposited cell-encapsulated hydrogels together with synthetic polymers in an integrated structure. In this study, 3D constructs were prepared using a multi-head system, where one head was loaded with cell-laden poly (ethylene glycol) diacrylate (PEGDA) pre-gel mixture and maintained at 37 °C. The other head contained poly (lactic acid) (PLA) filament (MakerBot, USA) and was set at 200 °C for polymer melting. The outcome of the Hu *et al.*, (2018) study was the generation of scaffolds with tailorable mechanical and degradation properties, which were regulated by the infill pattern and density of the PLA frameworks, as well as a high cell survival (~90%) and cell proliferation rate within PEGDA.

However, despite the advantageous use of cell-laden printing by Hu *et al.*, (2018) it can be stated that the work presented within these investigations failed to acknowledge a number of potential hindrances. The first example of this was the use of an UV-irradiation polymerisation process (365 nm, 50 mW/cm<sup>2</sup>). UV polymerisation a method which is known to be a common source of DNA-damaging radiation and consequently could have long-term implications on cell behaviour (Fischbach *et al.*, 2001; Munarin, Bozzini, Visai, Maria C Tanzi, *et al.*, 2013; Stoppel *et al.*, 2014; Dai *et al.*, 2016) and was not assessed in the Hu *et al.*, (2018) study. Furthermore, the integration between the two material types (PLA and GG- PEGDA) used for the hybrid scaffold production was not well addressed within the Hu *et al.*, (2018) publication. Wherein, without the chemical combination of print materials a phase separation between the material types is likely, and is a phenomena that has been known to cause inherent weaknesses at interface boundaries (Lopes, Silva and Carneiro, 2018). The effect of phase separation would be especially evident over time, due to the faster degradation rate of hydrogels relative to thermoplastics. However mechanical testing of the hybrid scaffolds was only performed for one week following fabrication in the Hu *et al.*, (2018) investigations, and thus should preferentially be considered over a longer duration. Furthermore, bone marrow stromal cells (as used by Hu *et al.*, (2018)) are progenitor cells for skeletal tissue and can subsequently differentiate along multiple lineages such as osteoblasts, chondrocytes and adipocytes (Bianco *et al.*, 2001). Despite this the Hu *et al.*, (2018) investigation did not assess the hybrid scaffolds effect on cell phenotype or resultant ECM (via methods such as gene expression analysis, histological staining or immunohistochemistry techniques) (Kular, Basu and Sharma, 2014). It was therefore unclear in the experiments by Hu *et al.*, (2018) as to whether a cell phenotype appropriate for IVD regeneration was achieved, wherein long term cell survival and chondrogenic phenotype maintenance within the hybrid scaffolds (PLA and GG- PEGDA) would be necessary to demonstrate the feasibility of this approach for IVD engineering.

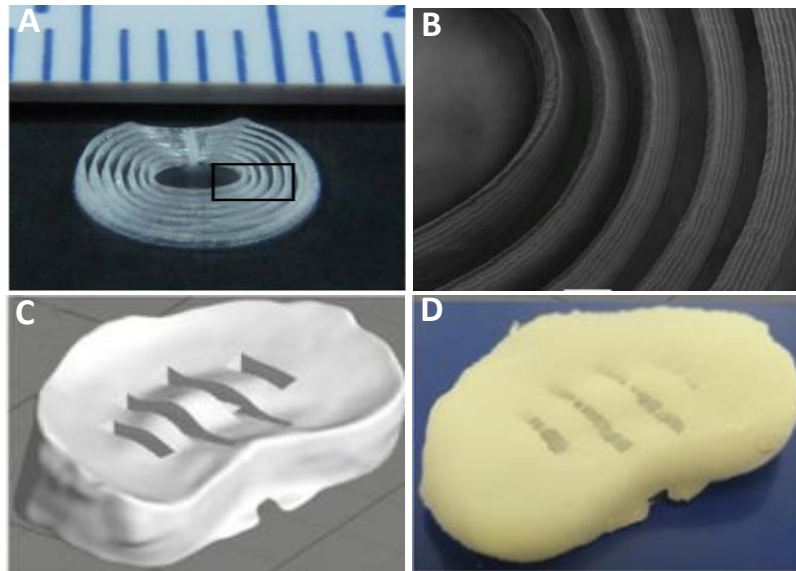


**Figure 2.10** Intervertebral disc models fabricated using additive manufacturing (A-B) fabricated using bioprinting by Whatley (2013), (C-D) using fused-filament modelling by van Uden *et al.*, 2015a. (A-B) High magnification scanning electron microscopy images of a chitosan/gelatin disc scaffold by Whatley (2013) with lamellae type structures similar to native annulus tissue. (C) Computer aided design model of a rabbit intervertebral disc at 200% scale. (D) Polycaprolactone disc scaffold after printing.

## 2.6 Bioprinting of articular cartilage for the guidance of intervertebral disc scaffold fabrication

In contrast to the lack of research on IVD cartilage engineering using additive manufacturing, there have been multiple attempts at bioprinting articular/hyaline cartilage (Zhang *et al.*, 2017; Petretta *et al.*, 2018; Wang *et al.*, 2019; Gálvez-Martín *et al.*, 2019). In part, this is due to the graded zonal organisation of articular cartilage tissue, which has been said to be well suited to the layer by layer approach of bioprinting, wherein the scaffold layers can be tailored towards the properties of the cartilage zones (Zhu *et al.*, 2018). As such, based on the ECM compositional similarities between IVDs and articular cartilage, the studies on articular/hyaline cartilage bioprinting should be used as a platform in establishing effective protocols for IVD generation.

Despite the advantages of scaffold fabrication using bioprinting technology the progress for cartilage engineering has been limited by the development of compatible biomaterials (Zhang *et al.*, 2018). The necessary balance between biocompatibility and bio-printability has represented a major challenge for the field (Gopinathan and Noh, 2018). Thus far, the materials used for cartilage bioprinting can be characterised as either natural or synthetic, or alternatively a hybrid of both natural and synthetic materials (López-Marcial *et al.*, 2018; Zhu *et al.*, 2018; Gálvez-Martín *et al.*, 2019). However, natural hydrogels have been stated to have a biological advantage over synthetic materials, due to their morphological similarity to cartilage as well as the presence of ligands, such as the adhesion molecules on laminin, fibronectin and collagen, which allow them to interact with cells and to assist ECM synthesis, cell migration and proliferation (Hunt and Grover, 2010; Jabbari, 2018). Commonly employed natural materials in cartilage research have included hydrogels such as agarose, alginate, chitosan, collagen, fibrin and hyaluronan (Zhao *et al.*, 2017; López-Marcial *et al.*, 2018; Gopinathan and Noh, 2018; Gilarska *et al.*, 2018) with each material demonstrating its own advantages and disadvantages (Table.2.3).

However, among the various hydrogels used it is alginate that has represented the most widely used bioink for cartilage research (Axpe and Oyen, 2016). The popularity of alginate bioprinting in cartilage applications has been attributed to the previously mentioned properties (1.4.1) including its high biocompatibility, easily controlled gelation, suitability for printing and modifiable stiffness (which can be influenced by the M to G ratio within its chemical structure) (Wang *et al.* 2003; Lee and Mooney, 2012). Among the cell types used with alginate both primary isolated articular chondrocytes (Nakamura, 2006; Fedorovich *et al.*, 2012; Park *et al.*, 2016) and mesenchymal stem cells (Luo *et al.*, 2013; Moshaverinia *et al.*, 2013; Bernhardt *et al.*, 2015) have been well evidenced to support cartilaginous tissue development. Furthermore, in the encouraging work by Cohen *et al.*, (2010) the use of alginate hydrogels has already been effectively employed in the treatment of chondral defects *in vivo*. The results of which, effectively demonstrated the feasibility of alginate additive manufacturing for cartilage regeneration Cohen *et al.*, (2010).

Furthermore, upon comparison of different alginate based approaches for bioprinting it was observed in the vast majority of investigations that a blend of alginate with other biomaterials was employed, rather than alginate alone (Axpe and Oyen, 2016).

Examples of this included: alginate–agarose (López-Marcial *et al.*, 2018; Marcial, 2018), alginate/fibrin (Landers *et al.*, 2002), alginate/gelatin (Naficy *et al.*, 2013; Chung *et al.*, 2013) and alginate-collagen (Zhao *et al.*, 2017) as well as alginate overlaid with agarose and calcium salts of polyphosphate compounds (Feng *et al.*, 2014; Neufurth *et al.*, 2014). The use of alginate hybrid hydrogels in these examples have been employed to enhance processability. This is due to the typical low viscosity and poor rheological properties of hydrogel precursor solutions before cross-linking, which prevent shape retention after printing (Pati *et al.*, 2015; Zhang *et al.*, 2018). The problem of low viscosity has also been addressed via the addition of viscosity modifiers, such as methyl cellulose (Ahlfeld *et al.*, 2017; Seidel *et al.*, 2017) nanocellulose (Müller *et al.*, 2017) and nanoclay (Jin *et al.*, 2017) to increase the viscosity of precursor solutions and to give them a yield point which is compatible with printing (Jang *et al.*, 2018). Consequently, the use of cell compatible viscosity modifiers and hybrid hydrogel combinations can be used to avoid the use of covalent or photo-mediated cross-linking and sacrificial materials for enhancing physical properties, which have been shown to negatively impact tissue growth (Marcial, 2018).

In addition to alginate, another frequented and more recent material approach within cartilage bioprinting has been gelatin methacryloyl 'GelMA' (Schuurman *et al.*, 2013; Abraham *et al.*, 2019). GelMA is a semi-synthetic hydrogel, which is prepared using a water-soluble protein derived from denatured collagen in porcine gelatin, and has been enhanced through the incorporation of methacrylate groups to improve printability (Pepelanova *et al.*, 2018). However, GelMA solutions have been associated with innately low viscosities at 37°C, which is a feature that is incompatible with bioprinting (Schuurman *et al.*, 2013). As a result, the GelMA bioink has been commonly used in combination with other materials such as hyaluronic acid, thermoplastics and alginate (Schuurman *et al.*, 2013). An example of this was evidenced in the publication by Schuurman *et al.*, (2013) who formulated and screened multiple hybrid GelMA solutions embedded with equine primary chondrocytes. In the research by Schuurman *et al.*, (2013), the bioinks composed of alginate with GelMA and chondroitin sulfate methacrylate were revealed as the best candidate for neocartilage formation, with the highest collagen type II: collagen type I ratio after four weeks of cell culture.

However, regardless of the variety of GelMA material combinations tested, the GelMA solutions depend on a UV polymerisation process (320–365 nm) to attain scaffold

integrity (Schuurman *et al.*, 2013; Chen and Glover, 2016; Abraham *et al.*, 2019). However, the use of UV light in combination with cells is a clinical concern which has been known to impart a negative influence on chromosomal and genetic stability (Dai *et al.*, 2016). As a result, although GelMA represents as a promising material for cartilage engineering using bioprinting its requirement for photo-crosslinking and the reliance on other materials for scaffold viability has made this bioink a less desirable choice. In addition, when using animal-derived natural polymers, such as gelatin, concerns on immunogenic reactions and infection must also be considered (Zhu and Marchant, 2011).

**Table 2.3** Advantages and disadvantages of biomaterials used in articular cartilage repair, taken from the review paper by Campos *et al.*, 2012.

Material	Advantages	Disadvantages
Agarose	Allows cell differentiation; high glycosaminoglycan/DNA; reparative ability	Difficult migration of cells when polymerized at a high concentration; needs to be exposed to mechanical overload
Alginate	Allows interaction with cells	Not ideal mechanical properties
Chitosan	Unlimited resource; contains glycosaminoglycans and hyaluronan, similarly to native cartilage	Lacks fast gelling properties (cannot be applied <i>in situ</i> )
Collagen	Main component present in the ECM; good cell adhesion properties; achieved good clinical results with young patients	Needs mechanical stimulation for improving loading capacity
Fibrin	Approved by the FDA; stimulates production of glycosaminoglycans; supports formation of the ECM	Success rate of 3 of 5 patients; results are dependent on cell seeding concentration
Hyaluronan	Glycosaminoglycan present in native cartilage; allows interaction with cells; improves expression of collagen type II	Needs growth factors for cell survival; decreases expression of collagen type I
Gellan gum	Water soluble; good rheological properties	Derived from microbial fermentation of <i>Sphingomonas paucimobilis</i> ; poor mechanical strength
PEG	Allows interaction with chondrocytes; does not support angiogenesis (beneficial for chondrocytes)	Not ideal strength and compression modulus
PNiPAAm	Copolymerization possible with AAC; gelling temperature around 37 °C; does not support angiogenesis; cells keep their phenotype	When polymerized, there is an output of water content; poor mechanical strength
PLA	Able to maintain 3-D structure when implanted <i>in vivo</i> ; expression of high levels of collagen types I and II	Needs growth factors for cell survival
Polyurethane	Ease of processing as injectable gel ( <i>in situ</i> polymerization); good mechanical properties	Not completely biocompatible (mild host response)
PVA	Water soluble; excellent adhesion properties; allows interaction with cells	Not completely degradable (semidegradable); culture in bioreactor needed to increase compression modulus
Scaffold free	Production of an ECM rich in proteoglycans; derives sizable tissues	Poor mechanical strength

: PEG = poly(ethylene glycol); PLA = polylactide acid; PVA = poly(vinyl alcohol); ECM = extracellular matrix.

## 2.7 Summary

Thus, in brief, based on the previous research publications which have employed bioprinting for IVD cartilage and articular cartilage generation it can be inferred that the use of alginate hydrogels will likely be the most prominent biomaterial candidate in the future of cartilage engineering. The next stage of research in this area should therefore focus on the standardisation of human IVD (hIVD) cell laden alginate bioprinting for clinical approval as well as the improvement of tissue engineering and cell culture methods, such as mechanical stimulation for the enhancement of ECM development closer to native IVD tissue composition.

## **Chapter 3 Experimental screening of alginate and collagen based biomaterials for the fabrication of scaffolds using bioprinting**

### 3.1 Introduction

The ultimate goal of tissue engineering is to restore the physiological properties of damaged tissue using a biomaterial-based implantable scaffold (Chan and Leong, 2008). To achieve the clinical implementation of tissue-engineered scaffolds a number of key criteria must be considered, including biocompatibility, biodegradability, sterility, mechanical efficacy, architectural stability and reproducibility (see Table.3.1) (O'Brien, 2011). Thus far, the main example of scaffold fabrication has been through the use of conventional techniques, with methods including solvent casting, gas foaming, phase separation and porogen leaching (see section 2.5.1) (Mikos and Temenoff, 2000; Leong *et al.*, 2008). However, due to the common limitations of conventional fabrication approaches such as batch-batch product variation, unconnected pore networks and the use of damaging chemicals and/or fabrication conditions (Nam *et al.*, 2000; Leong *et al.*, 2008), conventional scaffolds have demonstrated an overall incompatibility with clinical implementation (Lysaght and Hazlehurst, 2004, O'Brien, 2011). Consequently, in more recent years the application of additive manufacturing such as bioprinting for scaffold fabrication has gained popularity, due to its high resolution control ( $\mu\text{m}$ ) and capability for multi-material and cell-laden printing (see section 2.5.1.1) (Peltola *et al.*, 2008; Billiet *et al.*, 2012, Zhu and Chen, 2013, Chia and Wu, 2015).

Nevertheless, despite the advantages of bioprinting, so far only a few biomaterials which are favoured for conventional cartilage scaffolds have been adapted for bioprinting, with examples including polyglycolic acid (PGA)-polylactic acid (PLA) (Mizuno *et al.*, 2004), hybrid alginate/chitosan (Xinxin Shao, 2006) and poly(polycaprolactone-triol-malate) (Wan *et al.*, 2008). In part, the lack of materials for bioprinting is reliant on the specific material properties required for extrusion printing, such as a suitable viscosity, gelation rate and melting temperatures for a consistent fluid flow under pressure, as well as structural rigidity after deposition (Zhang *et al.*, 2018). Therefore, the characterisation of materials for bioprinting represents an important stage in scaffold development.

In this investigation bioprinter technology was employed for the screening of three different materials: collagen, alginate methyl cellulose (alg/MC) and alginate dialdehyde-gelatin (ADA-Gel) with the aim of producing macro-porous, reproducible scaffolds for cartilage engineering. The materials and the resultant scaffolds were assessed on their suitability for bioprinting i.e. ease of material preparation, material/scaffold reproducibility, prospect for cell compatibility and scaffold structural integrity as well as their feasibility for clinical implementation (Table.3.1) (Gopinathan and Noh, 2018; Topuz *et al.*, 2018; Zhang *et al.*, 2018). In addition, due to the popularity of PCL for bioprinting the material PCL was also screened (see Appendix A). However, due to the inherent cell incompatibility of PCL thermoplastic approaches which include high temperature extrusion (~80-95°C), low degradation rate, hydrophobicity, lack of micro-porosity and brittle tendencies this material was not included in the main investigation (Appendix A). Based on the outcomes of this study an appropriate biomaterial was taken forward for further investigation for the purpose of cell-inclusive cartilage engineering.

**Table 3.1** Biomaterial scaffold criteria for clinical implementation.

Biocompatibility	Biodegradability	Sterility	Mechanical properties	Scaffold architecture	Simple preparation and manufacture
Cells must adhere, function normally, migrate and maintain a desired phenotype	Scaffolds must be biodegradable to allow cells to produce their own extracellular matrix. The by-products should be non-toxic and able to exit the body.	Materials must be sterile before cell inclusion to prevent contamination and infection.	By the point of implantation the scaffold must have sufficient mechanical integrity to function in vivo.	Scaffolds must be free-standing without structural collapse and maintain open pore networks for cell penetration and mass transfer.	Material preparation and scaffold manufacture should be highly reproducible, cost-effective, achievable under good manufacturing practice and possible for scale-up to allow for regulatory approval.

## 3.2 Materials and Methods

### 3.2.1 List of Materials

Sodium alginate, alginic acid sodium salt from marine brown algae, suitable for immobilization of micro-organisms) with a molecular weight of 100K–200 Kg mol<sup>-1</sup> (Sigma-Aldrich), Methyl cellulose, approximate MW = 88 kDa (Sigma-Aldrich),

Calcium chloride di-hydrate ( $\text{CaCl}_2 \cdot 2\text{H}_2\text{O}$ ) (Sigma-Aldrich), Sodium metaperiodate (Sigma-Aldrich), Gelatine, Type A, Bloom 300, derived from porcine skin (Sigma-Aldrich), Silver Nitrate (Sigma-Aldrich), Collaplex, water soluble solution of 1% collagen type I and II, extracted from calf hides and preserved with 1,0 % phenoxyethanol (GfN Selco), Dulbecco's Modified Eagle Medium (DMEM), (ThermoFisher Scientific), Tannic Acid (TA), (Sigma-Aldrich).

### 3.2.2 Material Selection

Three different materials were selected for investigation, chosen due to their previously stated suitability for bioprinting or use with cartilage tissue engineering (Kundu *et al.*, 2013; Lee *et al.*, 2014; Hwang *et al.*, 2007; Kim, Lee and Kim, 2017; Zhao *et al.*, 2017; Seidel *et al.*, 2017; Schütz *et al.*, 2017; Sarker *et al.*, 2014a; Zehnder *et al.*, 2015).

Collagen - a major component of the cartilage extracellular matrix, with physiological and cell compatibility properties akin to native cartilage (Marques *et al.*, 2019).

Alginate methyl cellulose (alg/MC) – A simple to prepare material blend. Alginate hydrogels have been shown to be effective for cell culture and maintaining the chondrocyte phenotype, by mimicking cartilage physiology (Lee and Mooney, 2012). The added MC acts a releasable thickener agent to improve printability without compromising cell compatibility (Schütz *et al.*, 2017).

Partially oxidised Alginate-Gelatine (ADA-Gel) – an alginate–gelatine cross-linked hybrid which has been shown to promote the growth and repair of tissue. The purpose of ADA-Gel is to incorporate the high biocompatibility of gelatine, without inheriting the gelatines poor mechanical properties. The alginate component is modified to improve biodegradability by using ADA with different degrees of oxidation, to influence the materials hydrolysis properties (Zehnder *et al.*, 2015).

### 3.2.3 Material preparation for bioprinting

#### 3.2.3.1 Alginate methyl cellulose

The alg/MC hydrogel mixture was prepared using the methods described by Schütz *et al.*, (2017). In this approach, a 3% weight/volume percent (w/v%) alginate solution was made by mixing alginic acid sodium salt in phosphate-buffered saline (PBS) before autoclave sterilisation (Systec D-23; 121°C for 20 minutes). Autoclave sterilised MC powder was then added to the alginate solution (9% w/v). The mixture was stirred to obtain a homogeneous alg/MC paste and left to swell for one and a half hours before bioprinting.

Different PBS solutions and methods were trialled for the alginate dissolution step to assess the effects on alg/MC viscosity and printability. The stirring of the PBS and alginate solutions was performed using a Fisherbrand™ Isotemp™ Stirrer and magnetic stir bar. Preparation methods included:

- Batch one: Made with a pre-prepared liquid sterile-filtered ‘Dulbecco’s Phosphate Buffered Saline 10x’, modified without calcium chloride and magnesium chloride (Sigma). The solution was stirred overnight after alginate addition.
- Batch two: PBS tablets (Sigma-Aldrich) were dissolved in ddH<sub>2</sub>O to yield a 0.01 M phosphate buffer with 0.0027 M potassium chloride and 0.137 M sodium chloride at a pH of 7.4. The mixture was left to stir for five hours following alginate addition.
- Batch three: Was a repeat of batch two, but with an overnight stirring stage after the addition of alginate.
- Batch four: Used PBS tablets (Dulbecco A) dissolved in ddH<sub>2</sub>O to give a molarity of solute components equal to: Sodium chloride 0.137 M, potassium chloride 0.003 M, disodium hydrogen phosphate 0.008 M, potassium dihydrogen phosphate 0.0015 M. The solution was stirred overnight after alginate addition.

#### 3.2.3.2 Alginate-gelatine (ADA-Gel)

The covalently crosslinked ADA–Gel was formulated using the following protocol, as described by Sarker *et al.*, (2014), which was modified from Balakrishnan and

Jayakrishnan, (2005). Alginate di-aldehyde (ADA) was firstly synthesised by the controlled oxidation reaction of sodium alginate, performed in an equal volume of ethanol–water mixture. The ADA was prepared by the oxidation of alginate using sodium metaperiodate in an ethanol-water mixture (1:1). The alginate was prepared by the dispersion of alginic acid at a concentration of 1g/mL in ethanol, to which a 7.5 mmol periodate solution was added in deionized H<sub>2</sub>O. The mixture was stirred under dark conditions at room temperature for six hours, before stopping the reaction using an equal molar ratio of ethylene glycol to alginate, slowly added under continuous stirring for 30 minutes. The resultant suspension was then transferred into a semipermeable membrane (BioDesign Dialysis tubing, MWCO: 8000 Da, Fisher) and dialyzed against distilled water for seven days; numerous water changes were carried out to ensure the purification of the solution. The solution was confirmed to be periodate free via a silver nitrate test in which 1% (w/v) silver nitrate solution was added to equal volume taken from the produced dialysate. The lack of precipitation during this addition confirmed the absence of periodate. Following this the ADA solution was aliquoted into smaller volumes and lyophilized at -70°C/0.25mBar for 24 hours. For the preparation of the ADA–Gel hydrogel, a 5% (w/v) aqueous solution of gelatine in PBS was added drop-wise into a 5% (w/v) ADA solution (dissolved in HPLC grade water) at a pH of 7.4 under continuous stirring. Batches with decreasing sodium periodate addition were also prepared in an attempt to increase material printability, with the ratios of (0.25:1) and (0.5:1) in ethanol-water mixture.

### 3.2.3.3 Collagen

The preparation of non-fibrillar and fibrillar collagen pastes from the commercially available 'Collaplex 1.0 SF-solution' were novel formulations and represent the first demonstration of the following methodologies.

A non-fibrillar collagen solution (1%) was retrieved by the following steps: First, 110 g of 'Collaplex 1.0 SF-solution' (~1g collagen) was purified by precipitation with a 1M saline solution (Fig.3.1, A), which was left to stir for one hour at room temperature, and then kept at 4°C for two hours. The collagen was retrieved by centrifugation (3,000 x g) (Fig.3.1, B).

The purification steps were then repeated (purified with 1M saline solution for one hour at RT then two hours at 4°C, followed by centrifugation). The collected collagen was filled into a dialysis tube (BioDesign Dialysis tubing, MWCO: 8000 Da, Fisher), and incubated at 4°C for seven days in ddH<sub>2</sub>O (with a daily water change). Dialysis was performed to remove the preservatives only. The retrieved pure collaplex solution (GfN Selco) was centrifuged at 2°C (3,000 x g), and the pellets collected and weighed (Fig.3.1, C). The solution was frozen at -20°C and freeze dried (Christ, model Alpha 1-2, -40°C, 10<sup>-1</sup> mbar) (Fig.3.1, D). Freeze-dried collagen was dissolved to 4% in 0.1 M HCl. Homogenisation of the collagen in 0.1 M HCL was achieved with a hand-held foamer device (Ventuci). The mixture was neutralised using NaOH and tested via litmus paper (Mission). Paste variants with and without 1% MC w/v powder addition were prepared (MC sterilised by autoclave, 121°C for 20 minutes).

Alternatively, fibrillar collagen was formulated and proceeded the collection of non-fibrillar collagen after dialysis. At this stage, instead of freezing, the collected collagen 1.0 SF-solution was poured into a 2L Erlenmeyer flask and 0.1 M HCl and ddH<sub>2</sub>O added in a ratio of 1:4 and stirred for two hours at room temperature. Next a 2 M NaCl and 0.5 M phosphate buffer was added to the mixture and adjusted to a pH of 7.2 then made up to two litres with ddH<sub>2</sub>O and 0.1M HCl. The mixture was incubated over night at 37°C and subsequently stirred for 30 minutes prior to centrifugation at 4°C for 25 minutes (3,000 G). The collected fibrillated collagen was weighed and batches were frozen at -20°C and later freeze dried (Christ, model Alpha 1-2, -40°C, 10<sup>-1</sup> mbar).

Upon manual extrusion tests (using a syringe capped with a 0.51 mm tip) the non-fibrillar collagen with 1% added MC was the only paste capable of a continual extrusion. As a result, the fibrillar collagen paste was not taken forward for print parameter screening. Attempts to sterilise the un-fibrillated collagen was implored for the potential future incorporation with cells. The sterilisation methods used included the following:

- UV-irradiation: freeze dried collagen was cut into pieces and placed under a UVC lamp (wavelength 254 nm, Fisher Scientific) at a distance of 5 cm for two hours (conditions selected based on previously employed studies shown to be within the range effective for sterilisation (Fischbach *et al.*, 2001; Huebsch,

Gilbert and Healy, 2005; Munarin, Bozzini, Visai, Tanzi, *et al.*, 2013; Dai *et al.*, 2016). The process was performed within a laminar flow hood.

- Super critical carbon dioxide (scCO<sub>2</sub>): freeze dried collagen was placed into an autoclave and an additive mixture of 0.25 vol% water, 0.15 vol% H<sub>2</sub>O<sub>2</sub> and 0.5 vol% acetic anhydride was pipetted to the bottom of the vessel. The autoclave was then filled with 300 g liquid CO<sub>2</sub> (18°C, 5.5 MPa) and heated to transfer the liquid CO<sub>2</sub> to the supercritical state (~38°C, ~8.5 MPa) for 45 minutes, depressurisation was performed within 6.5 minutes.
- Ethanol: freeze dried collagen was left submerged in pure ethyl alcohol (98%) in a six-well plate with the lid ajar in a laminar flow hood overnight. The collagen was then washed with sterile PBS three times and left to dry over-night.
- $\gamma$ -irradiation: performed on freeze dried collagen using a Cobalt 60 source at minimal dose of 25 kGy by BBF Sterilisation Service (Kernen, Germany).
- Chloroform evaporation: carried out on the collagen pastes (4%) (after dissolution in HCl and neutralization). Chloroform was added underneath the collagen material (10% of the volume of collagen solution) inside a 50 ml falcon tube. The tube was closed and left at either room temperature or 4°C overnight. The top layer of collagen solution was then removed aseptically and rinsed with sterile tissue culture grade water.

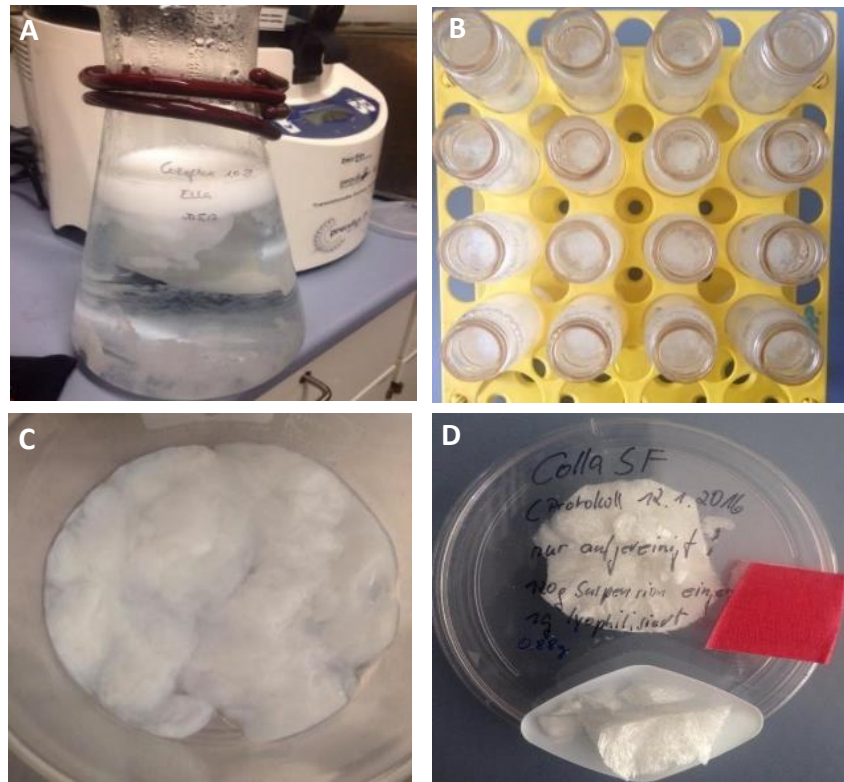


**Figure 3.1** Images showing stages of the non-fibrillar 4% collagen paste preparation (A) Precipitation in saline solution. (B) Pellet formation after centrifugation. (C) Collection of pellets. (D) Freeze-dried collagen.

### 3.2.4 Material characterisation

#### 3.2.4.1 Fourier transform infrared spectrometer analysis

Fourier transform infrared (FTIR) spectrometer (PerkinElmer Spectrum 65) was used to obtain an infrared spectrum of molecular absorption of the prepared materials, for chemical composition characterisation purposes. All wet samples (alginate, ADA-Gel and collagen) were freeze-dried before analysis to lower the distorting high-water peak.

#### 3.2.4.2 Shear Rheometer testing

Dynamic shear viscosity ( $\eta$ ) of alg/MC pastes and collagen pastes were determined by applying a constant shear rate ( $\dot{\gamma}$ ) of  $30 \text{ s}^{-1}$  for 300 s using a using a HAAKE Rheostress 1 plate rheometer (Thermo Scientific™) and a Physica MCR 300 rheometer (Anton Paar, Austria) respectively at  $25^\circ\text{C}$ . For both material types viscosity

was determined using a cone-plate ( $D = 35\text{mm}$ ) with a distance of  $0.1\text{ mm}$  ( $n = 4$ ). The paste viscosities were determined after a defined shear rate of  $1\text{ s}^{-1}$  (also stated as  $1/\text{s}$ ) had been used<sup>4</sup>. To evaluate both measurement reliability and batch-batch repeatability material batches ( $n = 4$ ) were tested six times. The dynamic shear viscosity values were then considered along with their material processability using the bioprinter to determine a dynamic viscosity range suitable for printing. Due to the physical properties of the ADA-gel formulation this material was not suitable for rheological testing. The ADA-gel was not sufficiently viscous and caused sample run-off during measurement.

For the alg/MC pastes (batches 1-4 prepared using different PBS sources) measurements were taken after 1.5 hours following MC addition to the alginate solution, as this was the swell time successfully used for bioprinting in previously published applications of alg/MC (Schütz *et al.*, 2017). In addition, viscosity measurements of alginate alone were monitored following 0.08, 1, 2, 4 and 24 hours after MC addition, and compared to measurements of alginate without MC addition (control) to provide insight into MC swelling on paste behaviour. For collagen pastes with and without MC addition, the viscosity was monitored over time, wherein measurements were taken immediately after paste formulation and then following 0.5 hours and 2 hours to observe the potential effects of MC swelling.

After an initial amplitude sweep test to detect the viscoelastic region, oscillatory frequency sweep tests ( $f = 0.01\text{--}10\text{ s}^{-1}$ ) were performed on the collagen + 1% MC paste. The storage modulus ( $G'$ ) and loss modulus ( $G''$ ) were measured as material properties which have been suggested to be predictive of printability (Law *et al.*, 2018), with high  $G'$  materials linked to the prevention of uniform extrusion (Law *et al.*, 2018). Shear thinning was tested by increasing rotational shear rate from  $0\text{--}100\text{ s}^{-1}$  over 5000 s (increment =  $0.08\text{ s}^{-1}$ ).

---

<sup>4</sup> The unit for shear rate is  $1/\text{s} = 1\text{ s}^{-1}$ , also called reciprocal seconds. Shear rate is the rate at which fluid layers move past each other during flow. The shear rate within a print tip is generally unknown wherein the material properties itself can influence shear rates generated in the dispensing tips. A measurement of viscosity after a fixed unit of shear rate has been applied is used to compare samples and not to infer viscosity during printing.

### 3.2.5 Plotting of materials

Material print parameter screening was performed, based upon protocols found in literature with systematic adjustments for bioprinting with the Bioscaffolder 3.1 (GeSiM, Germany) (Fig.3.2). The main parameters altered for improved material printing included those listed in Table 3.2. The settings used were optimised and determined according to material flow consistency (determined visually during material extrusion testing), strand definition (measured using microscopy) and structural integrity (i.e. the ability to maintain a defined shape whilst supporting subsequent layers without structural collapse). The screened conditions for the fabrication of alg/MC and non-fibrillar collagen + 1% MC scaffolds were documented in Table 3.3. For all scaffolds the pre-determined dimensions of 12 mm by 12 mm by 2 mm were employed, with an angle orientation change of 90° per layer. For the alg/MC scaffolds material crosslinking took place immediately after fabrication with 100 mM CaCl<sub>2</sub> for ten minutes. The collagen + 1% MC scaffolds were cross-linked with 2% tannic acid (TA) for 30 minutes. Subsequently, all scaffolds were washed in DMEM growth medium and kept under cell culture conditions of 37°C, 5% CO<sub>2</sub>.

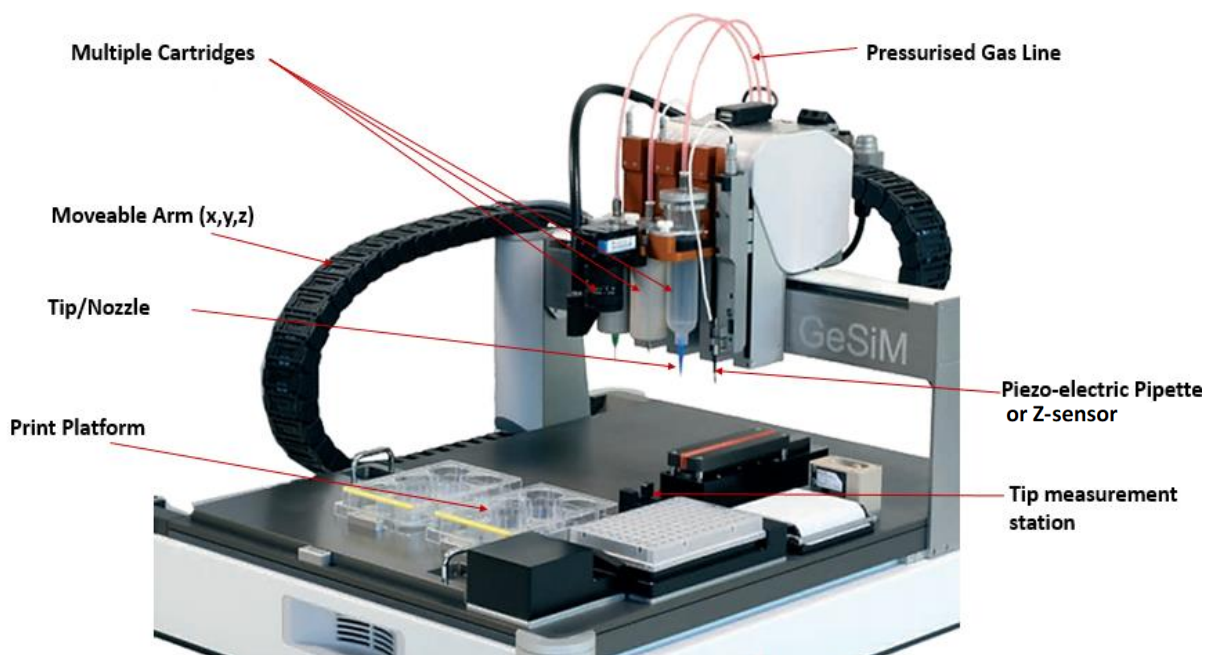


**Figure 3.2** Schematic of the 3D BioScaffolder 3.1 (GeSiM, Germany) with labelled elements. Modified image sourced from GeSiM online brochure <http://GeSiM-bioinstruments-microfluidics.com>.

**Table 3.2** Bioscaffolder 3.1 (GeSIM, Germany) print parameters, with definitions and ranges.

<b>Print parameter</b>	<b>Definition</b>	<b>Range</b>
Tip inner diameter (ID)	The diameter of the inside of the print tip. Influences material volume extruded during printing and resultant strand thickness.	0.2-1.8 mm (Nordson)
Needle z-offset	Represents the distance of the print tip from the print plate or a previous deposited material layer.	-50 to 100 mm
Start break	Duration of time that the print pressure is applied to the cartridge before the print commences. Often used to prime the tip with material.	-5 to 5 seconds
Interlayer pause	Length of time between the printing of material layers.	1 to 300 seconds
Strand number	Strands are the individual lines of material deposited which make up the final, often grid-like scaffold structures. Strand number pertains to how many lines of material will make up each layer of the scaffold.	1 to 50
Distance between strands	The predetermined spacing of adjacent material strands e.g. in mm.	0.1 to 100 mm
Cartridge temperature	The temperature of the material cartridge can be controlled using a thermoregulated jacket which surrounds the cartridge.	Room temperature to 100°C
Plotting speed	The velocity at which the print tip moves during a print i.e. from strand to strand.	1 to 115mm/s
Print pressure	The pressure of applied gas onto the plunger within the cartridge, influences the speed and volume at which the material is extruded.	0 to 1000 kPa

**Table 3.3** Screened print parameters for the printing of alginate methyl cellulose and non-fibrillar collagen + 1% methyl cellulose using the 3.1 Bioscaffolder (GeSIM, Germany).

Material	Print parameter ranges						
	Tip ID* (mm)	Z-offset (mm)	Pressure (kPa)	Speed (mm/s)	Start break (s)	Temperature (°C)	Interlayer pause (s)
Alg/MC	0.51	0.6	70	10	-0.5	20-25	0
	0.35	0.4					
Collagen	0.61 *	0.5	66	8	-0.05	20-25	0
+ 1% MC	0.84	0.7	55	12			

Alg/MC; alginate methyl cellulose. Tips used for printing were flexible tapered tips (Nordson) with the exception of collagen + 1% methyl cellulose with a tip inner diameter (ID) of 0.61mm \*which was printed using a steel cannula tip (Nordson). Batch three of alginate methyl cellulose was used to determine optimal printing conditions.

### 3.2.5.1 Multi-head printing

Multi-material printing of simple and computer-modelled scaffolds were trialed using the Bioscaffolder 3.1 (GeSIM, Germany) and employed the previously established print-parameters for alg/MC (Table.3.3).

#### Sequence based multi-head printing with alginate methyl cellulose

Simple scaffold designs (created within the GeSIM bioscaffolder software) were plotted with coloured alg/MC (achieved with red and green food colouring) using two separate print heads, labelled as 'A' and 'C'. Print sequences within the software were used to control the deposition from the different print heads, A or C. Cartridge A contained red alg/MC and cartridge C was filled with green alg/MC. Single layer scaffolds with sequences of: ACCAACCA, ACACA, AACCCCAA and AC were printed with the dimensions of 12 mm by 12 mm by 0.5 mm.

#### Upscaled disc model using coloured alginate methyl cellulose

Multi-material printing with coloured alg/MC was performed for the fabrication of a custom designed IVD model. The digital file of a full IVD was attained from an MRI scan of a human lumbar spine through the use of specialised biomodelling software

'Materialise Mimics®' (Fig.3.3, A). The anatomic area of interest was selected in 3D on a pixel by pixel bases using a 'mask' based on the greyscale intensity, which allowed for a visual distinction of the disc from the surrounding vertebrae. The sequence based option for multi-material printing on the Bioscaffolder 3.1 (GeSIM, Germany) software was not available for imported digital files. In addition, the GeSIM software was not compatible with commonplace 3D modelling and slicing softwares such as 'Slic3r®'. This was overcome via the following method: Using the 3D modelling software 'Blender®' the extracted IVD model was separated into two regions, which represented the AF and NP disc sections (Fig.3.3, B-D). For each region the model data was imported and tessellated as a separate STL file with the Bioscaffolder 3.1 software (GeSIM, Germany) and converted to a buildable 3D mesh model. A print file was generated for each model and subsequently copied into 'notepad'. The computer code generated for each file was manually combined and spatially edited to piece the models together into one print. Commands were manually written into the code to print the AF region with print head 'A' and the NP section with print head 'C' (Fig.3.3, E-F). The previously generated code was then replaced with the formatted version and the device instructed to print. Once fabricated the scaffold was cross-linked in CaCl<sub>2</sub> for 10 minutes.

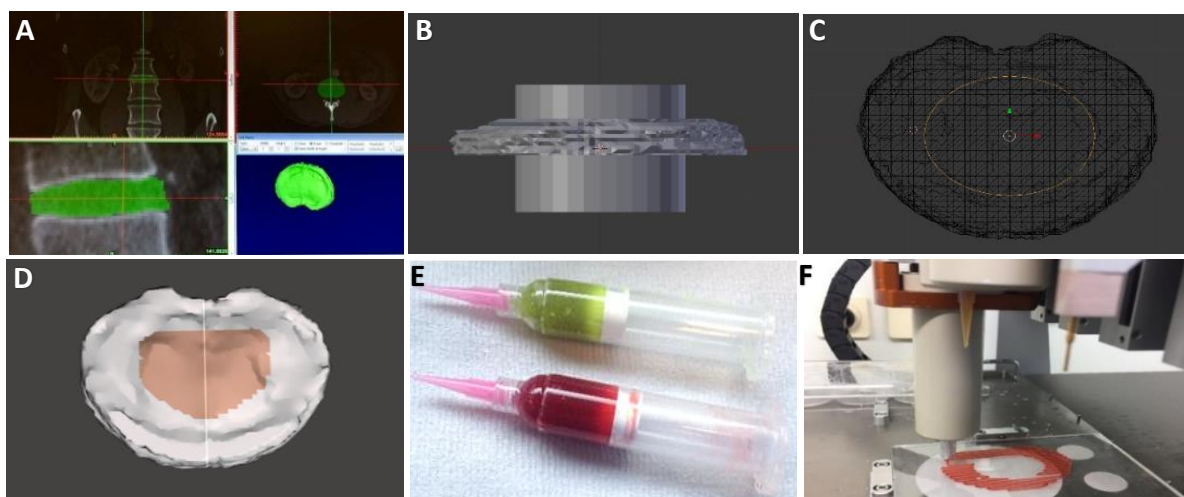


**Figure 3.3** The multi-material printing of an intervertebral disc model based on true dimensions. (A) The anatomical area of interest was isolated on a pixel by pixel bases in 3D using Mimics® software from a patients MRI scans. (B-D) The attained model was separated into two regions using Blender®. (E) Two cartridges of alginate methyl cellulose, coloured red or green were prepared. (F) The digital file was imported to the bioscaffolder 3.1 software (GeSIM, Germany) and a print code generated. The code script was edited for printing with two print heads and printing commenced.

### 3.2.6 Scaffold characterisation

Scaffolds were assessed based on their micro and macro architectures using optical/stereo and scanning electron microscopy (SEM). Imaging was performed to study strand-strand material spacing (pore size), pore morphology, strand width and overall structural consistency.

#### 3.2.6.1 Cryogenic-scanning electron microscopy of alginate methyl cellulose

##### scaffolds

The alg/MC scaffolds with strand numbers of six or eight, produced with tips of diameter size 0.51 mm or 0.61 mm were analysed using cryogenic-scanning electron microscopy (CRYO-SEM) on a Zeiss sigma field emission gun scanning transmission electron microscope (Carl Zeiss Ltd. UK, FEG-STEM) at the University of Brighton's

Image Analysis Unit (IAU). Portions of the scaffolds were cut to size with a scalpel and mounted onto sample stubs using cryogenic glue (EPO-TEK). The samples were measured individually. Prior to measurement each sample was attached to a holder and plunged into frozen liquid nitrogen slush. The sample was entered into the CRYO-SEM transfer chamber under a pulled vacuum of  $1 \times 10^{-2}$  mBar. The chamber was filled with argon and the sample sublimed at  $90^{\circ}\text{C}$  for 5 minutes before being spluttered with a 4 nm platinum conductive coating. The sample was docked for measurement under the microscope. The strut widths and pore dimensions were determined from SEM images using the smart Tiff imaging software package (Zeiss Zen 2) (Fig.3.4). Pore cross-sectional areas were calculated based on the following equation:

$$\text{Equation 3.1} \quad A = h \times w$$

whereby  $A$  is cross-sectional area ( $\text{mm}^2$ ),  $h$  denotes height (mm) and  $w$  is pore width (mm).

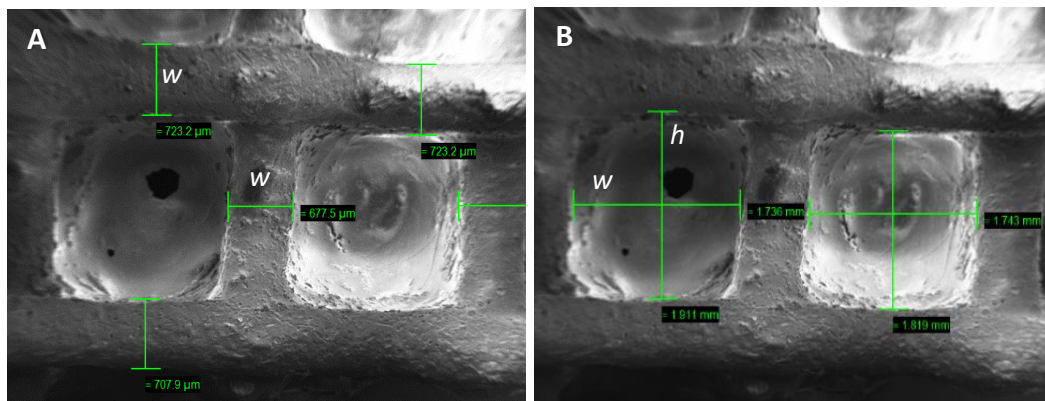


**Figure 3.4** Procedure for measuring (A) material strut widths ( $w$ ) and (B) macropore height ( $h$ ) and widths from Cryo-SEM images of alginate methyl cellulose scaffolds using the smart Tiff imaging software package (Zeiss Zen 2).

### 3.2.6.2 Stereo light microscopy of collagen methyl cellulose scaffolds

Images of the collagen + 1% MC scaffolds were taken using a stereo light microscope (Leica M205 C equipped with DFC295 camera, Germany). The strut widths were

determined using the Image J V1.44p analysis suite and images scaled by via normalisation to scalebars.

### 3.2.6.3 Compression testing

Compression experiments using an Electroforce WinTest® Digital Control System (BOSE corporation) were performed to characterize the compressive properties of the scaffolds. Dimensional measurements of each scaffold were taken prior to testing using digital callipers (Duratool, 50-100-900). Engineering stress and strain were then recorded to extract the Young's moduli, as calculated from load and displacement using the following calculations:

$$\text{Equation 3.2} \quad \sigma = \frac{F}{A}$$

$$\text{Equation 3.3} \quad \varepsilon = \frac{\Delta l}{l_0}$$

whereby  $\sigma$  denotes stress,  $F$  signifies the applied force (N),  $A$  is cross-sectional area ( $\text{mm}^2$ ),  $\varepsilon$  denotes strain,  $\Delta l$  represents the change in height (mm) and  $l_0$  original height (mm).

Static compression testing of alginate methyl cellulose and collagen + 1% methyl cellulose scaffolds

Both alg/MC (Batch 1 samples) and collagen + 1% MC scaffolds were kept in cell culture conditions overnight ( $37^\circ\text{C}$  in growth medium) before compression was performed at room temperature ( $20\text{-}22^\circ\text{C}$ ). The wet scaffolds were compressed to 20% of their initial height at a velocity of 0.3 mm/s for 30 cycles to mimic low stress cartilage compression (Schütz *et al.*, 2017). The compressive modulus was determined by linear regression of stress–strain curves plotted for cycles: 5,10,15,20,25 in order to understand how the behaviour of the structures varied throughout the progressive loading cycles.

The compression set up was controlled using a block waveform dynamic compression sequence (Fig.3.5), using the steps as follows;

- 1) Load ramped at 0.02 N/sec (approximately 5% scaffold height) to -0.1 N
- 2) Displacement ramped to compression of scaffold height by 20% at 0.3 mm/s

- 3) Load was ramped back to -0.1 N at 0.02 N/sec (5% scaffold height to release some pressurisation)
- 4) Load was held at -0.1 N for a dwell period of 20 seconds to allow for recovery
- 5) Stages 1-4 were repeated for 30 cycles

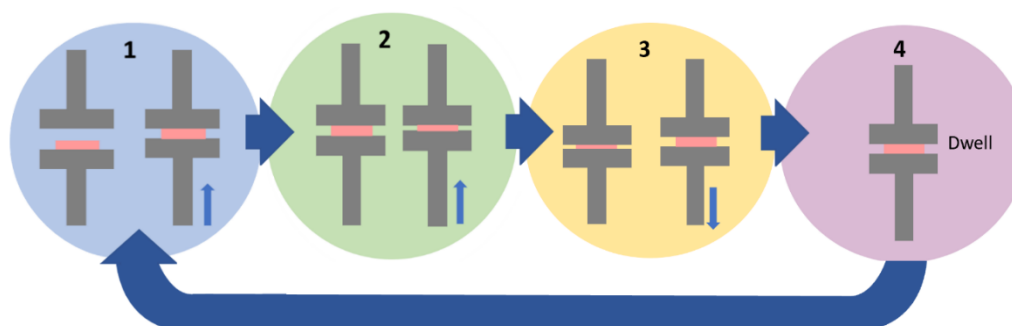


**Figure 3.5** Flow diagram to demonstrate the compression protocol (1-4) used for mechanical testing of alginate methyl cellulose and collagen + 1% methyl cellulose scaffolds.

#### Dynamic shear testing of alginate methyl cellulose scaffolds

Dynamic shear testing was performed on six stranded alg/MC scaffolds at 37°C, with a HAAKE Rheostress 1 rheometer (Thermo Scientific™) using oscillation rheology and parallel serrated plate ( $D = 20$  mm) measurement, with a gap distance of either 15% or 30% of the scaffold height measured with digital callipers (Duratool, 50-100-900), see Fig.3.6. The 15% and 30% strains employed were used to mimic physiological conditions with vertebral discs reported to be subjected to a constant baseline degree of compressive force at around 15% during rest *in vivo* and 30-45% under more severe spinal loading/activity (Latridis *et al.*, 1997; Baer *et al.*, 2001; Whatley *et al.*, 2011). Following this, each sample was subjected to a shear stress of 5 Pa (identified from an initial oscillation stress sweep of  $0.01\text{--}10$  s<sup>-1</sup>) at a frequency of 0.05-1.05 Hz to determine the viscoelastic behaviour of the cross-linked structures under strain (Fig.3.6). Dynamic shear properties  $G'$ ,  $G''$  and  $G^*$  (complex shear modulus) were measured.

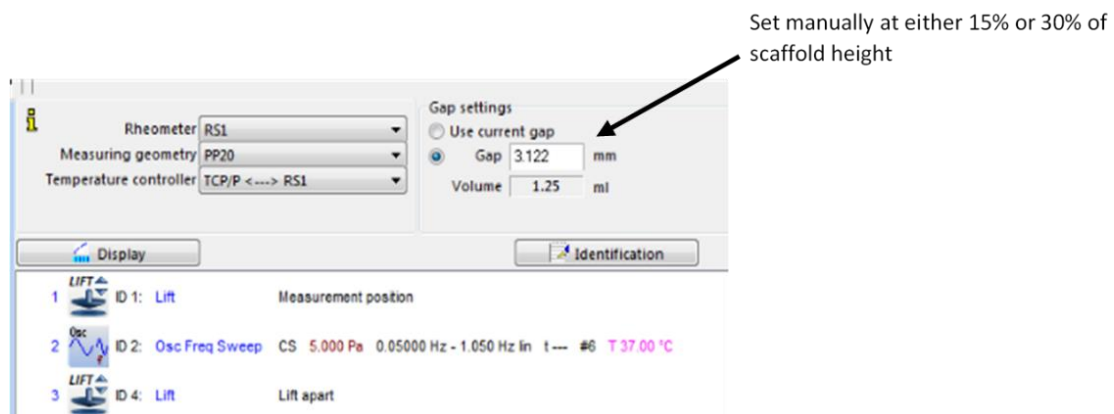


**Figure 3.6** Software interface of the AR G2 dynamic rheometer (TA Instruments) dynamic test set up on alginate methyl cellulose scaffolds. Demonstrating the use of the ‘gap settings’ to apply a defined compressive strain (entered as 3.791 for 15% and 3.122 for 30%) based on scaffold height. A step wise procedure was performed as follows: (1) Positioning/lifting of the lower plate to either 15% or 30% of the scaffold heights (as defined by gap setting) (2) Application of a compressive strain of 5 Pa and oscillation frequencies ranging from 0.05 Hz to 1.05 Hz, performed at 37°C (3) Separation of the plates to remove compressive force on the sample.

### 3.2.7 Statistical analysis

All measured data was analysed statistically using analysis of variance (ANOVA). When the ANOVA indicated a significant difference ( $P \leq 0.05$ ) between groups, the difference was evaluated with post hoc comparison of Bonferroni set at  $P \leq 0.05$  using IBM SPSS 24 statistical software platform® (UK).

### 3.3 Results

#### 3.3.1 Material Characterisation with Fourier transform infrared spectroscopy

FTIR is a technique used to measure how much infrared radiation a sample absorbs at each wavelength, whereby a materials absorption is specific to their chemical composition with different chemical bonds relating to specific peaks of absorbance. Thus, the infrared spectrum of absorption retrieved from materials can be used to identify and characterise materials.

##### 3.3.1.1 Fourier transform infrared spectroscopy of alginate methyl cellulose

The FTIR spectrums of the alginic salt (Fig.3.7, A) and MC powder (Fig.3.7, B) and their assignments were identified in Table.3.4. The spectra of the alg/MC scaffolds (Fig.3.7, C) demonstrated characteristic peaks of alginate which were shifted due to the presence of the ionic surfactant ( $\text{CaCl}_2$ ) and the combination with MC. Successful ionic cross-linking of the alginate was confirmed by the increased wavenumber of the carboxyl peak seen at  $1595\text{ cm}^{-1}$  in the alginic salt to  $1606\text{ cm}^{-1}$  in the alg/MC spectra, with a shift of the carboxyl absorption band by approximately  $11\text{ cm}^{-1}$ . Similarly, the band ( $-\text{CH}$ ) at  $1406.8\text{ cm}^{-1}$  in the alginic salt was also shifted to  $1412.63\text{ cm}^{-1}$  in the alg/MC blend. As was expected, alginate related peaks were present within the alg/MC spectra, including the  $1312\text{ cm}^{-1}$  (C-O) peak seen at  $1315\text{ cm}^{-1}$ , the  $1123\text{ cm}^{-1}$  (C-C) peak found at  $1192\text{ cm}^{-1}$ , the  $1024\text{ cm}^{-1}$  peak (C-O-C stretching) at  $1029.8\text{ cm}^{-1}$  and the  $946\text{ cm}^{-1}$  peak (C-O stretching) at  $947\text{ cm}^{-1}$  (Fig.3.7, C). Characteristic peaks of the MC could also be identified within the alg/MC spectrum, with C-H stretching bands of  $1372\text{ cm}^{-1}$  seen at  $1375\text{ cm}^{-1}$ ,  $1313\text{ cm}^{-1}$  at  $1315\text{ cm}^{-1}$ ,  $944\text{ cm}^{-1}$  at  $946\text{ cm}^{-1}$  and the distinguishing C-O-C band of  $1054\text{ cm}^{-1}$  slightly shifted to  $1056\text{ cm}^{-1}$ . The early hydroxyl  $3457\text{ cm}^{-1}$  band was also seen at  $3400\text{ cm}^{-1}$ , as well as the C-H stretching band at  $2922\text{ cm}^{-1}$ . The FTIR spectra of different alg/MC batches showed no apparent differences in peak heights or ratios between the batches prepared with different PBS diluents (Fig.3.7, C was representative of all batches).

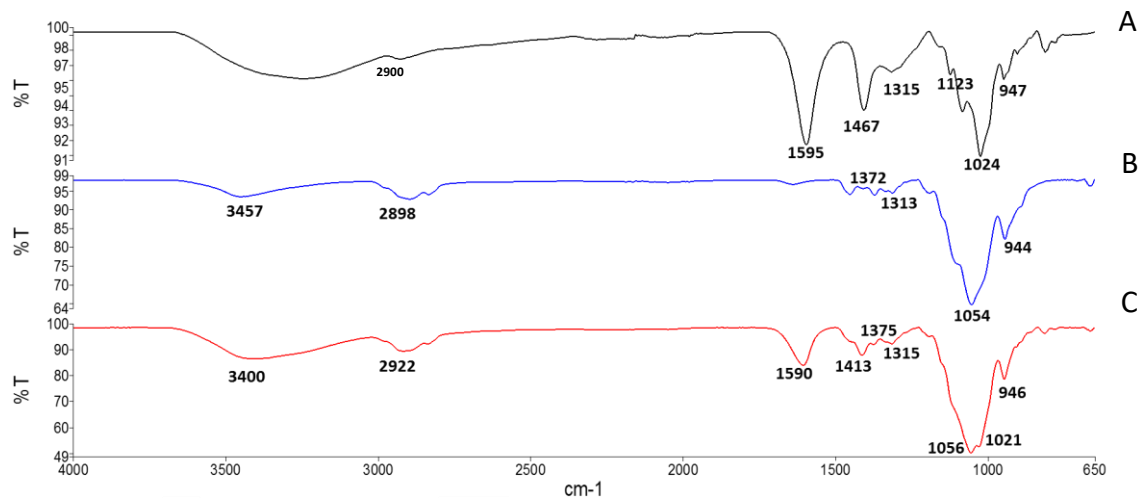


**Figure 3.7** Fourier transform infrared (FTIR) spectra of (A) alginate salt powder (B) methyl cellulose powder and (C) freeze-dried alginate methyl cellulose scaffolds ionically crosslinked with calcium chloride.

**Table 3.4** Chemical bond assignments of the Fourier transform infrared spectra for alginic salt and methyl cellulose.

Material	Position (cm <sup>-1</sup> )	Peak assignment
Alginic salt	1315	C-O, C-C, C-O-C and C-O stretching. Characteristic absorption bands of alginates native polysaccharide structure (Peretz <i>et al.</i> , 2014).
	1123	
	1024	
	947	
	1595	Asymmetric and symmetric stretching peaks of carboxylate salt groups, known to be present in alginate (Peretz <i>et al.</i> , 2014).
	1407	
Methyl cellulose	1372	Representative of C-H stretching of both the CH <sub>2</sub> and CH <sub>3</sub> groups (Schluffer and Heinze, 2010).
	1320	
	950	
	1054	C-O-C bonds, characteristic of cellulose ethers (Schluffer and Heinze, 2010).
	3457	Stretching of the O-H bond (hydroxyl groups) of cellulose (Oliveira <i>et al.</i> , 2015).
	2898	C-H stretching due to the presence of CH and CH <sub>2</sub> groups of cellulose and CH <sub>3</sub> of the MC (Oliveira <i>et al.</i> , 2015).

### 3.3.1.2 Fourier transform infrared spectroscopy of alginate di-aldehyde-gelatinmethyl cellulose

The combination of atoms within the ADA-Gel material provided a unique FTIR spectrum suitable for identification, with the size of the peaks in the spectrum representing direct indication of the amount of material present. The ADA material preparation was based on the methods taken from Sarker *et al.*, (2014). In this study

the spectrum of ADA demonstrated key peaks at 1594 and 1557  $\text{cm}^{-1}$  (Fig.3.8,A), which were stated to indicate the carboxyl groups of the oxidised alginate with the presence of aldehyde; characteristic of ADA formation. In comparison, the spectrum of the ADA recreated within this study (Fig.3.8, B) showed matching peaks at 1597 and 1405  $\text{cm}^{-1}$ , which confirmed that the material replication of ADA formation was achieved.

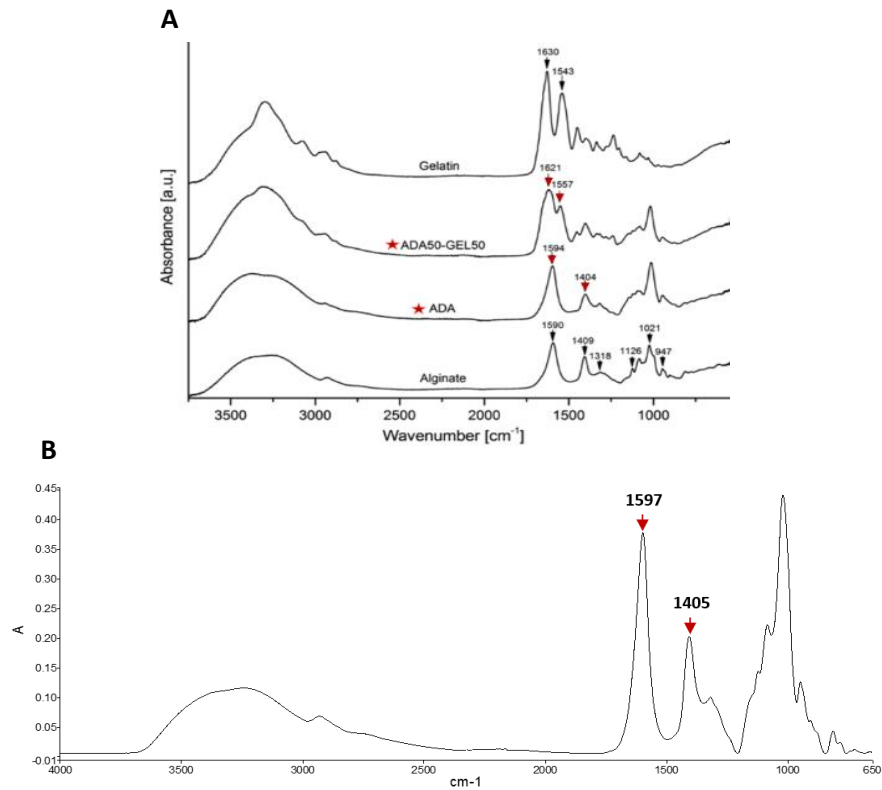


**Figure 3.8** (A) Fourier transform infrared (FTIR) spectrum of alginate dialdehyde and alginate dialdehyde-gelatin, alongside spectra of the material components alginate and gelatin taken from Sarker *et al.*, (2014) for comparison with (B) FTIR spectra of alginate dialdehyde and alginate dialdehyde-gelatin. Comparisons of the two spectrum show shared characteristic peaks for the alginate dialdehyde material.

### 3.3.1.2 Fourier transform infrared spectroscopy of collagen

Although a precise allocation of absorption bands for each collagen type present within the collaplex solution (GfN Selco) (stated to consist of type I and III collagens) were not distinctly obvious in the FTIR spectra (Fig.3.9, A) the absorptions bands at 1,452, 1,400, 1,337, 1,240, and 1,203  $\text{cm}^{-1}$  could be attributed to the  $\delta(\text{CH}_2)$ ,  $\delta(\text{CH}_3)$ ,  $\nu(\text{C}-\text{N})$ , and  $\delta(\text{N}-\text{H})$  absorptions related to collagens. In addition, the peaks at 1,629 and 1,545  $\text{cm}^{-1}$  can be assigned to amides I and II absorptions respectively (Fig.3.9, A) (Camacho *et al.*, 2000; Belbachir *et al.*, 2009; Cheheltani *et al.*, 2012). The FTIR spectra attained from the freeze-dried collagen in this study visually matched the collagen spectra seen within the previous publication by Belbachir *et al.*, 2009 (Fig.3.9, B). The comparison of spectra can be used to assume pure collagen presence, with no obvious additional peaks (between Fig.3.9, A-B).

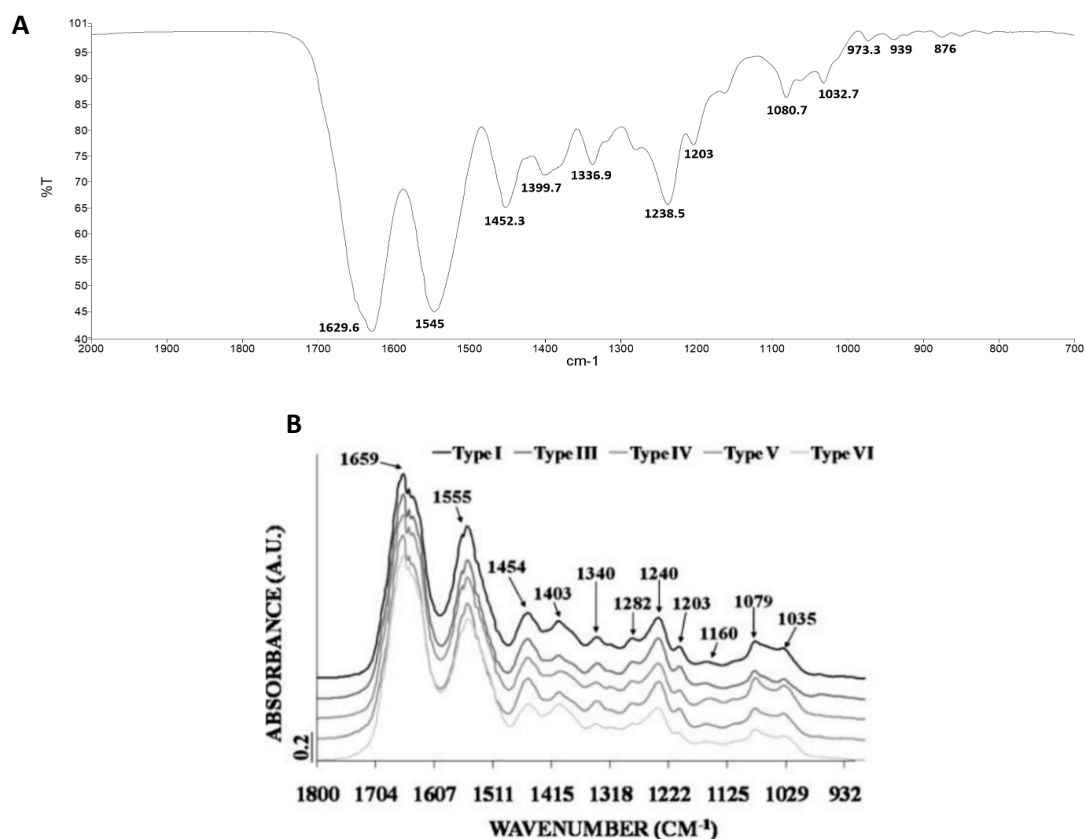


**Figure 3.9** Fourier transform infrared (FTIR) spectra of freeze-dried collagen (A) 1% collaplex (B) comparative spectra of five collagen types from the publication by Belbachir *et al.*, (2009).

### 3.3.2 Material properties

Dynamic shear viscosity and dynamic shear properties of the alg/MC and non-fibrillar collagen pastes were determined, whereby a material with shear thinning properties and a viscosity within the range of 30 mPa·s to  $>6 \times 10^7$  mPa·s is known to be essential for extrusion bioprinting (Murphy and Atala, 2014; Katja Hölzl *et al.*, 2016).

The alg/MC batches prepared with different PBS diluents (Batch one with liquid sterile-filtered PBS, batch two with PBS tablets from Sigma-Aldrich, batch three with PBS tablets from Sigma-Aldrich and stirred overnight and batch four using PBS tablets from Dulbecco A and stirred overnight) had different measured viscosities (Table.3.5, Fig.3.10). Batch one had the lowest viscosity ( $89.1 \pm 9.6$  Pa·s) relative to the other batches at  $s^{-1}$  ( $P = 0.019$ ) and batch four had a significantly higher viscosity ( $342.3 \pm 59.0$  Pa·s) compared to the other batches ( $P = 0.0014$ ). The batch numbers two and three, prepared with the same PBS source had no significant difference in viscosity at  $s^{-1}$ , with values of  $129.9 \pm 7.6$  Pa·s and  $117.04 \pm 5.8$  respectively ( $P = 0.133$ ). Repeated measurements within batches one-three showed no significant difference in viscosity, demonstrating material preparation consistency.

The dynamic viscosity measurements of MC addition to alginate suggested that the MC had an almost immediate and significant effect on material viscosity (Table.3.5, Fig.3.10). With an observed increase in viscosity from  $4.71 \pm 0.09$  Pa·s (alginate only) to  $72.92 \pm 3.43$  Pa·s after 0.08 hours of MC presence. Viscosity of the paste after MC addition continued to change over time with a significant increase between one hour ( $84.59 \pm 1.29$  Pa·s) to two hours ( $89.91 \pm 3.75$  Pa·s), as well as from two hours to four hours ( $105.6 \pm 4.99$  Pa·s). By four and 24 hours ( $109.23 \pm 3.56$  Pa·s), there was no further significant change to the alg/MC paste showing that viscosity plateaued between these later time-points (Fig.3.10).

From the rheogram plots (Fig.3.11-3.12), wherein dynamic viscosity was derived after a shear rate of  $1$ -s, the shape of the slopes seen inferred that alg/MC behaved as a pseudoplastic fluid. This was demonstrated by the evidence of fluid flow, in which the alg/MC paste responded instantaneously when changes to shear rate were applied i.e. the plot of shear stress against shear strain passed through the origin (Fig.3.11). Furthermore, the characteristic shear stress slope gradually decreased with increasing

shear rate, which demonstrated that the material viscosity was directly dependent on shear rate i.e. it was a non-Newtonian fluid (Fig.3.11); an essential property of bioinks. The dynamic viscosity derived from the slope of this curve was seen to decrease as the shear rate was increased, which is known as shear thinning, and was consistently observed between material replicates (Fig.3.12).

**Table 3.5** Dynamic shear viscosity for alginate methyl cellulose material batches prepared with different phosphate-buffered saline sources at  $s^{-1}$  of applied shear rate.

	<b>Shear rate at <math>s^{-1}</math></b>			
<b>alg/MC batch</b>	<b>1</b>	<b>2</b>	<b>3</b>	<b>4</b>
<b>Mean <math>\pm</math> stdev</b>	89.09	129.87	117.04	342.25
<b>(Pa·s)</b>	$\pm 9.63$	$\pm 7.62$	$\pm 5.76$	$\pm 58.95$

Values presented as the mean  $\pm$  standard deviation (n=4), whereby Pa·s refers to pascal-second a measurement unit of dynamic viscosity. Alginate methyl cellulose batches prepared with different phosphate buffer saline (PBS) diluents and stir conditions were as follows: Batch 1 was made with liquid sterile-filtered PBS (Dulbeccos) and stirred overnight after alginate addition. Batch 2 was prepared with PBS tablets from Sigma-Aldrich and stirred for five hours. Batch 3 was made using PBS tablets from Sigma-Aldrich but stirred overnight. Batch 4 was made with PBS tablets (Dulbeccos) then stirred overnight.

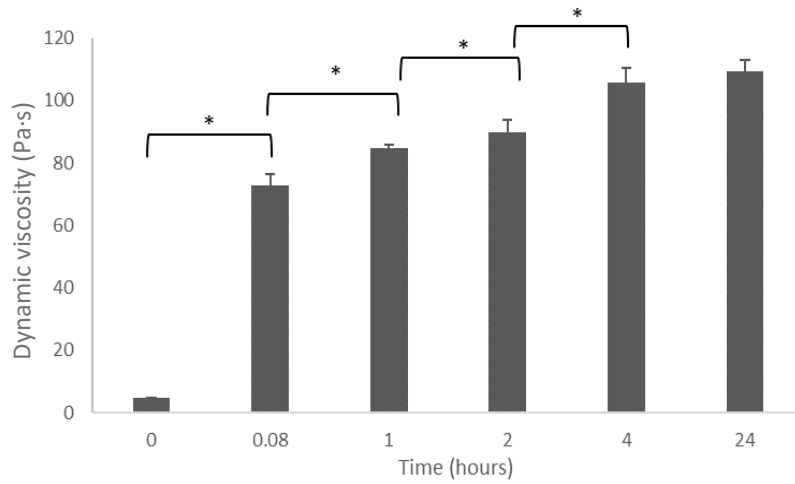


**Figure 3.10** Mean dynamic viscosity of alginate methyl cellulose (alg/MC batch 1) measured over time following initial MC addition, to monitor MC swelling effect on material viscosity, where time '0' represents the alginate only control (n=4,  $P \leq 0.05$ , mean  $\pm$  stdev). Batch 1 was made with liquid sterile-filtered phosphate buffer saline (Dulbeccos) and stirred overnight after alginate addition.

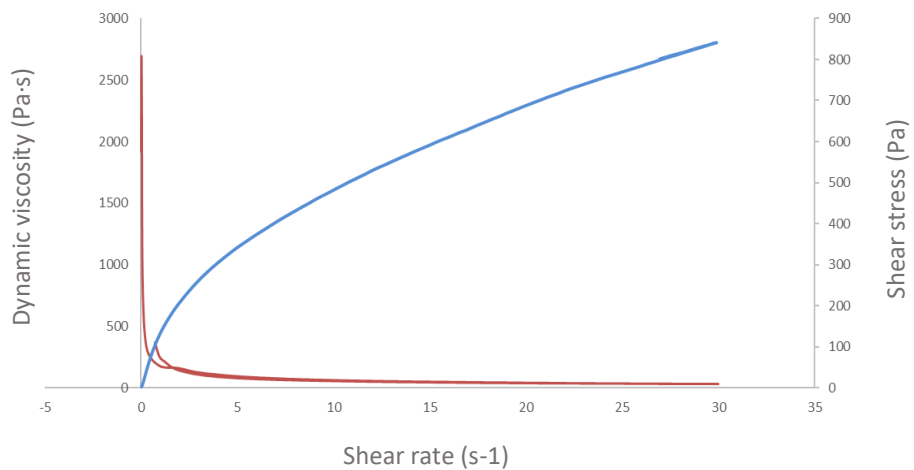


**Figure 3.11** Representative rheogram of alginate methyl cellulose paste from batch 2, (material before ionic cross-linking) the plotted curves represent the shear stress (blue line) and viscosity (red line) as a function of shear rate. Batch 2 was prepared with phosphate buffer saline tablets from Sigma-Aldrich and stirred for five hours.

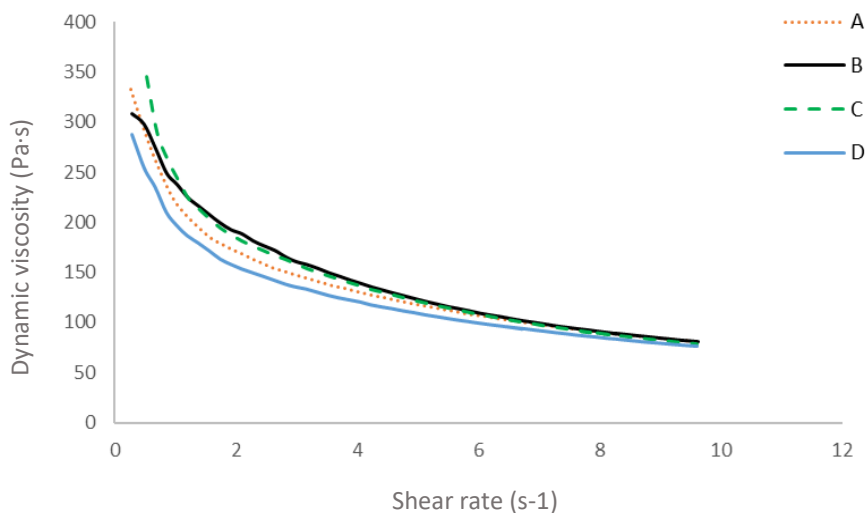


**Figure 3.12** Example rheometer curves of four (A-D) batch one alginate methyl cellulose replicates, demonstrating repeatability as well as a characteristic decreasing viscosity with increasing shear rate. Batch one was made with liquid sterile-filtered phosphate buffer saline (Dulbeccos) and stirred overnight after alginate addition.

It was shown that the fibrillar collagen 4% paste formulations did not produce a homogenous consistency and was deemed as incompatible with printing, whereas the non-fibrillar collagen 4% formulation produced a smooth paste consistency. Subsequently, the non-fibrillar collagen was taken forward for further characterisation, with and without the addition of 1% MC.

The measured dynamic viscosity of the non-fibrillar collagen pastes were shown to be significantly increased immediately following the addition of 1% MC, wherein the viscosity further increased after both a 30 minute and 2 hour swell time ( $P = 0.01$ ) (Table.3.6), with a greater viscosity corresponding to longer swell time ( $n = 4$ ). In comparison the recorded viscosity of the collagen paste alone did not significantly alter over time ( $P = 0.28$ ) (Table.3.6).

Furthermore, the dynamic shear properties of the non-fibrillar collagen paste with and without MC addition were also measured (Fig.3.13). Following the addition of MC to collagen it was apparent that there was a drop in both  $G'$  and  $G''$ . In which,  $G'$  denotes the elastic stored energy and represents the solid component of a material whereas

G'' represents the energy lost from the system (as heat) and characterises the liquid behaviour of a material. Thus, after the addition of MC the elasticity of the paste was lower, this feature coincided with increased printability. Another observation was that the stability of the G' and G'' decreased after 3500 seconds following MC addition and could have been related to MC swelling changing the material properties and viscosity over time (Fig.3.13).

Experiment attempts to sterilise the non-fibrillar collagen altered the collagen material properties which made it unsuitable for printing. Both the UV and  $\gamma$ -irradiation performed on the freeze-dried collagen resulted in material hardening and an inability to dissolve in HCL. When the scCO<sub>2</sub> treatment was used a partial dissolution of the collagen was possible, but remaining paste inhomogeneities prevented material extrusion. After ethanol soaking of the freeze-dried collagen a paste was prepared that was sticky and viscid, and despite additions of MC extrudable strands could not be achieved. The chloroform evaporation method performed on the pre-prepared collagen paste at both room temperature and 4 °C resulted in increased viscosity and material inhomogeneity compared to the untreated collagen + 1% MC and collagen alone (Appendix, Fig.S1B) subsequently the increase in viscosity hindered printing.

**Table 3.6** Mean dynamic shear viscosity of collagen and collagen + 1% methyl cellulose material batches after 0 minutes, 30 minutes or 2 hours after paste formulation at s<sup>-1</sup> of shear rate.

	Shear rate s <sup>-1</sup>					
	Collagen only (0 min)	Collagen +1% MC (0 min)	Collagen only (30 min)	Collagen +1% MC (30 min)	Collagen only (2hr)	Collagen +1% MC (2hr)
<b>Mean</b>	45.02	68.37	46.02	104.37	48.30	232.56
<b>± stdev (Pa·s)</b>	± 6.12	± 6.08	± 6.08	± 9.42	± 7.33	± 12.02

Values presented as mean ± standard deviation (stdev), n=6. MC denotes methyl cellulose and Pa·s is Pascal-second, a measurement unit of dynamic viscosity.

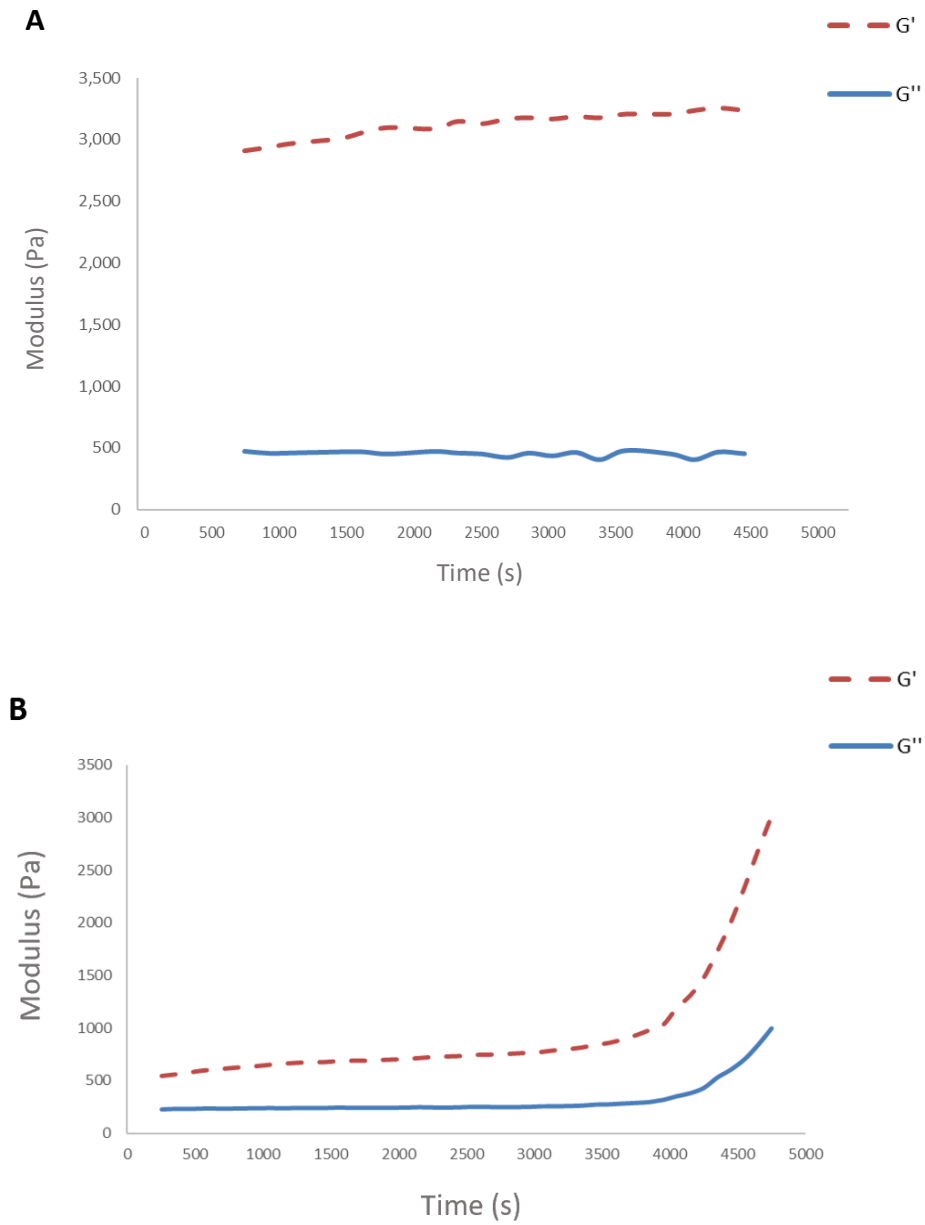


**Figure 3.13** Rheograms demonstrating the dynamic shear properties of the (A) collagen paste alone and (B) collagen + 1% methyl cellulose. Storage shear modulus ( $G'$ ) and loss modulus ( $G''$ ) were plotted over time.

### 3.3.3 Fabrication of scaffolds

The bioprinting of materials required the adjustment and optimisation of print parameters which were highly dependent on the material properties, wherein the lower viscosity pastes demanded lower print pressures and high print speeds. The adapted print parameters used for the consistent material extrusion of alg/MC and collagen + 1% MC materials were stated previously in Table.3.3.

With regards to the alg/MC printing, the batches prepared with PBS tablets from Sigma-Aldrich (batches two and three) demonstrated a consistent fluid flow behaviour that was suitable for reproducible bioprinting (Fig.3.14). However, the excessively high and low viscosity of batches four and one, respectively, led to the cessation of these material batches for bioprinting due to recurrent tip blockage or uncontrolled fluid flow. Key influential parameters identified for the accurate deposition of alg/MC included the applied start break (time of pressure applied before needle movement) which was necessary to prime the tip prior to print start, as well as the z-offset (tip distance from the plate or previous material layer). These factors proved essential for the formation of continuous strand deposition. Multi-head printing with alg/MC was also achieved and was capable of producing well defined simple scaffold structures (Fig.3.15, A-D) as well as a more complex anatomically shaped disc model (Fig.3.15, E).

Following the addition of 1% w/v MC non-fibrillar collagen pastes were found to be suitable for controlled bioprinting, within a window of ~15-70 minutes immediately after MC addition (Fig.3.16, A-D). It was identified that the flexible conical 0.84 mm ID tip and the 0.61 mm stainless steel cannula tips were the best for achieving collagen strand fidelity. As a result of the optimised print parameters structurally viable scaffolds composed of 12 layers with open macropores (Fig.3.16, A-D) were fabricated using the collagen + 1% MC paste. The TA cross-linking treatment of the scaffolds led to a hardening of the collagen + 1% MC scaffolds making them easier to handle without deformation. In comparison, scaffold fabrication was not achieved using fibrillar collagen due to an inability for homogenisation, wherein remaining fibres caused persistent clogging of print tips.

In addition, the ADA-Gel paste variants, prepared with differing ratios of periodate, were also found to be unsuitable for bioprinting even at the lowest print pressure

application (1 kPa) and the finest tip available (ID 0.2 mm). The ADA-Gel formulation was therefore disqualified for further study as no stable scaffolds could be formed.

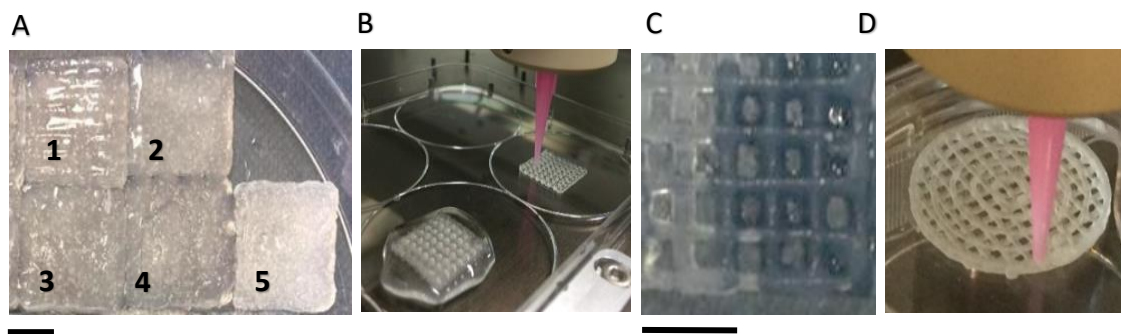


**Figure 3.14** The modification of print parameters for the printing of alginate methyl cellulose (alg/MC) through a 0.51 mm ID polyethylene tapered tip (Nordson) (A) alg/MC plotted using unrefined parameters of (1) 80 kPa, speed 10 mm/s (2) 80 kPa speed 15 mm/s (3) 75 kPa, speed 10 mm/s (4) 75 kPa speed 15 mm/s (5) 75 kPa speed 10 mm/s (B-D) alg/MC printed with adjusted settings of 70 kPa, speed 10 mm/s. Scale bars represent 5 mm.

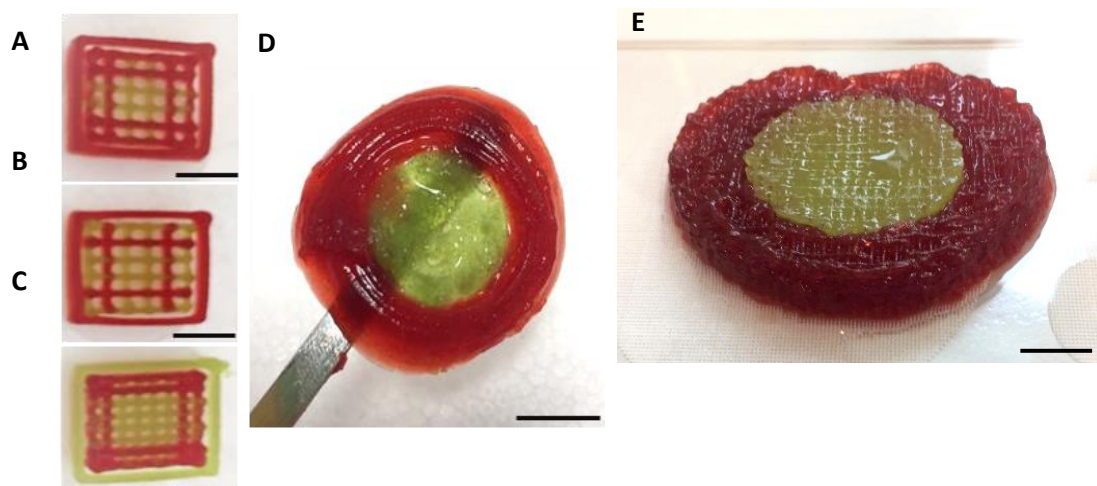


**Figure 3.15** Cartridges were prepared for multi-material printing containing coloured alginate methyl cellulose (alg/MC) paste and were loaded into the GeSIM bioscaffolder 3.1 to be recognised as print head A (red) and C (green) by the printer software. Multi-head printing of alg/MC scaffolds with different designs were achieved using the print sequences: (A) ACCAACCA (B) ACACA (C) AACCCCAA (D) AC. (E) An up-scaled intervertebral disc model comprised of two regions printed using separate print heads, with coloured alg/MC. Scale bars represent 10 mm.

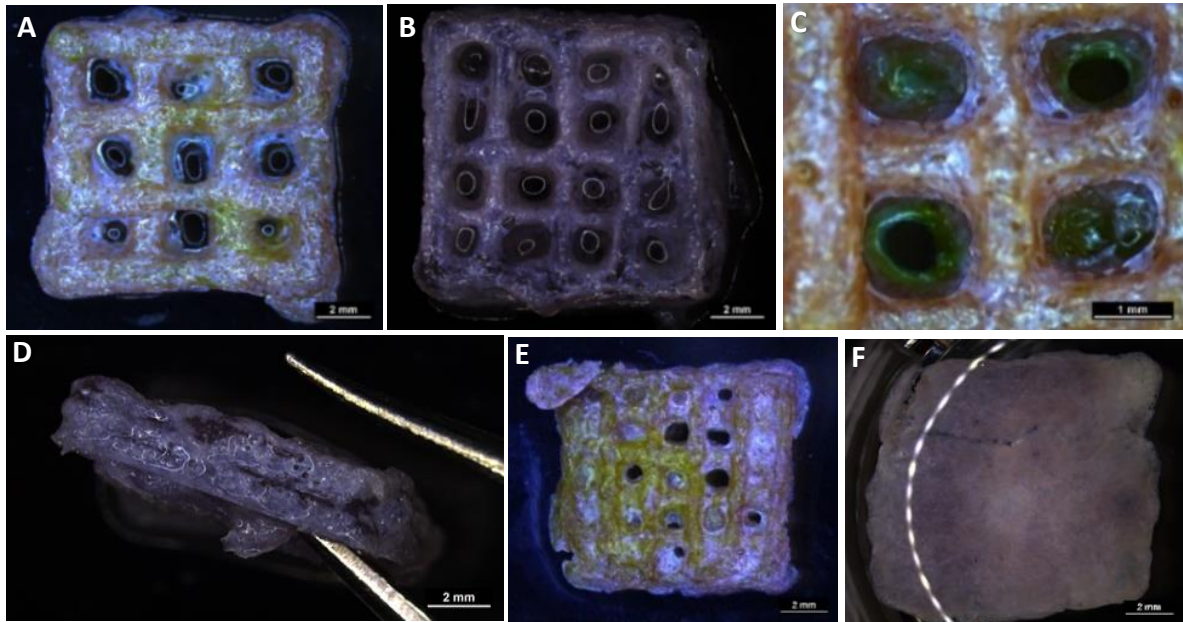


**Figure 3.16** 4% Collagen + 1% methyl cellulose scaffolds. Images taken with a stereo light microscope (Leica M205 C equipped with DFC295 camera, Germany). (A) Four strand scaffold plotted using stainless steel cannula tip, 0.84  $\mu\text{m}$  ID (mag x10). (B) Five strand scaffolds produced using a flexible conical nozzle, 0.61 mm ID, (mag x10). (C) Close-up view of five strand variant macropores, plotted with nozzle size 0.61 mm (mag x20). (D) Side view of a 12 layer five strand scaffold to demonstrate full height (mag x10). (E-F) Early collagen scaffolds produced with non-refined print parameters, (E) pressure of 70 kPa, speed 8 mm/s, (F) 80 kPa, speed 5 mm/s.

### 3.3.4 Morphological characterisation of scaffolds

Imaging (optical/stereo and SEM) was performed to study the micro and macro architectures of the fabricated scaffolds to assess for structural integrity and consistency of the parameters such as strand-strand material spacing (pore size), pore morphology, strand width and overall structural consistency.

### 3.3.4.1 Cryogenic-scanning electron microscopy of alginate methyl cellulose

#### scaffolds

The mean values of the dimension measurements taken from the Cryo-SEM images of alg/MC scaffolds (Fig.3.17, Table.3.7) demonstrated the differences caused by tip diameter on the produced structures, regarding material strand deposition. When a 0.61 mm tip and 0.51 mm tip type was used to plot an eight strand alg/MC scaffold a noticeable and expected reduction in strand width was seen ( $0.739 \pm 0.4\text{mm}$  to  $0.607 \pm 0.02\text{ mm}$ ). In addition, the use of the 0.51 mm tip resulted in larger pore cross-section areas than with the 0.61 mm tip size ( $1.43 \pm 0.1$  compared to  $1.13 \pm 0.08\text{ mm}^2$ ); due to the related reduction of strand width. Comparison of the six and eight strand alg/MC scaffolds printed using the 0.61 mm tip saw a distinct difference in pore size, whilst maintaining a similar strand width (Fig.3.17, Table.3.7). Thus, showing evidence of good structural control.

Statistical analysis to confirm the significance of the measurements taken between the tip types and strand variants were unavailable for Cryo-SEM images: as the sample loading tray used for the analysis only fit one sample (~4 x 4mm) at a time, and only a few pores could be observed per scaffold in the microscopes available field of view. However, the measurements taken strongly corresponded to the software specified measurements used for their production (strand number and tip diameter) with a low variance between measurements (Table.3.7) and so were considered an accurate representation of the printing outcome.

A consistent material deposition and connected geometry was apparent in the scaffolds plotted with the 0.61 mm tip (Fig.3.17, A-D). In comparison, images of alg/MC structures printed with the 0.51 mm tip showed evidence of material breakage (Fig.3.17, D) and this was likely associated with the reduced tip diameter. The narrower 0.51 mm tip reduced volumetric material flow rate compared to the 0.61 mm tip to produce struts with a lower material volume. This resulted in strand breakage as the strands could not support themselves over the free hanging gap of the macropore (Fig.3.17, D). The topography of the alg/MC material appeared mostly smooth, but some micro porosity and texture was apparent (Fig.3.17, A-D).

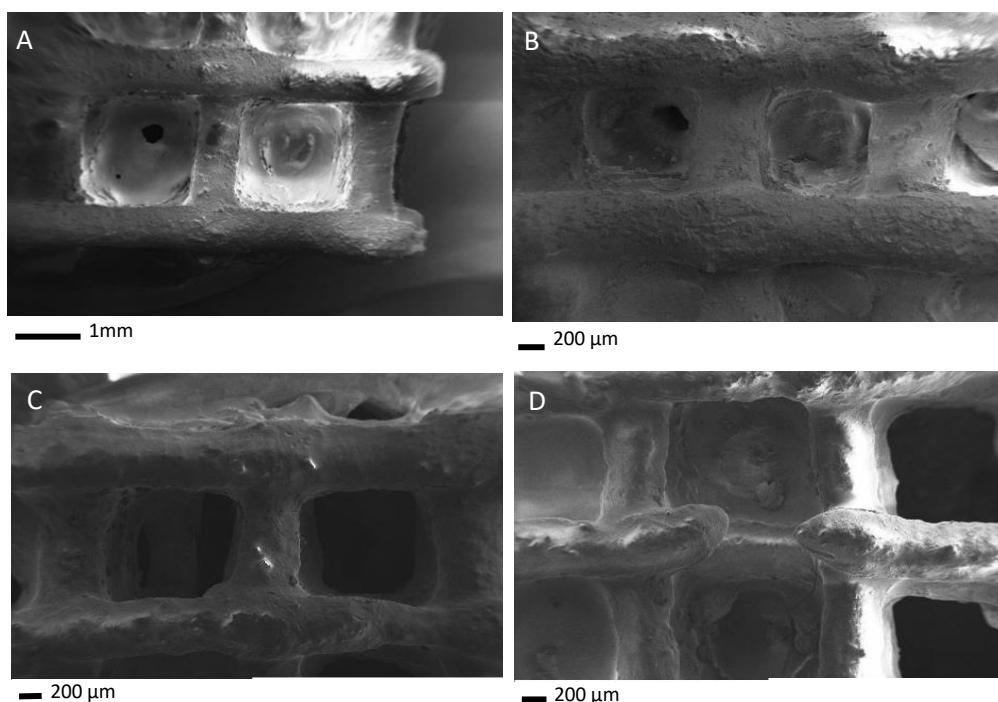


**Figure 3.17** Cryogenic-scanning electron microscopy images of alginate methyl cellulose (alg/MC) scaffolds. (A) Six strand scaffold printed using a tip with an inner diameter (ID) of 0.61 mm. (B) Eight strand scaffold printed using a tip with an ID 0.61 mm. (C) Six strand scaffold produced with a tip with the ID 0.51 mm. (D) Eight strand scaffold printed with ID of 0.51 mm with evidence of material breakage between struts.

**Table 3.7** Pore morphology measurements of alginate methyl cellulose scaffold variants printed with either six or eight materials strands using tips with the inner diameter of 0.61 mm or 0.51 mm

Measurement averages	alg/MC scaffold variants		
	ID 0.61 mm		ID 0.51 mm
	6 Strands	8 strands	8 strands
Pore cross-section area (mm <sup>2</sup> )	3.15 ± 0.13	1.13 ± 0.08	1.43 ± 0.10
Strut width (mm)	0.736 ± 0.3	0.739 ± 0.4	0.607 ± 0.02

Values are presented as the mean ± standard deviation (n=6). ID denotes inner diameter (of the print tip used), alg/MC denotes alginate methyl cellulose. The pore cross-sectional area measurements were calculated using Area= height × width. Strut width represents the diameter of a material strand.

### 3.3.4.2 Optical microscopy of collagen methyl cellulose scaffolds

Collagen (+ 1% MC) scaffolds printed with a 0.61 mm ID steel cannula needle type had a significantly lower mean strand width than structures plotted using a 0.84 mm flexible conical tip, with mean values of  $0.878 \pm 0.132$  (mm) and  $1.152 \pm 0.113$  (mm) respectively (Fig.3.18). When the optimised print parameter settings were used for each tip type (previously stated in Table.3.3) the scaffolds had visibly open and connected macropore networks (Fig.3.18). However, some pores within the collagen scaffolds were misshapen. In particular pore malformations occurred on the edges and corners of the scaffolds, whereas the central pores were visually more consistent in size and morphology (as seen in the top left corner of Fig.3.18, A-B). For this reason, measurements of pore cross-sectional area were not performed. Microscopy of the collagen topography revealed a fibrous and microporous surface (Fig.3.18, A-B).

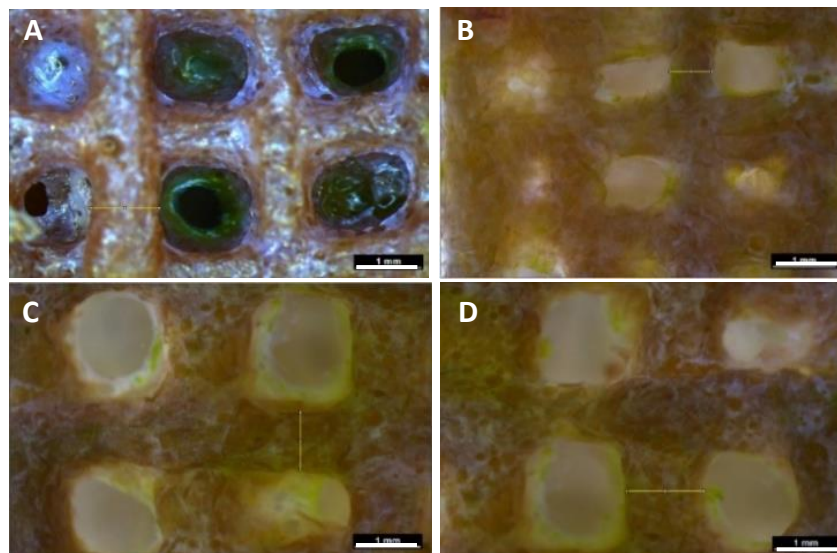


**Figure 3.18** Stereo microscopy images of collagen + 1% methyl cellulose scaffolds (A-B) printed with 0.61 mm inner diameter (ID) steel cannula tip (C-D) or 0.84 mm ID flexible conical tip (scalebar = 1 mm).

### 3.3.5 Scaffold mechanical properties

The mechanical properties of scaffolds can have an influence on structural integrity over time which can affect the feasibility of structures for supporting the growth of cells and was therefore an important factor for consideration when comparing samples.

#### 3.3.5.1 Shear testing of cross-linked alginate methyl cellulose scaffolds

The rheological testing of alg/MC scaffolds at both a 15% and 30% compressive strain demonstrated a ratio of  $G'$  and  $G''$  values with a significantly higher  $G'$  to  $G''$  modulus (Table 3.8). The  $G'$  denotes elastic stored energy and represents the solid component of a material and  $G''$  represents the energy lost from the system (as heat), which characterises liquid material behaviour. Thus, the higher  $G'$  to  $G''$  ratio which was observed for the alg/MC demonstrated that material behaved predominantly as a solid, but was still viscoelastic in nature (made up of both solid and liquid components) (Whatley, 2013).

The dynamic shear modulus ( $G^*$ ), comprised of both  $G'$  and  $G''$ , additionally provided important information about the material properties of alg/MC. For both the compressive strains tested the alg/MC  $G'$  and  $G^*$  measurements were not significantly different (Table 3.8). Thus, for both the 15% and 30% compressive strains the  $G^*$  was primarily governed by  $G'$ , meaning that the energy stored during deformation was mostly stored by the alg/MC material, which signified elastic behaviour.

**Table 3.8** Mean dynamic shear moduli values of the alginate methyl cellulose scaffolds under compressive strains of 15% and 30%.

		Degree of compression (strain)	Mean $\pm$ stdev (kPa)
<b>Storage (G')</b>	<b>Modulus</b>	15%	28.39 $\pm$ 2.7
		30%	35.67 $\pm$ 4.0
<b>Loss Modulus (G'')</b>		15%	5.16 $\pm$ 0.8
		30%	6.61 $\pm$ 0.7
<b>Dynamic (G*)</b>	<b>Modulus</b>	15%	28.88 $\pm$ 2.6
		30%	36.32 $\pm$ 3.8

Values are presented as the mean  $\pm$  standard deviation (n=6). Degree of compression represents the distance of the rheometer plates during testing, which were set at either 15% or 30% of the scaffold height. Scaffold heights were measured using digital callipers prior to testing (Duratool, 50-100-900).

### 3.3.5.2 Compression loading of alginate methyl cellulose scaffolds

The overall shape of the stress strain graph of the alg/MC scaffolds were found to be reasonably represented by a linear line of best. The recorded range of Young's moduli for the alg/MC scaffolds was from 43-60.4 kPa (Table.3.9). The Young's moduli calculated from the linear regression of all points decreased from early to late compression cycles, which showed a softening of the material over time, with a reduction in stiffness of 28% from cycle 5 to the 25<sup>th</sup> cycle (Table.3.9).

**Table 3.9** Young’s modulus values of the alginate methyl cellulose scaffold at cycles 5,10,15,20,25. Means calculated from linear regression curves of stress versus strain. A general trend of decreasing compressive modulus was seen over the course of the test.

<b>Cycle</b>	<b>Young’s modulus (kPa)</b>
<b>5</b>	60.4 ± 2.4
<b>10</b>	51.3 ± 3.3
<b>15</b>	49.2 ± 2.8
<b>20</b>	42.5 ± 1.9
<b>25</b>	43.3 ± 1.2

Values are presented as the mean ± standard deviation (n=6). Wet alginate methyl cellulose scaffolds were compressed to 20% of their initial height at a velocity of 0.3 mm/s for 30 cycles to mimic low stress cartilage compression. The Young’s modulus was determined by linear regression of stress–strain curves plotted for cycles: 5,10,15,20,25.

### 3.3.5.3 Successive compression testing of collagen methylcellulose scaffolds

During the compression testing of the collagen + 1% MC scaffolds no breaking stress point was observed and instead the test was manually stopped once 145 kPa of force had been applied. After pressurisation the collagen + 1% MC scaffold structure appeared visually intact but the internal fluid had been extruded out of the scaffold. The scaffold heights were measured with callipers (Duratool, 50-100-900) before and after testing (Table.3.10). After compression the scaffolds were returned to over-night incubation in DMEM + P/S and the scaffold heights were measured. Height recovery was seen after three daily rounds of compression with no significant difference in height before the start of each compressive test (Table.3.10). In addition, the measured Young’s modulus of the collagen scaffolds showed no significant reduction over time after two days of successive loading (Fig.3.19). With mean compression moduli values of 69.62 ± 2.10 kPa on day one of incubation (after one compressive loading) and 67.99 ± 2.65 kPa on day two of incubation (after a second compressive load). On the third day of incubation and compression the recorded Young’s moduli of the scaffolds was significantly reduced, with a moduli of 54.55 ± 3.76 kPa (Fig.3.19).

The samples could not be kept or tested for longer than three days due to the lack of sterility of both the collagen scaffolds and test conditions.

**Table 3.10** Measured heights of collagen + 1% methylcellulose scaffolds before and after compression testing on three successive days of incubation and mechanical testing.

	Day 1 before	Day 1 after	Day 2 before	Day 2 after	Day 3 after
Mean height (mm)	1.982 ± 0.106	1.124 ± 0.098	1.976 ± 0.110	1.02 ± 0.136	0.928 ± 0.024

Values are presented as the mean ± standard deviation (n=3). Collagen + 1% methyl cellulose scaffold heights recorded using digital callipers (Duratool, 50-100-900) before and after compression testing on three successive days. During loading scaffolds were loaded to 20% of their initial height at a velocity of 0.3 mm/s for 30 cycles, scaffolds were maintained under standard cell culture conditions in-between compressions (37°C, 5% CO<sub>2</sub>).

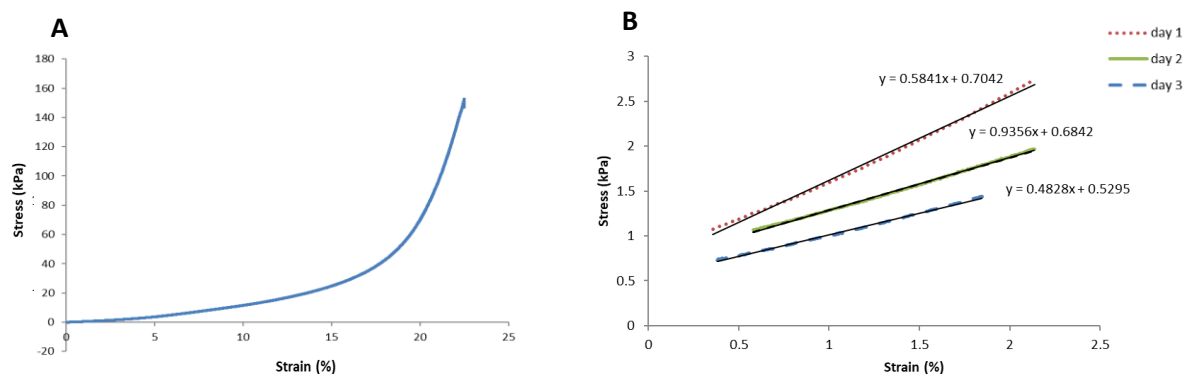


**Figure 3.19** Example stress-strain graphs of the same collagen + 1% methyl cellulose scaffold (A) full stress-strain curve recorded on day 1 of incubation. (B) The regions of linearity used for extrapolating the Young's moduli on days 1, 2 and 3 of recurrent compression, using a threshold of between 0.5-2.0% strain.

### 3.3.6 Biomaterial comparison

A comparison of the tested alg/MC, Collagen + 1% MC and ADA-gel materials was performed based on their feasibility for cell-laden bioprinting for the purpose of cartilage tissue engineering. Seven key properties were used for the assessment of the material variants which included: ease of material preparation, material/scaffold reproducibility, suitability for printing, material sterility, prospect for cell compatibility (dependent on the print conditions, material properties and material stabilisation methods required), structural integrity (maintenance of open and interconnected pore networks) and scaffold compressive moduli. The result of this screening determined that alg/MC was the favoured biomaterial candidate, with a high suitability for the bioprinting of stable and repeatable structures under conditions suitable for cell inclusion (Table.3.11).

**Table 3.11** A comparison of alginate methyl cellulose, non-fibrillar collagen + 1% methyl cellulose and alginate dialdehyde-gelatin materials based on their feasibility for bioprinting.

Material	Properties						
	Ease of preparation, 1-5 (1 easy, 5 hard)	Reproducibility (based on FTIR and viscosity)	Suitable for printing	Sterile	Prospect for cell compatibility	Scaffold structural integrity	Compressive moduli (kPa)
Alg/MC	2	Good	Yes	Yes	Good	Yes	49.3 ± 7.2
Collagen + 1% MC	3	Good	Yes	No	Good	Yes	69.6 ± 2.1
ADA-Gel	4	Good	No	No	Good	No	N/A

Ease of material preparation was ranked based on the complexity and time taken for material formulation. The rating for 'Reproducibility' was judged dependent on FTIR spectra and viscosity repeatability between batches. Factors considered for the assessment of the criteria 'Suitable for printing' included the consistency of fluid flow under pressure and was reliant on the viscosity and shear thinning properties of the materials. A material was confirmed as sterile if a sterilisation process was determined which allowed for sterile material printing. The property 'Prospect for cell compatibility' was evaluated based on the conditions used for printing as well as material toxicity, topography and composition. Scaffold structural integrity was gaged based on scaffold microarchitecture, such as open pore networks. The compressive moduli values were presented as the mean ± standard deviation (n=6).

### **3.4 Discussion**

The characterisation of the materials investigated in this study was initially achieved via FTIR spectroscopy. FTIR was used to identify the bonds within the formulated materials, based on their absorption. The spectra produced was used as a quick and reliable method for assessing material composition and as an index for material reproduction/batch quality control.

In the example of the ADA-Gel material formulated in this study (the accurate replication of the ADA-Gel chemical composition was confirmed. Wherein, the ADA-Gel peaks (Fig.3.8) visually matched those stated in the Sarker *et al.*, (2014) publication (the first formulators of ADA-Gel). Within the ADA-gel spectra, characteristic bands of ADA formation were observed at 1594 and 1557  $\text{cm}^{-1}$ . An occurrence which is based on the periodate oxidation of alginate. Without the formation of ADA, the hybridisation with gelatine would not occur and the degradation properties of alginate would be unchanged (Sarker *et al.*, 2014). However, despite the correct material preparation of ADA-Gel (confirmed by FTIR) the formulation was fluid in consistency which is an incompatible property with bioprinting for the fabrication of well-defined and stable structures (Zhang *et al.*, 2018). This issue was discussed with the Sarker *et al.*, group who stated that they had similarly experienced print incompatibility and had made alterations to their methods to increase material viscosity. The alterations made included a decrease in sodium periodate addition and editions to the molecular structure of the alginate. Despite the suggested changes to the material preparation Sarker *et al.*, claimed that the ADA-Gel would “still not be an ideal material for the fabrication of 3D structures, as it is not inherently a paste-like material”. Furthermore, the reduction of sodium periodate concentration to increase ADA-Gel thickness was explored in this work, with the ratios of 0.25:1 and 0.5:1 in ethanol-water mixture. However, this did not sufficiently improve the rheology of the material for bioprinting.

Conversely, for alg/MC the material characterisation using FTIR and rheology evidenced features which demonstrated an effective material preparation for bioprinting. An example of this, was the FTIR spectra of alg/MC which displayed a combination of peaks from both alginic salt and MC, as well as a visible alteration to

the alginate carboxylate groups caused by  $\text{CaCl}_2$  cross-linking. Thus, confirming the hybrid combination of materials and an effective crosslinking approach for structural stabilisation. Furthermore, the degree of carboxylate shifting, known to depend on the duration of cross-linking and  $\text{CaCl}_2$  concentration (Lee and Mooney, 2012) had no observable difference between the batch replicates, which suggested that a repeatable cross-linking method was achieved. The dynamic shear viscosity testing of alg/MC also revealed multiple attributes for bioprinting, including shear thinning and a non-Newtonian fluid behaviour (Fig.3.11-3.12).

Upon the comparison of the different alg/MC batches, prepared with different PBS diluents, a significant disparity in dynamic shear viscosity was observed. With measurements recorded from  $89.1 \pm 9.6$  Pa/s for batch one (prepared with sterile-filtered PBS, Dulbecco) to  $342.3 \pm 59.0$  Pa/s for batch four (made with PBS tablets, Dulbecco). This result demonstrated the importance of PBS selection on resultant alginate properties, whereby the underlying cause of the variation batches was likely the result of the trace element quantities present within the different PBS sources. Consequently, the presence of trace elements could have affected alginate dissolution; as alginate is known to cross-link ionically. For example, the significantly increased viscosity of batch four may have been due to additional ionic presence within the tablets (Dulbecco A, pH 7.3, Dulbecco), which were not specifically disclosed as calcium or magnesium chloride free.

Furthermore, no significant difference ( $P = 0.097$ ) was observed between the mean dynamic viscosity of batch two ( $129.9 \pm 7.6$  Pa·s; stirred for 5 hours) and three ( $117.04 \pm 5.8$  Pa·s; stirred overnight) of alg/MC which were prepared with PBS tablets (Sigma-Aldrich). A result which further suggested that that the disparity of viscosities seen in batch one and four were not the result of manual error, such as discrepancies in measurement or mixing. Wherein, the lack of significant difference between batch two and three of alg/MC which were prepared with the same PBS source suggested that a difference in PBS diluent was more influential than stir time for material preparation. Thus, based on this study the use of alg/MC batch three was employed for further investigation for bioprinting, due to its low variance between replicates and mid-range viscosity which was found to be highly-suitable for pressure-based extrusion.

The parameters used for bioprinting of alg/MC pastes resulted in the repeatable extrusion of the hydrogel under sterile conditions with mid-range pressures and print speeds of 60-70 kPa and 8-10 mm/s respectively, and cell compatible temperatures of 20-25 °C. The analysis of the alg/MC scaffolds by SEM demonstrated macropore networks that were open and connected (cross-sectional areas of  $1.13 \pm 0.08 \text{ mm}^2$ ) with consistent material strand dimensions ( $0.607 \pm 0.02 \text{ mm}$ ) (Fig.3.17, Table.3.7). Thus, the highly controlled microarchitectures of the alg/MC scaffolds are promising attributes for cell inclusion, to allow for effective nutrient/waste and mass-transfer when printed with embedded cells (Billiet, *et al.*, 2012).

An additional attribute of the alg/MC scaffolds for cell inclusion was the observed surface topography shown using SEM imaging, which appeared to reveal a subtly texturized material surface. The micro-porous architecture of alg/MC scaffolds has been previously reported (Schütz *et al.*, 2017) and was theorised to be caused by the release of MC from the scaffolds over time (Schütz *et al.*, 2017). Surface micro-porosity and micro-architecture is a desirable feature for biomaterials, which create spaces for cell attachment and integration (Chen *et al.*, 2018). Although, it should be stated that it is possible that the alg/MC topographical properties seen may have been influenced by the sample preparation required for SEM imaging (3.2.4). Nevertheless, alginate hydrogels have been well established in medicine as a result of their cell amicable properties and mild ionic cross-linking (Elder *et al.*, 2006; Kundu *et al.*, 2013; Gálvez-Martín *et al.*, 2019). In particular, alginate has been highly popular for cartilage engineering, with alginates high-water content and overall negative charge being similar to cartilage matrices (Lee and Mooney, 2012), and therefore represented a good candidate for further research with cells for IVD cartilage engineering.

However, a characteristic limitation for employing alginate in tissue engineering, remains the innately low physical strength of natural hydrogels. In this study, alg/MC scaffolds on day one of fabrication had a mean Young's moduli of  $49.3 \pm 7.2 \text{ kPa}$ , a value that is orders of magnitude lower than the maximum Young's modulus reported for whole IVDs of approximately 16.37 MPa (Pei *et al.*, 2013). Conversely, when compared to the Young's moduli of NP tissue alone, which has been previously recorded as 0.003-0.031 MPa (Mow *et al.*, 2004) the alg/MC scaffolds are not overly dissimilar to NP tissue ranges. Thus, despite the disparity of alg/MC with IVD strength, the leading positive attribute of alginate is its capability for supporting cell growth and

neocartilage development. As such, the matrix produced by the cells within the alginate would be the main contribution towards the restoration of cartilage properties, rather than a reliance on the material alone.

Similar to alg/MC, the novel non-fibrillar 4% collagen +1% MC paste formulated in this investigation also demonstrated multiple attributes for bioprinting. Upon the characterisation of the non-fibrillar collagen paste using FTIR, the key peaks identified were successfully matched with previously published collagen spectra (Belbachir *et al.*, 2009) (Fig.3.9, B). Wherein, no additional bands or shifting was observed upon the comparison of the two collagen spectras (Fig.3.9, A-B), which suggested that the isolation of pure collagen from the commercially available collaplex solution (GfN Selco) was achieved. The inferred purity of the collagen biomaterial, with the removal of potential toxic preservatives (found in collaplex) therefore represented an important feat. With pure collagen capable of permitting the biocompatible inclusion of living cells.

Furthermore, the rheological testing of the non-fibrillar collagen paste found that following the addition of 1% MC that the collagen pastes demonstrated shear thinning properties suitable for printing. After the addition of the MC component a large drop in both  $G'$  (2,484 Pa) and  $G''$  (272 Pa) was observed, i.e. the elastic portion of the paste was significantly lowered ( $P = 0.002$ ). In addition, the stability of the beneficial effect of MC on collagen elasticity was shown to decrease after 3500 seconds and was employed to identify an optimal printing window - within a range of 1000-3500 seconds after MC addition. Consequently, it was assumed that the time-dependent influence of MC on collagen properties was due to the result of MC swelling over time. Thus, the use of MC for the enhancement of collagen and alginate hydrogel properties for bioprinting was employed within this study and highlighted the potential widespread benefits of MC additives for biomaterials.

The bioprinting of 4% collagen + 1% MC pastes was shown to form stable scaffolds, with a continuous material flow under mid-range and cell amicable pressures of 55 or 66 kPa, with a 0.84 mm tapered tip or 0.61 steel cannula tip (Nordson), respectively. During printing it was noted that the print tip 'type' had a significant influence on collagen strand precision (Fig.3.16). Wherein, the burr-free, passivated stainless steel tips resulted in a more refined material strand deposition than the 'smooth flow'

tapered tip designs (Nordson), of  $0.878 \pm 0.132$  (mm) and  $1.152 \pm 0.113$  (mm) respectively. The difference in print precision was attributed to the influence of material properties and the difference in the interior tip designs and rigidity on material flow dynamics (Nair *et al.*, 2009; Aguado *et al.*, 2011).

Thus, the resolution of collagen + 1% MC was similar to alg/MC, within a micron range. However, despite the print parameter optimisation employed for collagen printing some limitations were experienced. In particular, the pores on the external edges of the collagen + 1% MC scaffolds were deformed compared to the central pore regions. The cause of the distortion was associated with physical displacement of the material during printing, or 'dragging off'. The material dragging occurred when extruded collagen strands remained attached to the print tip for longer than programmed, rather than directly depositing onto the print plate. In future development, a potential solution could be an adhesive print plate, such as one coated with gelatine to keep strands fixated immediately after deposition (Migliaresi, 2015). However, the preparation of a sufficient collagen material volume for further print optimisation was limited in this experiment (with 1 g of material attainable per litre of collaplex solution, GfN Selco) and as such the discrepancy was not resolved in this work. The issue of poor micro-architectural control was therefore a limiting factor for the collagen + 1% MC scaffolds, whereby high reproducibility is a requirement for the clinical feasibility of tissue-engineered structures (O'Brien, 2011).

Nonetheless, based on the scaffold physical properties the TA cross-linked collagen scaffolds had a Young's moduli of  $69.62 \pm 2.10$  kPa. The collagen scaffolds therefore demonstrated an increase relative to the alg/MC hydrogel scaffolds ( $49.3 \pm 7.2$  kPa), which was a Young's moduli within the range of NP measurements (0.003-0.031 MPa) reported by Mow *et al.*, (2004). Furthermore, the collagen scaffolds were capable of withstanding loads (maximum  $\sim 0.15$  MPa) without evidence of structural breakage and retained an ability to recover height between stress applications (Table 3.10, Fig.3.19). Thus, the collagen scaffolds demonstrated an endurance for low level loading, which is a desirable trait for potential *in vivo* applications and was not shared by the alg/MC structures.

Consequently, the use of the novel collagen + 1% formulation developed in this investigation, demonstrated a promising capability for bioprinting under cell amicable

print conditions with mild TA cross-linking (Kim, Lee and Kim, 2017). Wherein, the inherent physical properties of collagen as well as collagen's supportive role within native cartilage make it a sought after material for cartilage engineering. Conversely, animal derived hydrogels, such as collagen and gelatin, have been associated with concerns regarding immunogenic reactions and infection (Zhu and Marchant, 2011). Thus, in addition to the previously stated biomaterial criteria for tissue engineering (Table.3.1) the clinical feasibility of the collagen + 1% MC hydrogel was decidedly limited in contrast to alg/MC, in particular with regards to:

**Material preparation:** The extraction of medical grade collagen was time-consuming and in-efficient due to the week-long dialysis purification which resulted in a relatively low yield of purified collagen (1 g of material per 1 litre of collaplex solution, GfN Selco). In comparison, alginate and MC products are non-animal derived, widely available and cheaply sourced (Lee and Mooney, 2012; Li *et al.*, 2017) and their combination for alg/MC preparation is a quick and efficient process (Schütz *et al.*, 2017).

**Scaffold reproducibility:** An inconsistency in macropore morphology was repeatedly observed within the collagen + 1% MC scaffolds, whereby batch-batch reproducibility is a critical feature for the approval of medical and pharmaceutical products by the MHRA and FDA (Lysaght and Hazlehurst, 2004). Conversely, the alg/MC scaffolds demonstrated a high structural reproducibility upon printing that resulted in consistently produced macro-porous structures. The good resolution of alg/MC printing was further evidenced by the materials adaptability for multi-headed material printing for the generation of a human IVD model, which was based on medically derived dimensions with accurate regional representations of the AF and NP disc sections.

**Sterility:** Material sterility is an important consideration in scaffold production (Rutala and Weber, 2013), however despite the trialling of five different sterilisation approaches: UV and  $\gamma$ -irradiation, scCO<sub>2</sub> treatment, ethanol and chloroform soaking, a suitable sterilisation process for collagen was not identified. The sterilisation methods trialled on collagen all altered the paste material properties to a degree which forced trade-offs to be made with printability. Comparatively, the use of sterile alginate based biomaterials have been extensively used in medical research without detriment to cells or processability (Stoppel *et al.*, 2014; Axpe and Oyen, 2016).

As a result, it was the alg/MC hydrogel out of the ADA-gel and collagen formulations trialled that was deemed as the preferred biomaterial candidate for future investigation. In the proceeding work the potential for alg/MC as a suitable bioink for cartilage engineering using encapsulated chondrocyte-laden bioprinting is explored.

### 3.5 Summary

The work in this study demonstrated the preparation and comparison of three materials: alg/MC, ADA-Gel and collagen + 1% MC as potential candidates for the purposes of cartilage tissue engineering using bioprinting. The materials and resultant scaffolds were characterised and compared based on their molecular properties (FTIR analysis), printability (rheology), structural architecture and reproducibility (microscopy and mechanical testing). Of the formulations, the alg/MC and collagen + 1% MC pastes were successfully screened for printing (Table.3.3) Under optimised and defined conditions the two materials demonstrated a continuous and homogenous fluid flow and produced structurally intact scaffolds. Conversely, the innate low viscosity of the ADA-Gel hybrid prevented the formation of a stable, printable paste and was excluded from further investigation.

From material development for the purposes of cell-inclusive tissue engineering, alg/MC was surmised as the most favourable candidate. This decision was based upon the following criteria, in which alg/MC performed well across all analysis:

1. Ease of manufacture
2. Prospects for sterility
3. Cell compatibility
4. Application/compatibility of characterisation techniques

The high structural reproducibility of the scaffolds attained using alg/MC and collagen + 1% MC validated the approach of bioprinting using the bioscaffolder 3.1 (GeSIM, Germany) as an effective method for the fabrication of clinically relevant structures. This was concluded from the high-level multi-material print control achieved and the fabrication of patient defined bespoke IVD models. The optimal processing parameters identified in this study will be carried forward into the next experiments for the incorporation of chondrocytes during alg/MC scaffold fabrication.

## **Chapter 4 Investigating the effect of sterilisation methods on the physical properties and cytocompatibility of methyl cellulose used in combination with alginate for bioprinting chondrocytes**

### 4.1 Introduction

In the previous chapter the screening of biomaterials for bioprinting was performed. As a result, the biomaterial alg/MC was established as a leading candidate for cell encapsulation and precise material deposition. In the present study further characterisation of alg/MC as a bioink for the encapsulation of bovine primary chondrocytes was performed. With the effects of four sterilisation methods, autoclave, scCO<sub>2</sub> treatment, UV and  $\gamma$ -irradiation evaluated, regarding their impact on alg/MC material properties and cellular responses.

Alginate is a naturally occurring anionic polymer and represents one of the most extensively investigated hydrogels used for many biomedical applications (Lee and Mooney, 2012). Due to its simple crosslinking by multivalent cations and its suitability for cell encapsulation (Lee *et al.*, 2000) the transition of alginate for extrusion-based bioprinting has been commonly pursued (Fedorovich *et al.*, 2012; Kundu *et al.*, 2013). However, this has not been without challenge (Maher *et al.*, 2009). Materials suitable for extrusion must not only ensure continuous fluid-flow, but also maintain structural integrity upon deposition (Billiet *et al.*, 2012). Hence, viscous pastes are highly suitable whereas alginate solutions at low concentrations have a poor applicability for the plotting of 3D scaffolds due to their fluid like state (Maher *et al.*, 2009; Schütz *et al.*, 2017). However, a simple increase of its concentration to enhance the viscosity is restricted by a related decrease in cell survival after crosslinking. Alternative methods to improve hydrogel print capabilities without an increase in alginate network density include the use of complimentary material combinations, to utilise different gelation properties such as alginate/gelatine (Zehnder *et al.*, 2015), alginate/fibrin (Hwang *et al.*, 2013) and alg/MC (Schütz *et al.*, 2017).

The use of methyl cellulose (MC) as a thickening additive for alginate extrusion-based bioprinting is a relatively new approach, with the first formulation introduced by Schütz

*et al.*, (2017) (first available online in 2015). The addition of MC has since demonstrated a high potential for the bioprinting of different cell types (Lode *et al.*, 2015; Seidel *et al.*, 2017; Li *et al.*, 2017; Lode, Meyer and Brüggemeier, 2017) and its relevance for use in 3D printing was recently highlighted (Wang *et al.*, 2018). MC is obtained from the bacterium *Gluconacetobacter xylinus* and possesses high crystallinity, purity, and a large capacity for water absorption (as result of MC methyl groups) with excellent mechanical properties including shear thinning. MC is an easily mass produced, non-toxic and non-allergen substance with a current commercial importance across a range of industries, such as food and cosmetics (Nasatto *et al.*, 2015). MC is also commonly used in the study of the proliferation and differentiation of hematopoietic cells, as part of a colony forming cell (CFC) assay. Wherein, the number and the morphology of the colonies formed within an MC based semi-solid medium is used to assess the cells ability to differentiate and proliferate (Sarma, Takeda and Yaseen, 2010).

However, prior to both the incorporation of cells and future therapeutic applications, the sterility of a biomaterial must be ensured. Sterilisation refers to the complete destruction of life and biological agents including fungi, bacteria and viruses present within a targeted region (Munarin *et al.*, 2013). It is commonly achieved via the application of heat, chemicals, irradiation, high pressure or filtration through membranes with 0.22 µm pore sizes (Mendes, Brandão and Silva, 2007). However, by design common sterilisation techniques are intense, and can cause change to a material's chemical and physical properties (Mendes, Brandão and Silva, 2007; Munarin *et al.*, 2013). These alterations can affect its performance and feasibility for extrusion and tissue engineering. It is therefore of high importance to select the most appropriate sterilisation procedure, specific to the material used and its intended application.

Autoclaving is one of the most widely used health care sterilisation techniques due to its speed, efficacy and low cost (Dai *et al.*, 2016). The method uses pressurised steam and high temperature water for the thermal destruction of microbial life. However, high temperatures have been reported to adversely affect sensitive biomaterials such as polysaccharides (Mendes, Brandão and Silva, 2007; Ahmed, 2015).

A low temperature alternative for sterilisation is the application of super critical carbon dioxide (scCO<sub>2</sub>) in combination with low amounts of chemical additives. The basis of this sterilisation method is through the extreme pressurisation of CO<sub>2</sub> to nearly 10 times atmospheric pressure, above the critical point when the gas forms a solvent (Karajanagi *et al.*, 2011). Although the precise mechanism by which the scCO<sub>2</sub> method sterilises samples is not yet fully established, it is proposed to be the result of intracellular reactions upon solvent diffusion into the cell which cause the formation of carbonic acid, leading to acidification which along with chemical oxidation can kill bacteria (Damar and Balaban, 2006; Bernhardt *et al.*, 2015). The use of scCO<sub>2</sub> has been shown to achieve sterilisation without any notable negative physical or structural effects and has been suggested as a promising treatment for use with sensitive biomaterials (Spilimbergo *et al.*, 2003). In particular, the application of scCO<sub>2</sub> on MC was shown to be less compromising on mechanical and rheological properties when directly compared to ethylene oxide exposure, another low temperature alternative (Bernhardt *et al.*, 2015).

The use of  $\gamma$ -irradiation is the most common sterilisation technique for orthopaedic implants (Collier *et al.*, 1996), as well as various other fields including food preservation and pharmaceutical production (El-ashhab *et al.*, 2013), with between 25 and 40 kGy doses of radiation known to ensure sterility. Energy from photons of  $\gamma$  radiation is transferred to the electrons in the exposed material (Palmer *et al.*, 2012). The highly excited electrons then yield high doses of free radicals which disrupt the DNA double helix of any microorganism present. When the DNA is irreparably destroyed the cells are no longer able to function. However,  $\gamma$ -irradiation has been linked to crosslinking and chain scission in some polymers (Goldman *et al.*, 1996; Stoppel *et al.*, 2014; Maslennikova *et al.*, 2015).

UV light is employed in a comparable way to  $\gamma$ -irradiation but uses lower energy photons, with wavelengths between 290 and 200 nm considered optimal for disinfection purposes (Meechan and Wilson, 2006). The UV rays work by damaging DNA through initiating a reaction between two molecules of thymine within the nucleic acid. Dependent on the duration and proximity of the UV source, the DNA is irreparably destroyed, and the cells become inert (Huebsch, Gilbert and Healy, 2005). Although UV treatment is not considered a fully effective method for the terminal stage sterilisation of all biological life (Stoppel *et al.*, 2014), it is a common method of choice

for material sterilisation in research laboratories (Bryant and Anseth, 2002; Wilda and Gough, 2006; T.Reza and Nicoll, 2008; Pan *et al.*, 2016).

Acknowledging the high impact of sterilisation on biopolymer properties with respect to fabrication and scaffold characteristics, the intention of the present study was to systematically investigate the effect of four sterilisation methods on material properties relevant for bioprinting and cartilage tissue engineering. In addition to the easily accessible and commonly employed UV and autoclave treatments, the well-established  $\gamma$ -irradiation and the less utilised scCO<sub>2</sub> sterilisation (as a low temperature and irradiation-free method) were tested. The effect of sterilisation on MC was focused on, based on its role as a universal thickening agent for hydrogel plotting, to enable cell compatible and improved printing properties for the fabrication of volumetric, open-porous constructs. Hence, the sterilisation treatments were performed on powdered MC, as part of the alg/MC blend previously developed by Schütz *et al.*, (2017). The sterilisation of the alginate component by autoclaving was kept constant throughout, due to the low viscosity of 3% alginate solutions regardless of the sterilisation method employed (Leo, Mcloughlin and Malone, 1990; Stoppel *et al.*, 2014), and the already well established use of autoclave for alginate that has been used in research (Leo, Mcloughlin and Malone, 1990; Young *et al.*, 2012; Kundu *et al.*, 2013; Stoppel *et al.*, 2014; Park *et al.*, 2016). Furthermore, the constant treatment of the alginate component subsequently allowed for the reliable attribution of any observed changes in the paste and/or scaffolds to the effects of the MC only, as the primary material for conferring printability. By applying FTIR and gel permeation chromatography the chemical composition and molecular mass of the treated MC types were evaluated. The resulting alg/MC pastes were characterised with respect to viscosity and suitability for extrusion and the plotted scaffolds were analysed based on microstructure, composition, and mechanical properties. In addition, bovine primary chondrocytes (BPCs) were embedded in alg/MC prior to printing and cell viability as well as ECM deposition within the scaffolds was evaluated.

## 4.2 Materials and methods

### 4.2.1 List of materials

Dulbecco's modified eagle medium (DMEM), Hanks balanced salt solution (HBSS), penicillin/streptomycin and phosphate buffered saline solution (PBS) from Thermofisher, USA; Foetal calf serum (FCS), gentamycin, MQuant™ Peracetic Acid Test kit, sodium citrate and Trypan blue from Merck Millipore, USA; 5-chloromethylfluorescein diacetate (CMFDA) Green and ethidium homodimer from Molecular probes, USA; acetic anhydride, alginic acid sodium salt, hydrogen peroxide (H<sub>2</sub>O<sub>2</sub>), methyl cellulose and safranin O from Sigma-Aldrich, USA; calcium chloride (CaCl<sub>2</sub>) and chlorine–zinc–iodine solution from Roth, Germany; Mykoyal from Hund Wetzlar, Germany; QuantiFluor dsDNA system from Promega, USA; formaldehyde solution from SAV LP GmbH, Germany; QUANTOFIX® Fluitest CA CPC assay from Analyticon Biotechnologies, Germany; Peroxidetest strips from Macherey-Nagel, Germany.

### 4.2.2 Tissue processing and cell culture

Primary bovine articular cartilage was isolated from bovine metacarpal phalangeal joints of skeletally mature animals (~30 months) as previously described by Hall *et al.*, (1996). Briefly, bovine lower limbs were obtained from a local abattoir and used within four hours of animal death. Full depth articular cartilage was removed under aseptic conditions and incubated for ~20 hours in the presence of collagenase (Type II; 2 mg/ml<sup>-1</sup>) in high glucose DMEM with 10 µg/ml gentamycin at 37°C and 5% CO<sub>2</sub>. The digest was crudely filtered through a stainless-steel mesh followed by 70 µm nylon sieve (BD Bioscience, USA). The collected cell suspension was washed by centrifugation (5 minutes at 400xg) and counted by haemocytometer in the presence of trypan blue to determine cell viability. Cells were expanded for four days under normal cell culture conditions, seeded at 0.5 x 10<sup>6</sup> per T25 flask at 37°C and 5% CO<sub>2</sub> in standard culture medium consisting of DMEM with 10% FCS, 100 µg/ml penicillin and 100 µg/ml streptomycin. Viability of isolated cells typically varied between 80-90%

following incubation. The isolated cells were then frozen after one passage at  $-1^{\circ}\text{C}/\text{min}$  and stored in liquid nitrogen for use within two months. The BPCs were thawed and expanded in monolayer culture using previously stated cell culture conditions and standard growth medium. The medium was changed twice a week. Cells in suspension were counted using a haemocytometer and underwent four passages before use in bioprinting experiments.

#### 4.2.3 Sterilisation

For each approach, a pre-weighed amount of MC powder was transferred to Heat Seal Closure Pouches SteriBags™ (Fisher Scientific, USA).  $\text{scCO}_2$  treatment was performed in a 750 ml stainless steel autoclave (J&W Scientific, Inc., USA). The MC powder was placed into the autoclave and an additive mixture of 0.25 vol% water, 0.15 vol%  $\text{H}_2\text{O}_2$  and 0.5 vol% acetic anhydride was pipetted to the bottom of the vessel. The autoclave was then filled with 300 g liquid  $\text{CO}_2$  ( $18^{\circ}\text{C}$ , 5.5 MPa) and heated to transfer the liquid  $\text{CO}_2$  to the supercritical state ( $\sim 38^{\circ}\text{C}$ ,  $\sim 8.5$  MPa) for 45 minutes, depressurisation was performed within 6.5 minutes. To check for chemical residues, MC was dissolved at a concentration of 2 g/L in dd $\text{H}_2\text{O}$  after sterilisation with  $\text{scCO}_2$  and tested for  $\text{H}_2\text{O}_2$  and peracetic acid with semi-quantitative test strips. Untreated MC was tested as a negative control. For autoclaving, the MC powder was subjected to an autoclave cycle that consisted of high-pressure saturated steam at  $121^{\circ}\text{C}$  and held for 20 minutes before cooling in a Systec D-23 table-top autoclave. For UV-irradiation, the transparent MC bag was placed under a UVC lamp (wavelength 254 nm, Fisher Scientific) at a distance of 5 cm for two hours (conditions selected based on previously employed studies shown to be within the range for effective sterilisation (Fischbach *et al.*, 2001; Janorkar, Metters and Hirt, 2006; Yixiang *et al.*, 2008). The powder was spread out and evenly distributed to ensure a thin layer across the inside surface and re-adjusted after an hour interval to allow for full UV light exposure. The process was performed within a laminar flow hood. Treatment by  $\gamma$ -irradiation was carried out using a Cobalt 60 source at minimal dose of 25 kGy by BBF Sterilisation Service (Kernen, Germany). The sterilisation methods employed were previously validated using microbial cells by Bernhardt *et al.*, (2015), with the exception of UV which is a broadly

implemented but currently non-approved (medium inactivation level) method for sterilisation (Dai *et al.*, 2016).

#### 4.2.4 Plotting material preparation

The alg/MC hydrogel mixture was prepared as described in Chapter 3, as first demonstrated by Schütz *et al.*, (2017). In brief, a 3 w/v % alginate solution was made by mixing alginic acid sodium salt in PBS and stirred overnight before sterilisation using autoclave (121°C for 20 minutes) which has been shown to not alter the chemical structure of alginate (see Appendix, Fig.S2B). 9 w/v% sterilised MC was then added to the alginate solution. The mixture was stirred to obtain a homogeneous alg/MC paste and left to swell for one and a half hours before the addition of BPCs. The cells were suspended in culture medium (DMEM) with a ratio of cell suspension: plotting paste of 1:9, and a cell seeding density of  $5 \times 10^6$  per gram of material (based on the cell densities used in relevant literature by Hu and Athanasiou, (2006) and Elder and Athanasiou, (2008). Cell-free material was also printed to evaluate scaffold structure, material composition and mechanical properties.

#### 4.2.5 Bioprinting of alginate methyl cellulose constructs

The bioprinting system used in this study was the BioScaffolder 3.1 from GeSiM (Germany) operated under sterile conditions. The alg/MC material was dispensed through a dosing needle (Nordson) with an inner diameter of 0.61 mm and using a plotting speed of 10 mm/s and dosing pressure of 70-80 kPa. For the extrusion of the  $\gamma$ -treated material a reduced print pressure of 65 kPa bar and tip diameter of 0.45 mm were required. The 3D constructs were built up layer-by-layer into 12-well plates by plotting into air. The structures were designed with the defined overall dimensions of 9.5 mm by 9.5 mm, with a height of 1.4 mm per layer, comprised of 4 or 10 layers, 5 strands per layer, and an angle orientation change of 90° between the layers. After print completion the hydrogel scaffolds were crosslinked in sterile filtered (Merck™ Stericup™ Sterile Vacuum Filter Units; 0.10µm membrane) 100 mM CaCl<sub>2</sub> for ten

minutes. Both cell-laden and cell-free scaffolds were plotted under the same print conditions.

#### 4.2.6 Methyl cellulose characterisation

##### 4.2.6.1 Fourier Transform Infrared Spectroscopy

FTIR spectra were acquired from untreated and sterilised MC powders. The spectra were recorded with a 65 Fourier-transform infrared spectrometer (PerkinElmer), with an ATR crystal, in the spectral range of 400-4000  $\text{cm}^{-1}$  at a resolution of 4  $\text{cm}^{-1}$ .

##### 4.2.6.2 Gel permeation chromatography

The molecular mass of differently treated MC was determined by gel permeation chromatography. Samples with a concentration of 2 g/L were filtered through a 0.45  $\mu\text{m}$  filter, to remove particulates which could clog the fine tubing within the chromatography system, and measured at room temperature using a AZURA Assistant ASM 2.1 L (Knauer Wissenschaftliche Geräte GmbH, Germany) gel permeation chromatography system equipped with three columns (1x PSS Suprema 100 Å and 2x PSS Suprema 3000 Å), and a precolumn (PSS-Polymer -Standard-Service GmbH, Germany). The eluent consisted of 50 mM  $\text{NaNO}_3$  and 7.7 mM  $\text{NaN}_3$  in  $\text{dH}_2\text{O}$ . Calibration was carried out using Pullulan standards with defined molar masses ranging from 342 Da to 2560 kDa and a Smartline RI detector 2300. Molecular mass was calculated according to the following formulae:

$$\text{Equation 4.1} \quad M_w = \frac{\sum N_i M_i^2}{\sum N_i M_i}$$

$$\text{Equation 4.2} \quad M_n = \frac{\sum N_i M_i}{\sum N_i}$$

$$\text{Equation 4.3} \quad PDI = \frac{M_w}{M_n}$$

whereby  $M_w$  is the molecular mass average of the weight,  $M_n$  the number average molecular mass, and PDI the polydispersity index.  $M_i$  denotes the molecular mass of a polymer chain and  $N_i$  the number of chains within said molecular mass.

#### 4.2.7 Alginate methyl cellulose paste characterisation

##### 4.2.7.1 Viscosity

The viscosities of alg/MC pastes were determined at room temperature using a rheometer with plate-plate geometry (Rheotest RN 4, Germany), a plate diameter of 50 mm and a plate-plate distance of 1 mm. Shear thinning was tested for pastes with non-sterilised, autoclaved, UV and  $\gamma$ -irradiated MC by constantly increasing rotational shear rate from 0 to 100  $s^{-1}$  (increment 0.08  $s^{-1}$ ). Before measurement the alg/MC material was left to swell at 4°C overnight, to avoid the effects of swelling on viscosity over time and between measurements. The paste viscosities were determined after a defined shear rate of 10  $s^{-1}$  had been used.

#### 4.2.8 Scaffold evaluation – structure and composition

##### 4.2.8.1 Release of methyl cellulose

The MC content within bioprinted and  $Ca^{2+}$ -crosslinked alg/MC scaffolds was observed via staining with a chlorine–zinc–iodine solution after 1, 7, 14 and 21 days. Images were taken using a stereo light microscope (Leica M205 C equipped with DFC295 camera, Germany).

For quantitative analysis of MC release, alg/MC scaffolds were incubated in 2 mls of standard growth medium in cell culture conditions over the 21 day investigation period. On defined time points (2 hours and 1, 2, 4, 7, 11, 14, 19, 21 days) 1 ml of supernatant was collected and replaced by 1 ml of fresh medium. Mykoval™ (formerly distributed as Calcofluor, Blankoflor or Uvitex 2B) a fluorescence marker primarily applied for cellulose and chitin detection in fungal cell walls (Koch and Pimsler, 1987; Rasconi *et al.*, 2009) was used to determine the presence of soluble MC within the collected

supernatant (see calibration data, Appendix, Fig.S3B). To optimise the use of this method measurements were performed on scaffolds and pure MC solution samples at different concentrations (3-750  $\mu\text{g/ml}$ ) and temperatures (4°C, 26°C, 37°C) using media comprised of DMEM, HBSS, 1 M and 0.1 M  $\text{CaCl}_2$ . Each calibration series used for the MC release calculation of the sterilisation methods was set up using equally treated MC. For measurement 180  $\mu\text{l}$  of supernatant was mixed with 20  $\mu\text{l}$  of the Mykoval™ solution in a black 96-well plate (Greiner Bio-One, Germany). The samples were incubated for five minutes in the dark and measured on a microplate reader (Infinite M200 Pro; Tecan, Switzerland), with the excitation and emission wavelengths of 400 and 450 nm. Regression analysis to obtain calibrated MC concentration via the detected fluorescence signal was performed via non-linear regression using GraphPad Prism 7.0 for Windows (GraphPAD Software, USA).

#### 4.2.8.2 Scanning electron microscopy

Scaffolds were washed twice with HEPES buffered saline (HBS) containing  $\text{Ca}^{2+}$  and  $\text{Mg}^{2+}$  and dehydrated using a gradation series of ethanol/distilled water solutions. Critical point drying was performed with a CPD 030 apparatus (BAL-TEC, Liechtenstein). Dried samples were coated with gold and imaged using a Philips XL 30/ESEM with field emission gun, operating in SEM mode.

#### 4.2.8.3 Calcium release

The Fluitest CA CPC assay method was used to monitor the breakdown of the ionic cross-links by measuring the  $\text{Ca}^{2+}$  concentration within the culture supernatants at progressive intervals during scaffold incubation. Cell-free scaffolds used for compression testing were incubated in 2 ml cell culture medium, the medium was regularly changed (every three or four days) and 1 ml of the supernatant was assessed against a known calcium standard according to manufacturer's instructions. In brief, a standard was prepared by the serial dilution of the provided Ca-standard with using double distilled water (*ddH*<sub>2</sub>O) within the range of 0.2.5 mM. 10 $\mu\text{l}$  of the supernatant samples were then pipetted into a transparent 96-well plate (Greiner Bio-One, Germany) with duplicates and 200 $\mu\text{l}$  of the reagent solution added per well. The plate was then incubated for 15 minutes at room temperature under constant shaking before data was collected at an absorbance of 570 nm (Infinite M200 Pro; Tecan,

Switzerland). The data from the Ca-standards was used to plot a standard curve and the Ca<sup>2+</sup> concentration of the samples were determined.

#### 4.2.8.4 Compression testing

Uni-axial compression experiments were performed using an Instron 5566 materials testing device equipped with a 100 N load cell (Instron Wolpert, Germany). Scaffolds printed with 10 layers (and a minimal height of 2 mm) were investigated from culture in a wet state at room temperature with a compression load exerted at 5% of scaffold height/min until failure. The compressive strength was determined by the maximum peak breaking point. Dimensional measurements of each scaffold were taken prior to compression using digital callipers (PiCUS©) and were considered during measurement.

#### 4.2.9 Alginate methyl cellulose scaffold – cell compatibility

##### 4.2.9.1 Cell survival live/dead assay

Cell viability was determined via live/dead staining. After 1, 7, 14, and 21 days of incubation cell-laden scaffolds were incubated for 20 minutes in culture medium supplemented with 5 µM CMFDA green and 1.4 µM ethidium homodimer-1 per ml at 37°C and 5% CO<sub>2</sub>. Scaffolds were rinsed with HBSS, fixed in a 4% paraformaldehyde solution, and stored at 4°C for a maximum of two weeks before imaging.

##### Cell survival live/dead imaging

Imaging was performed using a Zeiss Observer Z.1, wide field system with ApoTome (Zeiss, Germany) equipped with an hxp100 fluorescence lamp, GFP (EX 470/40, BS 495, EM 525/50) and RFP (EX 550/25, BS 570, EM 605/70) fluorescence filter cubes and a *Monochromatic Camera AxioCam 503 mono*. The fluorophores CMFDA (live cells; excitation 492nm, emission 517nm maxima) and ethidium homodimer-1 (dead cells; excitation 528nm, emission 617nm maxima) were excited with a 495nm Argon laser and 525nm Helium/Neon lasers respectively. Sequential optical sections in the z-axis were acquired with a 1.5 µm step size, with the emission fluorescence measured at 490-570 nm for CMFDA and 590-710 nm for ethidium homodimer-1.

Image size was 1.5 mm<sup>2</sup>, comprising of 512 x 512 pixels. A pinhole diameter of 1 Airy unit was used.

#### Cell survival live/dead image analysis

For image analysis the multiple z-stack sections were superimposed into one image. The number of live and dead cells in an image were then quantified using Image J V1.44p (FIJI) analysis software based on the protocol by BRTI Life sciences (BTRI Life Sciences, 2015). In brief the steps consisted of (Fig.4.1):

1) The image colour channels were separated, with the living cells within the Green Channel and the dead cells in the Red Channel. The Blue channel was discarded. (Image > Colour > Split Channels)

2) Each channel was then individually converted to the 8-bit greyscale format to enable thresholding based on intensity analysis. (Image > Type > 8-bit)

3) The select 'Find Maxima' function was used to count the number of dead or live cells from each channel. The function "Point Selection" was then selected and a preview of the point selection was generated. The noise tolerance was adjusted until background staining was visually excluded and the same tolerance setting applied for image replicates of the same sample. The maximum number of points selected was automatically counted and represented the total number of cells positive for the stain of interest (Fig.4.1). (Process > Find Maxima)

Percent survival was then calculated using the following equation:

Equation 4.4

$$(\text{Number of living cells} / \text{Total number of cells}) \times 100$$

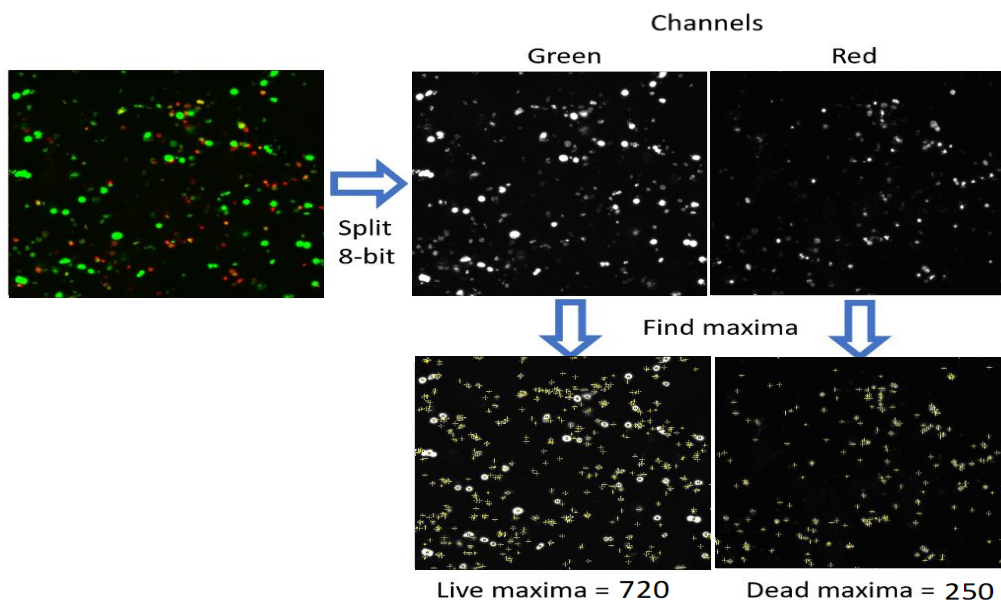


**Figure 4.1** Schematic to demonstrate live/dead cell quantification using Image J V1.44p (FIJI) analysis software. Step 1: Channels were split, Step 2: Files converted to 8-bit format, Step 3: Maxima point selection was found and the cell number per channel counted.

#### 4.2.9.2 DNA quantification

To extract the DNA the alg/MC scaffolds were frozen at  $-80^{\circ}\text{C}$  on the days 1, 7, 14, and 21 of culture, and dissolved in 3 ml of 100 mM sodium citrate. The cells were lysed at  $60^{\circ}\text{C}$  overnight followed by 10 minutes sonication. The lysate was stored at  $-80^{\circ}\text{C}$  until measurement of total DNA using the QuantiFluor dsDNA system as per the manufacturer's instructions. Wherein, the QuantiFluorR dsDNA System contains a fluorescent double-stranded DNA-binding dye (504nm Excitation/ 531nm Emission) that enables the sensitive quantitation of small amounts of double stranded DNA (dsDNA). In brief, a standard curve for DNA quantification was generated using Lambda DNA (Promega) which was serially diluted with 1x TE<sup>5</sup> buffer from 4000 ng/ml down to 31.25 ng/ml (dilution series 1:2). After this, 10  $\mu\text{l}$  of the cell lysate and prepared standards were pipetted into a black 96-well plate (Greiner Bio-One, Germany) with

<sup>5</sup> TE is derived from the components: Tris, a common pH buffer, and EDTA, a molecule that chelates cations like  $\text{Mg}^{2+}$ . The purpose of the TE buffer is to solubilise DNA while protecting it from degradation.

duplicates and 190 µl of the colouring solution (QuantiFluor 1:800 with 1x TE buffer) was added to the wells. In addition, blank samples containing 1x TE buffer were used to assess the background level of the assay. The plate was then incubated for five minutes on a shaker in the dark and the fluorescence measured at 485/535 nm with the Tecan-Reader (Infinite M200 Pro; Tecan, Switzerland). All samples were found to be within the range of the standard curve without further dilutions. Upon analysis the mean fluorescence of the blank sample (1x TE buffer) was subtracted from the standard and unknown samples. The corrected data from the DNA standards was then used to generate a standard curve of fluorescence versus DNA concentration and the DNA concentration of the samples were determined from the curve.

#### 4.2.9.3 Glycosaminoglycan histology

To localize sulphated glycosaminoglycans (sGAG) within the BPC-laden alg/MC constructs cultured for 21 days, histochemical analysis was performed using safranin O. Control samples included both cell-free scaffolds incubated for 21 days as well as BPC-laden constructs cultured for one day, to allow for the comparison with background alginate staining and the assessment of GAG production over time.

Scaffolds were fixed with 4% paraformaldehyde in HBSS (with Ca<sup>2+</sup> and Mg<sup>2+</sup>), and then paraffin embedded using a tissue processor (LEICA TP 1050) using the protocol outlined in Table 4.1. Microtome sections of 10 µm thickness were mounted onto poly-L-Lysine coated glass slides (Sigma), dried in a 50°C oven overnight, and proteoglycan presence analysed by staining with 0.1% safranin O, Weigerts Iron Hematoxylin solution, and 0.02% counter stain fast green. Images were obtained by photomicroscopy using brightfield illumination, with the same light settings applied for each sample (Nikon, inverted microscope, ECLIPSE, TE2000). Semi-quantitative results for safranin O stain intensity of the histological images were achieved using Image J software (Fiji, V1.44p) three images per sample were measured with three replicates per time point (n = 3).

The intensity of a pixel is typically expressed within a numerical range of 0 to 255, the higher the value therefore represents a greater intensity. For histological staining, increased staining results in a darker image of lower intensity. To avoid confusion of a high intensity value representing weaker staining within this study the image intensities were inverted. Therefore, a value of 0 represented the total absence of stain

(background/white) and 255 the total presence (solid black). Consequently, all histology images were converted into a greyscale 8-bit format and then inverted prior to the measurement of stain intensity (Fig.4.2).

Due to the macroporous architecture of the scaffolds, as well as sample degradation during paraffin embedding, the histological sections used for image analysis contained areas without cell matrix and as a result the safranin O stain was not spread evenly across the samples. Subsequently, during image analysis a thresholding protocol was employed to ensure that only the stained sections of the samples were measured for intensity. Firstly, thresholding was trialled on a number of images taken from samples at different stages in culture duration. From these test images a threshold at 40% of the maximum image intensity was identified which selectively covered the areas of safranin O staining without coverage of the unstained image areas (Fig.4.2). Following this, for all image analysis a fixed threshold cut-off of value of 40% was applied and was used to ensure consistency between samples (Fig.4.2). In the next stage of image analysis, the thresholding was inversed and the intensity of areas without stain measured. The background measurements were then subtracted from the total intensity to remove the influence of any differences in background colouration (Fig.4.2). Lastly, cell-laden sample measurements were normalised to adjust for the effect of non-specific alginate staining. To do this, the intensity measurements of cell-free alg/MC control samples (at matching timepoints e.g. after 1,7,14 or 21 days) were subtracted from the cell-laden sample measurements.

**Table 4.1** Protocol used to embed alginate methyl cellulose samples in paraffin using a *LEICA TP 1050* tissue processor.

<b>Reagent</b>	<b>Time (minutes)</b>	<b>Temperature (°C)</b>
<b>Formalin</b>	5	Ambient
<b>IMS 50%</b>	5	30
<b>IMS 70%</b>	10	40
<b>IMS 90%</b>	10	40
<b>IMS 100%</b>	15	40
<b>IMS</b>	15	40
<b>IMS</b>	15	40
<b>Xylene</b>	15	40
<b>Xylene</b>	15	40
<b>Xylene</b>	15	40
<b>Paraffin wax</b>	15	62
<b>Paraffin wax</b>	15	62
<b>Paraffin wax</b>	20	62

IMS denotes industrial methylated spirit.

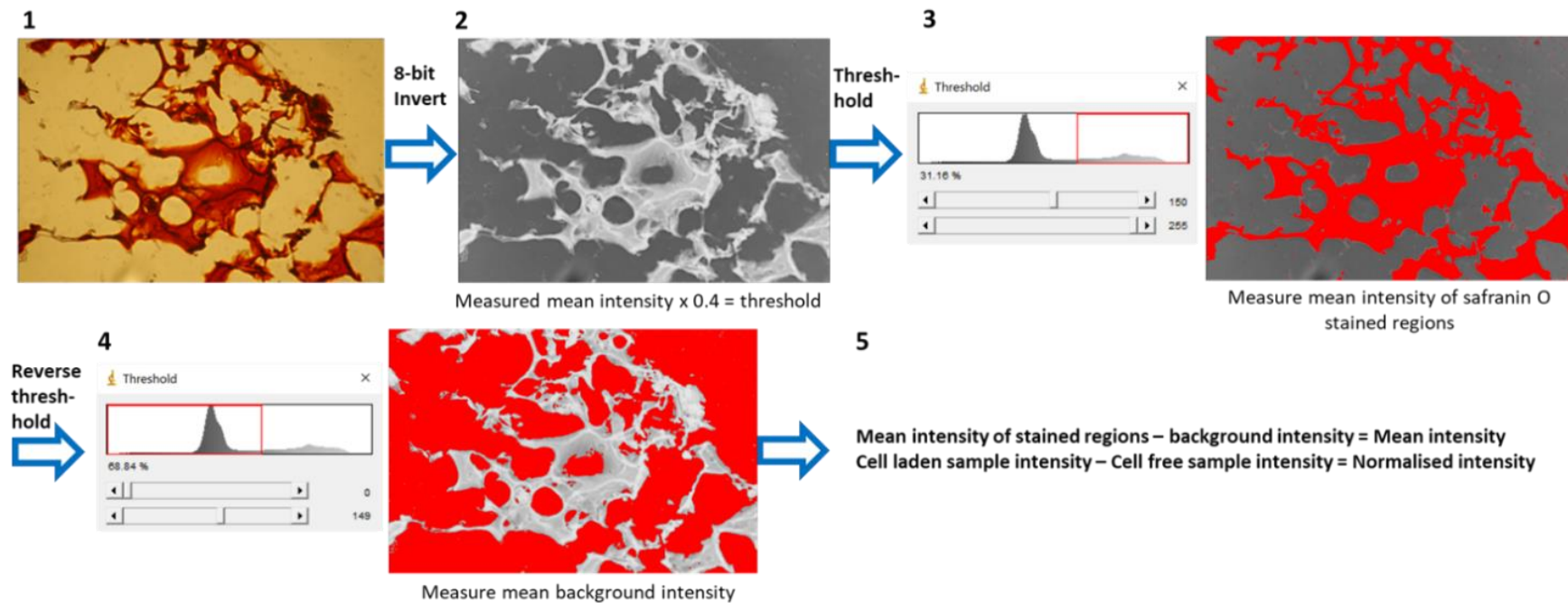


**Figure 4.2** Schematic to demonstrate the image analysis process prior to safranin O stain intensity measurement. (1) Original image. (2) Image converted to 8-bit and grayscale inverted, mean intensity measured and multiplied by a fixed value of 0.4 to give the threshold value for use in next step. (3) Image thresholded and the mean intensity of the safranin O regions measured. (4) Threshold reversed and the mean intensity of the unstained background measured. (5) Calculations were performed to correct for differences in background intensity, or for any false positive alginate staining.

#### 4.2.10 Statistical analysis

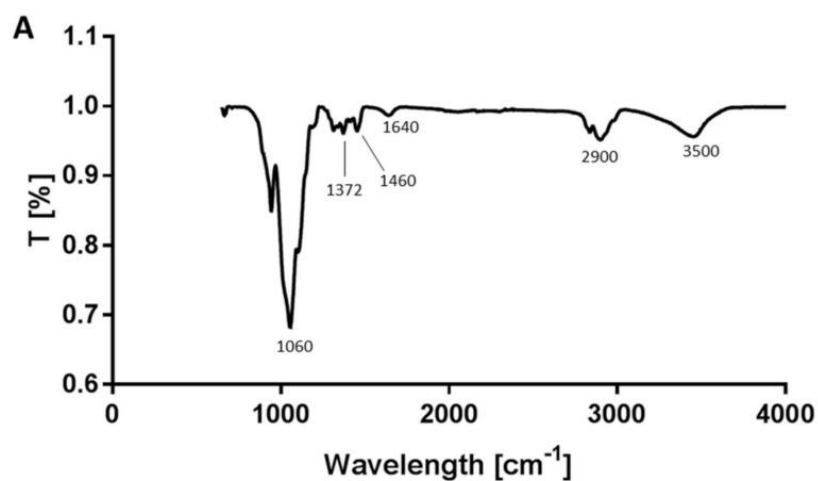
For quantitative MC release studies, statistical analysis for triplicate samples were performed on GraphPad Prism via multiple t-tests with Bonferroni-Dunn correction, to compare single time points of the MC release curves between groups. For all other statistics performed the Mini-tab software package was used, data were initially tested for normality using the Anderson-Darling Test. The differences between multiple means were then compared via a one-way ANOVA with post-hoc Tukey. The alpha level was set at  $P \leq 0.05$ .

### 4.3 Results

#### 4.3.1 Methyl cellulose characterisation

To evaluate the potential impact of the sterilisation methods on the chemical composition of MC, the treated powders were analysed by FTIR spectroscopy in comparison to untreated MC. The FTIR spectra revealed no significant difference between absorption bands for all MC variants tested, identified in Fig.4.3. The peak shapes and ratios were unchanged with no visual shifts or deformations (see Appendix, Fig.S4B), indicating that the UV, autoclaved, scCO<sub>2</sub>, and  $\gamma$ -irradiation sterilisation processes did not modify the MC composition detectable by FTIR.

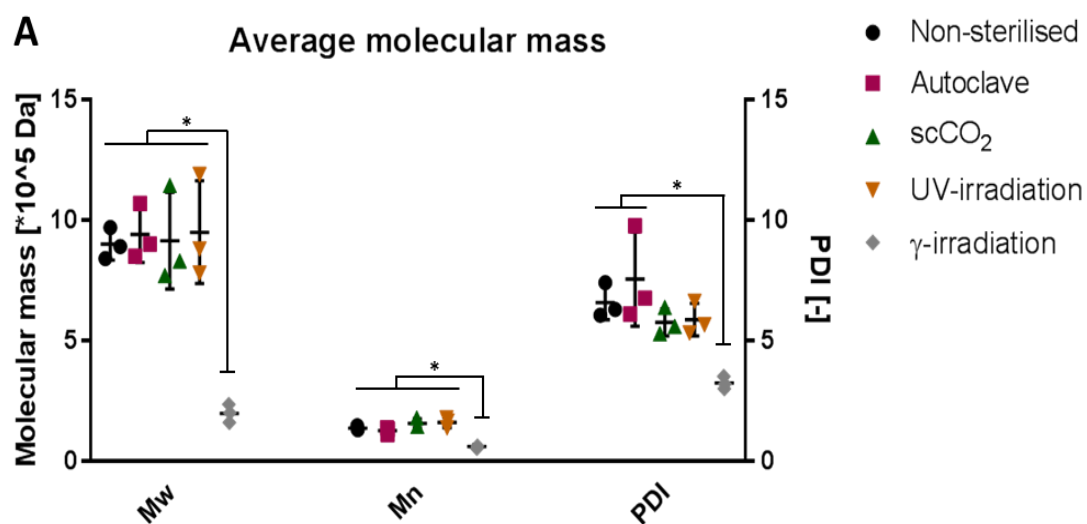
The influence of the sterilisation treatments on the MC molecular weight was studied by gel permeation chromatography (Fig.4.4, A-B). The  $M_w$  is calculated as the average of the molecular mass distribution considering the weight of each polymer fraction, whereas  $M_n$  takes the number of molecules of each fraction into consideration. Therefore, smaller molecules have a greater impact on  $M_n$  than on  $M_w$  (Fig.4.4, A-B). No significant differences in molecular mass were detected between the untreated, autoclaved, scCO<sub>2</sub> treated and UV-irradiated MC for either  $M_w$  or  $M_n$ . However, the  $\gamma$ -irradiated MC had a significantly reduced  $M_w$  and  $M_n$  (Fig.4.4, A-B). The measured polydispersity index used to indicate how far from a uniform distribution ( $PDI = 1$ ) a sample is, was seen to be significantly reduced for the  $\gamma$ -irradiated MC when compared to the non-sterilised and autoclaved samples, but not from UV and scCO<sub>2</sub> treated MC (Fig.4.4, A-B).



**B**

Peak wavenumber [cm <sup>-1</sup> ]	Bonds
3500	O-H bond (hydroxyl groups)
2900	C-H aliphatic
1372/2900	Ratio indicative of total crystallinity index (TCI)
1460	C-H, C-O deformation bending or stretching
1372	C-O-C and C-O deformation or stretching vibrations
1060	CH OCH stretching
1640	C=C stretch

**Fig 4.3** Fourier transform infra-red (FTIR) analysis of methyl cellulose (MC) powder treated by different sterilisation methods (A) Example FTIR spectrum of MC powder with labelled peaks. The spectra of all MC types measured (autoclaved, scCO<sub>2</sub> treated, UV and  $\gamma$ -irradiated) were identical in appearance. (B) Identification of MC spectrum peaks.



**B**

	$M_w$ [ $\cdot 10^5$ Da]	$M_n$ [ $\cdot 10^5$ Da]	PDI [-]
Non-sterilised	$9.0 \pm 0.7$	$1.4 \pm 0.1$	$6.6 \pm 0.7$
Autoclave	$9.4 \pm 1.2$	$1.3 \pm 0.2$	$7.6 \pm 2.0$
scCO <sub>2</sub>	$9.1 \pm 2.0$	$1.6 \pm 0.2$	$5.8 \pm 0.6$
UV-irradiation	$9.5 \pm 2.1$	$1.6 \pm 0.2$	$5.9 \pm 0.7$
γ-irradiation	$2.0 \pm 0.4$	$0.6 \pm 0.1$	$3.2 \pm 0.3$

**Figure 4.4** Gel permeation chromatography, weight and numerical average molecular mass ( $M_w$  and  $M_n$ ) as well as polydispersity index (PDI) of methyl cellulose (MC) powders prepared using non-sterilised MC and MC sterilised by autoclave, scCO<sub>2</sub>, UV and γ-irradiation. Mean  $\pm$  stdev,  $n=3$ ,  $*P \leq 0.05$ .

#### 4.3.2 Alginate methyl cellulose paste characterisation

The sterilised MC variants were used to prepare plotting pastes by mixing the MC powder with a 3% alginate solution, the untreated MC formulation served as a control. The rheological and printing properties of the pastes were compared.

All pastes demonstrated shear thinning behaviour with a decrease in viscosity under shear strain (Fig.4.5, A). At a defined shear rate of  $10 \text{ s}^{-1}$  the viscosity measurements of the alg/MC pastes showed no significant difference between the non-sterilised ( $308 \pm 7.5 \text{ Pa}\cdot\text{s}$ ), autoclaved ( $291 \pm 13.3 \text{ Pa}\cdot\text{s}$ ) and  $\text{scCO}_2$  ( $273 \pm 27.3 \text{ Pa}\cdot\text{s}$ ) group. The UV group had a significantly reduced viscosity of  $224 \pm 12.4 \text{ Pa}\cdot\text{s}$  followed by the  $\gamma$ -irradiation group with the strongly reduced viscosity of  $11 \pm 1.5 \text{ Pa}\cdot\text{s}$  (Fig.4.5, B).

All pastes were printable after one and a half hours of swell time. However, the increased flow rate and decreased viscosity of the  $\gamma$ -treated material required adaptation of the printing conditions (see section 4.2.5) with immediate crosslinking needed to achieve structural integrity and preserve macropores (Fig.4.5, C). The effects of the parameter changes to print pressure and speed would cause a different shear stress applied to the plotted cell-laden material as well as alter the material volume extruded per scaffold. Furthermore, the  $\gamma$ -sterilised scaffolds lacked form stability, especially with the layers printed at increasing height, and so was not appropriate for mechanical testing. Therefore, the use of  $\gamma$ -irradiation was not taken forward for cell-laden bioprinting as variation from the other types was considered too high for a fair comparison.

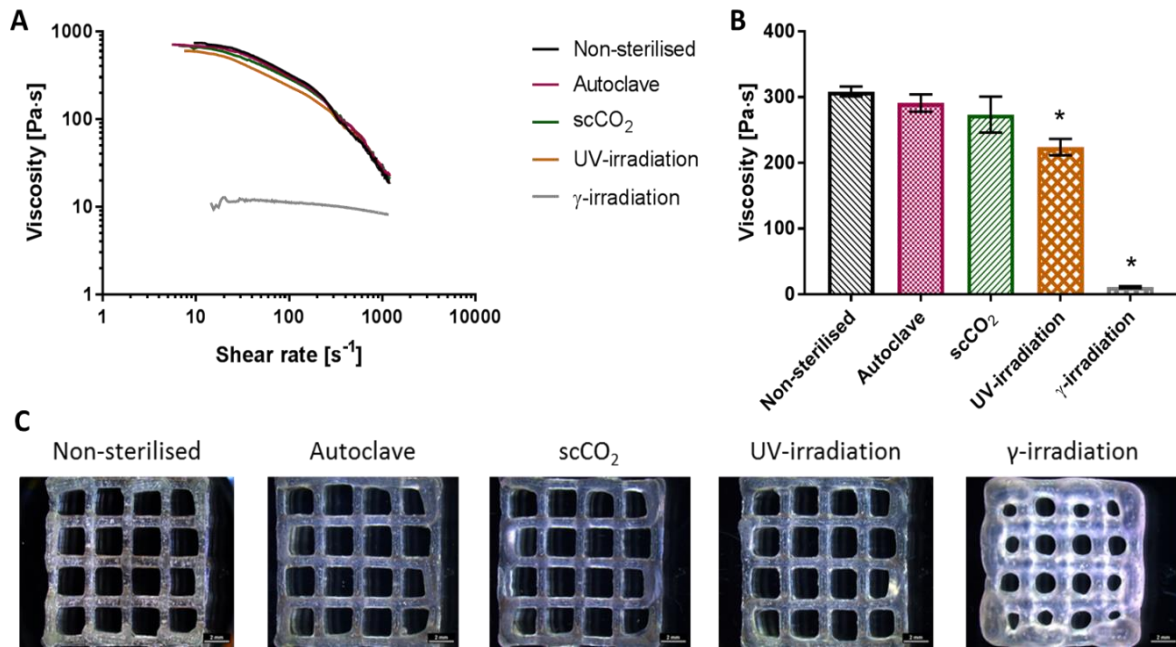


**Figure 4.5** Viscosity measurements of alginate methyl cellulose (alg/MC) pastes. MC was mixed into dissolved alginate and left to swell overnight (A) Viscosity over shear rate of alg/MC pastes prepared using non-sterilised MC and MC sterilised by autoclave, scCO<sub>2</sub>, UV and γ-irradiation. One representative measurement is shown from each variant to demonstrate material behaviour. At all-time points, the viscosity of the alg/MC paste with γ-irradiated MC was significantly lower than the other variants. (B) Viscosity of alg/MC pastes at a defined shear rate of 10 s<sup>-1</sup> prepared with non-sterilised MC and sterilised MC. Mean ± stdev, n = 3, \*P ≤ 0.05 compared to the non-sterilised MC. (C) Examples of plotted scaffolds prepared using non-sterilised MC and MC sterilised by autoclave, scCO<sub>2</sub>, UV and γ-irradiation (scale bars = 2 mm).

#### 4.3.3 Alginate methyl cellulose scaffold evaluation

MC as a thickener agent has been previously employed as a temporary additive used to improve alginate processability for bioprinting. The MC component is not ionically crosslinked by Ca<sup>2+</sup> and has been shown to be released from the scaffolds over time (Schütz *et al.*, 2017). In order to evaluate the potential impact of the sterilisation methods on the MC release behaviour, the MC content of the scaffolds prepared from the different alg/MC pastes was visualised by chlorine–zinc–iodine staining. After one

day of incubation under cell culture conditions all the stained scaffold types appeared dark violet without any apparent difference which indicated a high MC content (Fig.4.6, A, first column). After seven days (Fig.4.6, A, second column) the intensity was visually unchanged for all MC types except for the  $\gamma$ -irradiation group, which had almost completely released MC from the scaffold. Conversely, a dark staining remained within the UV, autoclaved and scCO<sub>2</sub> scaffolds until the end of the study at day 21 (Fig.4.6, A, third column).

To quantitatively assess the effects of the different sterilisation treatments on MC release over time, the concentration of released MC in collected supernatants was calculated cumulatively using the Mykoval™ fluorescence intensity measurements (Fig.4.6, B). It was found that the untreated variant had consistently the lowest MC release over the study duration. With approximately 20% of the total MC content measured in the untreated scaffolds supernatant following crosslinking with 2 hours incubation (depicted as one cumulative data point at the two hour mark in Fig.4.6, B) and only a marginal release after the 48 hour time point. Comparatively, the  $\gamma$ -irradiated MC was released to the significantly highest extent for all time points tested. After 11 days 100% of the  $\gamma$ -irradiated MC was released with 80% already present in the supernatants after crosslinking with two hours incubation. Conversely, the samples sterilised by scCO<sub>2</sub>, autoclaving and UV-irradiation evoked a release of approximately 25% of the total MC content after crosslinking with two hours of incubation, which was followed by a moderate release until 48 hours with no (autoclave) or very low (UV and scCO<sub>2</sub>) additional release later on. At the later time points (days 14, 19 and 21) the scCO<sub>2</sub> scaffolds released significantly higher amounts compared to the autoclave and UV scaffold types (Fig.4.6, B).

The investigation of the scaffold surface microstructures using SEM imaging showed evenly distributed micropores for all MC variants (Fig.4.6, C, I). This indicated that the presence of MC itself, independent of size or release, was sufficient to cause micropores in the otherwise even surface of alginate (as was shown by Schütz *et al.*, 2017). Furthermore, a variation in micropore structure was apparent on the alg/MC scaffolds which were prepared using the differently treated MC, this effect was most evident on the 10,000 x magnification images (Fig.4.6, C, II). Wherein, in the scaffolds prepared with the  $\gamma$ -irradiated MC presented micropores which were symmetrical, rounded and regularly distributed pores. However, in the scaffolds prepared with MC

treated by scCO<sub>2</sub>, UV or autoclave, in which a higher content of MC remained in the crosslinked alginate network, the pores were seen to be more fibrous and cavernous in appearance (Fig.4.6, C, II).

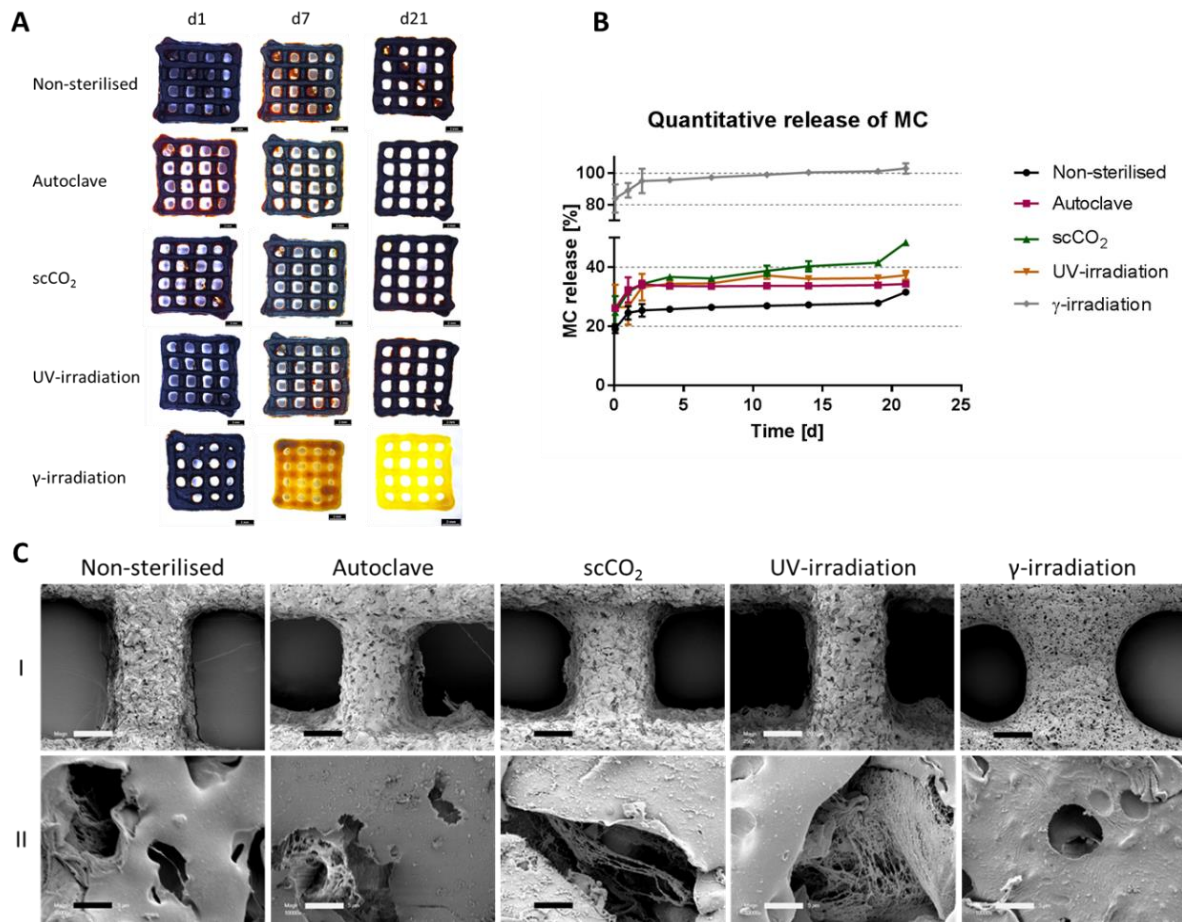


**Figure 4.6** Methyl cellulose (MC) content and microstructure of alginate methyl cellulose (alg/MC) scaffolds (A) Stereomicroscopy images of alg/MC scaffolds after 1, 7 and 21 days of cell culture stained with chlorine–zinc–iodine solution, prepared with untreated MC and sterilised MC via autoclave, scCO<sub>2</sub>, UV and γ-irradiation, (scale bars = 2 mm). (B) Quantitative measurement of cumulative percentage of MC release over time. Mean ± stdv, n = 3. At all time points, release of the γ-irradiated MC was significantly higher; at days 14, 19 and 21, release of the scCO<sub>2</sub>–treated MC was significantly higher than those of the autoclaved and UV-treated MC; after 21 days, release of all sterilised MC types was significantly higher than those of the untreated MC \**P* ≤ 0.05. (C) Representative scanning electron microscopy images of alg/MC scaffolds prepared with the different MC variants at a magnification of x250 (I) and x10,000 (II) after one day of incubation under cell culture conditions (scale bars for I = 200 μm and II = 50 μm).

The compressive strength of the alg/MC scaffolds was the highest on day one of testing for all MC variants but decreased significantly between days 1-10 (Fig.4.7, A). On day one the hydrogel scaffold of the UV group had the significantly highest compressive strength of  $45.2 \pm 8.0$  MPa. Conversely, no significant difference could be determined between the autoclaved and scCO<sub>2</sub> variants with values of  $32.1 \pm 6.8$  MPa and  $27.7 \pm 4.6$  MPa respectively (Fig.4.7, A). Between days 10 and 21, a significant decline was observed for the scCO<sub>2</sub> and UV-treated MC variants, whereas no significant differences were seen between the sterilised MC variants on day 10 or 21 of measurement.

A measurement used for the further indication of mechanical stability was the release of calcium ions during incubation. The amount of calcium released on days 1 and 10 (Fig.4.7, B) showed no significant differences between the different MC sterilisation groups. On day 21 the autoclaved variant had a significantly higher calcium release than the scCO<sub>2</sub> variant, with values of  $42.7 \pm 5.4$  (µmol) and  $28.8 \pm 3.9$  (µmol) measured in the supernatant respectively. The UV samples ( $31.3 \pm 7$  µmol) had no significant differences to either the autoclaved or scCO<sub>2</sub> measurements (Fig.4.7, B). For all MC types, there was a significant increase in calcium release from day 1 to day 10. Differences in calcium release between day 10 and 21 were not significant for the scCO<sub>2</sub> MC type but showed a significant increase in release for the UV and autoclave treated scaffolds (Fig.4.7, B).

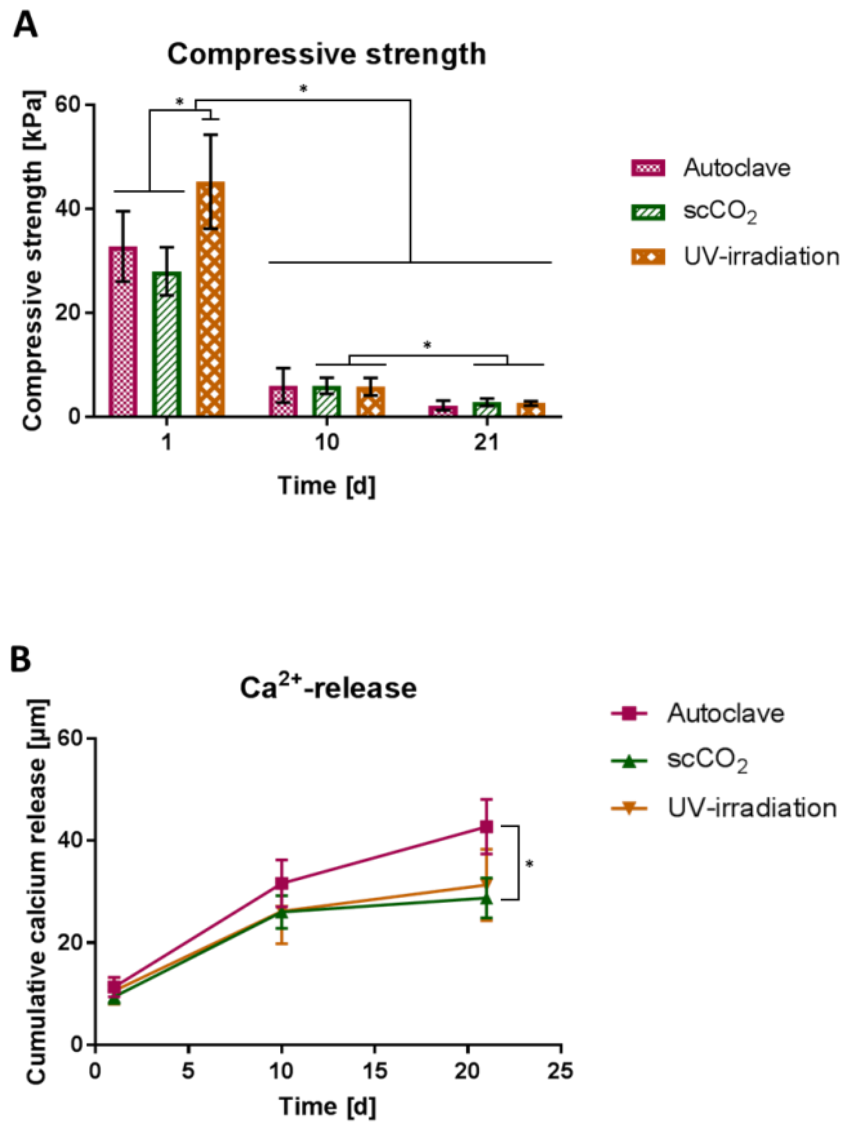


**Figure 4.7** The effect of different sterilisation procedures on scaffold stability of cell-free scaffolds kept under cell culture conditions (A) Compressive strength of alginate methyl cellulose (alg/MC) scaffolds prepared with the MC variants treated with autoclave, scCO<sub>2</sub> and UV on days 1, 10 and 21 of incubation. Mean  $\pm$  stdv,  $n = 12$ , \*  $P \leq 0.05$ . (B) Cumulative calcium release by alg/MC scaffolds prepared using the different MC sterilisation methods, autoclaving, scCO<sub>2</sub> and UV, measured after 1, 10 and 21 days of incubation. Mean  $\pm$  stdv,  $n = 9$ , \*  $P \leq 0.05$ .

#### 4.3.4 Cell compatibility of alginate methyl cellulose scaffolds – towards cartilage tissue engineering

For the bioprinting of BPC-laden alg/MC scaffolds, autoclaved, scCO<sub>2</sub> treated and UV-irradiated MC types were used and compared regarding their influence on cell compatibility.

The UV and the scCO<sub>2</sub> variants showed consistent survival across all time intervals. However, in the autoclaved group, values for the percent of live cells on day one (65.89% ± 10.6) were significantly higher than on day 21 (54.6 ± 9.4) but with no significant differences between days 7, 14 and 21 (Fig.4.8, A). Values determined for the MC variants treated with UV and autoclave had no significant differences in cell survival on days 1, 7, 14 and 21. The MC variants treated with UV and autoclave supported a significantly higher cell survival within the alg/MC hydrogel scaffolds than compared to the scCO<sub>2</sub>-treated MC type on days 1, 7 and 14. By day 21, only cell viability within UV scaffolds remained significantly higher than the scCO<sub>2</sub> scaffold (Fig.4.8, A). On the whole, a higher number of viable cells were visible in the autoclave and the UV group in comparison to the scCO<sub>2</sub> group (Fig.4.8, A).

The autoclaved MC type showed no significant change in DNA content over the whole cultivation time. DNA content of the scCO<sub>2</sub> variant was significantly higher on day 1 and 7 compared to day 14 and 21. The DNA content of the UV variant showed a significant increase between day one and day seven, which then plateaued (Fig.4.8, B).

On day one there was no significant difference in the DNA content between the MC treatment types tested (Fig.4.8, B). On day 7 the scaffolds derived from UV-irradiated MC had the highest DNA content. On days 14 and 21, both the UV and the autoclaved variant had a significant higher DNA content than the scCO<sub>2</sub> type (Fig.4.8, B).

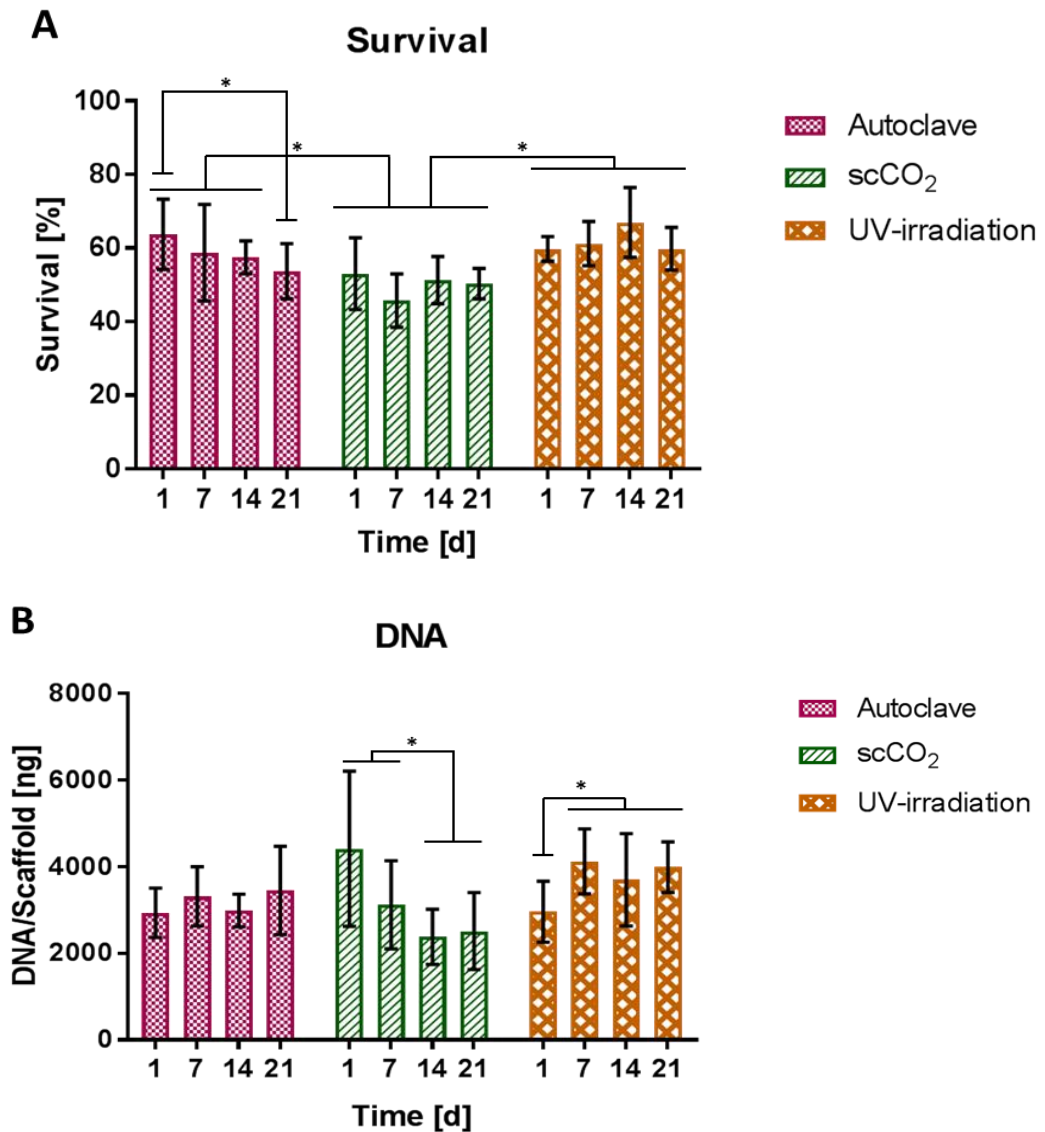


**Figure 4.8** Cytocompatibility of bovine primary chondrocyte (BPC)-laden alginate methyl cellulose (alg/MC) scaffolds prepared with MC treated by autoclave, scCO<sub>2</sub> and UV at days 1, 7, 14 and 21 of cell culture (A) Survival of live BPCs within the scaffolds, mean  $\pm$  stdv,  $n = 12$ , \*  $P \leq 0.05$ . (B) Total DNA content of BPCs embedded in the scaffolds, mean  $\pm$  stdv,  $n = 6$ , \*  $P \leq 0.05$ .

In order to study ECM production, the histological staining of proteoglycans was performed with safranin O on BPC-laden and BPC-free (control) scaffolds at regular intervals throughout culture duration. After 21 days in culture the scCO<sub>2</sub> samples showed a visibly lower safranin O stain intensity with sparse regions of proteoglycan when compared to the autoclaved and UV variants (Fig.4.9, A, I-III). Little or no

safranin O staining was present for day seven or cell-free samples for all MC treatment types tested confirming that the staining reveals matrix production by the cells (Fig.4.9, A, IV-V).

Image assessment for the UV and autoclaved sample types revealed no significant differences with regard to stain intensity (Fig.4.9, B). On days 7 and 21 safranin O stain intensity was higher in the UV and autoclave group than seen for the scCO<sub>2</sub> samples; on day 14 no significant difference could be stated between the autoclaved and scCO<sub>2</sub> variants (Fig.7, C). For the UV and autoclaved variants, the stain intensity increased from day 7 to day 21. The scCO<sub>2</sub> type showed a significant increase in intensity from day 7 to 14 but then showed no significant difference by day 21 (Fig.4.9, B).

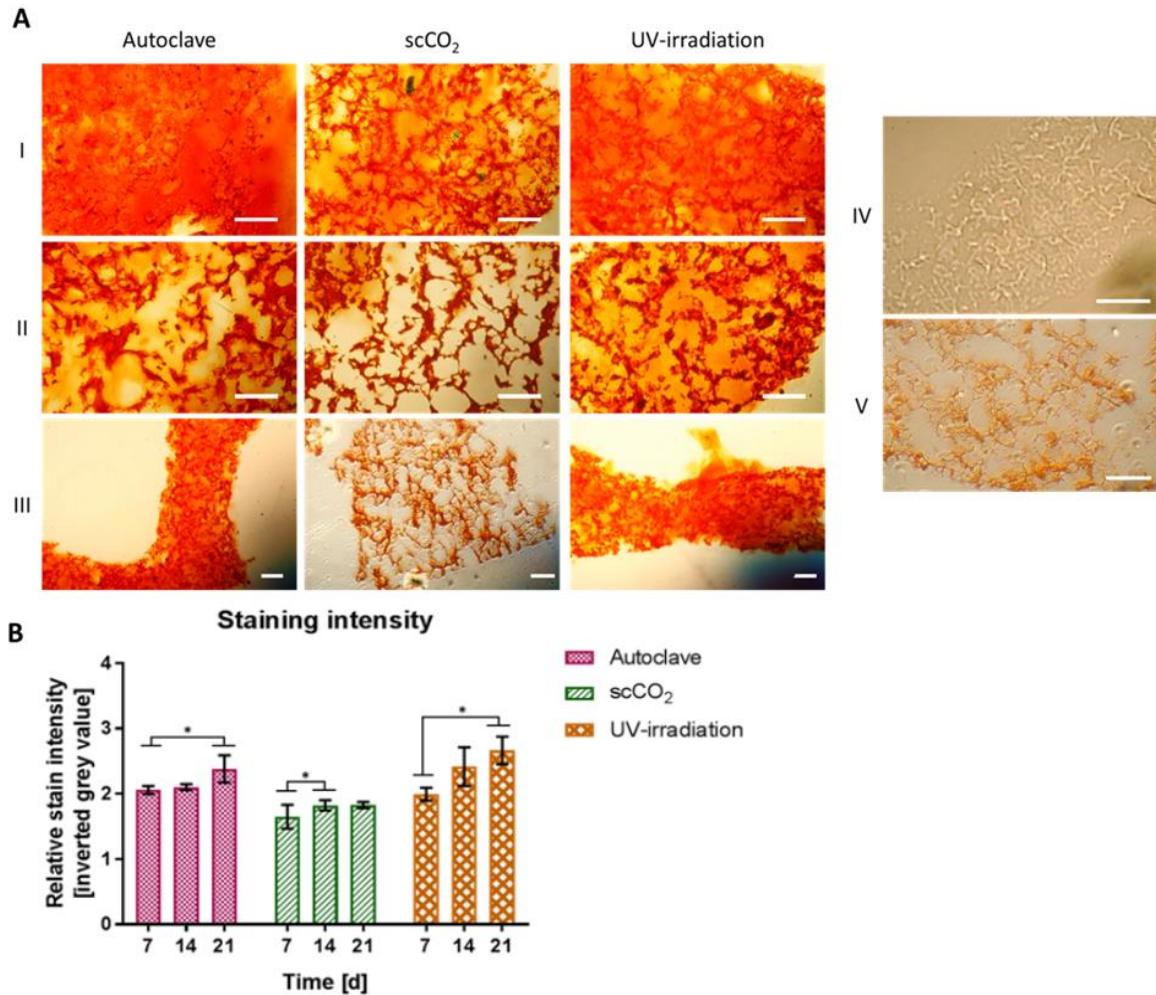


**Figure 4.9** Glycosaminoglycan histology staining of bovine primary chondrocyte (BPC)-laden and cell-free alginate methyl cellulose (alg/MC) scaffolds prepared with autoclave, scCO<sub>2</sub> and UV treated MC (A) Histological images of scaffold sections, fixed at day 21 of cell culture and stained with safranin O, taken by light microscopy (I) 20x magnification showing areas of high stain intensity (II) 20x magnification images to represent regions of low staining (III) 10x magnification images (IV) 10x magnification of a cell-free scaffold prepared with autoclaved MC and fixed at day 14 of incubation under cell culture conditions (V) 20x magnification of BPC-laden scaffold prepared with autoclaved MC and fixed at day 7 of culture scalebars for all images represent 10  $\mu$ m. (B) Relative intensity of safranin O staining taken from histology images (20x magnification) of scaffolds on days 7, 14 and 21 of cell culture. Mean  $\pm$  stdv, n = 9, \*  $P \leq 0.05$ .

## 4.4 Discussion

Tissue-engineered scaffolds for medical purposes must be manufactured in a reproducible, controlled and sterile fashion and should be achieved using conditions possible for the inclusion of biological components such as living cells (O'Brien, 2011). The use of suitable sterilisation methods is therefore an essential step in the development of a clinically feasible regenerative approach. However, the identification of appropriate sterilisation methods is often under-investigated and can hold numerous implications on material properties and cell behaviour, affecting both the feasibility for bioprinting and therapeutic validity. In the present study, we investigated the influence of four different sterilisation methods on the physiological and cell compatibility of MC, a relevant material in bioprinting (Wang *et al.*, 2018), which was used as a thickening additive to enhance alginate suitability for extrusion (Lode *et al.*, 2015; Seidel *et al.*, 2017; Lode, Meyer and Brüggemeier, 2017; Li *et al.*, 2017; Law *et al.*, 2018).

### 4.4.1 Effects of methyl cellulose sterilisation on alginate methyl cellulose properties for bioprinting

For bioprinting, the rheological properties of the bioink are essential parameters for achieving consistent extrusion. In this study the viscosity measurements revealed that in contrast to autoclaving and scCO<sub>2</sub> treatment, sterilisation of MC by irradiation based methods resulted in a significantly reduced alg/MC viscosity (Fig.4.5, B). However, the type and dose of irradiation energy determined the strength of this effect. Wherein, the non-ionizing lower energy photons of UV-irradiation resulted in a slight reduction relative to the high energy ionizing input from  $\gamma$ -irradiation which led to a dramatic reduction of viscosity. The alg/MC paste derived from  $\gamma$ -irradiated MC had a fluid like behaviour, which caused a loss of shape fidelity and limited scaffold height and macroporosity upon printing. Although use of  $\gamma$ -irradiation has been commonly applied for the sterilisation of biomaterials in biomedical products (Hugo, 1995) its destructive action is well known. With  $\gamma$ -irradiation exposure having been previously shown to degrade polysaccharides such as starch, cellulose and pectin, by the cleavage of the glycosidic bonds (El-ashhab *et al.*, 2013; Hermannova *et al.*, 2008). The common

result of material degradation by  $\gamma$  is a decreased viscosity and molecular mass (Elashhab *et al.*, 2013). Consequently, the strong decrease in viscosity observed for the alg/MC paste prepared with  $\gamma$ -irradiated MC was also accompanied by a marked reduction of the MC's molecular mass (Fig.4.4, A-B).

Conversely, the gel permeation chromatography measurements indicated that treatment of MC by autoclaving, scCO<sub>2</sub> and UV-irradiation did not result in a significant shift of the molecular mass. Although slight changes can be assumed, whereby the PDI of MC was slightly reduced after treatment with scCO<sub>2</sub> and UV. Thus, it could be argued that these methods led to cleavages in the larger molecules within MC as well, however this was not accompanied by a clear reduction in either M<sub>w</sub> or M<sub>n</sub> and therefore it is difficult to draw any definitive conclusions (Fig.4.4, A-B). On the other hand, the  $\gamma$ -irradiation of MC led to a marked decrease in both the number (M<sub>n</sub>) and size of larger molecules (M<sub>w</sub>), which led to a more even distribution of MC chain size and was indicated by a much lower PDI. In addition, it should be noted that non-sterilised MC showed a high variation in the M<sub>w</sub> measurements, as the material was inherently inhomogeneous with chain lengths ranging from hundreds to tens of thousands of molecules. However, sterilisation by  $\gamma$ -irradiation resulted in an increased cleavage of the larger molecules and consequently a decreased chain length variability. The loss of high molecular mass chains was most likely the cause for its much less viscous behaviour. As such, it can be surmised from this outcome that  $\gamma$ -sterilisation is not an appropriate method for MC treatment for the use of alg/MC extrusion due to its greatly altered material properties.

Furthermore, in the case of the alg/MC paste derived from UV treated MC the slight reduction of viscosity observed did not affect the printability or structural integrity of the material. In this study the viscosity measurements recorded were taken after a period of 18 hours following MC addition. The extended swelling period before measurement was done to limit the effects of swelling between measurements which would have affected the results. However, when singular measurements were taken after two hours (reflecting a similar swell time applied for the cell printing experiments) viscosity values within a range of 50-70 Pa-s were reported. Thus, when the two hour measurement is compared to the values following overnight swelling (200-300 Pa-s) it can be stated that the longer swell time likely maximised the different effects of MC sterilisation on viscosity (Fig.4.5, B). Therefore, although the viscosity of the UV type

was reduced relative to the scCO<sub>2</sub> and autoclaved variants following overnight swelling, this effect was not seen to markedly effect material behaviour after a shorter swell time. Upon bioprinting, similar plotting parameters were applied for the different alg/MC pastes (prepared with autoclaved, UV, scCO<sub>2</sub> treated or non-sterilised MC) whereby all the variants produced defined and structurally stable scaffolds, with little variation between strand diameters (Fig.4.6; for quantitative analysis see Appendix, Fig.S5B). In addition, throughout the 21 day investigation the structural integrity and shape fidelity of the different scaffold types were maintained (observed by stereo microscopy and SEM). It can therefore be stated that based on print quality alone that scCO<sub>2</sub>, autoclave and UV are all suitable MC sterilisation methods, with an equal feasibility for the successful extrusion of alg/MC.

#### 4.4.2 Effects of methyl cellulose sterilisation on alginate methyl cellulose scaffold characteristics

In previous work, the successive release of MC from the hydrogel scaffolds after ionic crosslinking of alginate has been observed (Schütz *et al.*, 2017). Subsequently, MC release behaviour was also investigated within this study, and it was found that the release of MC from the scaffolds was strongly dependent on the method used for MC sterilisation. The measurement of MC release was achieved through the application of chlorine-zinc-iodine whereby the result of this study confirmed the observation by Schütz *et al.*, (2017), with an apparent cumulative release of MC by alg/MC scaffolds prepared with  $\gamma$ -irradiated MC. However, no visual MC release over time was seen from the samples treated using the other sterilisation methods (Fig.4.6, A). On day 21 of investigation a dark chlorine-zinc-iodine stain was present in the autoclave, UV or scCO<sub>2</sub> type scaffolds, which subsequently indicated that no successive release of MC occurred. However, considering the oversaturated nature of chlorine-zinc-iodine staining a more differentiated insight into MC release was explored. Subsequently, the scaffold variants were analysed by an assay based on Mykoyal™ fluorescence staining, which was described by Hodder *et al.*, (2018) for the first time as a quantitative detection method for MC in solution. The outcome of this assay further verified that the complete release of MC was seen in alg/MC scaffolds made with  $\gamma$ -

irradiated MC whereas the results also revealed a partial release of untreated MC and MC sterilised by autoclave, UV and scCO<sub>2</sub> (Fig.4.6, A-B).

Despite the corroboration of the Mykoval™ quantification approach with the chlorine-zinc-iodine results a few problems did arise upon the development of the Mykoval™ method. An example of this included the issue which effected the higher MC concentrations (used to determine the assay range) whereby the measurements may have been limited due to fluorescence extinction. However, in the lower range that was relevant for MC concentration in the supernatant samples this effect was not apparent. Furthermore, there was a slight discrepancy with the calibration series, wherein all samples were prepared in culture medium with the exception of the those taken immediately after crosslinking, which were in a 100 mM CaCl<sub>2</sub> solution. Therefore, a slight deviation of fluorescence intensity could have occurred in these early samples, due to the effects of different ionic strength and/or optic properties (phenol red, proteins in DMEM medium). Nevertheless, the Mykoval™ assay method presented an attractive new option for the sensitive quantification of MC release.

In summation with regards to the MC release behaviour, a correlation between the MC molecule size  $M_w$  (Fig.4.4, A-B) and the overall MC release (Fig.4.6, B) was discovered and subsequently indicated that larger molecules in MC resulted in lower MC release. For instance, this finding was exemplified by the high bulk release of MC from the  $\gamma$ -type scaffolds. Wherein, the shorter MC chains in the  $\gamma$ -irradiated MC led to an increased mobility and ultimately resulted in a nearly MC-free alginate scaffold by day 21. In line with this view was the assumption that large molecule cleavages occurred in the scCO<sub>2</sub> and UV-treated MC fractions, which was deduced from the slightly reduced PDI values (Fig.4.4, A-B), whereby these samples showed slightly higher MC release rates than the untreated or the autoclaved groups.

In addition, the use of SEM provided an insight into the scaffold microstructure, with variances observed between the tested sterilisation types (Fig.4.6, C). The apparent differences in alg/MC microarchitecture were especially evident for the  $\gamma$ -type scaffolds, which appeared to have smaller and more symmetrical pores compared to the other samples. The finer porosity in the  $\gamma$ -type scaffolds could be theorised to reflect the less disturbed nature of the alginate matrix using  $\gamma$ -irradiated MC, due to the shorter MC chains and the earlier MC release from these samples (which

happened to a large extent during incubation in the crosslinking solution). Further to this, the more fibrous and cavernous pores which were observed in the autoclaved, scCO<sub>2</sub> and UV-treated groups could have been induced by the presence of MC molecules with higher M<sub>w</sub> breaking up the alginate network.

Lastly, the observation of calcium release from the alg/MC scaffolds showed an increase with time, which was expected of ionically crosslinked alginate (Shahriari *et al.*, 2016) and corresponded with the decreasing mechanical strength of the samples. In brief, on day 1 and 10 of cell culture no significant difference in calcium release between the different scaffolds was observed, whereas on day 21 the autoclaved type had the significantly highest release and the UV type the lowest (Fig.4.7, B). Although, the effect of these differences in calcium release was not markedly observed in the physical attributes of the day 21 scaffolds (Fig.4.7, A). In addition, despite the decrease in strength over time and the internal degradation caused by cumulative calcium release, the volumetric and external appearance of the scaffolds remained unchanged throughout for all MC types, which was demonstrated by consistent strand width measurements (Appendix, Fig.S5B).

#### 4.4.3 Sterilisation effects of methyl cellulose on cell survival and matrix production in alginate methyl cellulose scaffolds

The viability of BPCs in alg/MC, which was indicated by live/dead staining, clearly demonstrated a significantly higher cell survival in the scaffolds prepared with autoclaved and UV treated MC, relative to scCO<sub>2</sub> sterilisation (Fig.4.8, A). Wherein, despite their very different methods of sterilisation, the UV and autoclaved variants showed no significant difference in cell survival on days 1, 7 or 21 of scaffold culture. Furthermore, the significantly decreased cell survival of the scCO<sub>2</sub> scaffold types was an important outcome of this work, in which scCO<sub>2</sub> for biomaterial sterilisation is a relatively new application that has not yet been widely utilised. Thus, although the method of scCO<sub>2</sub> has been previously reported to be a gentle, non-cytotoxic and low-temperature alternative for the sterilisation of sensitive biomaterials (Bernhardt *et al.*, 2015; Meyer *et al.*, 2015) it is clear from this study that further development of the

scCO<sub>2</sub> methodology is required. For example, although it has been stated that after scCO<sub>2</sub> sterilisation the treated sample should be left to ventilate prior to contact with cells (Bernhardt *et al.*, 2015; Meyer *et al.*, 2015) the timing of this has not been optimised. Therefore, it could be theorised that a possible reason for the reduced cell survival in alg/MC derived from scCO<sub>2</sub> treated MC could be associated with the chemical additives used in the scCO<sub>2</sub> sterilisation process.

In relation to this, within post-experiment testing it was found that notable levels of hydrogen peroxide were present in scCO<sub>2</sub> treated MC for up to seven days after sterilisation, following ventilated storage at room temperature. In comparison, after 14 days of scCO<sub>2</sub> treatment only trace amounts of hydrogen peroxide remained, with no residue observed in samples after 21 days of sample aeration (see Appendix, Fig.S6B). Conversely, no evidence of peracetic acid was detected in the scCO<sub>2</sub> treated MC, even at the earliest time points analysed (another chemical additive used during scCO<sub>2</sub> sterilisation). Within this investigation, following scCO<sub>2</sub> treatment a 10 day minimum of MC sample ventilation was used prior to cell printing. Thus, it is possible that trace amounts of hydrogen peroxide could have contributed to the reduced cell survival within the scCO<sub>2</sub> derived scaffolds. Therefore, the outcome of this study highlights that scCO<sub>2</sub> as a sterilisation method for biomaterials requires additional optimisation and careful verification before it is considered a valid option for clinical applications. Furthermore, it was shown that the both UV-irradiation and autoclaving, despite being considered as harsh sterilisation methods for biopolymers (Dai *et al.*, 2016) did not have a negative influence on MC, and are much more widely available in research than scCO<sub>2</sub>.

Moreover, the DNA content results additionally corresponded with the cell survival data retrieved and was a result which further promoted the favoured use of UV-irradiation and autoclaving for biomaterial sterilisation (Fig.4.8, B). On day seven of cell culture it was observed that the UV and autoclaved MC scaffold types had a higher DNA content than the scCO<sub>2</sub> group. Similarly, for the autoclaved and UV treated MC type scaffolds a cumulative DNA content was apparent, whereas for the scCO<sub>2</sub> samples the DNA content decreased over time. Likewise, the findings of the safranin O staining additionally corroborated the beneficial effects of UV and autoclave (Fig.4.9, A-B) relative to scCO<sub>2</sub>, with a marked visual decrease in stain intensity for the scCO<sub>2</sub> type samples on days 7, 14 and 21. Thus, for each time point tested using

safranin O staining the scCO<sub>2</sub> samples evidenced lower proteoglycan contents, which indicated that a lower percent of living and metabolically active cells were present to produce ECM.

#### 4.5 Conclusion

Upon the comparison of sterilisation treatments for MC, as a component of alg/MC bioinks, UV-irradiation, autoclave and scCO<sub>2</sub> treatments were highly comparable with regards to paste printability. Wherein, the three treatment types resulted in an alg/MC paste that was capable of high resolution printing, with defined material strands for the production of structurally stable scaffolds over a 21 day testing period. However, in comparison the use of  $\gamma$ -irradiated MC powders formulated an alg/MC paste with a substantial reduction in viscosity, and subsequently led to poorly formed scaffolds. The apparent difference in material behaviour using  $\gamma$ -irradiated MC was ultimately attributed to its marked decrease in molecular mass, which in addition led to the complete release of MC over time. Conversely, only slight variations between scaffold properties were observed for the other sterilisation methods tested with molecular masses closer in range and indicated that autoclaving was not more intense than the low temperature scCO<sub>2</sub> treatment. Furthermore, the investigations of cell compatibility and resultant proteoglycan production revealed that the UV-irradiated and autoclaved MC treatments were the best candidates for alg/MC cell-laden printing. Nevertheless, UV treatment is not considered a fully effective method for terminal stage sterilisation. Therefore, it can be proposed that autoclaving for the sterilisation of powdered MC presents a more viable alternative than UV-irradiation, and in addition is a widely accessible and clinically approved method. Comparatively, the application of scCO<sub>2</sub> for the sterilisation of sensitive biopolymers was shown to require further optimisation before it is considered a valid approach within tissue engineering. Moreover, the results of this study demonstrated the highly compatible use of MC with alginate for the 3D culture of chondrocytes, with wider implications as a promising material for cartilage regeneration using bioprinting.

In summation, this investigation effectively established that sterilisation method can have a direct impact on biomaterial physical properties as well as on cell behaviour, and thus has a large influence on a materials suitability for cell-laden bioprinting. The exact mechanism of the interactions of the sterilisation approach on material

properties could not be fully elucidated. However, the results suggested that the difference between the MC sterilisation types was not due to a chemical change, as shown by consistent FTIR spectra, but the result of a physical alteration to matrix distributions caused by the observed differences in molecular mass. The outcome of this investigation subsequently highlighted the necessity for appropriate sterilisation method selection for biomaterial compatibility and feasibility for bioprinting, with a particular relevance for recently explored cellulose based bioinks.

## **Chapter 5 The effect of hydrostatic pressure application on proteoglycan production in mammalian articular cartilage *in vitro*: a meta-analysis review**

### 5.1 Introduction

The functional repair of cartilage defects is known to be a difficult task, mostly the result of cartilage tissue's inability to self-repair which has been linked to its lack of blood supply (Hunziker, Quinn and Häuselmann, 2002). However, with advancements in the field of tissue engineering multiple promising solutions to cartilage restoration have been demonstrated (Dzobo *et al.*, 2018; Petretta *et al.*, 2018; Zhu *et al.*, 2018). Furthermore, it is now commonly accepted that chondrocytes, especially from articular regions, demonstrate improved cartilaginous physiology when cultured with exposure to mechanical forces which comprise of hydrostatic pressure (HP) (Mizuno, 2011; Correia *et al.*, 2012; S F Carroll, Buckley and Kelly, 2014), compression (AufderHeide and Athanasiou, 2004; Sharma, Saxena and Mishra, 2008; Pörtner *et al.*, 2009) and shear stress (Nakai, Shogo and Jun, 2015; Lu, Yan and Chen, 2016; Fukuda *et al.*, 2017). These mechanical stimuli replicate physiological forces and can be employed to improve the biomimicry of tissue-engineered constructs, by regulating chondrocyte differentiation, maturation and ECM formation via mechanotransduction (O'Connor, Case and Guilak, 2013).

Mechanotransduction is the process by which mechanical signals modulate biochemical activity and changes in cell behaviour (Brown and Hu, 2015). The biophysical and biochemical events involved in mechanotransduction are still not fully understood challenged by the complexity of the ECM and the cell. However, it has been suggested that mechanosensitive ion channels and integrins found within chondrocytes are likely to be involved (Martinac, 2004; Yamamura, Suzuki and Imaizumi, 2018; Lee *et al.*, 2019). With anabolic responses to mechanotransduction resulting in the production of new tissue (aggrecan and/or collagen II) or catabolic reactions, causing the removal of damaged cells (Martinac, 2004; Lee *et al.*, 2019). The maintenance of healthy tissue depends on the balance between matrix anabolism and catabolism and has been shown to be directly influenced by mechanical parameters, including the magnitude and frequency of their application (Ramage, Nuki and Salter, 2009; Lee *et al.*, 2019).

The potential beneficial effects of mechanical stimulation for cartilage synthesis is not a new finding. Numerous investigations over the past decades have been designed to understand the cellular response to forces found within articular joints, including compression (Pörtner *et al.*, 2009), shear (Nakai, Shogo and Jun, 2015), hydrostatic (Carroll, Buckley and Kelly, 2014), and osmotic-pressure (Guilak, Erickson and Tingbeall, 2002). The commonly used marker for a successful anabolic response after mechanical stimulation has been reported as the upregulation of proteoglycan expression and in some publications collagen type II (Toyoda *et al.*, 2003; Kawanishi *et al.*, 2007; Kunitomo *et al.*, 2009; Tatsumura *et al.* 2013; Li *et al.*, 2016). The most extensive studies for cartilage mechanical stimulation thus far have been performed using uniaxial compression, whereby unconfined specimens are loaded axially up to failure or a pre-set level of deformation (Anderson and Johnstone, 2017). However, the effects of compression cannot be easily separated from other forces. Soon after compressive loading occurs an increase in internal HP also arises in the tissue, as well as osmotic stresses (Mow, Wang and Hung, 1999; Lu, Yan and Chen, 2016). It has been stated that when compression occurs *in vivo* the majority of the force is instead transformed to HP, due to the interstitial fluid content of the joint (Eckstein *et al.* 2001; Mow and Wang 1999; Soltz and Ateshian 1998). Thus, in essence the indirect application of HP is the most prevalent load occurring in joints for cartilage maintenance (Maik and Augustinus, 2007). Additionally, HP provides the least detrimental mechanical stimulation approach, with equal forces acting from every side of a sample via the compression of its surrounding fluid, without causing direct impact damage (Foster *et al.*, 2015). When HP is applied alone no internal fluid flow results, unlike under compression, which has been associated with damage to cartilage ECM (Maik and Augustinus, 2007).

The potential stimulatory effects of HP on cartilaginous synthesis has long been known, with relevant published studies dating back thirty years (Lippiello *et al.*, 1985) and remains an influence on present day research (Chen, 2017; Cheleschi *et al.*, 2017; Choi, Yong and Choi, 2018). However, despite its popularised application the methods of HP stimulation have varied greatly between studies, with no uniform approach for the effective use of HP in cartilage engineering. Examples of this disparity among experiments have included a wide variation in pressure magnitude application, ranging from 0.3 MPa (Heyland *et al.*, 2006) and 0.35 MPa (Hutton *et al.*, 2001) to 10 MPa

(Kunitomo *et al.*, 2009)(Hu and Athanasiou, 2006; Elder and Athanasiou, 2008). Similarly, the method of HP application for 3D cultured chondrocytes has been diverse, with papers utilising either dynamic HP loading strategies such as repetitive or cyclical HP applications (Suzuki *et al.*, 2006; Heyland *et al.*, 2006; Kawanishi *et al.*, 2007; Tatsumura *et al.*, 2013) or static loading approaches (daily or one-off loading) (Toyoda *et al.*, 2003; Kunitomo *et al.*, 2009). Furthermore, the durations of HP studies have varied, with studies lasting for hours (Toyoda *et al.*, 2003; Toyoda *et al.*, 2006), days (Kawanishi *et al.*, 2007), weeks (Kunitomo *et al.*, 2009) and months (Hu and Athanasiou, 2006). Thus, this suggests that the key attributes needed to trigger a successful HP induced mechanotransductive response are not yet clear. Therefore, the purpose of this study was to use an aggregate meta-analytical approach to investigate the effect of HP experimental factors on the upregulation of proteoglycan expression and GAG content in primary articular chondrocytes, including the effect of magnitude, application style, duration of pressure applied and observation time.

## 5.2 Methodology

### 5.2.1 Study Eligibility Criteria

Studies were included if they met the following criteria: 1) primary research studies published between 2000-2018; 2) utilised mammalian primary articular chondrocytes; 3) the cells were grown in 3D culture (either embedded, cartilage explant, self-assembling or pellet culture); 4) utilised HP as the only mechanical stimulus, 5) analysed proteoglycan expression or GAG content using RT-PCR or DMMB assay; 6) had a comparative control group. Studies that did not meet all criteria were excluded.

### 5.2.2 Data Sources

Studies were retrieved from three electronic database sources (PubMed, EMBASE and Web of Science). The following keywords were utilised in all searches 'hydrostatic pressure', 'chondrocytes' and 'cartilage', and a collective search output of 2,340 citation papers was obtained.

### 5.2.3 Study Selection

The author and a second party selected all studies independently, before reviewing their selections for accuracy and consistency. Discrepancies were resolved by consensus, and by a third party arbitrator if required. Trials published as duplicate reports (parallel publications) were only included once, ensuring that the trial data were not duplicated in the review. From the original 2,340 citations, initial screening excluded 2,277 studies. Following this initial screening 63 articles were assessed for eligibility with 48 excluded for the following reasons: 26 did not employ proteoglycan gene expression or DMMB colorimetric assay analysis or consider the ECM response at all, 6 did not use mammalian articular chondrocytes, 6 used monolayer culture, 4 were reviews, 4 did not test HP in isolation and 2 were congress abstracts. This led to 15 citations that fulfilled the inclusion criteria (Fig.5.1).

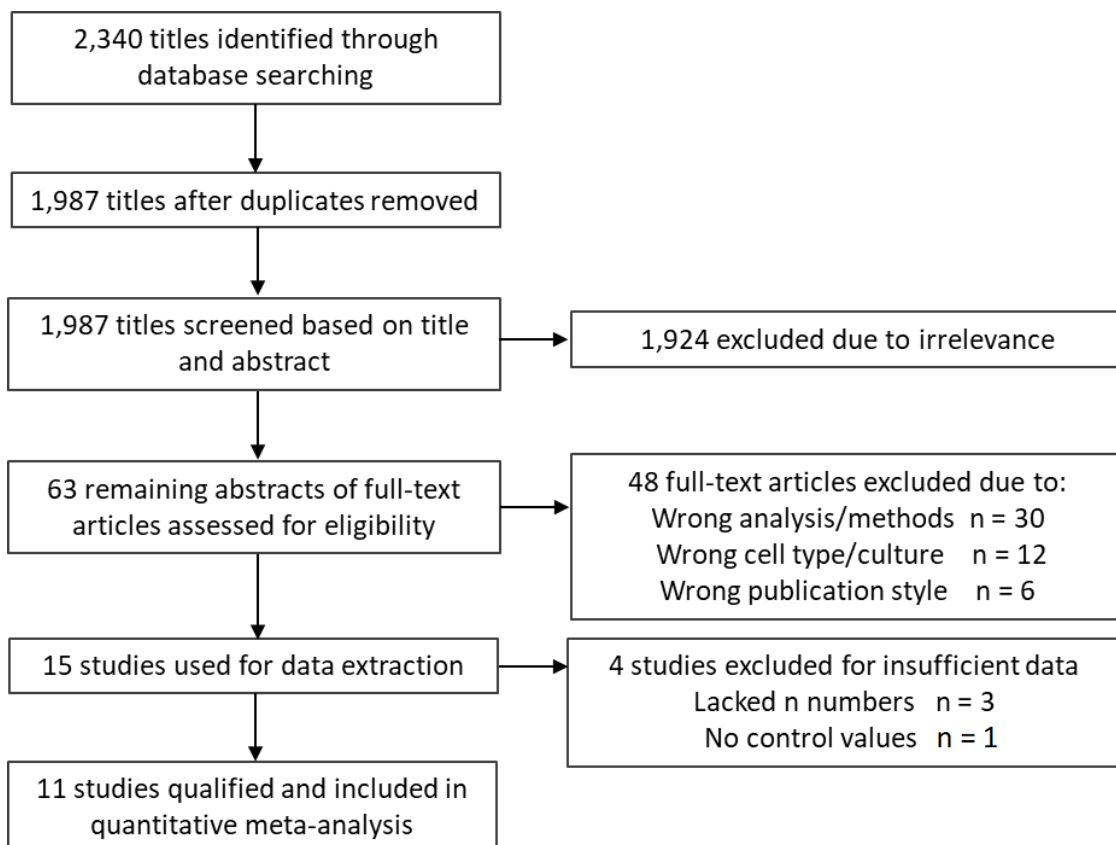


**Figure 5.1** Visual demonstration of the publication selection process.

#### 5.2.4 Data Extraction

Each study was independently evaluated and either the relative proteoglycan expression or total GAG content data were extracted. Where possible, missing raw data (sometimes due to normalisation of data to control groups) were sought from the authors of studies for inclusion. Papers with authors who replied included Jarvelainent and Tammi, (1994); Kaarniranta *et al.*, (2000); Lane Smith *et al.*, (2000); Toyoda *et al.*, (2003) and Elder *et al.*, (2006). However, with the exception of Elder *et al.*, (2006), no additional information was obtained from these communications. Therefore, in publications which included suitable graphs the raw data was extrapolated using a graph digitising software 'engage digitiser'. At this stage four publications were dismissed due to a lack of data availability, unavailable contact information and/or inadequate graph information. This led to a final number of 11 citations that fulfilled the inclusion criteria (Fig.5.1).

#### 5.2.5 Missing Data Extraction

Figures from the publications by Mizuno *et al.*, (2002), Elder *et al.*, (2006), Kawanishi *et al.*, (2007); Elder and Athanasiou (2008) and Tatsumura *et al.*, (2013) were individually imported into Engauge Digitizer (version 10.5). The co-ordinates of the axis were then manually defined by placing three points on the figure axis at the origin (0,0), and the maximum values on both the x and y axis (in examples in which the x-axis were not related to numerical values then a dummy value was input and the x-axis co-ordinate for this later disregarded) (Fig.5.2, A). Once values were given to these points the software was able to estimate the graph scale. Co-ordinates were then drawn over the data values and at the top of each error bar (Fig.5.2, B), and the relative data were retrieved and exported (Fig.5.2, C).

Tests to ensure the accuracy of the engage digitizer extraction protocol were performed. Ten graphs were manually created using known means and each graph was measured using engage digitizer; the extracted values were compared to the

actual values plotted (n = 3), and the coefficient of variation (CV) calculated using the following equation:

$$\text{Equation 5.1} \quad CV = (SD / \bar{X}) \times 100.$$

For all ten graphs the derived CV was 0.18% which demonstrated high repeatability. In addition, there was no significant difference between known values and the extracted values (averaged, n = 3); performed via Mann–Whitney U test ( $P = 0.79$ ), which implied a minimal margin of error.

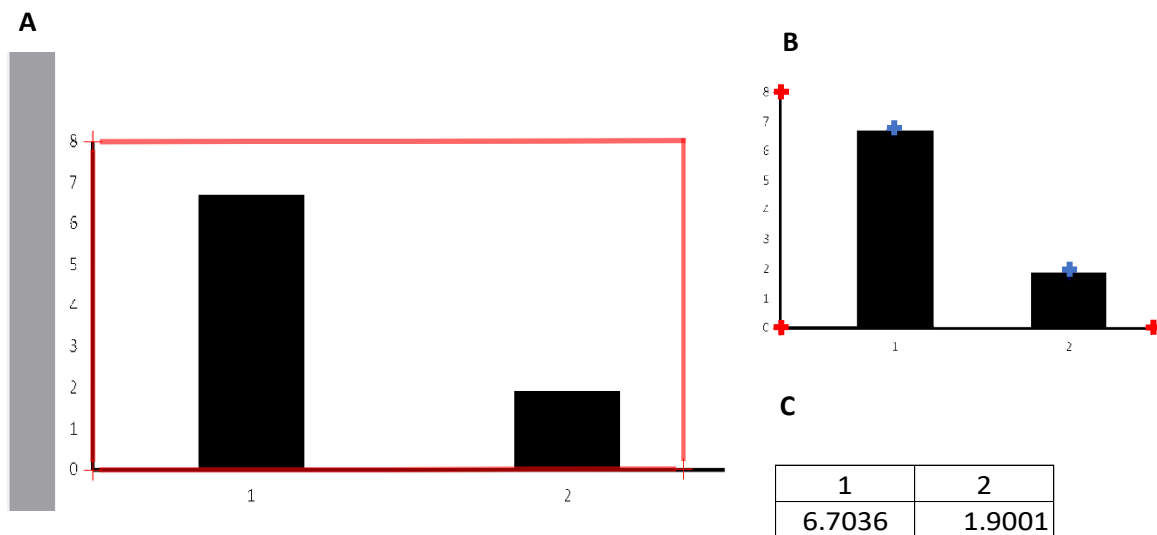


**Figure 5.2** Representation of how the raw data was extracted from graphs using engage digitizer (10.5) software. (A) Screen shot of the engage digitizer software after three axis co-ordinates had been allocated to define the graph area. (B) Example of co-ordinate plotting for the extraction of data values using a bar graph. (C) Exported y-axis data from the plotted co-ordinates.

### 5.2.6 Statistical Analysis

#### Calculation of Effect Sizes.

The primary outcome measures, that is changes in X and Y, were calculated using the standardised effect size  $g$  using the following equation:

Equation 5.2 
$$g = \frac{\bar{X}_t - \bar{X}_c}{SD_{pooled}}$$

whereby  $g$  is the standardised effect size,  $\bar{X}_t$  is the mean of HP treated,  $\bar{X}_c$  the mean average of the control group, and  $SD_{pooled}$  is the pooled standard deviation of both groups combined. The data were then manually imported into Review Manager 5 (RevMan 5, Cochrane Collaboration). Mean difference was used as the measure of effect for continuous data, using a random effects model and a 95% confidence interval. Next the data sets were sorted based on the following attributes: pressure magnitude, pressure application i.e. static (one-off or daily motionless load) or dynamic (cyclic, intermittent or repetitive motion loading) and study duration (Table.5.1).

In addition to the mechanical experiment factors analysed some additional cell-based experimental factors were considered and compared (Table.5.2). These factors included; cell source, 3D culture type, seeding density, preculture time and the growth medium and supplements used.

**Table 5.1** Overview of physical hydrostatic pressure factors selected for meta-analysis taken from papers reviewed in this study.

	Study	Pressure (MPa)	Load Duration	Frequency (Hz)	Length of Study
PG gene expression	Toyoda <i>et al.</i> , 2003	5.0	4 hr/day	0 or 1	20 hrs
	Toyoda <i>et al.</i> , 2006	4.0	4 hr	0 or 1	4 hrs
	Kawanishi <i>et al.</i> , 2007	5.0	4hr/day	0.5	4 days
	Kunitomo <i>et al.</i> , 2009	10.0	12 hr	0	3 hrs or 2 wks
	Li <i>et al.</i> , 2016	5.0	4 hr/day	0.5	1, 2, or 4 wks
GAG content	Elder and Athansiou, 2008	1.0, 5.10, 10.0	1 hr/d	0, 0.1, 1	4 wks
	Mizuno <i>et al.</i> , 2002	2.8	continual	0 or 0.015	5 or 15 days
	Elder <i>et al.</i> , 2006	0.4-4.0	45 min x2	1	1 wk
	Heyland <i>et al.</i> , 2006	0.3	6 hr	50 l/h	1 wk
	Hu and Athansiou, 2006	10.0	4 hr/day/5 day per wk continual	1.0	8 wks
	Tatsumura <i>et al.</i> 2013	0-0.5	7d/cHP, 4d/cHP, 4d x 2 cHP	0.5	2 wks

PG; proteoglycan, GAG; glycosaminoglycans (proteoglycans are formed of glycosaminoglycans) cHP; cyclic hydrostatic pressure, hrs; hours, Hz; Hertz, min; minutes, MPa; mega-pascal, wk(s); week(s)

**Table 5.2** Overview of the cell-based experiment factors within the studies selected for meta-analysis review.

	Study	Cell Source	Culture Type	Seeding Density	Preculture (days)	Medium
Gene Expression	Toyoda <i>et al.</i> , 2003	Bovine	Agarose	2 x 10 <sup>6</sup> cells/ml	2	DMEM, 10% FCS
	Toyoda <i>et al.</i> , 2006	Human	Alginate	2 x 10 <sup>5</sup> /10 beads	3	DMEM, 10% FBS, antimyotic, pen/strep, amphotericin B, HEPES
	Kawanishi <i>et al.</i> , 2007	Bovine	Pellet	2.5 x 10 <sup>5</sup>	3	Chondrogenic medium*1
	Kunitomo <i>et al.</i> , 2009	Rabbit	Alginate	4 x 10 <sup>6</sup> cells/ml	0 or 14	DMEM, 10% FCS, pen/strep
	Li <i>et al.</i> , 2016	Rabbit	Alginate	NS	7	DMEM, 10% FBS (preculture with chondrogenic medium)
DMMB Assay	Elder and Athansiou, 2008	Bovine	Self-assembled	5.5 x 10 <sup>6</sup> cells/well	1	Chondrogenic medium*2
	Mizuno <i>et al.</i> , 2002	Bovine	Collagen Sponge	3 x 10 <sup>6</sup> cells/sponge	3	Ham's F12, 10 % FCS
	Elder <i>et al.</i> , 2006	Porcine	Pellet	5 x 10 <sup>5</sup> cells/mL	2	Ham's F10, 10 % FBS, Ascorbic Acid (daily 25 µg/ml)
			Alginate	10 <sup>7</sup> cells/mL, 25 µL = 1 bead		
	Heyland <i>et al.</i> , 2006	Porcine	Alginate or cartilage carrier	NS	NS	NS
	Hu and Athansiou, 2006	Bovine	Self-assembled	5.1x 10 <sup>6</sup> per well	14	Chondrogenic medium*3
	Tatsumura <i>et al.</i> 2013	Bovine	Collagen gel	5.5 x 10 <sup>5</sup> /55 µl	Overnight	DMEM/F-12 [50:50], 10% FBS, pen/strep

---

NS; not stated, DMEM; Dulbecco's modified eagle medium, FCS/FBS; fetal calf/bovine serum, HEPES; 4-(2-hydroxyethyl)-1-piperazineethanesulfonic acid) buffering agent, ml; millilitres,  $\mu$ L; microlitres,  $\mu$ g; microgram, pen/strep; penicillin/streptomycin, \*1 high-glucose DMEM, ITS + Premix, insulin, transferrin, selenous acid, linoleic acid, bovine serum albumin, ascorbic acid 2-phosphate, sodium pyruvate, proline, pen/strep, amphotericin \*DMEM, 10% FBS, recombinant human BMP-2, and antibiotic/antimycotic \*3 DMEM, 10% FBS, glucose, L-glutamine, 1% fungizone (Biowhit- taker), 1% penicillin/streptomycin, 1% non-essential amino acids, proline, HEPES, L-ascorbic acid

## 5.3 Results

### 5.3.1 Hydrostatic pressure interventions

#### 5.3.1.1 Proteoglycan gene expression

Eleven effects representing 66 repeated experiments from 5 studies (Toyoda *et al.*, 2003; Toyoda *et al.*, 2006; Kawanishi *et al.*, 2007; Kunitomo *et al.*, 2009; Li *et al.*, 2016) resulted in an overall significant and positive effect favouring HP conditions compared with control conditions, ( $g = 0.45$ , 95% CI 0.07, 0.84,  $Z = 2.29$ ,  $P = 0.02$ ,  $X^2=286.26$ ,  $P<0.00001$ ,  $I_2 = 97\%$ , Fig.5.3).

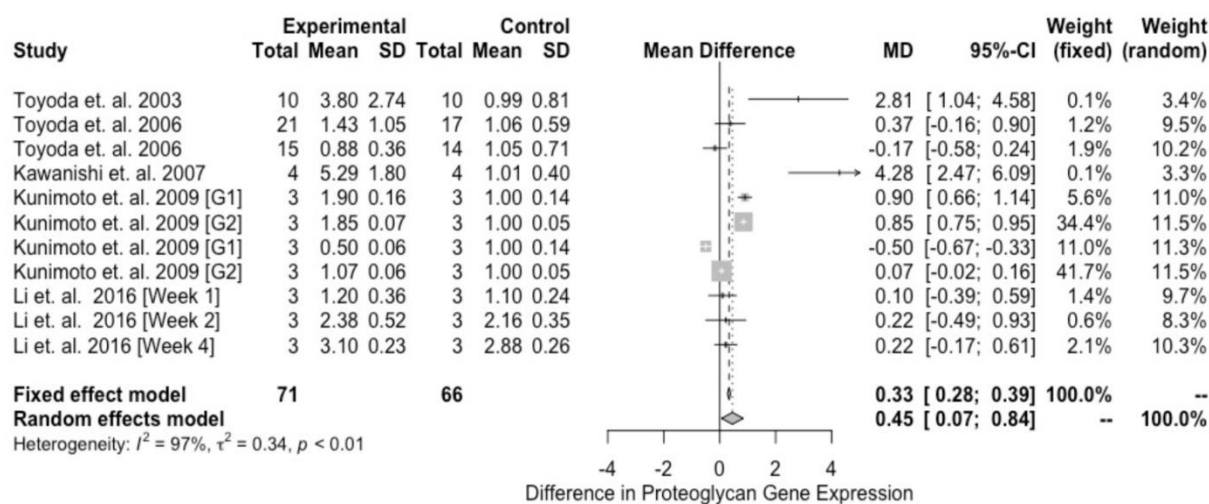


**Figure 5.3** Forest plots representing the relationship between hydrostatic pressure (HP) stimulated 3D cultured samples on proteoglycan gene expression measured via RT-PCR compared to control samples kept at atmospheric pressures.

#### 5.3.1.2 Glycosaminoglycan content

Twenty-seven effects representing 137 repeated experiments and 6 studies resulted in an overall significant positive effect favouring an HP treatment versus atmospheric

control conditions ( $g = 2.18$ , 95% CI 1.29,3.08,  $Z = 4.79$ ,  $P < 0.00001$ ,  $X^2 = 707.69$ ,  $P < 0.00001$ ,  $I_2 = 96\%$ , Fig.5.4).

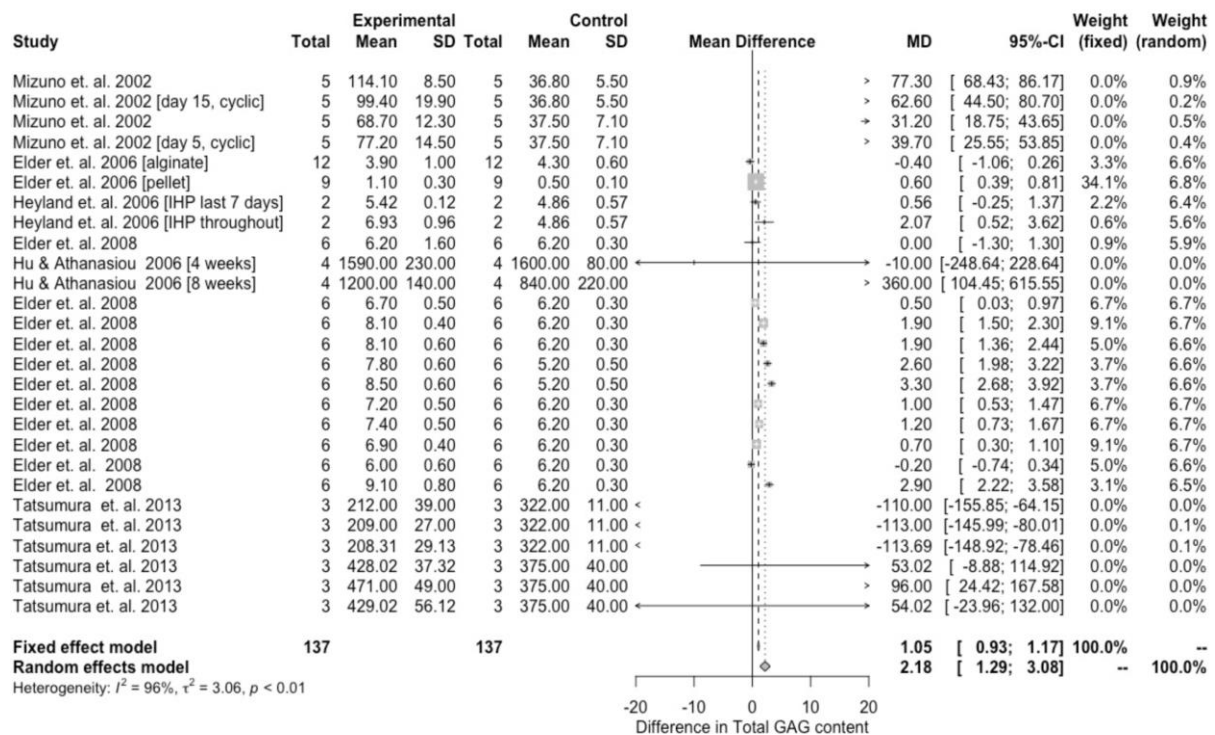


**Figure 5.4** Forest plot representing the relationship between hydrostatic pressure stimulated 3D cultured samples on total glycosaminoglycan content measured via DMMB colorimetric assay relative to samples kept at atmospheric pressure conditions.

### 5.3.2 Static and dynamic hydrostatic pressure

#### 5.3.2.1 Proteoglycan gene expression

Static HP was seen to have a significant effect on proteoglycan upregulation compared to control conditions with a cumulative effect size from four effects representing 31 experimental repeats across three studies, of 0.70 (95% CI = 0.23, 1.16,  $Z = 2.94$ ,  $P = 0.003$ ,  $X^2 = 27.80$ ,  $P < 0.0001$ ,  $I_2 = 89\%$ , Fig.5.5). A non-significant effect was seen for the dynamic HP conditions, from five effect values representing three studies and 34 experimental conditions ( $g = 0.55$ , 95% CI = -0.05,1.16,  $Z = 1.79$ ,  $P = 0.07$ ,  $X^2 = 19.56$ ,  $P < 0.00001$ ,  $I_2 = 80\%$ , Fig.5.5). The test for subgroup differences, which tested the difference between the pooled effect estimates for each subgroup i.e. in this case

the subgroups 'statically applied HP' and 'dynamic HP' demonstrated no significant difference between groups ( $\text{Chi}^2 = 0.14$ ,  $\text{df} = 1$ ,  $P = 0.71$ ,  $I^2 = 0\%$ ).

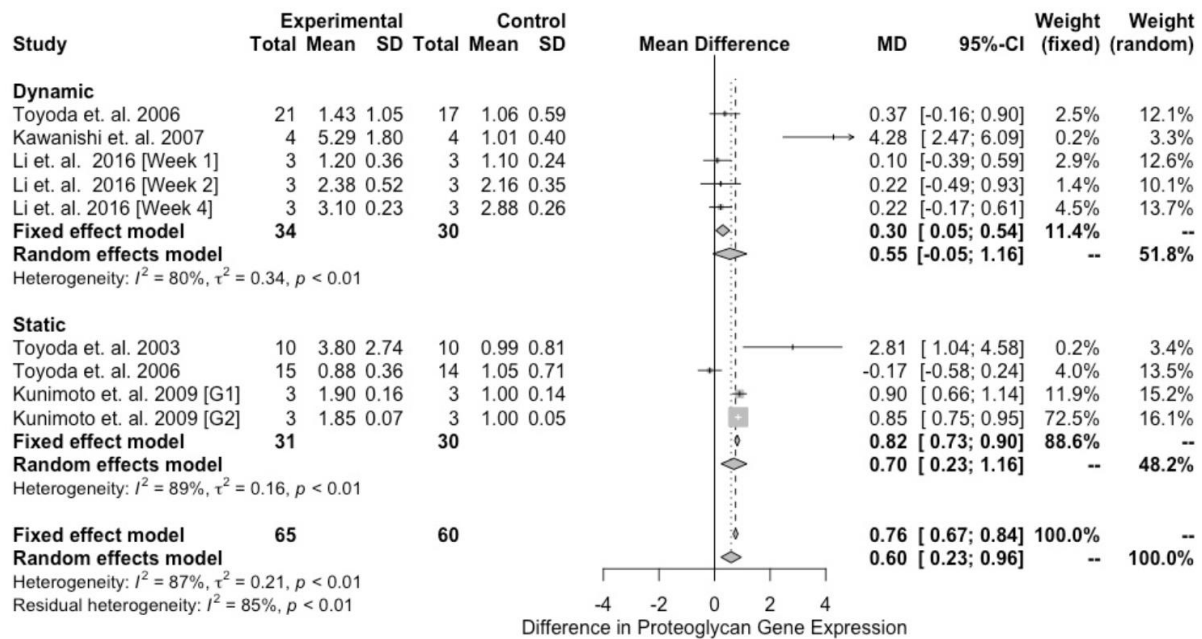


**Figure 5.5** Forest plots representing the relationship between hydrostatic pressure stimulated 3D cultured samples applied either as static or dynamic loads on proteoglycan gene expression measured via real time-polymerase chain reaction compared to control samples cultured under atmospheric pressures.

### 5.3.2.2 Glycosaminoglycan content

Static HP applications were found to significantly favour GAG content upregulation with values of  $g = 6.00$ ,  $95\% \text{ CI} = 3.9, 8.10$ ,  $Z = 5.61$ ,  $P < 0.00001$ ,  $X^2 = 357.29$ ,  $P < 0.00001$ ,  $I^2 = 98\%$ , Fig.5.6). Comparatively, dynamically applied HP also significantly favoured the experimental conditions over the control but to a lesser extent ( $g = 0.96$ ,  $95\% \text{ CI} = 0.08, 1.83$ ,  $Z = 2.15$ ,  $P = 0.03$ ,  $X^2 = 273.96$ ,  $P < 0.00001$ ,  $I^2 = 93\%$ , Fig.5.6) for GAG content. The test for subgroup differences between the static and dynamic HP experimental conditions revealed that static HP had a significantly greater positive influence on GAG content than dynamically applied HP, ( $\text{Chi}^2 = 18.95$ ,  $\text{df} = 1$ ,  $P < 0.0001$ ,  $I^2 = 94.7\%$ ) when using data from DMMB colorimetric assay measurements.

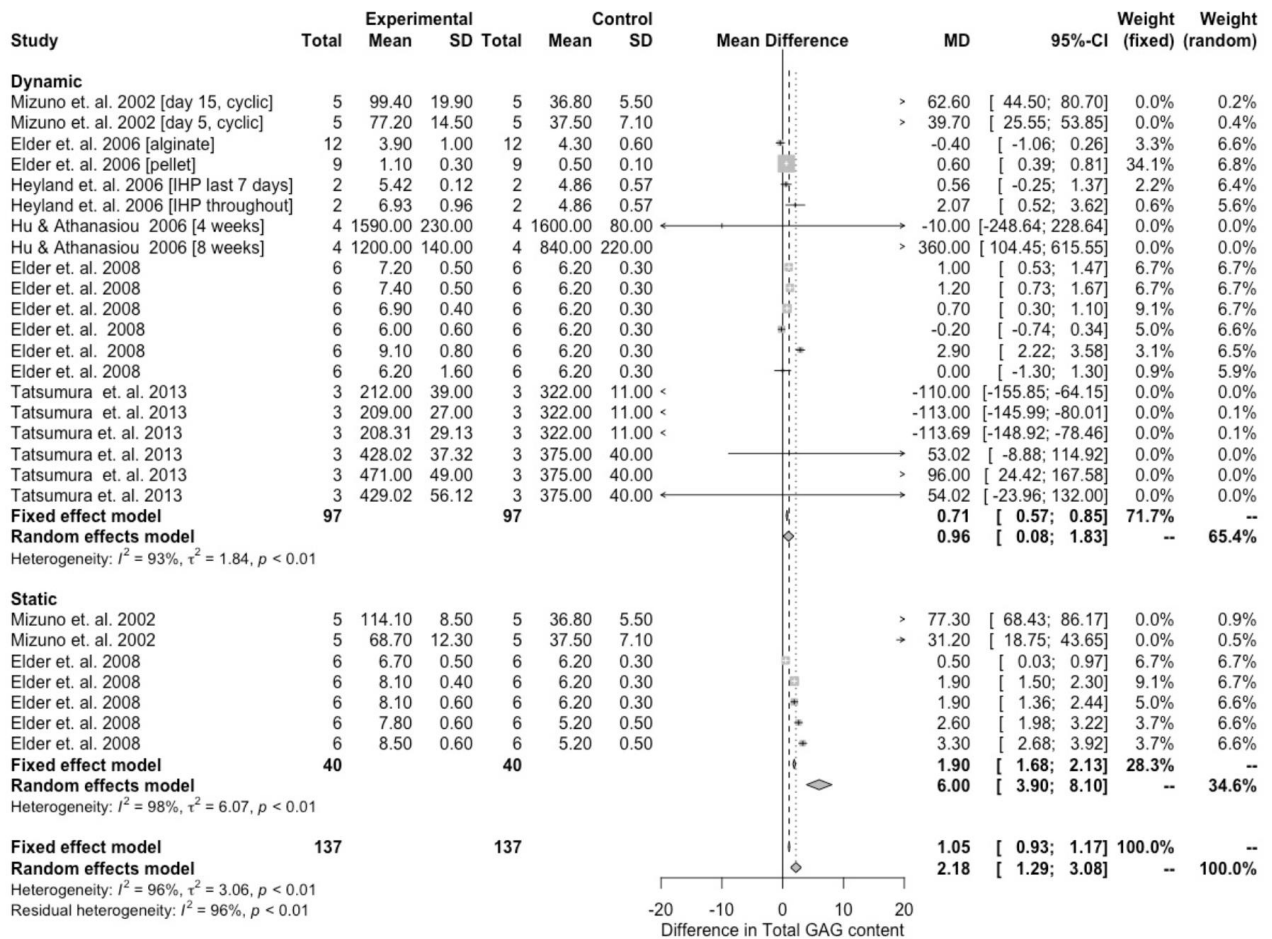


**Figure 5.6** Forest plots representing the relationship between hydrostatic pressure stimulated 3D cultured samples applied as either static or dynamic loads on measured glycosaminoglycan content, via DMMB colorimetric assay, compared to control samples cultured under atmospheric pressure.

### 5.3.3 Pressure magnitude

#### 5.3.3.1 Proteoglycan gene expression

The  $\leq 5$  MPa of HP subgroup was associated with no significant overall effect compared with normal pressure controls ( $g = 0.58$ , 95% CI = 0.03, 1.12,  $P = 0.05$ ,  $Z = 2.07$ ,  $X^2 = 31.62$ ,  $P < 0.0001$ ,  $I^2 = 81%$ , Fig. 5.7). A non-significant effect was also seen for the HP magnitude of 50 MPa, compared with normal pressure controls ( $g = -0.21$ , 95% CI = -0.77, 0.35,  $P = 0.46$ ,  $Z = 0.74$ ,  $X^2 = 33.27$ ,  $P < 0.00001$ ,  $I^2 = 97%$ , Fig. 5.7). However, when an HP of 10 MPa was applied there was a significant effect favouring the experimental condition ( $g = 0.86$ , 95% CI = 0.77, 0.95,  $P < 0.00001$ ,  $Z = 18.62$ ,  $X^2$

= 0.14,  $P = 0.70$ ,  $I^2 = 0\%$ , Fig.5.7). The test for subgroup differences confirmed there was a measurable significant difference between the outcomes related to the three magnitude groups difference ( $\text{Chi}^2 = 14.48$ ,  $\text{df} = 2$ ,  $P = 0.0007$ ,  $I^2 = 86.2\%$ ); in which 10 MPa had the greatest influence on proteoglycan gene expression.

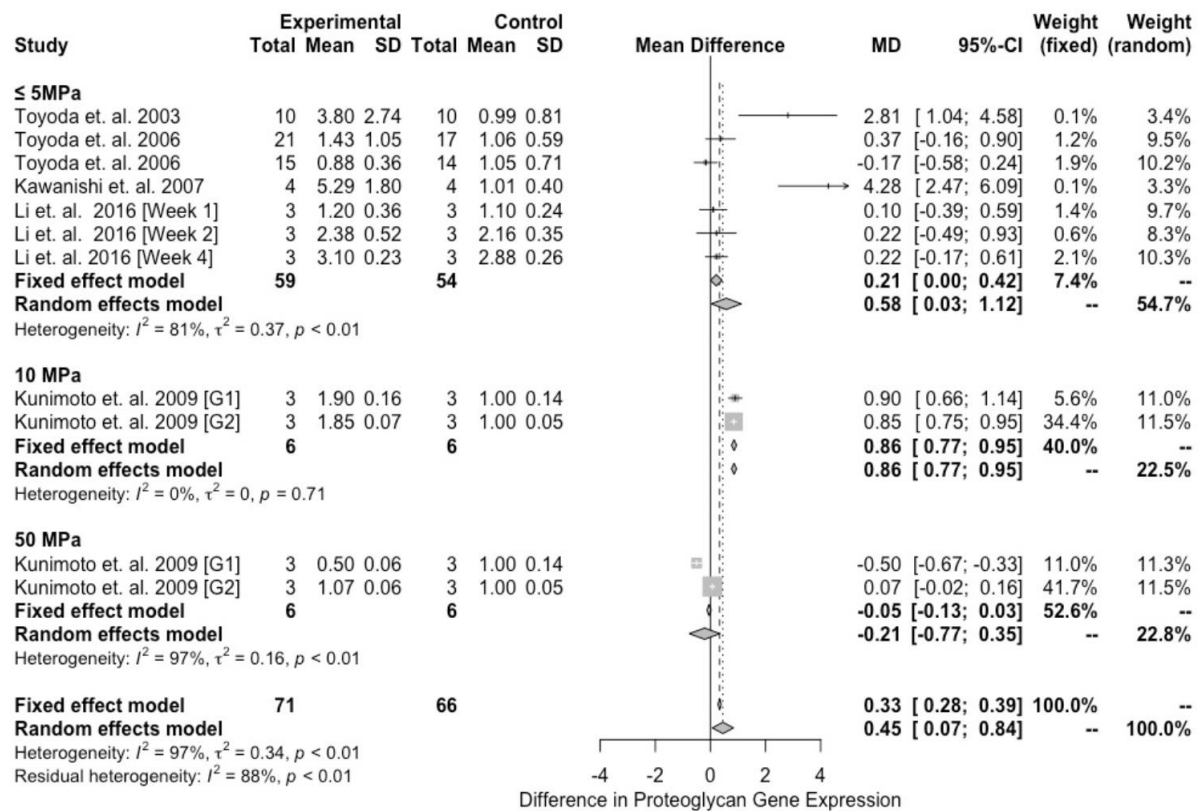


**Figure 5.7** Forest plots demonstrating the relationship between hydrostatic pressure stimulated 3D cultured samples using magnitudes of ≤ 5 MPa, 10 MPa and 50 MPa applied as either static or dynamic loads on measured proteoglycan gene expression, via RT-PCR analysis, compared to control samples kept at atmospheric pressure.

### 5.3.3.2 Glycosaminoglycan content

When pressure magnitudes were examined based in GAG content data an overall significant effect was seen for all magnitudes employed. The <1 MPa of HP gave a result of  $g = -11.78$ , 95% CI=-20.28, -3.28,  $P = 0.007$ ,  $Z = 2.72$ ,  $X^2 = 122.95$ ,  $P < 0.00001$ ,  $I^2 = 94\%$  (Fig.5.8) thus significantly favouring control conditions. The pressure magnitude of <5 MPa (but >1 MPa) significantly favoured HP over control

samples with values of  $g = 4.70$ , 95% CI 2.89, 6.52,  $P < 0.00001$ ,  $Z = 5.09$ ,  $X^2 = 404.50$ ,  $P < 0.00001$ ,  $I^2 = 98\%$  (Fig.5.8) and the higher magnitude subgroups of 5 MPa ( $g = 1.38$ , 95% CI = 0.35, 2.40,  $Z = 2.63$ ,  $P = 0.009$ ,  $X^2 = 33.65$ ,  $P < 0.00001$ ,  $I^2 = 91\%$ , Fig.5.8) and 10 MPa ( $g = 2.31$ , 95% CI = 1.35, 3.27  $P < 0.00001$ ,  $Z = 4.71$ ,  $X^2 = 42.14$ ,  $P < 0.00001$ ,  $I^2 = 88\%$ , Fig.5.8) also demonstrated a significant positive effect on GAG content. The test for subgroup differences showed there was measurable significant difference between the four magnitude subgroups difference ( $\text{Chi}^2 = 20.24$ ,  $\text{df} = 3$ ,  $P = 0.0002$ ,  $I^2 = 85.2\%$ ); confirming that a difference in pressure magnitude can have a direct influence on the extent of HP's stimulatory effect on GAG content.

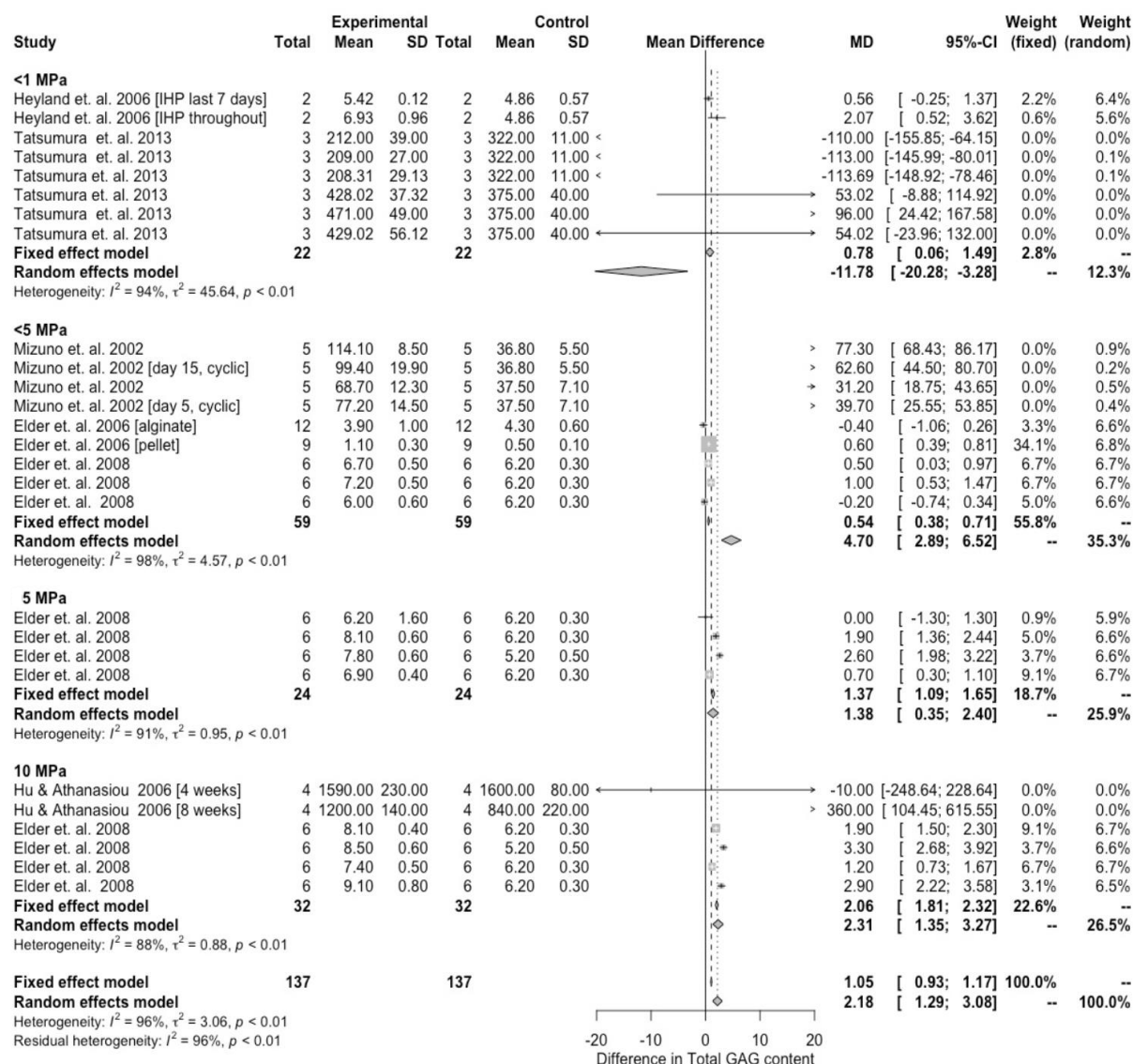


**Figure 5.8** Forest plots representing the relationship between hydrostatic pressure stimulated 3D cultured samples using pressure magnitudes of under 1 MPa, 5 MPa and 10 MPa on measured glycosaminoglycan content, via DMMB colorimetric assay, compared to unpressurised control samples.

### 5.3.4 Study Duration

#### 5.3.4.1 Gene expression

Based on the test for difference between subgroups when the proteoglycan gene expression data was separated by HP experiment durations of  $\leq 1$  week and  $> 1$  week no significant difference was observed between groups ( $\text{Chi}^2 = 0.09$ ,  $\text{df} = 1$ ,  $P = 0.77$ ,  $I_2 = 0\%$ ). Studies lasting  $\leq 1$  week did not significantly favour HP when compared to

the control condition ( $g = 0.49$ , 95% CI = -0.21, 1.19,  $P = 0.17$ ,  $Z = 1.37$ ,  $X^2 = 110.39$ ,  $P < 0.00001$ ,  $I^2 = 95\%$ , Fig.5.9). Studies of  $\geq 2$  weeks also did not infer a significant effect on proteoglycan expression with ( $g = 0.35$ , 95% CI = -0.19, 0.90,  $P = 0.06$ ,  $Z = 1.85$ ,  $X^2 = 278.84$ ,  $P < 0.0001$ ,  $I^2 = 98\%$ , Fig.5.9).

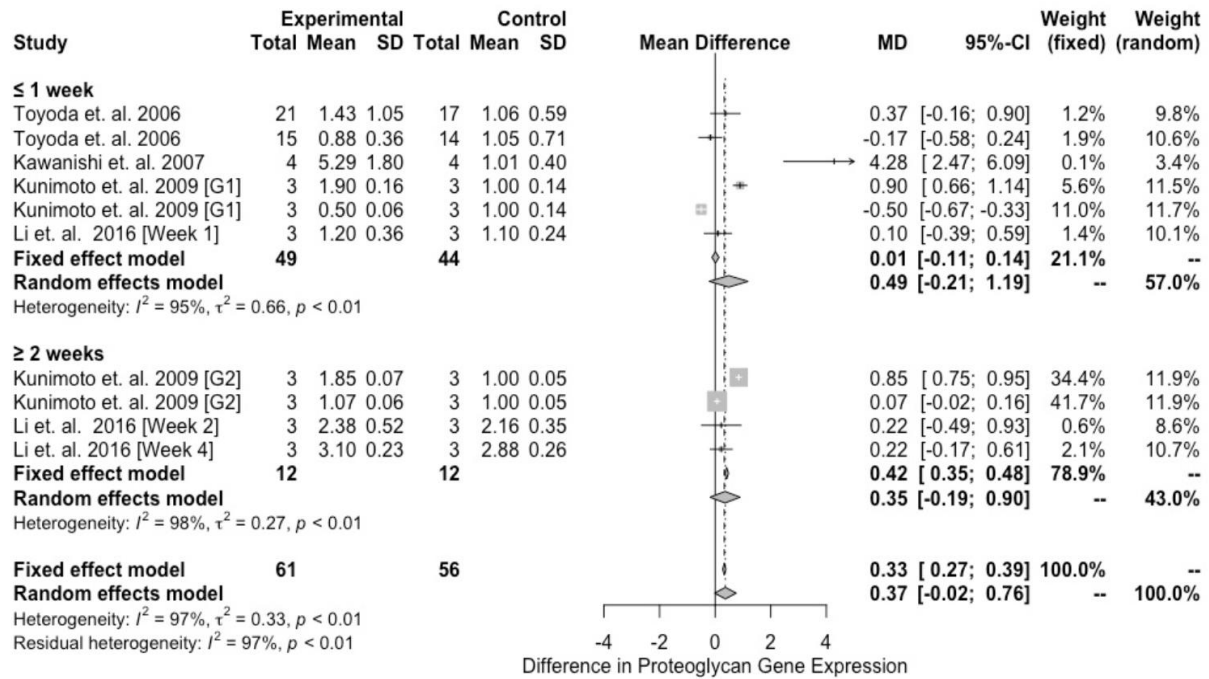


**Figure 5.9** Forest plots demonstrating the relationship between proteoglycan gene expression measured by RT-PCR of hydrostatic pressure stimulated 3D cultured chondrocytes and experiment duration; of one week or under and two weeks or over, compared to unpressurised control samples.

### 5.3.4.2 Glycosaminoglycan content

When GAG content values were compared and divided into subgroups based on experiment longevity with durations of  $\leq 1$  week and  $\geq 2$  week no significant difference between subgroups was seen ( $\text{Chi}^2 = 1.19$ ,  $\text{df} = 1$ ,  $P = 0.27$ ,  $I^2 = 16.2\%$ ) (Fig.5.10). Although the effect size for experiments lasting  $\leq 1$  week showed no significant influence on GAG content ( $g = 1.02$ ,  $95\% \text{ CI} = -1.67, 3.72$ ,  $P = 0.46$ ,  $Z = 0.74$ ,  $X^2 = 168.99$ ,  $P < 0.0001$ ,  $I^2 = 96\%$ , Figure 10). The  $\geq 2$  week subgroup demonstrated a significant positive effect on GAG content favouring HP with ( $g = 2.64$ ,  $95\% \text{ CI} = 1.59, 3.68$ ,  $P = 0.0001$ ,  $Z = 4.96$ ,  $X^2 = 490.03$ ,  $P < 0.00001$ ,  $I^2 = 96\%$ , Fig.5.10).

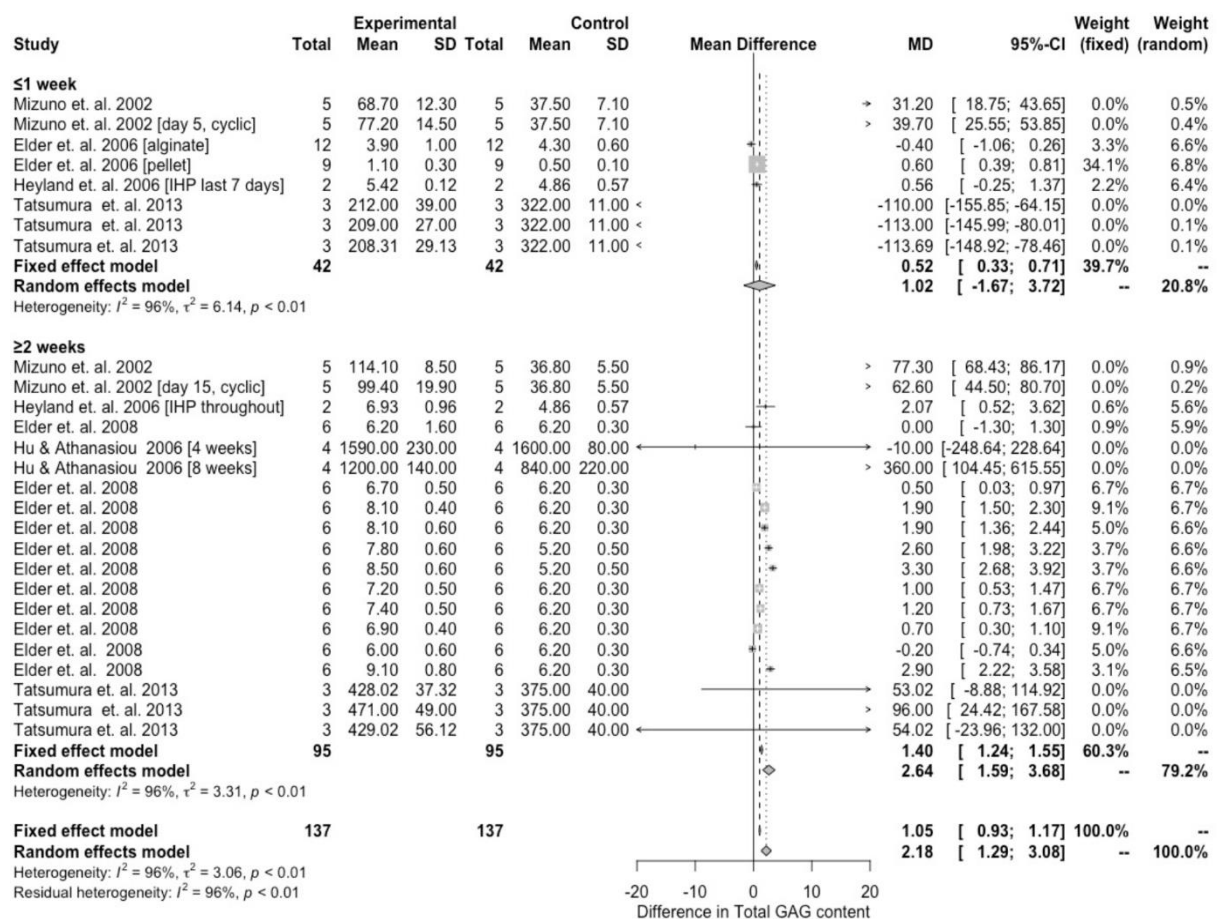


**Figure 5.10** Forest plots showing the relationship between glycosaminoglycan content measured by DMMB colorimetric assay in stimulated 3D cultured chondrocytes and experiment duration; of under one week, one week or over, and two weeks or over, compared to unpressurised control samples.

## 5.4 Discussion - summary of main results

### 5.4.1 Methodology criteria

The eligibility of the papers included within this comparative study were based upon their applicability for the improvement of human cartilage tissue engineering using 3D cultured chondrocytes, as was the focus of this thesis. It was identified that [<sup>35</sup>S]-sulfate incorporation as a method of quantifying proteoglycan synthesis was popular during the early study of HP on chondrocytes (prior to 2000) (Kato and Gospodarowicz, 1985; Hall, Urban and Gehl, 1991; Ishihara *et al.*, 1996). However, the [<sup>35</sup>S]-sulfate incorporation method is no longer commonly employed, as a result of the safety issues involved with handling radioactive reagents. In more recent studies the standard measurement of proteoglycan production has been through the use of DMMB colorimetric assay for GAG content (Barbosa *et al.*, 2003; Sakao *et al.*, 2008; Li *et al.*, 2016) and RT-PCR for aggrecan gene expression analysis (Kawanishi *et al.*, 2007; Kunitomo *et al.*, 2009; Li *et al.*, 2016). For this reason, studies prior to 2000 were not included within this review and the papers which employed DMMB and RT-PCR for proteoglycan measurement were selected. In addition, only the experiments which involved the 3D culture of mammalian chondrocytes from articular cartilage were considered for investigation, with the exclusion of cartilage explants or the use of stem cells. The choice of cell source was based on the cell phenotype used within the bulk of this thesis (BPCs). Furthermore, cells of different phenotypic origins (T.Reza and Nicoll, 2008; Le Maitre *et al.*, 2008) and cell culture methods (Parkkinen, 1993; Lu, Yan and Chen, 2016) have been shown to behave differently in response to HP. Therefore, to focus solely on the effects of HP during comparison only one cell type was considered. Lastly, studies which employed the paired analysis of HP exposed samples with atmospheric control groups without additional mechanical stimuli were chosen for review. The reason for the decision to focus solely on HP application was to limit the chances of false positives caused by linked stimuli.

#### 5.4.2 The overall outcome of hydrostatic pressure versus control conditions

When comparing HP treatment versus non-pressurised controls, regardless of the different intervention methods used, a significantly greater overall positive effect on proteoglycan was seen following HP ( $g = 0.45$ ,  $P = 0.02$  for gene expression (Fig.5.3) and  $g = 2.18$ ,  $P < 0.00001$  for GAG content (Fig.5.4). Thus, an overall positive outcome of generically applied HP stimuli on the upregulation of proteoglycan was observed for both the gene expression and total GAG content datasets, which subsequently supported the use of HP for improved cartilage ECM production using 3D cultured chondrocytes. However, on closer examination it was apparent that not all strategies of HP were as effective as each other, with multiple outcomes resulting in either no effect or favouring control groups (Fig.5.3-5.4).

The observed sensitivity of cells to mechanotransduction in some studies, relative to a lack of response in others, implied that differences between the experimental protocols could be the cause of the variance in effect size seen. The process of mechanotransduction signalling has been proposed to occur via membrane ion channels and cytoskeletal mechanotransduction, as well as through ECM related integrins and a range of other mechanosensitive proteins, whereby a response is triggered following cell deformation caused by cartilage pressurisation (Guilak, Ratcliffe and Mow, 1995; Guilak, Jones, *et al.*, 1999; Foster *et al.*, 2015; Yamamura, Suzuki and Imaizumi, 2018). A variety of mechanical stimuli is present within articular cartilage environments including shear, compressive and HP (Elder *et al.*, 2009b). Subsequently, the extent of a mechanotransductive response depends on the approach of the stimulation applied as well as the proportion of the different pressurisations that occur (Elder *et al.*, 2009b). Thus, although the exact cause for mechanotransduction in cartilage remains unclear, the mechanical requirements needed to induce a mechanotransductive response can be elucidated through experimental screening. Therefore, the experiment findings which showed no effect or a catabolic response to HP highlighted the necessity of this systematic review, to understand what potential experimental factors are involved in the determination of a beneficial or non-advantageous effect when HP is applied.

#### 5.4.3 The effect of static versus dynamic hydrostatic pressure application

The first factor that was isolated for consideration in the meta-analysis review was the style of pressure loading i.e. static or dynamic HP (cyclic or intermittent). The debate of a static versus dynamic HP application has long been surrounded by uncertainty, with early studies by Kampen and Kuijer (1985), Lippiello *et al.*, (1985) and Kimura (1985) having demonstrated the nuanced influence of HP application style. Upon the comparison of these studies, all published in 1985, a variety of different HP methods were shown to result in a range of different outcomes (Parkkinen, 1993). For example, in the work by Kampen and Kuijer (1985) a dynamic HP on chick epiphyseal explants was shown to result in a 120% increase to proteoglycan synthesis relative to controls. However, in similar experiments by Lippiello *et al.*, (1985) which used a static HP on cartilage segments a 10-15% increase in proteoglycan synthesis ( $[^{35}\text{S}]$ -sulfate incorporation) was measured, whereas, in the work by Kimura (1985) a static application had no significant effect on proteoglycan content when applied to bovine cartilage (Kimura, 1985). Thus, the comparison of these studies effectively demonstrated the ambiguity around HP applications for mechanotransduction. However, the issue of conflicting findings following static or dynamic approaches is an issue which has remained in more recent literature (Elder and Athansiou, 2008; Elder and Athansiou, 2008, Kunitomo *et al.*, 2009). Subsequently, the disparity between static and dynamic HP studies has evidenced a need for a meta-analysis approach, to determine the significant differences between static versus dynamic HP experiments.

In this meta-analysis review 11 final publications qualified for comparison, in which four of the selected papers investigated used both a dynamic and static HP (Toyoda *et al.*, 2003; Toyoda *et al.*, 2006; Elder and Athansiou, 2008; Mizuno *et al.*, 2012), six papers looked at dynamic HP alone (Kawanishi *et al.*, 2007; Li *et al.*, 2016; Elder *et al.*, 2006; Heyland *et al.*, 2006, Hu and Athansiou, 2006; Tatsumura *et al.*, 2013) and only one publication considered a solely static approach (Kunitomo *et al.*, 2009) (see Table 5.1, frequency column). However, of the studies which did employ a static HP a significant positive effect on both proteoglycan gene expression ( $g = 0.70$ ,  $P = 0.003$ ) and GAG content was observed ( $g = 6.00$ ,  $P < 0.00001$ ), with a significantly greater effect than dynamic HP when based on GAG content (difference between subgroups

of  $P < 0.0001$ ). Furthermore, the results of the proteoglycan gene expression data set demonstrated no significant influence on proteoglycan upregulation for dynamic HP ( $g = 0.55$ ,  $P = 0.07$ ). In addition, in the papers which investigated the direct comparison of static and dynamic HP on 3D cultured chondrocytes the same overall outcome was observed, with a static HP application shown to significantly favour proteoglycan production relative to dynamic approaches (Mizuno *et al.*, 2002; Toyoda *et al.*, 2003; Elder and Athanasiou, 2008). An example of the effect of static versus dynamic applications was clearly evidenced in the work by Mizuno *et al.*, (2002). Within the study by Mizuno *et al.*, (2002) a static HP of 2.8 MPa applied to 3D cultured bovine chondrocytes was shown to significantly increase GAG production on both days 5 and 15 of study, but significantly decreased GAG content when the pressure was applied cyclically (Fig.5.6). Similarly, in the work by Toyoda *et al.*, (2003) it was demonstrated that a static HP of 5 MPa was shown to result in a 4-fold increase in aggrecan gene expression relative to dynamic HP (1 Hz).

However, despite the accumulation of evidence for a static versus a dynamic HP approach on proteoglycan synthesis in 3D cultured chondrocytes the cause of this occurrence remains unclear and appears counter-intuitive relative to the dynamic conditions known to occur in cartilage *in vivo*. Native articular cartilage environments are consistently exposed to recurrent pressures (Hodge and Harris, 1986; Conzen and Eckstein, 2000; Correia *et al.*, 2012) and this has been commonly used as the justification for dynamic HP in 3D cell culture, to mimic *in vivo* conditions (Candiani *et al.*, 2008; Vinardell *et al.*, 2012; Correia *et al.*, 2012). Despite this, one potential reason for the preference of static mechanical stimulation is that when pressure is applied frequently (such as during dynamic stimulation) that it is more likely to cause excessive stress on cells (Iwata, 1993; Guilak *et al.*, 1999). Where, much like how repetitive stress injuries can negatively affect articular cartilage (Clements *et al.*, 2001), high frequency mechanical loading has been linked to a reduced cell productivity (Completo, Bandejas and Fonseca, 2017). In early examples of mechanical stimulation experiments it has been demonstrated that high frequency strains can have a long-lasting negative influence on cells (Ishihara *et al.*, 1992; Guilak *et al.*, 1999).

#### 5.4.4 The influence of pressure magnitude

##### 5.4.4.1 Gene expression analysis

The magnitude of HP pressure represents a well-known influential factor in mechanotransduction, with high pressure magnitudes known to impart a deleterious effect on cell matrix production (Brown and Hu, 2015) as well as damaging effects on mRNA stability (Crenshaw *et al.*, 1996; Sironen *et al.*, 2002; Elo *et al.*, 2005). Furthermore, the loading of cartilage tissues with magnitudes excessive to healthy joint ranges has been repeatedly linked to cellular catabolic response and osteoarthritis (Crenshaw *et al.*, 1996; Sironen *et al.*, 2002; Elo *et al.*, 2005).

In articular cartilage, such as from the hip and knee, an average HP loading of about 0.5-10 MPa has been measured during normal movement (Hodge *et al.*, 1986; AufderHeide and Athanasiou 2004; Elder *et al.*, 2009b). As a result, the majority of studies which were included for meta-analysis review were seen to employ HP magnitudes within the physiological range of cartilage, with only one publication demonstrating an exception to this, with an excessive magnitude of 50 MPa (Kunitomo *et al.*, 2009). Furthermore, amongst the publications used an HP of ~5 MPa was identified as the most commonly selected magnitude and is comfortably within the physiological range of articular cartilage (Elder *et al.*, 2009b). For the publications included within the gene expression dataset a total of three out of six studies employed a magnitude of 5 MPa (Kawanishi *et al.*, 2007, Li *et al.*, 2016, Toyoda and Susuki *et al.*, 2006), with the remaining experiments by Toyoda *et al.*, (2003) using an HP of 4 MPa was applied and the studies by Kunitomo *et al.*, (2009) employing magnitudes of 10 MPa or 50 MPa.

Subsequently, the meta-analysis based on proteoglycan gene expression data confirmed that the use of a 4-5 MPa HP magnitude (the  $\leq 5$  MPa subgroup) could be used to significantly enhance proteoglycan synthesis ( $g = 0.58$ ,  $P = 0.05$ ) (Fig.5.7). However, the level of significance reported for the use of a  $\leq 5$  MPa magnitude on gene expression was considered to be borderline (with a threshold of  $P \leq 0.05$ ) and therefore should be carefully implemented in future studies for effective mechanotransduction. In comparison, the application of a 10 MPa HP, as was demonstrated in the experiments by Kunitomo *et al.*, (2009), resulted in a highly significant effect on

proteoglycan gene expression ( $g = 0.86$ ,  $P < 0.00001$ ) with a greater effect on proteoglycan promotion than both the Li *et al.*, 2016 study (5 MPa) and Toyoda and Susuki *et al.*, 2006 (4 MPa) experiments, as well as a significant difference between magnitude subgroups of  $P = 0.0007$ . Lastly, in the experiments which employed a HP magnitude of 50 MPa a negative effect on proteoglycan production was observed ( $g = -0.21$ ,  $P = 0.46$ ). Subsequently, the results of the gene expression data analysis inferred that a magnitude of 10 MPa can be successfully used for inducing proteoglycan production in 3D cultured chondrocytes, whereas a magnitude of 50 MPa verified the non-advantageous use of excessive HP loading for mechanotransduction. However, despite the outcome of the gene expression analysis, the decision between a magnitude application of 5 MPa or 10 MPa for preferential proteoglycan upregulation requires further evidence, whereby the only experiment which used 10 MPa was by Kunitomo *et al.*, (2009).

Furthermore, the appropriate selection of a HP magnitude for cell stimulation may also depend on the sensitivity of the cells and culture type employed. For instance, in the case of Kunitomo *et al.*, (2009) a 10 MPa HP was applied to rabbit chondrocytes embedded in alginate, whereas, if a pellet culture was employed then the cells may have been less compatible with high range pressurisation. This theory is based on the findings of Elder *et al.*, (2006), which inferred that pelleted cultures had a higher sensitivity to HP than encapsulated cells, wherein it was demonstrated that pelleted cultures had a significantly increased anabolic response to HP stimulation than alginate embedded cultures. The observed decreased response of encapsulated cells was subsequently attributed to a reduction in cell sensitivity caused by increased cell spacing, separated by the encapsulating material, which resulted in less cell–cell signalling and a lower integrin expression (Elder *et al.*, 2006). However, it should be stated that although cell-cell interaction effects on mechanotransduction have been comprehensively explored in bone (Scott *et a.*, 2008; Yavropoulou and Yovos, 2016; Martino *et al.*, 2018), the effects of gap-junction propagation in cartilage research has been subsequently less founded (Mayan *et al.*, 2017), and as a result further evidence to support the approach of an increased HP magnitude for encapsulated chondrocyte culture relative to pellet cultures should be more thoroughly investigated.

#### 5.4.4.2 Glycosaminoglycan content

In comparison to the gene expression data set, the publications which employed GAG content analysis demonstrated a wider screening of HP magnitudes, with pressure ranges of <1 MPa, <5 MPa, 5 MPa and 10 MPa used amongst experiments. Subsequently the analysis of the different magnitudes demonstrated that the application of a 10 MPa HP had the greatest increase in GAG content relative to the lower pressures ( $g = 2.31$ ,  $P < 0.00001$ ), a result which corresponded with the findings of the gene expression analysis (5.4.4.1). Furthermore, the lowest HP magnitude (<1 MPa) was shown to impart a significant negative effect on GAG production ( $g = -11.81$ ,  $P = 0.007$ ), whereas, the mid-range sub-groups of <5 MPa and 5 MPa significantly favoured proteoglycan production with results of  $g = 4.70$ ,  $p < 0.00001$  and  $g = 1.38$ ,  $P = 0.009$ , respectively.

Thus, the GAG content analysis demonstrated that a high range 10 MPa was the best magnitude candidate for attaining an anabolic response in 3D cultured chondrocytes, whereas mid-range pressures were sufficient to induce a positive response in proteoglycan production. However, the low range physiological joint pressures resulted in a significant catabolic outcome. Therefore, the findings of this study effectively evidenced the fine balance necessary between adequate stimulation and detrimental response dependent on HP magnitude, and represents a promising source of knowledge for the future implementation of HP experiments. However, it should be stated that upon inspection of the GAG content data that the majority of the experiments performed using a 10 MPa magnitude were carried out by Elder and Athanasiou (2008), and was subsequently the leading determinant within the 10 MPa subgroup. Furthermore, within the work by Elder and Athanasiou (2008) the comparative effects of 5 MPa and 10 MPa HP magnitude applications were directly investigated and showed no significant difference between the two approaches. Therefore, despite the meta-analysis result, which evidenced an overall significant difference between the 5 MPa and 10 MPa subgroups, the paired analysis results of the Elder and Athanasiou (2008) investigation should also be taken into consideration when deciding between a 5 MPa or 10 MPa HP application approach.

#### 5.4.5 The impact of experiment duration

The influence of experiment duration was also considered within this review. The factor of experiment duration was chosen based on a potential for the delayed measurement of HP upregulation, caused by the limitations of the analysis used (specifically the DMMB assay) as well as cellular response time.

In early HP experiments (prior to 2000) the application of radio-assays for the monitoring of proteoglycan synthesis were commonplace. In particular [<sup>35</sup>S]-sulfate incorporation was popularly employed for HP studies, and is a highly sensitive method capable of quantifiably measuring differences in proteoglycan synthesis within just a few seconds of HP stimulation (Mans and Novell, 1960; Prince, Rahemtulla and Butler, 2015). However, due to the strict safety regulations and approval required for handling radiation, as well as the relative expense of radioactive reagents, the use of [<sup>35</sup>S]-sulfate incorporation has since been favoured by the use of DMMB assays and gene expression analysis. Consequently, the sensitivity of proteoglycan detection has been reduced in more recent experiments which use methods that rely on a mass change in gene expression (gene expression analysis) and the subsequent synthesis and accumulation of full proteoglycan proteins (DMMB assay) to a detectable level. Thus, in the HP experiments which employed DMMB and gene expression analysis for proteoglycan detection the time taken for the cells to generate a measurable change in gene expression and GAG content following HP stimulation could represent a key determining factor in the timely detection of a mechanotransductive response. As a result, it was theorised within this review that short-term studies (hours) would not be sufficient to capture the accumulation of cellular changes in gene expression and downstream proteoglycan production following HP stimuli, due to the limited sensitivity of the methods employed.

Consequently, upon the comparative analysis of proteoglycan gene expression measurements there was no significant difference between the studies which lasted for durations of <1 ( $g = 0.49$ ,  $P = 0.46$ ) and  $\geq 2$  weeks ( $g = 0.37$ ,  $P = 0.056$ ). However, it was observed that for the studies which lasted  $\geq 2$  weeks ( $P = 0.056$ ) that a  $P$  value approaching significance was measured (with a threshold of  $P \leq 0.05$ ) whereas for the experiments lasting <1 week no marginal significance was apparent  $P = 0.46$ .

Therefore, the access to a larger sample size for the analysis of gene expression data could influence the outcome of this result to favour the significance of increased proteoglycan upregulation in experiments with extended durations. Furthermore, upon the analysis of the GAG content data it was observed that the experiments with durations of  $\leq 1$  week resulted in no significant change to GAG content ( $g = 1.02$ ,  $P = 0.46$ ), whereas in the experiments of  $\geq 2$  weeks a significant increase was measured ( $g = 2.64$ ,  $P = 0.0001$ ). Thus, it was inferred that for studies which employed DMMB assays for proteoglycan quantification that an experiment duration of  $\geq 2$  weeks was a key factor for the significant detection GAG content upregulation following HP stimulation.

Therefore, as was previously theorised, the potential explanation for the delayed response in the measurement of increased GAG content ( $\geq 2$  weeks) in relation to HP stimuli was likely related to both cell development and assay sensitivity. It has been suggested that the process of mechanotransduction functions use integrin binding receptors, however these receptors are not yet present in cells until the pericellular matrix (PCM) has been synthesised (Zhang, 2014). Consequently, the delay in a response to HP could be reflective of the time taken for the integrin receptors to be produced, and for the PCM to become sufficiently formed to enable a mechanotransductive effect. This theory of PCM involvement in the delayed measurement of proteoglycan stimulation was supported by the findings of Zhang (2014). In the report by Zhang (2014) it was found that isolated chondrocytes cultured in hydrogels required a period of 24 hours to synthesise type VI collagen, decorin, and fibronectin proteins as well as taking approximately one week of culture time to fully rebuild their PCM (Vigfúsdóttir *et al.*, 2010; Twomey *et al.*, 2014).

#### 5.4.6 The influence of loading time

The final factor considered in this review, was the influence of pressure loading time. In previous studies the effects of HP duration have been recognised as a potentially determining factor in HP experiments, with various HP lengths examined in literature (Hall *et al.*, 1991; Parkkinen *et al.*, 1994; Smith *et al.*, 2000; Hu and Athansiou, 2006; Nakamura *et al.*, 2006; Elder and Athanasiou, 2008; Correia *et al.*, 2012). However,

despite investigation the length of an optimal loading period has yet to be elucidated and instead a HP protocol that mimics human activity levels is commonly employed. Consequently, a protocol of 4 hours/day has been the most popular HP application method in literature and was used in five of the 11 studies screened in this review and four of the five papers which used gene expression analysis (see Table.5.1, Load duration column). Conversely, due to the variability of person to person activity levels (caused by factors including age, mobility, and lifestyle) a wide disparity of HP lengths has also been employed in literature (see Table.5.1). Wherein, all the selected studies which used GAG content analysis utilised a different HP duration, with applications of 1 hour a day (Elder and Athanasiou, 2008), 4 hours a day (Hu and Athansiou, 2006) two rounds of 45 minutes a day (Elder *et al.*, 2006), 6 hours a day (Heyland *et al.*, 2006), continual application (Mizuno *et al.*, 2011) and dynamic HP with intermittent days of atmospheric pressure (Tatsumura *et al.*, 2013). Thus, as a result of the homogeneity seen within the proteoglycan gene expression data set and the heterogeneity of the GAG content data set (insufficient number of experiments per subgroup), the influence of loading time could not be examined by a meta-analysis approach within this review.

However, based on a comparative assessment of the HP studies the significance of loading time on proteoglycan production was supported. For instance, it was observed that only two (Toyoda *et al.*, 2003; Kawanishi *et al.*, 2007) out of four studies which used a 4 hour/day HP strategy resulted in a significant increase in proteoglycan gene expression. Therefore, only 50% of the studies which employed a 4 hour/day HP protocol led to an up-regulatory effect on proteoglycan gene expression, a result which does not confer the advantage of the most popular HP approach. Furthermore, within the GAG content data set a mixed effect size was observed in response to varied HP durations, with a positive influence evident in samples exposed to 4 hours/day of pressurisation (Hu and Athansiou, 2006), continual HP (Mizuno *et al.*, 2011) and a 1 hour pressure application (Elder and Athanasiou, 2008). Thus, upon consideration of both the gene expression and GAG content data it was apparent that differences in HP duration resulted in a mixed HP response with no identifiable optimal duration. As a result, further work should be investigated to illucidate an ideal HP duration for the effective employment of mechanotransduction in 3D chondrocytes. Furthermore, screenings of short HP periods should be considered, wherein HP studies outside the

scope of this review have previously utilised shorter loading durations of 30 minutes/day (Luo and Seedhom, 2007) and 20 seconds or 5 minute a day (said to simulate rest periods or standing) with significant success (Hall *et al.*,1991; Luo and Seedhom, 2007).

## 5.5 Conclusion

In conclusion, the meta-analysis of proteoglycan gene expression and GAG content data sets taken from relevant HP papers revealed multiple significant and factor reliant outcomes. Initial comparisons of a generic HP exposure compared to atmospheric control conditions demonstrated that an anabolic response was significantly favoured by HP stimulation. However, it was apparent that not all HP strategies resulted in a significant impact on proteoglycan production. Upon further analysis it was identified that proteoglycan synthesis was significantly promoted by the use of a static HP protocol in comparison to dynamic stimulation (cyclic or intermittent) and was evidenced by both the gene expression and GAG content data sets. In addition, pressure magnitude was proven as a significant influential factor, with the greatest proteoglycan output achieved following a magnitude within the mid-high range of native articular joint pressure ( $\leq 5-10$  MPa), and a significantly decreased response after the exposure to low range ( $<1$  MPa) and excess HP (50 MPa). Furthermore, based on the meta-analysis of study duration an experiment length of  $\geq 2$  weeks was seen to be optimal for proteoglycan production, wherein in a significantly greater GAG content was observed in experiments lasting  $\geq 2$  weeks relative to durations of  $\leq 1$  week (which showed no significant anabolic response), as well as a marginally significant proteoglycan gene upregulation in samples measured after  $\geq 2$  weeks ( $P = 0.06$ ), that was not seen in samples after  $\leq 1$  week ( $P = 0.17$ ). It was subsequently theorised that the influence of experiment duration on anabolic response was related to the sensitivity of the proteoglycan quantification methods used, as well as the time required for PCM synthesis by the growing cells containing the key proteins and receptors needed for mechanotransduction. Lastly, in the final comparisons performed it was observed that the frequented use of a 4 hour/day HP loading time was not favoured by the experimental outcomes within this review and was a result which suggested the need for further research towards the optimisation of HP load duration.

Thus, overall HP for cartilage tissue engineering using 3D cultured chondrocytes relies on a fine balance between potential stimulation and detrimental effect, with many factors involved in triggering the mechanotransduction process, both physical and cellular. However, it was evidenced in this review that through the use of certain mechanical factors it is possible to improve experimental outcome. Wherein, the results of this study showed that a successful anabolic response was most likely achieved when the following factors were employed; a static HP application, a magnitude within the mid-high physiological range of cartilage ( $\leq 5-10$  MPa) and a study duration of  $\geq 2$  weeks. The factors identified in this review can be reliably used as a guideline for future tissue engineering experiments using 3D cultured chondrocytes, for the improved generation of cartilage via HP stimulation. Moreover, further research towards the influence of HP load duration and differences in 3D culture method (pellet versus embedded cells) on mechanotransduction sensitivity should be investigated as additional areas of potential significance.

The results obtained from the meta-analysis performed in this work were used to directly influence the factor selection in the following experimental chapter, which employed HP application on 3D cultured BPCs and human IVD cells.

## **Chapter 6 Hydrostatic pressure stimulated cell culture of bioprinted alginate methyl cellulose scaffolds embedded with BPCs or hVD cells for the purposes of cartilage tissue engineering**

### 6.1 Introduction

Alg/MC is a promising material for cartilage tissue engineering using bioprinting. In Chapter four of this thesis alg/MC as a BPC-laden bioink was characterised and shown to be capable of supporting a chondrogenic phenotype. The BPCs were cultured in alg/MC for 21 days and showed high ratios of collagen type II: collagen type I, similar to native cartilage. However, in order to fully replicate a cartilaginous ECM, a high concentration of proteoglycan proteins must also be present and are essential for cartilage hydration and swelling (Fox, Bedi and Rodeo, 2009). The role of proteoglycans in cartilage is to provide the ECM with resilience and elasticity by drawing water into the tissue and working in synchronicity with collagen fibrils to resist physical loading (Muir, 1978). Together collagen and proteoglycan macromolecules play an essential role in buffering external stresses and maintaining cartilage health (Fox, Bedi and Rodeo, 2009; Gentili and Cancedda, 2009). In the intervertebral disc proteoglycan is the major component of the central NP disc region, alongside water, and is crucial to overall disc function and health (Gullbrand *et al.*, 2018). A decrease in proteoglycan level within cartilage is one of the first signs of degeneration, and thus represents an important consideration in regenerative approaches (Urban and Roberts, 2003; Ludescher *et al.*, 2008; Iatridis and Mwale, 2014).

In previous literature, various regimes of hydrostatic pressurisation have been demonstrated as effective enhancers of proteoglycan and collagen synthesis using chondrocytes (Hall, Urban and Gehl, 1991; Kawanishi *et al.*, 2007; Sharma, Saxena and Mishra, 2007; Elder and Athanasiou, 2008). Wherein, stimulation by HP is achieved by triggering a mechanotransduction response i.e. the process in which mechanical signals modulate biochemical activity and changes in cell behaviour (Brown and Hu, 2015). The anabolic influence of mechanotransduction has been demonstrated using a range of HP factors, cell types and culture systems (Wheeler, Fitzgerald and Grodzinsky, 2005; Scott *et al.*, 2008; Shioji *et al.*, 2014; Choi, Yong and

Choi, 2018). The use of HP mechanical stimuli represents an easily controlled and well-researched method for the enhancement of tissue biomimicry, without chemical manipulation or functionalised drug/growth factor inclusion (Suh *et al.*, 1999; Elder *et al.*, 2008; Li *et al.*, 2016a; Chen, 2017).

In the previous Chapter 5 a meta-analysis study of 13 relevant publications was performed and the results confirmed the positive influence of HP culture on chondrogenesis. However, despite the known benefits of HP for cartilage development a universally accepted and replicable HP approach has yet to be established. Consequently, the use of HP mechanotransduction in combination with bioprinted chondrocyte scaffolds has not been evidenced in literature and remains a highly promising avenue for future investigation within cartilage engineering. The appropriate application of HP therefore presents a promising method for supporting cartilage synthesis, which once established will likely be considered critical methodology for the development of tissue-engineered cartilage matrices (Elder and Athanasiou, 2008; Correia *et al.*, 2012). Thus, the overall purpose of this study was to determine an effective HP protocol for improving cartilage production, with a particular interest in the enhancement of proteoglycan synthesis within bioprinted alg/MC embedded with either BPCs or human IVD cells.

Within the meta-analysis study (Chapter 5) it was revealed that the mechanotransductive response of 3D cultured chondrocytes to HP stimuli was significantly dependent on three main experiment factors: a static pressurisation application, a study duration of  $\geq$  two weeks and a magnitude within the mid-high physiological range of the native cartilage tissue. The outcome of this research was subsequently employed to guide the set-up of the experiments within this investigation. This included the implementation of a static HP with a magnitude of 6 MPa for BPC cells from articulated cartilage and 1 MPa for hAF and hNP cells sourced from human lumbar discs. Furthermore, an additional finding of the meta-analysis review (Chapter 5) revealed that the experimental factor 'HP duration' was poorly elucidated within literature. Amongst the studies considered within the meta-analysis review an HP application of 4 hours/day was identified as the most commonly employed approach (Toyoda *et al.*, 2003; Toyoda *et al.*, 2006; Hu and Athanasiou *et al.*, 2006; Kawanishi *et al.*, 2007; Li *et al.*, 2016). However, the justification of the popular 4 hour/day HP

methodology was lacking and examples of HP studies using shorter pressurisation times with positive outcomes were found (Hall, Urban and Gehl, 1991; Luo and Seedhom, 2007; Elder and Athanasiou, 2008). For these reasons, the initial experiment within this investigation was set-up to screen a range of HP durations, and the favoured outcome, based on proteoglycan synthesis, was used in the following experiments.

## 6.2 Methods

The experimental set-up of this investigation was divided into three parts (Fig.6.1). In the first set of experiments the effect of HP duration was investigated on BPCs in alg/MC applied daily (5 days on/ 2 days off). In the second experiment a 45 minute HP duration was taken forward and applied to BPC-laden alg/MC scaffolds over a culture time of 21 days. In the final and third phase of experiments the HP protocol was adjusted for use with human IVD (hIVD) cells in alg/MC (Fig.6.1). A static pre-culture time of seven days was given for all experiments immediately following scaffold fabrication, to allow time for cell development and integrin deposition (implicated in mediating mechanotransduction) during PCM formation (Vigfúsdóttir *et al.*, 2010; Zhang, 2014, Twomey *et al.*, 2014).

It has been suggested that hydrogel embedding, though excellent for maintaining a chondrogenic phenotype, can hinder the cellular response to HP by reducing inter-cellular interactions due to increased cell spacing (Elder *et al.*, 2006). Thus, the influence of cell-cell interaction was taken into consideration in the experimental set-up of this investigation, with a high cell seeding density of  $5 \times 10^6$  used in all three experiments to minimise cell spacing. In addition, based on the outcome of the meta-analysis review (Chapter 5) a HP magnitude towards the high end of normal physiological pressures was used for the respective cell types (Elder *et al.*, 2009b). In the case of BPC cells, a static application of 6 MPa was employed and was similar to pressures successfully tested by Toyoda *et al.*, 2003 and Kunitomo *et al.*, 2006 using chondrocyte-hydrogel culture. Alternatively, for hIVD cells a HP of 1 MPa was used, due to the lower range of magnitudes endured in spinal loading than in articular joints (Hodge *et al.*, 1986; Chen *et al.*, 2013; Oxland, 2015).

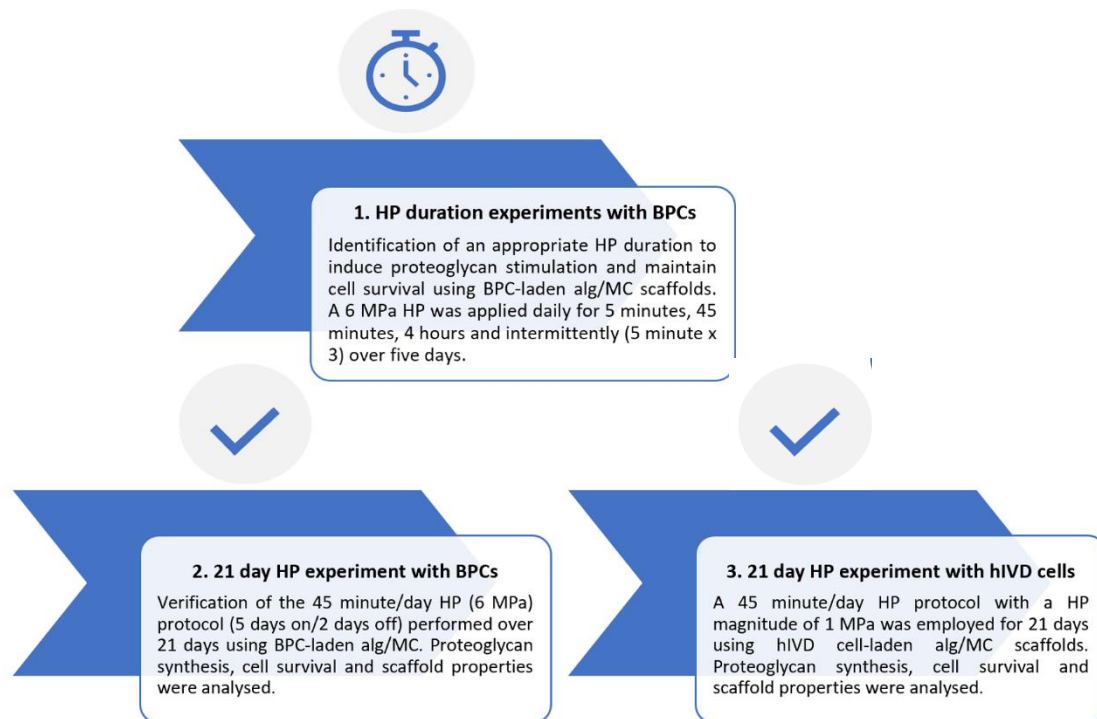


**Figure 6.1** Flow diagram schematic of the experimental layout within this chapter: (1) Duration experiments with bovine primary chondrocytes (BPCs). (2) 21 day hydrostatic pressure experiment with BPCs. (3) 21 day hydrostatic pressure experiment with human intervertebral disc cells.

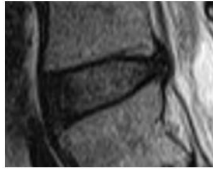
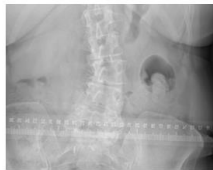
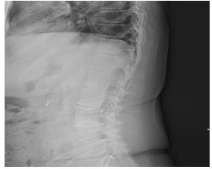
#### 4.2.1.1 Isolation of bovine primary chondrocytes

Primary bovine articular chondrocytes were isolated from the cartilage of bovine metacarpal phalangeal joints of skeletally mature animals (~30 months) as previously described in Chapter 4.2.2, following methods initially published by Hall *et al.*, (1996). Cells were expanded under normal cell culture conditions, at 37°C and 5% CO<sub>2</sub> in standard culture medium consisting of DMEM with 10% FCS, 100 µg/ml penicillin and 100 µg/ml streptomycin. Cells were counted in suspension using a haemocytometer and underwent four passages before use in scaffold fabrication. In all experiments cells from different joints/animals were kept separate, with each experiment representing a biological repeat.

## 6.2.1 Isolation of human intervertebral disc cells

Primary hAF and hNP cells (passage 1) aseptically isolated from adult human patient sources with lumbar disk pathology were sourced from the University of Basel, department of biomedicine (Table.6.1). The cells were obtained with ethical approval from the Swiss research ethics committee and also complied with England and Wales tissue authority regulations (see Appendix C, Doc.S1C and Doc.S2C for the ethics approval and consent forms). The cells were stored at -80°C until expansion (passage four) in standard culture medium (DMEM + 10% FCS) for scaffold fabrication (counted with a haemocytometer). Information on the patient sources are listed below and were kept anonymous (Table.6.1).

**Table 6.1** Human intervertebral disc tissue information

Sample details	Harvested tissue		MRI
	AF	NP	
<p><b>Patient 1</b></p> <p><b>Sex:</b> Male <b>Age:</b> 68 <b>Level:</b> L4/5  <b>Pathology:</b> Bulge  <b>Pfirrmann Scale:</b> 2</p>			
<p><b>Patient 2</b></p> <p><b>Sex:</b> Female <b>Age:</b> 66 <b>Level:</b> L2/3  <b>Pathology:</b> Unknown  <b>Pfirrmann Scale:</b> Unknown</p>			
<p><b>Patient 3</b></p> <p><b>Sex:</b> Female <b>Age:</b> 67 <b>Level:</b> L3/4  <b>Pathology:</b> Unknown  <b>Pfirrmann Scale:</b> Unknown</p>			
<p><b>Patient 4</b></p> <p><b>Sex:</b> Male <b>Age:</b> 53 <b>Level:</b> L2/3  <b>Pathology:</b> Herniation  <b>Pfirrmann Scale:</b> 2</p>			

\*Pfirrmann scale is a quantitative disc degeneration grading system from 1-5, with a higher numeric value relating to a higher level of degeneration. A disc bulge pathology pertains to the nucleus pressing outward onto a weakened annulus wall. A herniated disc is when the nucleus protrudes through a ruptured annulus.

### 6.2.2 Bioprinting material preparation

The alg/MC hydrogel mixture was prepared according to the methodology outlined in Chapter 3 section 3.2.3.1 and Chapter 4 section 4.2.4, which follows the approach originally used by Schütz *et al.*, (2017). The alg/MC paste was obtained using a 3 w/v % alginate solution stirred overnight before sterilisation using autoclave. Autoclave sterilised MC (9 w/v %) was then stirred into room temperature alginate and left to swell for 30 minutes before the addition of BPCs or hIVDs at a seeding density of  $5 \times 10^6$  cells per gram of material.

### 6.2.3 Bioprinting of alginate methyl cellulose constructs

Alg/MC scaffolds were bioprinted with the BioScaffolder 3.1 from GeSiM (Radeberg, Germany) using the print parameters outlined in Chapter 3 section 3.2.5 (Table 3.3) and Chapter 4 section 4.2.5 with the dimensions of 9.5 mm by 9.5 mm by 6 mm and a tip diameter of 0.61 mm carried out under sterile conditions. After print completion the hydrogel scaffolds were crosslinked in 100 mM CaCl<sub>2</sub> for 10 minutes. Both cell-laden and cell-free scaffolds were bioprinted under the same conditions. In all experiments the scaffolds were incubated in standard culture medium at 37°C and 5% CO<sub>2</sub> for seven days before HP application.

### 6.2.4 Hydrostatic pressure application

#### 6.2.4.1 Sample preparation

Prior to pressurisation, scaffolds were transferred into sterile 5ml syringes (BD Plastipak), with two scaffolds per syringe, suspended in 4 ml of culture medium (Fig.6.2 and Fig.6.3, A). The syringes were then divided into two groups: control and HP. During incubation all syringe ends were fitted with 0.25-micron filters (Cole-Parmer) to allow for gas exchange. For the HP samples before pressurisation the syringe filters were replaced with Luer lock caps to prevent contamination.

#### 6.2.4.2 The hydrostatic pressure vessel

HP was applied via compression of the fluid phase. The method involved the connection of a fluid-filled vessel, connected via a hose to a piston attached directly to a hand-driven hydraulic pump (Fig.6.2-6.3). Initial pressurisation resulted in gas coming out of solution, which was bled off (using the outlet valve) before the desired pressure could be achieved (Fig.6.2,6.3, C).

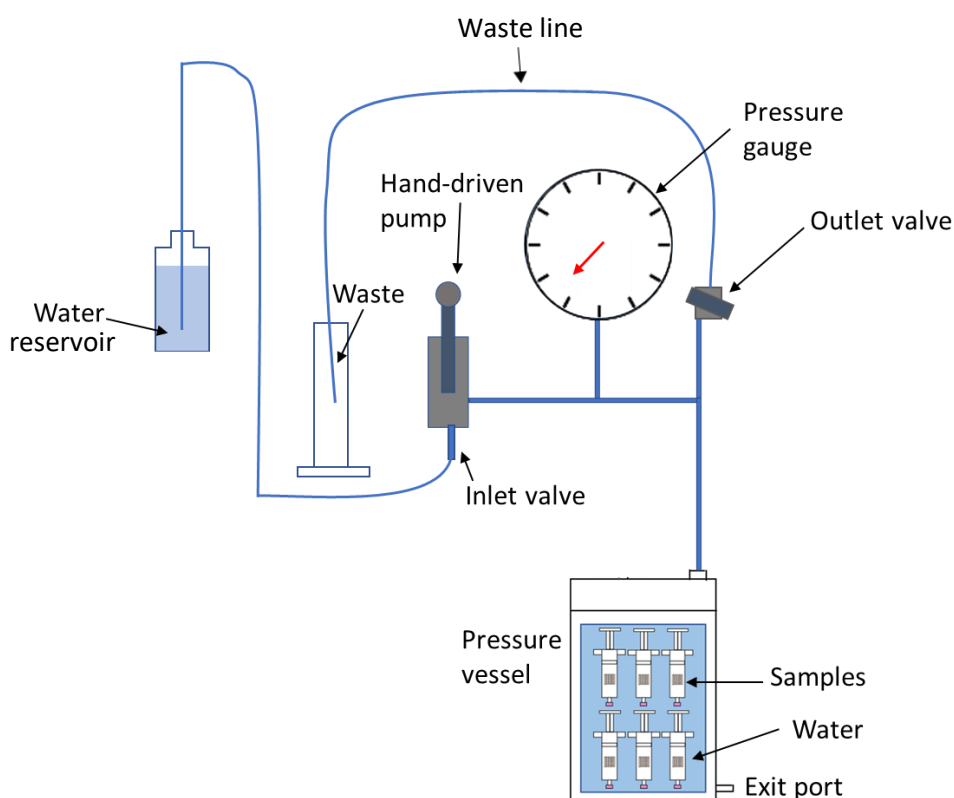


**Figure 6.2** Schematic diagram of the hydrostatic pressure vessel set up. Water from the reservoir was manually pumped through the inlet valve and into the top of the full pressure vessel. Gas from solution was released using the outlet valve into the waste line. Once all gas was removed the outlet valve was closed and pressure within the vessel was raised to the desired magnitude using the hand-driven pump at approximately 0.04 MPa/sec. Once pressurisation was completed the outlet valve was gradually opened to allow for depressurisation into the waste line at approximately 0.04 MPa/sec. Image created by author.

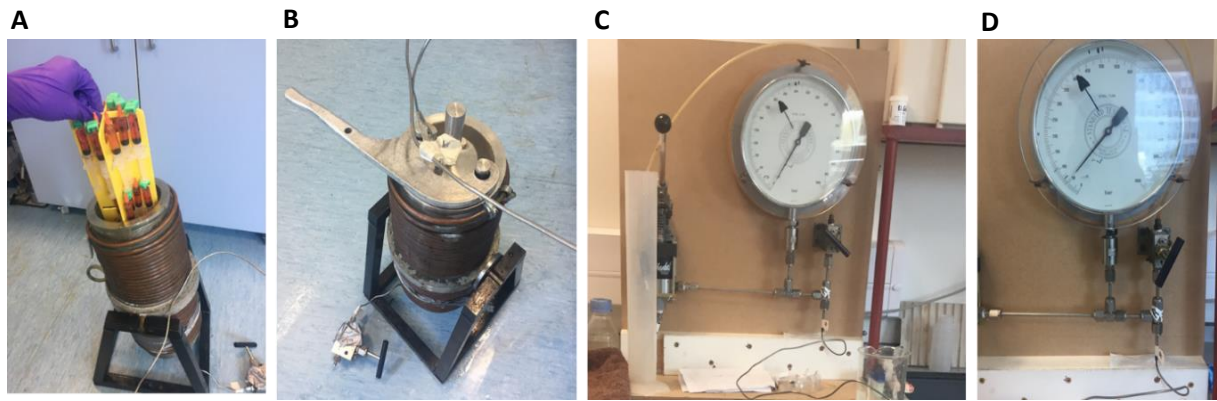


**Figure 6.3** Images to demonstrate the hydrostatic pressure vessel in use (A) Loading of samples into the vessel. (B) Tightening of the vessel lid. (C) Clearing the line of gas by opening the outlet valve to release pressure into the waste line. (D) Pressurisation of the vessel (as indicated on the gauge).

#### 6.2.4.3 Hydrostatic pressure application protocol

Luer lock sealed syringes (BD Plastipak) were secured to a custom-made syringe rack before lowering into the stainless-steel vessel (Fig.6.3, A-B). The HP was generated by a hand-driven pump, which delivered dH<sub>2</sub>O into the vessel (Haskel MCP188, Burbank, CA, U.S.A.) and was raised from atmospheric pressure to 6 MPa for the BPC laden scaffolds, or to 1 MPa for the human IVD embedded samples, over a controlled ramp up of approximately 0.04 MPa/sec and was depressurised at the same rate. The pressure within the vessel was measured using a calibrated (21%) Bourdon-type gauge (Budenberg Ltd., Broadheath, England) (Hall, Urban and Gehl, 1991). HP was applied once a day with a protocol of five days on/two days off. Between rounds of HP the syringes were returned to atmospheric incubation at 37°C and 5% CO<sub>2</sub>. Culture medium was changed every other day at least one hour before HP application and was changed within the same hour as control samples.

In the first experimental phase using BPC samples the scaffolds for pressurisation were sub-divided and pressurised in separate sessions for five days using the following duration times: 5 minutes, 45 minutes, 4 hours, or IHP (5 minutes HP followed by 2 minutes at atmospheric pressure, repeated three times in immediate succession). For the second and third experiment using BPC or hIVD laden alg/MC

respectively, the HP group was subjected to 45 minutes of HP/day, for two sets of five day stimulation sessions, over the course of two weeks (see Fig.6.4). Following the same five days on, two days off protocol as before. For BPC cells the pressure magnitude employed was 6 MPa, and for human IVD cells (AF and hNP) the magnitude used was 1 MPa.

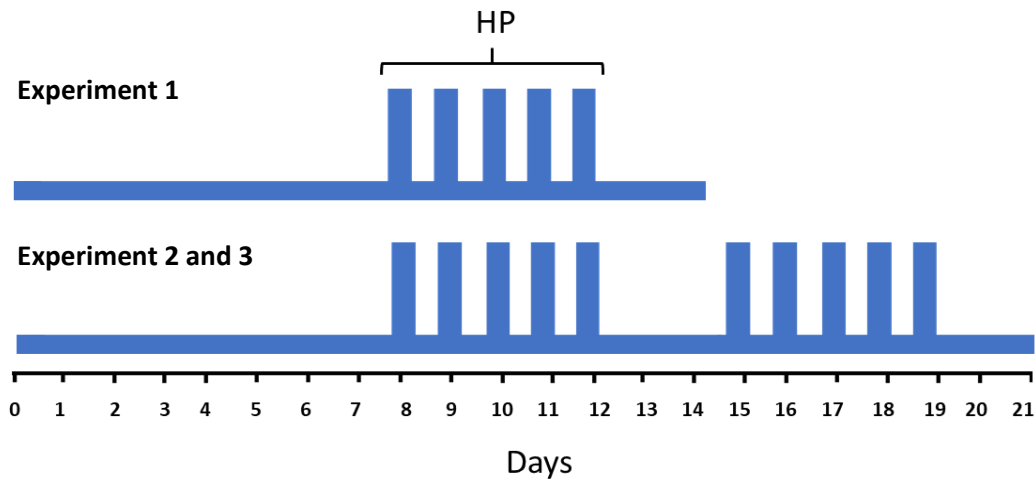


**Figure 6.4** Hydrostatic pressure (HP) application timeline: For the duration screening in Experiment 1 the HP pressurisation started on day eight of bovine primary chondrocyte (BPC) scaffold culture, 6 MPa was applied once a day for five days for either 5 or 45 minutes, 4 hours or dynamically (5 min on/ 2 min off, x3). Two days after the last pressurisation the final samples were taken for analysis. For the 21 day investigations in Experiment 2 and 3 the HP pressurisation started on day eight of BPC or human intervertebral disc cell culture, HP was applied for 45 minutes a day for 5 days, followed by a two day rest period, this was then repeated and the final samples taken on day 21 after a two day period at atmospheric conditions. For all experiments the control samples were kept under atmospheric incubation conditions for the entire study duration. Image created by author.

### 6.2.5 Cell survival

To ascertain cell survival before, during and after exposure to HP the cell viability was determined using two methods: live/dead staining with CMFDA Green and ethidium homodimer-1 solutions and MTT.

#### 6.2.5.1 Cell survival live/dead

For the live/dead assay the cell-laden scaffolds were incubated for 20 minutes in culture medium supplemented with 5  $\mu$ M CMFDA green and 1.4  $\mu$ M ethidium homodimer-1 at 37°C and 5% CO<sub>2</sub>. Scaffolds were rinsed with HBSS, fixed in a 4% paraformaldehyde solution, and stored at 4°C for a maximum of two weeks before imaging. The live/dead staining was performed on days 1, 8 and 15 for scaffolds in the HP duration studies of Experiment 1, on days 1, 8, 15 and 21 for the BPC investigations in Experiment 2, and on days 1 and 21 for samples from the hIVD cell work in Experiment 3. Imaging was performed using an upright Leica TCS SP5 confocal laser scanning (CLSM; Leica Microsystems, Milton Keynes, UK) microscope fitted with a 20x dry objective, equipped with a 488nm Argon laser and 543nm Helium/Neon lasers for the excitation of fluorophores CMFDA (live cells) and ethidium homodimer-1 (dead cells) respectively. Image acquisition of multiple z-stack sections and the subsequent image analysis for percent survival determination was performed as detailed in Chapter 4, section 4.2.9.1 (Fig.4.1).

#### 6.2.5.2 Cell survival using MTT dye compound

On the same time points used for live/dead sampling, scaffold sections were also taken for 3-(4,5-Dimethylthiazol-2-yl)-2,5-diphenyltetrazolium bromide (MTT) staining. The MTT protocol for assessing cell viability within the alg/MC scaffolds was performed based on the protocol outlined in Chapter 4, section 4.12. In brief, both cell-laden samples and cell-free samples were incubated for two hours in culture medium (DMEM) supplemented with 5 mg/ml MTT, a yellow tetrazole which is reduced to purple coloured formazan in living cells. Scaffolds were then washed in DMEM and light microscopy images of the scaffolds taken by digital photography next to a ruler for scale (Axiovert-25, Carl-Zeiss).

### 6.2.6 Gene expression analysis

The cell-laden scaffolds were digested in a 100 mM sodium citrate solution for 30 minutes, and the retrieved cell pellet was lysed with 600  $\mu$ l RLT (RNeasy Kit, Qiagen) and RNA purified and eluted out using the RNeasy kit (Qiagen) following manufacturer's instructions (Qiagen, 2016). Briefly,  $\sim 5 \times 10^6$  cells were pelleted and 600  $\mu$ l of RLT buffer added followed by 600  $\mu$ l of 70% ethanol and the sample mixed before transferring into a RNeasy Mini spin column. The mixture was then centrifuged for 15 s at  $\geq 8000 \times g$  and the flow-through discarded. In the next stage, 700  $\mu$ l of buffer RW1 was added to the RNeasy spin column and the sample was centrifuged for another 15 s at  $\geq 8000 \times g$ . Afterwards 500  $\mu$ l of the RPE buffer was added to the column and then centrifuged for 15 s at  $\geq 8000 \times g$ . The addition of the RPE buffer was then repeated and followed by a centrifuge step of two minutes ( $\geq 8000 \times g$ ). In the final step, 50  $\mu$ l of RNase-free water was pipetted directly onto the spin column membrane and centrifuged for one minute ( $\geq 8000 \times g$ ) to elute the RNA. The tubes were then immediately placed on ice before placing into a Freezing Container (Thermo Scientific™, Mr. Frosty™) at  $-20^\circ\text{C}$ . After two days the samples were transferred to a  $-80^\circ\text{C}$  freezer.

#### 6.2.6.1 RNA ScreenTape analysis

A sampling of the extracted RNA samples were measured using RNA ScreenTape analysis (Agilent technologies), to assess the integrity and quantity of RNA isolated from the alg/MC scaffolds. The ScreenTape analysis allowed for the electrophoretic separation of total RNA down to 5 ng/ $\mu$ l and was performed following manufacturer's instructions (Agilent Technologies, 2015):

- 1) RNA sample buffer was allowed to equilibrate at room temperature for 30 minutes
- 2) The RNA ScreenTape device was loaded into the 4200 TapeStation instrument and RNA assay mode was selected
- 3) The RNA ladder was prepared using 5  $\mu$ L of the RNA sample Buffer and 1  $\mu$ L of RNA ladder
- 4) Test samples were prepared containing 5  $\mu$ L of the RNA sample Buffer and 1  $\mu$ L of RNA

- 5) All samples were mixed by vortex (Whirlimixer, Fisherbrand) at 2000 rpm for one minute
- 6) The samples were placed at 72 °C for three minutes for denaturing before being placed on ice for two minutes and spun down
- 7) All samples were loaded into the Agilent 4200 TapeStation instrument and the RNA ladder placed in position A1 of the tube strip holder
- 8) The required sample positions on the 4200 TapeStation Controller Software were selected and the protocol started

The output of the ScreenTape analysis was the evaluation of the RNA degradation which was inferred by the generated RNA Integrity Number (RIN<sup>e</sup>) using 'TapeStation Analysis software A.02.02' (Agilent technologies). A RIN<sup>e</sup> number of 8 or above was considered acceptable and was used as a minimal threshold for all RNA samples.

Subsequently, the collected RNA was further analysed using a nano-spectrophotometer (QIAxpert), wherein 2 µl of each RNA sample was pipetted onto a QIAxpert Slide and inserted into the QIAxpert instrument. Quantification of nucleic acids and proteins within the samples was inferred by traditional absorbance readings (at A260 and A280). Following this the RNA was reverse transcribed to create cDNA using the Reverse transcriptase (QuantiTect Reverse Transcription Kit, Qiagen). Briefly, the purified RNA sample was incubated in gDNA Wipeout Buffer at 42°C for two minutes to effectively remove contaminating genomic DNA. Following decontamination, the RNA sample was reverse transcribed using a master mix prepared from Quantiscript Reverse Transcriptase, Quantiscript RT Buffer, and RT Primer Mix, the reaction occurred at 42°C and was then inactivated at 95°C.

RT-PCR was performed using the Syber Green method (Ponchel *et al.*, 2003) with the cDNA samples using the primers as detailed in Tables 6.2 and 6.3 and a reaction mixture composition as listed in Table 6.4.

**Table 6.2** Bovine primer sequences.

<b>Primer Name</b>	<b>Primer sequence (5' to 3')</b>
<b>Collagen I Forward</b>	TGAGAGAGGGGTTGTTGGAC
<b>Collagen I Reverse</b>	AGGTTCACCTTCACACCTG
<b>Collagen II Forward</b>	CATCCCACCCTCTCACAGTT
<b>Collagen II Reverse</b>	GTCTCTGCCTTGACCCAAAG
<b>L30 (Housekeeping) Forward</b>	AGGAAGGCTCAACGAGAACA
<b>L30 (Housekeeping) Reverse</b>	CGAGGAGCAGAAACCTTCAC

**Table 6.3** Human intervertebral disc primer sequences.

<b>Primer Name</b>	<b>Primer sequence (5' to 3')</b>
<b>Collagen I Forward</b>	CAGCCGCTTCACCTACAGC
<b>Collagen I Reverse</b>	TTTTGTATTCAATCACTGTCTTGCC
<b>Collagen II Forward</b>	GGCAATAGCAGGTTACGTACA
<b>Collagen II Reverse</b>	CGATAACAGTCTTGCCCCACTT
<b>GAPDH (Housekeeping) Forward</b>	TGGACTCCACGACGTACTIONCA
<b>GAPDH (Housekeeping) Reverse</b>	GGAAGCTTGTCATCAATGGAA

**Table 6.4** RT-PCR reaction mixture composition.

<b>Reagent</b>	<b>Volume (µl)</b>
<b>Primer</b>	1.0
<b>cDNA sample</b>	2.0
<b>RNAse free water</b>	10.5
<b>Syber Green</b>	12.5

cDNA denotes complimentary Deoxyribo Nucleic acid.

Samples were run on a Rotor-Gene Q real time instrument for 40 cycles of denaturing at 95 °C for five minutes, followed by annealing at 60 °C for 10 seconds. The PCR amplification was monitored using fluorescence detection at 521 nm. Reference gene controls were sourced from cells extracted from flasks at the same passage number as those used to seed the scaffolds. Negative controls without the addition of DNA were also run, to check results against possible primer-dimer false positives. RT-PCR standards were run for each primer pair used and the PCR efficiency calculated from standard curves of the serially diluted samples. The relative cycle threshold (Ct) values for all samples were extrapolated from the fluorescent gradients generated by the real-time instrument. Wherein, the Ct value represents the number of RT-PCR cycles required for the fluorescent signal (Syber green) to exceed background levels and is inversely proportional to the target gene abundance. The Ct values for target gene samples were normalised by comparison to the housekeeping genes employed in each run and the relative gene expression calculated using the Pfaffl Method. A method which took into consideration the reference gene controls and the PCR efficiency of each primer (Pfaffl, 2001). The ratio of collagen I: collagen II was then determined for all samples and the percent difference in proteoglycan gene expression calculated between atmospheric control samples and HP exposed samples.

### 6.2.7 Glycosaminoglycan content

#### 6.2.7.1 DMMB assay

The GAG content within the cell-laden scaffolds was spectrophotometrically determined with 9-dimethylmethylene blue chloride (DMMB) using a modification of the DMMB colorimetric assay as described by Farndale, Buttle and Barrett (1986).

For the duration studies within Experiment 1 the samples for DMMB were collected on days 8 and 15, for the 21 day BPC experiments (Experiment 2) the samples were taken on days 8, 15 and 21, and for the 21 day hIVD cell studies in Experiment 3 the samples were tested on days 8 and 21 only. Immediately following sampling, the alg/MC scaffolds were transferred to Eppendorf tubes and frozen at -20°C for a maximum of two weeks. Once thawed the samples were first digested overnight at

60°C in a 55 mM EDTA solution prepared using 100 mM Sodium citrate, to solubilise the alginate. Subsequently, the cells were pelleted by centrifugation (three minutes at 800 ×g). The retrieved cells were then homogenised by vortex (Whirlimixer, Fisherbrand) at 2000 rpm for one minute and incubated overnight at 60°C in an aqueous solution composed of 50 mM sodium phosphate pH 6.5, 2 mM EDTA, 5 mM N-acetyl-cysteine and 10 ug/mL papain (Sigma).

The released GAG within the digest solution was combined with filtered DMMB assay reagent: 0.038 mM DMMB (Sigma-Aldrich), 0.04 mM glycine (Sigma-Aldrich), 0.027 mM NaCl (Sigma), 100 mM HCl (in dH<sub>2</sub>O) using a microplate reader (Biochrom ASYS, UVM 340) and the absorbance measured at 525 nm. A standard curve for the GAG analysis was generated using chondroitin sulfate (Sigma-Aldrich). GAG content was normalised to the dry weights of scaffolds, wherein three scaffolds from each cell source per time-point were weighed before and after drying overnight in an oven at 60 °C (Thermofisher). To remove the influence of false positives caused by residual negatively charged alginate, cell-free scaffolds were also digested and measured, and their calculated concentration subtracted from cell-laden sample values.

#### 6.2.7.2 Histochemical analysis

In the 21 day BPC studies within Experiment 2, histological staining was used to localise GAGs and was performed on cell-free and cell-laden scaffolds from days 8, 15 and 21. Histochemical analysis was performed using safranin O; as described previously in Chapter 4, section 4.2.9.3 (Fig.4.2). Briefly, the samples were fixed with 4% paraformaldehyde in HBSS (with Ca<sup>2+</sup> and Mg<sup>2+</sup>), and paraffin embedded using a tissue processor (LEICA TP 1050) using the protocol outlined in Chapter 4, section 4.2.9.3 (Table 4.1). Microtome sections of 10-micron thickness were then mounted onto poly-L-Lysine coated glass slides (Sigma) and proteoglycan analysed by staining with 0.1% safranin O, Weigerts Iron Hematoxylin solution, and 0.02% counter stain fast green. Images were obtained by photo-microscopy using brightfield illumination, with the same light settings applied for each sample (Nikon, inverted microscope, ECLIPSE, TE2000). Semi-quantitative results for the histological images were achieved using thresholding analysis on Image J V1.44p for stain intensity. All histology images were converted into a greyscale 8-bit format and then inverted prior to the measurement of stain intensity. Three images per scaffold were analysed with

three replicates per time point. For all image analysis a fixed threshold cut-off of value of 40% was applied and was used to ensure consistency between samples. Measurements were normalised based on the background measurements and cell-free alg/MC control samples.

#### 6.2.8 Mechanical properties

Uni-axial compression experiments were performed using an Electroforce WinTest® Digital Control System (BOSE corporation). Testing was carried out on BPC samples from Experiment 2 only. Four scaffolds from each cell source (n = 4) were measured on day 8, 15 and 21 to characterise the Young's modulus (stiffness) of the alg/MC structures. The cell-free and cell-laden scaffolds were kept in cell culture conditions until immediately before compression tests were performed at room temperature (20-22°C). The wet scaffolds were compressed according to the following determined protocol (Fig.6.5):

- 1) Load ramped at 0.02 N/sec (touching scaffold) to -0.1 N
- 2) Displacement ramped at 0.06 mm/sec to 0.6 mm  
(to compress to around 50% of scaffold measured height)
- 3) Displacement ramped at -0.2 mm/sec to -2mm (to release pressurisation)

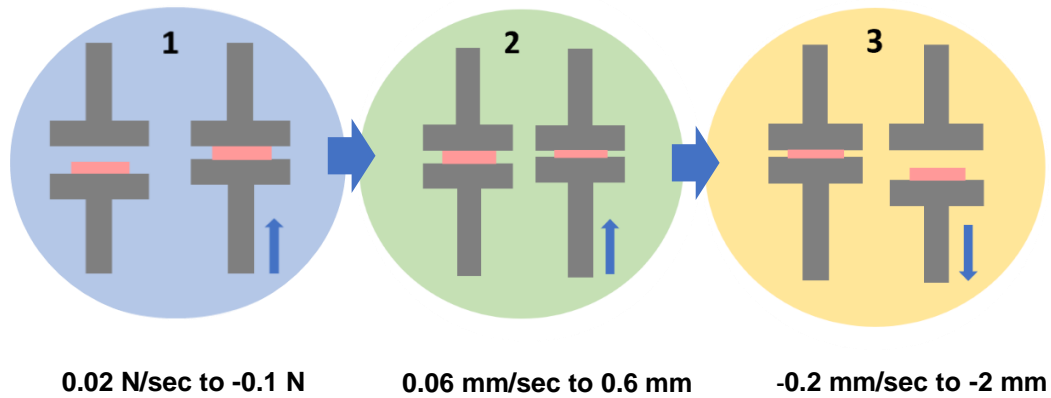


**Figure 6.5** Flow diagram to demonstrate the compression protocol used for mechanical testing in Experiment 2 on bovine primary chondrocyte-laden alginate methyl cellulose scaffolds.

Dimensional measurements of each sample were taken prior to testing using electronic callipers. Engineering stress and strain were then recorded to extract the Young's moduli, as calculated from load and displacement using the calculations previously stated in Chapter 3 (section 3.17, equations 3.2 and 3.3). The Young's moduli were determined using the secant method, defined as the slope of a line from the origin of the curve to a specific point on the stress-strain curve. An example of this method can be seen below in Fig.6.6. The maximum stress (kPa) and percent strain (%) values from each test were recorded and the secant modulus (kPa per % strain) calculated using the following formula:

$$\text{Equation 6.3} \quad \textit{Secant modulus} = \frac{\textit{max stress}}{\textit{strain at max stress}} \times 100$$

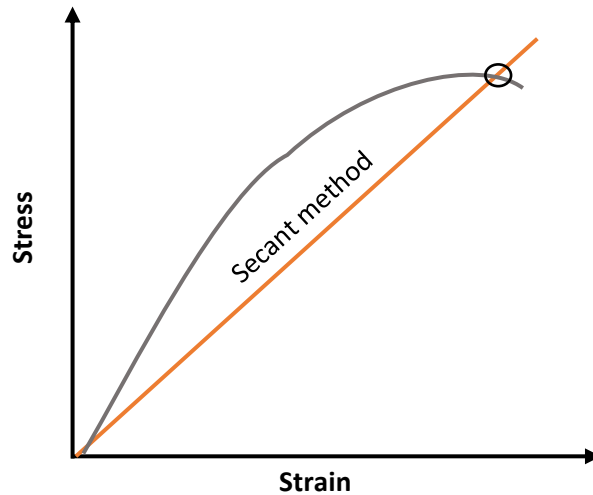


**Figure 6.6** Diagram to demonstrate the secant method used to extract the Young's moduli of alginate methyl cellulose scaffolds.

### 6.2.9 Statistical analysis

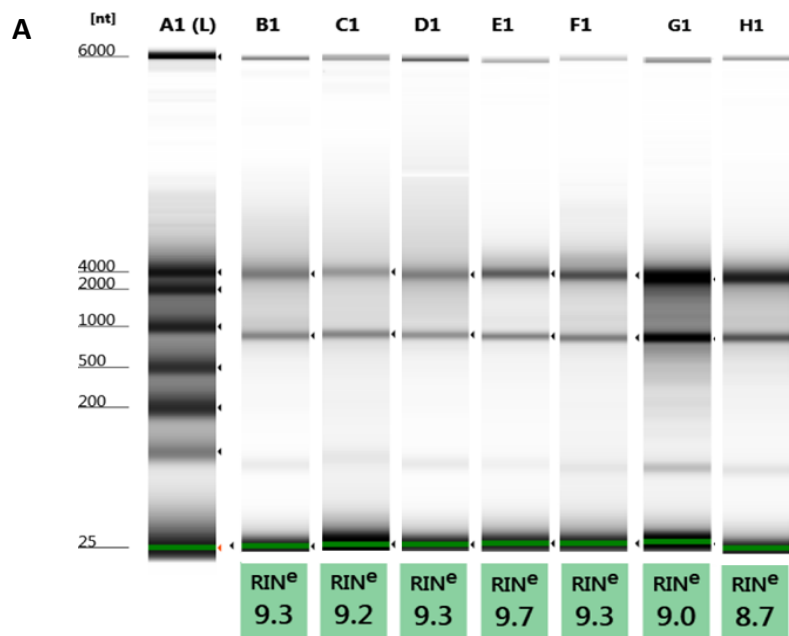
All raw data was analysed statistically using ANOVA. When the ANOVA indicated a significant difference ( $P \leq 0.05$ ) between groups, the difference was evaluated with post hoc comparison of Bonferroni set at  $P \leq 0.05$  using IBM SPSS 24 statistical software platform® (UK).

## 6.3 Results

### 6.3.1 Screen-tape analysis

The integrity and quantity of the RNA obtained from a selection of BPC and hIVD cells within alg/MC scaffolds (isolated using the RNeasy kit, Qiagen) across the three experiments performed were assessed. The output of the ScreenTape analysis (Agilent technologies) demonstrated a high RNA integrity of the tested RNA samples (purified from alg/MC scaffolds using the RNeasy kit (Qiagen) (Fig.6.7, A). The evaluation of RNA degradation was inferred by the generated RNA Integrity Number (RIN<sup>e</sup>) using 'TapeStation Analysis software A.02.02' (Agilent technologies). A RIN<sup>e</sup> number of 8 or above was measured for all the RNA samples tested and was

consequently considered acceptable (Fig.6.7, A). In addition, the sampled RNA quantities measured using a nano-spectrophotometer (QIAxpert) provided a sufficient quantity of nucleic acids for RT-PCR (Fig.6.7, B). The concentration and purity of the nucleic acids was inferred by the ratio of absorbance at 260 nm and 280 nm. The RNA samples all displayed a ratio of approximately 2.0, which is the value typically accepted as “pure” for RNA.



**B**

Sample	Quantity (ng/μl)	Ratio (260/280)
B1	13.68 ± 3.11	2.26 ± 0.36
C1	11.78 ± 3.02	2.30 ± 0.44
D1	12.73 ± 2.11	2.23 ± 0.33
E1	13.32 ± 2.30	2.34 ± 0.21
G1	25.05 ± 1.74	1.98 ± 0.11
H1	22.35 ± 2.18	2.01 ± 0.16

**Figure 6.7** Screen-tape analysis and nano-spectrophotometer results of RNA isolated using the RNeasy kit (Qiagen) from bovine primary chondrocytes (BPC) or human annulus fibrosus (hAF) and nucleus pulposus (hNP) cells at successive time-points, purified from alginate methyl cellulose scaffolds which were cultured under control conditions or with hydrostatic pressure (HP) exposure. (A1) RNA ladder (B1) BPC Day 7 control (C1) BPC Day 14 control (D1) BPC Day 21 control (E1) BPC Day 14 HP (F1) BPC Day 21 HP (G1) hAF Day 14 control (H1) hNP Day 14 Control. (A) RNA RIN<sup>e</sup> values provided by the ‘TapeStation Analysis software A.02.02’ (Agilent technologies). (B) Nano-spectrophotometer (QIAXpert) results of measured RNA quantity (ng/μl) and 260/280 ratio, values presented as mean ± standard deviation of three repeated measurements.

## Experiment 1- Hydrostatic pressure duration experiments using bovine primary chondrocytes

### 6.3.2.1 Cell survival

Cell survival was assessed using two independent methods which included a live/dead viability assay and an MTT protocol.

#### 6.3.2.1.1 Percent survival (Live/Dead)

The physical and biochemical properties of cell-laden scaffolds can be determined by the cell population, it is therefore critical to ensure sufficient cell numbers. Consequently, the percent of cell survival was measured in scaffolds with and without exposure to HP. On day one following scaffold fabrication a high average percent of BPC survival of  $90.29\% \pm 4.24$  was seen using live/dead staining (Fig.6.8, A). By the final point of cell culture (15 days) there was no significant change in cell survival for the samples exposed to static HP durations (5 min, 45 min or 4 hours), relative to the day one measurements. In addition, no significant difference in percent cell survival was found between the samples kept under atmospheric conditions ( $87.21\% \pm 3.20$ ) and the scaffolds exposed to HP durations of 5 or 45 minutes ( $85.72\% \pm 3.32$  and  $91.06\% \pm 4.80$  respectively) (Fig.6.8, A). However, the scaffolds subjected to dynamic HP (3 x 5 minutes) did have a significantly lower survival ( $82\% \pm 2.17$ ) than samples exposed to 5 and 45 minutes of statically applied HP (Fig.6.8, A).

#### 6.3.2.1.2 Stain intensity (MTT)

The images of the MTT stained scaffold sections confirmed a high cell survival on day 15 for all pressurisation protocols tested as well as control samples. This was evident by the intensity of purple formazan staining seen for the cell-laden scaffolds, which was not apparent in the cell-free samples (Fig.6.8, B).

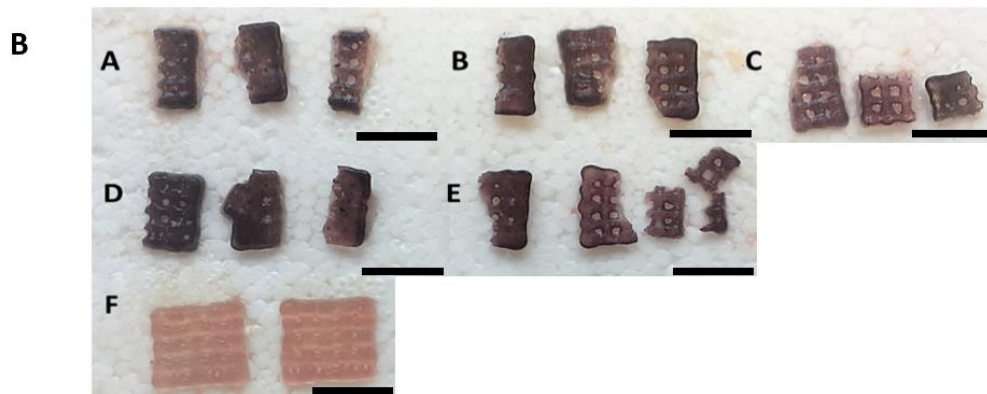
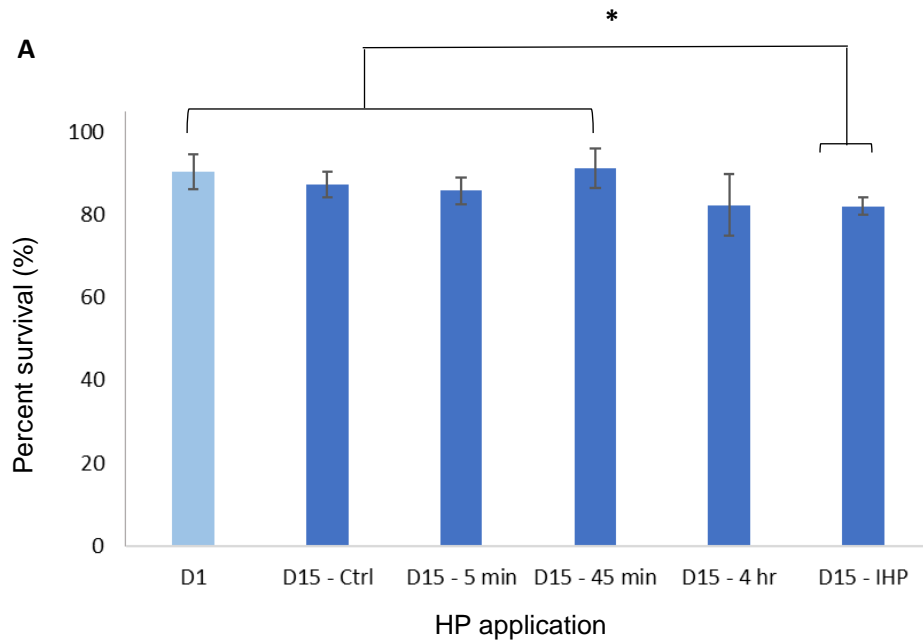


**Figure 6.8** (A) Percent bovine primary chondrocyte survival in alginate methyl cellulose scaffolds calculated via live/dead staining analysis on day one (D1) and day 15 (D15) of culture. Measurements were taken of samples kept at atmospheric control conditions (Ctrl) or exposed to five days of HP (6 MPa) applied for 5 minutes, 45 minutes, 4 hours or dynamic intermittent applications (IHP) of 5 minutes on/2 minutes off x3, (mean  $\pm$  stdv)  $n = 4$ ,  $*P \leq 0.05$ . (B) Examples of MTT stained scaffold sections taken on day 15 of incubation, taken from samples subjected to the different HP duration protocols A) 5 minutes B) 45 minutes C) IHP D) 4 hours or from scaffolds kept under atmospheric conditions E) cell-laden controls F) cell-free controls. The three scaffold sections for each sample type represent one sample from three different cell sources ( $n=3$ ).

### 6.3.2.2 Proteoglycan production

There was a large variability in proteoglycan synthesis between samples, seen for the both gene expression and total GAG content measurements. Consequently, the four different cell sources used for the duration studies in Experiment 1 (isolated from four different bovine joints) demonstrated varied quantities of proteoglycan presence and extents in response to the different mechanical stimuli protocols (Table.6.5). For this reason, the gene expression and GAG content values on day 15 of incubation were calculated as a percentage difference from the control groups.

For the proteoglycan gene expression data, the influence of each pressurisation protocol tested had a positive effect on proteoglycan expression compared to the atmospheric control groups by day 15 of incubation (5 days of pressurisation). With the exception of the 5 minute application, which did not demonstrate a significant increase in proteoglycan expression relative to control samples ( $P = 6.5$ ) (Table.6.5).

The positive influence on relative proteoglycan gene expression compared to control samples was significant and the most consistent (with the lowest standard deviations) for the 45 minute and 4 hour HP applications, with a  $72.2\% \pm 9.98$  and  $62.4\% \pm 20.62$  increase in proteoglycan expression respectively (Table.6.5). However, due to variability between cell sources, especially for the 5 minute ( $\pm 47.77$ ) and IHP ( $\pm 41.60$ ) applications, a significant difference between the HP protocols could not be stated.

Similarly, the GAG content of the BPC cells in alg/MC after 15 days of culture showed an increase following an HP of 45 minutes and an intermittently applied HP when compared to control groups, with a percent increase of  $56.64\% \pm 15.86$  and  $42.62\% \pm 14.84$  respectively (Table.6.5). Whereas, no significant difference between the control samples and the 5 minute ( $P = 0.003$ ) and 4 hour HP ( $P = 0.008$ ) durations was determined. In addition, no significant difference was observed between the different HP durations due to high variance between cell sources.

**Table 6.5** Percent difference in proteoglycan gene expression and glycosaminoglycan content relative to controls measured in bovine primary chondrocytes extracted from bioprinted alginate methyl cellulose scaffolds exposed to either 5 minutes, 45 minutes, 4 hours or intermittent hydrostatic pressure (6 MPa for 5 days on/2 days off) taken on day 15 of cell culture.

Analysis	Measurement	5 min	45 min	4 hr	IHP (5 min on/2 min off x3)
PG gene expression (RT-PCR)		20.25 ±	72.2 ±	62.4 ±	42.09 ±
	% Difference from control	47.77	9.98**	20.62*	41.60
GAG content (DMMB)		7.21 ±	56.64 ±	22.1 ±	42.62 ±
		63.47	15.86*	55.66	14.84*

Values are presented as the mean percent difference ± standard deviation. PG; proteoglycan, RT-PCR; real time polymerase chain reaction, GAG; glycosaminoglycan, min; minutes, hr; hours; IHP; intermittent hydrostatic pressure. Relative proteoglycan gene expression was measured by RT-PCR (n=4) whereas GAG content was quantified by 1,9-dimethylmethylene blue assay (n=3). Significant difference from control groups was marked by either a \* or \*\* with \* representing a significance of  $P \leq 0.05$  and \*\* a significance of ( $P \leq 0.01$ ).

### Experiment 2 - 21 day hydrostatic pressure experiment with bovine primary chondrocytes

#### 6.3.2.2 Cell survival

The percent cell survival in all scaffolds immediately after printing (day one) was high with an average cell survival of 88.6% ± 1.1 (Fig.6.9, A). By day 21 both the control and HP treated samples (control 85.9% ± 0.9, HP 83.8% ± 1.5) demonstrated a significant decline in cell survival from days one and eight. With percent cell survival values of 87.3% ± 1.03 (control) and 89.3% ± 1.8 (HP) on day eight of incubation. Whereas, there was no significant difference to cell survival between days 15 and 21 of cell culture for HP (86.4% ± 0.6 control) or control samples (86.6% ± 0.6 HP) (Fig.6.9, A). Thus, cell survival for both the control and HP treated samples showed a

slight, but significant, decline over time. The direct comparison of HP and control samples saw no significant difference in cell survival at any time point (Fig.6.9, A).

In addition, the MTT staining confirmed a consistently high cell survival from days one (day of scaffold fabrication) to day 21 of scaffold incubation (Fig.6.9, B), with a strong purple formazan presence in all scaffolds except the cell-free samples. This was observable macroscopically (Fig.6.9, B) and via light microscopy (Fig.6.9, C). Due to the high cell density within the alg/MC material scaffolds the purple colouration was shown throughout the structure (Fig.6.9, B). Upon microscopy (x10) it was evident that the stain was retained within the BPC cells (Fig.6.9, C, A-H). Although the cell-free samples showed some background MTT staining (Fig.6.9, C, I-K) a clear distinction from the cell-laden scaffolds was apparent.

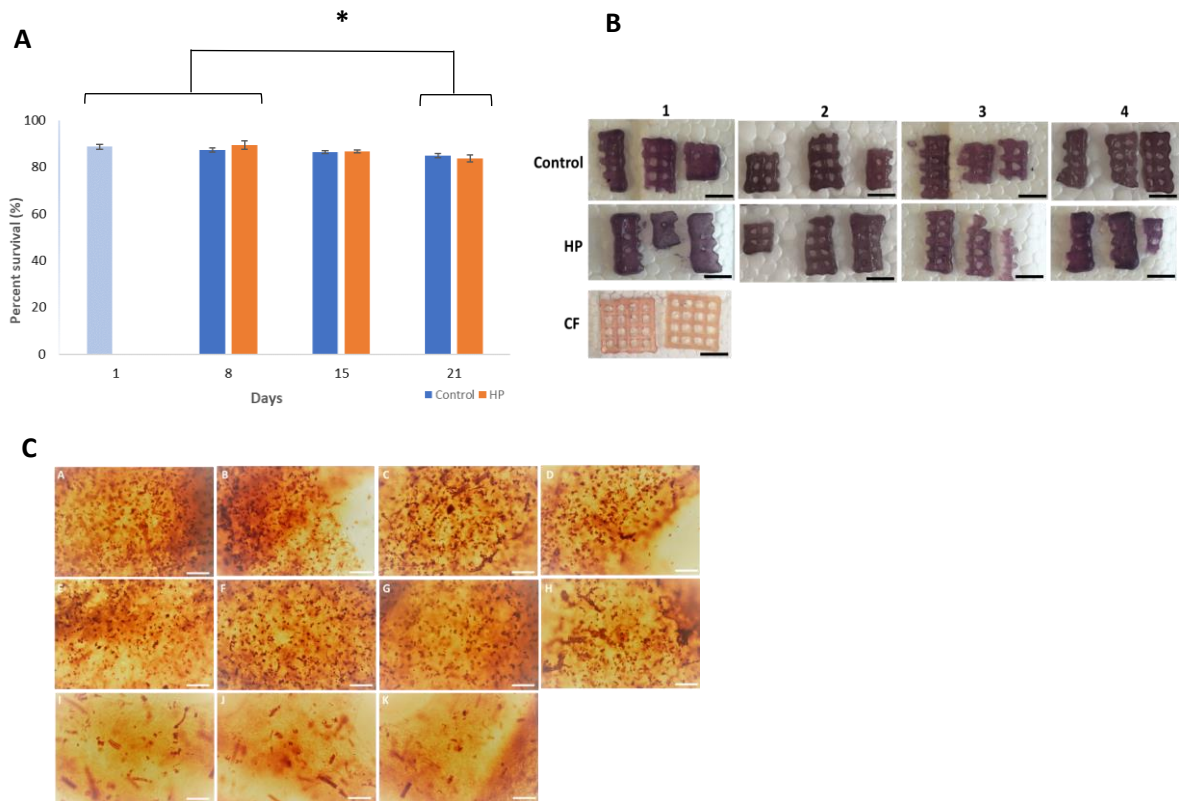


**Figure 6.9** (A) Percent survival of bovine primary chondrocytes (BPCs) within alginate methyl cellulose (alg/MC) scaffolds over time on days 1,8,15 and 21 of incubation, separated by sample type; atmospheric controls or those exposed to 6 MPa of HP 5 days on/ 2 days off, after seven days of static atmospheric culture. Mean  $\pm$  stdv,  $n=4$ , \*  $P \leq 0.05$ . (B) MTT staining of BPC cells within scaffolds taken on day 21 of incubation, following culture under atmospheric conditions for the entire study duration (controls) or subjected to HP. Samples represent sections taken from three separate scaffolds and are grouped by their cell source (1-4). Cell-free (CF) samples were also stained for comparison. Scalebar represents 5 mm. (C) Examples of MTT staining of BPC-laden (A-H) and cell-free alg/MC scaffolds (I-K) on day 21 of incubation (A-D) control samples, (E-H) samples exposed to the 45 minute/day HP protocol. Each column represents samples from a different cell source ( $n=4$ ), with the exception of the cell-free samples (I-K). Images taken by light microscopy (Axiovert-25, Carl- Zeiss), magnification  $\times 10$ , scalebar represents 10  $\mu\text{m}$ .

### 6.3.2.3 Proteoglycan production

Gene expression analysis was performed after the first day of pressurisation (day eight of incubation) and on the final day of the study (day 21) after the scaffolds were subjected to two sets of HP (five days on/two days off).

The results showed a significant percent increase in proteoglycan expression (relative to control) following HP exposure on both the first and final day of mechanical stimuli (Table.6.6). For the samples measured on day 21 the percent increase in proteoglycan expression relative to controls was over 11 fold greater ( $78.1\% \pm 16.1$ , percent difference from controls) than the change seen after the first day of HP ( $7.0\% \pm 5.0$ , percent difference from controls) (Table.6.6)

In addition, a high collagen type II: collagen type I was seen on day 21 for both the control and HP treated samples (Table.6.7), with no significant differences between the groups for the expression of either collagen type.

With regards to GAG content, there was no significant increase in GAG content relative to control samples following the first day of HP application, with a mean percent change of  $4.9\% \pm 12.9$  (Table.6.6). However, by day 21 of incubation the GAG concentration was significantly increased relative to the control samples, with a percentage increase of  $71.3\% \pm 11.1$  (Table.6.6).

Similarly, the semi-quantitative analysis of histology images indicated no significant difference in safranin O stain intensity (inverted grayscale) on day one of HP, between the HP stimulated samples and control samples, with a mean percent change of  $79.0\% \pm 144.2$  (Table.6.6). Yet, by day 15 of incubation, the HP exposed samples demonstrated a significantly increased safranin O stain intensity, with a  $206.0\% \pm 7.8$  increase. On day 21 of culture the HP treated samples saw a significant percent increase in stain intensity  $99.2\% \pm 17.3$  relative to the day 21 control samples (Table.6.6). In addition, a significant and progressive increase in stain intensity (inverted grayscale) was seen between days 8, 15 and 21 for the HP treated samples. For the control samples a significant increase in stain intensity (inverted grayscale) was only seen between days 15 and 21 of cell culture (Table.6.6).

**Table 6.6** Relative aggrecan gene expression, glycosaminoglycan content and safranin O stain intensity of bovine primary chondrocytes alginate methyl cellulose samples subjected to 6 MPa of hydrostatic pressure (5 days on/2 days off) after 8 days of incubation (one day of hydrostatic pressure exposure), 15 days (5 days of pressurisation) and 21 days of incubation (10 days of total hydrostatic pressurisation).

Analysis	Measurement	Day 8	Day 15	Day 21
<b>Proteoglycan gene expression (RT-PCR)</b>	% Difference from control	7.0 ± 5.0*	-	78.1 ± 16.1*
<b>GAG content (DMMB)</b>		4.9 ± 12.9	-	71.3 ± 11.1*
<b>Intensity (safranin O)</b>		79.0 ± 144.2	206.0 ± 7.8**	99.2 ± 17.3*

Values are presented as the mean percent difference ± standard deviation. RT-PCR; real time polymerase chain reaction, GAG; glycosaminoglycan, DMMB; 1,9-dimethylmethylene blue assay. Relative proteoglycan gene expression was measured by RT-PCR (n = 4), GAG content was quantified by DMMB (n = 4) and intensity measured from safranin O stained histological slices (n = 4). A significant difference from control groups was marked by either a \* or \*\* with \* representing a significance of  $P \leq 0.05$  and \*\* a significance of  $P \leq 0.01$ .

**Table 6.7** The calculated mean ratio of collagen type I : collagen type II relative gene expression in bovine primary chondrocytes isolated from alginate methyl cellulose scaffolds exposed to hydrostatic pressure (6 MPa; 5 days on/2 days off) or atmospheric control conditions taken on day 21 of cell culture.

<b>Sample</b>	<b>Collagen I</b>	<b>Collagen II</b>	<b>Stdv</b>
<b>Control</b>	0.45	99.55	0.45
<b>HP</b>	1.50	98.50	1.96

Values were presented as the mean ratio of collagen type I: collagen type II relative gene expression  $\pm$  standard deviation (Stdv). HP denotes hydrostatic pressure. Relative gene expression was measured by RT-PCR (n=4).

### 6.3.3.3 Mechanical properties

The mechanical properties of cell-laden scaffolds can have an influence on both cell properties and structural integrity over time and was therefore an important factor for consideration when comparing HP treated and control samples. On days 8,15 and 21 of cell culture no significant difference to Young's modulus was observed between the samples, regardless of whether they were kept under atmospheric control conditions, exposed to HP or were fabricated without cell inclusion (Fig.6.10). In addition, the Young's modulus within sample types showed no significant difference between days 8,15 and 21 of incubation (Fig.6.10).

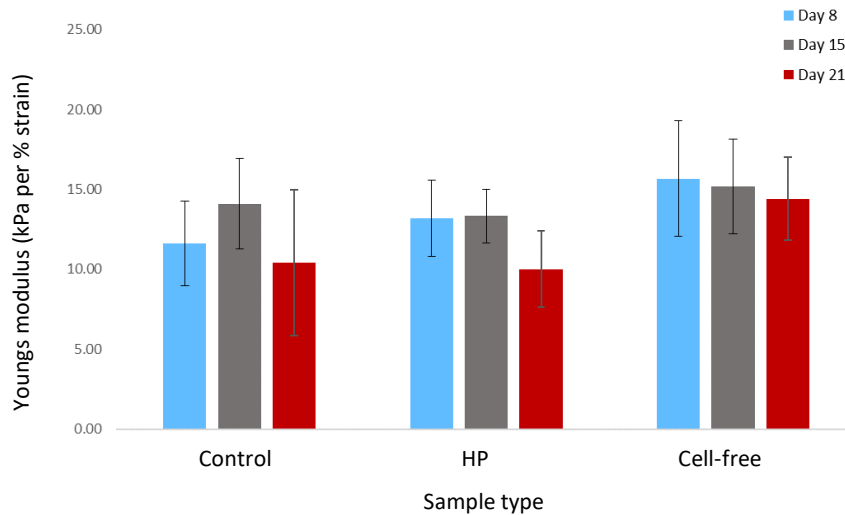


**Figure 6.10** Young's modulus of bovine primary chondrocyte-laden and cell-free alginate methyl cellulose scaffolds over time, measured on days 8, 15 and 21 of incubation. Samples were either kept consistently under atmospheric conditions (control) or exposed to a daily 45 minute 6 MPa hydrostatic pressure protocol starting on day 8 (5 days on/2 days off). Mean  $\pm$  stdv,  $n=4$ , \*  $P \leq 0.05$ .

#### 6.3.4 Experiment 3- 21 day hydrostatic pressure experiment with human intervertebral disc cells

##### 6.3.4.1 Cell survival

Cell survival after day 8 of culture was high, with a mean cell survival of  $93.1\% \pm 5.5$  and  $88.6\% \pm 5.5$  for hAF and hNP cells kept under control conditions, and  $93.1\% \pm 5.5$  and  $93.6\% \pm 2.7$  for the hAF and hNP cells following the first round of HP (Fig.6.11, A). On day 21 of culture both the control and HP treated AF samples (control  $65.2\% \pm 9.3$ , HP  $72.8\% \pm 10.3$ ) demonstrated a significant decline in cell survival compared to day eight (Fig.6.11, A). The hNP cells did not show a significant decrease in survival from day eight, with a mean survival rate of  $83.0\% \pm 4.4$  for the control samples and  $82.0\% \pm 7.7$  for cells from HP treated samples (Fig.6.11, A). For both the hAF and

hNP cells there was no significant difference in cell survival between the control and HP treated samples, on either day 8 or day 21 of culture. On day 21 the hAF cell control samples showed a significantly decreased cell survival compared to the hNP control samples at the same time point (Fig.6.11, A). MTT staining of the cell-laden scaffolds showed a high formazan presence on both day one (the day of scaffold fabrication) as well as on day 21 of cell culture for all sample types (regardless of the culture conditions used) with no obvious visual disparities in colour intensity. The cell-free samples showed no apparent formazan presence (Fig.6.11, B).

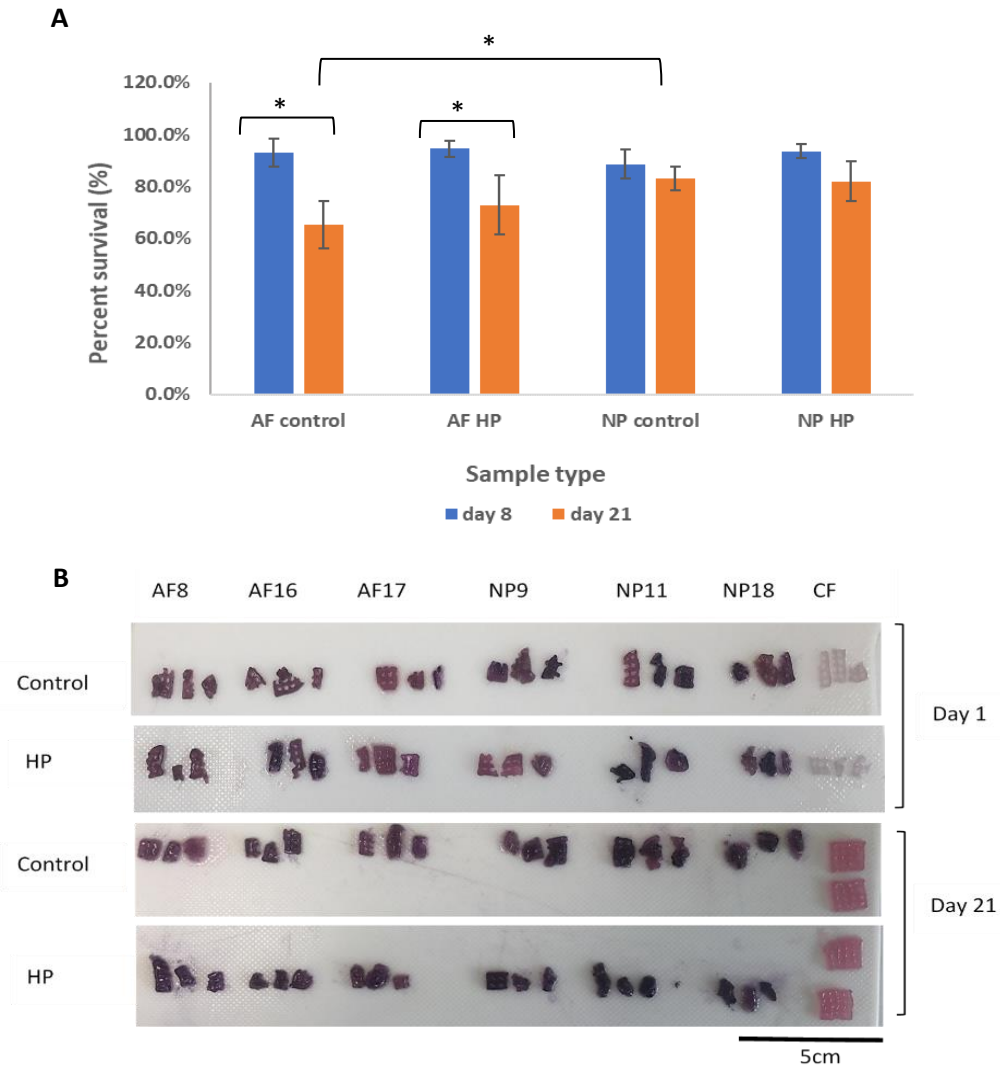


**Figure 6.11** (A) Percent cell survival calculated from live/dead imaging of human annulus fibrosis (hAF) and nucleus pulposus (hNP) cells in alginate methyl cellulose (alg/MC) scaffolds after 8 or 21 days of incubation, including samples cultured under atmospheric control conditions or hydrostatic pressure (HP). Mean  $\pm$  stdv,  $n=4$ ,  $*P \leq 0.05$ . (B) MTT staining of alg/MC scaffold sections embedded with hAF or hNP cells, sorted by cell source, on day one (the day of scaffold fabrication) or day 21 of culture under atmospheric control or HP conditions,  $n=3$ , scale bar represents 5cm. Images taken with iphone v6.

#### 6.3.4.2 Proteoglycan production

Gene expression analysis was performed after the first day of culture within the alg/MC scaffolds, on both atmospheric control samples and samples subjected to one session of 45 minute HP. The mean relative proteoglycan gene expression for samples exposed to one HP application was not significantly different to the control samples, and a high variation was seen between cell sources (Table.6.8). Conversely, the day 21 samples did show a significant increase in proteoglycan expression relative to the control samples, with an average percent increase of  $187.4\% \pm 122.4$  for the HP exposed hAF cells and  $81.9\% \pm 26.4$  for the HP treated hNP cells (Table.6.8)

Regarding the ratio of collagen type I to collagen type II, the proportions of collagen presence were shown to shift over the duration of cell culture (Table.6.9). In day one samples the collagen type I presence was significantly lower than collagen type II, with a mean ratio of  $39.3: 60.7 \pm 6.1$  across all sample types. However, the difference observed was significantly greater in the day 21 samples with a mean ratio of  $0.87: 99.2 \pm 0.8$  for all samples collectively, regardless of cell type or treatment. Measurements of the relative collagen contents on days 8 and 21 demonstrated no significant difference between the atmospheric controls and the HP treated samples (Table.6.9).

On day 21 of culture both the hAF and hNP alg/MC embedded cells treated with daily HP demonstrated an increase in GAG content ( $\mu\text{g/scaffold}$ ) relative to the atmospheric controls (Table.6.8). This was seen to be significant in all hNP samples, with an overall mean percentage increase of  $87.1\% \pm 7.0$ . For the HP treated hAF cells the sample from patients one and three demonstrated a positive influence on GAG content with mean increases of  $80.2\% \pm 2.2$  and  $86.2\% \pm 3.1$  respectively (Table.6.8). Comparatively, the hAF cells from patient two had a negative effect on GAG content with a mean decrease of  $-72.4\% \pm 19.2$  relative to controls, which resulted in an overall percentage increase of  $31.3\% \pm 89.5$  for the hAF cell type (Table.6.8). For DMMB measurements taken on day one of HP application (day eight of culture) a GAG content value could not be determined from background values (the mean false positive values recorded for cell-free scaffolds due to negatively charged alginate) (Table.6.8).

Semi-quantitative analysis of safranin O stained hAF or hNP-laden alg/MC scaffolds measured on day 21 of culture showed a significant increase in stain intensity (inverted grayscale) for HP treated cells relative to the controls (Table.6.8). With a mean percentage increase in intensity (inverted grayscale) of 99.6%  $\pm$  45.6 for hAF cells, and 112.7%  $\pm$  65.8 for hNP cells.

**Table 6.8** Mean measurements of the relative aggrecan gene expression, glycosaminoglycan content and safranin O stain intensity of human annulus fibrosus nucleus pulposus cells cultured in alginate methyl cellulose subjected to 1 MPa of hydrostatic pressure (5 days on/2 days off) represented as percent change from control samples.

Analysis	Measurement	Day 8		Day 21	
		hAF	hNP	hAF	hNP
<b>Proteoglycan</b>					
gene		4.4 $\pm$	7.5 $\pm$	187.4 $\pm$	81.9 $\pm$ 26.4
expression (RT-PCR)	% Difference from control	13.2	8.6	122.4*	*
<b>GAG content</b>					
(DMMB)		-	-	31.3 $\pm$ 89.5	87.1 $\pm$ 7.0**
<b>Intensity</b>					
(safranin-O)		-	-	99.6 $\pm$ 45.6*	112.7 $\pm$ 65.8*

Values are presented as the mean percent difference  $\pm$  standard deviation. RT-PCR; real time polymerase chain reaction, GAG; glycosaminoglycan, DMMB; 1,9-dimethylmethylene blue assay. Relative proteoglycan gene expression was measured by RT-PCR (n=4), GAG content was quantified by 1,9-dimethylmethylene blue assay (n=4) and intensity measured from safranin O stained histological slices (n=4). A significant difference from control groups was marked by either a \* or \*\* with \* representing a significance of  $P \leq 0.05$  and \*\* a significance of  $P \leq 0.01$

**Table 6.9** Relative gene expression ratios of collagen type I: collagen type II in human annulus fibrosus and nucleus pulposus cells cultured in alginate methyl cellulose scaffolds on day 8 or 21 of cell culture. Measurements taken from samples exposed to 1 MPa of hydrostatic pressure (5 days on/2 days off) or cultured under constant atmospheric control conditions.

<b>Control</b>	<b>Cell type</b>	<b>Collagen type</b>	<b>Collagen type</b>	<b>Stdv</b>
		<b>I</b>	<b>II</b>	
<b>Day 8</b>	hAF	33.5	66.5	0.47
	hNP	48.3	51.7	0.34
<b>Day 21</b>	hAF	1.8	98.2	0.65
	hNP	0.15	99.7	0.02
<b>HP</b>	<b>Cell type</b>	<b>Collagen type</b>	<b>Collagen type</b>	<b>Stdev</b>
		<b>I</b>	<b>II</b>	
<b>Day 8</b>	hAF	42.2	57.8	0.42
	hNP	39.2	60.8	0.31
<b>Day 21</b>	hAF	0.32	99.8	0.45
	hNP	1.1	98.9	0.46

Values were presented as the mean ratio of collagen type I: collagen type II relative gene expression  $\pm$  standard deviation (Stdv). hAF; human annulus fibrosus cells, hNP; human nucleus pulposus cells. Relative gene expression was measured by RT-PCR (n=4).

#### 6.4 Discussion

The purpose of this chapter was to further the identification of optimal HP experiment factors for the up-regulation of proteoglycan production in 3D cultured chondrocytes based on the findings of the previous meta-analysis review (Chapter 5). The intentions of this study were met via the application of a static HP (45 minutes; 5 days on, 2 days off) on bioprinted BPC-laden alg/MC scaffolds and was subsequently translated for application with hIVD cells for the purposes of disc cartilage engineering.

#### 6.4.1 Experiment 1 – Hydrostatic pressure duration experiments using bovine primary chondrocytes

Due to a lack of sufficient data in literature an ideal HP duration was not identified in the previous meta-analysis review of HP experiment factors (Chapter 5) and therefore the identification of an optimised HP duration was the primary purpose of the first experiment performed in this investigation.

In the review of previous HP literature for cartilage engineering (Chapter 5) it was found that an HP duration of 4 hours/day was the most frequented pressure duration used in mechanotransduction experiments. The selection of a 4 hour HP period was commonly based on the justification that it mimicked the typical physiological loading time of human cartilage in a day (Smith *et al.*, 2000; Hu and Athanasiou, 2006; Li *et al.*, 2016). However, according to the HP application lengths tested in the first experiment within this study, the results suggested that a HP time of 45 minutes was the favoured method for achieving a significant stimulatory response in chondrocytes, when compared to durations of 4 hours, 5 minutes and a dynamic application of 3 x 5 minutes (IHP). In the duration experiment, both the 45 minute and 4 hour HP applications resulted in a significant increase to proteoglycan gene expression, with no significant difference between the two durations. However, the 45 minute HP duration demonstrated a more consistent stimulatory response (with a percent increase of  $72.2\% \pm 10.0$  in proteoglycan gene expression relative to controls,  $P = 0.006$ ) than the 4 hour application (with an increase of  $62.4\% \pm 20.6$ ,  $P = 0.03$ ). Furthermore, based on GAG content measurements the samples exposed to the 45 minute HP exposure conditions saw a significant increase of  $56.6\% \pm 15.9$  relative to control samples, which was a result that corroborated with the gene expression analysis. Conversely, for the samples subjected to a 4 hour HP protocol, although an increase in GAG was observed in two of the four BPC cell sources, no significant overall change in GAG content was observed relative to controls ( $22.1\% \pm 55.7$ ,  $P = 0.07$ ), and was a result which did not support the gene expression analysis. Wherein, the observed disparity in the GAG content and gene expression results for the 4 hour duration was likely due to a delayed proteoglycan production in some donor cells.

The total length of culture employed in the first experiment phase was 15 days and comprised of 7 days of atmospheric conditions followed by 5 days of HP and then a further 2 days of atmospheric culture for the HP treated samples. On the 14<sup>th</sup> day of cell-laden culture a significant upregulation of proteoglycan gene expression was observed in the 4 hour HP exposed samples, whereas no marked difference in GAG content was measured. Thus, considering that protein production is the downstream effect of gene expression, the lack of significant increase in GAG content on day 14 suggested that a GAG production response was delayed or not yet measurable by DMMB for all cells at this time-point. This theory of experiment duration on a measurable proteoglycan response was additionally supported by the previous meta-analysis review, in which the effects of HP were more significantly observed in experiments which consisted of  $\geq 2$  weeks of HP application (Mizuno *et al.*, 2002; Elder *et al.*, 2006; Heyland *et al.*, 2006; Elder and Athanasiou, 2008; Kunitomo *et al.*, 2009; Tatsumura *et al.*, 2013; Li *et al.*, 2016). Thus, it could be suggested that with a longer experiment time that a 4 hour static HP approach would have demonstrated an upregulation to GAG content, which corresponded with the significant increase seen in proteoglycan gene expression. In addition, it should be noted that alginate contamination was an issue for the DMMB assay protocol. Alginate polysaccharides carry an innate negative charge and as a result the DMMB stain is attracted to both alginate and negatively charged proteoglycans (Zheng and Levenston, 2015). Due to the known occurrence of alginate interference during DMMB, cell-free alg/MC samples were used as a negative control for DMMB measurement, and the mean concentrations of the cell-free samples were subtracted from all cell-laden samples. However, it is possible that any unexpected differences in alginate content between the scaffolds could have affected results. Conversely, it can be stated with confidence that alginate presence did not alter the gene expression results, based on the ScreenTape analysis (Agilent technologies) of RNA retrieved from alg/MC samples, which demonstrated RNA of good integrity and purity (6.3.1, Fig.6.7). Thus, the gene expression analysis of the samples exposed to four hours of HP were assumed as reliable.

The application of a five minute HP duration used in this study was chosen based on the outcome of an early HP experiment published by Hall, Urban and Gehl (1991). In the work by Hall, Urban and Gehl (1991) an HP duration of five minutes was found to

sufficiently induce proteoglycan production (monitored via [<sup>35</sup>S]- sulfate incorporation) in explanted bovine cartilage. Conversely, the results of this study using BPC-laden alg/MC did not demonstrate a significant up-regulatory effect after a five minute HP duration, (20.3% ± 47.8 difference in proteoglycan gene expression relative to controls,  $P = 0.09$ ). The disparity between the results of these experiments was unexpected. However, upon further consideration the reason for the differences in the results can likely be explained by the sensitivity of the analysis used for proteoglycan quantification.

In the Hall, Urban and Gehl (1991) experiments the highly sensitive [<sup>35</sup>S]-sulfate incorporation radio-assay was utilised for proteoglycan analysis, and is a method capable of monitoring changes in [<sup>35</sup>S]-sulfate incorporation (used in proteoglycan synthesis) within seconds of stimuli application (Beeley, 1985). However, due to the higher regulatory approval and health concerns associated with handling radiation the utilisation of radio-assays are no longer standard practice. Instead, in more recent literature the detection of proteoglycans is commonly performed via the use of colorimetric DMMB assays and gene expression analysis. However, these methods of detection are less sensitive. Thus, based on the protocols employed in this study (DMMB and gene expression analysis) the reason for the lack of response in proteoglycan production observed after a 5 minute HP duration was likely related to the reduced sensitivity of analysis. It was therefore an interesting observation that the increased HP exposure duration of 45 minutes was capable of eliciting an observable anabolic response (following 14 days of cell culture with 5 days of HP). However, due to the limited durations tested in Experiment 1 it was unclear whether an upregulation in proteoglycan could also have been triggered using a duration between 5 and 45 minutes.

Furthermore, an additional observation identified in the HP duration experiment was the presence of donor-donor variation between BPC cell sources. For the four hour, five minute and dynamic five minute test durations used in this study, two of the four sources (from donors two and four) did not invoke a stimulatory response following HP. A difference in cell susceptibility to mechanical stimuli between cell donors is not an unprecedented occurrence and has been identified in previous mechanotransduction studies (Meyer *et al.*, 2011; Steward *et al.*, 2012). However, the 45 minute HP application demonstrated an up-regulatory effect in all four donor

sources. For this reason, the utilisation of a 45 minute HP duration was carried forward for the subsequent experiments within this chapter, for the 21 day HP experiments using BPC or hIVD cells. In addition, the identification of the optimised 45 minute HP duration contributed to the previous outcomes of the meta-analysis review (Chapter 5), towards the improvement of HP use in experiments for the enhancement of cartilage engineering. In continuation, the direct comparison of the static 5 minute and intermittent 5 minute HP protocol applied in the duration experiment further demonstrated that a dynamic HP approach does not significantly favour proteoglycan production relative to static applications, as was suggested in the meta-analysis review (Chapter 5).

#### 6.4.2 Experiment 2 -21 day hydrostatic pressure experiment with bovine primary chondrocytes

In the second phase of experiments within this study a 45 minute/day HP protocol was taken forward for a longer BPC culture period of 21 days and was shown to support the increase of proteoglycan production relative to control conditions, based on gene expression analysis ( $78.1\% \pm 16.1$ ), GAG content ( $71.3\% \pm 11.1$ ) and safranin O stain intensity ( $99.2\% \pm 17.2$ ) (Table.6.6).

Following one day of HP exposure a significant up-regulation of proteoglycan gene expression was observed in BPC-laden alg/MC samples relative to control samples ( $7.0\% \pm 5.0$ ,  $P = 0.04$ ), but was not supported by a significant increase in either GAG content or safranin O stain intensity. It could therefore be assumed that the early response to HP stimuli in the form of proteoglycan gene expression up-regulation, had not yet resulted in an increase in protein synthesis that was detectable by the DMMB or safranin O analysis, and suggested a need for an extended experiment length. In line with this, in both the 21 day experiments employed using either BPC (Experiment 2) or hNP cells (Experiment 3) the highest production of proteoglycan was measured at the final point of cell culture (for both GAG content and gene expression analysis). Notably, the accumulative effect of HP exposure on proteoglycan production validates the finding of the previous meta-analysis review (Chapter 5) which presented a

significant positive correlation between HP experiment length ( $\geq 2$  week) and effect size.

Furthermore, within the 21 day HP experiment with BPC cells a high cell survival was measured throughout in both the HP exposed cells and those maintained under atmospheric control conditions, with no significant difference between sample types (cell survival of  $85.9\% \pm 0.9$  and  $83.8\% \pm 1.5$  on day 21 of cell culture, for control and HP samples respectively). The high cell survival of the HP treated samples subsequently demonstrated that the cell viability was not negatively affected by the HP protocol used (6 MPa; 45 minutes; 5 days on/2 days off) and as a result the cell survival could not be instigated in the difference in proteoglycan content measured between the control and HP samples.

Similarly, the mechanical properties of the BPC-laden scaffolds monitored over the 21 day culture period demonstrated no significant difference in Young's moduli between the HP and control samples (Fig.6.10). Wherein, the consistency of the mechanical properties between sample types, alongside the cell survival results, further evidenced the non-destructive nature of HP. In addition, based on the Young's moduli results, it can be stated that a culture period longer than 21 days will be required for a measurable improvement in scaffold physical properties caused by ECM synthesis.

#### 6.4.3 Experiment 3- 21 day hydrostatic pressure experiment with human intervertebral disc cells

In the final experiment performed in this study the transition from BPCs to human IVD cell-laden bioprinting followed by HP stimulated cell culture was achieved. Within this work, a high cell survival for both hAF and hNP cells printed within alg/MC was confirmed using live/dead staining, with a survival of  $93.1\% \pm 5.5$  (hAF) and  $88.6\% \pm 5.5$  (hNP) immediately after fabrication and  $93.1\% \pm 5.5$  (hAF) and  $93.6\% \pm 2.7$  (hNP) after a 45 minute HP duration (1 MPa). Wherein, the hNP cells showed no significant decrease in survival between days 8-21 of culture. Subsequently, the results of this experiment inferred that alg/MC has a good cytocompatibility with hNP cells and was the first evidence of bioprinted hIVD cell-laden alg/MC in literature.

However, it should be stated that with regards to the hAF cells a significant decline in percent survival was observed between day 8 and 21 of cell culture, with a survival of  $65.2\% \pm 9.3$  (control) and  $72.8\% \pm 10.3$  (HP treated) on day 21. A potential reason for the difference between the IVD cell types was likely due to the high water content of the alg/MC hydrogel environment, which mimics the native NP composition. Comparatively, the ECM of an AF disc region is fibrous in nature and therefore is not well simulated by hydrogel matrices (Horner *et al.*, 2002). However, due to the high cell seeding density that was employed in this study ( $5 \times 10^6$ ), the ~20% decrease in survival observed for hAF cells by day 21 of culture meant that  $\sim 4 \times 10^6$  (per gram of material) of living cells still remained within the hAF cell-laden alg/MC samples. Moreover, the results attained on day 21 of hAF culture demonstrated that the remaining live cells were capable of an up-regulated proteoglycan production with a significant percent increase in both gene expression ( $187.4 \pm 122.4$ ) and safranin O staining ( $99.6 \pm 45.6$ ). Nonetheless, the presence of dead cells is not desirable in cell culture, whereby a greater upregulation of ECM synthesis would have been likely in hAF samples with a higher percent survival. Thus, additional investigation into improving hAF cell survival and longevity in alg/MC scaffolds should be pursued.

Furthermore, a chondrogenic phenotype was confirmed for hAF and hNP cells following 21 days of alg/MC embedded culture and was evidenced by the gene expression ratios of collagen type II: type I of 1.8: 98.2 (AF) and 0.15: 99.7 (NP). In addition, a cumulative production of proteoglycan was observed in the hIVD cell cultures which was shown to be successfully up-regulated by HP stimulation (1 MPa; 45 minutes; 5 days on/2 days off) with an increase of  $4.4\% \pm 13.2$  (hAF) and  $7.5\% \pm 8.6$  (hNP) on day 8, to an increase of  $187.4\% \pm 122.4$  and  $81.9\% \pm 26.4$  by day 21 of culture. Therefore, the outcome of this experiment effectively demonstrated that alg/MC can be used for the culture of hIVD cells, as well as evidencing the effective use of HP stimulation with hIVD cell-laden alg/MC for enhanced proteoglycan production.

## 6.5 Conclusion

The experiments in this investigation confirmed that alg/MC bioprinted scaffolds can support both a high cell survival (Fig.6.8, A-B, Fig.6.9, A, Fig.6.11, A-B) and a chondrogenic phenotype when using either BPC or hIVD cell-laden culture (Table.6.7,

Table 6.9). In particular, isolated BPC and hNP cells maintained a high percent survival of over 80% throughout the 21 culture periods employed (Experiments 2 and 3) with a high ratio of collagen type II: type I gene expression by day 21 of culture (Table.6.7, Table 6.9). In addition, it was shown that the repeated exposure of cell-laden alg/MC samples to a static HP (of 6 MPa for BPC cells and 1 MPa for hIVD cells; 45 minutes; 5 days on/2 days off) had no significant negative impact on either cell survival or scaffold physical properties relative to controls. Thus, the combination of these findings effectively demonstrated that a static HP approach used in combination with bioprinted alg/MC scaffolds was a cell compatible and non-destructive method for the culture of BPC and hIVD cells.

In addition, the application of a static 45 minute HP over a 21 day culture period was shown to significantly up-regulate proteoglycan production within both BPC and hIVD cell-laden alg/MC scaffolds (5 days on/2 days off). Wherein, the results of the 21 day BPC-laden experiment evidenced a total percent increase of proteoglycan gene expression by  $78.1\% \pm 16.1$ , with a GAG content increase of  $71.3\% \pm 11.1$  and a safranin O stain intensity increase of  $99.2\% \pm 17.2$  following HP exposure, relative to controls. While in the third experiment hNP cells exposed to HP (1 MPa; 45 minutes; 5 days on/2 days off) saw a significant increase in proteoglycan gene expression ( $81.9\% \pm 26.4$ ), GAG content ( $87.1\% \pm 7.0$ ) and safranin O stain intensity ( $112.7\% \pm 65.8$ ), relative to controls. Similarly, the use of HP exposure on hAF cell-laden alg/MC samples also had a significant influence on both proteoglycan gene expression of  $187.4\% \pm 122.4$  and safranin O stain intensity of  $99.6\% \pm 45.6$ , relative to controls. However, the effect of HP stimulation using hAF cells was significantly reduced when compared to hNP and BPC cells, and was related to a decreased cell-survival and increased variation in cell response dependent on patient source. Despite this, it can still be stated that the translation of a static 45 minute HP method, which was first applied on BPC cells, was successfully employed for the culture of hIVD cell-laden alg/MC scaffolds for the significant up-regulation of cartilaginous ECM production.

Furthermore, based on the first experiment in this investigation, an HP duration of 45 minutes was identified to be capable of significantly up-regulating proteoglycan synthesis in BPC-laden alg/MC scaffolds after 14 days of culture, assessed using both gene expression and GAG content analysis. In this preliminary experiment, a 45 minute HP protocol was shown to favour a consistent mechanotransductive response

in BPC cells relative to the other HP durations trialled of 5 minutes, dynamic 3 x 5 minutes and 4 hours. For this reason, the 45 minute duration was selected as the preferred candidate for employment in the further experimental phases. Consequently, the successful application of a 45 minute HP approach in these experiments challenges the previously popularised 4 hour duration, (which has been the most commonly used in literature) and could be used to improve the HP stimulation approach for cartilage engineering.

Thus, the work presented in this investigation effectively confirmed that the application of a 45 minute/day (5 days on/2 days off) static HP culture approach can be used as an effective and cell compatible approach for the stimulation of proteoglycan production via mechanotransduction, when used in combination with bioprinted alg/MC scaffolds with relevance to both articular and IVD cartilage tissue engineering.

## **Chapter 7 Characterisation of macromolecular composition in healthy intervertebral discs and BPC-laden alginate methyl cellulose scaffolds using quantitative magnetic resonance imaging and spectroscopy**

### 7.1 Introduction

The current use of qMRI in the field of tissue engineering and regenerative medicine has two main applications: 1) the assessment of injury/tissue sites to inform and instruct surgeons/physicians 2) to follow up on medical device implantation and integration following surgical-intervention (Shindle *et al.*, 2006; Schulz *et al.*, 2007; Weber *et al.*, 2012; Jungmann *et al.*, 2014). In this investigation a novel application of qMRI was employed to assess the feasibility of qMRI using clinically available field strengths (1.5 T or 3 T) as a method of monitoring tissue-engineered scaffold development, using parameters established on human IVDs *in vivo*.

The overall aim of a tissue-engineered scaffold is to replicate an ECM environment which mimics native tissues (Fisher and Mauck, 2013). It is therefore standard practice to monitor the internal properties of tissue-engineered constructs using methods which detect the macromolecules and proteins associated with the intended tissue type (such as histological staining, gene expression analysis and micro-assays). However, there are limited techniques available which can assess the macromolecular properties of developing tissues both quantitatively and progressively without causing a detriment to cellular processes (Kotecha, Yin and Magin, 2013). The use of qMRI in this way, has the potential as a non-invasive tool to provide insight into the microstructural progress of growing tissue (Miyata *et al.*, 2007; Li *et al.*, 2010; Irrechukwu *et al.*, 2012).

The aim of this investigation was to establish qMRI parameters which were capable of analysing the molecular compositions of both healthy human discs and tissue-engineered cartilage constructs. The use of qMRI was then applied as a tool to aid the screening of cell culture conditions (either atmospheric or using HP stimulation) for improved IVD tissue biomimicry using bioprinted chondrocyte-laden alg/MC scaffolds.

The qMRI techniques used in this study were chosen based on their sensitivity to key macromolecules known for their essential roles in IVD function and maintenance. For example, the transverse relaxation time ' $T_2$ '<sup>6</sup> was selected due to its high sensitivity to water content (Grunert *et al.*, 2015), wherein  $T_2$  is affected by the rate of movement of protons and so is sensitive to whether water within a sample is free-flowing or bound (such as within collagen protein matrices). In addition, MR spectroscopy (MRS) was employed to detect signal from hydrogen ( $^1\text{H}$ ) nuclei associated with proteoglycans at 2.04 ppm, which are essential for cartilage hydration and function (Renema *et al.*, 2007).

The novel application of qMRI for monitoring ECM development in engineered tissues offers a non-invasive method for the screening and fine-tuning of BPC-laden alg/MC scaffold fabrication and cell-culture. As well as providing a method capable of monitoring tissue-engineered scaffolds both prior to and following surgical implantation. Thus, in addition to the laboratory based molecular analysis, as was performed in Chapter 6, qMRI analysis will form an important role in the formation of a standardised protocol for cartilage tissue engineering.

## 7.2 Materials and Methods

The work in this investigation was split into two separate experiments: the first was an *in vivo* assessment of IVDs using the MR techniques  $T_2$ ,  $T_2^*$  and spectroscopy, where the repeatability and viability of the methods were studied. The second was an *in vitro* study of bioprinted alg/MC scaffolds, with and without BPC cell embedding, and used  $T_2$  and MRS. The *in vitro* work was employed to determine whether the qMRI techniques could be used with tissue-engineered hydrogel scaffolds as a method of monitoring differences in ECM development depending on the cell culture methods used for scaffold growth. Wherein, within this study the qMRI analysed scaffolds were cultured using either HP stimulation or standard atmospheric growth conditions (based on the methods developed in Chapter 6).

---

<sup>6</sup>  $T_2$  relaxation refers to the time constant which determines the rate at which excited protons reach equilibrium or go out of phase with each other. It is a measure which is influenced by tissue-particular characteristics, primarily those which affect the rate of movement of protons, most of which are found in water molecules.

### 7.2.1 In vivo quantitative MRI disc study – human volunteers

The qMRI parameters  $T_2$ ,  $T_2^*$  and MRS were established for the measurement of water and proteoglycan content within the lumbar discs of healthy human participants.

Ten healthy volunteers (5 male; 5 female, mean age 26 years, range 23-33 years) were scanned using a Siemens Avanto 1.5T imager. All participants provided written consent and the study was approved by the local research ethics committee (see Appendix D, Doc.S1D-Doc.S2D for the consent form and participant information sheet). All images were arranged in the transverse plane with the centre slice positioned in the middle of an IVD from the lumbar spine at position L3-L4 or L4-L5, whichever was visually the thickest (see Fig.7.1). The phase-encoding was assigned to the left-right direction to minimise unwanted signal artefacts caused by movement during breathing, which occurs in the anterior-posterior and head-foot dimensions (Honal *et al.*, 2010). The protocol included: a series of 2D spin echo sequences for measuring  $T_2$ , a series of 2D gradient echo sequences for measuring  $T_2^*$  (see details below in section 7.2.1.1), anatomical scans for the purpose of manual voxel placement; and single-voxel MRS as detailed in section 7.2.1.2.

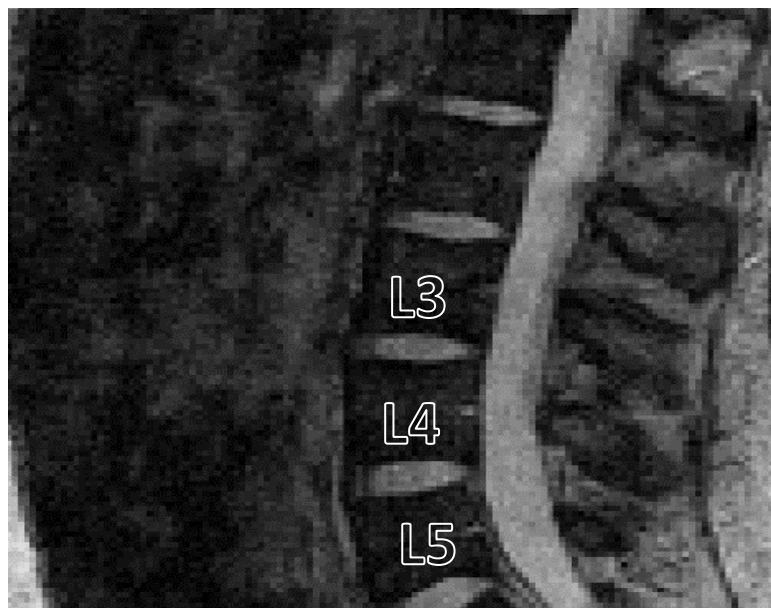


**Figure 7.1** Sagittal  $T_2$ -weighted magnetic resonance image of the lumbar spine labelled to show the level 3,4 and 5 vertebrae. The lumbar discs chosen for voxel placement in this study were located between either L3-L4 or L4-L5.

### 7.2.1.1 Transverse relaxation time $T_2$ and $T_2^*$

For the measurement of  $T_2$  a series of five separate 2D spin echo acquisitions were used, with a matrix size of 192 x 192, composed of 22 slices with voxel dimensions of 1.25 x 1.25 x 1.3cm<sup>3</sup>, repetition time (TR) of 4110 ms and echo times (TE) of 24, 36, 47, 59, 107 ms. The total acquisition time was 10 minutes.

A 3D Gradient Echo (GRE) sequence was used to measure  $T_2^*$  with acquisition parameters: matrix size = 128 x 128, slice number = 20, voxel dimensions = 1.5 x 1.5 x 1.5 cm<sup>3</sup>, TR = 100 ms and TE = 5, 10, 20, 35, 50 ms. The acquisition time for  $T_2^*$  was 13 minutes.

Analysis was performed in three main regions of interest: the whole disc (WD), the AF and the NP as shown in Fig.7.2. ImageJ software (Fiji, V1.44p) was used to manually define the disc regions from the MR images that passed through the centre of the IVD in the transverse plane (slice 11 for  $T_2$ , and slice 16 for  $T_2^*$ ). ImageJ (Fiji, V1.44p) was used to extract the mean signal values (S) for each ROI across all volumes/echo time measured. The signal is known to decay according to the equations (Boulby, 2003; Tofts and Steens, 2003):

$$\text{Equation 1} \quad S = MO \times \exp\{-TE / T_2\} \quad \text{for spin echo}$$

$$\text{Equation 2} \quad S = MO \times \exp\{-TE / T_2^*\} \quad \text{for gradient echo}$$

The relationship between signal and TE becomes linear when it is expressed logarithmically:

$$\text{Equation 3} \quad \ln(S) = \ln(MO) - TE/T_2 \quad \text{for spin echo}$$

$$\text{Equation 4} \quad \ln(S) = \ln(MO) - TE/T_2^* \quad \text{for gradient echo}$$

Plotting the  $\ln S$  vs TE gives a straight-line plot with gradient  $M = -1/T_2$  for spin echo and  $M = -1/T_2^*$  for gradient echo. Gradients were calculated from a line of best fit plotted using Microsoft Excel (see Fig.7.3).

Quantitative analysis was performed on the mean ROI values. The between-subject repeatability of values measured from the AF, NP and WD considered all 10 volunteers

and was assessed using ANOVA across all disc regions, and a paired T-test to look for statistical differences between the AF and NP regions only.

Parameter maps of  $T_2$  and  $T_2^*$  were generated using voxel-wise fitting in the AF and NP using ImageJ (Fiji, V1.44p) and the 'Fire' Lookup Table colour scheme.

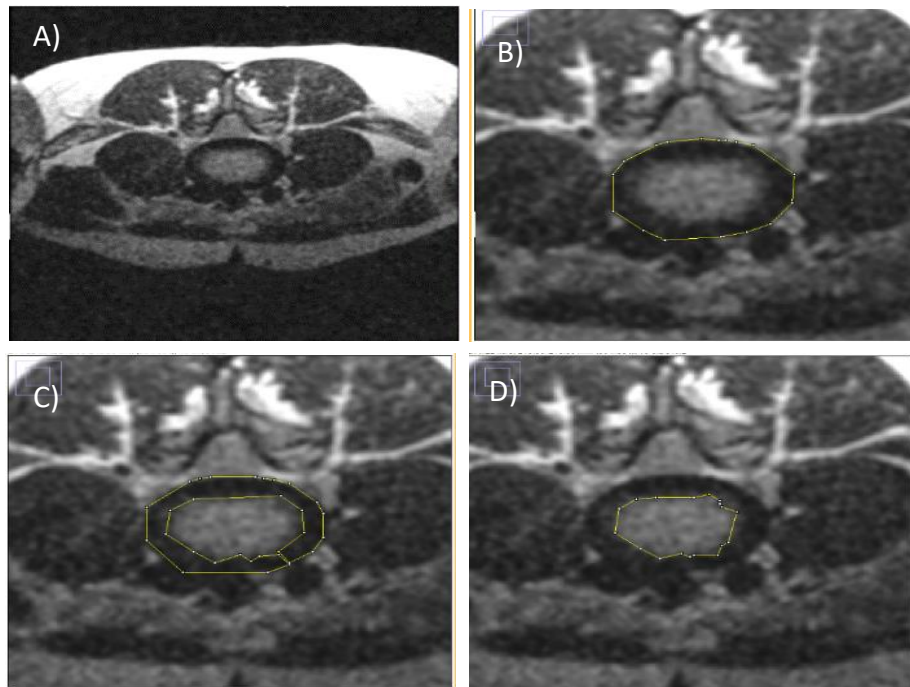


**Figure 7.2** The manual region of interest (ROI) selection process taken from the slice positioned at the centre of the IVD. Regions were defined using ImageJ software (Fiji, V1.44p). (A) Un-edited image (B) ROI of the whole disc (WD) (C) ROI drawn around the annulus fibrosus region (D) ROI of the nucleus pulposus.

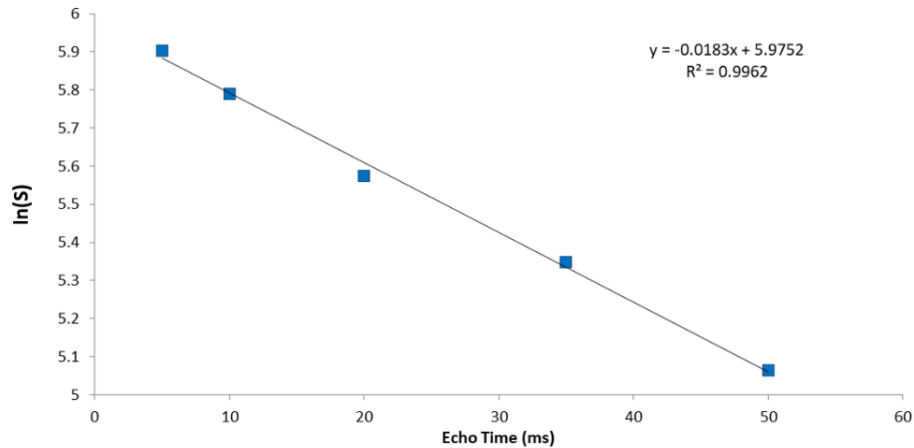


**Figure 7.3** Example linear regression plot of the Log of Signal against Echo Time, gradient used to extrapolate the  $T_2/T_2^*$  values.

#### 7.2.1.2 Quantitative spectroscopy

The  $^1\text{H}$  MRS was performed to assess proteoglycan content within the IVD using the acquisition conditions: point-resolved (single-voxel) spectroscopy (PRESS), TE = 30ms, TR = 1500ms, with 256 averages and strong water suppression. A second spectrum (the “water spectrum”) was obtained without water suppression using matching acquisition parameters, except that only 16 averages were used. The relative proteoglycan concentrations were then quantified as a ratio of the water peak in the water spectrum to the proteoglycan peak.

Ten participants were scanned as part of this study. The region-of-interest was positioned in the middle of the chosen IVD using localising scans acquired in three orthogonal planes. The selected voxel dimensions for MRS measurements were 25 x 20 x 8mm and care was taken to ensure the measured region was contained fully within the disc tissue to minimise the infiltration of signal from neighbouring vertebrae. To further limit the signal originating from surrounding tissue and vertebrae a pre-pulse of radio frequency was selectively applied to saturate signal from these areas prior to MRS data collection (Haase *et al.*, 1985; Ozhinsky, Vigneron and Nelson, 2011). This was achieved by the manual placing of saturation bands around the region of interest

(see Fig.7.4). Shimming of the localised electromagnet currents around the disc was performed manually to achieve heterogeneity in the magnetic field, to obtain the narrowest possible water peak linewidth (indicative of magnetic field homogeneity). The total acquisition time was approximately seven minutes.

The proteoglycan proteins were identified by their characteristic disaccharide 'N-acetyl regions' as based on the work by Renema *et al.*, (2007) arising at 2.04ppm. However, there is appreciable overlap between the proteoglycan resonance and the nearby peaks originating from carbohydrates and lipid. Spectra were fitted using the jMRUI processing tool with the 'Advanced Method for Accurate, Robust and Efficient Spectral fitting' (AMARES) (Fig.7.5) to identify and quantify the contribution of individual components to the spectrum, based on their differences in resonance frequencies (Zuo *et al.*, 2012).

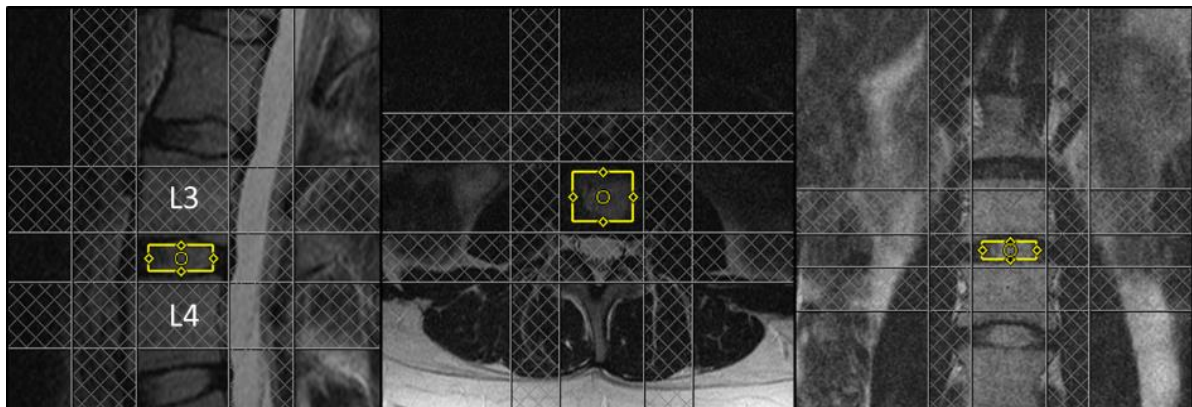


**Figure 7.4** Voxel placement shown in three orthogonal planes, in which the voxel was fully contained within the intervertebral disc between the third lumbar disc (L3) and the fourth lumbar disc (L4). The hatched lines represent the saturation bands which were placed surrounding the voxel to remove external signal.

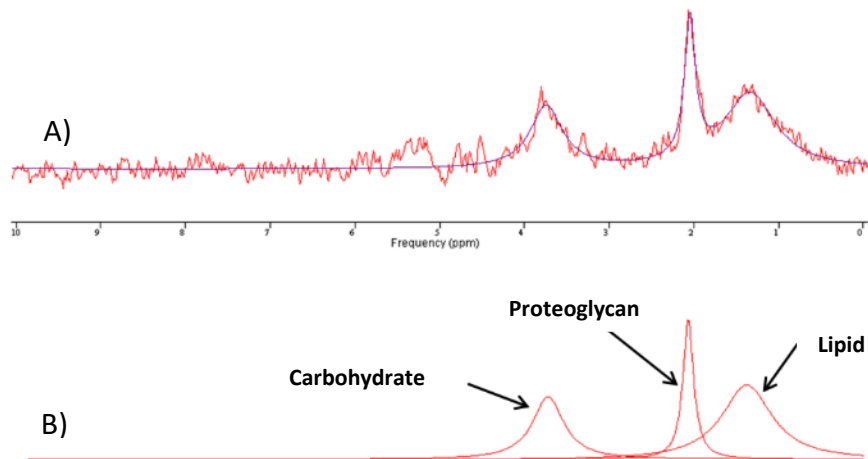


**Figure 7.5** (A) AMARES fitting of disc spectra. (B) Observable peaks including carbohydrate at 3.54 ppm, lipids and macromolecules at 1.3 ppm and the proteoglycan (N-Acetyl) peak of interest at 2.04 ppm.

### 7.2.2 Experiment 2 - *in vitro* quantitative MRI study of bioprinted scaffolds

In the second stage of experiments the qMRI parameters  $T_2$  and MRS as established on the lumbar disc of healthy human participants were translated to alg/MC scaffolds, with or without BPCs. The cell-laden scaffolds were cultured under control conditions (37°C and 5%  $CO_2$ ) or exposed to a statically applied HP protocol (45 minutes; 6 MPa; 5 days on/2 days off).

#### 7.2.2.1 Cell preparation

Primary bovine articular cartilage was isolated from bovine metacarpal phalangeal joints of skeletally mature animals (~30 months) (Hall *et al.*, 1996) as previously described in Chapter 4, section 4.2.2. Cells in passage 4 were used for bioprinting experiments.

### 7.2.2.2 Scaffold fabrication

The alg/MC bioink was prepared as previously stated in Chapter 6, section 6.2.2 with autoclave treated MC. The scaffolds were fabricated using the BioScaffolder 3.1 from GeSiM GmbH (Germany) operated under sterile conditions using the print parameters for alg/MC which were previously identified in Chapter 3, section 3.2.3 (Table.3.2). For the purposes of the qMRI investigation (to accommodate voxel placement) the scaffolds were designed with the dimensions of 12 by 12 mm, with a height of 1.4 mm per layer, comprised of 100 layers, 14 strands per layer, and an angle orientation change of 90° between the layers and printed with a tip diameter of 0.6 mm. Three scaffolds were fabricated per print session (Fig.7.6, A-B). Cells from combined sources were pooled and used for embedding, this was due to the demand of printing large volume scaffolds with a high cell seeding density ( $5 \times 10^6$  cells per gram of material). The process was then repeated three times ( $n = 3$ ). In addition, the structures were purposefully fabricated without macropores (spaces between strands). This was to prevent internal interfaces between the alg/MC material and the surrounding medium i.e. avoid trapped air bubbles which cause a disruption to the magnetic field and make qMRI measurements difficult (Shatil, Matsuda and Figley, 2016). Two scaffold variants 'cell-free' and 'cell-laden' were plotted and were fabricated and cultured under identical conditions. Immediately after print completion the hydrogel scaffolds were crosslinked with 100mM  $\text{CaCl}_2$  for ten minutes. The scaffolds were then transferred to 50ml syringes (BD Plastipak) containing 40ml of DMEM + 10% FCS culture medium (one scaffold per syringe) and capped with Luer lock 0.25-micron filters (Cole-Parmer) (Fig.7.6, A-B). The scaffolds were incubated under the standard conditions (37°C and 5%  $\text{CO}_2$ ) in culture medium for seven days. After this point the cell-laden scaffolds were divided into two categories, control and HP. For all sample types (control, HP and cell-free) the culture medium was changed every other day and all scaffolds were kept for a total culture period of 28 days.

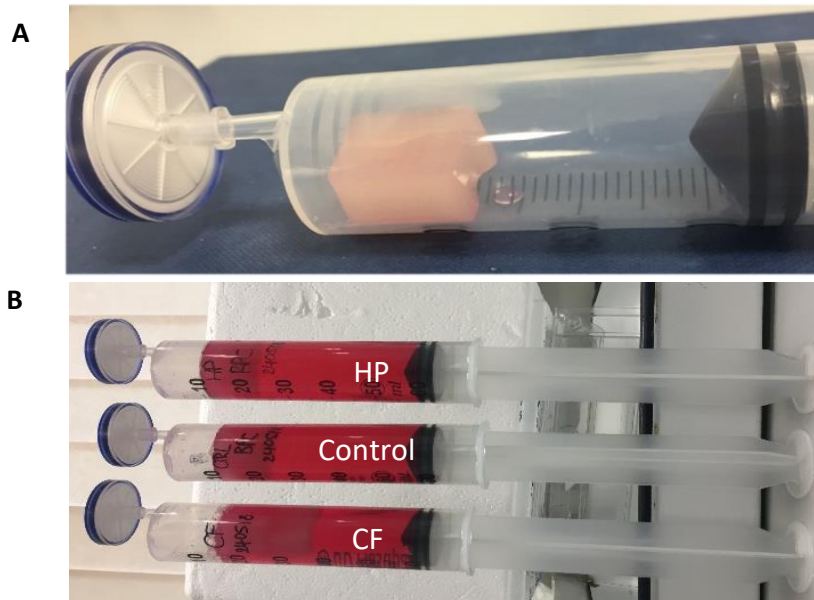


**Figure 7.6** (A) Scaffolds transferred into 50ml syringes (B) Cell-free (CF), control and hydrostatic pressure (HP) treated scaffolds were divided into separate syringes and filled with 40mls of culture medium. All syringes were capped with Luer lock 0.2-micron filters during incubation to allow for gas-exchange.

### 7.2.2.3 Hydrostatic pressure application

Prior to HP treatment the syringes were taken out of the standard atmospheric culture conditions (37°C and 5% CO<sub>2</sub>) and closed off with Luer lock caps. The HP samples were then placed into a water filled chamber inside a pressure vessel (previously described in Chapter 6, section 6.2.4.3). The HP was generated by a hand-driven pump which delivered dH<sub>2</sub>O into the vessel (Haskel MCP188, Burbank, CA, U.S.A.) and was raised from atmospheric pressure to 6 MPa over a controlled ramp up of approximately 0.04 MPa/sec, which was held for 45 minutes and subsequently depressurised (~0.04 MPa/sec). The HP was applied once a day with a protocol of 5 days on/2 days off for a total duration of 21 days. Between rounds of HP the syringes were returned to atmospheric incubation conditions alongside the control and cell-free samples, and re-capped with 0.2 micron filters.

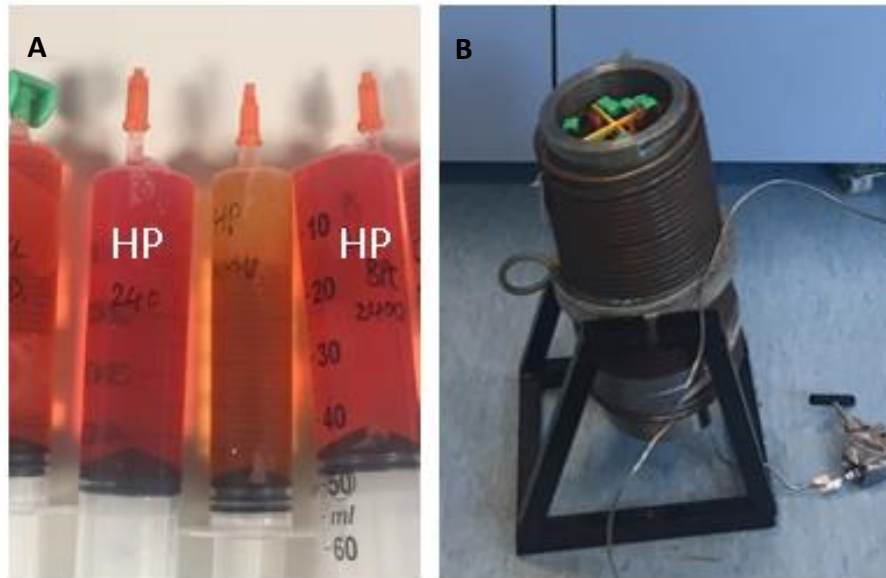


**Figure 7.7** Luer lock capped syringes containing scaffolds for hydrostatic pressurisation (HP) treatment (B) Syringes inside the pressure vessel chamber.

#### 7.2.2.4 Quantitative MRI of bioprinted alginate methyl cellulose structures

During MR imaging the scaffolds were suspended in culture medium filled and capped with Luer lock capped syringes. The syringes were then placed into a 20 channel head coil and scanned within a Siemens Avanto 3T imager (Fig.7.8, A-B). The scans were performed on days 14, 21 and 28 of cell culture. After imaging the scaffolds were returned to standard culture conditions (37°C and 5% CO<sub>2</sub>), which allowed the re-use of samples for subsequent scan sessions.

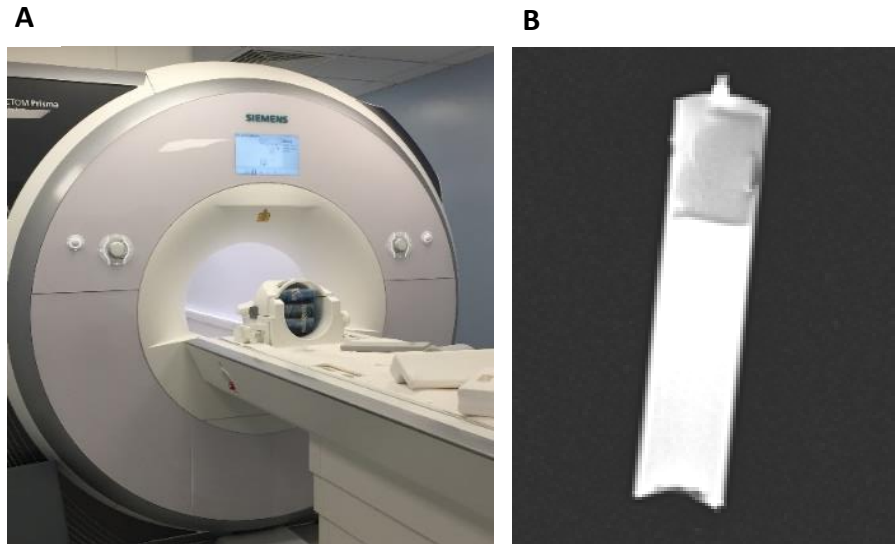


**Figure 7.8** (A) Scaffold samples entering the Siemens Avanto 3 Tesla scanner, placed inside a 20-channel receive-only head-coil (B) Localisation scan image of an alginate methyl cellulose scaffold inside a syringe.

#### Transverse relaxation time

A 2D spin echo pulse sequence was used to measure the  $T_2$  of the cell-free and cell-laden scaffolds using protocols based on the sequences used for the *in vivo* IVD experiment, with adapted acquisition parameters and echo times.

$T_2$  mapping was chosen over the use of  $T_2^*$  due to  $T_2^*$  image sensitivity to magnetic field inhomogeneities, which are caused by the different magnetic susceptibility of nearby objects (Chavhan *et al.*, 2009). In this case, the surrounding phases of air, plastic syringe, alginate and bubbles within the alginate were present and had different magnetic susceptibilities which caused extensive signal dropout and image distortion. This rendered the  $T_2^*$  data for the *in vitro* scaffolds unusable. For this reason,  $T_2$  was pursued, as the Spin Echo sequence for  $T_2$  mapping was able to refocus the  $T_2^*$  effects and gave a usable image.

$T_2$  mapping was performed on each syringe using a 2D spin echo pulse sequence with acquisition parameters: TR = 11.01 s, number of slices = 10, slice thickness = 2mm, FOV = 140 x 140mm<sup>2</sup>, matrix size = 320 x 240 interpolated to 320 x 320 to give voxel

size = 0.4 x 0.4 x 2mm<sup>3</sup> (Fig.7.9, A). Echo times of 53, 93, 253, 293 ms were used. The total acquisition time was ten minutes.

Analysis was performed on ImageJ (Fiji, V1.44p), using manually defined regions of interest determined from MR images that passed through the centre of the scaffolds in the transverse plane (Fig.7.9, B). ImageJ (Fiji, V1.44p) was used to extract the mean signal values (S) for each ROI across all echo times measured. Scaffold T<sub>2</sub> values were obtained using the protocol from section 7.2.1.2, with the use of equation 1 and a linear regression plot of Log of Signal against Echo Time.

The mean percent difference ( $\pm$  standard deviation) in T<sub>2</sub> for each sample condition (HP, control or cell-free) was calculated between days 14-21, 21-28 and 14-28 days of culture (n = 3).

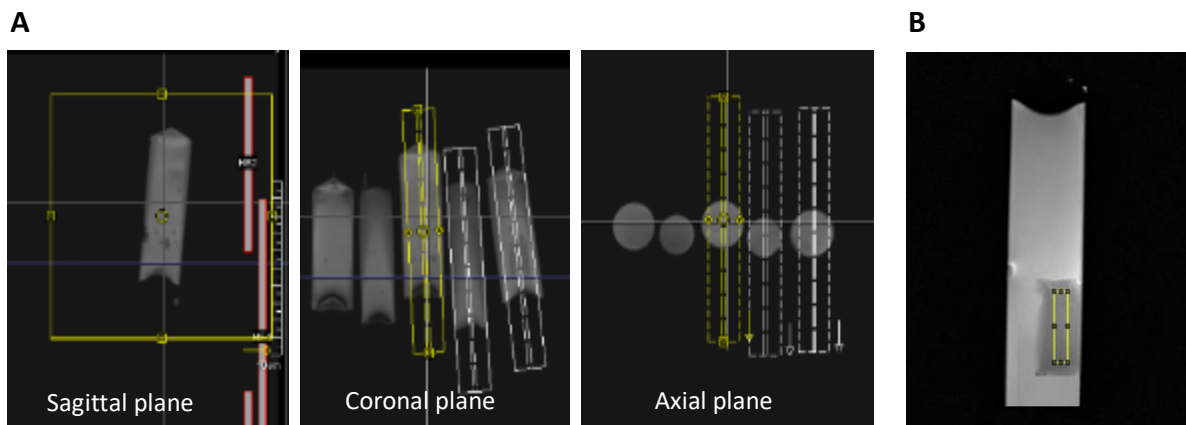


**Figure 7.9** (A) The positioning of imaging slices for T<sub>2</sub> mapping in the three imaging planes sagittal, coronal and axial, using the Siemens Avanto 3T software interface (B) Shows the positioning of the region of interest on T<sub>2</sub> scans of scaffolds using ImageJ software (Fiji, V1.44p).

### Quantitative Spectroscopy

The <sup>1</sup>H MRS method previously employed in section 7.2.1.2 on human IVDs *in vivo* was replicated for the alg/MC scaffolds, with the only alteration pertaining to voxel shape and size which was adjusted to fit the scaffold dimensions (approximately 22 x 20 x 6 mm). Scans of syringes containing culture medium alone as well as cell-free,

control and HP treated samples were run for each session. Spectral RMS noise level<sup>7</sup> for each measurement was calculated using Tarquin software analysis tool and represents an estimate of the spectral RMS noise level.

### 7.2.3 Statistical analysis

One-way ANOVA was performed on all measured data with a post hoc comparison of Bonferroni set at  $P \leq 0.05$  using IBM SPSS 24 statistical software platform® (UK).

## 7.3 Results

### 7.3.1 Experiment 1 - *in vivo* quantitative MRI of human intervertebral discs

#### 7.3.1.1 Transverse relaxation constant $T_2$ and $T_2^*$

When the  $T_2$  and  $T_2^*$  values of IVDs were compared an apparent trend was identified, with higher  $T_2$  and  $T_2^*$  measurements in the NP region and lower values in the AF (Table.7.1, Fig.7.10). A distinction between the AF and NP regionally dependent values was confirmed to be significant for the  $T_2^*$  values, across the 10 volunteers (Fig.7.10). Conversely, a difference between the mean  $T_2$  values for the AF and NP regions was not significant due to the high variation of the AF values, with a high standard deviation of  $\pm 32\text{ms}$  (Table.7.1). However, the regional dependent pattern was affirmed by a visual colour difference between the AF and NP, seen in Fig.7.11, via  $T_2$  parameter mapping.

---

<sup>7</sup> The noise level in an electronic system is typically measured as an electrical power  $N$  in a root mean square (RMS) voltage. Spectral RMS noise level is an estimate of the level of noise in the spectrum. Higher noise levels suggest higher interference or added variability to the received signal which could mask a genuine peak, especially if it has a low intensity.

**Table 7.1** Mean  $T_2$  and  $T_2^*$  relaxation parameters measured *in vivo* for the whole disc as well as the annulus fibrosus and nucleus pulposus disc regions.

Disc Region	$T_2$			$T_2^*$		
	WD	AF	NP	WD	AF	NP
<b>Mean</b>	102.4	101.2	112.9	49.1	34.3	76.5
<b>± Stdev (ms)</b>	± 13.9	± 32.2	± 13.3	± 5.6	± 4.2	± 13.8

Values are presented as the mean ± standard deviation (Stdev); n = 10. WD denotes whole disc, AF the annulus fibrosus, NP the nucleus pulposus.

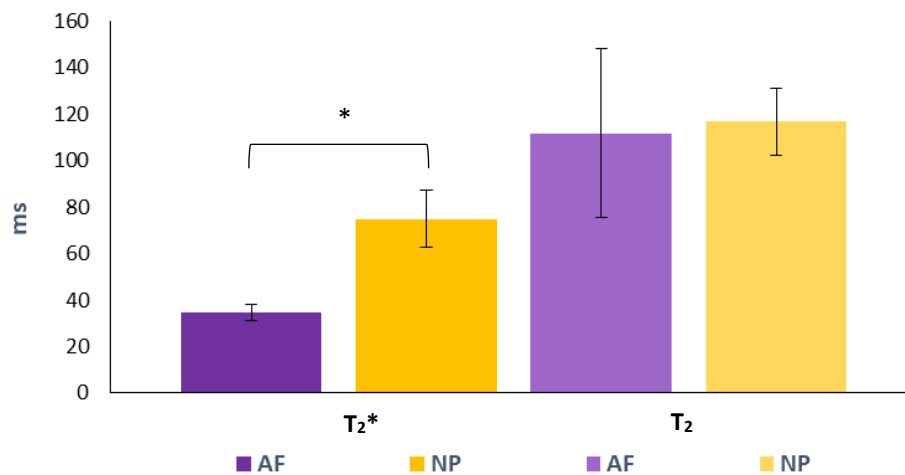


**Figure 7.10** Mean  $T_2$  and  $T_2^*$  values (ms) of the annulus fibrosus (AF) and nucleus pulposus (NP) disc regions. Error bars represent standard deviations; n=10.  $P \leq 0.05$ .

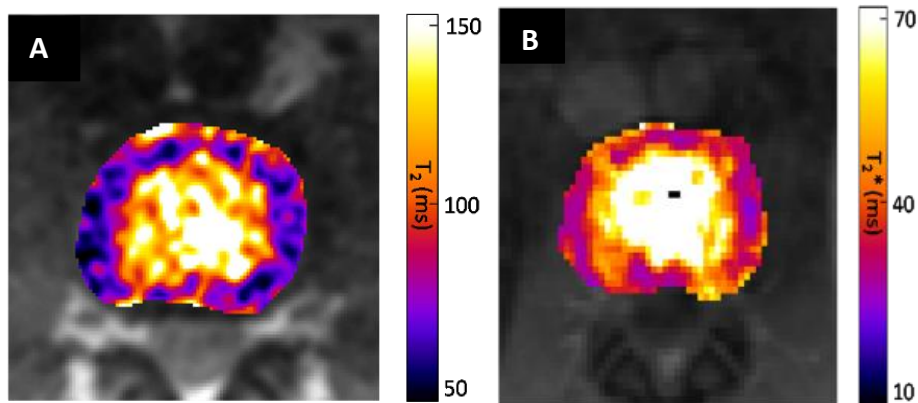


**Figure 7.11** Example parameter maps generated using ImageJ (Fiji, V1.44p) of a lumbar disc in a healthy 29 year old male participant (A)  $T_2$  and (B)  $T_2^*$ .

### 7.3.1.2 Quantitative Spectroscopy

A clear single peak from the N-acetyl resonance associated with proteoglycan (2.04ppm) was seen in all ten spectra (Fig.7.12, A) and was measured with an average relative concentration of  $301.4 \pm 61.2$  water/proteoglycan ratio (Fig.7.12, B). The quality of this measurement seemed to be of an acceptable standard for all spectra based on the line width of  $8.0 \pm 2.0$ Hz and signal-to-noise-ratio (SNR) =  $11.2 \pm 6.8$  (Fig.7.12, C). Wherein, the linewidth is indicative of the shim quality and the ability to resolve nearby peaks. A linewidth of under 10 Hz has been commonly accepted in literature as an indication of accuracy, whereby increased linewidths have been shown to directly lead to an increase in fitting inaccuracies (Kreis, 2004).

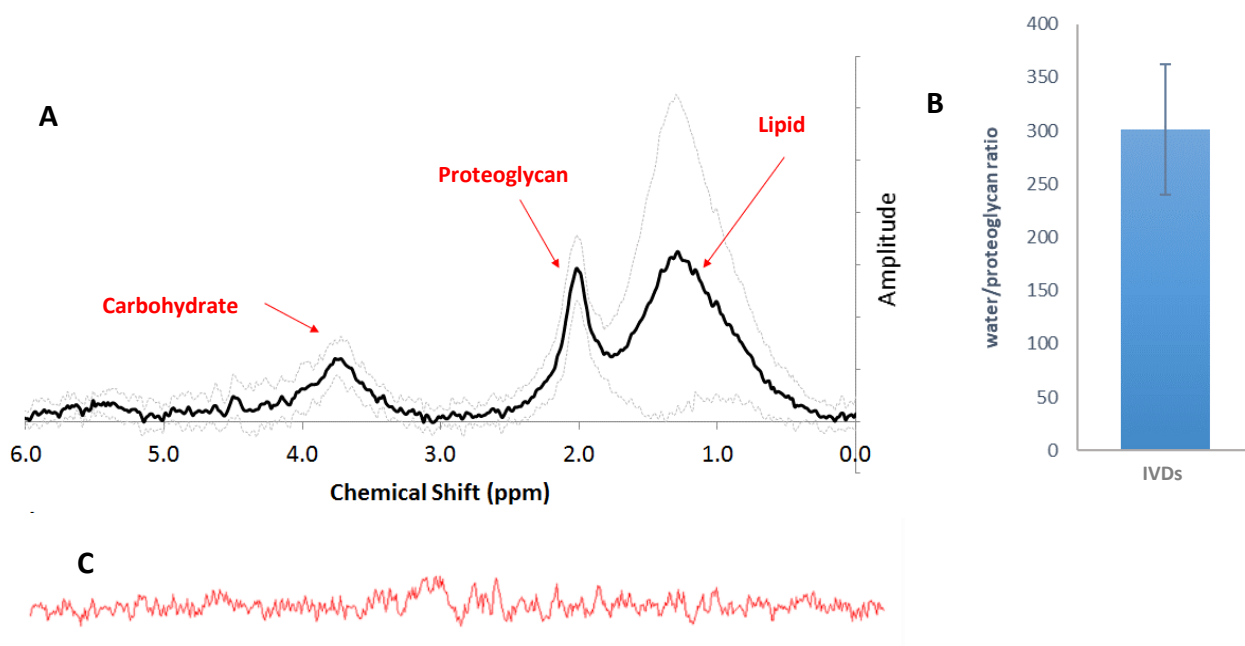


**Figure 7.12** AMARES fit to the intervertebral disc spectrum (A) The black line represents the mean spectrum of all 10 study volunteers, and the grey line is the  $\pm$  standard deviation. Notable peaks are labelled and include Carbohydrate at 3.54 ppm, Proteoglycan (N-Acetyl) peak at 2.02 ppm and a Lipids and Macromolecules peak at 1.3 ppm. (B) Mean relative proteoglycan content of  $301.4 \pm 61.2$  water/proteoglycan ratio (error bars represent standard deviation,  $n = 13$ ). (C) Mean residual background noise measured (fitted model was subtracted from the spectrum data).

### 7.3.2 Experiment 2 – *in vitro* quantitative MRI of bioprinted scaffolds

#### 7.3.2.1 Transverse relaxation constant $T_2$

The recorded mean  $T_2$  of the cell-free samples demonstrated high variation between scaffolds ( $n = 3$ ) with no significant difference observed over time (Fig.7.13). Conversely, for the cell-laden scaffolds cultured under control conditions there was a marked significant increase in  $T_2$  between days 21 and day 28 of measurement (from

249.2 ± 24.1 ms to 305.5 ± 22.2 ms, respectively). A significant difference between the mean T<sub>2</sub> values for control cells on day 14 (277.4 ± 36.9 ms) relative to the day 21 and 28 values was not apparent (Fig.7.13). For the HP treated samples a significant increase in T<sub>2</sub> was seen between each progressive timepoint, with an approximate increase of 58.7 ms on days 14-21 and an increase of ~74.5 ms between days 21-28. On day 21 the mean T<sub>2</sub> of HP samples was significantly greater than the control samples measured on the same timepoint (by approximately 71.3 ms) but was not significantly different from the cell-free measurements (Fig.7.13). In addition, the day 28 HP scaffolds demonstrated a mean T<sub>2</sub> of 395.0 ± 39.7 ms which was significantly higher than all other T<sub>2</sub> values measured, regardless of the sample type or day of measurement (Fig.7.13).

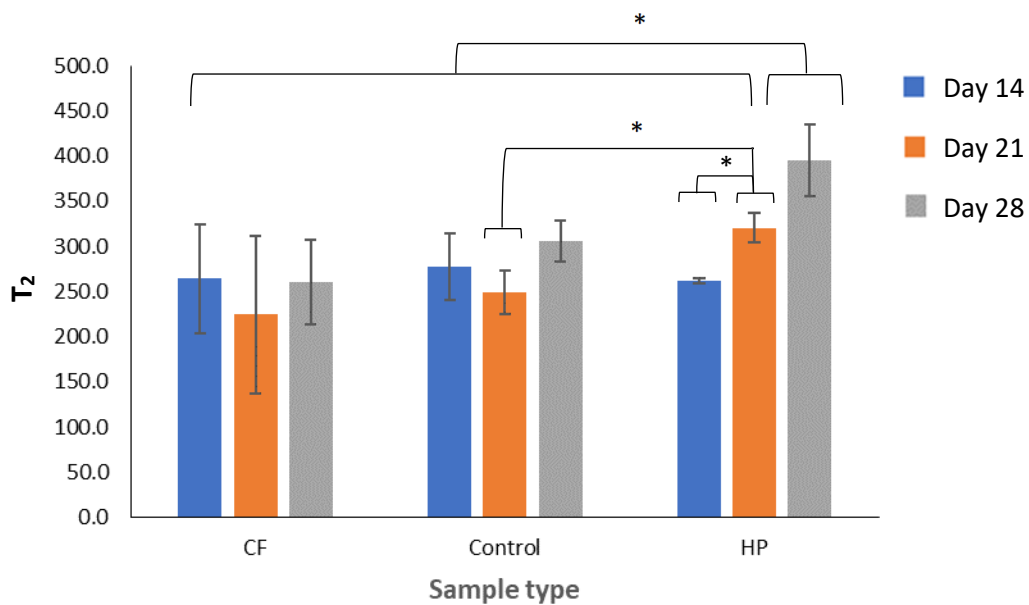


**Figure 7.13** Mean T<sub>2</sub> measurements of bovine primary chondrocyte-laden and cell-free alginate methyl cellulose scaffolds on days 14, 21 and 28 which were either subjected to daily hydrostatic pressure (HP) treatment or cultured under atmospheric control conditions, error bars represent standard deviations, (n=3). *P* ≤ 0.05.

### 7.3.2.2 Quantitative spectroscopy

A clear singlet peak from the N-acetyl resonance associated with proteoglycan (2.04ppm) was not observable in the cell-free or BPC-laden scaffolds when cultured under control conditions, on days 14, 21 or 28 (three weeks of HP) of measurement (Table.7.2). After 21 days of culture (with two weeks of HP) BPC-laden scaffolds demonstrated an apparent peak for proteoglycan (Fig.7.14, D), with an average relative concentration of 14.5 water/proteoglycan ratio and amplitude of 18.07 (Table.7.2). The samples subjected to HP after 28 days showed a visibly reduced peak at 2.04 ppm, with an average relative concentration of 6.9 water/proteoglycan ratio and amplitude of 6.51 (Fig.7.14, E), (Table.7.2). Additional full versions of the obtained spectra from the samples as well as spectra of the growth medium alone are available in Appendix D, Fig.S3D-Fig.S5D.

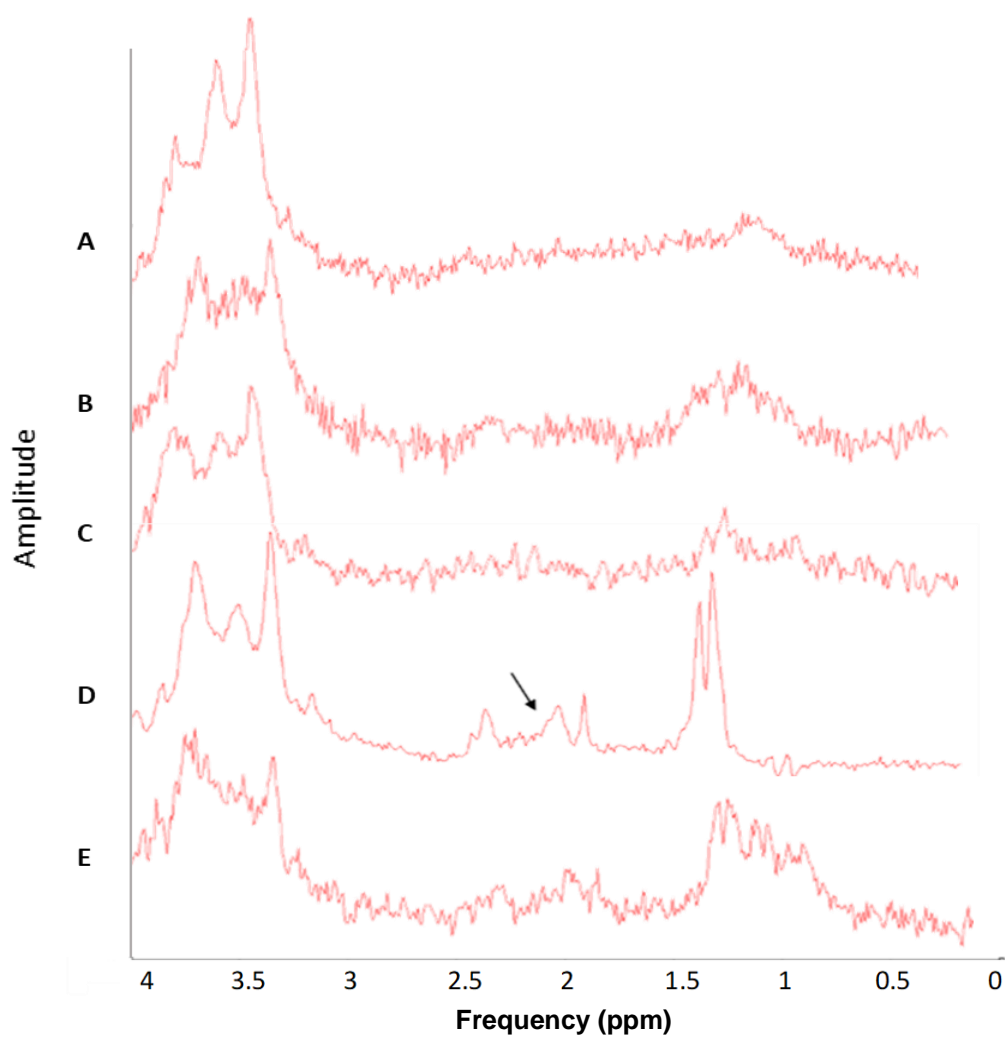


**Figure 7.14** Examples of clipped <sup>1</sup>H-spectra obtained for the alginate methyl cellulose scaffolds. (A) Cell-free scaffold after 21 days (B) Control scaffold after 21 days of culture. (C) Hydrostatic pressure (HP) treated scaffold after 14 days. (D) HP treated scaffold after 21 days. (E) HP treated scaffold after 28 days.

**Table 7.2** Values of spectral noise level measured in root mean square voltage (RMS), proteoglycan amplitude and water/proteoglycan ratio taken from the <sup>1</sup>H-spectra of cell-free and bovine primary chondrocyte laden alginate methyl cellulose scaffolds exposed to hydrostatic pressure or control conditions after 14, 21 and 28 days of cell culture conditions. All values were attained using Tarquin software.

Days	Hydrostatic pressure			Control	Cell-free
	Spectral (N <sub>rms</sub> )	Proteoglycan amplitude	Water/proteoglycan ratio	Spectral (N <sub>rms</sub> )	Spectral (N <sub>rms</sub> )
<b>14</b>	5.8	3.0	4.8	3.8	No data
<b>21</b>	2.8	18.1	14.5	2.3	1.9
<b>28</b>	2.6	6.5	6.9	3.6	1.9

Spectral (N<sub>rms</sub>) denotes Spectral RMS noise which is an estimate of the noise level (spectral RMS - which denotes root mean squared) in a system. A higher spectral RMS noise levels represents a noisier system which reduces the clarity of the spectral peaks for accurate measurement relative to the background. The values presented are single measurements, due to the absence of readable water/proteoglycan ratios within all the spectra obtained. All values were attained using Tarquin software.

## 7.4 Discussion

### 7.4.1 quantitative MRI for the investigation of human intervertebral discs *in vivo*

Upon, the application of qMR parameters for the analysis of hIVDs *in vivo* a significant pattern of increased T<sub>2</sub>\* in the NP disc regions relative to the AF was seen. The recorded T<sub>2</sub>\* subsequently followed the characteristic variation of water content across internal IVD phases, which is known to progressively increase from the fibre dense AF exterior (~60-70% water by weight) towards the water-rich nucleus centre (~77-90% by weight) (Baldit, 2018). Thus, the observed corroboration of measurements with disc physiology suggested that the employed T<sub>2</sub>\* methodology was sensitive enough to

effectively monitor changes in water content across human IVDs *in vivo*. Furthermore, the  $T_2^*$  data values obtained in the *in vivo* disc experiments from the AF and NP regions, of  $76.5 \pm 13.8$  ms and  $34.3 \pm 4.2$  ms respectively, were similar to values reported in literature with measurements of  $\sim 60$ -80 ms in the NP and  $\sim 20$ -40 ms for the AF (Hoppe, Quirbach, Marnisch *et al.*, 2012).

However, despite a similar observation with the  $T_2$  measurements, the difference between the AF and NP  $T_2$  values were not found to be significant. In addition, the recorded  $T_2$  values of  $101.2 \pm 32.2$  ms and  $112.9 \pm 13.2$  ms for the NP and AF regions respectively, were comparatively high relative to the previously published values of NP  $\sim 80$  ms and AF  $\sim 30$ -40 ms by Watanabe *et al.*, (2007). Although, it should be stated that the difference in  $T_2$  may have been influenced by the lower age range of participants in this investigation, since disc de-hydration and degeneration is linked with increased age (Menezes-Reis *et al.*, 2016).

The origin of the variability between the  $T_2^*$  and  $T_2$  measurements could be associated to the inherent sensitivity difference between the two transverse relaxation parameters. Although, both  $T_2$  and  $T_2^*$  are sensitive to water content, the  $T_2^*$  measurement is known to be more sensitive to magnetic susceptibility which is not necessarily dependent on the tissue composition (Chavhan *et al.*, 2009). Conversely,  $T_2$  is intrinsic to the sample only, with any nearby inhomogeneities within the magnetic field re-focused and corrected for by the spin echo acquisition technique (Boulby, 2003). Furthermore, due to the collagen rich laminae structure of the AF disc region, the AF composition likely affected  $T_2^*$  more than  $T_2$  and could have been the reason for the more significant change seen in  $T_2^*$ . This is due to the known trait of  $T_2^*$  being sensitive to the orientation of semisolid structures, with respect to the main field ( $B_0$ ), and so the laminar collagenous network of the AF region might have resulted in this effect (Gründer, 2006).

A continued parameter optimisation of  $T_2$  acquisition with an increase in scan averages, to suppress the effects of random variations or artefacts<sup>8</sup>, may be sufficient for reducing the  $T_2$  data variability which was seen for the hIVD measurements<sup>8</sup>. However, an increase in the number of scan averages performed would result in

---

<sup>8</sup> Increased signal averaging for a signal-to-noise (SNR) improvement is accomplished by taking the average of several MRI signals made under similar conditions to suppress the effects of random variations or random artefacts. The number of averages is also referred to as the number of excitations or the number of acquisitions.

longer scan times and is not favourable for use with patients. Alternatively, the use of an MRI with a greater magnetic field strength will increase the signal to noise ratio of MR measurements as well as the peak resolution for MRS. Subsequently, a 3 T MRI was employed in the *in vitro* phase of experiments.

Similar to the  $T_2^*$  data, the mean MRS values attained in the *in vivo* IVD experiment, were found to favourably compare with current literature, including studies which were performed using a higher field strength (3 T MRI machine by Zuo *et al.*, 2009; Zuo, *et al.*, 2012). In the disc degeneration study by Zuo *et al.*, in 2009 and 2012) values of  $299 \pm 62$  (water/proteoglycan) were measured for control participants. This data was similar to the mean relative proteoglycan content of  $301.4 \pm 61.2$  (water/proteoglycan) ratio measured in the *in vivo* disc studies presented in this investigation. Thus, this finding of proteoglycan concentration measurements using clinical 1.5 T MRI represents the first of its kind and is supported by the agreement of results with previously published data. Furthermore, based on the narrow average line width of  $8.0 \pm 2.0$  Hz and high signal to noise ratio of  $11.2 \pm 6.8$  the quality of the overall spectra was considered to be an acceptable standard (Fig.7.12, C), with a magnetic field homogeneity across the region of interest comparable to established literature (Zuo *et al.*, 2009; Zuo, *et al.*, 2012).

#### 7.4.2 Quantitative MRI for the investigation of bioprinted chondrocyte-laden scaffolds

Correspondingly in the *in vitro* experiment, which employed the use of qMRI on cell-free and BPC-laden alg/MC scaffolds, the  $T_2$  values of HP stimulated scaffolds significantly increased over the culture duration (total of 28 days) and were significantly higher than the control samples on both day 21 and 28 of culture. This outcome of increased  $T_2$  in HP exposed samples inferred that a higher water content was present in the HP stimulated scaffolds relative to controls and was potentially the result of increased proteoglycan production stimulated by mechanotransduction (demonstrated in Chapter 6). Wherein, proteoglycan is an essential ECM protein and its presence has been directly linked to tissue hydration, due to its inherent negative charge which promote osmosis (Urban *et al.*, 1979; Urban and Maroudas, 1981). For this reason, the higher water content seen in the HP treated BPC-scaffolds could correlate to a

higher proteoglycan concentration. However, it was only by day 28 of cell culture that the HP exposed scaffolds reached a mean  $T_2$  value significantly higher than the alg/MC samples without cells. Comparatively, the cell-free scaffolds which were maintained under standard cell culture conditions had a high and significantly stable water content over time, but with high variation between measurements. Furthermore, the cell-laden control samples demonstrated a mean  $T_2$  which was not significantly different from the cell-free samples at any of the time points tested. Nonetheless, the observed high  $T_2$  values reported for the alg/MC material without cells was an expected outcome, due to the high water content of the alginate hydrogel. However, the cell-free samples did not show any significant difference in  $T_2$  over time, which implied that a constant water content was maintained. Alternatively, for the HP exposed samples a significant increase in  $T_2$  was monitored over time, which suggested that a change in water content dynamics occurred.

Consequently, the lack of a significant difference in  $T_2$  measurement over time seen for the cell-free samples and cell-laden samples (on days 14,21 and 28 for cells kept under control conditions and on days 14 and 21 for HP treated cells) could be attributed to differences in alginate degradation rates. Wherein, the rate of alginate degradation in cell-free samples would have been slowed in comparison to the cell-laden scaffolds, due to a lack of enzymes and by-products produced during cell metabolism (Davison, Groot and Grijpma, 2015). Thus, the cell-free samples likely maintained their water content, with a stable  $T_2$  over time, due to a slower matrix degradation. This theory was supported by the significance of the day 28 HP exposed samples, in which a cumulative production of proteoglycan was high enough by day 28 to differentiate from the values of cell-free samples (Fig.7.14, Table.7.2). Moreover, the quantifiable change in water composition observed for the HP treated cell samples suggested that the increase in  $T_2$  and thus inferred water content, was directly linked to the use of HP exposure.

In addition, the MRS measurements of the alg/MC scaffolds effectively supported the observations demonstrated by  $T_2$  (Fig.7.14, D), whereby the significant increase in water content measured by  $T_2$  in HP treated samples after two weeks corresponded with a visible increase in proteoglycan presence (with a water/proteoglycan of 14.52 and amplitude of 18.07). Therefore, the outcomes of the MRS and  $T_2$  measurements *in vitro* reinforced the earlier finding (from Chapter 6) that mechanical stimulation using

HP causes increased proteoglycan production (and by association increased water through swelling) within BPC-laden alg/MC scaffolds. However, it was also observed within the MRS measurements that by the third week of HP culture there was a visible decrease in the proteoglycan peak relative to week two (with a water/proteoglycan of 6.9 and amplitude of 6.5) which would have been expected to increase if cumulative proteoglycan production had occurred. In connection with this outcome, the week three spectra for HP treated samples also presented peaks at ~1.3 ppm, which is associated with lactate (Harris *et al.*, 2015). This finding suggested that the embedded cells experienced a reduction in oxygen between the second and third week of incubation, in which lactate is a known by-product of anaerobic metabolism (Ohshima and Urban, 1992).

The scaffolds employed in the qMRI study were designed without internal macropore networks to remove internal interfaces (such as material and growth medium, and material with trapped bubbles of gas) which give rise to magnetic susceptibility distortions. However, the cause of the reduced ability for gas mass-transfer within the alg/MC scaffolds was likely due to the lack of macro-porosity. Furthermore, to achieve the voxel dimensions appropriate for <sup>1</sup>H-spectroscopy (approximately 10 by 10 by 14 mm) the scaffolds were designed to fit these dimensions and were much larger (14 by 14 by 14 mm) than the previously tested 12 by 12 by 3 mm cell-laden scaffolds used in Chapters 4 and 6. Thus, the combined effect of the large scaffold size and lack of macro-porosity would have impaired oxygen delivery to the embedded cells relative to the previously printed alg/MC structures (Chapters 4 and 6). In this instance, the week three samples, which had endured the longest period of reduced mass-transfer, experienced some cell death with a subsequent loss of cells capable of producing proteoglycan as well as existing proteoglycan break-down due to necrosis (Lu *et al.*, 2011; Li *et al.*, 2012). Therefore, the decrease in observable proteoglycan and the increased lactate within the HP treated samples after three weeks of encapsulation can likely be contributed to the scaffold design requirements, as opposed to an issue with progressive HP stimulation. A theory which is supported by the lactate presence within the control samples after three weeks. Thus, the magnetic distortion caused by macro-porosity is an important issue that needs to be addressed. As macro-porous structures will be a necessary feature for long-term cell survival in large scaffolds, such as those required for full disc replacement, wherein the mean disc heights in the

human spine include 11.6 +/- 1.8 mm for L3/4 discs, 11.3 +/- 2.1 mm for L4/5 discs, and 10.7 +/- 2.1 mm for the L5/S1 level discs with an average surface area of 1,492 mm<sup>2</sup> (Zhou *et al.*, 2000)

Furthermore, for the *in vitro* scaffold studies, it was not possible to collect usable T<sub>2</sub>\* mapping data, due to the extensive geometric distortions present in the gradient echo images. The distortions, which were theorised to be caused by external inhomogeneities in the magnetic field, such as the plastic surrounding the samples, were reflected by the marked increase in the T<sub>2</sub>\* spectral RMS noise level values relative to those seen for the IVD measurements *in vivo* (Table.7.2). However, the successful use of T<sub>2</sub>\* for tissue-engineered *in vitro* samples would likely give more sensitive measurements than the use of T<sub>2</sub>, based on the findings of the *in vivo* study with IVDs. In which the measured T<sub>2</sub>\* values provided a significant distinction between the AF and NP disc regions but was not observed with T<sub>2</sub> (Fig.7.10, Table.7.1). Thus, the influence of internal interfaces (caused by macropores) and external interfaces (sample container plastic) were a major hindrance in this study. Subsequently, the development of approaches which allow for both macro-porosity and *in vitro* T<sub>2</sub>\* measurement should be investigated to accommodate for the improved imaging of bioprinted scaffolds, and could be attempted through the use of bespoke sample holders (Shatil, Matsuda and Figley, 2016), sample submersion in 'MR-invisible' Fomblin (McNab *et al.*, 2009; Miller *et al.*, 2011) and the use of increased magnetic field strengths (Kraff *et al.*, 2015), which are explained in the following sections:

#### 7.4.2.1 Bespoke sample holders

A probable cause of the increased noise within the spectroscopy measurements was the presence of artefacts which originated from magnetic susceptibility differences of air, syringe plastic, liquid media and bubbles (trapped within the scaffolds). To improve this for further study, a custom designed chamber could be used, which would suspend the samples in large volumes of liquid and subsequently reduce nearby inhomogeneities by increasing the distance of the air/media interface from the samples (Shatil, Matsuda and Figley, 2016). Additionally, custom holders which can hold the samples using an MRI 'invisible' support material such as reticulated foams have also been developed and could be used to remove the interference of external interfaces (Materka, 2000). However, the use of larger vessels for sample containment during

measurement would prevent the simultaneous scanning of multiple samples, which was achieved in this study, and thus would result in longer scan durations.

#### 7.4.2.2 Sample submersion in Fomblin

A further option for consideration, would be the use of a proton-free fluid called Fomblin (a chemically inert perfluoropolyether fluorocarbon; Solvay Solexis, Inc.), (McNab *et al.*, 2009; Miller *et al.*, 2011). Fomblin is a liquid which produces no MRI signal and has a similar magnetic susceptibility to tissue (McNab *et al.*, 2009; Miller *et al.*, 2011) its use for sample submersion is therefore a widely favoured approach for *ex vivo* MR. Thus, the immersion of porous alg/MC samples in Fomblin could provide a promising solution to the issues of microporous scaffolds and magnetic distortion. However, there are several draw-backs to the use of Fomblin, including its expense (>£290 per litre), lack of availability and oil-like consistency (Shatil, Matsuda and Figley, 2016), which could influence sample properties such as hydrophobicity and subsequent nutrient exchange.

#### 7.4.2.3 High field strength MRI

An alternative approach to improve the data quality of *in vitro* measurements would be to use MR technology with an increased magnetic field or narrower bore to accommodate for small samples (Kraff *et al.*, 2015). Examples of these MRI models exist and include MRI machines employed for scanning small animals (Madularu *et al.*, 2017, Lehto *et al.*, 2018) or for the specialised observation of *ex vivo* tissue samples such as tumour explants (Schopp and Whitman, 2014). However, this technology is not widely accessible and is highly expensive to use, wherein the measurement of *in vitro* samples using clinical MRI (with 1.5 T or 3 T field strengths) would be a more optimal solution (Tanenbaum, 2006; Miyata *et al.*, 2007).

#### 7.4.3 Comparison of quantitative MRI experiments performed *in vivo* and *in vitro*

A final consideration for discussion was the difference in the qMRI values obtained from the human discs in comparison to the measurements of the neocartilage within the alg/MC scaffolds suspended in media. With regard to the T<sub>2</sub> values from both experiments it was seen that the T<sub>2</sub> measurements were significantly higher for the

BPC-laden scaffolds, with approximately a three-fold increase relative to the whole-disc values. However, for the *in vitro* samples the free liquid (growth medium) was expected to have a much longer  $T_2$  than the *in vivo* water which is bound up in the ECM of discs. Thus, the microstructural differences of the underdeveloped ECM within the alg/MC *in vitro* samples relative to the complex native disc tissue was likely the main reason for the large difference seen between the absolute  $T_2$  values reported (Lalande *et al.*, 2011). Therefore, a longer monitoring period would be recommended for achieving  $T_2$  measurements closer to native disc tissues using the BPC-laden alg/MC scaffolds. Similarly, the accumulation of proteoglycans in later-stage tissue development would likely result in a more consistent capability for proteoglycan measurement using MRS.

Furthermore, the direct comparison between the absolute  $T_2$  values of native *in vivo* tissue and *in vitro* tissue was not the main observation of this study. Instead, the principal finding of interest was the change in  $T_2$  measured *in vitro* over time within HP treated scaffolds, with a marked increase in  $T_2$  between days 14 and day 21 of cell culture, as well as the observed change in proteoglycan measured by MRS. This result could be attributed to the development of a neocartilage ECM within the alg/MC samples (Irrechukwu *et al.*, 2012; Kotecha, Yin and Magin 2013). Consequently, this outcome confirmed what was previously shown in Chapter 6, that the HP stimulated culture of chondrocytes in alg/MC has an up-regulatory effect on proteoglycan production. Thus, the observation that the *in vitro*  $T_2$  and MRS measurements of cell-laden alg/MC scaffolds were sensitive to macromolecular changes over time as well as differences in culture conditions were the foremost findings from this study. Further characterisation which allows for the direct comparison of  $T_2$  and MRS values from scaffolds and healthy IVDs will subsequently be more relevant once the scaffold is implanted *in vivo* and subjected to the same environmental conditions.

#### 7.4.4 Overall confidence in the quantitative MRI measurements obtained

In this study, changes in  $T_2$  in the *in vitro* scaffold were assumed to be due to changes in water content. However, it is important to note that the  $T_2$  parameter is not specific to water content. There are a number of factors which could affect  $T_2$  to different extents, primarily these include temperature and paramagnetic concentration (Tofts and Steens, 2003). When  $T_2$  is linked to water content changes the assumption is

made that all other conditions are unchanged in the measurements or that they would only have a minor effect compared to water content (Tofts and Steens, 2003). In the *in vitro* studies performed, it can be considered unlikely that the effects of temperature or paramagnetic concentrations influenced the  $T_2$  increase observed for HP exposed scaffolds. This is because all the alg/MC samples were scanned at a constant temperature and were suspended within the same batch of liquid growth medium. In addition, any paramagnetic species which were potentially removed from the system during regular medium change-overs would have been consistent between the control and HP exposed scaffolds and could therefore not have solely accounted for the  $T_2$  differences seen only in HP treated samples. Furthermore, if paramagnetic (chemical) species production occurred within the cell-laden samples then this would have led to a shortened  $T_2$  (higher paramagnetic concentration = lower  $T_2$ ), which was not observed. Thus, it can be fairly assumed that the increase in  $T_2$  seen for the HP treated scaffolds over time was the result of a rise in water content, and that this can be linked to the higher proteoglycan production found in the HP stimulated chondrocyte cell cultures.

## 7.5 Conclusion

In conclusion, using the qMRI methods established in this study it was feasible to obtain repeatable and representative values for the macromolecular properties of native hIVDs and tissue-engineered alg/MC constructs.

The  $T_2^*$  3D Gradient Echo (GRE) sequence employed in the *in vivo* disc experiment proved to be an effective method of measuring relative water contents within IVDs, with a statistically significant sensitivity to the characteristic water content variations between internal disc compartments. The corroboration with published data for the mean  $T_2^*$  disc values further confirmed the effectiveness of this technique. In addition, this work demonstrated the first known and successful quantification of proteoglycan concentrations via spectroscopy within human discs using a 1.5 T strength clinical MRI. Data replicability of this was evidenced by the agreement of mean values with those recorded in literature using a stronger 3 T strength MRI scanner. This outcome is a finding which would appeal to many medical centres, which due to their reduced cost relative to higher strength MR are commonly equipped with only 1.5 T MRI

machines. Therefore, measurements using a 1.5 T MRI would allow for the medical assessment of patients on more widely available equipment (Wood *et al.*, 2012).

In comparison to the  $T_2^*$  data the *in vivo*  $T_2$  measurements demonstrated a loss of statistical correlation with disc regions, which was accounted for due to the difference in parameter sensitivity. Within the  $T_2$  mapping of IVDs a basic data trend was apparent, however the values recorded were not precise enough to make a valid distinction between the disc AF and NP regions. For this reason, to enhance  $T_2$  measurement sensitivity, a 3 T strength MRI scanner was employed in the second set of experiments on the BPC-laden or cell-free alg/MC scaffolds.

The  $T_2$  values obtained in the *in vitro* scaffold experiment provided a novel insight on the macromolecular composition of BPC-alg/MC samples over the course of a 28 day culture period. A significant trend of increasing  $T_2$  was identified in cell-laden scaffolds which were subjected to HP (5 days on/ 2 days off) when compared to atmospheric controls. The trend of increased water content was linked to the stimulated production of proteoglycan in HP treated samples caused by mechanotransduction (previously identified in Chapter 6), whereby proteoglycans are responsible for the osmotic swelling in cartilage tissues (Gentili and Cancedda, 2009). The demonstrated corroboration of  $T_2$  measurements with increased proteoglycan content in HP treated samples suggested that the  $T_2$  parameters employed were sensitive enough to monitor water content changes in the developing BPC tissue samples. Furthermore, both the  $T_2$  and spectroscopy data in the *in vitro* scaffold experiment supported findings reported in Chapter 6, that the application of HP (6 MPa; 45 minutes; 5 days on/2 days off) can significantly upregulate proteoglycan production in BPC-laden alg/MC scaffolds when compared to atmospheric control culture conditions.

Future work should aim to progress the development of chondrocyte-laden alg/MC scaffolds to achieve ECM production with qMRI values closer in range to native IVD tissue, such as through the extended duration of HP stimulated culture experiments (over multiple months).

## Chapter 8 Discussion

The work contained within this thesis aimed to build upon the previous research lead primarily by Whatley *et al.*, (2011a), Whatley (2013), Rosenzweig *et al.*, (2015), van Uden *et al.*, (2015a) and Hu *et al.*, (2018) in the development of tissue engineering approaches using additive manufacturing for disc regeneration, with the specific purpose of providing a clinically feasible bioprinting method for the generation of cartilage matrices. The challenge was approached via a series of investigations, which started with the screening of various biomaterials and was subsequently followed by the characterisation of an alg/MC bioink for primary chondrocyte-laden culture. In addition, the use of HP was explored and effectively utilised as a method to improve cartilaginous ECM production in alg/MC embedded chondrocytes. In a final proof of concept, hIVD cells were bioprinted within alg/MC and cultured using HP stimulation. The principle outcomes of these investigations and their implication on the development of bioprinting for disc generation will be discussed in the following sections.

### 8.1 Bioink selection

Accurately mimicking natural ECM properties represents one of the critical barriers in tissue engineering and has been especially limiting for cell-inclusive additive manufacturing. The availability of materials suitable for both printing and cell compatibility has been a major hindrance to biomimicry, in particular for tissues with viscoelastic properties such as the IVD (Chen, Liang and Thouas, 2013). Comparatively, cell-free and commercially available fused-filament methods of 3D printing have been able to fabricate elastic structures (Reppel and Weinberg, 2018) and has been achieved via the printing of flexible filaments such as polyurethane or 'ninja-flex' (Reppel and Weinberg, 2018). Consequently, the printing of an up-scaled disc model using ninja-flex filament on a fused-filament printer (MakerBot) was exemplified in this thesis as a proof of concept model (see Appendix E, Fig.S1E, Fig.S2E). However, the melting point of synthetic ninja-flex materials (typically 210 -

225°C) is commonly above the parameter settings available on generic bioplotter devices, as well as being non-conductive to live cells. Thus, biomaterial science for biological scaffold fabrication has become a prime area of research within the field of tissue engineering. Amongst the biomaterials screened, silk fibroins and collagens have become increasingly recognised as promising materials for elastic and resilient scaffold generation (Ngiam *et al.*, 2009; Pereira *et al.*, 2013; Yin *et al.*, 2014; Frauchiger *et al.*, 2017) wherein the fibrous orientation of silk and collagens is what provides their advantageous physical features (Puppi *et al.*, 2010). Subsequently, the use of silk and collagen in tissue engineering has demonstrated promising and cell compatible outcomes in literature (Lin *et al.*, 2011; Das *et al.*, 2015). However, fibrous materials represent a specifically challenging medium for bioprinting devices (Gill *et al.*, 2018), and was a problem which was made evident in the early material screening stage of this project (Chapter 3). Wherein, during the inspection of materials for bioprinting both a fibrillated and non-fibrillar collagen paste was investigated. Consequently, the fibrous collagen was found to be ineffective for bioprinting due to the consistent clogging of the print tip, whereas the non-fibrillar collagen paste was printable following homogenisation (blending) (Table.3.2). Thus, the inherent need for smooth and shear thinning materials for bioprinting has rendered the use of collagen and silk fibril architectures unsuitable for extrusion based printing (Gill *et al.*, 2018) and as a result elastic materials for bioprinting still remain at a loss (Gopinathan and Noh, 2018). Conversely, an alternative fabrication approach which has the capability for generating scaffolds using fibrous materials is the method known as ‘electrospinning’. However, thus far, electrospinning does not permit cell inclusion and relies on a chaotic deposition of fibres for randomised pore generation, which has led to poor repeatability (Dalton *et al.*, 2013). Subsequently, attempts to combine the processes of bioprinting hydrogels with electro-spun fibres could offer a promising solution for the achievement of elastic scaffolds (Dalton *et al.*, 2013). Examples of scaffold fabrication using both bioprinting and electro spun methods have already been evidenced in literature, such as the work by Xu *et al.*, (2010) who created fibre–hydrogel composites for cortical bone as well as the studies by Hu *et al.*, (2012) who combined electro-spun PCL fibres with inkjet printed chondrocyte laden fibrin–collagen hydrogels. Thus, the combined attributes of bioprinting and electrospinning may well offer a solution for IVD scaffolding. However, the full integration and the decomposition dynamics of the different scaffold phases (Lopes, Silva and Carneiro, 2018), as well as improved

reproducibility of electro-spun networks would first need to be established before this is a clinically viable option (Dalton *et al.*, 2013).

Consequently, to tackle the aim posed in this thesis which was to achieve medically feasible cartilaginous scaffolds using bioprinting, an alternative route to the use of thermoplastics (see Appendix A for work on PCL) and fibrous materials was explored. Wherein, rather than focusing on the mechanical attributes of the materials selected for scaffold generation, a cell based approach was utilised. The intent of this research was therefore to fabricate highly cell-laden scaffolds guided by cell compatible biomaterials and 3D culture methods for the production of ECMs with properties matching native IVD tissue.

The use of scaffolds composed of living cells is a concept that has been well demonstrated in research, with established clinical trials for the regeneration of a wide variety of tissues including tracheal replacement, skin epidermis, corneal epithelial regeneration and periodontal ligament transplantation (Yang *et al.*, 2007; Murphy and Atala, 2014). However, in comparison to traditional acellular approaches the concept of cell-laden scaffolds require time (typically multiple months of cell culture) to develop a cell matrix which has the physical attributes required for implantation (Fullhase *et al.*, 2009; Murphy and Atala, 2014; Kang *et al.*, 2016). In spite of this disadvantage, cellular scaffolds have effectively demonstrated the potential to overcome the common inadequacies of acellular tissue replacements, by improving scaffold integration and restoring biological functions (Yang *et al.*, 2007). Thus, based on the promise of cellular scaffolds alongside the technological advancements of bioprinting, the potential to develop cell-laden scaffolds which can effectively mimic IVD composition was considered an attainable goal for investigation.

The early stage of bioink selection carried out in Chapter 3 reflected the start of the cell focused route of investigation within this thesis, wherein ADA-Gel, alg/MC and collagen materials were screened for bioprinting. Subsequently, the alg/MC hydrogel was identified as the most optimal material candidate, based on its ability for precise plotting and promise for cell compatibility (Ahlfeld *et al.*, 2017; Schütz *et al.*, 2017; Seidel *et al.*, 2017). The choice of alg/MC as the material for further development with cell inclusion was solely rivalled at this stage by the non-fibrous collagen paste, which demonstrated similar attributes conducive to cells, including a high-water content and

a capability for cross-linking and fabrication under mild conditions. However, despite the multiple attempts of identifying a suitable sterilisation method for the non-fibrillar collagen, no treatment was found which did not impart a negative influence on the materials processability, and thus cell inclusion could not be explored for this material type. In comparison, alginate hydrogels sterilised by autoclave have been a long established and popular cell culture approach in medical research (Leo, Mcloughlin and Malone, 1990; Lee and Mooney, 2012; Detsch *et al.*, 2015) and subsequently it was the alg/MC that was chosen to be the most suitable bioink for cell-laden scaffold fabrication.

## 8.2 Bioprinted alginate methyl cellulose scaffolds for chondrocyte culture

Alginate has been commonly referenced as an excellent material for the culture of chondrocytes, wherein the highly hydrated 3D alginate polymer matrix is similar in composition to the native cartilage ECM environment and has been demonstrated to support chondrogenesis and prevent de-differentiation (Cohen *et al.*, 2010; Duarte Campos *et al.*, 2012). However, the requirement of a constant fluid flow during extrusion bioprinting has restricted the use of alginate bioinks in additive manufacturing, whereby only low-weight alginate hydrogels have a viscosity suitable for continuous extrusion, but then subsequently exhibit poor mechanical properties upon deposition (Cohen *et al.*, 2006; Le Maitre *et al.*, 2008). To overcome this issue, the addition of a MC viscosity modifier was employed to provide the alginate with print compatible attributes. Wherein, the methyl groups of the MC component enable water storage, and thus enhance hydrogel swelling and viscosity. The use of MC ultimately presented the alginate with an increased viscosity (from  $4.71 \pm 0.09$  Pa to  $84.59 \pm 1.29$  Pa after an hour of MC addition), shear-thinning and fast crosslinking features (Schütz *et al.*, 2017). Moreover, the effective use of MC as a biomaterial thickener demonstrated potential for the assisted availability of other natural materials with innately low viscosities (e.g. fibrin, hyaluronic acid and chitosan) and is an area of high relevance for the continued development of bioprinting (Zhang *et al.*, 2018).

In previous literature, the conducive use of alg/MC for embedded cell culture has been shown using three different cell phenotypes including L929 adipose derived cells (Li

*et al.*, 2017), plant cells (Seidel *et al.*, 2017) and human mesenchymal stem cells (Schütz *et al.*, 2017; Ahlfeld *et al.*, 2017). The behaviour of cells within material carriers has been shown to vary depending on biomaterial composition and cell source, with the cells responding to differences in material properties, such as stiffness, net charge and surface topography (Ronken, 2009). However, the development of chondrocytes within alg/MC scaffolds had not yet been previously investigated. Thus, the confirmation of alg/MC as a suitable material for chondrocyte culture was an important component of this thesis and was screened using MC sterilised via autoclave, scCO<sub>2</sub>, UV or  $\gamma$ -irradiation over a 21 day culture period (Chapter 4, n = 4). Wherein, the effects of sterilisation methods on polysaccharides have been known to influence the physiochemical, cell compatibility and biological properties of biomaterials, and therefore was an imperative factor for investigation (Hugo, 1995; Buchanan *et al.*, 2012; Meyer *et al.*, 2015).

The main outcome of the MC sterilisation study (Chapter 4; Hodder *et al.*, 2019) demonstrated that both the UV and autoclave treated MC resulted in an alg/MC paste which was the most favourable for BPC cell survival and ECM production relative to scCO<sub>2</sub> sterilised MC. The preferred use of UV and autoclave was effectively evidenced by the increase in percent cell survival within the resultant alg/MC scaffolds with an increase of 27% (UV) and 23% (autoclave) compared to scCO<sub>2</sub> treated samples, as well as a 130% and 127% increase in safranin O stain coverage by day 21. In comparison, the MC treated with  $\gamma$ -irradiation resulted in an alg/MC paste was not suitable for printing. Subsequently, this work presented the potentially critical influence of sterilisation method on bioink behaviour as well as optimising the sterilisation of alg/MC for cell incorporation and clinical approval.

Thus, the use of sterile alg/MC for the fabrication of tissue-engineered scaffolds was well supported within this thesis, based on its mild preparation, amicable crosslinking, high cell compatibility and ease of application for cell-laden bioprinting. In addition, the evidenced capability of the alg/MC culture model for supporting a cartilaginous ECM effectively contributed towards the achievement of the thesis aim, which was to achieve a clinically feasible bioprinting method for the fabrication of cartilage scaffolds.

### 8.3 Hydrostatic pressure and supplement based stimulated culture of alginate methyl cellulose chondrocyte-laden scaffolds

The development of alg/MC as a material for chondrocyte culture was further pursued in Chapter 6 via the application of HP and was employed to enhance the cartilage matrix through the process of mechanotransduction (Chapter 6). A valuable contribution to the work with HP was the meta-analysis review carried out in Chapter 5. The meta-analysis chapter quantifiably compared the results of previous HP studies and was used to identify the key factors in the successful stimulation of ECM synthesis in 3D cultured chondrocytes. The main factors revealed in this review were an application of pressure within the mid-high physiological range i.e. between 5 -10 MPa for articular cartilage, a study duration of  $\geq$  two weeks and a static HP application (i.e. not intermittent or cyclic approaches). Thus, the outcomes of the meta-analysis review provided a series of findings that represented the most reliable experimental factors for achieving a significant anabolic in response to HP, a result which has not yet been covered in literature. In this way, the findings of the meta-analysis review could be readily employed to assist the development of engineered cartilage using 3D cultured chondrocytes, without the timely preliminary screening of experiment conditions. Furthermore, the relevance of the findings from the HP meta-analysis review (Chapter 5) were evidenced by the experimental work performed in Chapter 6 using within cell-laden alg/MC scaffolds. Wherein, the adoption of the recommended HP parameters, as outlined in the meta-analysis review were employed i.e. the use of a static HP within the mid-high physiological range of cartilage tissue (6 MPa for BPCs or 1 MPa for human IVDs) and an experiment duration greater than two weeks to allow for the detection of a significant mechanotransductive response. The positive outcome of HP on BPC-laden and hIVD cell-laden alg/MC cultured chondrocytes was effectively evidenced by the markedly enhanced GAG content and proteoglycan gene expression relative to atmospheric controls. In addition, the work presented in the HP experiments of Chapter 6 further verified the use of bioprinted alg/MC for the maintenance of a chondrogenic phenotype, with a high ratio of collagen type II to collagen type I relative gene expression, such as that seen in the BPC samples on day 21 of cell culture: 99.5:0.5. Furthermore, the capability of the alg/MC 3D environment to support a

chondrogenic phenotype in this thesis was demonstrated without a reliance on specialised differentiation medium.

Differentiation medium is commonly used for the directed culture of unspecialised stem cells, which have a broad capacity for differentiation (Soleimanifar *et al.*, 2019). Unlike stem cells for cartilage engineering, chondrocytes in 3D culture have a limited cell phenotype (with the exception of the potential to de-differentiate to fibroblasts). Thus, 3D chondrocyte culture can be relatively easily coerced to maintain a chondrogenic lineage (Galois *et al.*, 2006). However, despite the known phenotypic distinction between chondrocytes and stem cells, the use of chondrogenic differentiation medium has been popularised for both cell cultures within cartilage tissue engineering (Hu and Athansiou, 2006; Kawanishi *et al.*, 2007; Elder and Athanasiou, 2008).

The components and quantities of chondrogenic medium used in cartilage research have typically comprised of the following main supplements: ascorbic acid, L-proline, dexamethasone, insulin transferrin selenium and transforming growth factor- $\beta$ 3 (TGF- $\beta$ 3) (Luo and Seedhom, 2007; Elder and Athanasiou, 2008; Carroll, Buckley and Kelly, 2014). In particular, the addition of the growth factors TGF- $\beta$ 1 or - $\beta$ 3 have been found to significantly influence the success of HP on cartilaginous matrix production, and is an outcome that has been demonstrated in multiple studies (Miyaniishi, 2006; Gunja, Uthamanthil and Athanasiou, 2009). For example, in the work by Elder and Athanasiou (2008) the addition of growth factors alongside HP on primary chondrocytes in alginate demonstrated a synergistic influence, wherein a statically loaded 10 MPa combined with 30ng/ml TGF- $\beta$ 1 resulted in a significant increase for both GAG/WW% and CollagenII/WW% relative to HP alone. Thus, based on previous findings, it can be accepted that the combined use of growth factors with HP stimuli can be employed to maintain chondrogenesis and to subsequently attain an improved ECM protein production (Miyaniishi, 2006; Gunja, Uthamanthil and Athanasiou, 2009; Mahdian *et al.*, 2012). As such, it could therefore be assumed that the addition of TGF supplements to the experiments performed in Chapter 6 (HP stimulated cell culture of alg/MC scaffolds embedded with BPCs or hIVD cells) would have enhanced the proteoglycan production seen and could present a future area of investigation.

However, despite the evidence of TGFs as a promising additive to improve tissue engineering outcomes, there has been concern over the use of high TGF concentrations and their potential to cause negative and potentially life-threatening side effects in patients such as an increased cancer risk or ectopic tissue formation (Mitchell *et al.*, 2016). Furthermore, the leading issue with cellular constructs being cultured in the presence of TGFs is the potential implications following scaffold implantation (Kaplan *et al.*, 2003; Mitchell *et al.*, 2016). Wherein, the use of growth factors at the concentrations employed for cell culture are not commonly present in native cartilage, and therefore do not accurately replicate the physiological state (Fortier *et al.*, 2011). Consequently, the effects of excess growth factors *in vivo* such as the injected use of BMP-2 during lumbar spinal arthrodesis (fusion) procedures have been associated with an increased risk of cancer development (Carragee *et al.*, 2013; Wang *et al.*, 2017). The study by Carragee *et al.*, (2013) used publicly available data from an FDA approved multicentre, randomized controlled trial on patients with degenerative lumbar spine conditions who underwent a single-level spinal fusion procedure with either high-dose BMP-2 in a compression-resistant matrix (CRM) (BMP-2/CRM; n = 239) or autogenous bone graft (control group; n = 224). The outcome of this investigation demonstrated that for every 100 patients exposed to high-dose rhBMP-2 additional cancer events occurred over five years when compared with control patients. Wherein, at five years, the cumulative incidence of cancer events per 100 patients was 10.75 in the BMP-2/CRM group and 2.99 in the control group. Thus, understandably, the use of TGFs in medicine are commonly avoided or alternatively have been used at low concentrations which are carefully moderated (Carragee *et al.*, 2013).

However, despite the lack of differentiation medium used within the experiments in this thesis, the use of FCS supplementation was employed, and ultimately represented the main hindrance towards clinical feasibility within this culture model. FCS is an animal derived product which is harvested from bovine foetuses and represents the most widely used growth supplement for traditional cell culture media, which is employed to enhance cell attachment and proliferation (Cho, Lee and Kim, 2018). The characterisation of FCS batches used in cell culture has been performed by ELISAs (Lindl, 2002; Thermo Scientific, 2007) and was used to confirm the presence of the growth factors IGF-1, TGF- $\beta$ 1 and FGF-2 within the serum (Thermo Scientific, 2007).

The concentrations of TGF- $\beta$ 1 with FCS batches were shown to vary from approximately  $2.7 \pm 0.37$  to  $20.9 \pm 2.2$  ng/ml. However, similar to the direct use of growth factor supplementation, FCS is not present in the physiological environment of cartilage and furthermore due to its animal origins comes with serum-related biosafety concerns including an immune response to nonself antigens and the risk of disease transmission by pathogens (Gstraunthaler, 2003). Wherein, cases of zoonotic infections (caused by bacteria, viruses and parasites that spread between animals and humans) pose a significant threat to human health, with examples including both 'foot and mouth disease' caused by the coxsackievirus A16 virus, and 'bird flu' caused by influenza strains H5N1 and H7N9 (Tomley and Shirley, 2009).

Consequently, the use of medium without FCS supplementation for cartilage engineering would improve scaffold safety of use for clinical implementation. However, serum free cell cultures have been repeatedly shown to significantly lower the proliferative ability of cells as well as ECM production (Kato and Gospodarowicz, 1985; Lane Smith *et al.*, 1996). In the early publication by Lane Smith *et al.*, (1996) the difference between serum free and 1% FCS medium on bovine articular chondrocytes was established. The results demonstrated that following the use of 1% FCS supplemented medium an increase in both aggrecan and collagen production was observed, which over doubled what was seen in serum free cultures. Furthermore, with relevance to HP stimulation, the work by Gunja, Uthamanthil and Athanasiou (2009) investigated the effects of lowered FCS concentration on HP response. The findings of Gunja, Uthamanthil and Athanasiou (2009) subsequently showed that HP stimulated meniscus cells cultured in medium with a 1% FCS concentration resulted in a 50% decrease in both collagen and GAG deposition when compared to constructs that were grown with 10% FCS.

In summation, FCS supplements are a well-known and powerful stimulatory modulator for ECM production. However, its use for cell culture in clinical settings remains open for debate (Gstraunthaler, 2003; van der Valk *et al.*, 2018). In part, this is due to the variable differences in serum composition that have been shown between donor animals (Stein, 2007). Thus, although FCS and TGF's should ideally not be employed in tissue engineering, without these supplements *in vitro* the ECM production by cells would be reduced and would be unlikely to develop the properties required to replace native tissues. Subsequently, novel methods which reduce the reliance on TGF's or

FCS in cell culture should be investigated, such as the alternative use of human derived sera (i.e. platelet derived growth factors obtained from the patient) which have been proposed to be less likely to cause unregulated side effects, spread disease or trigger immune rejection (Gstraunthaler, 2003; Rauch *et al.*, 2011).

An additional area of investigation which could be pursued to encourage ECM development during 3D cell culture is the control of osmolarity levels. In which, osmolarity is defined as the concentration of a solution expressed as the total number of solute particles present per litre (Li *et al.*, 2016). In previous studies using NP tissue fragments and NP cells it has been shown that different osmolarity levels can diversely affect ECM gene expression and biosynthesis activity (Li *et al.*, 2016). For example, Chen *et al.*, (2002) demonstrated that the gene expression of proteoglycan within NP cells encapsulated in alginate was down-regulated in hypo-osmotic (255mOsm/kg) or hyper-osmotic (450mOsm/kg) culture conditions when compared to iso-osmotic conditions (293mOsm/kg). Similarly, in the work by Ishihara *et al.* (1997) it was reported that the proteoglycan synthesis rate within bovine NP tissue was increased by 200% when the culture medium osmolarity was raised from 280mOsm/kg to 430mOsm/kg. However, it should be stated that in both the Chen *et al.*, (2002) and Ishihara *et al.* (1997) studies the culture mediums employed, regardless of osmolarity, were supplemented with FCS and thus the anabolic response to osmolarity changes may be reliant on FCS presence. Therefore, the optimisation of osmolarity levels without FCS presence for NP cell culture should be explored as a potential alternative to TGF or FCS supplementation. Furthermore, the control of osmolarity levels for NP cell culture could be investigated in combination with both bioprinted scaffolds and HP stimuli to assess the influence of cumulative factors on the enhancement of IVD tissue generation.

#### 8.4 Translation from bovine primary cells to human intervertebral disc cells in alginate methylcellulose with hydrostatic pressure stimulated culture

The overall intention of the work performed in this thesis was the application of bioprinting for the purposes of IVD regeneration. However, the access to substantial

quantities of IVD tissue from abattoirs for research purposes is limited, wherein bovine IVD tissue carries the risk of bovine spongiform encephalopathy (BSE) contamination. Consequently, in the majority of experiments employed the use of BPC cells from metacarpal phalangeal joints were utilised, which presented an easily accessed and comparable chondrocyte cell source to IVD cells. Upon completion of the preliminary investigative work i.e. the establishment of high cell survival during bioprinting and HP stimulated culture in alg/MC, the translation to hIVD cells was implemented.

In the experiments using hIVDs the cells were isolated from either AF or NP disc regions and bioprinted within alg/MC for 3D culture which was employed using the same conditions as was used with BPC cells (DMEM +10% FCS; 37°C, 5% CO<sub>2</sub>; Chapter 4 and 6). Consequently, the results of hIVD cells within the bioplotted alg/MC scaffolds were highly promising and demonstrated both a good initial cell survival (93.1% ± 5.5 and 88.6 % ± 5.5 for AF and NP cells) as well as chondrogenic phenotype maintenance over the course of 21 days (with collagen type I: collagen type II gene expression ratios of 0.32:99.8 for AF cells and 1.1:98.9 for NP cells). Therefore, the 3D culture of hAF and hNP cells evidenced a similar cellular behaviour to the BPC-laden alg/MC samples *in vitro*.

Furthermore, upon the application of HP on the alg/MC hIVD cultures an up-regulatory response was observed by day 21 of culture, with a significant increase in both proteoglycan gene expression (187.4 ± 122.4% for AF cells and 81.9 ± 26.4% for NP cells, relative to controls) and safranin O stain intensity (99.6 ± 45.6% for AF cells and 112.7 ± 65.8% for NP cells, relative to controls). Thus, the response of hIVD cells to an HP mechanical stimuli was highly comparable to the response observed in BPC cells, wherein based on the percent change from controls no significant difference was seen between the cellular response of BPC or hIVD cells based on proteoglycan gene expression ( $P = 0.02$  for AF cells,  $P = 0.003$  for NP cells) or safranin O stain intensity ( $P = 0.0008$  for AF cells,  $P = 0.01$  for NP cells). Therefore, the use of a static HP approach over a duration of 21 days was found to be effective for the enhanced generation of ECM using both bioprinted BPC and hIVD cells. Thus, the positive outcome with hIVD cells further validated the findings of the meta-analysis review (Chapter 5), as well as supporting the use of bioprinted alg/MC as a viable culture system for the generation of neo-cartilage.

However, based on the results of the hAF cells alone it was evident that an up-regulatory effect in response to HP was not equally reliable across disc cell sources. A high variability was observed within the measurements for proteoglycan gene expression and safranin O stain intensity in relation to the hAF samples (Table.6.6), with no observable significant difference in GAG content over time ( $P = 0.09$ ). Furthermore, the alg/MC embedded hAF cells also demonstrated a significantly reduced cell survival in alg/MC by day 21 when compared to both the hNP ( $P = 0.02$ ) and BPC cells ( $P = 0.01$ ) and therefore it was inferred that alg/MC culture was less suitable for hAF cells. Consequently, similar observations of NP cells responding more favourably in hydrogel culture compared to AF derived cells has been reported in earlier literature (Horner *et al.*, 2002; Gruber *et al.*, 2004), with the reasoning that the innately soft environment of hydrogels does not effectively mimic the tough and fibrous nature of the AF disc region (Horner *et al.*, 2002).

For some years, the use of alginate as a culture system for disc cells has been used and was evidenced to maintain the phenotype of mature NP and inner AF cells (Maldonado and Oegema, 1992; Chelberg *et al.*, 1995). However, in the work by Horner *et al.*, (2002) it was suggested that bovine nucleus and outer annulus cells may require different culture systems to maintain their phenotypes, wherein alginate or agarose cultures were found to be favoured by NP cells. Comparatively, the outer AF cells did not survive well in alginate with their morphology and matrix expression significantly altered from *in vivo*. However, the morphology of the outer AF cells were also modified when they were cultured in collagen gels or in monolayer (Horner *et al.*, 2002). Subsequently, within the work by Horner *et al.*, (2002) an appropriate culture system to maintain outer AF cell morphology and matrix synthesis was not identified.

Thus, the studies by Horner *et al.*, (2002) identified a key distinction between the inner and outer annulus cells based on their production of proteoglycan, wherein the incorporation of sulfated glycosaminoglycans were always the highest for the nucleus cells and inner AF cells than for the outer AF cells (regardless of the culture method used). The production of proteoglycans in this way therefore reflected the profile seen in native discs, where proteoglycan concentrations in the NP are much greater than in the AF. Thus, the results of the Horner *et al.*, (2002) study suggested that differences in disc cell phenotype were responsible for producing and maintaining the ECM gradient of proteoglycan concentration within native discs.

Furthermore, in the investigations by Ishihara *et al.*, (1996) which applied HP to different regions of bovine caudal IVDs *in vitro*, mechanotransduction was observed in both the NP and inner AF disc sections, with proteoglycan synthesis rates within the inner AF shown to double after HP exposure. However, in the outer annulus, no significant response was seen following HP tested over a range of 1-10 MPa. The reported indifference of the outer AF cells to HP in this study were associated to the outer AF tissue regions role in pressure distribution *in vivo*, whereby due to the pump like action of disc tissue spinal loading leads to a rise in HP within the IVDs, but does not cause an increase in HP in the outer annulus (Ishihara *et al.*, 1996).

Consequently, based on the corroboration of the previous findings (Ishihara *et al.*, 1996; Horner *et al.*, 2002) with the work presented within this thesis, it is likely that the differences observed between the hNP cells and the hAF cells following HP exposure were associated to cell phenotype. Wherein, outer AF cells have been reported to have an innately lower proteoglycan production as well as a decreased HP sensitivity and lower survival in 3D culture systems than NP cells (Horner *et al.*, 2002). It is therefore also important to mention that the hAF cells used in this thesis (donated from the University Hospital of Basel) were not isolated based on their inner or outer AF placement, and thus a mixed distribution of inner and outer hAF cells would have occurred. Subsequently the mix of hAF cells used in these experiments (Chaper 6) likely influenced the cellular response to an alginate environment and the overall proteoglycan synthesis (with and without HP).

Thus, the separation of outer and inner AF cells is an approach which will likely be required for the improved hAF survival and ECM production in alg/MC, wherein alternative 3D culture methods should also be investigated for the involvement of cells from outer AF tissue. Furthermore, another experimental factor that may have affected the work in this thesis, is that the human IVD cells employed in this thesis were isolated from patient discs with reported pathology. Therefore, it is feasible that hIVD cells sourced from healthy discs could have behaved more favourably to alg/MC HP culture, due to an overall improved well-being. Evidence supporting this phenomena was found in the previously published work by Le Maitre *et al.*, (2008) which compared the response to HP in human disc cells attained from healthy sources to those isolated from degenerate IVDs. The result of this study found that cells from healthy disc sources demonstrated a significantly greater anabolic response following HP

stimulation than those from degenerate discs (Le Maitre *et al.*, 2008). Although, the influence of tissue health on human disc cell culture would be difficult to assess due to the limited availability of healthy human disc cells for research, which would need to be sourced promptly post-mortem.

### 8.5 The application of biomedical imaging for the guidance of engineered tissues

At present, artificial IVD replacements do not utilise a 'made to fit' approach, instead surgeons access implants of varying sizes and decide during surgery on which is the most suitable for the injury site (Bao *et al.*, 1996;Gloria *et al.*, 2007;Punt *et al.*, 2012). However, this method is not fool proof and has in cases been linked with implant dislodgement and migration due to bad fitting (Guterl *et al.*, 2013; Beer and Merwe, 2013; Salzmann *et al.*, 2017). In addition, when it comes to tissue engineering the generic implant method may not be practical due to the cellular cost of producing multiple scaffolds. For these reasons, the work in this thesis considered the use of clinically applicable imaging for the retrieval of IVD dimensions for personalised scaffold designs. In the print parameter screening section (Chapter 3) an IVD model was fabricated using alg/MC and based on 3D spatial information extracted from a medical scan of a patient's spine. The proof of concept disc was effectively designed with biologically representative AF and NP disc regions, which were then printed with different material cartridges simultaneously (Fig.3.15, E).

The use of customised 3D printing has already demonstrated great potential in producing functional scaffolds for biomedical applications (Chuen Wong, 2016; Honigmann *et al.*, 2018). In particular 3D modelled implants have been highly effective within the field of prosthetics (Kate, Smit and Breedveld, 2017; Young, Pierce and Zuniga, 2019) and reconstructive surgery (Payne *et al.*, 2014; Tovar *et al.*, 2018). With the use of 3D printed parts having been linked to improved integration and lowered likelihood of implant dislodgement and migration following implantation (Hunziker, 2002; Beer and Merwe, 2013; van Uden *et al.*, 2015a; Gullbrand *et al.*, 2018). Understandably therefore, the potential benefits of 3D guided implant design has also been considered for use with IVD surgery. In the work by Bowles *et al.*, (2012) the MRI and microcomputed tomography images of a rat spine were used to design anatomically customised disc implants. The implants were fabricated using injection

moulding and subsequently were implanted into the lumbar spine of rats. The reported results of this study showed both a good scaffold-vertebral body integration and disc height maintenance following surgery and was the first published evidence of how a 3D custom engineered disc can perform in a native disc space (Bowles *et al.*, 2012).

Thus, it can be predicted that with the added precision and customisability of 3D printing, alongside the broadening choices of printable biomaterials, that functional IVD scaffolds can be developed which will overcome the fitting issues linked with current artificial disc implantation (Guterl *et al.*, 2013; van Uden *et al.*, 2015a). In particular, the facilitation of multi-material printing which was evidenced in the bespoke alg/MC disc model (Fig.3.15, E.) promises to be an essential aspect for full disc tissue engineering. Wherein, the multi-material design of discs will likely be required to generate region specific disc scaffolds, with materials tailored to support the different cell types within disc tissues (Este, Eglin and Alini, 2018). As well as a potential third osteochondral based material on the external of disc scaffolds to facilitate integration with adjacent vertebral disc plates.

In addition to the MRI imaging modalities which were used for the design of disc scaffolds in Chapter 3, further MR parameters were also employed in the later studies of this thesis (Chapter 7). In these experiments MRI was used for the quantification of macromolecules within human discs and cell-laden scaffolds. In particular, the biologically significant qMRI parameters  $T_2$  (for inferring water content) and  $^1H$  MRS (for measuring proteoglycan content) were screened and subsequently identified within IVDs *in vivo* ( $T_2$  values of  $102.4 \pm 13.9$  ms and water/proteoglycan ratio measurements of  $301.4 \pm 61.2$  in whole discs) as well as in alg/MC BPC-laden scaffolds (*in vitro*) ( $T_2$  of  $322.2 \pm 18.3$  ms and a water/proteoglycan ratio of 14.5 in HP stimulated samples on day 21 of culture). In addition, the qMR techniques used were capable of monitoring changes in the cell-laden scaffold development over time as well as being able to distinguish between the culture methods used. Wherein, the HP stimulated alg/MC BPC cultures had a markedly different  $T_2$  mean value and  $^1H$  MR spectra when compared to samples which remained under atmospheric conditions, with a measurable increase in both proteoglycan and water content over time in HP exposed scaffolds (Fig.7.13, Fig.7.14, Table.7.2).

Furthermore, the successful monitoring of proteoglycan within human discs and tissue-engineered scaffolds using 1.5 T clinical strength MRS is an area that has not been previously demonstrated and evidenced a novel aspect of this work. The importance of the MRS work being achieved on a 1.5 T MRI is based on the wide availability of this scanner type, in which 1.5 T MRI are cheaper than higher strength MRI machines and thus more available in clinics (Wood *et al.*, 2012), and would therefore be more easily accessible to patients for medical assessment. In addition, the use of non-invasive clinical MRI as a method for assisting the characterisation and development of tissue-engineered scaffolds for cartilage has also been an underutilised area in literature and will likely be an essential component in the acceptance of these devices for clinical use (Kotecha *et al.*, 2013a; Kotecha, Klatt and Magin, 2013). Before implantation in patients engineered scaffolds will need to be evaluated based on their physiological characteristics to confirm their feasibility for endurance and survival post-surgery (Miyata *et al.*, 2007; Lalande *et al.*, 2011). Ideally, a method of scaffold assessment should therefore be achievable on widely available technology and without sample destruction (commonly involved in current laboratory based methods such as RT-PCR, protein assays, histology and immunohistochemistry). Consequently, the qMR screening of IVDs and cell-laden scaffolds (Chapter 7) effectively contributed towards the use of non-invasive macromolecular analysis with medically available MRI for the quantitative assessment of essential ECM components, both *in vivo* and within engineered tissues. The results of these investigations are relevant to the field of regenerative medicine for the compositional assessment of engineered cartilage matrices prior to scaffold implantation.

## 8.6 Summary

In brief, the findings of studies performed in this thesis revealed that alg/MC embedded bioprinted scaffolds can elicit a cell compatible effect on both BPC and hIVD cells, which is capable of supporting and maintaining a chondrogenic phenotype and cartilaginous tissue formation. Furthermore, for both the BPC and hIVD cell types tested in these experiments the generation of a proteoglycan rich ECM was markedly

enhanced by the application of static HP stimulation during culture and was an outcome which was confirmed using both laboratory based methods and non-invasive clinical strength qMRI. Subsequently, the results of these investigations effectively evidenced the high potential of using the combination of alg/MC bioprinting and HP stimulation for the generation of new cartilage tissue. On the other hand, the innately low proteoglycan production rate of outer AF cells was raised as a limitation within this work. Thus, further exploration on how to adequately support the cells from all three disc regions (outer AF, inner AF and NP) is recommended to continue the development of a full-disc regeneration approach for the treatment of IVD degeneration and associated disorders.

## Chapter 9 Conclusion

In conclusion the series of experiments within this thesis achieved the development, generation and characterisation of bioprinted alg/MC scaffolds for the purpose of cartilage engineering and was undertaken with consideration for medical feasibility.

The work performed in this study included the fabrication of cell-laden tissue scaffolds using alg/MC bioprinting encapsulated with BPC and hIVD cells. The use of alg/MC as a carrier for these cell types has not been previously demonstrated in literature and effectively supported chondrogenesis with a high collagen II: collagen I ratio and the accumulation of proteoglycan over time.

The screening of biomaterial sterilisation methods and their implications on MC as a compatible and printable hydrogel component was an important addition to this thesis. Wherein, bioink sterility is an essential feature for their clinical implementation. Thus, the evidenced favourable use of autoclave for MC sterilisation, based on cell compatibility and printability relative to the methods of scCO<sub>2</sub>, UV and ( $\gamma$ )-irradiation, was a key outcome and one which was used to aid the effectiveness of alg/MC for supporting chondrogenesis. Consequently, the verification of autoclaved MC as an appropriate viscosity modifier for cell culture purposes, could be used to promote the future formulation of highly sought after medically relevant bioinks.

Furthermore, the comparative and quantitative investigation of optimal HP factors for the promotion of cartilage ECM using 3D cultured chondrocytes (Chapter 5) demonstrated another significant finding of this thesis. In which, the meta-analysis of literature revealed three main factors which are likely to be key in the upregulation of proteoglycan production: a static HP application, a magnitude within the mid-high physiological range of articular cartilage ( $\leq 5$ -10 MPa) and a study duration of  $\geq$  two weeks. Thus, the findings of this work have a high applicability for the future research of HP for cartilage engineering, by providing a standardised HP approach proven to be effective for ECM generation. In addition, the successful application of the identified HP experiment factors was performed in Chapter 6, wherein a static two-week HP protocol was employed for the culture of BPC and hIVD cells within bioprinted alg/MC. The outcome of the HP cell culture experiments resulted in a significantly increased

proteoglycan production, based on gene expression analysis, GAG content measurements and histological staining. Which subsequently confirmed the relevance of the meta-analysis, as well as demonstrating the potential of bioprinted alg/MC with HP as a promising method for the enhancement of ECM formation.

The final finding of note generated by this project, was the use of medically available qMRI for internal compositional detection within IVDs and bioengineered scaffolds. In Chapter 7, the quantitative parameters of  $T_2$  and  $^1\text{H}$  MRS, which were first determined on IVDs, were shown to be directly transferrable to bioprinted cell-laden alg/MC scaffolds. In particular the use of  $^1\text{H}$  MRS demonstrated the first known evidence of accurate macromolecular measurements in IVDs *in vivo* achieved using 1.5 T field strength MR, wherein, previous studies have used higher field strengths for this purpose (Zuo *et al.*, 2012). Furthermore, the novelty of the 1.5 T approach means that proteoglycan measurement in discs could be performed on a wider range of scanners and would therefore potentially offer an easier route of access for medical assessment (Wood *et al.*, 2012). In addition, the  $T_2^*$  values obtained in the *in vivo* disc experiments were similar to values reported in literature (Hoppe *et al.*, 2012) and thus provided further confidence in the methods employed.

Despite some difficulty during data acquisition of the alg/MC scaffolds compared to the qMR measurements taken *in vivo* (with a higher noise level and greater likelihood of measurement failure) the  $T_2$  and  $^1\text{H}$  MRS values retrieved for the scaffolds were sensitive enough to determine significant differences between the control and HP sample groups. In addition, both  $T_2$  and  $^1\text{H}$  MRS were sensitive to the accumulation of water and proteoglycan in the HP treated alg/MC samples over time. Thus, qMRI was shown to be an appropriate non-invasive technique for the quantification of cartilage ECM macromolecules within the bioprinted alg/MC scaffolds. This work could be further developed to promote engineered tissues in medicine by using qMR as a non-destructive tool for the assessment of ECM composition prior to implantation.

Therefore, the research produced in this thesis stands as a proof of concept for a clinically feasible scaffold fabrication approach using hIVD cell-laden alg/MC bioprinting, alongside HP stimulation and non-invasive qMR evaluation for the enhanced generation of cartilage neo-tissue similar in composition to native IVDs.

## Chapter 10 Future research

A number of research areas could be explored to further the development of the experimental findings of this thesis, towards the goal of a clinically feasible, bioprinted scaffold for IVD regeneration. Subsequently, the main issues which were raised during this project and would therefore benefit the most from additional study included the following:

### 10.1 Biomaterial development for improved human annulus fibrosus cell compatibility

The limited availability of biomaterials suitable for cell-inclusivity and printing is a major hindrance to the advancement of bioprinted tissue-engineered scaffolds (Billiet, Vandenhaute, Schelfhout, Van Vlierberghe, *et al.*, 2012). In this thesis, it was observed that hIVD cells isolated from AF disc regions had a significantly reduced cell survival within alg/MC when compared to embedded NP disc cells or BPCs. Based on previous publications it was theorised that a reason for the reduced hAF cell viability was the hydrogel environment, in which a matrix that better mimics the fibrous nature of the AF disc region may be more suitable for the AF cell type (Chang *et al.*, 2007; Park *et al.*, 2012). However, fibrillated materials, such as collagens and silk fibroins represent a major challenge for precise bioprinting. Wherein, materials with intact fibrous architectures do not have the appropriate material attributes for printing and are unable to produce a consistent fluid flow without clogging (Murphy and Atala, 2014; Pati *et al.*, 2015). Thus, further research into materials which can mimic elastic matrices, whilst maintaining properties suitable for printing and cell compatibility are an area of priority for bioprinting. In addition, sterilisation approaches for these materials must also be determined, which was highlighted as a factor of relevance in the early material screening of this thesis (Chapter 3, section 3.3.2) as well as in Chapter 4; Hodder *et al.*, (2019).

Once a suitable bioink has been formulated to simulate the AF environment, combinatory printing with alg/MC should be tested. In which, work to establish a fully incorporated bi-phasic material structure would be performed with a particular focus on multi-material integration to prevent weakness or breakage at the material interfaces. In this proposed model, two print heads would be used, with one head

printing the alg/MC hNP cell-laden central disc region, and a second print head depositing a second material into a concentric ring like AF structure. Wherein, the AF region of the scaffold would be printed with a stiffer material component, such as a higher concentration of alg/MC or a bioink composite. Furthermore, it could be suggested that for the AF region of the bi-phasic scaffolds that hAF cells would be deposited on top of the printed structures, as opposed to encapsulated within the print material. The deposition of cells onto the scaffold during fabrication would be performed by the piezoelectric component (electrically charged print nozzle) of the GeSIM biplotter (see Fig.3.2), which would allow for the highly controlled and spatiotemporal placement of single cells (Kim JD *et al.*, 2010). The proposition of the piezoelectric hAF cell placement onto the scaffold surface instead of cell encapsulation is based on the cell phenotype of the hAF cells in an alg/MC hydrogel environment. In which, it was shown in Chapter 6 of this thesis that encapsulated alg/MC printing of hAF cells promoted a chondrogenic phenotype, as was demonstrated by the high collagen II: collagen I gene expression ratio.

However, in native IVD tissue hAF cells are fibroblastic and produce an ECM composed predominantly of collagen type I. It could therefore be suggested that hAF cells grown over the surface of a material, in a more 2D environment, would maintain their fibroblastic phenotype and produce a more relevant ECM for the generation of a matrix which mimics the AF. Furthermore, the piezoelectric deposition of the hAF cells onto a stiff material structure, which has been printed to mimic the ring like architecture of the AF, should promote cell alignment. Whereby, the pattern of the material that cells are cultured on can cause the cells to extend and spread in an orientation that follows the material architecture. The alignment of AF cell culture on a microarchitecture that mimicked the AF lamellae has been previously demonstrated in the work by Whatley (2013) and represents a method which will likely be key in the production of an AF matrix orientation that mimics the properties of native AF tissue. Thus, the result of this future study would ideally yield a multi-material scaffold capable of supporting the generation of distinct but integrated AF and NP cartilage matrices within a single scaffold, whilst maintaining both hAF and hNP cell survival and phenotype maintenance.

## 10.2 Clinical feasibility

The research presented in this thesis employed an emphasis on the clinical feasibility of the materials and methodologies used throughout. However, it was realised that current cell culture practices remain highly dependent on growth medium supplementation such as the use of FCS or TGF additives (Cho, Lee and Kim, 2018; van der Valk *et al.*, 2018). As a result of the animal derived nature of FCS and the excess levels of TGF concentrations employed, the likelihood of the clinical approval of these methods is markedly reduced (Gstraunthaler, 2003; Rauch *et al.*, 2011). Future research into cell culture approaches which can positively influence cell adhesion, growth and survival without a reliance on FCS or TGFs should therefore be investigated. Alternative routes of research include the potential use of patient derived growth serums, low level TGF supplementation, or an advanced, combinatory employment of mechanobiology and osmolarity for cell stimulation (Gstraunthaler, 2003; Morlock *et al.*, 2009; Rauch *et al.*, 2011; Li *et al.*, 2016).

A further way of demonstrating the medical feasibility of the alg/MC model developed in this thesis, would be to employ long term cell-culture experiments (multiple months) using chondrocyte-laden alg/MC to investigate cell survival, matrix development and matrix physical properties over an extended time period. In addition, *in vivo* studies within small animal models could also be envisaged as potential future research. As such, the investigation of implanted cell-laden alg/MC structures within animals would be highly indicative of their feasibility for integration and immunogenicity. Within this, qMRI could be utilised in combination with laboratory based analysis on explanted tissues for the assessment of matrix production. In addition, the explanted tissue could also be assayed for inflammatory mediators such as IL-1 and TNF- $\alpha$ , to assess for a potential immune response upon implantation.

Finally, mesenchymal stem cell (MSC) behaviour in alg/MC with and without HP stimulation could also be studied to assess alg/MC bioink's feasibility for MSC compatibility and phenotypic effect. MSC cells represent a popular cell source for IVD tissue engineering and these may provide a valid alternative in the absence of suitable IVD donors or chondrocyte sources.

### 10.3 Analysis of tissue-engineered matrix development using medical imaging

The use of accessible MRI as a tool for monitoring tissue-engineered scaffolds would offer a novel, non-invasive method for scaffold evaluation prior to implantation which is a process likely to be essential in the progression of cell-laden implants for clinical approval. However, when the 3 T strength MR was employed on alg/MC cellular scaffolds some difficulty occurred. The results of which led to noisy T<sub>2</sub> and <sup>1</sup>H MRS measurements relative to those achieved from *in vivo* IVD tissue. Primarily, the issues with this method related to the interfaces (i.e. boundaries) between phases. Examples of such issues could include trapped air within a scaffold sample in the form of bubbles or where samples are surrounded by a vessel (a plastic container), which can have a considerable influence on the MR measurement (see Chapter 7).

Thus, future efforts towards minimising the presence or influence of disturbing phase interfaces during *in vitro* scanning should be explored. The reduction of external interfaces could be achieved through the use of bespoke sample holders and can be constructed using MR 'invisible' materials to suspend samples within large volumes of liquid, to avoid external interface intrusion on measurements. However, for the concern of internal interfaces a solution is less simple. Within the investigations performed in this thesis the scaffolds for MR scanning had to be produced without internal macro-porosity as alg/MC structures with macropores produced distorted and unreadable MR scans. However, the porosity of scaffolds is considered an essential element for cell survival, since it permits nutrient and gas exchange as well as cell ingrowth (Hoffman, 2002). As a result, the lack of macropores within the alg/MC caused a reduction in cell survival within the samples, a result which was exacerbated following 14 days of culture. A method which could be employed within future work to assist this issue could be the culture of the samples without macropores within a bioreactor system to improve nutrient flow dynamics and thus cell survival (Maik and Augustinus, 2007; Mabvuure, Hindocha and Khan, 2012). However, ideally, scaffolds with highly interconnected macro-porosity should be designed and fabricated for effective tissue growth (Woodfield *et al.*, 2004), and so a qMR method that can work with macroporous structures should be sought.

The alternative approach to improve the data quality of *in vitro* measurements would be to use MR technology with an increased magnetic field or narrower bore. Examples

of these MRI models exist and could include MRI machines already employed for scanning small animals (Madularu *et al.*, 2017, Lehto *et al.*, 2018) or for the specialised observation of *ex vivo* tissue samples, primarily tumour explants (Schopp and Whitman, 2014). However, this technology is not widely accessible and is highly expensive to use. Whereas, the generation of reliable spectra from *in vitro* samples using clinical MRI (3 T field strength) would be a more optimal solution to improve the medical feasibility of qMRI as a tool for monitoring engineered tissues. Thus, research into a methodology to overcome or reduce the effects of macropores on MR distortion will be necessary to improve the use of 3 T MR for tissue-engineered scaffold development.

## References

- Abi-Hanna D, Kerferd J, Phan K, Rao P, Mobbs R (2018) 'Lumbar Disk Arthroplasty for Degenerative Disk Disease: Literature Review', *World Neurosurgery*, 109, 188–196.
- Abraham G A, Aldana A A, Malatto L, Rehman M A U, Boccaccini A R (2019) 'Fabrication of Gelatin Methacrylate (GelMA) Scaffolds with Nano- and Micro-Topographical and Morphological Features', *Nanomaterials*, 9, (120), 1-12.
- Agilent Technologies (2015) 'Agilent RNA ScreenTape Assay Quick Guide for 4200 TapeStation', 1–4.
- Aguado B A, Mulyasmita W, Su J, Lampe K J, Heilshorn S C (2011) 'Improving Viability of Stem Cells During Syringe Needle Flow Through the Design of Hydrogel Cell Carriers', *Tissue Engineering Part A*, 18 (7–8), 806–815.
- Ahlfeld T, Cidonio G, Kilian D, Duin S, Akkineni A R, Dawson J I, Yang S, Lode A, Oreffo R O C, Gelinsky M (2017) 'Development of a clay based bioink for 3D cell printing for skeletal application', *Biofabrication*, 9, (3), 034103.
- Ahmed E M (2015) 'Hydrogel: Preparation, characterization, and applications: A review', *Journal of Advanced Research*, 6 (2), 105–121.
- Aimar A, Palermo A, Innocenti B (2019) 'The Role of 3D Printing in Medical Applications: A State of the Art', *Journal of Healthcare Engineering*.
- Akella S V, Regatte R R, Gougoutas A J, Borthakur A, Shapiro E M, Kneeland J B, Leigh J S, Reddy R (2001) 'Proteoglycan-induced changes in T1 rho-relaxation of articular cartilage at 4T', *Magnetic resonance in medicine*, 46 (3), 419–423.
- Aldaadaa A, Owji N, Knowles J (2018) 'Three-dimensional Printing in Maxillofacial Surgery: Hype versus Reality', *Journal of Tissue Engineering*, 9, 1–5.
- Alger J (2010) 'Quantitative Proton Magnetic Resonance Spectroscopy and Spectroscopic Imaging of the Brain: A Didactic Review', *Topics Magnetic Resonance Imaging*, 21 (2), 115–128.
- Andersen T, Auk-Emblem P, Dornish M (2015) '3D Cell Culture in Alginate Hydrogels', *Microarrays*, 4 (2), 133–161.
- Anderson D E, Johnstone B (2017) 'Dynamic Mechanical Compression of Chondrocytes for Tissue Engineering: A Critical Review', *Frontiers in Bioengineering and Biotechnology*, 5 (Dec), 1–20.
- Andersson G B J (1998) 'What are the age-related changes in the spine?', *Bailliere's Clinical Rheumatology*, 12 (1), 161–173.
- Antoniou J, Steffen T, Nelson F, Winterbottom N, Hollander AP, Poole RA, Aebi M, Alini M (1996) 'The human lumbar intervertebral disc: Evidence for changes in the biosynthesis and denaturation of the

extracellular matrix with growth, maturation, ageing, and degeneration', *Journal of Clinical Investigation*, 98 (4), 996–1003.

Arafat M T, Gibson I, Li X (2013) 'State of the art and future direction of additive manufactured scaffolds-based bone tissue engineering', *Rapid Prototyping Journal*, 20, 13–26.

Arcaute K, Mann B, Wicker R (2010) 'Stereolithography of spatially controlled multi-material bioactive poly (ethylene glycol) scaffolds', *Acta biomaterialia*, 6 (3), 1047–54.

AufderHeide A C, Athanasiou K A (2004) 'Mechanical Stimulation Toward Tissue Engineering of the Knee Meniscus', *Annals of Biomedical Engineering*, 32 (8), 1163–1176.

Auricchio F, Marconi S (2016) '3D printing: clinical applications in orthopaedics and traumatology', *EFORT Open Reviews*, 1 (5), 121–127.

Axpe E, Oyen M L (2016) 'Applications of alginate-based bioinks in 3D bioprinting', *International Journal of Molecular Sciences*, 17 (12).

Baer A E, Wange J Y, Kraus V B, Setton L A (2001) 'Collagen gene expression and mechanical properties of intervertebral disc cell-alginate cultures', *Journal of orthopaedic research*, 19 (1), 2–10.

Balakrishnan B, Jayakrishnan A (2005) 'Self-cross-linking biopolymers as injectable in situ forming biodegradable scaffolds', *Biomaterials*, 26 (18), 3941–3951.

Baldit A (2018) 'Micromechanics of the Intervertebral Disk', *Multiscale biomechanics*, 455-467

Bao Q B, McCullen G M, Higham P, Dumbleton JH, Yuan H A (1996) 'The artificial disc: theory, design and materials', *Biomaterials*, 17 (12), 1157–1167.

Barbosa I, Garcia S, Barbier-Chassefière, Caruelle J-P, Martelly I, Papy-Garcia D (2003) 'Improved and simple micro assay for sulfated glycosaminoglycans quantification in biological extracts and its use in skin and muscle tissue studies', *Glycobiology*, 13 (9), 647–653.

Beeley J G (1985) 'Radioactive labelling techniques', *Laboratory Techniques in Biochemistry and Molecular Biology*, 365–425.

Beer N De, Merwe A Van Der (2013) 'Patient-specific intervertebral disc implants using rapid manufacturing technology', *Rapid Prototyping Journal*, 19 (May 2012), 126–139.

Belbachir K, Noreen R, Gouspillou G, Petibois C (2009) 'Collagen types analysis and differentiation by FTIR spectroscopy', *Analytical and Bioanalytical Chemistry*, 395 (3), 829–837.

Bernhardt A, Wehrl M, Paul B, Hochmuth T, Schaumacher M, Schütz K, Gelinsky M (2015) 'Improved Sterilization of Sensitive Biomaterials with Supercritical Carbon Dioxide at Low Temperature', *PLoS one*, 10 (6), 0129205.

- Best B A, Guilak F, Setton L, Zhu W, Saed-Nejad F, Ratcliffe A, Weidenbaum M (1994) 'Compressive mechanical properties of the human annulus fibrosus and their relationship to biochemical composition', *Spine*, 212–221.
- Bhardwaj N, Nguyen Q T, Chen AC, Kaplan D L, Sah R L, Kundu S C (2011) 'Potential of 3-D tissue constructs engineered from bovine chondrocytes/silk fibroin-chitosan for in vitro cartilage tissue engineering', *Biomaterials*, 32 (25), 5773–5781.
- Bhardwaj N, Devi D, Mandal B B (2015) 'Tissue-Engineered Cartilage: The Crossroads of Biomaterials, Cells and Stimulating Factors', *Macromolecular Bioscience*, 153–182.
- Bianco P, Riminucci M, Gronthos S, Robey P G (2001) 'Bone Marrow Stromal Stem Cells: Nature, Biology, and Potential Applications', *Stem Cells*, 19, 180–192.
- Billiet T, Vandenhoute M, Schelfhout J, Van Vlierberghe S (2012) 'A review of trends and limitations in hydrogel-rapid prototyping for tissue engineering', *Biomaterials*, 33 (26), 6020–6041.
- Bittersohl B, Hosalkar H S, Miese F R, Schibensky J, König D P, Herten M, Antoch G, Krauspe R, Zilkens C (2015) 'Zonal T2\* and T1Gd assessment of knee joint cartilage in various histological grades of cartilage degeneration: an observational in vitro study', *BMJ open*, 5 (2), e006895.
- Bono C M, Garfin S R. 'History and evolution of disc replacement', *The spine journal: official journal of the North American Spine Society*, 4 (6 Suppl), 145S-150S.
- Bouhadir K H, Lee K Y, Alsberg E, Damm K L, Anderson K W, Mooney D J (2001) 'Degradation of partially oxidized alginate and its potential application for tissue engineering', *Biotechnology Progress*, 17 (5), 945–950.
- Boulby P (2003) 'Chapter 6 T<sub>2</sub>: the transverse relaxation time, Quantitative MRI of the brain: measuring changes caused by disease', 141-199.
- Bowles R D, Gebhard H H, Dyke J P, Ballon D J, Tomasino A, Cunningham M E, Härtl R, Bonassar L J (2012) 'Image-based tissue engineering of a total intervertebral disc implant for restoration of function to the rat lumbar spine', *NMR in Biomedicine*, 25 (3), 443–451.
- Brockbank, K G M (2013) 'Tissue Engineering Constructs and Commercialization' *Madame Curie Bioscience Database* [Internet] 05/12/2018, <https://www.ncbi.nlm.nih.gov/books/NBK6008/>.
- Van den Broeck J, Vereecke E, Wirex-Speetjens R, Vander Sloten J (2014) 'Segmentation accuracy of long bones', *Medical Engineering and Physics*, 36 (7), 949–953.
- Brown W E, Hu J C (2015) 'Harnessing Biomechanics to Develop Cartilage Regeneration Strategies', *Journal of Biomechanical Engineering*, 137.
- Bryant S J, Anseth K S (2002) 'Hydrogel properties influence ECM production by chondrocytes photoencapsulated in poly (ethylene glycol) hydrogels', *Journal of Biomedical Material Research*

BTRI Life Sciences (2015) 'Quantification of Live/Dead Staining Using Fiji Software Analyze' [Internet] 21/02/2016, www.BRTILifeSciences.com.

Camacho N, West P, Torzilli P A, Mendelsohn R (2000) 'FTIR Microscopic Imaging of Collagen and Proteoglycan in Bovine Cartilage', *Biopolymers*, 62, 1–8.

Candiani G, Raimondi M T, Aurora R, Laganà K, Dubini G (2008) 'Chondrocyte response to high regimens of cyclic hydrostatic pressure in 3-dimensional engineered constructs', *International Journal of Artificial Organs*, 31 (6), 490–499.

Carragee E J, Chu G, Rohatgi R, Hurwitz E L, Weiner B K, Yoon S T, Comer G, Kopjar B (2013) 'Cancer Risk After Use of Recombinant Bone', *Journal of Bone and Joint Surgery*, 95 (17), 1537–1545.

Carroll S F, Buckley C T, Kelly D J (2014) 'Cyclic hydrostatic pressure promotes a stable cartilage phenotype and enhances the functional development of cartilaginous grafts engineered using multipotent stromal cells isolated from bone marrow and infrapatellar fat pad', *Journal of Biomechanics*, 47 (9), 2115–2121.

Carroll S F, Buckley C T, Kelly D J (2014) 'Cyclic hydrostatic pressure promotes a stable cartilage phenotype and enhances the functional development of cartilaginous grafts engineered using multipotent stromal cells isolated from bone marrow and infrapatellar fat pad', *Journal of Biomechanics*.

Carvalho C, Landers R, Mülhaupt R (2004) 'Soft and hard implant fabrication using 3D-Bioplotting', *Solid Freeform Fabrication Proceedings*, 732–741.

Chae M P, Rozen W M, McMenamin P G, Findlay M W, Spychal R T, Hunter-Smith D J (2015) Emerging Applications of Bedside 3D Printing in Plastic Surgery', *Frontiers in Surgery*, 2 (June), 1–14.

Chan B P, Leong K W (2008) 'Scaffolding in tissue engineering: general approaches and tissue-specific considerations', *European spine journal*, 17 (Suppl 4), 467–79.

Chang G, Kim H J, Kaplan D, Vunjak-Novakovic G, Kandel R A (2007) 'Porous silk scaffolds can be used for tissue engineering annulus fibrosus', *European Spine Journal*, 16 (11), 1848–1857.

Chang N J, Jhung Y R, Yao C K, Yeh M L (2012) 'Hydrophilic gelatin and hyaluronic acid-treated PLGA scaffolds for cartilage tissue engineering', *Journal of Applied Biomaterials & Biomechanics*, 11 (1), 45-52.

Chavhan G B, Babyn P S, Thomas B, Shroff M M, Haacke E M (2009) 'Principles, techniques, and applications of T2\*-based MR imaging and its special applications', *Radiographics*, 29 (5), 1433–1449.

Cheheltani R, Rosano J M, Wang B, Sabri A K, Pleshko N, Kiani M F (2012) 'Fourier transform infrared spectroscopic infarction collagen deposition after myocardial imaging of cardiac tissue to detect', *Journal of biomedical optics*, 17 (5), 1–9.

Chelberg M K, Banks G M, Geiger D F, Oegema T R (1995) 'Identification of heterogeneous cell populations in normal human intervertebral disc', *Journal of anatomy*, 186 (Pt1), 43-53.

- Cheleschi S, Palma A D, Pecorelli A, Pascarelli N A, Valacchi G, Belmonte G, Carta S, Galeazzi M, Fioravanti A (2017) 'Hydrostatic pressure regulates MicroRNA expression levels in osteoarthritic chondrocyte cultures via the Wnt/ $\beta$ -catenin pathway', *International Journal of Molecular Sciences*, 18 (1).
- Chen J, Baer A E, Paik P Y (2002) 'Matrix protein gene expression in intervertebral disc cells subjected to altered osmolarity' *Biochemical and Biophysical Research*, 293, 932–938.
- Chen J, Yuan Z, Liu Y, Zheng R, Dai Y, Tao R, Xia H, Liu H, Zhang Z, Zhang W, Liu W, Cao Y, Zhou G (2017) 'Improvement of In Vitro Three-Dimensional Cartilage Regeneration by a Novel Hydrostatic Pressure Bioreactor', *Stem Cells Translational Medicine*, 6 (3), 982-991.
- Chen C, Tambe DT, Deng L, Yang L (2013) 'Biomechanical properties and mechanobiology of the articular chondrocyte', *American Journal of Physiology*, 305 (15), 1202–1208.
- Chen J E, Glover G H (2016) 'Functional Magnetic Resonance Imaging Methods', *Neuropsychological Review*, 25(3), 289–313.
- Chen Q, Liang S, Thouas G (2013) 'Elastomeric biomaterials for tissue engineering', *Progress in Polymer Science*, 38 (3–4), 584–671.
- Chen X, Fan H, Deng X, Wu L, Yi T, Gu L, Zhou C, Fan Y, Zhang X (2018) 'Scaffold Structural Microenvironmental Cues to Guide Tissue Regeneration in Bone Tissue Applications', *Nanomaterials*, 8 (11).
- Cheng H L M, Loai Y, Farhat W A (2012) 'Monitoring tissue development in acellular matrix-based regeneration for bladder tissue engineering: Multiexponential diffusion and T2\* for improved specificity', *NMR in Biomedicine*, 25 (3), 418–426.
- Chia H N, Wu B M (2015) 'Recent advances in 3D printing of biomaterials', *Journal of Biological Engineering*, 9 (1).
- Cho H, Lee A, Kim K (2018) 'The effect of serum types on Chondrogenic differentiation of adipose-derived stem cells', *Biomaterials Research*, 22 (1), 1–10.
- Choi J R, Yong K W, Choi J Y (2018) 'Effects of mechanical loading on human mesenchymal stem cells for cartilage tissue engineering', *Journal of Cellular Physiology*, 233 (3), 1913–1928.
- Choy A T H, Chan B P (2015) 'A Structurally and Functionally Biomimetic Biphasic Scaffold for Intervertebral Disc Tissue Engineering', *Plos One*, 10 (6).
- Chuen Wong K (2016) '3D-printed patient-specific applications in orthopedics', *Orthopedic research and reviews*, (8), 57–66.
- De Ciurana J, Serenó L, Vallès È (2013) 'Selecting process parameters in RepRap additive manufacturing system for PLA scaffolds manufacture', *Procedia CIRP*, 5, 152–157.

- Clements K M, Bee Z C, Crossingham G V, Adams M A, Sharif M (2001) 'How severe must repetitive loading be to kill chondrocytes in articular cartilage?', *Osteoarthritis and Cartilage*, 9 (5), 499–507.
- Cohen D L, Malone E, Lipson H, Bonassar L J (2006) 'Direct Freeform Fabrication of Seeded Hydrogels in Arbitrary Geometries', *Tissue Engineering*, 12 (5), 1325–1335.
- Cohen D L, Lipton J I, Bonassar L J, Lipson H (2010) 'Additive manufacturing for in situ repair of osteochondral defects', *Biofabrication*, 2 (3).
- Collier J P, Sperling D K, Currier J H, Sutula L C, Saum K A, Mayor M B (1996) 'Impact of gamma sterilization on clinical performance of polyethylene in the knee', *Journal of Arthroplasty*, 11 (4), 377–389.
- Completo A, Bandejas C, Fonseca F (2017) 'Comparative assessment of intrinsic mechanical stimuli on knee cartilage and compressed agarose constructs', *Medical Engineering and Physics*, 44, 87–93.
- Conzen A, Eckstein F (2000) 'Quantitative determination of articular pressure in the human shoulder joint', *Journal of Shoulder Elbow Surgery*, 9 (3), 196–204.
- Correia C, Pereira A L, Duarte A R, Frias A M, Pedro A J, Oliveira J T, Sousa R A, Reis R L (2012) 'Dynamic Culturing of Cartilage Tissue: The Significance of Hydrostatic Pressure', *Tissue Engineering Part A*, 18 (19-20), 1979-1991.
- Crema M D, Roemer F W, Marra M D, Burstein D, Gold G E, Eckstein F, Baum T, Mosher T J, Carrino J A, Guermazi A (2011) 'Articular cartilage in the knee: current MR imaging techniques and applications in clinical practice and research', *Radiographics: a review publication of the Radiological Society of North America*, 31 (1), 37–61.
- Crenshaw H C, Allen J A, Skeen V, Harris A, Salmon E D (1996) 'Hydrostatic pressure has different effects on the assembly of tubulin, actin, myosin II, vinculin, talin, vimentin, and cytokeratin in mammalian tissue cells', *Experimental Cell Research*, 227 (2), 285–297.
- Cui H, Nowicki M, Fisher J P, Zhang L G (2017) '3D Bioprinting for Organ Regeneration', *Advanced Healthcare Materials*, 6 (1), 1–54.
- Cuidi L, Kan W, Xiaojun Z, Tao L, Yan X, Lei Q, Mingzheng P, Yuanjing X, Le X, Chuanglong H (2019) 'Controllable fabrication of hydroxybutyl chitosan/oxidized chondroitin sulfate hydrogels by 3D bioprinting technique for cartilage tissue engineering', *Biomedical Materials*, 14 (2), 1–17.
- Dai Z, Ronholm J, Tian Y, Sethi B, Cao X (2016) 'Sterilization techniques for biodegradable scaffolds in tissue engineering applications', *Journal of Tissue Engineering*, 7, 1-13.
- Dalton P D, Vaquette C, Farrugia B L, Dargaville T R, Brown T D, Hutmacher D W (2013) 'Electrospinning and additive manufacturing: Converging technologies', *Biomaterials Science*, 1 (2), 171–185.

- Damar S, Balaban M O (2006) 'Review of dense phase CO<sub>2</sub> technology: Microbial and enzyme inactivation, and effects on food quality', *Journal of Food Science*, 71 (1), 1–11.
- Das S, Pati F, Choi Y J, Rijal G, Shim J H, Kim S W, Ray A R, Cho D W, Ghosh S (2015) 'Bioprintable, cell-laden silk fibroin-gelatin hydrogel supporting multilineage differentiation of stem cells for fabrication of three-dimensional tissue constructs', *Acta Biomaterialia*, 11 (1), 233–246.
- Davison N L, Groot F B, Grijpma D W (2015) 'Degradation of Biomaterials'. *Tissue Engineering*, (Second Edition), 177-215.
- Detsch R, Sarker B, Zehnder T, Boccaccini A R, Douglas T E L (2014) 'Additive manufacturing of cell-loaded alginate enriched with alkaline phosphatase for bone tissue engineering application', *BioNanoMaterials*, 15 (3–4), 79–87.
- Detsch R, Sarker B, Zehnder T, Frank G, Boccaccini A R (2015) 'Advanced alginate-based hydrogels', *Materials Today*, 18 (10), 590–591.
- Difederico E, Shelton J C (2017) 'Complex Mechanical Conditioning of Cell-Seeded Agarose Constructs Can Influence Chondrocyte Biosynthetic Activity', *Biotechnology and Bioengineering*, 114 (7), 1614–1625.
- Do A V, Khorsand B, Geary S M, Salem A K (2015) '3D Printing of Scaffolds for Tissue Regeneration Applications', *Advanced Healthcare Materials*, 4 (12), 1742-1762.
- Domingos M, Chiellini F, Gloria L, Ambrosia P, Bartolo P, Chiellini E (2012) 'Effect of process parameters on the morphological and mechanical properties of 3D Bioextruded poly(1-caprolactone) scaffolds', *Rapid Prototyping Journal*, 18 (1), 56–67.
- Duarte C, Drescher W, Rath B, Tingart M, Fischer H (2012) 'Supporting Biomaterials for Articular Cartilage Repair', *Cartilage*, 3 (3), 205–221.
- Ducheyne P, Healy K, Hutmacher D E, Grainger D W (2015) 'Comprehensive Biomaterials' Volume 5.
- Dzobo K, Thomford N E, Senthebane D A, Shipanga H, Rowe A, Dandara C, Pillay M, Motaung K S C M (2018) 'Advances in regenerative medicine and tissue engineering: Innovation and transformation of medicine', *Stem Cells International*.
- El-ashhab F, Sheha L, Abdalkhalek M, Hussein A K (2013) 'The influence of gamma irradiation on the intrinsic properties of cellulose acetate polymers', *Journal of the Association of Arab Universities for Basic and Applied Sciences*, 14 (1), 46–50.
- Elder B D, Athanasiou K A (2009a) 'Effects of Temporal Hydrostatic Pressure on Tissue-Engineered Bovine Articular Cartilage Constructs', *Tissue Engineering Part A*, 15 (5), 1151-1158.
- Elder B D, Athanasiou K A (2009b) 'Hydrostatic Pressure in Articular Cartilage Tissue Engineering: From Chondrocytes to Tissue Regeneration', *Tissue Engineering Part B*, 15 (1), 43-53.

- Elder B D, Athanasiou K A (2008) 'Synergistic and Additive Effects of Hydrostatic Pressure and Growth Factors on Tissue Formation', *PLoS One*, 3 (6).
- Elder S H, Sanders SW, McCulley WR, Marr ML, Shim JW, Hasty K A (2006) 'Chondrocyte Response to Cyclic Hydrostatic Pressure in Alginate Versus Pellet Culture', *Journal of Orthopaedic Research*, (April), 740–747.
- Elder S H, Shim J W, Borazjani A, Robertson H M, Smith K E, Warnock J N (2008) 'Influence of hydrostatic and distortional stress on chondroinduction', *Biorheology*, 45, 479–486.
- Elliott D M, Wright A C, Vresilovic E J, Johannessen W (2004) 'Intervertebral disc mechanics are restored following cyclic loading and unloaded recovery', *Annals of Biomedical Engineering*, 32 (1), 70–76.
- Ellingson A M, Nagel T M, Polly D W, Ellermann J, Nuckley D J (2014) *Journal of orthopaedic research*, 32 (8), 1083-10839.
- Elo M A, Karjalainen H M, Sironen R K, Valmu L, Redpath N T, Browne G J, Kalkkinen N, Helminen H J, Lammi M J (2005) 'High hydrostatic pressure inhibits the biosynthesis of eukaryotic elongation factor-2', *Journal of Cellular Biochemistry*, 94 (3), 497–507.
- Eltorai A E M, Nguyen E, Daniels A H (2015) 'Three-Dimensional Printing in Orthopedic Surgery', *Orthopedics*, 38 (11), 684–687.
- Este M D, Eglin D, Alini M (2018) 'Acta Biomaterialia Lessons to be learned and future directions for intervertebral disc biomaterials', *Acta Biomaterialia*, 78, 13–22.
- Farndale R W, Buttle D J, Barrett A J (1986) 'Improved quantitation and discrimination of sulphated glycosaminoglycans by use of dimethylmethylene blue', *BBA - General Subjects*, 883 (2), 173–177.
- FDA U.S. Food and drug administration (2019) 'Preparation and review of investigational device exemption applications (IDEs) for total artificial discs' fda.gov [Internet] 02/06/2019, <http://www.fda.gov/regulatory-information/search-fda-guidance-documents/preparations-and-review-investigational-device-exempton-applications-ides-total-artificial-discs>
- Fedorovich N E, Schuurman W, Wjinberg H M, Prins H J, van Weeren P R, Malda J, Alblas J, Dhert W J (2012) 'Biofabrication of Osteochondral Tissue Equivalents by Printing Topologically Defined, Cell-Laden Hydrogel Scaffolds', *Tissue Engineering Part C*, 18 (1), 33–44.
- Feng Q, Wang X, Schröder H C, Feng Q, Diehl-Seifert B, Ziebert T, Steffen R, Wang S, Müller W E G (2014) 'Engineering a morphogenetically active hydrogel for bioprinting of bioartificial tissue derived from human osteoblast-like SaOS-2 cells', *Biomaterials*, 35 (31), 8810–8819.
- Fields A J, Lee G L, Keaveny T M (2010) 'Mechanisms of initial endplate failure in the human vertebral body', *Journal of Biomechanics*, 43 (16), 3126–3131.

- Fischbach C, Tessmar J, Lucke A, Schnell E, Schmeer G, Blunk T, Göpferich A (2001) 'Does UV irradiation affect polymer properties relevant to tissue engineering?', *Surface Science*, 491 (3), 333–345.
- Fisher M B, Mauck R L (2013) 'Tissue engineering and regenerative medicine: recent innovations and the transition to translation', *Tissue engineering Part B*, 19 (1), 1–13.
- Fitzgerald J B, Jin M, Grodzinsky A J (2006) 'Shear and compression differentially regulate clusters of functionally related temporal transcription patterns in cartilage tissue', *Journal of Biological Chemistry*, 281 (34), 24095–24103.
- Fortier L A, Barker J U, Strauss E J, McCarrel T M, Cole B J (2011) 'The role of growth factors in cartilage repair', *Clinical Orthopaedics and Related Research*, 469 (10), 2706–2715.
- Foster N C, Henstock J R, Reinwald Y, El Haj A J (2015) 'Dynamic 3D Culture: Models of Chondrogenesis and Endochondral Ossification', *Birth Defects Research C Embryo Today*, 105 (1), 19–33.
- Fox A, Bedi A, Rodeo S (2009) 'The Basic Science of Articular Cartilage', *Orthopedics*, 1 (6), 461–468.
- Frauchiger D A, Tekari A, Wöltje M, Fortunato G, Benneker L M, Gantenbein B (2017) 'A review of the application of reinforced hydrogels and silk as biomaterials for intervertebral disc repair', *European Cell Materials*, 34, 271–290.
- Fukuda K, Shigyo Y, Ariura H, Omata S, Morita T, Yamaguchi T, Sawae Y (2017) 'Relationship between dynamic stress field and ECM production in regenerated cartilage tissue', *Institute of electrical and electronics engineers*, 3–5.
- Fullhase C, Atala A, Soler R, Andersson K-E, Yoo J (2009) 'A Novel Hybrid Printing System for the Generation of Organized Bladder Tissue', *Journal of Urology*, 181 (4S), 282–283.
- Galois L, Hutasse S, Cortial D, Rousseau C F, Grossin L, Ronziere M C, Herbage D, Freyria A M (2006) 'Bovine chondrocyte behaviour in three-dimensional type I collagen gel in terms of gel contraction, proliferation and gene expression', *Biomaterials*, 27 (1), 79–90.
- Gálvez-Martín P, Marchal J A, Perán M, Griñán-Lisón C, Antich C, López-Ruiz E, Jiménez G, Baena J M (2019) 'Volume-by-volume bioprinting of chondrocytes-alginate bioinks in high temperature thermoplastic scaffolds for cartilage regeneration', *Experimental Biology and Medicine*, 244 (1), 13–21.
- Gebhard H, Bowles R, Dyke J, Saleh T, Doty S, Bonassar L, Härtl R (2010) 'Total disc replacement using a tissue-engineered intervertebral disc in vivo: new animal model and initial results', *Evidence-Based Spine-Care Journal*, 1 (02), 62–66.
- Gelber P E, Batista P J, Patthauer L, Millan-Billi A, Vera S, Monllau J C, Masdeu M G (2014) 'Magnetic resonance evaluation of TruFit® plugs for the treatment of osteochondral lesions of the knee shows the poor characteristics of the repair tissue', *The Knee*, 21 (4), 827–832.

- Gentili C, Cancedda R (2009) 'Cartilage and Bone Extracellular Matrix', *Current Pharmaceutical Design*, 15 (12), 1334–1348.
- Gilarska A, Lewandowska-Łańcucka J, Horak W, Nowakowska M (2018) 'Collagen/chitosan/hyaluronic acid – based injectable hydrogels for tissue engineering applications – design, physicochemical and biological characterization', *Colloids and Surfaces B: Biointerfaces*, 170 (June), 152–162.
- Gill E L, Li X, Birch M A, Shery Huang Y Y (2018) 'Multi-length scale bioprinting towards simulating microenvironmental cues', *Bio-Design and Manufacturing*, 1 (2), 77–88.
- Gleadall A, Visscher D, Yang J (2018) 'Review of additive manufactured tissue engineering scaffolds: relationship between geometry and performance', *Burns & Trauma*, 6 (1), 1–16.
- Gloria A, Causa F, De Santis R, Netti P A, Ambrosia L (2007) 'Dynamic-mechanical properties of a novel composite intervertebral disc prosthesis', *Journal of Materials Science: Materials in Medicine*, 18 (11), 2159–2165.
- Goldman M, Gronsky R, Ranganathan R, Pruitt L (1996) 'The effects of gamma radiation sterilization and ageing on the structure and morphology of medical grade ultra high molecular weight polyethylene', *Polymer*, 37 (14), 2909–2913.
- Gopinathan J, Noh I (2018) 'Recent trends in bioinks for 3D printing', *Biomaterials Research*, 22 (1), 1–15.
- Grane P, Lindqvist M (2009) 'Evaluation of the post-operative lumbar spine with MR imaging', *Acta Radiologica*, 38 (6), 1035–1042.
- Groll J, Burdick J A, Cho D-W, Derby B, Gelinksy M, Heilshorn S C, Jüngst T, Malda J, Mirinov V A, Nakayama K (2019) 'A definition of bioinks and their distinction from biomaterial inks', *Biofabrication*, 11, p.13001.
- Gründer W (2006) 'MRI assessment of cartilage ultrastructure', *NMR in Biomedicine*, 19 (7), 855–876.
- Gruber H E (2004) 'Cell-based tissue engineering for the intervertebral disc: In vitro studies of human disc cell gene expression and matrix production within selected cell carriers', *Spine Journal*, 4(1), 44–55.
- Grunert P (2015) 'Quantitative MRI Analysis: an in vivo study', *Spine*, 39(6), 1–23.
- Gstraunthaler G (2003) 'Alternatives to the use of fetal bovine serum: serum-free cell culture', *Altex*, 20 (4), 275–281.
- Guarino V, Gentile G, Sorrentino L, Ambrosio L (2017) Polycaprolactone: Synthesis, Properties, and Applications, *Encyclopedia of Polymer Science and Technology*.
- Guilak F, Jones W (1999) 'The deformation behavior and viscoelastic properties of chondrocytes in articular cartilage', *Biorheology*, 37 (1-2), 27-44.

- Guilak F, Ting-beall H P, Baer A E, Trickey W R, Erickson G R, Setton L A (1999) 'Viscoelastic Properties of Intervertebral Disc Cells Identification of Two Biomechanically Distinct Cell Populations', *Spine*, 24 (23), 2475–2483.
- Guilak F, Erickson G R, Ting-beall H P (2002) 'The Effects of Osmotic Stress on the Viscoelastic and Physical Properties of Articular Chondrocytes', *Biophysical Journal*, 82 (2), 720–727.
- Guilak F, Ratcliffe A, Mow V C (1995) 'Chondrocyte deformation and local tissue strain in articular cartilage: A confocal microscopy study', *Journal of Orthopaedic Research*, 13 (3), 410–421.
- Guillemot F, Souquet A, Catros S, Guillotin B, Lopez J, Faucon M, Pippenger B, Bareille R, Remy M, Bellance S, Chabassier P, Fricain J C, Amédée J (2010) 'High-throughput laser printing of cells and biomaterials for tissue engineering', *Acta biomaterialia*, 6 (7), 2494–500.
- Gullbrand S E, Ashinsky B G (2018) 'Long-term mechanical function and integration of an implanted tissue-engineered intervertebral disc', *Science Translational Medicine*, 10 (468).
- Gullbrand S E, Smith L J, Smith H, Mauck R L (2018) 'Promise, progress, and problems in whole disc tissue engineering', *JOR Spine*, 1(2).
- Gunja N J, Uthamanthil R K, Athanasiou K A (2009) 'Biomaterials Effects of TGF-  $\beta$ 1 and hydrostatic pressure on meniscus cell-seeded scaffolds', *Biomaterials*, 30 (4), 565–573.
- Guterl C, See E Y, Blanquer S B, Pandit A, Ferguson S J, Benneker L M, Grijpma D W, Sakai D, Eglin D, Alini M, Iatridis J C, Grad S (2013) 'Challenges and strategies in the repair of ruptured annulus fibrosus', *European Cell Materials*, 25, 1–21.
- Haase A (1985) '1H NMR chemical shift selective (CHESS) imaging', *Plasma Sources Science and Technology*, 30 (4), 341–344.
- Haberstroh K, Ritter K, Kushnierz J, Bormann K H, Kaps C, Carvalho C, Mülhaupt R, Sittlinger M, Gellrich N C (2010) 'Bone repair by cell-seeded 3D-bioplotting composite scaffolds made of collagen treated tricalciumphosphate or tricalciumphosphate-chitosan-collagen hydrogel or PLGA in ovine critical-sized calvarial defects', *Journal of biomedical materials research Part B*, 93 (2), 520–30.
- Hall A C, Starks I, Shoultz C L, Rashidbigi S (1996) 'Pathways for K<sup>+</sup> transport across the bovine articular chondrocyte membrane and their sensitivity to cell volume', *American Journal of Physiology*, 270 (5 Pt 1), C1300-10.
- Hall A C, Urban J P G, Gehl K A (1991) 'The Effects of Hydrostatic Pressure on Matrix Synthesis in Articular Cartilage', *Journal of Orthopaedic Research*, (28).
- Hangge P (2018) 'Three-dimensional (3D) printing and its applications for aortic diseases', *Cardiovascular Diagnosis and Therapy*, 8 (S1), S19–S25.

- Harris L M, Tunariu N, Messiou C, Hughes J, Wallace T, DeSouza N M, Leach M O, Payne G S (2015) 'Evaluation of lactate detection using selective multiple quantum coherence in phantoms and brain tumours', *NMR Biomedicine*, 28 (3), 338–343.
- Hennink W, van Nostrum C (2002) 'Novel crosslinking methods to design hydrogels', *Advanced Drug Delivery Reviews*, 54 (1), 13–36.
- Hermannova M, Dřimalová E, Malovíková A, Ebringerová A, Velebný V (2008) 'Effect of microwave irradiation on the molecular and structural properties of hyaluronan', *Carbohydrate Polymers*, 73, 640–646.
- Heyland J, Wiegandt K, Goepfert C, Nagel-Heyer S, Ilinich E, Schumacher U, Pörtner R (2006) 'Redifferentiation of chondrocytes and cartilage formation under intermittent hydrostatic pressure', *Biotechnology Letters*, 28 (20), 1641-1648.
- Hodder E, Duin S, Killian D, Ahlfeld T, Seidel J, Nachtigall C, Bush P, Covill D, Gelinsky M, Lode A (2019) 'Investigating the effect of sterilisation methods on the physical properties and cytocompatibility of methyl cellulose used in combination with alginate for 3D-bioplotting of chondrocytes', *Journal of Materials Science: Materials in Medicine*, 30 (1).
- Hodge W A, Harris W H (1986) 'Contact pressures in the human hip joint measured in vivo', *Proceedings of the National Academy of Sciences U S A*, 83 (May), 2879–2883.
- Hoffman A S (2002) 'Hydrogels for biomedical applications', *Advanced drug delivery reviews*, 64, 18–23.
- Hözl K, Lin S, Tytgat L, Van Vlierberghe S, Gu L, Osvianikov A (2016) 'Bioink properties before, during and after 3D bioprinting', *Biofabrication*, 8 (3).
- Honal M, Leupold J, Huff S, Baumann T, Ludwig U (2010) 'Compensation of breathing motion artifacts for MRI with continuously moving table', *Magnetic Resonance in Medicine*, 63 (3), 701–712.
- Honigmann P, Sharma N, Okolo B, Popp U, Msallem B, Theringer F M (2018) 'Patient-Specific Surgical Implants Made of 3D Printed PEEK: Material, Technology, and Scope of Surgical Application', *BioMed Research International*, 1–8.
- Hoppe S, Quirbach S, Mamisch Tallal C (2012) 'Axial T2\* mapping in intervertebral discs: A new technique for assessment of intervertebral disc degeneration', *European Radiology*, 22 (9), 2013–2019.
- Horner H A, Roberts S, Bielby R C, Menage J, Evans H, Urban J P (2002) 'Cells from different regions of the intervertebral disc', *Spine*, 27(10), 1018–1028.
- Hsieh A H, Twomey J D (2010) 'Cellular mechanobiology of the intervertebral disc: New directions and approaches', *Journal of Biomechanics*, 43 (1), 137–145.
- Hu D, Wu D, Huang L, Jiao Y, Li L, Lu L, Zhou C (2018) '3D bioprinting of cell-laden scaffolds for intervertebral disc regeneration', *Materials Letters*, 223, 219–222.

- Hu J C, Athanasiou K A (2006) 'The Effects of Intermittent Hydrostatic Pressure on self-assembled articular cartilage constructs', *Tissue Engineering*, 12 (5), 1337-1344.
- Huang W, Zhang X (2014) '3D printing: Print the future of ophthalmology', *Investigative Ophthalmology and Visual Science*, 55 (8), 5380–5381.
- Huebsch N, Gilbert M, Healy K E (2005) 'Analysis of sterilization protocols for peptide-modified hydrogels', *Journal of Biomedical Materials Research Part B Applied Biomaterials*, 74 (1), 440–447.
- Hugo W B (1995) 'A brief history of heat, chemical and radiation preservation and disinfection', *International Biodeterioration and Biodegradation*, 36 (3–4), 197–217.
- Hunt J, Chen R, van Veen T, Bryan N (2014) 'Hydrogels for tissue engineering and regenerative medicine', *Journal of Materials Chemistry B*, 33.
- Hunt N C, Grover L M (2010) 'Cell encapsulation using biopolymer gels for regenerative medicine', *Biotechnology Letters*, 32 (6), 733–742.
- Hunziker E B (2002) 'Articular cartilage repair: Basic science and clinical progress. A review of the current status and prospects', *Osteoarthritis and Cartilage*, 10 (6), 432–463.
- Hunziker E B, Quinn T M, Häuselmann H J (2002) 'Quantitative structural organization of normal adult human articular cartilage', *Osteoarthritis and Cartilage*, 10 (7), 564–572.
- Hutmacher D W, Schantz T, Zein T, Kee W N, Hin Teoh S, Cheng Tan K (2001) 'Mechanical properties and cell cultural response of polycaprolactone scaffolds designed and fabricated via fused deposition modeling', *Journal of Biomedical Materials Research*, 55 (2), 203–216.
- Hutton W C, Elmer W A, Bryce L M, Kozłowska E E, Boden S D, Kozłowski M (2001) 'Do the intervertebral disc cells respond to different levels of hydrostatic pressure?', *Clinical Biomechanics*, 16 (9), 728-734.
- Hwang C M, Ay B, Kaplan D L, Rubin J P, Marra K G, Atala A, Yoo J J, Lee S J (2013) 'Assessments of injectable alginate particle-embedded fibrin hydrogels for soft tissue reconstruction', *Biomedical Materials*, 8 (1).
- Hwang N S (2007) 'Response of zonal chondrocytes to extracellular matrix-hydrogels', *FEBS Letters*, 581, 4172–4178.
- Hyeryeon J, Kyojin K, Su A P, Wan D K, Seung S P, Sang-Hun L, Jaemin J, Dongho C (2017) 'Generation of multilayered 3D structures of HepG2 cells using a bio-printing technique', *Gut and Liver*, 11 (1), 121–128.
- Iatridis J C, Setton L, Weidenbaum M, Mow V (1997) 'The viscoelastic behavior of the non-degenerate human lumbar nucleus pulposus in shear', *Journal of Biomechanics*, 30 (10), 1005–1013.
- Iatridis J C, Mwale F (2014) 'Grades of Degeneration', *Journal of Magnetic Resonance Imaging*, 38 (6), 1–27.

- Irrechukwu O N, Reiter D A, Lin P C, Roque R A, Fishbein K W, Spencer R G (2012) 'Characterization of Engineered Cartilage Constructs Using Multiexponential T2 Relaxation Analysis and Support Vector Regression', *Tissue Engineering Part C: Methods*, 18 (6), 433–443.
- Ishihara H, Tsuji H, Hirano N, Oshima H, Terahata N (1992) 'Effects of continuous quantitative vibration on rheological and biological behaviours of the intervertebral disc', *Spine*, 17 (3), 7–12.
- Ishihara H, McNally D S, Urban J P, Hall A C (1996) 'Effects of hydrostatic pressure on matrix synthesis in different regions of the intervertebral disk', *Journal of Applied Physiology*, 80 (3), 839–846.
- Ishihara H, Warensjo K, Roberts S, Urban J P (1997) 'Proteoglycan synthesis in the intervertebral disk nucleus: the role of extracellular osmolality', *The American Journal of Physiology-Cell Physiology*, 272 (5 Pt 1), 1499-1506.
- Iwata H (1993) 'Pharmacologic and Clinical Aspects of Intraarticular Injection of Hyaluronate', *Clinical Orthopaedics and Related Research*, (289), 285–291.
- Jabbari E (2018) 'Hydrogels for Cell Delivery', *Gels*, 4 (3), 58.
- Jang, T-S, Jung H-D, Matthew Pan H, Han W T, Chen S, Song J (2018) '3D printing of hydrogel composite systems: Recent advances in technology for tissue engineering', *International Journal of Bioprinting*, 4 (1), 1–28.
- Janorkar A, Metters A, Hirt D (2006) 'Degradation of Poly(L-Lactide) Films Under Ultraviolet- Induced Photografting and Sterilization Conditions Amol', *Polymers and Polymer Composites*, 106 (2).
- Jarvelainen H T, Tammi M (1994) 'Expression of reduced amounts of structurally altered aggrecan in articular cartilage chondrocytes exposed to high hydrostatic pressure', *Biochemistry Journal*, 304 (Pt 3), 723–730.
- Jayakumar R, Chennazhi K P, Srinivasan S, Shantikumar V N, Tetsuya F, Hiroshi T (2011) 'Chitin scaffolds in tissue engineering', *International Journal of Molecular Sciences*, 12, 1876–1887
- Jeffries R E, Macdonald J M (2012) 'New advances in MR-compatible bioartificial liver', *NMR in Biomedicine*, 25 (3), 427–442.
- Jin Y, Liu C, Chai W, Compaan A, Huang Y (2017) 'Self-Supporting Nanoclay as Internal Scaffold Material for Direct Printing of Soft Hydrogel Composite Structures in Air', *ACS Applied Materials and Interfaces*, 9 (20), 17456–17465.
- Johnson W E B, Wootton A, El Haj A, Eisenstein S M, Curtis A S, Roberts S (2005) 'Topographical guidance of intervertebral disc cell growth in vitro: Towards the development of tissue repair strategies for the anulus fibrosus', *European Cells and Materials*, 10 (Suppl.3), 44.
- Jung J W, Lee J S, Cho D W (2016) 'Computer-aided multiple-head 3D printing system for printing of heterogeneous organ/tissue constructs', *Scientific reports*, 6 (November 2015), 21685.

- Jungmann P M, Baum T, Bauer J S, Karampinos D C, Erdle B, Link T M, Li X, Trattng S, Rummeny E J, Woertler K, Welsch G H (2014) 'Cartilage Repair Surgery: Outcome Evaluation by Using Noninvasive Cartilage Biomarkers Based on Quantitative MRI Techniques?' *Biomedical Research International*.
- Kaarniranta K, Sironen R, Elo M, Kaarniranta K, Helminen H J, Lammi M J (2000) 'Transcriptional activation in chondrocytes submitted to hydrostatic pressure', *Biorheology*, 37 (1-2), 85-93.
- Kang H W, Lee S J, Ko I K, Kengla C, Yoo J J, Atala A (2016) 'A 3D bioprinting system to produce human-scale tissue constructs with structural integrity', *Nature Biotechnology*, 34 (3), 312–319.
- Kaplan B A, Gorman C R, Gupta A K, Taylor S R, Lezzoni J C, Park S S (2003) 'Effects of transforming growth factor  $\beta$  and insulinlike growth factor 1 on the biomechanical and histologic properties of tissue-engineered cartilage', *Archives of Facial Plastic Surgery*, 5 (1), 96–101.
- Karajanagi S S, Yoganathan R, Mammucari R, Park H, Cox J, Zeitels S M, Langer R, Foster N R (2011) 'Application of a dense gas technique for sterilizing soft biomaterials', *Biotechnology and Bioengineering*, 108 (7), 1716–1725.
- Kate T J, Smit G, Breedveld P (2017) '3D-printed upper limb prostheses: a review', *Disability and Rehabilitation: Assistive Technology*, 12 (3), 300–314.
- Kato Y, Gospodarowicz D (1985) 'Stimulation by glucocorticoid of the synthesis of cartilage-matrix proteoglycans produced by rabbit costal chondrocytes in vitro', *Journal of Biological Chemistry*, 260 (4), 2364–2373.
- Kato Y, Gospodarowicz D (1985) 'Sulfated Proteoglycan Synthesis by Confluent Cultures of Rabbit Costal Chondrocytes Grown in the Presence of Fibroblast Growth Factor', *Cell Biology*, 100 (447–485).
- Kawanishi M, Oura A, Furukawa K, Fukubayashi T, Nakamura K, Tateishi T, Ushida T (2007) 'Redifferentiation of Dedifferentiated Bovine Articular a Gas-Controlled System', *Tissue engineering*, 13 (5), 957–964.
- Keenan K, Besier T F, Pauly J M, Han E, Rosenberg J, Smith R L, Delp S L, Beaupre G S, Gold G E (2011) 'Prediction of Glycosaminoglycan Content in Human Cartilage by Age, T1 $\rho$  and T2 MRI', *Osteoarthritis Cartilage*, 19 (2), 171–179.
- Kemper A R, McNally C, Duma S M (2007) 'The influence of strain rate on the compressive stiffness properties of human lumbar intervertebral discs', *Biomedical Sciences Instrumentation*, 43, 176–181.
- Kim W, Lee H, Kim Y (2017) 'Regeneration A cell-printing approach for obtaining hASC-laden scaffolds by using a collagen / polyphenol bioink', *Biofabrication*, 9 (2).
- Kim J D, Choi J S, Kim B S, Choi Y C, Cho Y W (2010) 'Piezoelectric inkjet printing of polymers: Stem cell patterning on polymer substrates' *Polymer*, 51, 2147-2154.

- Kingma I, Staudenmann D, van Dieën J H (2007) 'Trunk muscle activation and associated lumbar spine joint shear forces under different levels of external forward force applied to the trunk', *Journal of electromyography and kinesiology*, 17 (1), 14–24.
- Kisiday J D, Jin M, DiMicco M A, Kurz B, Grodzinsky A J (2004) 'Effects of dynamic compressive loading on chondrocyte biosynthesis in self-assembling peptide scaffolds', *Journal of Biomechanics*, 37 (5), 595–604.
- Klein-Nulend J, Veldhuijzen J P, van de Stadt R J, van Kampen G P, Kuijjer R, Burger E H (1987) 'Influence of intermittent compressive force on proteoglycan content in calcifying growth plate cartilage in vitro', *Journal of Biological Chemistry*, 262 (32), 15490–15495.
- Klein T J, Malda J, Sah R L, Hutmacher D W (2009) 'Tissue engineering of articular cartilage with biomimetic zones', *Tissue engineering Part B: Reviews*, 15 (2), 143–157.
- Klisch S M, Lotz J C (2002) 'A Special Theory of Biphasic Mixtures and Experimental Results for Human Annulus Fibrosus Tested in Confined Compression', *Journal of Biomechanical Engineering*, 122 (2), 180.
- Koch H H, Pimsler M (1987) 'Evaluation of Uvitex 2B: a nonspecific fluorescent stain for detecting and identifying fungi and algae in tissue', *Laboratory Medicine*, 18 (9), 603–606.
- Kotecha M, Ravindran S, Schmid T M, Vaidyanathan A, George A, Magin L R (2013a) 'The application of sodium triple-quantum coherence NMR spectroscopy for the study of growth dynamics in cartilage tissue engineering', *NMR in biomedicine*, 26 (6), 709–717.
- Kotecha M, Klatt D, Magin R L (2013) 'Monitoring Cartilage Tissue Engineering Using Magnetic Resonance Spectroscopy, Imaging, and Elastography', *Tissue Engineering Part B: Reviews*, 19 (6), 470–484.
- Kraff O, Fischer A, Nagel A M, Mönninghoff C, Ladd M E, (2015) 'MRI at 7 Tesla and Above: Demonstrated and Potential Capabilities', *Journal of Magnetic Resonance Imaging*, 33, 13–33.
- Krismer M, Haid C, Bechensky H, Kapfinger P, Landauer F, Rachbauer F (2000) 'Motion in lumbar functional spine units during side bending and axial rotation moments depending on the degree of degeneration', *Spine*, 25 (16), 2020–2027.
- Kreis, R (2004) 'Issues of spectral quality in clinical 1H-magnetic resonance spectroscopy and a gallery of artifacts', *NMR Biomedicine*, 17, 361-381.
- Kular J K, Basu S, Sharma R I (2014) 'The extracellular matrix: Structure, composition, age-related differences, tools for analysis and applications for tissue engineering', *Journal of Tissue Engineering*, 5, 1–17.
- Kumar A, Mandal S, Barui S, Vasireddi R, Gbureck U, Gelinsky M, Basu B (2016) 'Low temperature additive manufacturing of three dimensional scaffolds for bone-tissue engineering applications:

Processing related challenges and property assessment', *Materials Science and Engineering: R: Reports*, 103, 1–39.

Kundu J, Shim J-H, Jang J, Kim S W, Cho D W (2013) 'An additive manufacturing-based PCL–alginate–chondrocyte bioprinted scaffold for cartilage tissue engineering Joydip', *Journal of tissue engineering and regenerative medicine*, 9 (11), 1286–1297.

Kunitomo T, Takahashi K A, Arai Y, Sakao K, Honjo K, Saito M, Inoue A, Tonomura H, Morihara T, Mazda O, Imanashi J, Kubo T (2009) 'Influence of extracellular matrix on the expression of inflammatory cytokines, proteases, and apoptosis-related genes induced by hydrostatic pressure in three-dimensionally cultured chondrocytes', *Journal of Orthopaedic Science*, 776–783.

Kurenov S N, Ionita C, Sammons D, Demmy T L (2015) 'Three-dimensional printing to facilitate anatomic study, device development, simulation, and planning in thoracic surgery', *Journal of Thoracic and Cardiovascular Surgery*, 149 (4), 973-979.

Lafeber F, Veldhuijzen J P, Vanroy J L A M, Huber-Bruning O, Bijlsma J W J (1992) 'Intermittent Hydrostatic Compressive Force Stimulates Exclusively the Proteoglycan Synthesis of Osteoarthritic Human Cartilage', *British Journal of Rheumatology*, 31, 437–442.

Lalande C, Miraux S, Derkaoui S M, Mornet S, Bareille R, Fricain J C, Franconi J M, Le Visage C, Letourneur D, Amédée J, Bouzier-Sore A K (2011) 'Magnetic resonance imaging tracking of human adipose derived stromal cells within three-dimensional scaffolds for bone tissue engineering', *European cells and materials*, 21, 341–354.

Landers R, Pfister U, Hübner U, Schmelzeisen J R, Mülhaupt R (2002) 'Fabrication of soft tissue engineering scaffolds by means of rapid prototyping techniques', *Journal of Materials Science*, 37 (15), 3107–3116.

Law N, Doney B, Glover H, Qin Y, Aman Z M, Sercombe T B, Liew L J, Dilley R J, Doyle B J (2018) 'Characterisation of hyaluronic acid methylcellulose hydrogels for 3D bioprinting', *Journal of the Mechanical Behaviour of Biomedical Materials*, 77 (June 2017), 389–399.

Lee D, Erickson A, You T, Dudley A T, Ryu S (2018) 'Pneumatic microfluidic cell compression device for high-throughput study of chondrocyte mechanobiology', *Lab on a Chip Royal Society of Chemistry*, 18 (14), 2077–2086.

Lee H, SeungHyun A, Bonassar L, Kim G (2013) 'Alginate Hybrid Scaffolds for Tissue Regeneration', *Macromolecular journals*, 34, 142–149.

Lee J-S, Hong J M, Jung J W, Shim J H, Oh J H, Cho D W (2014) '3D printing of composite tissue with complex shape applied to ear regeneration', *Biofabrication*, 6 (2), p. 024103.

Lee J H, Kim D-H, Lee H-H, Kim H-W (2019) 'Role of nuclear mechanosensitivity in determining cellular responses to forces and biomaterials', *Biomaterials*, 197, 60–71.

- Lee K Y, Rowley J A, Eiselt P, Moy E M, Bouhadir K H, Mooney D J (2000) 'Controlling mechanical and swelling properties of alginate hydrogels independently by cross-linker type and cross-linking density', *Macromolecules*, 33 (11), 4291–4294.
- Lee K Y, Mooney D J (2012) 'Alginate: Properties and biomedical applications', *Progress in Polymer Science*, 37 (1), 106–126.
- Lehto L J, Idiyattullin D, Zhang J, Utecht L, Adriany G, Garwood M, Gröhn O, Michaeli S, Mangia S (2018) 'MB-SWIFT functional MRI during deep brain stimulation in rats', *NeuroImage*, 159 (612), 443–448.
- Leijten, J, Georgi, N, Wu, L, Blitterswijk C A, Karperien M (2013) 'Cell sources for articular repair strategies shifting from monocultures to cocultures', *Tissue engineering Part B*, 19 (1), 31-40.
- Leo, William J, Mcloughlin A J, Malone D M (1990) 'Effects of Sterilization Treatments on Some Properties of Alginate Solutions and Gels', *Biotechnology Progress*, 6 (2), 51–53.
- Leong K F, Chua C K, Sudarmadj N, Yeong W Y (2008) 'Engineering functionally graded tissue engineering scaffolds', *Journal of the Mechanical Behaviour of Biomedical Materials*, 1 (2), 140–152.
- Leong K-F, Llo D, Chua C K (2014) 'Tissue-engineering applications of additive-manufacturing', *Comprehensive Materials Processing*, 10, 251-264.
- Li H, Jun Tan Y, Leong K F, Li L (2017) '3D Bioprinting of Highly Thixotropic Alginate/Methylcellulose Hydrogel with Strong Interface Bonding', *ACS Applied Materials and Interfaces*, 9 (23), 20086–20097.
- Li J, Illeperuma R K, Suo Z, Vlassak J J (2014) 'Hybrid hydrogels with extremely high stiffness and toughness', *ACS Macro Letters*, 3 (6), 520–523.
- Li P, Gan Y, Xu Y, Li S, Song Lei, Li S, Li H, Zhou Q (2016) 'Osmolarity Affects Matrix Synthesis in the Nucleus Pulposus Associated With the Involvement of MAPK Pathways: A Study of Ex Vivo Disc Organ Culture System', *Journal of Orthopaedic Research*, 34 (6), 1092-1100.
- Li S, Cao J, Caterson B, Hughes C E (2012) 'Proteoglycan metabolism, cell death and Kashin-Beck Disease', *Glycoconjugate Journal*, 29, 241–248.
- Li W, Hong L, Hu L, Magin R L (2010) 'Magnetization Transfer Imaging Provides a Quantitative Measure of Chondrogenic Differentiation and Tissue Development', *Tissue Engineering Part C: Methods*, 16 (6), 1407–1415.
- Li X, Cheng J, Lin K, Saadat E, Bolbos R I, Jobke B, Ries M D, Horvai A, Link T M, Majumdar S (2011) 'Quantitative MRI using T1 $\rho$  and T2 in human osteoarthritic cartilage specimens: Correlation with biochemical measurements and histology', *Magnetic Resonance Imaging*, 29 (3), 324–334.
- Li Y, Zhou J, Yang X, Gui J (2016a) 'Intermittent hydrostatic pressure maintains and enhances the chondrogenic differentiation of cartilage progenitor cells cultivated in alginate beads', *Development Growth and Differentiation*, 58 (2), 180-193.

- Liaw C-Y, Guvendiren M (2017) 'Current and emerging applications of 3D printing in medicine', *Biofabrication*, 9 (2), 024102.
- Lin S, Sangaj N, Razafiarison T, Zhang C, Varghese S (2011) 'Influence of Physical Properties of Biomaterials on Cellular Behavior', *Pharmaceutical Research*, 28 (6), 1422–1430.
- Lin Z, Fitzgerald J B, Xu J, Willers C, Wood D, Grodzinsky A J, Zheng M H (2008) 'Gene expression profiles of human chondrocytes during passaged monolayer cultivation', *Journal of Orthopaedic Research*, 26 (9), 1230-1237.
- Lindl T (2002) *Zell und Gewebekultur*. 5th edn.
- Lippiello L, Kaye C, Neumata T, Mankin H J (1985) 'In Vitro Metabolic Response of Articular Cartilage Segments to Low Levels of Hydrostatic Pressure', *Connective Tissue Research*, 13 (2), 99–107.
- Liu C, Kamara A, Yan Y (2018) 'Investigation into the biomechanics of lumbar spine micro-dynamic pedicle screw', *BMC Musculoskeletal Disorders*, 19 (1), 1–11.
- Liu X, Ma P X (2010) 'Gelatin Scaffolds', *Biomaterials*, 30 (25), 4094–4103.
- Lode A, Krujatz F, Brüggemeier S, Quade M, Schütz K, Knaack S, Weber J, Bley T, Gelinsky M (2015) 'Green bioprinting: Fabrication of photosynthetic algae-laden hydrogel scaffolds for biotechnological and medical applications', *Engineering in Life Sciences*, 15 (2), 177–183.
- Lode A, Ahlfeld T, Cidonio G, Kilian D, Duin S, Akkineni AR, Dawson JI, Yang S, Oreffo ROC, Gelinsky M (2017) 'Development of a clay based bioink for 3D cell printing for skeletal application', *Biofabrication*, 9 (3).
- Lopes L R, Silva A F, Carneiro O S (2018) 'Multi-material 3D printing: The relevance of materials affinity on the boundary interface performance', *Additive Manufacturing*, 23 (July), 45–52.
- López-Marcial G R, Zeng A Y, Osuna C, Dennis J, Garcia J M, O'Connell G (2018) 'Agarose-Based Hydrogels as Suitable Bioprinting Materials for Tissue Engineering', *ACS Biomaterials Science and Engineering*, 4 (10), 3610–3616.
- Loupasis G A, Stamos K, Katonis P G, Sapkas G, Korres D S, Hartofilakidis (1999) 'Seven- to 20-year outcome of lumbar discectomy', *Spine*, 24 (22), 2313–2317.
- Lu P, Takai K, Weaver V M, Werb Z (2011) 'Extracellular Matrix Degradation and Remodeling in Development and Disease', *Cold Spring Harbor Laboratory Press Biol*, 3, 1–25.
- Lu Y, Yan F, Chen Z (2016) 'The function of mechanical loading on chondrogenesis', *Frontiers in Bioscience*, 21 (6), 1222–1232.
- Ludescher B, Effelsberg J, Martirosian P, Steidle G, Markert B, Claussen C, Schick F (2008) 'T2- and diffusion-maps reveal diurnal changes of intervertebral disc composition: An in vivo MRI study at 1.5 tesla', *Journal of Magnetic Resonance Imaging*, 28 (1), 252–257.

- Luo Y, Lode A, Sonntag F, Niles B, Gelinsky M (2013) 'Well-ordered biphasic calcium phosphate–alginate scaffolds fabricated by multi-channel 3D plotting under mild conditions', *Journal of Materials Chemistry B*, 1 (33), 4088.
- Luo Z-J, Seedhom B B (2007) 'Light and low-frequency pulsatile hydrostatic pressure enhances extracellular matrix formation by bone marrow mesenchymal cells: An in-vitro study with special reference to cartilage repair', *Journal of Engineering in Medicine*, 221, 499–507.
- Lysaght M J, Hazlehurst A L (2004) 'Tissue engineering: the end of the beginning', *Tissue engineering*, 10 (1–2), 309–20.
- Lysaght M J, Jaklenec A, Deweerd E (2008) 'Great expectations: private sector activity in tissue engineering, regenerative medicine, and stem cell therapeutics', *Tissue engineering Part A*, 14 (2), 305–15.
- Mabvuure N, Hindocha S, Khan W S (2012) 'The Role of Bioreactors in Cartilage Tissue Engineering', *Current Stem Cell Research Therapy*, 287–292.
- Madularu D, Kumaragamage C, Mathieu A P, Kulkarni P, Rajah M N, Gratton A P, Near J (2017) 'A chronic in situ coil system adapted for intracerebral stimulation during MRI in rats', *Journal of Neuroscience Methods*, 284, 85–95.
- Maher P S, Keatch R P, Donnelly K, Mackay R E, Paxton J Z (2009) 'Construction of 3D biological matrices using rapid prototyping technology', *Rapid Prototyping Journal*, 15 (3), 204–210.
- Maher P S, Keatch R P, Donnelly K, Paxton J Z (2009) 'Formed 3D Bio-Scaffolds via Rapid Prototyping Technology', *4th European conference of the international federation for medical and biological engineering*, 22 (1–3), 2200–2204.
- Maik R, Augustinus S (2007) 'Cartilage tissue engineering and bioreactor systems for the cultivation and stimulation of chondrocytes', *European Biophysiology Journal*, 539–568.
- Maitre CL, Frain J, Fotheringham A P, Freemont A J, Hoyland J A (2008) 'Human cells derived from degenerate intervertebral discs respond differently to those derived from non-degenerate intervertebral discs following application of dynamic hydrostatic pressure', *Biorheology*, 45 (5), 563–575.
- Malda J, Visser J, Melchels F P, Jüngst T, Hennink W E, Dhert W J, Groll J, Huttmacher D W (2013) '25th anniversary article: Engineering hydrogels for biofabrication', *Advanced Materials*, 25 (36), 5011–5028.
- Maldonado B A, Oegema T R (1992) 'Initial characterization of the metabolism of intervertebral disc cells encapsulated in microspheres', *Journal of Orthopaedic Research*, 10 (5), 677–690.
- Manabe N, Furuya Y, Nagano N, Yagi M, Kuramitsu K, Miyamoto H (1995) 'Immunohistochemical Quantitation for Extracellular Matrix Proteins in Rats with Glomerulonephritis Induced by Monoclonal Anti-Thy-1.1 Antibody', *Nephron*, 71, 79–86.

- Maniadakis N, Gray, A (2000) 'The economic burden of back pain in the UK', *Pain*, 84 (1), 95–103.
- Mano F, Reis R L, Gasperini L (2014) 'Natural polymers for the microencapsulation of cells-Revision', *Journal of the royal society interface*, 11, 20140817.
- Mans R J, Novell D G (1960) 'A convenient, rapid and sensitive method for measuring the incorporation of radioactive amino acids into protein', *biochemical and biophysical research communications*, 3 (5), 540–543.
- Marchand F, Ahmed A (1990) 'Investigation of the Laminate Structure of Lumbar Disc Anulus Fibrosus', *Spine*, 15 (5), 402–410.
- Marchioli G, van Gorp L, van Krieken P P, Stamatialis D, Engelse M, van Blitterswijk C A, Karperien M B, de Koning E, Alblas J, Moroni L, van Apeldoorn A A (2015) 'Fabrication of three-dimensional bioprinted hydrogel scaffolds for islets of Langerhans transplantation', *Biofabrication*, 7 (2), 025009.
- Marques C F, Diogo GS, Pina S, Oliveira J M, Silva T H, Reis R L (2019) 'Collagen-based bioinks for hard tissue engineering applications: a comprehensive review', *Journal of Materials Science: Materials in Medicine*, 30 (3).
- Martino F, Perestrelo A R, Vinarský V, Pagliari S, Forte G (2018) 'Cellular mechanotransduction: From tension to function', *Frontiers in Physiology*, 9 (824), 1–21.
- Martino S, D'Angelo F, Armentano I, Kenny J M, Orlacchio A (2012) 'Stem cell-biomaterial interactions for regenerative medicine', *Biotechnology advances*, 30 (1), 338–351.
- Maslennikova A, Kochueva M, Ignatieva N, Vitkin A, Zakharkina O, Kamensky V, Sergeeva E, Kiseleva E, Bagratashvili V (2015) 'Effects of gamma irradiation on collagen damage and remodeling', *International Journal of Radiation Biology*, 91 (3), 240–247.
- Matyas J R, Huang D, Chung M, Adams M E (2002) 'Regional quantification of cartilage type II collagen and aggrecan messenger RNA in joints with early experimental osteoarthritis', *Arthritis and Rheumatism*, 46 (6), 1536–1543.
- Matzat S J, van Tiel J, Gold G E, Oei E H (2013) 'Quantitative MRI techniques of cartilage composition', *Quantitative imaging in medicine and surgery*, 3 (3), 162–174.
- Mayan M D, Gago-Fuentes R, Carpintero-Fernandez P, Fernandez-Puente P, Filgueira-Fernandez P, Goyanes N, Valiunas V, Brink P R, Goldberg G S, Blanco F J. (2017) 'Articular chondrocyte network mediated by gap junctions: role in metabolic cartilage homeostasis', *Annals of the Rheumatic Diseases*, 74 (1), 275–284.
- McNab J A, Jbabdi S, Deoni S C, Douaud G, Behrens T E, Miller K L (2009) 'High resolution diffusion-weighted imaging in fixed human brain using diffusion-weighted steady state free precession', *NeuroImage*, 46 (3), 775–785.

Meechan P, Wilson C (2006) 'Use of ultraviolet lights in biological safety cabinets: A contrarian view', *Applied Biosafety*, 11 (4), 222–227.

Melchels F P W, Domingos M A N, J.Kleina T, Malda J, Bartolo P, Hutmacher D W (2012) 'Additive manufacturing of tissues and organs', *Progress in Polymer Science*, 37 (8), 1079–1104.

Melton J T K, Wilson A J, Chapman-Sheath P, Cossey A J (2010) 'TruFit CB bone plug: chondral repair, scaffold design, surgical technique and early experiences', *Expert review of medical devices*, 7 (3), 333–341.

Mendes G C C, Brandão T R S, Silva C L M (2007) 'Ethylene oxide sterilization of medical devices: A review', *American Journal of Infection Control*, 35 (9), 574–581.

Menezes-Reis R, Garrido Salmon C, Bonugli G P, Mazoroski D, Tamashiro M H, Savarese L G, Nogueira-Barbosa M H (2016) 'Lumbar intervertebral discs T2 relaxometry and T1 $\rho$  relaxometry correlation with age in asymptomatic young adults', *Quantitative Imaging in Medicine and Surgery*, 6 (4), 402–412.

Meyer M, Prade I, Leppchen-Fröhlich K, Felix A, Herdegen V, Haseneder R, Repke J-U (2015) 'Sterilisation of collagen materials using hydrogen peroxide doted supercritical carbon dioxide and its effects on the materials properties', *Journal of Supercritical Fluids*, 102, 32–39.

Migliaresi C, Maniglio D, Motta A, Gasperini L (2015) 'An Electrohydrodynamic Bioprinter for Alginate', *Tissue Engineering Part C: Methods*, 21 (2), 123–132.

Mikos A G, Temenoff J S (2000) 'Formation of highly porous biodegradable scaffolds for tissue engineering', *Electronic Journal of Biotechnology*, 3 (2).

Miller K L, , Stagg C J, Douaud G, Jbabdi S, Smith S M, Behrens T E J, Jenkinson M, Chance S A, Esiri M M, Voets N L, Jenkinson N, Aziz T Z, Turner M R, Johansen-Berg H, McNab J A (2011) 'Diffusion imaging of whole, post-mortem human brains on a clinical MRI scanner', *NeuroImage*, 57 (1), 167–181.

Mitchell A C, Briquez P S, Hubbell J A, Cochran J R (2016) 'Engineering growth factors for regenerative medicine applications', *Acta Biomaterialia*, (30), 1–12.

Miyaniishi K, Trindade M C, Lindsey D P, Beaupré G S, Carter D R, Goodman S B, Schurman D J, Smith R L (2006) 'Dose- and Time-Dependent Effects of Cyclic Hydrostatic Pressure on Transforming Growth Factor- $\beta$  3-Induced Chondrogenesis', *Tissue Engineering*, 12 (8), 2253-2262.

Miyata S, Numano T, Homma K, Tateishi T, Ushida T (2007) 'Feasibility of noninvasive evaluation of biophysical properties of tissue-engineered cartilage by using quantitative MRI', *Journal of Biomechanics*, 40 (13), 2990–2998.

Mizuno H, Roy A K, Vacanti C A, Kojima K, Ueda M, Bonassar L J (2004) 'Tissue-engineered composites of annulus fibrosus and nucleus pulposus for intervertebral disc replacement', *Spine*, 29 (12), 1290–1297.

Mizuno S, Tateishi T, Ushida T, Glowacki J (2002) 'Hydrostatic Fluid Pressure Enhances Matrix Synthesis and Accumulation by Bovine Chondrocytes in Three-Dimensional Culture', *Journal of Cell Physiology*, 193 (3), 319–327.

Mizuno S (2011) 'Novel cell culture model using pure hydrostatic pressure and a semipermeable membrane pouch', *Cell Transplantation*, 20 (5), 767–774.

Moshaverinia A, Xu X, DDS, Chen C, Akiyama K, Snead ML (2013) 'Dental mesenchymal stem cells encapsulated in alginate hydrogel co-delivery microencapsulation system for cartilage regeneration', *National Institute of Health*, 9 (12).

Mota C, Puppi D, Chiellini F, Chiellini E (2012) 'Additive manufacturing techniques for the production of tissue engineering constructs', *Journal of Tissue Engineering and Regenerative Medicine*, 6, 135–143.

Mow V C, Huijskes R, Abreu E (2005) 'Review of Basic Orthopaedic Biomechanics and Mechano-Biology', *Biomedical engineering Online*, 4 (28).

Mow V C, Wang C C, Hung C T (1999) 'The extracellular matrix, interstitial fluid and ions as a mechanical signal transducer in articular cartilage', *Osteoarthritis and Cartilage*, 7 (1), 41–58.

Muir H (1978) 'Proteoglycans of cartilage', *Journal of Clinical Pathology*, 31 (12), 67–81.

Müller M, Öztürk E, Arlov Ø, Gatenholm P, Zenobi-Wong M (2017) 'Alginate Sulfate–Nanocellulose Bioinks for Cartilage Bioprinting Applications', *Annals of Biomedical Engineering*, 45 (1), 210–223.

Munarin F, Bozzini S, Visai L, Tanzi Maria C (2013) 'Sterilization treatments on polysaccharides: Effects and side effects on pectin', *Food Hydrocolloids*, 31 (1), 74–84.

Murphy S V, Atala A (2014) '3D bioprinting of tissues and organs', *Nature biotechnology*, 32 (8), 773–785.

Murray C J L, Vos T, Lozano R, Naghavi M, Flaxman AD, Michaud C, Ezzati M, Shibuya K, Salomon JA, Abdalla S, Aboyans V, Abraham J, Ackerman I, Aggarwal R, Ahn SY, Ali MK, Alvarado M et al., (2012) 'Disability-adjusted life years (DALYs) for 291 diseases and injuries in 21 regions, 1990-2010: a systematic analysis for the Global Burden of Disease Study 2010', *Lancet (London, England)*, 380 (9859), 2197–223.

Mwale F, Iatridis J C, Antoniou J (2008) 'Quantitative MRI as a diagnostic tool of intervertebral disc matrix composition and integrity', *European Spine Journal*, 17 (SUPPL. 4), 432–440.

Naficy S, Chung J H Y, Yue Z, Kapsa R, Quigley A, Moulton S E, Wallace G G (2013) 'Bio-ink properties and printability for extrusion printing living cells', *Biomaterials Science*, 1 (7), 763.

Naghieh S, Sarker I A, Keramooz M R, McInnes A D, Chen X (2018) 'Modeling of the Mechanical Behavior of 3D Bioprinted Scaffolds Considering the Penetration in Interlocked Strands', *Applied Sciences*, 8 (9), 1422.

Nair K, Gandhi M, Khalil S, Yan KC, Marcolongo M, Barbee K, Sun W (2009) 'Characterization of cell viability during bioprinting processes', *Biotechnology Journal*, 4 (8), 1168–1177.

Nakai S, Shogo M, Jun K (2015) 'Effect of Complex Stimuli of Shear Stress and Surface Modification on Proliferation and Phenotype of Chondrocyte', *The Japan Institute of Metals and Materials*, 79 (6), 324–329.

Nakamura S, Arai Y, Takahashi KA, Terauchi R, Ohashi S, Mazda O, Imanishi J, Inoue A, Tonomura H, Kubo T (2006) 'Hydrostatic Pressure Induces Apoptosis of Chondrocytes Cultured in Alginate Beads', *Journal of Orthopaedic Research*, 24 (4), 733-739.

Nam Y S, Yoon J J, Park T G (2000) 'A novel fabrication method of macroporous biodegradable polymer scaffolds using gas foaming salt as a porogen additive', *Journal of Biomedical Materials Research*, 53 (1), 1–7.

Nasatto P L, Pignon F, Silviera J L M, Duarte M E R, Noseda M D, Rinuado M (2015) 'Methylcellulose, a Cellulose Derivative with Original Physical Properties and Extended Applications', *Polymers*, 777–803.

Nerurkar N L, Elliott D M, Mauck R L (2010) 'Mechanical design criteria for intervertebral disc', *Journal of Biomechanics*, 43 (6), 1017–1030.

Ngiam M, Liao S, Patil AJ, Cheng Z, Chan CK, Ramakrishna S (2009) 'The fabrication of nano-hydroxyapatite on PLGA and PLGA/collagen nanofibrous composite scaffolds and their effects in osteoblastic behaviour for bone tissue engineering', *Bone*, 45 (1), 4–16.

Nguyen L H, Kudva A K, Guckert N L, Linse K D, Roy K (2011) 'Unique biomaterial compositions direct bone marrow stem cells into specific chondrocytic phenotypes corresponding to the various zones of articular cartilage', *Biomaterials*, 32 (5), 1327–1338.

Nguyen T H, Randolph D C, Talmage J, Succop P, Travis R (2011) 'Long-term Outcomes of Lumbar Fusion Among Workers Compensation Subjects', *Spine*, 36 (4), 320–331.

NHS digital (2010) 'Hospital episode statistics' [Internet] 07/06/2018 <http://www.hesonline.nhs.uk>

Ning F, Cong W, Qiu J, Wei J, Wang S (2015) 'Additive manufacturing of carbon fiber reinforced thermoplastic composites using fused deposition modeling', *Composites Part B: Engineering*, 80, 369–378.

Nitzsche H, Wegener T, Metz H, Peschel D, Hause G, Howitz S, Groth T, Mäder K (2016) 'Different Strategies for Production and Characterisation of Collagen-Chitosan-Scaffolds Experimental methods', Conference poster.

Nijeholt G J, van Walderveen MA, Castelijns JA, van Waesberghe JH, Polman C, Scheltens P, Rosier PF, Jongen PJ, Barkhof F (1998) 'Brain and spinal cord abnormalities in multiple sclerosis: Correlation between MRI parameters, clinical subtypes and symptoms', *Brain*, 121, 687–697.

- Nowogrodzki A (2018) 'The world's strongest MRI machines are pushing human imaging to new limits', *Nature*, 563 (7729), 24–26.
- Nugent G E, Aneloski N M, Schmidt T A, Schumacher B L, Voegtline M S, Sah R L (2006) 'Dynamic shear stimulation of bovine cartilage biosynthesis of proteoglycan 4', *Arthritis and Rheumatism*, 54 (6), 1888–1896.
- O'Brien F J (2011) 'Biomaterials & scaffolds for tissue engineering', *Materials Today*, 14 (3), 88–95.
- O'Connell G D, Leach J K, Klineberg E (2015a) 'Tissue Engineering a Biological Repair Strategy for Lumbar Disc Herniation', *BioResearch Open Access*, 4 (1), 431–445.
- O'Connor C J, Case N, Guilak F (2013) 'Mechanical regulation of chondrogenesis', *Stem Cell Research and Therapy*, 4 (4), 1.
- Oh S H, Kang S G, Lee J H (2006) 'Degradation behavior of hydrophilized PLGA scaffolds prepared by melt-molding particulate-leaching method: comparison with control hydrophobic one', *Journal of Materials Science: Materials in medicine*, 17 (2), 131–137.
- Ohshima H, Urban J (1992) 'The effect of lactate and pH on proteoglycan and protein synthesis rates in the intervertebral disc', *Spine*, 17 (9), 1079–1082.
- Okay O (2009) 'General Properties of Hydrogels', *Hydrogel Sensors and Actuators*, 6, 1–15.
- Oliveira J T, Martins L, Picciochi R, Malafaya P B, Sousa R A, Neves N M, Mano J F, Reis R L (2009) 'Gellan gum: A new biomaterial for cartilage tissue engineering applications', *Journal of Biomedical Materials Research Part A*, 9999A.
- Oliveira R L, Vieira J G, Barud H S, Assunção R M N, Filho G R, Ribeiro S J L, Messadeqq (2015) 'Synthesis and characterization of methylcellulose produced from bacterial cellulose under heterogeneous condition', *Journal of the Brazilian Chemical Society*, 26 (9), 1861–1870.
- Orakdogan N, Okay O (2006) 'Correlation between crosslinking efficiency and spatial inhomogeneity in poly(acrylamide) hydrogels', *Polymer Bulletin*, 57 (5), 631–641.
- Oxland T R (2015) 'Fundamental Biomechanics of the Spine-What we have learned in the past 25 years and future directions', *Journal of Biomechanics*, 49 (6), 1–16.
- Ozawa H, Imamura K, Abe E, Takahashi N, Hiraide T, Shibasaki Y, Fukuhara T, Suda T (1990) 'Effect of a Continuously Applied Compressive Pressure on Mouse Osteoblast-like Cells (MC3T3-E1) In Vitro', *Journal of Cell Physiology*, 142 (1), 177-185.
- Ozhinsky E, Vigneron D, Nelson S (2011) 'Improved Spatial Coverage for Brain 3D PRESS MRSI by Automatic Placement of Outer-Volume Suppression Saturation Bands', *Journal of Magnetic Resonance Imaging*, 33 (4), 792–802.

Palmer I, Clarke S, Nelson J, Schatton W, Dunne N, Buchanan F (2012) 'Identification of a suitable sterilisation method for collagen derived from a marine Demosponge', *International Journal of Nano and Biomaterials*, 4, 148–163.

Pan T, Song W, Cao X, Wang Y (2016) '3D Bioplotting of Gelatin/Alginate Scaffolds for Tissue Engineering: Influence of Crosslinking Degree and Pore Architecture on Physicochemical Properties', *Journal of Materials Science & Technology*, 32 (9), 889-900.

Park J Y, Choi YJ, Shim J H, Park J H, Cho D W (2016) 'Development of a 3D cell printed structure as an alternative to autologous cartilage for auricular reconstruction', *Journal of Biomedical Materials Research - Part B Applied Biomaterials*, 105 (5), 1016–1028.

Park S-H, Gil E S, Cho H, Mandal B B, Tien L W, Min B H, Kaplan D L (2012) 'Intervertebral Disk Tissue Engineering Using Biphasic Silk Composite Scaffolds', *Tissue Engineering Part A*, 18 (5–6), 447–458.

Parkkinen J J, Ikonen J, Lammi M J, Laakkonen J, Tammi M, Helminen H J (1993) 'effects of cyclic hydrostatic pressure on proteoglycan synthesis in cultured chondrocytes and articular cartilage explants', *Archives of Biochemistry and Biophysics*, 300 (1), 458-465.

Pati F, Jang J, Woo Lee J, Cho D-W (2015) 'Chapter 7 Extrusion Bioprinting, Essentials of 3D Biofabrication and Translation', *Academic Press*, 123-152.

Payne K F, Balasundaram I, Deb S, Di Silvio L, Fan K F (2014) 'Tissue engineering technology and its possible applications in oral and maxillofacial surgery', *British Journal of Oral and Maxillofacial Surgery*, 52 (1), 7–15.

Pei B-Q, Li H, Zhu G, Li D-Y, Fan Y-B, Wu S-Q (2013) 'The Application of Fiber-Reinforced Materials in Disc Repair', *BioMed Research International*, 2013, 1–10.

Peltola S M, Melchels F P, Grijpma D W, Kellomäki M (2008) 'A review of rapid prototyping techniques for tissue engineering purposes', *Annals of medicine*, 40 (4), 268–80.

Pepelanova I, Kruppa K, Scheper T, Lavrentieva A (2018) 'Gelatin-Methacryloyl (GelMA) Hydrogels with Defined Degree of Functionalization as a Versatile Toolkit for 3D Cell Culture and Extrusion Bioprinting', *Bioengineering*, 5 (3), 55.

Pereira H, Silva-Correia J, Yan L P, Oliveira A L, Oliveira J M, Espregueira-Mendes J D, Reis R L (2013) 'Combined application of Silk-fibroin/methacrylated gellan gum hydrogel in tissue engineering approaches for partial and/or total meniscus replacement while enabling control of neovascularization', *Revue de Chirurgie Orthopédique et Traumatologique*, 99 (8), e18–e19.

Peretz S, Florea-spiroiu M, Anghel D-F, Bala D, Stoian C, Zgherea G (2014) 'Preparation of Porous Calcium Alginate Beads and Their Use for Adsorption of O-Nitrophenol from Aqueous Solutions', *New Applications of Nanomaterials*, 123-136.

Périeré D, Korda D, Iatridis J C (2005) 'Confined compression experiments on bovine nucleus pulposus and annulus fibrosus: Sensitivity of the experiment in the determination of compressive modulus and hydraulic permeability', *Journal of Biomechanics*, 38 (11), 2164–2171.

Pescosolido L, Schuurman W, Malda J, Matricardi P, Alhaique F, Coviello T, van Weeren P R, Dhert W J, Hennink W E, Vermonden T (2011) 'Hyaluronic acid and dextran-based semi-IPN hydrogels as biomaterials for bioprinting', *Biomacromolecules*, 12 (5), 1831–1838.

Petretta M, Bartolotti I, Grigolo B, Roseti L, Cavallo C, Desando G, Parisi V (2018) 'Three-Dimensional Bioprinting of Cartilage by the Use of Stem Cells: A Strategy to Improve Regeneration', *Materials*, 11 (9), 1749.

Pfaffl M W (2001) 'A new mathematical model for relative quantification in real-time RT-PCR', *Nucleic acids research*, 29 (9), e45.

Phillipson K, Hay J N, Jenkins M J (2014) 'Thermal analysis FTIR spectroscopy of poly( $\epsilon$ -caprolactone)', *Thermochimica Acta*, 595, 74–82.

Ponchel F, Toomes C, Bransfield K, Leong F T, Douglas S H, Field S L, Bell S M, Combaret V, Puisieux A, Mighell A J, Robinson P A, Inglehearn C F, Isaacs J D, Markham A F (2003) 'Real-time PCR based on SYBR-Green I fluorescence: An alternative to the TaqMan assay for a relative quantification of gene rearrangements, gene amplifications and micro gene deletions', *BMC Biotechnology*, 3 (18).

Pradeep S, Hunter D J, Jouve C, Hartigan C, Limke J, Pena E, Swaim B, Li Ling, Rainville J (2010) 'Inciting Events Associated with Lumbar Disk Herniation', *Spine Journal*, 10 (5), 388–395.

Prince C W, Rahemtulla F, Butler W T (2015) 'Incorporation of [ 35 S] sulphate into glycosaminoglycans by mineralized tissues in vivo', *Biochemical Journal*, 224 (3), 941–945.

Punt I, Willems P, Kurtz S, van Rhijn L, van Ooij A (2012) 'Clinical outcomes of two revision strategies for failed total disc replacements', *European Spine Journal*, 21 (12), 2558–2564.

Puppi D, Chiellini F, Piras A M, Chiellini E (2010) 'Polymeric materials for bone and cartilage repair', *Topical Issue on Biomaterials*, 35 (4), 403–440.

Pörtner R, Goepfert C, Wiegandt K, Janssen R, Ilinich E, Paetzold H, Eisenbarth E (2009) 'Technical Strategies to Improve Tissue Engineering of Cartilage-Carrier-Constructs', *Advances in Biochemical Engineering Biotechnology*, 112, 145-181.

Qiagen (2016) Quick-Start Protocol, RNeasy® Mini Kit. Available at: [www.qiagen.com/safety](http://www.qiagen.com/safety) (04/03/2018).

Rajaram A, Schreyer D, Chen D (2014) 'Bioplotting Alginate/Hyaluronic Acid Hydrogel Scaffolds with Structural Integrity and Preserved Schwann Cell Viability', *3D Printing and Additive Manufacturing*, 1 (4), 194–203.

- Ramage L, Nuki G, Salter D M (2009) 'Signalling cascades in mechanotransduction: cell – matrix interactions and mechanical loading', *Scandinavian Journal of Science and Medicine in Sports*, 457–469.
- Randazzo M (2016) '3D printing in neurosurgery: A systematic review', *Surgical Neurology International*, 7 (Suppl 33), 801-809.
- Rasconi S (2009) 'Use of calcofluor white for detection, identification, and quantification of phytoplanktonic fungal parasites', *Applied and Environmental Microbiology*, 75 (8), 2545–2553.
- Rauch C, Feifel E, Amann E M, Spötl H P, Schennach H, Pfaller W, Gstraunthaler G (2011) 'Alternatives to the use of fetal bovine serum: human platelet lysates as a serum substitute in cell culture media', *Altex*, 28 (4), 305–316.
- Rebuzzi M, Vinicola V, Taggi F, Sabatini U, Wehrli FW, Capuani S (2013) 'Potential diagnostic role of the MRI-derived internal magnetic field gradient in calcaneus cancellous bone for evaluating postmenopausal osteoporosis at 3T', *Bone*, 57 (1), 155–163.
- Reeks J, Liang H (2015) 'Materials and Their Failure Mechanisms in Total Disc Replacement', *Lubricants*, 3 (2), 346–364.
- Reinhart L, Knight W, Roberts L, Mendes C (2012) 'HHS Public Access Global Burden of Disease Study 2010', *Lancet*, 380 (9859), 2163–2196.
- Reitmaier S, Kreja L, Gruchenberg K, Kanter B, Silva-Correia J, Oliveira J M, Reis RL, Perugini V, Santin M, Ignatius A, Wilke H J (2014) 'In vivo biofunctional evaluation of hydrogels for disc regeneration', *European Spine Journal*, 23 (1), 19–26.
- Renema W K, Kan H E, Wiering B, Heerschap A (2007) 'In vivo magnetic resonance spectroscopy of transgenic mouse models with altered high-energy phosphoryl transfer metabolism', *NMR in Biomedicine*, 20 (4), 448–467.
- Reppel T, Weinberg K (2018) 'Experimental Determination of Elastic and Rupture Properties of Printed Ninjabflex', *Technische Mechanik*, 38, 104–112.
- Ronken S (2009) 'Influence of material choice and surface structure on cell behaviour', Thesis, Eindhoven University of Technology.
- Rosen C, Kiester P D, Lee T Q (2009) 'Lumbar Disk Replacement Failures: Review of 29 Patients and Rationale for Revision', *Orthopedics*, 32 (8), 562–569.
- Rosenzweig, D, Carelli E, Steffen T, Jarzem P, Haglund L (2015) '3D-Printed ABS and PLA Scaffolds for Cartilage and Nucleus Pulposus Tissue Regeneration', *International Journal of Molecular Sciences*, 16 (7), 15118–15135.

- Rosenzweig D H, Matmati M, Khayat G, Chaudhry S, Hinz B, Quinn T M (2012) 'Culture of primary bovine chondrocytes on a continuously expanding surface inhibits dedifferentiation', *Tissue engineering Part A Mary Ann Liebert*, 18 (23–24), 2466–2476.
- Rutala W A, Weber D J (2013) 'Disinfection and sterilization: An overview', *American Journal of Infection Control*, 41 (5 Suppl), S2–S5.
- Sabzalisenjani A, Nikraz H (2013) 'Priority Medicines for Europe and the World 2013 Update. Background Paper 6 - Priority Diseases and Reasons for Inclusion BP 6.24 - Low Back Pain', *Priority Medicines for Europe and the World 2013 Update*, (Mar), 833–842.
- Safshekan F, Tafazzoli-Shadpour M, Ali Shokrgozar M, Haghhighipour N, Mahdian R, Alireza H (2012) 'Intermittent Hydrostatic Pressure Enhances Growth Factor-Induced Chondroinduction of Human Adipose-Derived Mesenchymal Stem Cells', *Journal of Artificial Organs*, 36 (12), 1065-1071.
- Saijo H, Igawa K, Kanno Y, Mori Y, Kondo K, Shimizu K, Suzuki S, Chikazu D, Iino M, Anzai M, Sasaki N, Chung UI, Takato T (2009) 'Maxillofacial reconstruction using custom-made artificial bones fabricated by inkjet printing technology', *Journal of Artificial Organs*, 12 (3), 200–205.
- Sakao K, Takahashi K A, Arai Y, Inoue A, Tonomura H, Saito M, Yamamoto T, Kanamura N, Imanishi J, Mazda O, Kubo T (2008) 'Induction of chondrogenic phenotype in synovium-derived progenitor cells by intermittent hydrostatic pressure', *Osteoarthritis Cartilage*, 16 (7), 805-814.
- Salzmann S N, Plais N, Shue J, Girardi F P (2017) 'Lumbar disc replacement surgery—successes and obstacles to widespread adoption', *Current Reviews in Musculoskeletal Medicine*, 10 (2), 153–159.
- Sarker B, Papageorgiou D G, Silva R, Zehnder T, Gul-E-Noor F, Bertmer M, Kaschta J, Chrissafis K, Detscha R, R. Boccaccini A (2014) 'Fabrication of alginate–gelatin crosslinked hydrogel microcapsules and evaluation of the microstructure and physico-chemical properties', *Journal of Materials Chemistry B*, 2 (11), 1470.
- Sarma N J, Takeda A, Yaseen N R (2010) 'Colony Forming Cell (CFC) Assay for Human Hematopoietic Cells', *Journal of Visualized Experiments*, (46), 3–7.
- Schluffer K, Heinze T (2010) 'Carboxymethylation of bacterial cellulose', *Macromolecular Symposia*, 294 (2), 117–124.
- Schmitz N, Laverty S, Kraus V B, Aigner T (2010) 'Basic methods in histopathology of joint tissues', *Osteoarthritis and Cartilage*, 18 (Suppl 3), S113–S116.
- Schopp J G, Whitman G J (2014) 'Ex vivo MRI evaluation of breast tumors: A novel tool for verifying resection of nonpalpable only MRI detected lesions', *Breast Diseases*, 25 (2), 134–135.
- Schulz J, Pretzsch M, Khalaf I, Deiwick A, Scheidt H A, Salis-Soglio G, Bader A, Huster D (2007) 'Quantitative monitoring of extracellular matrix production in bone implants by <sup>13</sup>C and <sup>31</sup>P solid-state nuclear magnetic resonance spectroscopy', *Calcified Tissue International*, 80 (4), 275–285.

- Schütz A-M P, Birgit P, Brüggemeier S, Gelinsky M, Lode A (2017) 'Three-dimensional plotting of a cell-laden alginate/ methylcellulose blend: towards biofabrication of tissue engineering constructs with clinically relevant dimensions', *Journal of tissue engineering and regenerative medicine*, 11 (5), 1574-1587.
- Schuurman W, Levett P A, Pot M W, van Weeren P R, Dhert W J, Hutmacher D W, Melchels FP, Klein T J, Malda J (2013) 'Gelatin-methacrylamide hydrogels as potential biomaterials for fabrication of tissue-engineered cartilage constructs', *Macromolecular Bioscience*, 13 (5), 551–561.
- Scott A, Khan K M, Duronio V, Hart D A (2008) 'Mechanotransduction in human bone: In vitro cellular physiology that underpins bone changes with exercise', *Sports Medicine*, 38 (2), 139–160.
- Sechriest V F, Miao Y J, Niyibizi C, Westerhausen-Larson A, Matthew H W, Evans C H, Fu F H, Suh J K (2000) 'GAG-augmented polysaccharide hydrogel: a novel biocompatible and biodegradable material to support chondrogenesis', *Journal of biomedical materials research*, 49 (4), 534–41.
- Seidel J, Ahlfeld T, Adolph M, Kümmitz S, Steingroewer J, Krujatz F, Bley T, Gelinsky M, Lode A (2017) 'Green bioprinting: extrusion-based fabrication of plant cell-laden biopolymer hydrogel scaffolds', *Biofabrication*, 9 (4), 045011.
- Setton L A, Bonassar L J, Masuda K (2007) 'Regeneration and replacement of the intervertebral disc', *Principles of Tissue Engineering*, 877–896.
- Shahriari D, Koffler J, Lynam D A, Tuszynski M H, Sakamoto J S (2016) 'Characterizing the degradation of alginate hydrogel for use in multilumen scaffolds for spinal cord repair', *Journal of Biomedical Materials Research Part A*, 104 (3), 611–619.
- Sharifi S, Bulstra S K, Grijpma D W, Kuijjer R (2015) 'Treatment of the degenerated intervertebral disc; closure, repair and regeneration of the annulus fibrosus', *Journal of Tissue Engineering and Regenerative Medicine*, 9 (10), 1120–1132.
- Sharma G, Saxena R K, Mishra P (2007) 'Differential effects of cyclic and static pressure on biochemical and morphological properties of chondrocytes from articular cartilage', *Clinical Biomechanics*, 22 (2), 248–255.
- Sharma G, Saxena R K, Mishra P (2008) 'Synergistic effect of chondroitin sulfate and cyclic pressure on biochemical and morphological properties of chondrocytes from articular cartilage', *Osteoarthritis and Cartilage*, 16 (11), 1387–1394.
- Shatil A S, Matsuda K M, Figley C R (2016) 'A method for whole brain ex vivo magnetic resonance imaging with minimal susceptibility artifacts', *Frontiers in Neurology*, 7 (Nov), 1–10.
- Shindle M K, Foo L F, Kelly B T, Khanna A J, Domb B G, Farber A, Wanich T, Potter H G (2006) 'Magnetic resonance imaging of cartilage in the athlete: current techniques and spectrum of disease', *The Journal of bone and joint surgery*, 88 (Suppl 4), 27–46.

- Shioji S, Imai S, Ando K, Kumagai K, Matsusue Y (2014) 'Extracellular and intracellular mechanisms of mechanotransduction in three- Dimensionally embedded rat chondrocytes', *PLoS ONE*, 9 (12), 1–13.
- Shuff C, An H S (2005) 'Artificial disc replacement: the new solution for discogenic low back pain?', *American Journal of Orthopedics*, 34 (1), 8–12.
- Sin D, Miao X, Liu G, Wei F, Chadwick G, Yan C, Friis T (2010) 'Polyurethane (PU) scaffolds prepared by solvent casting/particulate leaching (SCPL) combined with centrifugation', *Materials Science and Engineering C*, 30 (1), 78–85.
- Singh R, Sarker B, Silva R, Detsch R, Dietel B, Alexiou C, Boccaccini A R, Cicha I (2015) 'Evaluation of hydrogel matrices for vessel bioplotting: Vascular cell growth and viability', *Journal of biomedical materials research. Part A*, 104 (3), 577-585.
- Sironen R K, Karjalainen H M, Törrönen K, Elo M A, Kaarniranta K, Takigawa M, Helminen H J, Lammi M J (2002) 'High pressure effects on cellular expression profile and mRNA stability. A cDNA array analysis', *Biorheology*, 39 (1–2), 111–117.
- Smith R L, Rusk S F, Ellison B E, Wessells P, Tsuchiya K, Carter D R, Caler W E, Sandell L J, Schurman D J. (1996) 'In Vitro Stimulation of Articular Chondrocyte mRNA and Extracellular Matrix Synthesis by Hydrostatic Pressure', *Journal of Orthopaedic Research*, (34), 53–60.
- Smith R L, Lin J, Shida J, Kajiyama G, Hoffman A R, van der Meulen M C H, Goodman S B, Schurman D J (2000) 'Time-dependent effects of intermittent hydrostatic pressure on articular chondrocyte type II collagen and aggrecan mRNA expression', *Journal of rehabilitation research and development*, 37 (2), 153–161.
- Soleimanifar F, Hosseini F S, Atabati H, Behdari A, Kabiri L, Enderami S E, Khani M M, Ardeshiryajimi A, Saburi E (2019) 'Adipose-derived stem cells-conditioned medium improved osteogenic differentiation of induced pluripotent stem cells when grown on polycaprolactone nanofibers', *Journal of Cellular Physiology*, 234 (7), 10315–10323.
- Spilimbergo S, Dehghani F, Bertuccio A, Foster N R (2003) 'Inactivation of bacteria and spores by pulse electric field and high pressure CO<sub>2</sub> at low temperature', *Biotechnology and Bioengineering*, 82 (1), 118–125.
- Steele J A, McCullen S D, Callanan A, Autefage H, Accardi M A, Dini D, Stevens M M (2014) 'Combinatorial scaffold morphologies for zonal articular cartilage engineering', *Acta Biomaterialia*, 10 (5), 2065–2075.
- Stein A (2007) 'Decreasing variability in your cell culture', *BioTechniques*, 43 (2), 228–229.
- Stergar J (2019) 'Intervertebral disc tissue engineering: A brief review', *Bosnian Journal of Basic Medical Sciences*, 19 (2), 130–137.
- Steward A J, Thorpe S D, Buckley C T, Wagner D R, Kelly D J (2012) 'Cell-matrix interactions regulate mesenchymal stem cell response to hydrostatic pressure' *Acta Biomaterialia*, 8 (6), 2153-2159.

Stoppel W L, White J C, Horava S D, Henry A C, Roberts S C, Bhatia S R (2014) 'Terminal sterilization of alginate hydrogels: Efficacy and impact on mechanical properties', *Journal of Biomedical Materials Research - Part B Applied Biomaterials*, 102 (4), 877–884.

Suh J-K, Baek G H, Arøen A, Malin C M, Niyibizi C, Evans C H, Westerhausen-Larson A (1999) 'Intermittent sub-ambient interstitial hydrostatic pressure as a potential mechanical stimulator for chondrocyte metabolism', *Osteoarthritis Cartilage*, 7, 71–80.

Suzuki T, Toyoda T, Suzuki H, Hisamori N, Matsumoto H, Toyama Y (2006) 'Hydrostatic pressure modulates mRNA expressions for matrix proteins in human meniscal cells', *Biorheology*, 43 (5), 611–622.

Tan Z, Parisi C, Di Silvio L, Dini D, Elia Forte A (2017) 'Cryo-genic 3D printing of super soft hydrogels' *Scientific reports*, 7, 1-11.

Tanenbaum L N (2006) 'Clinical 3T MR imaging: Mastering the challenges', *Magnetic Resonance Imaging Clinics of North America*, 14 (1), 1–15.

Tatumura M, Sakane M, Ochiai N, Mizuno S (2013) 'Off-loading of cyclic hydrostatic pressure promotes production of extracellular matrix by chondrocytes', *Cells Tissues Organs*, 198 (6), 405–413.

Taylor A J, Salerno M, Dharmakumar R, Jerosch-Herold M (2016) 'T1 Mapping Basic Techniques and Clinical Applications', *JACC: Cardiovascular Imaging*, 9 (1), 67–81.

Terzic A, Nelson T J (2013) 'Regenerative medicine primer', *Mayo Clinic proceedings*, 88 (7), 766–775.

Thermo Scientific (2007) 'Growth Factors in Thermo Scientific HyClone Cell Culture Serum', Thermo Scientific, 19 (1), 2–3.

Thompson D (1917) 'On growth and form' *Cambridge University Press*.

Tofts P S (2010) 'Introduction: What do we mean by quantitative MRI?', In: Proceedings of the Joint Annual Meeting of ISMRM-ESMRMB, Brighton and Sussex Medical School Weekend educational course.

Tofts P, Steens S, van Bucham M A (2003) 'Magnetization Transfer 1', Chapter 8 Quantitative MRI of the Brain: Measuring Changes Caused by Disease.

Tomley, F M, Shirley M W (2009) 'Livestock infectious diseases and zoonoses' *Philosophical Transactions of The Royal Society*, 364, 2637-2642.

Topuz M, Dikici B, Yilmazer H, Gavkali M (2018) 'A Review on the Hydrogels Used in 3D Bio-Printing', *International Journal of 3D Printing Technologies and Digital Industry*, 2 (2), 68–75.

Tovar N, Witek L, Atria P, Sobieraj M, Bowers M, Lopez C D, Cronstein B N, Coelho P G (2018) 'Form and functional repair of long bone using 3D-printed bioactive scaffolds', *Journal of Tissue Engineering and Regenerative Medicine*, 12 (9), 1986–1999.

- Toyoda T, Seedhom B B, Yao J Q, Kirkham J, Brookes S, Bonass W A (2003) 'Hydrostatic Pressure Modulates Proteoglycan Metabolism in Chondrocytes Seeded in Agarose', *Arthritis Rheumatology*, 48 (10), 2865–2872.
- Trachtenberg J E, Mountziaris P M, Miller J S, Wettergreen M, Kasper F K, Mikos A G (2014) 'Open-source three-dimensional printing of biodegradable polymer scaffolds for tissue engineering', *Journal of Biomedical Materials Research - Part A*, 102 (12), 4326–4335.
- T.Reza A, B.Nicoll S (2008) 'Hydrostatic Pressure Differentially Regulates Outer and Inner Annulus Fibrosus Cell Matrix Production in 3D Scaffolds', *Annals of Biomedical Engineering*, 36 (2), 204–213.
- Twomey J D, Thakore P I, Hartman D A, Myers E G, Hsieh A H (2014) 'Roles of type VI collagen and decorin in human mesenchymal stem cell biophysics during chondrogenic differentiation', *European Cells and Materials*, 27, 237–250.
- Urban G, Hall A C (1987) 'The Effects of Hydrostatic and Osmotic Pressures on Chondrocyte Metabolism', *Cell Mechanics and Cellular Engineering*, 398–399.
- Urban J P G, Maroudas A, Bayliss M T, Dillon J (1979) 'Swelling pressures of proteoglycans at the concentrations found in cartilaginous tissues', *Biorheology*, 16 (6), 447–464.
- Urban J P G, Maroudas A (1981) 'Swelling of the intervertebral disc in vitro', *Connective Tissue Research*, 9 (1), 1–10.
- Urban J P G, Roberts S (2003) 'Degeneration of the intervertebral disc', *Arthritis research and therapy*, 5 (3), 120–130.
- Van Den Eerenbeemt K D, Ostelo R W, van Boyen B J, Peul W C, van Tulder M W (2010) 'Total disc replacement surgery for symptomatic degenerative lumbar disc disease: A systematic review of the literature', *European Spine Journal*, 19 (8), 1262–1280.
- Van der Valk J, Bieback K, Buta C, Cochrane B, Dirks W G, Fu J, Hickman J J, Hohensee C, Kolar R, Liebsch M, Pistollato F, Schulz M, Thieme D, Weber T, Wiest J, Winkler S, Gstraunthaler G (2018) 'Fetal Bovine Serum (FBS): Past - Present - Future', *Altex*, 35 (1), 99–118.
- Van Rossom S, Robert Smith C, Zevenbergen L, Thelan D G, Vanwanseele B, Van Assche D, Jonkers Ilse (2017) 'Knee cartilage thickness, T1ρ and T2 relaxation time are related to articular cartilage loading in healthy adults', *PLoS ONE*, 12 (1), 1–16.
- Van Uden S, Silva-Correia J, Correlo V M, Oliveira J M, Reis R L (2015b) 'Custom-tailored tissue engineered polycaprolactone scaffolds for total disc replacement', *Biofabrication*, 7 (1), 015008.
- Ventola C L (2014) 'Medical Applications for 3D Printing: Current and Projected Uses', *P & T: a peer-reviewed journal for formulary management*, 39 (10), 704–11.
- Veres S P, Robertson P A, Broom N D (2009) 'The Morphology of Acute Disc Herniation', *Spine*, 34 (21), 2288–2296.

- Vigfúsdóttir Á T, Pasrija C, Thakore P I, Schmidt R B, Hsieh A H (2010) 'Role of pericellular matrix in mesenchymal stem cell deformation during chondrogenic differentiation', *Cellular and Molecular Bioengineering*, 3 (4), 387–397.
- Vinardell T, Rolfe R A, Buckley C T, Meyer E G, Ahearne M, Murphy P, Kelly D J (2012) 'Hydrostatic pressure acts to stabilise a chondrogenic phenotype in porcine joint tissue derived stem cells', *Europeans Cells and Materials*, 121 (32), 133–134.
- Vukicevic M, Mosadegh B, Min J K, Little S H (2017) 'Cardiac 3D Printing and its Future Directions', *JACC: Cardiovascular Imaging*, 10 (2), 171–184.
- Wade K R, Robertson P A, Thambyah A, Broom N D (2014) 'How Healthy Discs Herniate', *Spine*, 39 (13), 1018–1028.
- Wan Y, Feng G, Shen F H, Laurencin C T, Li X (2008) 'Biphasic scaffold for annulus fibrosus tissue regeneration', *Biomaterials*, 29 (6), 643–652.
- Wang Q, Sun J, Yao Q, Ji C, Liu J, Zhu Q (2018) '3D printing with cellulose materials', *Cellulose*, 25 (8), 4275–4301
- Wang Y (2012) 'Influence of degenerative changes of intervertebral disc on its material properties and pathology', *Chinese journal of traumatology*, 15 (2), 67–76.
- Wang Z, Wang Z, Weijia L W, Zhen W, Yang D, Peng S (2017) 'Novel biomaterial strategies for controlled growth factor delivery for biomedical applications', *NPG Asia Materials Nature Publishing Group*, 9 (10), e435.
- Watanabe A, Benneker L M, Boesch C, Watanabe T, Obata T, Anderson S E (2007) 'Classification of intervertebral disk degeneration with axial T2 mapping', *American Journal of Roentgenology*, 189 (4), 936–942.
- Weber F, Böhme J, Scheidt HA, Gründer W, Rammelt S, Hacker M, Schulz-Siegmund M, Huster D (2012) '31P and 13C solid-state NMR spectroscopy to study collagen synthesis and biomineralization in polymer-based bone implants', *NMR in Biomedicine*, 25 (3), 464–475.
- Weber K T, Jacobsen T D, Maidhof R, Virojanapa J, Overby C, Bloom O, Quraishi S, Levine M, Chahine N O (2015) 'Developments in intervertebral disc disease research: pathophysiology, mechanobiology, and therapeutics', *Current Reviews in Musculoskeletal Medicine*, 8 (1), 18–31.
- Whatley B (2013) 'Biofabrication of Scaffolds for Intervertebral Disc Tissue Regeneration', Thesis, Clemson University
- Whatley B, Kuo J, Shuai C (2011a) 'Fabrication of a biomimetic elastic intervertebral disk scaffold using additive manufacturing', *Biofabrication*, 3 (1), 015004.
- Wheeler-Kingshott C A M, Barker G J (2003) 'Chapter 7 D: the diffusion of water', *Quantitative MRI of the Brain*

- Wheeler C A, Fitzgerald J B, Grodzinsky A J (2005) 'Cartilage mechanobiology: The response of chondrocytes to mechanical force', *Current Opinion in Orthopaedics*, 16 (5), 346–353.
- White A A (1989) 'Clinical biomechanics of cervical spine implants', *Spine*, 14 (10), 1040–1045.
- Wilda H, Gough J E (2006) 'In vitro studies of annulus fibrosus disc cell attachment, differentiation and matrix production on PDLLA/45S5 Bioglass composite films', *Biomaterials*, 27 (30), 5220–5229.
- Wilke H-J, Neef P, Caimi M, Hoogland T, Claes L E (1999) 'New In-vivo measurements of pressures in disc in daily life', *Spine*, 24 (8), 755–762.
- Williams C, James A, Chae M P, Hunter-Smith D J (2015) '3D printing in clinical podiatry: a pilot study and review', *Journal of Foot and Ankle Research*, 8 (S2), 2015.
- Wilson W C, Boland T (2003) 'Cell and organ printing 1: protein and cell printers', *The anatomical record. Part A, Discoveries in molecular, cellular, and evolutionary biology*, 272 (2), 491–496.
- Wohlers Associates, Inc (2013) 'Technical, Market and strategic advice on additive manufacturing 3D printing rapid product development' [Internet] 16/05/2019, <http://wohlersassociates.com/>
- Wong T S, Teo N, Kyaw M O (2010) 'Prevalence and Risk Factors Associated with Low Back Pain Among Health Care Providers in a District Hospital', *Malaysian Orthopaedic Journal*, 4 (2), 23–28.
- Wood R, Bassett K, Foerster V, Spry C, Tong L (2012) '1.5 Tesla Magnetic Resonance Imaging Scanners Compared With 3.0 Tesla Magnetic Resonance Imaging Scanners: Systematic Review of Clinical Effectiveness', *CADTH technology overviews*, 2 (2), e2201.
- Woodfield T B F, Malda J, de Wijn J, Péters F, Riesle J, van Blitterswijk C A (2004) 'Design of porous scaffolds for cartilage tissue engineering using a three-dimensional fiber-deposition technique', *Biomaterials*, 25 (18), 4149–4161.
- Woodfield T B F, Moroni L, Malda J (2009) 'Combinatorial approaches to controlling cell behaviour and tissue formation in 3D via rapid-prototyping and smart scaffold design', *Combinatorial chemistry & high throughput screening*, 12, 562–579.
- Woodruff M A, Hutmacher D W (2010) 'The return of a forgotten polymer - Polycaprolactone in the 21st century', *Progress in Polymer Science*, 35 (10), 1217–1256.
- Wu X, Liu Y, Li X, Wen P, Zhang Y, Long Y, Wang X, Guo Y, Xing F, Gao J (2010) 'Preparation of aligned porous gelatin scaffolds by unidirectional freeze-drying method', *Acta Biomaterialia*, 6 (3), 1167–1177.
- Xian J F, Chen M, Jin Z Y (2015) 'Magnetic resonance imaging in clinical medicine: Current status and potential future developments in China', *Chinese Medical Journal*, 128 (5), 569–570.
- Xinxin S, Hunter C J (2006) 'Developing an alginate/chitosan hybrid fiber scaffold for annulus fibrosus cells', *Journal of Biomedical Materials Research Part A*, 81 (4), 771–780.

- Xiongfa J, Hao Z, Liming Z, Jun X (2018) 'Recent advances in 3D bioprinting for the regeneration of functional cartilage', *Regenerative Medicine*, 13 (1), 73–87.
- Xu H, Othman S F, Magin R L (2008) 'Monitoring tissue engineering using magnetic resonance imaging', *Journal of Bioscience and Bioengineering*, 106 (6), 515–527.
- Yamamura H, Suzuki Y, Imaizumi Y (2018) 'Ion Channels as Therapeutic Targets for the Immune, Inflammatory, and Metabolic Disorders Role of Thermo-Sensitive Transient Receptor Potential Channels in Brown Adipose Tissue', *Biological and Pharmaceutical Bulletin*, 41 (8), 1145–1151.
- Yang J, Yamato M, Shimizu T, Sekine H, Ohashi K, Kanzaki M, Ohki T, Nishida K, Okano T (2007) 'Reconstruction of functional tissues with cell sheet engineering', *Biomaterials*, 28 (34), 5033–5043.
- Yavropoulou M P, Yovos J G. (2016) 'The molecular basis of bone mechanotransduction', *Journal of Musculoskeletal Neuronal Interactions*, 16 (3), 221–236.
- Yin D, Wu H, Liu C, Zhang J, Zhou T, Wu J, Wan Y (2014a) 'Fabrication of composition-graded collagen/chitosan–polylactide scaffolds with gradient architecture and properties', *Reactive and Functional Polymers*, 83, 98–106.
- Yixiang D, Yong T, Liao S, Chan CK, Ramakrishna S (2008) 'Degradation of Electrospun Nanofiber Scaffold by Short Wavelength Ultraviolet Radiation Treatment and Its Potential Applications in Tissue Engineering', *Tissue Engineering Part A*, 14 (8), 1321–1329.
- Young K J, Pierce J E, Zuniga J M (2019) 'Assessment of body-powered 3D printed partial finger prostheses: a case study', *3D Printing in Medicine*, 5 (7).
- Zehnder T, Sarker B, Boccaccini A R, Detsch R (2015) 'Evaluation of an alginate-gelatine crosslinked hydrogel for bioplotting', *Biofabrication*, 7 (2), 025001.
- Zein I, Hutmacher D W, Cheng Tan K, Teoh S H (2002) 'Fused deposition modeling of novel scaffold architectures for tissue engineering applications', *Biomaterials*, 23 (4), 1169–1185.
- Zein N, Hanouneh I A, Bishop P D, Samaan M, Eghtesad B, Quintini C, Miller C, Yerian L, Klatt R (2013) '3-Dimensional (3D) print of liver for preoperative planning in live donor liver transplantation', *Hepatology*, 58 (4 Suppl. 1), 784A-785A.
- Zeng C, Yang Q, Zhu M, Du L, Zhang J, Ma X, Xu B, Wang L (2014) 'Silk fibroin porous scaffolds for nucleus pulposus tissue engineering', *Materials Science and Engineering C*, 37 (1), 232–240.
- Zhang Y S, Yue K, Aleman J, Moghaddam K M, Bakht S M, Yang J, Jia W, Dell'Erba V, Assawes P, Shin S R, Dokmeci M R, Oklu R, Khademhosseini A (2017) '3D Bioprinting for Tissue and Organ Fabrication', *Annals of Biomedical Engineering*, 45 (1), 148–163.
- Zhang L, Hu J, Athanasiou K A (2009) 'The role of tissue engineering in articular cartilage repair and regeneration', *Critical Reviews in Biomedical Engineering*, 37 (1–2), 1–57.

- Zhang Y, Chen S, Pei M (2016) 'Biomechanical signals guiding stem cell cartilage engineering: From molecular adaption to tissue functionality', *European Cells and Materials*, 5 (31), 59-78.
- Zhang Z (2014) 'Chondrons and the Pericellular Matrix of Chondrocytes', *Tissue Engineering Part B: Reviews*, 21 (3), 267–277.
- Zhang Z, Jin Y, Yin J, Xu C, Xiong R, Christensen K, Ringeisen B R, Chrisey D B (2018) 'Evaluation of bioink printability for bioprinting applications', *Applied Physics Reviews*, 5 (4).
- Zhao J, Lu Z, Wu H, Li W, Zheng L, Zhao J (2017) 'Collagen-alginate as bioink for three-dimensional (3D) cell printing based cartilage tissue engineering', *Materials Science and Engineering: C*, 83, 195–201.
- Zheng C, Levenston, M E (2015) 'Fact versus artifact: Avoiding erroneous estimates of sulfated glycosaminoglycan content using the dimethylmethylene blue colorimetric assay for tissue-engineered constructs', *European Cells and Materials*, 29, 224–236.
- Zhou S, McCarthy I D, McGregor A H, Coombs R R H, Hughes S P F (2000) 'Geometrical dimensions of the lower lumbar vertebrae', *European Spine Journal*, 9 (3), 242–248.
- Zhu H (2018) 'Chapter 3: Three-dimensional bioprinting for cartilage regeneration', *Frontiers in Nanobiomedical Research*, 10, 49–74.
- Zhu J, Marchant R E (2011) 'Design properties of hydrogel tissue-engineering scaffolds', *Expert Review of Medical Devices*, 8 (5), 607–26.
- Zhu N, Chen X (2013) 'Biofabrication of Tissue Scaffolds', *Advances in Biomaterials Science and Biomedical Applications*, 315–328.
- Zuo J, Saadat E, Romero A, Loo K, Li X, Link T M, Kurhanewicz J, Majumdar S (2009) 'Assessment of intervertebral disc degeneration with magnetic resonance single-voxel spectroscopy', *Magnetic Resonance in Medicine*, 62 (5), 1140–1146.
- Zuo J, Joseph G, Li X, Link T M, Hu S S, Berven S H, Kurhanewicz J, Majumdar S (2012) 'In-vivo Intervertebral Disc Characterization using Magnetic Resonance Spectroscopy and T1p Imaging: Association with Discography and Oswestry Disability Index and SF-36', *Spine*, 37 (3), 214–221.

## **Appendix**

### Appendix A: Preliminary investigation of polycaprolactone for bioprinting – Relating to Chapter 3

#### Introduction

In previous research using additive manufacturing for tissue-engineered IVDs the most common type of material that has been used is thermoplastics or thermoplastic/hydrogel hybrids (Rosenzweig *et al.*, 2015; van Uden *et al.*, 2015b; Hu *et al.*, 2018). The selection of thermoplastics for disc scaffold generation has been justified by the incentive to mimic the strength of the whole disc (inclusive of the fibrous annulus disc region) typically in the region of 16.37 Mpa (Pei *et al.*, 2013). Based on this approach, PCL thermoplastic was investigated for bioplotting, chosen for its preestablished use in biomedical applications (Guarino *et al.*, 2017). In addition, a multi-material printing method using alginate and PCL was also achieved.

#### Methods

##### Material Selection

PCL is a frequently used synthetic material in medical devices and in conventional 3D printing (such as fused filament fabrication), known to provide structures with a high stability (slow degradation rate of 1–2 years) and strength (to endure loading) (Woodruff and Hutmacher, 2010).

##### Polycaprolactone preparation

PCL granules MW = 14,000 kDa (Sigma-Aldrich) were melted at 87-90°C within the plotting device, using a custom cartridge heat jacket, until the material turned clear and homogenous (minimum of 20 minutes).

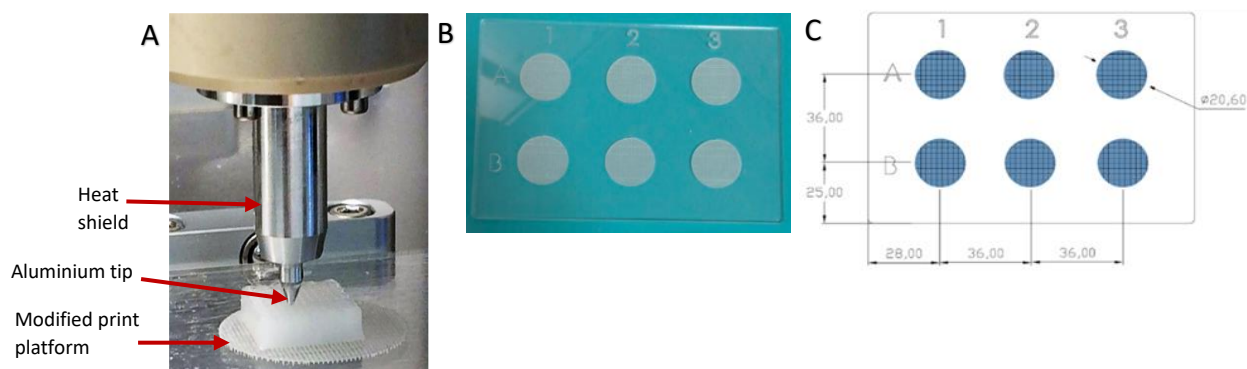
##### Polycaprolactone printing

Material print parameter screening was performed, based upon protocols found in literature with systematic adjustments for bioprinting with the Bioscaffolder 3.1 (GeSiM, Germany) (figure 27). The settings used were optimised and determined according to material flow consistency (determined visually during material extrusion

testing), strand definition (measured using microscopy), and structural integrity (i.e. the ability to maintain a defined shape whilst supporting subsequent layers without structural collapse). The screened conditions for the fabrication of PCL can be seen in Table.S1A. The pre-determined dimensions of 12 mm by 12 mm by 2 mm were employed for scaffold printing, with an angle orientation change of 90 ° per layer and a steel cannula tip with a heat shield to prevent temperature change within the tip (Nordson). Three scaffold variants were fabricated using PCL with strand numbers of six, eight or ten. An additional modification to improve printing included the use of a modified laser-etched print plate, which was designed to increase traction to prevent scaffolds from lifting during printing (due to material cooling and contraction) (Fig.S1A, A-C).

**Supplementary Table S1A** Screened print parameters for the printing of polycaprolactone, alginate methyl cellulose and non-fibrillar collagen + 1% methyl cellulose using the 3.1 Bioscaffolder (GeSIM, Germany)

Print parameter ranges							
Material	Tip ID* (mm)	Z-offset (mm)	Pressure (kPa)	Speed (mm/s)	Start break (s)	Temperature (°C)	Interlayer pause (s)
Polycaprolactone	0.35	0.11	115	5	-0.5	88	20



**Supplementary Figure S1A** (A) Plotting of a polycaprolactone (PCL) scaffolds with a 0.35 mm diameter tapered-aluminium tip with attached heat-shield (Vieweg, Dresden) (B) PCL was plotted onto a modified print platform to prevent scaffold lifting during material cooling and contraction. (C) Drawing dimensions of the laser-etched print platform custom made from Poly-ethylene to increase surface traction.

#### Multi-material plotting

Multi-material plotting of simple and computer-modelled scaffolds were trialed using the Bioscaffolder 3.1 (GeSIM, Germany) and employed the previously established print-parameters for alg/MC (Chapter 3, section 3.2.3.1) and for PCL (Table.S1A).

#### Polycaprolactone and alginate methyl cellulose

Multi-material printing of alg/MC with PCL was trialed using adjusted scaffold dimensions of dimensions of 12 mm by 12 mm by 12 mm, with 90 layers. Firstly, 30 layers of PCL were printed. Subsequently, alternate PCL and alginate strands were plotted for 10 layers, with a 40 second interlayer pause duration and print sequence of 'AC'. The next 20 layers consisted of alg/MC only and the remaining layers printed with PCL alone. Upon completion the scaffolds were submerged in CaCl<sub>2</sub> to cross-link the alg/MC. After 10 minutes the scaffolds were washed with DMEM culture medium and kept under cell culture conditions (5% CO<sub>2</sub>, 37°C).

#### Scaffold characterisation

The PCL scaffolds were assessed based on their macro architectures using optical and scanning electron microscopy (SEM). Imaging was performed to study strand-

strand material spacing (pore size), pore morphology, strand width and overall structural consistency.

### Scanning Electron Microscopy of polycaprolactone scaffolds

The PCL scaffold samples were prepared for SEM by taking intact sub-sections excised with a scalpel. Pieces from PCL scaffolds with strand numbers of 6, 8, 10 or 12 were fixed to SEM stubs using adhesive carbon tabs (Agar scientific Ltd., UK). The stubs were loaded into a sputter coating device (Quorum Technologies Ltd. Q150T ES) using a vacuum of  $1 \times 10^{-2}$  mBar. Argon gas filled the sputter coating chamber and a 4 nm conductive platinum layer was applied to the samples (Fig.S2A). SEM imaging was performed on a Zeiss sigma field emission gun scanning transmission electron microscope (Carl Zeiss Ltd. UK, FEG-STEM) at the University of Brighton's Image Analysis Unit (IAU). Measurements were determined from the SEM images using the smart Tiff imaging software package (Zeiss Zen 2).



**Supplementary Figure S2A** Sections of polycaprolactone scaffold samples prepared for Scanning Electron Microscopy (with strand numbers of 6, 8, 10 and 12 from left to right) mounted on stubs, spluttered with a 4nm layer of platinum.

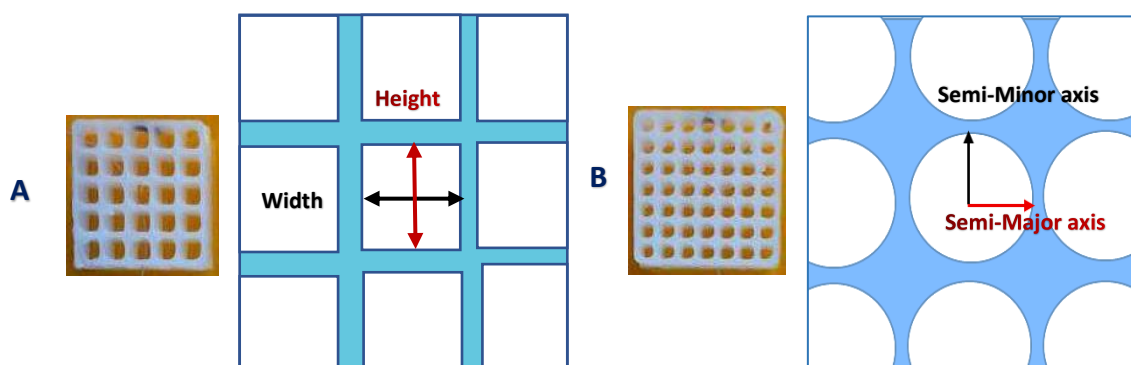
### Optical microscopy of polycaprolactone scaffolds

Scaffold structure was observed with bright field microscopy (Motic, Carl Zeiss). Strand widths and internal pore cross-sectional areas of the scaffolds were determined (figure 42) from light microscope images using 'motic images plus 2.0' digital microscopy software suite. Measurements were taken of the first 12 pores from each

scaffold edge (left to right). The pore cross-section measurements were based on the morphology of the pores. The pores of scaffolds with six strands were considered as square (Fig.S3, A) and the area calculated by the formula (S1A). Whereas, the eight and ten strand pores were considered elliptical in shape (Fig.S3, B), and as such the area was calculated using formula (S2A):

Supplementary Equation S1A  $Area = height \times width$

Supplementary Equation S2A  $Area = \pi \times (Semi - Major Axis \times Semi - Minor Axis)$



**Supplementary Figure S3A** Diagram to indicate the measurement of pore areas for different pore morphologies (A) pores of the six strand scaffolds were treated as square, and used the equation:  $Area = width \times height$  (B) for the eight and ten strand scaffolds elliptical pore morphologies were assumed, and areas were calculated using:  $Area = \pi \times semi-major axis \times semi-minor axis$ .

### Compression testing

Compression experiments using an Electroforce WinTest® Digital Control System (BOSE corporation) were performed to characterize the compressive properties of the PCL scaffolds. Dimensional measurements of each scaffold were taken prior to testing using digital callipers (Duratool, 50-100-900). Engineering stress and strain were then recorded to extract the compressive moduli, which was calculated based on the method described in Chapter 3, section 3.2.4.

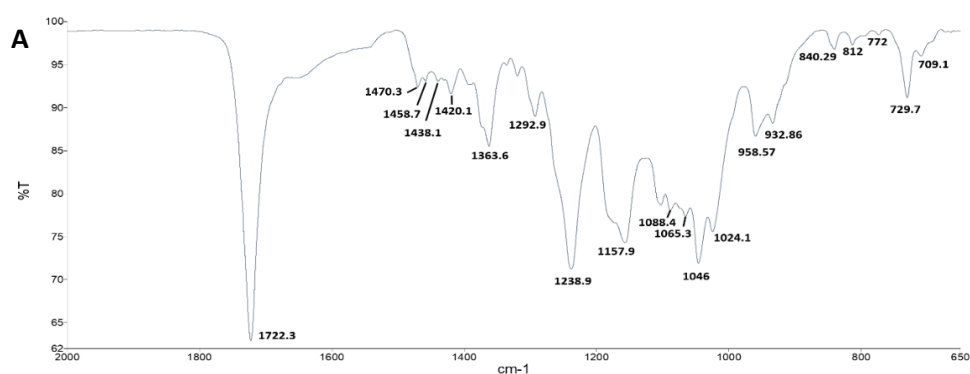
## Static compression testing of polycaprolactone scaffolds

Dry static compression testing of the PCL scaffold variations (six, eight, and ten strands) were performed using a ramp compression rate of 0.1mm/s and carried out at room temperature (20-21°C). The mass of the scaffolds was measured prior to testing for all samples using an analytical balance (Fisherbrand, RS232). The compressive moduli was determined by linear regression of stress–strain curves up to 5% strain of the original scaffold heights (3.5mm). Typical graphs retrieved from the PCL compression testing demonstrated a bi-linear nature. Compressive moduli was calculated from the stiffer end of the bi-linear region, between 0.035-0.045 compressive strain, corresponding to values of higher strain.

## Results

### Material Characterisation with Fourier transform infrared spectroscopy

Regarding the FTIR spectrum of PCL (Fig.S4A, A) the strongest bands and their assigned chemical bonds were identified (see Fig.S4A, B).



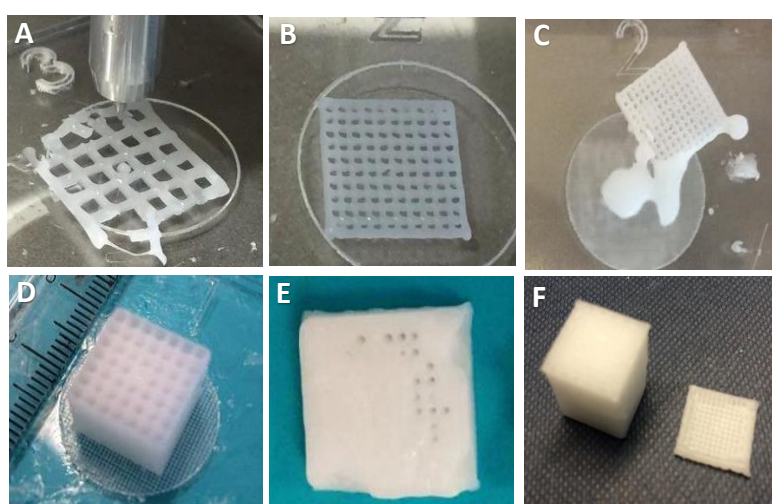
**B**

Position (cm <sup>-1</sup> )	Peak assignment
<b>1722</b>	Carbonyl stretching
<b>1293</b>	C=O and C=C stretching in the crystalline phase
<b>1239</b>	Asymmetric COC stretching
<b>1158</b>	C=O and C=C stretching in the amorphous phase

**Supplementary Figure S4A** (A) Fourier transform infra-red spectra of polycaprolactone material (measurements performed after material printing). (B) The corresponding peak assignments

## Fabrication of scaffolds

Reproducible and uniform PCL scaffolds were achieved via the use of the trialled print conditions in combination with a laser-etched print plate. The screening of parameters for PCL printing (Table.S1A) overcame recurrent issues with architectural inconsistencies caused by the high temperatures required for melted extrusion (Fig.S5A). In particular, an extended interlayer pause of 20 seconds with a reduced print temperature of 87°C (from 90°C) were essential for the stable deposition of PCL.



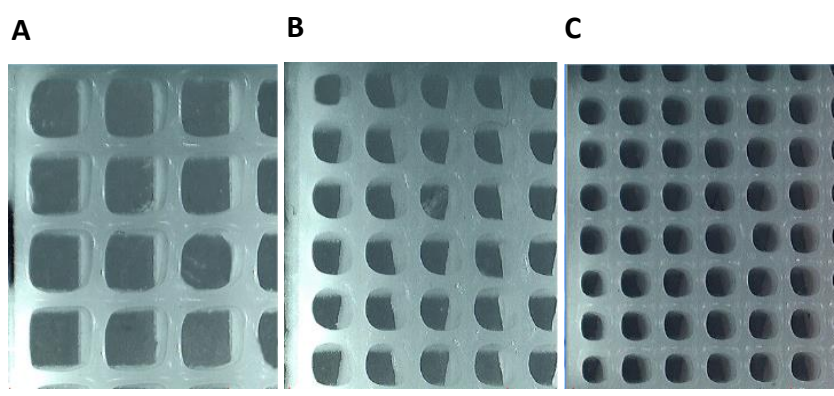
**Supplementary Figure S5A** The effects of parameter optimisation on PCL plotting; A, C, E represents issues occurred and B, D, F correspond to their respective solutions. (A) material breakage due to high temperature (90°C) resolved in (B) by lowering print temperature to 87°C. (C) Scaffold dislodged from the platform during printing which limited scaffold height. (D) Overcome by the use of an etched print platform. (E) Molten pooling of material at high layers (F) Resolved by an increased interlayer pause duration of 20 seconds.

## Morphological characterisation of scaffolds

### Optical Microscopy of polycaprolactone scaffolds

Optical microscopy of PCL scaffolds (Fig.S6A) demonstrated that the internal geometry and uniformity of the macropore distribution within scaffolds was directly determined by the number of material strands. With the mean values of both the pore cross-sectional area and material strut widths (Table.S2A) dependent on strand number. The pore cross-sectional area measurements were shown to decrease in relation to the increased number of strands printed *i.e.* the pore area measured for the six strand variant was almost three times the volume of the eight strand variant and approximately five times larger than for the ten strand scaffolds (Table.S2A). Low standard deviations were attained for the pore-area measurements taken between scaffolds of the same strand number variant, which inferred a repeatable print performance.

A visible difference in macropore morphology was apparent between scaffolds with different strand numbers (Fig.S6A). This disparity was most likely the result of material melt behaviour in combination with material spatial deposition. Due to the visible difference in pore morphology with decreasing strand distance. For the six strand structures the strands were plotted the furthest apart and the pores were square in shape (Fig.S6A, A). Comparatively, the eight and ten strand scaffolds which had a closer strand alignment, the macropores were visibly more circular in morphology (caused by an increased amount of melted material at the pore intersections) (Fig.S6A, B-C).



**Supplementary Figure S6A** Optical microscopy of polycaprolactone scaffold variants with (A) six strands, (B) eight strands and (C) ten strands, (scale bars = 1 mm), images taken at 0.5x magnification

**Supplementary Table S2A** Table to show the mean values ( $\pm$  standard deviations) of pore-cross sectional area and strut widths taken from 12 measurements for each PCL scaffold variant, printed with six, eight or ten strands ( $n = 4$ )

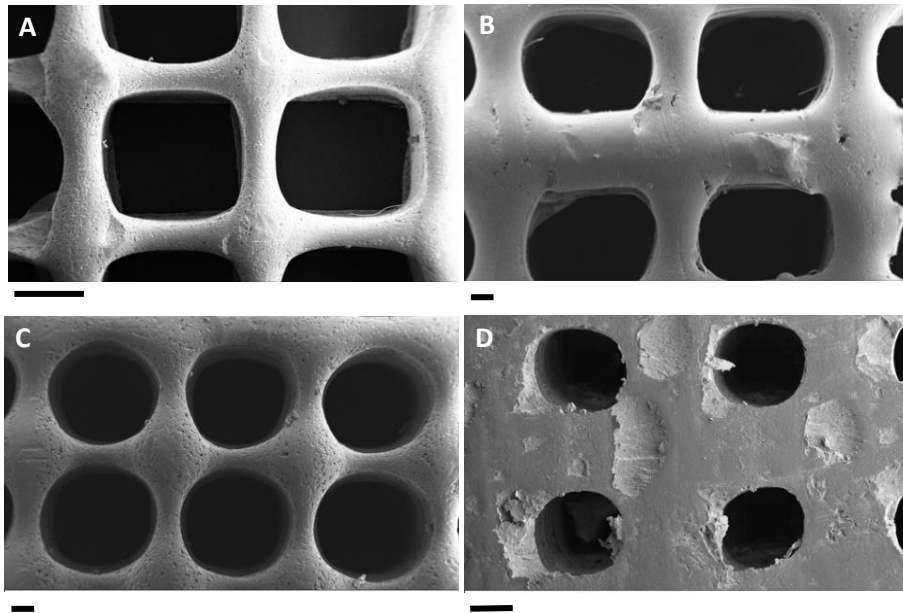
Structure variant (n=4)	6 strand	8 strand	10 strand
Pore cross-section area (mm <sup>2</sup> )	3.94 $\pm$ 0.18	1.36 $\pm$ 0.06	0.76 $\pm$ 0.05
Strut Width (mm)	0.48 $\pm$ 0.06	0.43 $\pm$ 0.02	0.36 $\pm$ 0.01

Values are presented as the mean  $\pm$  standard deviation ( $n = 4$ ). Strand denotes the lines/struts of material within a scaffold. The pore cross-sectional area measurements for the 6 strand scaffolds were calculated using Area = height  $\times$  width whereas pore cross-sectional areas of the 8 and 10 strand scaffolds were calculated using: Area =  $\pi \times$  semi-major axis  $\times$  semi-minor axis.

#### Scanning electron microscopy of PCL scaffolds

The SEM micrographs of the PCL scaffolds demonstrated a clear image of the internal pore systems achieved by varying strand number/distance (Fig.S7A). The pores for each structural variant were well-defined, uniform and un-obstructed with a smooth material topography. Measurements taken using the SEM images positively

corroborated the measurements and observations taken from the optical microscopy images.



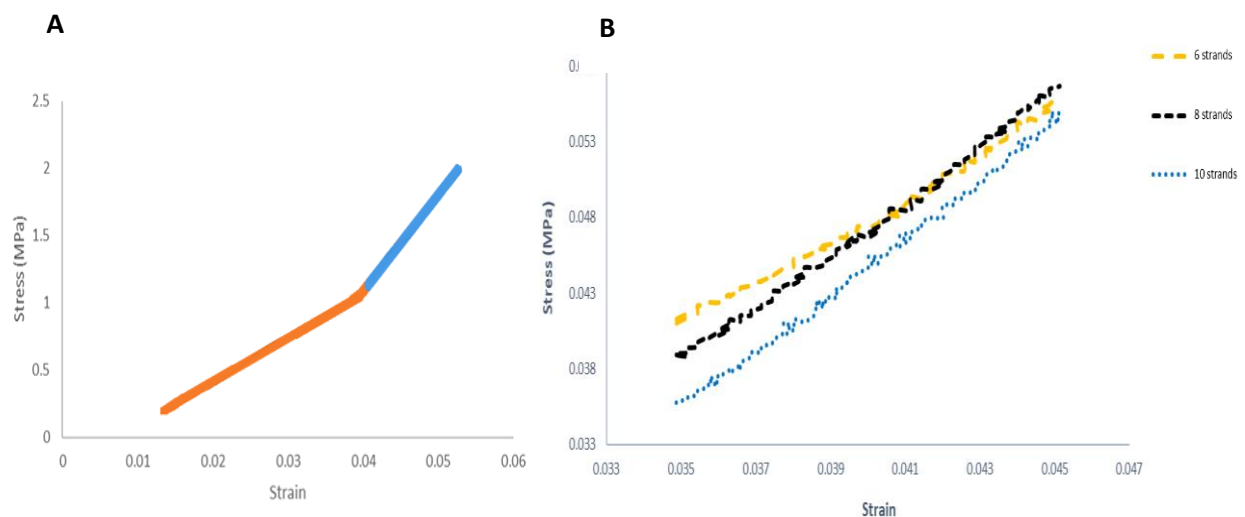
**Supplementary Figure S7A** Scanning electron images of PCL scaffold variants printed with (A) six (Mag 47 x) (B) eight (Mag 70 x) (C) ten (Mag 68 x) (D) and 12 strands of material (Mag 133 x). The change to the material surface as seen on (D) were due to post-processing (sanding) treatment. Scale bar for (A) equal to 1 mm, scale bars for (B-D) equal to 200  $\mu\text{m}$ .

#### Static compression of polycaprolactone scaffolds with and without alginate methyl

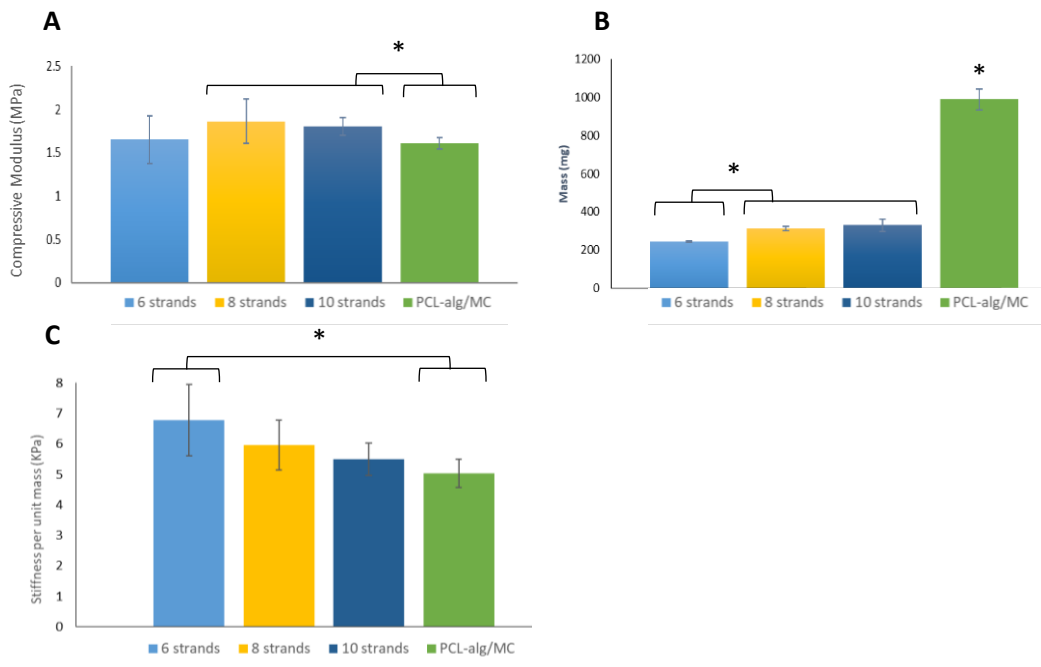
##### cellulose

Compressive moduli was calculated from the stress-strain curves of PCL scaffolds (Fig.S8A). The results of the compression testing demonstrated that the PCL scaffolds printed with different strands numbers (six, eight or ten) had no significant influence on overall compressive modulus relative to the eight and ten strand scaffolds (Fig.S9A). With the PCL structures demonstrating a mean compressive moduli of  $1.65 \pm 0.27$  MPa,  $1.861 \pm 0.25$  MPa and  $1.80 \pm 0.09$  MPa for the six, eight and ten strand scaffolds respectively (Fig.S9A). In comparison, the PCL-alg/MC scaffolds had a compressive modulus that was significantly below the ten and eight strand scaffolds

but was not significantly lower than the six strand PCL structures (Fig.S9A). The calculated stiffness to mass ratio (extracted via normalising the compressive stiffness data with scaffold mass for each variant) showed no significant difference between the PCL only scaffold types. Comparatively, the PCL-alg/MC multi-material scaffolds had a significantly lower stiffness to mass ratio than the six stranded PCL scaffolds (Fig.S9A). Thus, scaffold strand number did not influence compressive capacity, with no measurable difference to stiffness between scaffold stand variants relating to either mass or geometry. Although the alg/MC PCL scaffold hybrids had a markedly reduced overall compressive modulus compared to eight and ten strand scaffolds, this effect was not significant when calculated relative to the scaffold mass. Furthermore, within the strand variant groups ( $n = 3$ ) the standard deviations for both mean mass and mean compressive moduli were low (Fig.S9A) which inferred print reproducibility.



**Supplementary Figure S8A** Example stress-strain graph for the static compression of polycaprolactone (PCL) scaffolds, the curves demonstrated a bi-linear nature showing two linear regions (orange and red). Compressive moduli were calculated from the stiffer end between 0.04-0.055 compressive strain, corresponding to values of higher strain (blue). (B) Example truncated stress vs strain plots for the three PCL scaffold variants (with six, eight or ten material strands) within 0.04-0.055 compressive strain. Linear regression data for each plot was used to calculate the compressive modulus for all samples ( $n = 3$ ).



**Supplementary Figure S9A** (A) Mean compressive modulus, (B) mean mass and (C) mean stiffness per unit mass of scaffolds printed with six, eight or ten strands of polycaprolactone (PCL) only compared to 10 strand PCL-alginate methyl cellulose multi-material structures (error bars = standard deviation),  $n = 3$ ,  $P = \leq 0.05$ .

## Discussion

The characterisation of the materials investigated in this study was initially achieved via FTIR spectroscopy. FTIR was used to identify the bonds within the formulated materials, based on their vibration frequencies. The spectra produced was used as a quick and reliable method for assessing material composition and as an index for material reproduction / batch quality control. In PCL samples, crystallinity can be inferred by FTIR, and represents a highly influential factor for polymer properties, affecting strength, impact to resistance, melting point and rigidity. It would therefore be important to consistently replicate an appropriate degree of crystallinity as a parameter that determines its applicability for medical implants. Importantly, comparative measurements taken from the PCL scaffolds in this study demonstrated that there was no significant shift in peak alignment or ratios within the crystallinity

region (1600–900  $\text{cm}^{-1}$ ) between replicates; and this inferred that consistency was achieved (Phillipson, Hay and Jenkins, 2014).

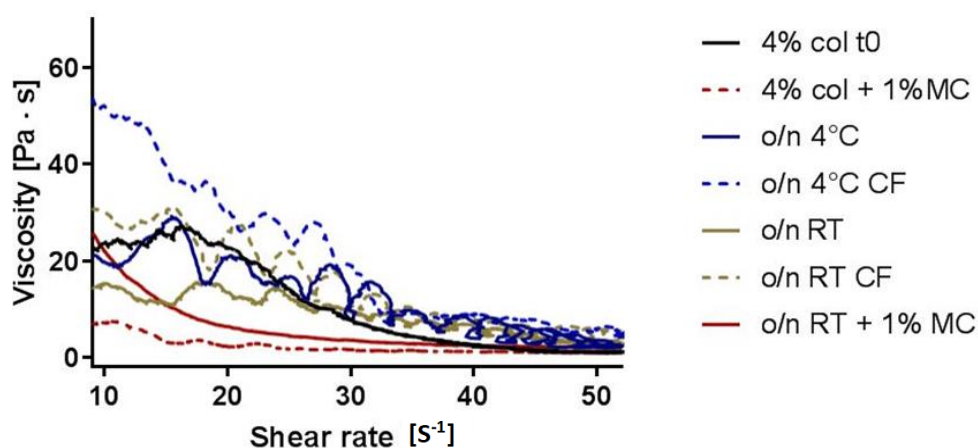
However, the mean compressive moduli of the PCL structures ( $1.861 \pm 0.25$  MPa for 8 stranded scaffolds) was measured to be approximately 10-fold lower than the maximum reported for whole discs of approximately 16.37 MPa (Pei *et al.*, 2013), but was within the range reported for AF tissue alone (0.116-2.3 MPa) as measured by Mow *et al.*, (2004) . Thus, although the compressive moduli of the PCL scaffolds were higher than the maximum values reported for the alg/MC and 4% collagen + 1% MC scaffolds ( $60.4 \pm 2.4$  kPa and  $69.62 \pm 2.10$  kPa, respectively) a disparity from whole native IVD cartilage remained. Further to this, the PCL material was brittle upon loading (a clear detrimental feature for biomaterials intended for implantation). Lowering the degree of crystallinity in PCL is likely to decrease rigidity and thus potentially providing a better candidate for applications in cartilage engineering. But this approach has limitations for bioprinting, with decreased crystallinity in PCL associated with a higher molecular weight, and by association a higher melting point. In this investigation, the high temperature (87-89°C) needed for consistent PCL extrusion proved challenging for reproducible scaffold production (Fig.S5A), likely due to cooling time. This was most prevalent in the multi-material printing with alg/MC printing, which required extended interlayer pause times of 40 seconds to allow for material cooling and resulted in a long print duration. In combination with PCL's innately poor cell compatibility (due to the combined effect of high temperature printing, surface hydrophobicity and lack of micro-porosity (Fig.S7A), the decision was taken to exclude the use of PCL from further investigation

## Conclusion

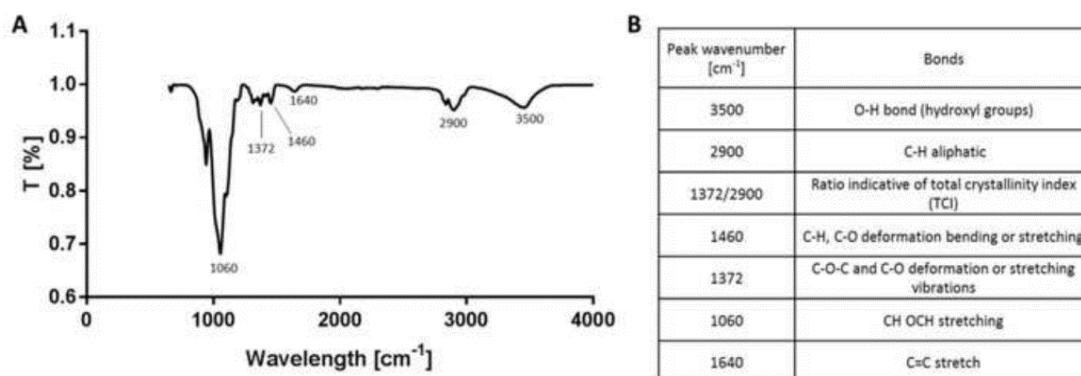
The attempted application of PCL as a biomaterial for scaffold fabrication resulted in several issues. As a result of PCL's dependence on high temperature extrusion, with a melting point ranging between 59 and 64 °C, cell inclusion was not possible during fabrication and precision printing was challenging. Problems with the PCL bioprinting were primarily caused by an inability for the control of material cooling which resulted in melted material pooling, undefined microarchitectures and material contraction.

Furthermore, despite the trialling of different architectural modifications the compressive moduli of the PCL structures measured below those reported for whole IVDs ( $1.86 \pm 0.25$  MPa for 8 stranded scaffolds) (Fig.S9A). In addition, upon mechanical loading the PCL material became brittle and prone to breakage. Whereas, the PCL-alginate hybrid scaffolds demonstrated a weakness at the material interfaces under compression, which resulted in hydrogel leakage. Thus, based on the observations using PCL and upon consideration of thermoplastics' inherent cell incompatible properties (hydrophobicity and smooth topography) the use of PCL was concluded.

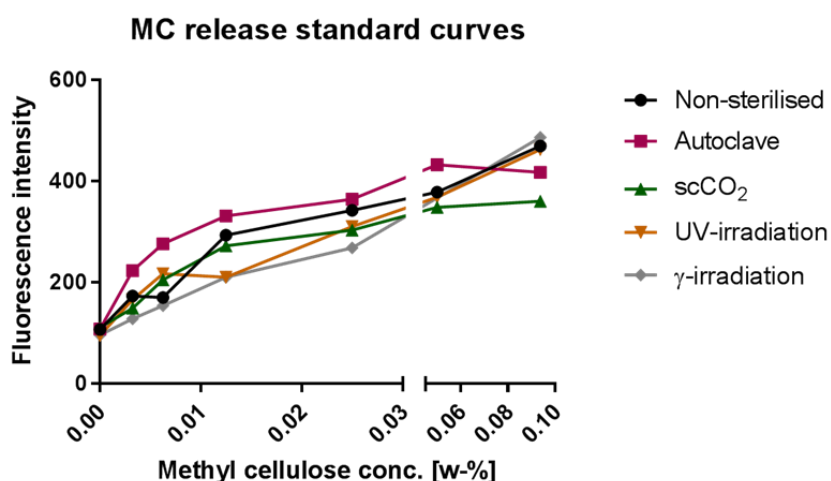
#### Appendix B: Supplementary figures related to Chapter 4



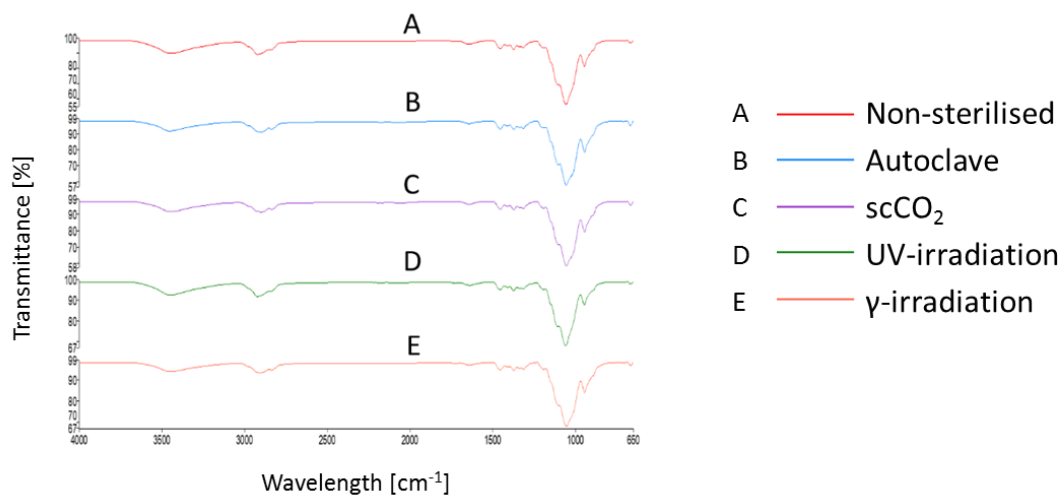
**Supplementary Figure S1B** Rheological profiles of collagen pastes with or without the addition of 1% methyl cellulose (MC), and with or without treatment with chloroform (CF), performed overnight (o/n) at either room temperature (RT) or 4°C



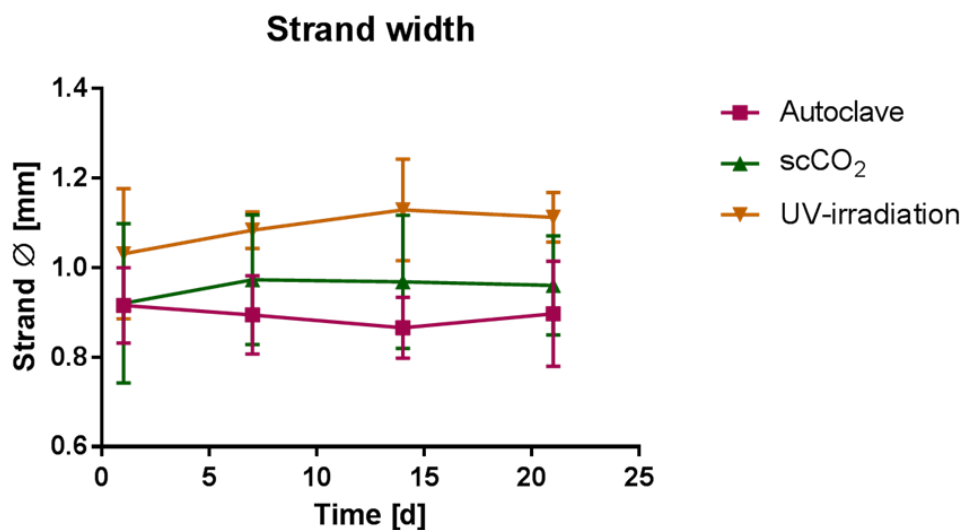
**Supplementary Figure S2B** FTIR spectra of a 5% alginate solution (A) before autoclaving and (B) after autoclaving. Samples were measured four times each, and the average major peak values were recorded. No significant differences between major peak values from the autoclaved and non-autoclaved alginate samples were detected and the spectra showed no apparent visible changes.



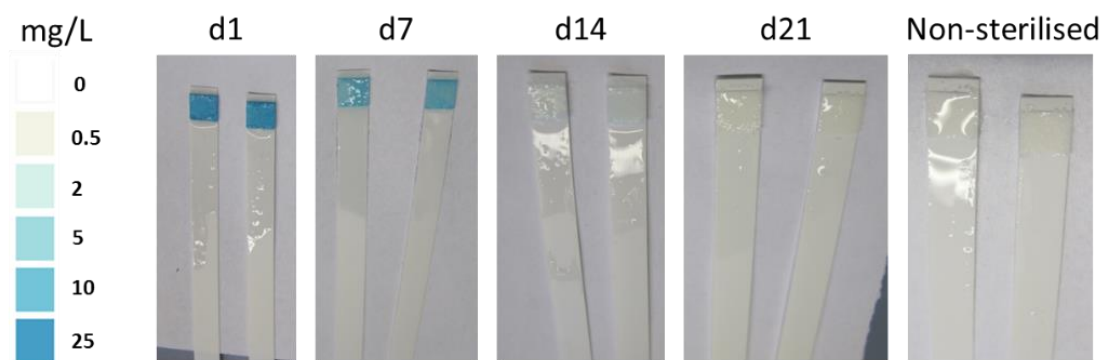
**Supplementary Figure S3B** Calibrated MC concentration curves via detected Mykoval™ fluorescence signal intensity, performed for each MC treatment type, excitation 400 nm and emission 450 nm



**Supplementary Figure S4B:** Normalised FT-IR spectra of MC powders non-sterilised and sterilised using the different methods.



**Supplementary Figure S5B** Mean width of alg/MC strands ( $\pm$  stdv) produced by 3D bioplotting of alg/MC pastes prepared with sterilised MC via autoclave,  $\text{scCO}_2$  or UV-irradiation after 1, 7, 14 and 21 days of incubation. Mean  $\pm$  stdv,  $n = 3$ .



**Supplementary Figure S6B** Hydrogen peroxide test strip results using non-sterilised and scCO<sub>2</sub> treated MC dissolved in ddH<sub>2</sub>O tested 1, 7, 14 and 21 days after sterilisation.

Appendix C: Documents related to Chapter 6

A



HTA Licence number: 12583  
 Designated individual: Professor Paul Gard  
 Head of School: Professor David Timson  
 HTA.SLA.0001

**Service Level Agreement to supply human tissue to the School of Pharmacy and Biomolecular Sciences at the University of Brighton for 'The 3D extrusion of cell encapsulated hydrogels using human intervertebral disc cells for tissue engineering' subject to the restrictions of the PABS Human Tissue Licence (No 12583) and compliance with the Human Tissues Act (2004) and HTA Codes of Practice. Please ensure that any electronic addition of information to this form does not move the signature sections onto the following page.**

I Dr. Arne Mehrkens MD confirm that the human tissue samples to be provided to the School of Pharmacy and Biomolecular Sciences, University of Brighton, and described in the attached Schedule A, were obtained in accordance with the ethics approved protocol together with the requirements of the HTA Act (2004), as amended from time to time, and the HTA Code of Practice relating to the seeking and acquisition of appropriate consent.

HTA licence number of Sender's Institute (if applicable; i.e. if samples have been stored under an HTA licence) \_EKNZ 2015-305\_ (Ethik Commission Northwest and Central Switzerland)

NHS REC number and short title (if applicable) \_\_\_\_\_

\_\_\_\_\_ Start date \_\_\_\_\_

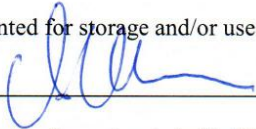
Finish date \_\_\_\_\_

PABS REC number and short title (if applicable) \_\_\_\_\_

\_\_\_\_\_ Start date \_\_\_\_\_

Finish date \_\_\_\_\_

Is consent granted for storage and/or use outside the limits of the ethics approval? YES

Signature 

Authorised to sign for and on behalf of [Department of Biomedicine, University Hospital Basel]

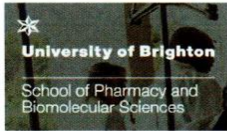
Print Name: Arne Mehrkens.....

Title: MD.....

Date Basel, Dec. 15th. 2017

University Hospital Basel  
 Spinal Chirurgie  
 Dr. med. Arne Mehrkens  
 Oberarzt  
 Spitalstrasse 21, CH-4031 Basel

B



HTA Licence number: 12583
Designated individual: Professor Paul Gard
Head of School: Professor David Timson
HTA.SLA.0001

1 Schedule A – Development of Intervertebral Disc scaffolds using 3D-Bioplotting in Regenerative Medicine

This Service Level Agreement is made on the 15.11.17

BETWEEN

- (1) Department of Biomedicine at the University Hospital Basel, Hebelstrasse 20, 4031 Basel
(2) The University of Brighton ("the Recipient") whose principal place of business is at Cockcroft building, Lewes Road, Brighton, East Sussex BN2 4GJ

Please specify the type and quantity (if known) of Materials that are to be supplied by the Department of Biomedicine.

Tissue details:

The cells were isolated from the tissue of human Nucleus Pulposus and Annulus Fibrosus of patients undergoing discectomies in the Department for Spinal Surgery at the University Hospital Basel.

Additional information to be complete (if appropriate) by supplying unit: The precise amount cannot be specified at the moment.

Is consent granted for the donated sample to be

- used for genetic research YES
- stored for future unspecified (but ethics approved) use\* YES

Any further restriction on use? NO
If yes, please specify

Any storage requirements to protect integrity of tissue sample? YES
If yes, please specify
Vials of frozen cells should be kept in liquid nitrogen for long term storage.

Any specific instructions regarding the disposal of any unused sample? NO
If yes, please specify

Signature [Handwritten Signature] Dec 1st 2017

University Hospital Basel
Schule Chirurgie
Dr. med. Arne Mehrkens
Chirurg
Schulstrasse 21, CH-4031 Basel

Authorised to sign for and on behalf of Department of Biomedicine, University Hospital Basel

The University of Brighton confirm that use of the received cells will be acknowledged in any resulting publication or written document.

\* This may be an option on the consent form for each individual donor. If the option is present please indicate 'yes' here and comment under 'any further restriction on use' that a label will accompany each sample where consent for future use is granted or withheld

Supplementary Figure S2C Human tissue authority approval for use of human intervertebral disc cells from the University Hospital Basel (A) Page one (B) Page two.

## Aufklärungsdokument über:

### Die Weiterverwendung von biologischem Material für die Forschung in verschlüsselter Form (Art. 29 HFV)

Sehr geehrte Dame oder Herr

- **Wer wir sind:**

Seit dem 1. November 2014 gibt es am Universitätsspital Basel die neue Abteilung für Spinale Chirurgie. Diese Abteilung besteht aus einem Team von orthopädischen und neurochirurgischen Wirbelsäulen-Spezialisten unter der cheftätlichen Leitung von Prof. Dr. Stefan Schären. Neben Behandlung von Wirbelsäulen Pathologien setzt sich die Abteilung für die Entwicklung von innovativen Methoden zur Behandlung von Rückenschmerzen ein, die durch degenerierte Bandscheiben verursacht werden. Für diesen Zweck arbeitet die Spinale Chirurgie mit unserer Forschungsgruppe zusammen. Unsere Forschungsgruppe beschäftigt sich mit der Züchtung von Geweben (Tissue Engineering) und wird geleitet von Prof. Dr. Ivan Martin, am Universitätsspital Basel. Mit Hilfe des Tissue Engineering werden Zellen vermehrt und aus verschiedenen Zelltypen unterschiedliche Gewebe gezüchtet, die auch klinisch eingesetzt werden können.

In unserem aktuellen Projekt geht es darum günstige Zelltypen zu bestimmen, die für die Regeneration von degenerierten Bandscheiben gebraucht werden können. In den letzten Jahren haben verschiedene Klinische Studien gezeigt, dass Schmerzen in Patienten gelindert wurden nachdem in ihre degenerierten Bandscheiben Knorpel- oder Stammzellen injiziert wurden. Die Resultate dieser Studien begünstigen Zelltransplantation als eine mögliche Therapie für die Regeneration von Bandscheiben, aber ein optimaler Zelltyp ist noch unbestimmt.

Vor kurzem hat unsere Forschungsgruppe gezeigt, dass Knorpelzellen von der Nase für die Wiederherstellung von Knorpel vorteilhafter sind als Knorpelzellen von Gelenkknorpel. Um eine klinische Applikationen Anwendung dieser Zellen in der Bandscheibenregeneration anzustreben, muss zuerst festgestellt werden wie sich die Knorpelzellen in einer Bandscheibe verhalten. Ziel unseres Forschungsprojektes ist es festzustellen, ob sich Nasenknorpelzellen für die Bandscheibenregeneration eignen.

- **Weshalb wir Sie anfragen:**

Wir möchten Sie hiermit einladen, die medizinische Forschung zu unterstützen.

Ihnen steht eine Operation bevor bei der ihnen die Bandscheibe oder Gewebe von der Bandscheibe entnommen wird. Im Rahmen der Operation haben Sie die Möglichkeit das entnommene Gewebe für das oben beschriebene Forschungsprojekt zu spenden. Die Studie wird ab dem 1. September 2015 durchgeführt. Von diesem Datum an werden Bandscheibenspenden gesammelt und anonymisiert in die Studie eingeschlossen. Durch die Spende entstehen keine Nachteile oder Risiken für Sie. Das Gewebe wird nur zu klinischen Forschungszwecken verwendet und würde ansonsten verworfen werden. Wir erwarten für Sie keinen direkten klinischen Vorteil von der Spende, allerdings können vielleicht andere Patienten dank Ihrer Teilnahme in Zukunft von den Resultaten profitieren.

Wir bitten Sie deshalb, Ihrem Arzt/Ihrer Ärztin zu erlauben, das Bandscheibengewebe zu Forschungszwecken verschlüsselt an uns weiterzugeben.

- **Rechte der Spendenden**

Sie geben nur dann das Bandscheibengewebe für die Weiterverwendung zu Forschungszwecken frei, wenn Sie es wollen. Niemand darf Sie dazu in irgendeiner Weise drängen oder dazu überreden wollen. Sie müssen nicht begründen, warum Sie es nicht freigeben wollen.

Wenn Sie sich zur Freigabe entscheiden, können sie diesen Entscheid jederzeit zurücknehmen. Sie müssen nicht begründen, warum Sie die Freigabe zurücknehmen wollen.

- **Vertraulichkeit**

Wir verwenden Ihr Bandscheibengewebe in verschlüsselter Form. Das bedeutet, dass das Material mit einer Nummer beschriftet wird. Ihr Name, Ihre Adresse, Ihr genaues Geburtsdatum oder ähnliche Angaben werden nicht an uns weitergegeben. Der Schlüssel, das heisst die Liste, die die Nummer mit Ihrem Namen verbindet, liegt sicher und streng verwahrt bei Dr.med. Arne Mehrkens, Oberarzt in der Spinalen Chirurgie des Universitätsspitals Basel.

Nur Mitarbeiter der Ethischen Kommission sowie der Swissmedic dürfen diese Liste einsehen.

Für Aussenstehende ist es folglich unmöglich, das Körpermaterial und die Daten mit Ihnen in Verbindung zu bringen. Wir selbst dürfen die Verschlüsselung nur in eindeutig definierten Fällen aufheben:

- wenn es zum Schutz Ihrer Gesundheit oder Ihrer Rechte (zum Beispiel, weil Sie Ihre Einwilligung widerrufen wollen) notwendig ist, oder
- wenn ein Gesetz es verlangt, zum Beispiel im Rahmen einer Strafuntersuchung.

Falls eine entsprechende Anfrage vorliegt, werden wir Ihre Materialien und Daten in dieser verschlüsselten Form auch an Dritte weitergeben. Der Schlüssel bleibt dabei aber unverändert bei der genannten Person. Die Empfänger Ihres Materials haben auch nur in den eben genannten Fällen das Recht zu erfahren, dass die Materialien von Ihnen stammten.

C

swissethics

Schweizerische Ethikkommissionen für die Forschung am Menschen  
Commissions d'éthique suisses relative à la recherche sur l'être humain  
Commissioni etiche svizzere per la ricerca sull'essere umano  
Swiss Ethics Committees on research involving humans

---

**Einwilligungserklärung zur:**

**Weiterverwendung von biologischem Material zu Forschungszwecken in verschlüsselter Form (Art. 29 HFV)**

Name und Vorname der/s Patienten/in / der betroffenen Person:

Operationsdatum:

---

Ich willige hiermit ein, dass biologisches Material von mir, das aus einer medizinischen Behandlung oder anderweitig vorhanden ist, in verschlüsselter Form zu Forschungszwecken weiterverwendet werden darf.

Ich bestätige, dass

- ich das zu dieser Einwilligungserklärung gehörende Aufklärungsdokument erhalten habe.
- ich darüber informiert wurde, dass meine Einwilligung freiwillig ist.
- ich weiss, dass ich diese Einwilligung jederzeit widerrufen kann, ohne Angabe von Gründen.
- ich weiss, wie mein Material geschützt ist.
- ich weiss, dass mein Material zu Forschungszwecken an Dritte weitergegeben werden kann.
- ich weiss, dass die Forschungsergebnisse in anonymisierter Weise veröffentlicht werden.

Ort, Datum, rechtsgültige Unterschrift der Patientin / des Patienten / der betroffenen Person oder ihre / seine berechnigte Vertretungsperson

Ort, Datum, rechtsgültige Unterschrift der aufklärenden Person

**Supplementary Figure S3C** Patient clarification and consent forms (Swiss ethics written in German) (A) Page one (B) Page two (C) Page three.

## Appendix D: Documents related to Chapter 7

### R&D OFFICE

Research Director Prof Kevin Davies  
R&D Manager: Scott Harfield  
Research Governance Officer: Linda Rudden

E-mail: [scott.harfield@bsuh.nhs.uk](mailto:scott.harfield@bsuh.nhs.uk)  
[Linda.rudden@bsuh.nhs.uk](mailto:Linda.rudden@bsuh.nhs.uk)

Tel: 01273 696955 ext 3538 / 7497



Research & Development Directorate  
Royal Sussex County Hospital  
Clinical Investigation & Research Unit  
Eastern Road  
Brighton  
BN2 5BE

26/11/2009

Professor Paul Tofts  
Brighton & Sussex Medical School  
University of Sussex  
Falmer  
Brighton  
BN1 9PS

Dear Professor Paul Tofts

**Full Study Title:** Quantitative MR in Healthy Volunteers  
**R&D Ref No. :** 09/156/TOF

I am writing to inform you that you have Research Governance approval to proceed with the above named project. This letter acknowledges that you have all the necessary internal and external regulatory approvals. The sites covered by this approval include:

- University of Sussex

### Conditions of Approval

The approval covers the period stated in the Research Ethics Committee (REC) application and will be extended in line with any amendments agreed by the REC. Research must commence within 12 months of the issue date of this letter. Any delay beyond this may require a new review of the project resources.

Please note this approval does not apply to the earlier request to include MRI examinations of the eye. A separate application and information sheet should be submitted for this project, as the intervention requires the administration of an anaesthetic.

### Amendments

Project amendment details dated after the issue of this approval letter should be emailed to the R&D Office for formal approval.

### ICH-GCP Monitoring

The Medical School has a duty to ensure that all research is conducted in accordance with the Research Governance Framework and to ICH-GCP standards. The R&D Department will take responsibility for the ongoing monitoring of the study and reporting of any adverse events. In order to ensure compliance the department undertakes random audits. If your project is selected you will be given 4 weeks notice to prepare all documentation for inspection.

I wish you luck with your project and would be grateful if you could inform me when the project is complete or due to be closed on this site.

Yours sincerely

A handwritten signature in black ink, appearing to read 'S Harfield'.

Scott Harfield  
Research & Development Manager

**Supplementary Figure S1D** Ethics approval for MRI work with healthy human patients.

## Development of New MRI Sequences

### Dear Participant

You are being invited to take part in a research study. Before you decide it is important for you to understand why the research is being done and what it will involve. Please take time to read the following information carefully. Talk to others about the study if you wish.

- Part 1 tells you the purpose of this study and what will happen to you if you take part.
- Part 2 gives you more detailed information about the conduct of the study.

Ask us if there is anything that is not clear or if you would like more information. Take time to decide whether or not you wish to take part.

#### 1. What is the purpose of the study?

The purpose is to develop and assess the performance of quantitative MRI techniques implemented on our scanner in healthy people. It is important that the quantities we measure on the scanner are accurate and reproducible and, in order to test this, we need to perform our imaging techniques on a group of healthy volunteers.

#### 2. Why have I been chosen?

You have been chosen because you have expressed an interest in helping out with our research project.

#### 3. Do I have to take part?

No. It is up to you to decide whether or not to take part. If you do, you will be given this information sheet to keep and be asked to sign a consent form. You are still free to withdraw at any time and without giving a reason. A decision to withdraw at any time, or a decision not to take part, will not affect the standard of care you receive.

#### 4. What will happen to me if I take part?

You will undergo a MRI scan that lasts no longer than 1 hour.

#### 5. What do I have to do?

You will need to attend the Clinical Imaging Sciences Centre at the University of Sussex. Here you will be asked to fill in a safety questionnaire to confirm your suitability for the scan. You will then be required to lie in the MRI scanner for up to one hour. Normally, you will be asked to relax and do nothing, although, on occasion, you may be asked to perform simple tasks, such as looking at an image or listening to a sound and asked to respond via a button box. You will be notified in advance if any tasks are planned.

Development of New MRI Sequences  
Version 4  
February 2012

B

**6. What are the side effects of any treatment received when taking part?**

The technique has been used for over 20 years in medicine and every year approximately 10 million people are scanned worldwide. There are no known side effects and MRI causes no pain or damage.

**7. What are the other possible disadvantages and risks of taking part?**

There are no disadvantages unless you are afraid of small spaces or loud noises. However occasionally unexpected findings are revealed by imaging. In this instance we will advise you to contact your GP who can arrange for further tests. It is important to note that the images are not being obtained for diagnosis. Therefore, you should not volunteer for the study as an alternative to seeking medical attention.

**8. What are the possible benefits of taking part?**

There are no immediate benefits in taking part, however you will be helping the development and testing of new MRI methods that will benefit many clinical projects.

**9. What if there is a problem?**

Any complaint about the way you have been dealt with during the study or any possible harm you might suffer will be addressed. Please contact the researchers in the first instance (contact details in section 11)

**10. Will my taking part in the study be kept confidential?**

Yes. All the information about your participation in this study will be kept confidential. The details are included in Part 2.

**11. Contact Details:**

Professor Mara Cercignani, CISC, Brighton and Sussex Medical School, Brighton, BN1 9RR ([m.cercignani@bsms.ac.uk](mailto:m.cercignani@bsms.ac.uk)). Tel: 01273 877879  
Dr Nicholas Dowell, CISC, Brighton and Sussex Medical School, Brighton, BN1 9RR ([n.g.dowell@bsms.ac.uk](mailto:n.g.dowell@bsms.ac.uk)). Tel: 01273 876770  
Dr Marica Cutajar, CISC, Brighton and Sussex Medical School, Brighton, BN1 9RR ([m.cutajar@gmail.com](mailto:m.cutajar@gmail.com)). Tel: 01273 876769

**Part 2**

**1. What can I expect in the MRI scanner?**

The MRI examination is performed in a special room that houses the MR system or “scanner”. The scanner consists of a circular magnetic tunnel which contains the radio coils. During your scan you will lie on a padded bed, which will move slowly into the scanner.

Development of New MRI Sequences  
Version 4  
February 2012

## C

In preparation for the MRI examination, you will be asked to wear headphones or earplugs to protect your hearing as the scanner produces loud noises. These loud noises are normal and should not worry you.

A number of scans will be taken with a pause in between so do not be alarmed if the scanner goes quiet. The most important thing is to relax and try to keep still. It is not

dangerous if you move, but the resulting pictures may be blurred. Some minor movement of your body is possible between the scans. The radiographer will be able to hear and see you throughout the session and you will be provided with a call button to alert them if you have any concerns. The whole session will take approximately 45 mins – 1 hour.



### **2. Complaints**

If you have a concern about any aspect of this study, you should ask to speak with the researchers who will do their best to answer your questions (contact details are in part 1, section 11).

### **3. Harm**

In the event that something does go wrong and you are harmed during the research study there are no special compensation arrangements. If you are harmed and this is due to someone's negligence then you may have grounds for a legal action for compensation against the Brighton and Sussex Medical School, but you may have to pay your legal costs.

### **4. Will my taking part in this study be kept confidential?**

All information which is collected about you during the course of the research will be kept strictly confidential. All MRI images are anonymized and do not contain participant names.

### **5. What will happen to my MR Images?**

The results gained during this experiment will be confidential and your scans will be stored in an anonymous form. The results will be used to assess our improvements, and the accuracy and reproducibility of these scans.

### **6. What will happen to the results of the research study?**

The results of the research study will be written and up and published in a scientific journal.

### **7. Who is organising and funding the research?**

Development of New MRI Sequences  
Version 4  
February 2012

D

The research is funded by CISC and BSMS.

**8. Who has reviewed the study?**

This study was given a favourable ethical opinion by the Research Governance Ethics Committee:

Research & Development Directorate, Royal Sussex County Hospital, Clinical Investigation & Research Unit, Eastern Road, Brighton, BN2 5BE

Thank you for taking the time to read this information sheet.



**CONSENT FORM**

**Title of Project: Development of New MRI Sequences**

**Name of Researchers:**

**Professor Mara Cercignani  
Dr Nicholas Dowell  
Dr Marica Cutajar**

**Please initial  
box**

I confirm that I have read and understand the information sheet dated February 2012 (Version 4) for the above study. I have had the opportunity to consider the information, ask questions and have had these answered satisfactorily.

I understand that my participation is voluntary and that I am free to withdraw at any time, without giving any reason, without my medical care or legal rights being affected.

I agree that my images may be used for educational purposes on the understanding that they will be fully anonymized before being used in such a way.

I agree to my GP being informed of my participation in the study, if necessary.

I agree to take part in the above study.

\_\_\_\_\_  
Name of Participant

\_\_\_\_\_  
Date

\_\_\_\_\_  
Signature

\_\_\_\_\_  
Name of Person taking consent  
(if different from researcher)

\_\_\_\_\_  
Date

\_\_\_\_\_  
Signature

\_\_\_\_\_  
Researcher

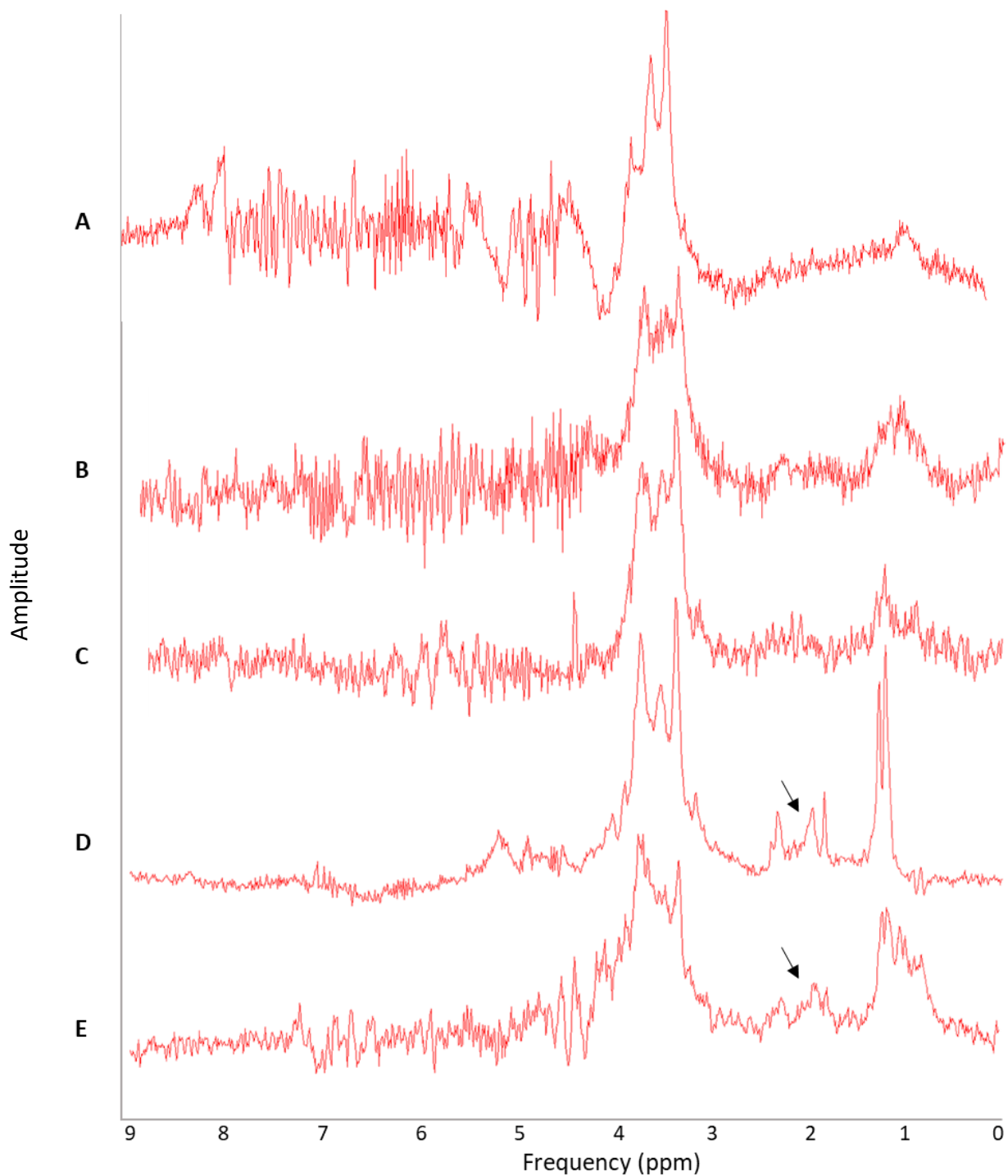
\_\_\_\_\_  
Date

\_\_\_\_\_  
Signature

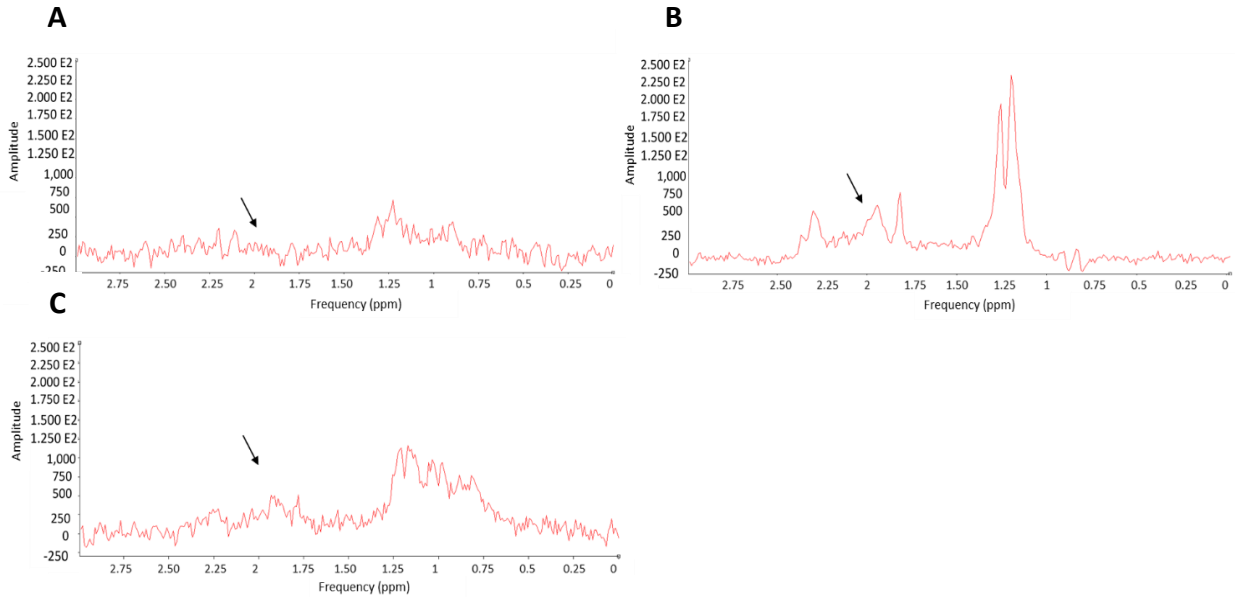
When completed, 1 for participant; 1 for researcher site file.

CONSENT FORM  
VERSION NUMBER 4  
DATE February 2012

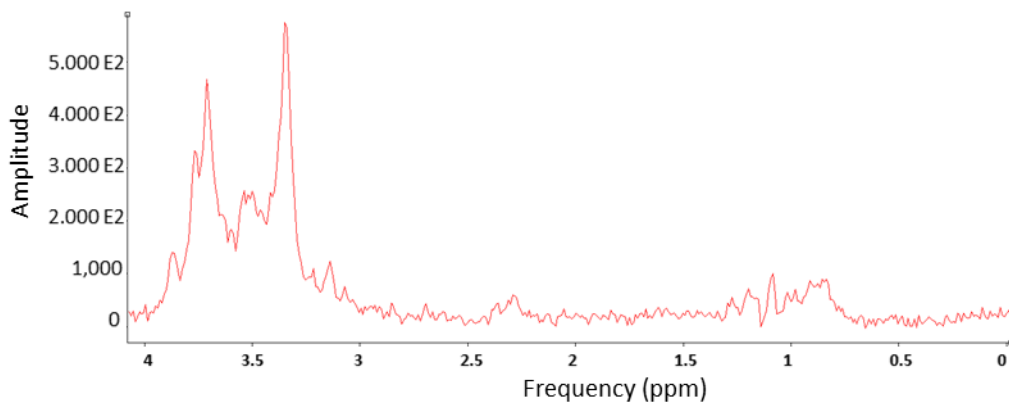
**Supplementary Figure S3C** Patient clarification and consent forms for MRI work with healthy volunteers (A) Page one (B) Page two (C) Page three (D) Page four.



**Supplementary Figure S3D** Full <sup>1</sup>H-spectra obtained for the alginate methyl cellulose scaffolds. (A) Cell-free scaffold after 21 days. (B) Control scaffold after 21 days of culture. (C) Hydrostatic pressure (HP) treated scaffold after 14 days. (D) HP treated scaffold after 21 days. (E) HP treated scaffold after 28 days.



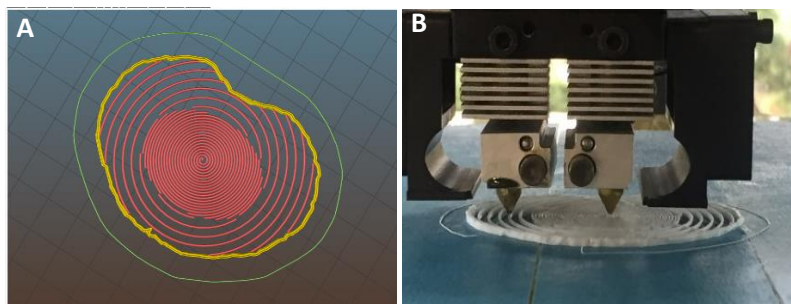
**Supplementary Figure S4D** Clipped  $^1\text{H}$ -spectra obtained for the alginate methyl cellulose scaffolds. (A) Hydrostatic pressure exposed samples after 14 days of cell culture. (B) Hydrostatic pressure exposed samples after 21 days of cell culture. (C) Hydrostatic pressure exposed samples after 14 days of cell culture.



**Supplementary Figure S5D** Clipped spectra of standard culture medium, DMEM + 10% Fetal calf serum, performed as a background measurement.

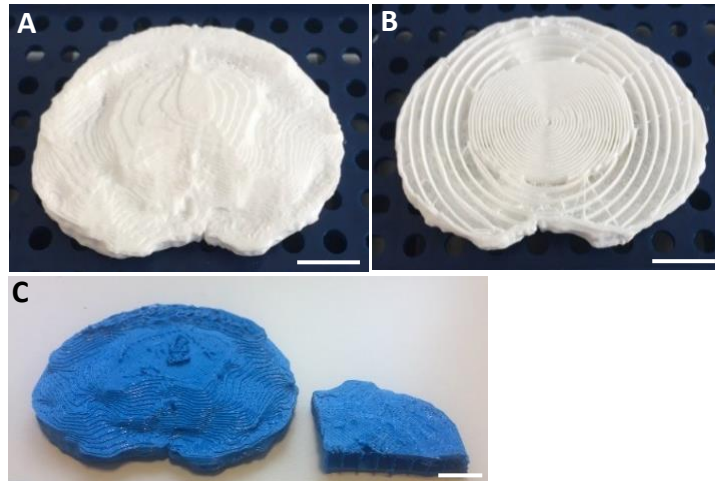
## Appendix E: Makerbot fabrication of anatomic disc model - related to Chapter 8

A disc scaffold model was produced based on medically derived dimensions with accurate regional representations of AF and NP disc sections to effectively demonstrate the customisability of 3D printing (Fig.S1E). The anatomical disc model (designed using Mimics® in Chapter 3.2.3) was fabricated using MakerBot Raise3D, Pro2 and replicator 2x technology, with polyvinyl alcohol (FilaPrint) and Flexi-fill (FilaPrint) filament (Fig.), respectively. A controlled material infill was designed via the use of slicing software 'Slic3r®'.



**Supplementary Figure S1E** 3D printed disc model with anatomical dimensions designed using Mimics® and 'Slic3r® software. (A) The Slic3r® software was used to control the regional infill density of two separate sections within the model, to mimic native microarchitecture of the annulus and nucleus disc regions. (B) A disc model being printed in polyvinyl alcohol on a MakerBot (Raise3D, Pro2).

The proof of concept disc model printed with polyvinyl alcohol filament (FilaPrint) on a MakerBot (Raise3D, Pro2) effectively demonstrated the use of compatible slicing software. Graded internal architecture was used to produce clinically relevant models with interiors which mimicked the structures of native discs (Fig.S2E). Similarly, the disc model printed with flexi-fill (FilaPrint) on a MakerBot (replicator 2x) produced a scaffold with honey-comb shaped interior and elasticity (Fig.S2E). The proof of concept disc models which were printed using filament-based MakerBot devices, represented the full potential of 3D printing for the design of scaffolds with custom infill patterns and densities, which is a feature currently unavailable on the bioscaffolder 3.1 (GeSIM, Germany).



**Supplementary Figure S2E** (A) Disc model printed with polyvinyl alcohol filament (FilaPrint) using a MakerBot (Raise3D, Pro2). (B) The cross-sectional image of the polyvinyl alcohol (FilaPrint) disc model, to reveal an internal graded structure. (C) A disc model printed with flexi-fill material (FilaPrint) on a MakerBot (replicator 2x). Scale bars represent 10 mm.